

REPORT DOCUMENTATION PAGE

Form Approved OMB No. 0704-0188

Public reporting burden for this collection of information is estimated to average 1 hour per response, including the time for reviewing instructions, searching existing data sources, gathering and maintaining the data needed, and completing and reviewing the collection of information. Send comments regarding this burden estimate or any other aspect of this collection of information, including suggestions for reducing this burden to Washington Headquarters Services, Directorate for Information Operations and Reports, 1215 Jefferson Davis Highway, Suite 1204, Arlington, VA 22202-4302, and to the Office of Management and Budget, Paperwork Reduction Project (0704-0188), Washington, DC 20503.

1. AGENCY USE ONLY (Leave blank)		2. REPORT DATE 1998	3. REPORT TYPE AND DATES COVERED Conference Proceedings	
4. TITLE AND SUBTITLE International Conference on the Methods of Aerophysical Research 98 "ICMAR 98"			5. FUNDING NUMBERS F61775-98-WE002	
6. AUTHOR(S) Conference Committee				
7. PERFORMING ORGANIZATION NAME(S) AND ADDRESS(ES) Institute of Theoretical and Applied Mechanics Novosibirsk 630090 Russia			8. PERFORMING ORGANIZATION REPORT NUMBER N/A	
9. SPONSORING/MONITORING AGENCY NAME(S) AND ADDRESS(ES) EOARD PSC 802 BOX 14 FPO 09499-0200			10. SPONSORING/MONITORING AGENCY REPORT NUMBER CSP 98-1025	
11. SUPPLEMENTARY NOTES Part III of the conference proceedings. (I've already sent you volumes I and II, this volume just came in and is to be added to the existing proceedings.)				
12a. DISTRIBUTION/AVAILABILITY STATEMENT Approved for public release; distribution is unlimited.			12b. DISTRIBUTION CODE A	
13. ABSTRACT (Maximum 200 words) The Final Proceedings for International Conference on Methods of Aerophysical Research (ICMAR'98), 29 June 1998 - 3 July 1998 This is an interdisciplinary conference. Topics include: Problems of Modeling at sub/trans/super/hypersonic velocities; Methods of flow diagnostics; Instrumentation for aerophysical experiments; Verification of CFD models and methods.				
14. SUBJECT TERMS EOARD, Aerodynamics, Flow Diagnostics, Computational Fluid Dynamics			15. NUMBER OF PAGES 306	
			16. PRICE CODE N/A	
17. SECURITY CLASSIFICATION OF REPORT UNCLASSIFIED	18. SECURITY CLASSIFICATION OF THIS PAGE UNCLASSIFIED	19. SECURITY CLASSIFICATION OF ABSTRACT UNCLASSIFIED	20. LIMITATION OF ABSTRACT UL	

19990119 043

NSN 7540-01-280-5500

Standard Form 298 (Rev. 2-89)
Prescribed by ANSI Std. Z39-18
298-102

ICMAR'98



Novosibirsk, Russia

**RUSSIAN ACADEMY OF SCIENCES SIBERIAN DIVISION
RUSSIAN NATIONAL COMMITTEE
ON THEORETICAL AND APPLIED MECHANICS
INSTITUTE OF THEORETICAL AND APPLIED MECHANICS
INTERNATIONAL CENTER OF AEROPHYSICAL RESEARCH
NOVOSIBIRSK UNITED RESEARCH UNIVERSITY
OF HIGH TECHNOLOGIES**

**INTERNATIONAL CONFERENCE
ON THE METHODS OF AEROPHYSICAL RESEARCH**

29 June – 3 July, 1998, Novosibirsk, Russia

**Proceedings
Part III**

**Novosibirsk
1998**

AQ F 99-04-0673

ICMAR'98 is sponsored by:

- Russian National Committee on
Theoretical and Applied Mechanics
 - Russian Foundation for Basic Research (RFBR)
 - American Institute of Aeronautics
and Astronautics (AIAA)
-

We wish to thank

**The United States Air Force European Office
of Aerospace Research and Development (EOARD)**

for its contribution to the success of the Conference



We thank the Novosibirsk
Branch of TOKOBANK
for its financial support

6 Lavrent'eva av., 630090, Novosibirsk, Russia,

Phone: (3832) 35-23-62,

Fax: (3832) 32-41-46

**The ICMAR'98 Organizing Committee Office is equipped with
computers of FRACTAL Company:**



*Institutskaya 4, Building 18
630090, Novosibirsk, RUSSIA*

Phone: (3832) 35-75-15

(3832) 39-75-15

Fax: (3832) 35-65-15

HTTP: // www.fractal.ru

**The papers are printed by direct reproduction from the authors' originals.
The authors are responsible for possible misprints and the quality of translations.**

© Institute of Theoretical and Applied
Mechanics, 1998, Composing

STUDY ON DRAG-THRUST FORCES OF A SCRAMJET MODEL IN BLOW-DOWN AND HOT-SHOT WIND TUNNELS

N.P. Adamov, Yu.P. Goon'ko, A.M. Kharitonov,
A.F. Latypov, I.I. Mazhul, M.I. Yaroslavtsev,
Institute of Theoretical and Applied Mechanics (ITAM) SB RAS,
630090, Novosibirsk, Russia

F.Chalot, P.Perrier, Ph.Rostand
Dassault Aviation, Paris, France

One of the main problems determining the prospects of creating aerospace planes and hypersonic aircraft is the development of an air-breathing engine with supersonic combustion (scramjet). The gas dynamics of internal scramjet flows, including the inlet/combustor interaction, the combustion and mixing processes in a supersonic flow, etc., and also the integral characteristics of the engine as a whole are still poorly studied. This hinders the prediction of scramjet characteristics in the system of a flying vehicle. The use of numerical methods for simulation of the integral scramjet characteristics is also hampered by the absence of representative experimental data that would meet all demands of verification of numerical models and methods [1]. Results of an experimental investigation of the total thrust-aerodynamic characteristics of a scramjet are described in the present paper. The objective of this work was to obtain experimental data both for extending the knowledge about the gas dynamic processes and scramjet characteristics and for verification of numerical algorithms and computational methods [1].

To perform this study, a special scramjet model was designed, which allowed to test the complete engine configuration and its truncated variants corresponding to the inlet alone and the engine without the nozzle. The experiments with this model were performed in two wind tunnels based at ITAM. The hot-shot wind tunnel IT-302 with a discharge chamber was used to study the thrust-aerodynamic characteristics at Mach numbers $M=6$ and 8 in the combustion mode, with gaseous hydrogen supplying as a fuel, and without combustion. The flow structure in the inlet was studied in detail and the longitudinal force characteristics of the all model versions in regimes without fuel injection were studied in the blow-down wind tunnel T-313. The aerodynamic characteristics of the model versions obtained in both wind tunnels at Mach numbers close to $M=6$ were compared.

CONFIGURATION OF THE MODEL

The general configuration of the scramjet model is shown in Fig.1. The model length is $L_{\text{model}}=860$ mm, the mid-section is 153.8×102 mm. The configuration of the model engine was determined by the necessity of reflecting the typical features of 3D flow in scramjet ducts. At the same time, the model is simplified and non-optimized, but workable and representative for the purposes of the conducted study.

The 3D inlet configuration of the model is akin to that of the inlets with side compression wedges studied in NASA Langley and CIAM. The external compression of the stream captured by the inlet is ensured by a ramp wedge with an angle $\delta_{rw}=12.5^\circ$ and a non-swept leading edge, as well as by two side wedges with angles $\delta_{sw}=10^\circ$ and a sweep angle $\chi_{sw}=45^\circ$.

© N.P. Adamov, Yu.P. Goon'ko, A.M. Kharitonov, A.F. Latypov, I.I. Mazhul, M.I. Yaroslavtsev,
F.Chalot, P.Perrier, Ph.Rostand, 1998

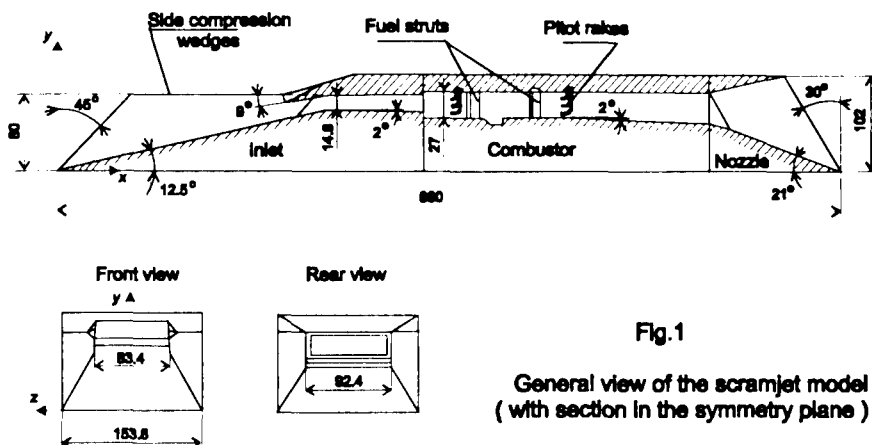


Fig.1

General view of the scramjet model
(with section in the symmetry plane)

The choice of the geometric parameters of internal compression section of the inlet was determined, first of all, by the conditions of model testing with combustion in IT-302. Taking into account these conditions, the relative throat area was preset as $A_{throat}/A_{inlet}=0.1$, where A_{inlet} is the frontal area of the inlet. In addition, it was necessary to obtain satisfactory characteristics of the model with a fixed inlet geometry in the examined range of Mach numbers $M=4-8$ in the both wind tunnels. In particular, the inlet cowl lip angle $\delta_{cowl}=9^\circ$ and the inlet duct entry contraction $A_{throat}/A_{entry}=0.543$ were determined by the inlet starting conditions at the lowest Mach number $M=4$ of the examined Mach range. Preliminary testing of the inlet flow regimes confirmed the characteristics of its starting within the range of operating parameters.

The inlet duct has a rectangular cross-section. The inlet throat is a short duct section of constant cross-section area (the throat length is about one height of its cross-section). Downstream of the inlet throat the duct is expanded due to a small angle between the lower wall and the model axis $\delta_{dif}=2^\circ$. The diffuser ends giving a backward-facing step with a sudden expansion of the duct cross-section up to the area ratio $A_{comb}/A_{dif}\approx 2$ where A_{comb} corresponds to the cross-section of the combustor beginning section.

The combustor is a channel of rectangular cross-section with an initial section of constant area $A_{comb}=\text{const}$ and a subsequent divergent section whose lower wall is inclined to the model axis at an angle $\delta_{comb}=2^\circ$. The initial section of combustor contains two rows of vertical fuel struts for injection of gaseous hydrogen. The first row of the strut-injectors is located behind the diffuser step at a distance of 50 mm from the combustor entrance, the second one is located at a distance of 118 mm from the latter.

The 3D nozzle is constructed very simply by flat walls as an "opposite inlet". Its exit cross-section is skewed at an angle $\chi_{nozzle}=30^\circ$ and has the relative area $A_{nozzle}/A_{inlet}\approx 1.3$. The asymmetric three-dimensional configuration of the nozzle ensures the divergence of the exhausted jet in the horizontal and vertical planes.

The external surfaces of the model excluding those of the inlet cowl are parallel with the free-stream direction and so $A_{nozzle}/A_{mid}=1$.

TEST CONDITIONS

The axial component of the resulting forces acting upon the model was measured by a special external strain-gage balance in the both wind tunnels. The balance was fastened in a special housing in the lower wall of the model and the model together with this balance was mounted on vertical pylon-struts, the balance was covered by a fairing shield. When the model was tested in T-313, the longitudinal force measurement performed by the strain-gage balance was verified by simultaneous measurement performed by the mechanical aerodynamic balance. At testing the model in IT-302, regimes with and without combustion in the engine were investigated, the balance measurements were performed in the both regimes. The influence of the fuel supply system on the balance measurements was negligibly small, which was confirmed by testing the model with a detached fuel manifold and by testing a special calibration model, which was a plate mounted on the strain-gage balance shield.

In the course of experiments, the flow pattern in the inlet duct was visualized, the static pressure and heat flux distributions on the inlet ramp and in the engine duct were measured, and the pitot pressure was measured by two rakes installed in the combustor (Fig. 1). On regimes with and without combustion, the pitot pressure distribution in the duct exit cross-section and the static pressure on the base face were measured for the inlet alone and for the engine without the nozzle, as well as the pitot pressure distribution in the nozzle exit cross-section of the complete engine model.

The IT-302 tests were conducted for wind tunnel operation with the pressure stabilization in the plenum chamber. The test conditions are listed below.

Wind tunnel	Mach number M_∞	P_0 , [bar]	T_0 , [K]	Re_1 (10^6), [1/m]
T-313	4.05	8.2-10.6	280-295	38.5-54
	5.85-6.0	8.3	280-430	20-9.3
IT-302	5.58-5.88	15.7-28.4	1450-1630	1.4-2.1
	7.61-7.89	113.7-124.5	2130-2350	1.2-1.6

FLOW REGIMES IN THE ENGINE DUCT OBTAINED ON THE BASIS OF MEASURED PRESSURE AND HEAT FLUX DISTRIBUTIONS

The schlieren pictures of the flow obtained in T-313 tests of the inlet equipped with optical glasses showed that a system of oblique shock waves forms in the duct and so a supersonic flow occurs in the duct and at its exit. Figure 2 shows the flow pattern in the symmetry plane, which is based on the data of optical visualization and calculated estimates of the shock structure over the external compression section of the inlet. Detailed studies of the inlet flow structure showed that it is characterized by a multiple complex three-dimensional interaction of shock waves between themselves and with the boundary layer. Glancing shocks induce multiple oblique separations and reattachments of the boundary layer with formation of spiral curls. A complex system of shocks, expansion waves and spiral separation vortices forms a significant non-uniformity of velocity field in the exit cross-section.

Based on data of the inlet model tests with the natural boundary layer development, the flow about the external compression section of the inlet in T-313 at $M=6$ was identified as

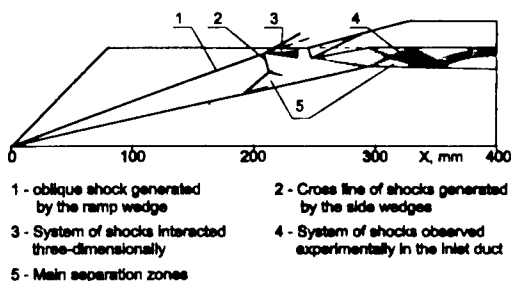


Fig.2. Inlet flow picture in the symmetry plane at $M = 6$

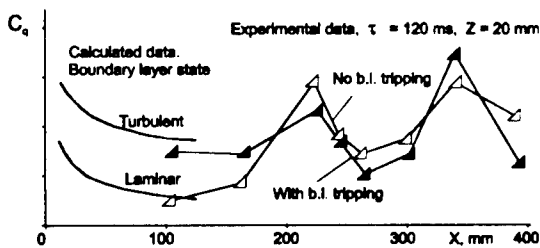


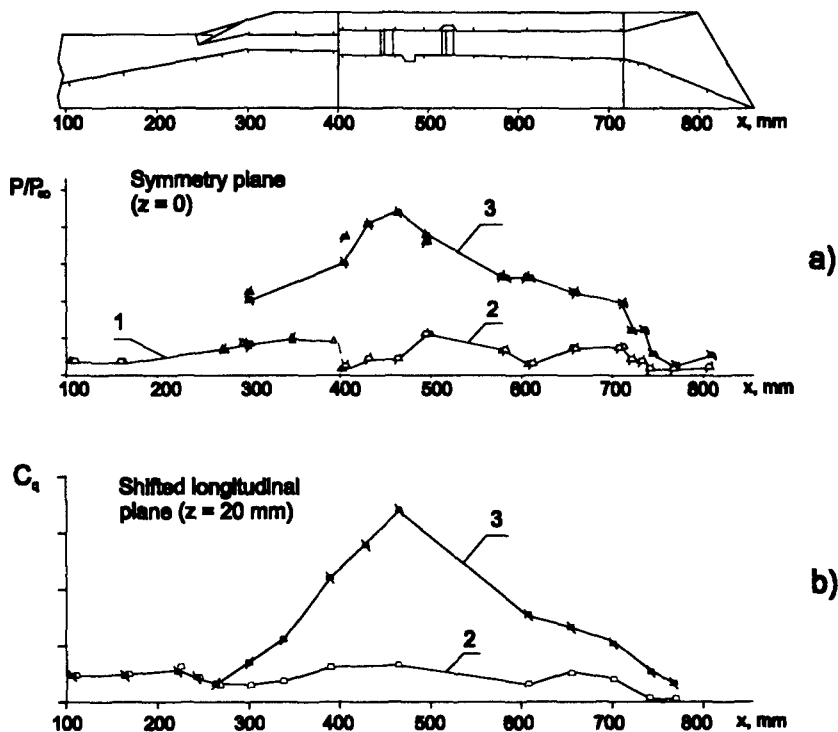
Fig.3. Lengthwise heat flux distribution in the inlet (lower wall), $M_\infty = 5.7$

rather corresponding to a transitional boundary layer. The boundary layer in IT-302 at $M=6$ and 8 is laminar. When the inlet model was tested with boundary layer tripping, the flow both in T-313 at $M=6$ and in IT-302 at $M=6$ and 8 had a turbulent boundary layer on the surfaces of external compression wedges. The efficiency of the boundary layer tripping was confirmed by special tests with the oil-film visualization of the surface streamlines and the pressure and heat flux measurements on the surfaces of the ramp and side wedges.

Figure 3 shows the heat flux distribution over the lower wall of the inlet by the model tests with and without boundary layer tripping at $M=6$ in IT-302. The characteristics presented refer to the time moment about $\tau=120$ ms at the end of the wind tunnel operation regime when the heat exchange in the model duct is already almost a steady process. The

heat flux is normalized to the flux of specific kinetic energy, $C_q = q_w / (\rho_\infty \cdot V_\infty \cdot V_\infty^2 / 2)$. Here ρ_∞ , V_∞ are the density and flow velocity of the free-stream, q_w is the specific heat flux. Note, the heat flux distribution was measured in a longitudinal plane shifted by 20 mm from the symmetry plane. The maxima and minima of the heat flux changing along the model length correspond to the transition through the lines of flow separation and reattachment in separation regions induced by shock waves, which can be seen by comparing Figs.2 and 3. Figure 3 also shows the calculated heat flux estimates for the measure point located on the ramp wedge at the distance $x=105$ mm from the leading edge. This point does not experience the influence of quasi-conical separation regions induced by glancing shocks from the side compression wedges. It is seen that the calculated estimates for the laminar and turbulent boundary layers, respectively, confirm the boundary layer state determined in tests without and with boundary layer tripping.

In model testing with combustion at $M=6$, the hydrogen was supplied in the regime with a falling pressure in the fuel tank, and the fuel-to-air ratio was $f=0.7-1.6$. At $M=8$, the pressure in the fuel tank was kept practically constant and $f=0.9-1.4$. When analyzing the experimental data on combustion we determined the flow pattern in the engine duct indirectly from the pressure and heat flux distributions in comparison with the calculated one-dimensional estimates of characteristics of the duct flow with the heat input in the combustor and taking into account the flow velocity values obtained from pitot pressure measurements in the combustor. The level and the character of pressure and heat flux variations over the engine duct and depending on the time show that a quasi-steady flow regime with thermal choking was observed in the engine duct both for $M=8$ and $M=6$ within the time range $\tau=80-120$ ms, a flow pattern with X-like shock waveforms forms here in the inlet. The flow structure in the inlet duct and in the beginning of the combustor in this case can be identified as rather a pseudo-shock.



$M_\infty = 7.6-7.7$, $p_\infty = (1.2-1.3) \cdot 10^4$ kPa, $t_{a,\infty} = 2100-2300$ K, $Re_\infty = (1.5-1.8) \cdot 10^6$ 1/m;
 1 - Inlet alone; 2 - Complete model, no fuel supply;
 3 - Combustion mode, hydrogen fuel, $f = 0.7-1.0$

Fig.4. Lengthwise static pressure (a) and heat flux (b) distribution (lower wall)

Figure 4 shows the static pressure and heat flux distributions on the inlet ramp and on the lower wall of the engine duct for $M=8$ in the said time range. The data presented were obtained in model testing with and without combustion. The pressure is related to the free-stream pressure, the heat flux is normalized to the flux of specific kinetic energy. One can see in Figure 4 that the beginning of heat flux increase in the pseudo-shock establishes in the beginning of the inlet duct, upstream of the throat, but the pseudo-shock, apparently, does not come upstream from the duct to the position in front of the inlet entry.

CHARACTERISTICS OF THE THRUST-AERODYNAMIC FORCES

The results of balance measurement are illustrated below as a diagram of the longitudinal force coefficients of the model $C_X = X/(q_\infty \cdot A_0)$ at $M=6$ for different tested model variants (Fig.5) and as a plot of the same coefficients versus the Mach number (Fig.6). Here X is the axial component of the resulting force acting upon the model in the downstream direction, $A_0 = 0.0123$ m² is the reference area of the model, which is equal to the frontal area of the inlet ($A_0 = A_{\text{inlet}}$), and q_∞ is the free stream dynamic pressure. A reasonable agreement between the aerodynamic forces measured by mechanical and strain-gage balances is observed for the

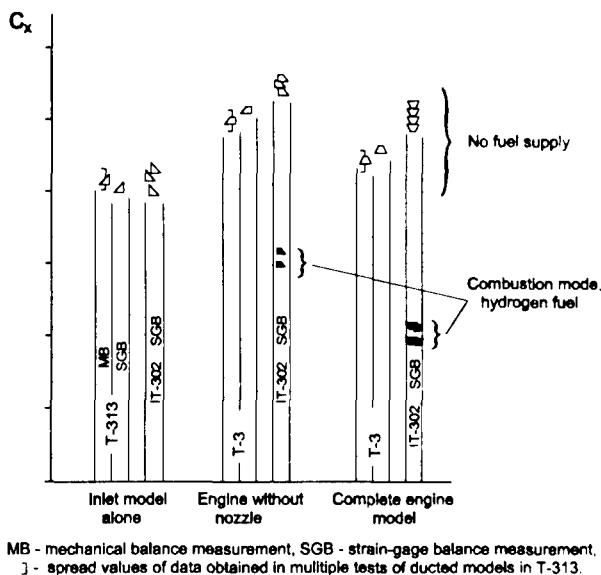


Fig.5. Diagram of drag force coefficients for different model versions at $M = 6$

systematically slightly higher than the data obtained in T-313. This can be attributed to the difference in flow parameters (total pressure and temperature) accessible in the wind tunnels under consideration. In IT-302 test conditions, the Reynolds number per meter was noticeably lower than in T-313 (see the table above). In particular, there are $Re_1 \approx 18 \cdot 10^6$ for T-313 and $Re_1 = 2 \cdot 2.5 \cdot 10^6$ for IT-302 in the comparative tests at $M \approx 6$. Besides, some difference in C_x is caused by the lower free-stream Mach number $M_\infty = 5.6-5.8$ obtained in IT-302 in comparison with $M \approx 6$ in T-313. The calculated estimates of the inlet drag show that we can expect a 10-15% increment of this drag due to smaller values of the Mach and Reynolds numbers in IT-302. The possible estimated increment of C_x is in agreement with the difference in experimental data obtained in the said wind tunnels. On the whole, taking into account the difference in total flow parameters in the wind tunnels under consideration, the agreement of the characteristics of the longitudinal aerodynamic force obtained for the examined scramjet model can be considered as quite satisfactory.

The longitudinal force coefficients obtained in model testing of the inlet alone, the engine without the nozzle and that of the complete configuration without combustion are in agreement with their expected variation depending on the examined configuration (Fig.5). The drag force of the engine without the nozzle increases in comparison with the inlet alone due to both internal drag of the combustor, which is blocked by fuel struts, and additional friction drag because of increasing wetted area of external surfaces. For the complete engine model in comparison with its truncated variant without the nozzle, the drag decreases because the air stream passing through the duct engine expands in the nozzle. At the same time, the complete model drag is slightly higher than the drag of inlet alone with the base face. This can be attributed to the internal drag of the combustor duct and the friction drag of external surfaces with a larger wetted area.

The diagram in Fig.5 shows also the data for the complete engine model and its truncated variant without the nozzle in the combustion mode with hydrogen supply as a fuel. The axial force directed downstream is significantly lower in the combustion mode, i.e., internal thrust

models at their testing in T-313, at $M=6$ the difference is less than 4% for the complete model. The IT-302 tests were performed in small series, and a good agreement of balance measurements was observed, which is seen in Figs. 5 and 6.

The results of model testing at $M=6$ with boundary layer tripping allowed for direct comparison of aerodynamic characteristics of the model obtained in wind tunnels with different operation principles. The analysis of pressure distributions in comparative tests showed that identical flow regimes around the inlet formed in T-313 and IT-302. At the same time, it follows from the results presented in Figs. 5 and 6 that the drag of the models in IT-302 tests without fuel injection are

of the engine is obtained. The drag reduction due to internal thrust at $M=6$ is about 30% for the model without the nozzle and about 60% for the complete model. At $M=8$ the drag reduction of the complete engine model due to internal thrust is about 80%.

The evolution in the model drag coefficients versus the Mach number, which were obtained in tests without fuel supply both in T-313 and IT-302, is shown in Fig. 6. An identical character of this evolution in both wind tunnels can be noted, which is evidenced by almost equal slope of the $C_x(M)$ curves for $M=4-6$ in T-313 and $M=6-8$ in IT-302. The base drag of the inlet alone and the engine without the nozzle is close in value. For $M=4$ and 6 it is, respectively, 18% and 7.5% of the total drag, for $M=8$ the base drag is negligibly small.

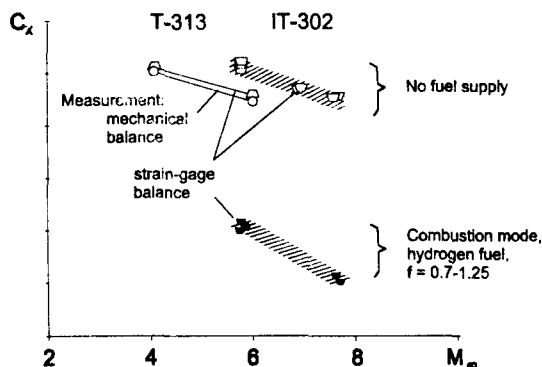


Fig.6. Coefficient of the total axial aerodynamic-thrust force for the complete model versus free-stream Mach number

CONCLUSION

A scramjet model with a three-dimensional inlet was tested in blow-down and hot-shot wind tunnels at Mach numbers $M=4-8$ on regimes with and without combustion (in the former case, gaseous hydrogen was used as a fuel). The aerodynamic drag of the engine constituents (the inlet alone and the engine without the nozzle) were determined taking into account the base drag. The total thrust-aerodynamic characteristics of the examined scramjet model and its variants were obtained. New experimental data obtained expand significantly the knowledge about the processes in scramjets of complex three-dimensional configuration and can be used for verification of numerical methods of flow simulation and for calculating the engine characteristics.

1. Chalot F., Rostand Ph., Perrier P., Goon'ko Yu., Kharitonov A., Latypov A., Mazhul I., Yaroslavtsev M. Validation of global aeropropulsive characteristics of integrated configurations. AIAA Paper 98-1624, 1998.

HIGH-VOLTAGE PULSE GENERATOR FOR VELOCITY MEASUREMENT IN GAS FLOWS BY SPARK TRACER METHOD

Yu.V.Afonin and A.P.Petrov

Institute of Theoretical and Applied Mechanics SB RAS, 630090,
Novosibirsk, Russia

Dozens of principally different methods are used now for flow velocity measurement. These methods are classified into kinematic, dynamic, and physical ones [1]. In the kinematic method, a label is somehow created in the flow, the label motion is registered by appropriate equipment, and then either the time of label passage along a certain trajectory or the distance covered by it during a certain time is measured.

The method of flow tracing by periodic electric discharges is rather evident and based on the use of high ionization of the spark discharge channel, which is preserved for a time of about 10^{-4} [2]. To detect the spark discharge repeated after a fixed time is used. If the time between the two discharges is rather small, the second discharge passes along the channel of the first one, the sections of this channel being shifted during this time at distances proportional to local flow velocities.

A multichannel generator of high-voltage pulses was developed for implementation of the above method in various gas dynamic facilities with a wide range of gas flow velocity. A sketch of this generator is shown in Fig. 1.

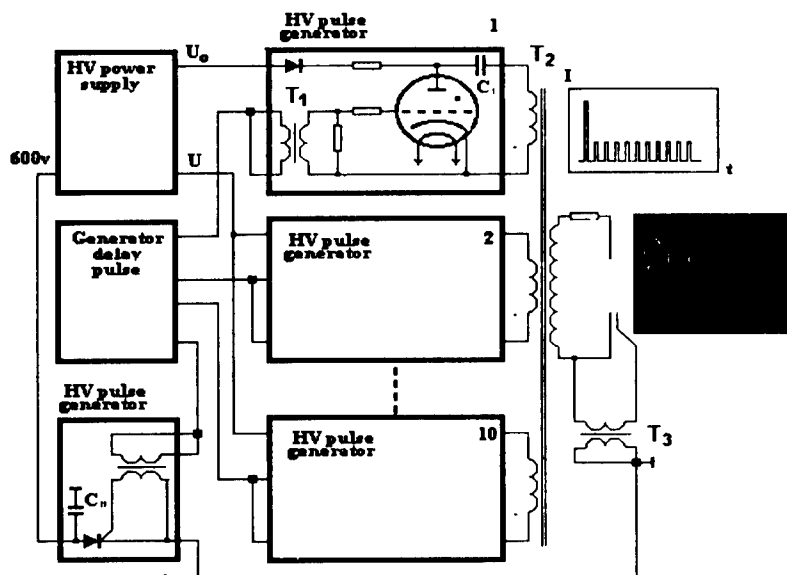


Fig. 1. Multichannel generator of high-voltage pulses. T_1 -control transformer, T_2 - output step-up transformer, T_3 -preliminary ionization transformer

Generator consists of 10 independent channels, each of them being assembled following

© Yu.V.Afonin, A.P.Petrov, 1998

a typical scheme. When the triggering pulse from the external generator comes to the primary winding of a control transformer T_1 , the thyatron switch tube works, and the capacitor C_1 , being primarily charged from a high-voltage source, discharges rapidly to the primary winding of the output transformer T_2 . Due to low resistance of the hydrogen thyatron and low inductance of the primary circuit of the pulse step-up transformer, a voltage pulse of small duration ($3 \cdot 10^{-7}$ s) with the transformation ratio of 10 is formed at the secondary winding. To ensure a high (~ 0.9) coupling coefficient, the primary windings of all ten channels and the secondary winding are located on one circular core made of ferromagnetic material K 180x120x20, 400 HH. Thus, a galvanic disconnection between the windings and from the load is achieved.

It should be noted that the operation of one thyatron induces the electromotive force on the primary windings of the remaining thyatrons, its minus being applied to anodes of other thyatrons. Preliminary tests showed, however, that this polarity and duration of the pulse did not cause the operation of other thyatrons at a three-fold nominal value of anode voltage. To provide electrical insulation, the windings are reeled up in one layer by a cable with polyethylene insulation without braiding and separated from each other by a small gap.

The study of recovery time of electric strength of the air gap for a flow velocity of up to 20 m/s and atmospheric pressure showed that the initial break-down of a 30-mm gap between $\varnothing 16$ -mm electrodes requires the pulse amplitude $U_0 = 100$ kV with duration of $\sim 3 \cdot 10^{-7}$ s (see Fig. 2a), while much lower amplitude ($0.1 \div 0.25 U_0$) is needed for the second pulse repeated after 100–200 μ s.

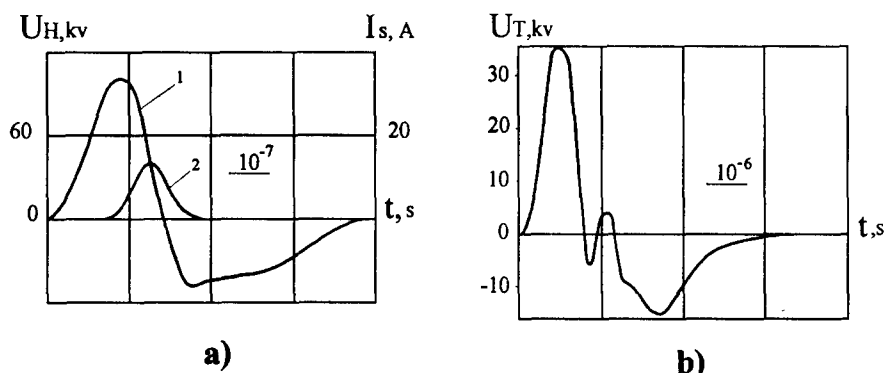


Fig. 2. a) no-load voltage oscillograms on the discharge gap (1) and spark current (2)
b) pre-ionization voltage pulse of thyristor generator.

The no-load voltage on the discharge gap and the spark discharge current were measured using a potentiometer-type voltage divider and high-speed oscilloscope. The total recovery of electric strength takes place within a millisecond range, and its mechanism at this stage is apparently connected with heat processes [3], while the second break-down has no information about the initial velocity distribution in the gas flow. The ionized trace of the previous discharge retains apparently for $2 \cdot 10^{-4}$ s.

In connection with the above said, the first channel for the primary break-down in this device is constructed on the basis of thyatron TGI-1000/25, the capacitor being charged from

a voltage source up to 15 kV. Nine remaining channels utilize thyatrons TGI-50/5 fed from a source up to 5 kV. The both sources of high voltage allow one to ensure a smooth adjustment of voltage from zero to the maximum value.

To reduce the mass-size dimensions of the entire device, high-voltage sources of d.c. voltage were developed. They have a 5 W power and a high-frequency (~ 10 kHz) transformation of 12-V d.c. voltage to a.c. unipolar voltage with amplitude of 5 kV on the basis of inductive charge integrator, the TVS-110L1 being used for that. A 15-kV voltage is generated by a three-cascade diode-capacity multiplier. The weight of one source does not exceed 1 kg.

It is known that the spark discharge time consists of the static delay time t_s and formation time t_f . For low-duration (t_d) pulses, the discharge can be absent because of the absence of initial electrons in the discharge gap, i.e., $t_d < t_s$. To avoid this effect, the present device has an additional generator of high-voltage pulses for preliminary ionization of the discharge gap by an auxiliary spark discharge located near the main discharge zone. Instead of thyatron, a fast-response thyristor TChI-100 is used in the generator as a switch tube element, with a 600-V charge of capacitor C_{11} . The output voltage pulse with amplitude of ~ 35 kV removed from the secondary winding of the circular transformer T_3 on the ferrite core K 120x80x12 is shown in Fig. 2 b.

Operation of thyatrons is controlled by two standard generators GZI-6. Each of them is a six-channel source of pulses with amplitude of 250 V and growth front of $0.5 \cdot 10^{-7}$ s, and all channels can be switched on in a certain sequence with a 0 to 10^{-3} s delay relative to each

other and have individual outputs. The pulses from GZI-6 come to thyatron nets through a coaxial cable and pulse transformer, and determine a specified sequence of high-voltage pulses on the discharge gap. A sketch of the device is shown in Fig. 3. The device dimensions are 1500x500x500 mm.

Thus, a 10-channel generator of high-voltage pulses for gas flow velocity measurements has been developed and manufactured. It has the following features.

The use of hydrogen thyatrons as switch tubes in generators of high-voltage pulses with a transformer output allows one to obtain steep fronts (10^{-7} s) of the pulses and increase the accuracy of determining the gas flow velocity.

The multichannel structure of this device, consisting of independent generators, can increase the pulse repetition frequency up to 2 MHz and extend the applicability limits of the method to the high-speed region.

Independent adjustment of the amplitude of repeated pulses creates conditions for minimizing gasdynamic disturbance due to energy production of a spark discharge in a controlled gas flow.



Fig.3. A sketch of multichannel generator.

References

1. Трохан А.М.. Гидроаэрофизические измерения.- Москва: Из-во Стандартов, 1981.
2. Bomelburg H.J., Herzog J., Weske J.R. The electric spark method for quantitative measurement in flowing gases // Z.Flughiss.- 1959.- Vol. 7.- №. 11.- P. 322.
3. Бельков Е.П.. Охлаждение газа и восстановление электрической прочности после искрового разряда // ЖТФ.- 1971.- Т. 41.- Вып. 8.- Стр. 1678.

THE CONDITIONS OF USING THE MULTI-SPARK DISCHARGE FOR GAS FLOW VELOCITY MEASUREMENTS

Yu.V.Afonin and A.P.Petrov

Institute of Theoretical and Applied Mechanics SB RAS,
630090, Novosibirsk

The method of gas flow tracing by periodic discharges is based on the use of high ionization of the spark channel, which is preserved for a considerable time $\sim 10^{-7}$ s [1]. The use of this method in particular conditions of gas dynamic experiment is primarily related to obtaining information about the voltage of impulse breakdown of the discharge gap and the lifetime of an ionized "trace" of primary discharge.

Besides, the spark discharge is a source of gas dynamic disturbances, which can distort the velocity field of examined flow. Thus, the study of ignition conditions of spark discharge with the minimum energy release in the channel is important. However, the current value should be sufficient for its photoregistration.

In the present paper we report some results on this topic, obtained using a two-pulse high-voltage generator with independent control of pulse amplitude. The duration of a bell-shaped voltage pulse was $3 \cdot 10^{-7}$ s. The amplitude of the first pulse could be varied within 20 to 160 kV, the repeated pulse amplitude was within zero to 45 kV, the spark discharge current being less than 50 A.

Figure 1 shows the spark discharge voltage versus the discharge gap for two electrode configurations at atmospheric pressure: 2 - "spike-spike" with diameter 0.1 mm, 1, 3 - "sphere-sphere" with diameter 28 mm.

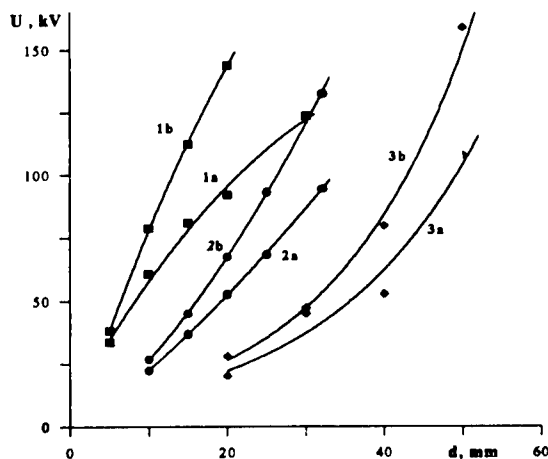


Fig. 1. Voltage of a pulse spark discharge for various configurations of electrode system. 1, 3 - spherical, 2 - spike, 3 - two-pulse regime.

Curves "b" correspond to voltage values for which a definite spark discharge takes place, curves "a" describe a breakdown with a 50% probability. It is seen from the figures that using spike electrodes the spark can be obtained at a distance between the electrodes approximately twice as large as the gap between spherical electrodes. A decrease in voltage leads to unfinished spark discharge and diffuse discharge shape. The smaller the voltage pulse dura-

© Yu.V.Afonin, A.P. Petrov, 1998

tion, the higher the accuracy of determining the discharge channel position, but the worse the conditions for obtaining a channel form of the discharge.

Figure 2 shows a set of typical photographs of discharge shapes for different voltage values lower curve 1a with the distance between the electrodes $d=20$ mm.

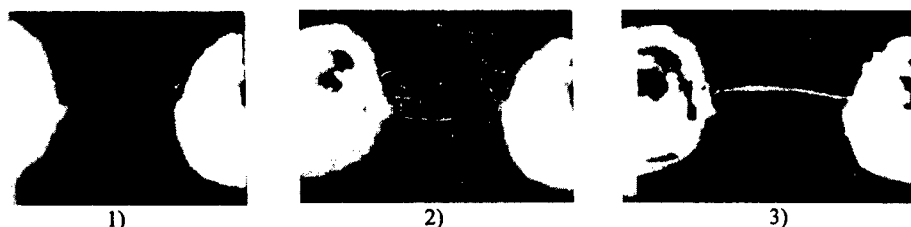


Fig. 2. Photographs of pulse discharge for various amplitude of voltage pulse. A spherical configuration of the electrode system 1+3 corresponds to $U_1=45, 50, 60$ kV.

When the voltage shifts below the 50% spark breakdown curve, the discharge shape is different. At first, the probability of appearance of a spark discharge decreases. Then incomplete streamers arise on the background of long-channel diffuse discharge. As the voltage further decreases, only a diffusion, weakly glowing discharge exists in a certain range. This discharge vanishes completely when a certain lower threshold voltage is achieved. This voltage is about 50 kV for spherical electrodes with discharge gaps larger than 10 mm.

A considerable decrease in initial breakdown voltage of the first pulse could be achieved by using a sequence of two pulses with equal duration (see Fig. 1, curve 3). The first pulse with an 80 kV amplitude "prepares" the gap (no spark discharge), and the second pulse breaks it with significantly lower voltage. This organization of spark discharge allows one to move to the region of large gaps, reduce energy release in the spark channel, and increase the accuracy of its temporal fixation. To choose the amplitude of the repeated pulse at a minimum level sufficient to form a spark discharge, we obtained the voltage of the repeated spark breakdown versus the time period that passed after the first spark.

Figure 3 shows the curve of recovery of electric strength of a spike gap with a 15 mm distance between the electrodes.

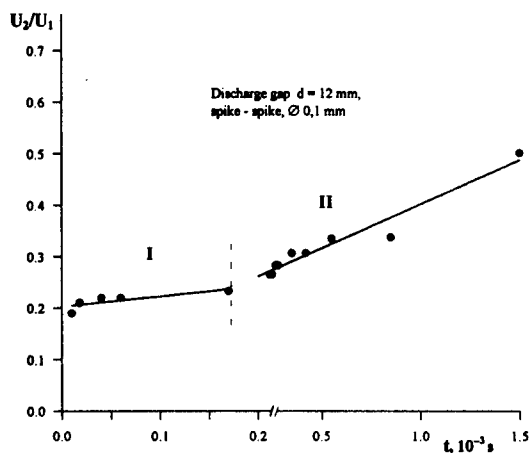


Fig. 3. Voltage of the repeated spark breakdown versus the time interval between the pulses. Discharge gap spike-spike, $\varnothing 0.1$ mm, $d=15$ mm.

It is seen from the figure that the process of electric strength recovery is characterized by two different sections. At the first, gently inclined section up to $180\text{ }\mu\text{s}$, the electric strength of the gap is roughly constant, the mean value of the repeated breakdown pulse is $0.23 U_1$. At the second section the breakdown voltage increases up to the level of the primary breakdown. To trace the gas flow, it is necessary to use the first section, since at this stage the gap strength is determined by the electric strength of plasma column remaining after the previous discharge [2].

Secondary spark discharges occur at the first stage following the existing channel and require substantially smaller voltages, while the energy contribution can be regulated by an external ballast resistor up to a level determined by photomaterial sensitivity.

Experiments in the gas at rest showed that after $500\text{ }\mu\text{s}$ the secondary spark does not repeat the shape of the primary spark and can deflect from it at a distance up to 2 mm , which is most probably connected with gas dynamic disturbances from the first spark.

In our conditions an energy release of 10^{-2} - 10^{-3} J/cm in the spark channel is equivalent to thermal explosion. The gas is heated up to temperature of $10^4\text{ }^\circ\text{K}$. Up to 10% of energy are spent on radiation, which is useful for photoregistration. The remaining energy is transformed into thermal energy. This results in the formation of a shock wave propagating to all directions from the spark discharge. A four-channel shadow chronograph was used to visualize the pattern of gas dynamic disturbances [4].

A typical picture of disturbance evolution for two sparks with an interval $10\text{ }\mu\text{s}$ with different moments fotoregistration is shown in Fig. 4. The observation direction coincides with the discharge channel axis.



Fig. 4. Shadowgraphs of shock waves of spark discharges with equal intervals between the pulses $10\text{ }\mu\text{s}$, but with different moments fotoregistration after first spark : a) $t=25\text{ }\mu\text{s}$, b) $t=60\text{ }\mu\text{s}$.

It was found that the second shock wave is not observed for intervals between the sparks less than $3\text{ }\mu\text{s}$, and the density gradient of gas disturbed by the second spark is outside the limits of sensitivity of the shadow chronograph. This circumstance is apparently explained by a high conductivity of plasma at this time interval and, as a consequence, by low energy release in the repeated spark discharge.

Thus, the following conclusions can be drawn from the results of conducted work.

1. Ignition conditions of a spark discharge with duration of $\approx 3 \cdot 10^{-7}\text{ s}$ both in uniform and strongly nonuniform electric field were determined.
2. A two-pulse regime of spark discharge ignition was obtained, which allows for a 2-3-fold increase of the controlled gas flow region.

3. The minimum amplitude of voltage pulse for obtaining a repeated spark discharge and the maximum time interval sufficient for tracing the primary spark were determined.

References

1. Bomelburg H.J., Herzog J., Weske J.R. The electric spark method for quantitative measurement in flowing gases // Z. Flugwiss.-1959.- Vol. 7.-№. 11.- P.322.
2. Slepian I. // Trans. AIEE.-1930.- Vol. 49.- P. 421.
3. Бельков Е.П. // ПТЭ.-1978.- № 1.- стр. 230.
4. Петров А.П. Четырехканальный теневой хронограф // 13 Всесоюзная научно-техническая конференция "Высокоскоростная фотография, фотоника и метрология быстропротекающих процессов", Тезисы докладов.- Москва,ВНИИОФИ, 1987, с. 8.

EXPERIMENTAL RESEARCH OF ATOMIC POWER STATION BUILDING LARGE-SCALE MODEL AERODYNAMICS IN AERODYNAMIC SUBSONIC VELOCITIES WIND TUNNEL WITH VISUALIZATION OF FLOW

L.S.Alekseeva, V.M.Berkovich, M.M.Grigorev, G.S.Taranov, E.F.Shirokov-Bryukhov
Institute AtomEnergoProject, Moscow, Russia

K.A.Kolinko

Central Aerohydrodynamic Institute, Zhukovsky, Moscow Region, Russia

A.N.Prokhorov, L.I.Semernyak

Central Institute of Aviation Motors, Moscow, Russia

ABSTRACT

The results of experimental research of influence of a direction of wind on performance of air channels of passive heat removal system (PHRS) of power generating unit of Novo-Voronezh nuclear power station. The researches were conducted in subsonic aerodynamic tunnel with opened working part on model of nuclear power station building, made in model-prototype relationship 1:80, at 60 m/s flow speed with action of wind from all directions.

The measurements of pressure difference on air shafts, and also massflows of air through shaft were carried out under various conditions of wind action.

It is shown that in case, when the wind blows on the annex side of protective shell, there is not a significant performance degradation of windward side group of PHRS shafts, in spite of the fact, that occurs rarefaction in the inlet collector of shafts caused by extensive recirculation zone at airflowing of annex.

INTRODUCTION

The safety of atomic electric power station is one of main problems, which should be solved at designing stage.

With the purposes of safety increase of new generation nuclear stations with water reactors (which Novo-Voronezh Nuclear Power Station - NV NPS-2 - is related too), it is supposed to equip them by PHRS with air condensers and draft shafts located on the outer side of protective shell of main building. The system consists of four groups of air shafts located in regular intervals on a circle of containment dome. In the lower ends of shafts the heat exchangers are located. The ventilation of heat exchangers implements at the expense of a natural convection of air shaft. For decrease of influence of wind on PHRS activity the design solutions such as a general annular collector at air condenser input and output collector with the deflector at draft shaft exit were offered (all right reserved - patent in Russia № 94044806/25/(045040) from 21.12.94. The owner of the patent is the Institute AtomEnergoProject).

The purpose of experimental researches under discussion was the quantitative estimation of influence of wind direction on PHRS activity and confirmation of developed construction solutions.

© L.S.Alekseeva, V.M.Berkovich, M.M.Grigorev, G.S.Taranov, E.F.Shirokov-Bryukhov,
K.A.Kolinko, A.N.Prokhorov, L.I.Semernyak, 1998

THE DESCRIPTION OF EXPERIMENTAL MODEL

To realize tests on assessment of NV NPS-2 PHRS effectiveness its model was developed and created in model-prototype relationship 1:80.

The NPS model was prepared by pressure sensors, which measured a static pressure difference between points located inside input collector-tunnel near every PHRS shaft and output collector. Static pressure inside output collector of protective shell also was measured. To measure small pressure difference the method of "thermal balance" was developed. For this aims the models of all sixteen shafts were equipped with electrical heaters of air and prepared by thermocouples for measurement of temperature difference between entrance and exit of shafts.

For visualization of external flow picture the model was prepared by silk threads (≈ 1200 pieces). The airflow pattern was registered by video- and photo-apparatus.

The tests of model NV NPS-2 were conducted in aerodynamic wind tunnel (AWT) of closed contour with opened working part. The model was fixed on rotary table. It has ensured capability of model airflying under any angle in range of $-178^\circ \dots +178^\circ$. The scheme of NPS model layout in working part of AWT is shown in Fig.1.

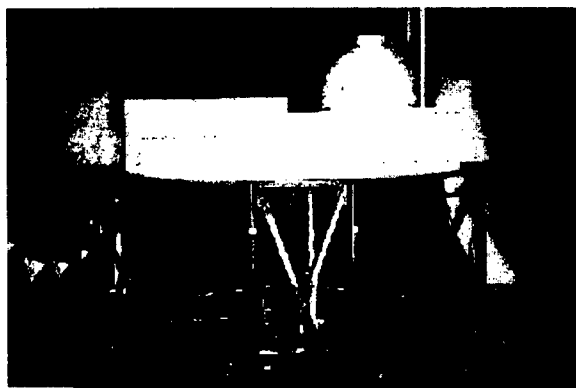


Fig.1.

THE DETERMINATION OF PRESSURE DIFFERENCE IN SHAFTS BY METHOD OF "THERMAL BALANCE"

With the purpose of measurement of small pressure differences on shafts, when accuracy of pressure sensors is already insufficient, the method of "thermal balance" was used. For this purpose inside a housing of the shaft model heat exchanger the electrical spiral heater of air by power of 190 W (see Fig.2) was mounted. At the entrances of PHRS shafts - in the input collector - the thermocouples were placed with probe head placed in center of input hole of shafts. In output funnels of shafts thermocouples also were placed with probe head placed at the upper wall of shaft.

On method of "thermal balance" it is assumed, that at constant heating power the value of air massflow is inversely as temperature difference at entrance and at exit of shaft. Knowing value of massflow, it is possible to calculate flow velocity in shaft and value of pressure difference on shaft.

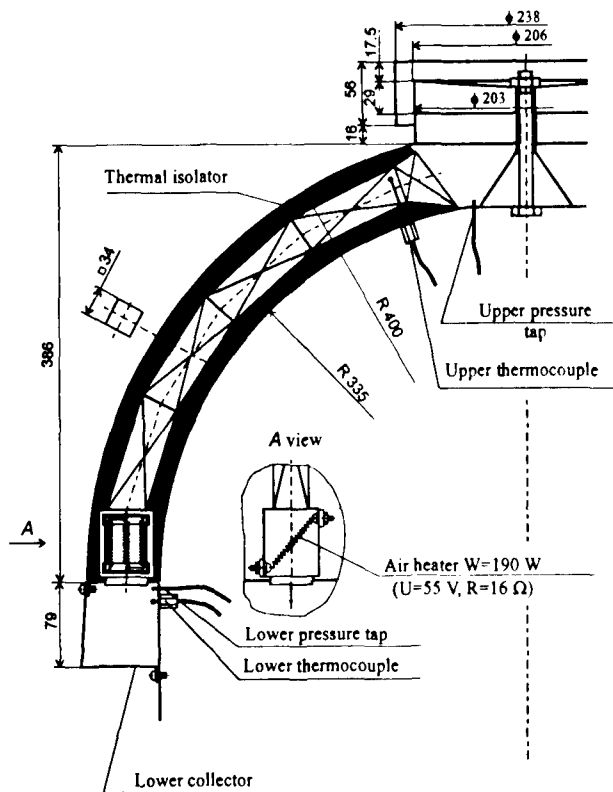


Fig.2.

The dependencies $G=G(\Delta T)$ and $\xi=\xi(G)$ (Fig.3) (where G - mass flowrate of air through shaft (positive massflow - from down to up), $\Delta T=(T_U-T_L)$, T_L - air temperature at entrance shaft, T_U - air temperature at shaft exit, ξ - hydraulic resistance factor of shaft) for shaft were measured in processes of calibration (see Fig.3).

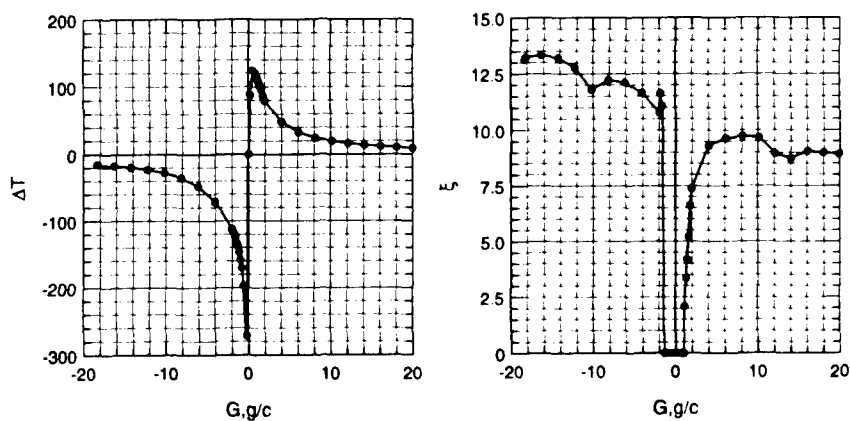


Fig.3.

RESULTS OF EXPERIMENTAL RESEARCHES

Within the frame of these researches the work parameters of shaft air duct of PHRS were investigated at flow speed $V=60$ m/s and angles of wind direction $\beta=-175^\circ\dots+175^\circ$. Reynold's number calculated on diameter of NPS containment dome was $Re=3.18\times 10^6$, that exceeds value of critical Reynold's number for sphere.

The relations of values of air massflow through the shafts from angle of wind direction determined on method of "thermal balance" are shown in Fig.4. The order of numbering of shaft groups, shafts in group and the scheme of model airflow angle readout is shown in Fig.5.

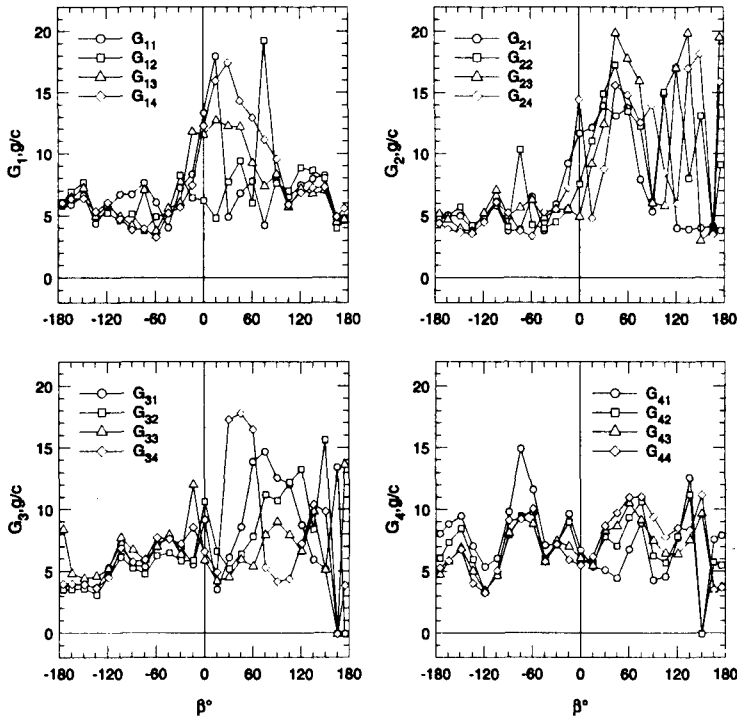


Fig.4.

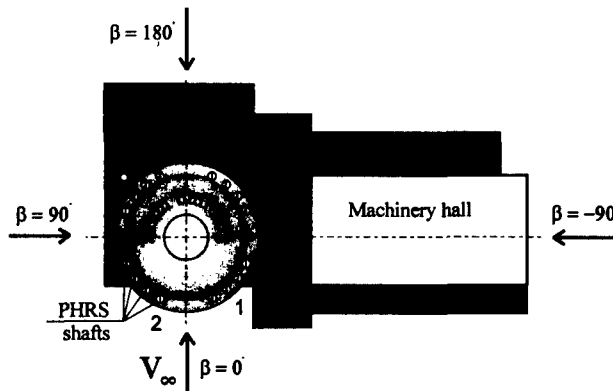


Fig.5.

The appropriate relations of total pressure drop on shafts evaluated also on method of "thermal balance" are shown in Fig.6.

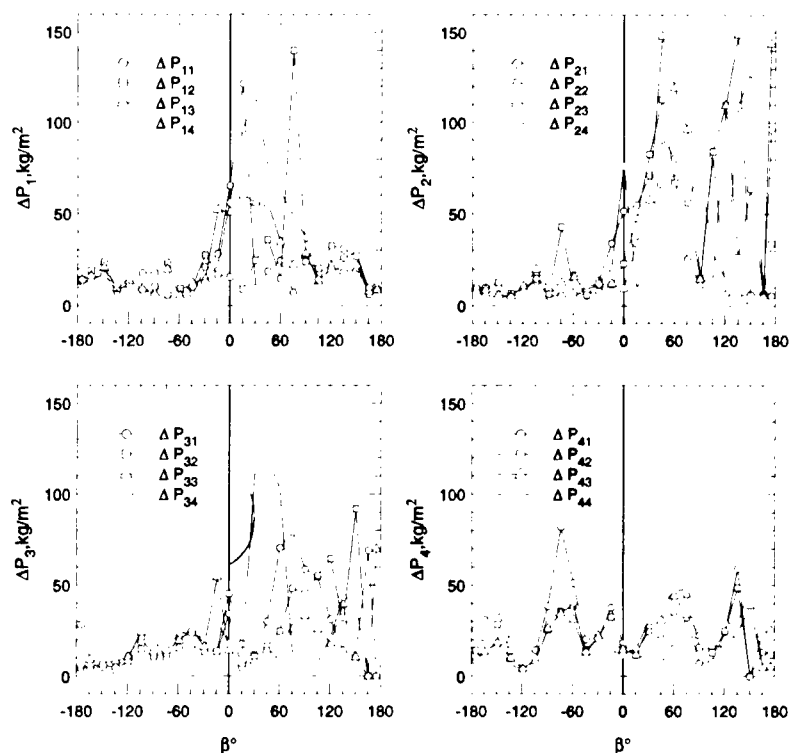


Fig 6.

PHRS SHAFT WORK IN CONDITIONS OF WIND ACTION

As the results of NV NPS-2 building airflow visualization have shown, airflow near the protective shell of main building of NPS, the upper deflector and zone of input slot of the lower collector of PHRS is determined by an interference of incident flow and vortexes formed at main building elements airflowing. Owing to obvious asymmetry of annexes of main building, the parameters of the working of air channels of PHRS depend on a direction of wind. It is confirmed by obtained results of parameter measurements of flow in shaft ducts.

As follows from the shown data, in the whole the design of the lower collector and deflector of NV NPS-2 PHRS provides effective work of system in conditions of wind action.

So in the first group of shafts, due to rarefaction created by the deflector, the value of the massflow is not lowered below 3 g/s (see Fig.4). In case, when the wind blows on shafts ($\beta = -30^\circ \dots +60^\circ$) the value of G through shafts reaches 15 g/s, that is explained by significant ramming arising at incident flow stagnating at the base of NPS main building.

The flow in the second group of shafts, as was emphasized above, is formed in conditions of the least influence of constructions ambient main building. Therefore at air onflowing from this group of shafts in range of angles $\beta = 0^\circ \dots 120^\circ$ the sharp increase of massflow (up to $G \approx 15 \dots 20$ g/s) is marked in all shafts of this group (see Fig.4) and in some

shafts of the first and third groups.

The decrease of overall performance of the third and fourth shaft group at $\beta=175^\circ$ is obviously connected with negative action of vortex appeared at airflowing of lateral wall and jetty upper part of annex.

Analyzing relations of massflow variation for shafts of the third group it is possible to note that, as well as for first two groups of shafts, massflow through shaft arising at wind action practically in all range of angles β is not less than 4 g/s. At flow stagnation in the field of entrance into the lower collector of shafts ($\beta=60^\circ \dots 135^\circ$), the massflow through all shafts grows and especially in first two one located near aperture formed between ventilating hall and the base of main building. The appreciable decrease of draft in the fourth shaft of group, which occurs at airflow with $\beta=75^\circ \dots 105^\circ$, apparently, is connected with significant acceleration of air in slot formed between cover of NPS ventilating hall and lower wall of annular collector (see Fig.4). The most essential decrease of overall performance of the third group of shafts is observed at wind action from the annex to protective shell building $\beta=165^\circ \dots 175^\circ$. In this case the additional pressure difference generated by wind is practically absent.

The appearance of significant rarefaction in the field of the lower collector is caused by action of high-power vortex formed on cover of annex. As it is specified in [1], at transversal flowing of parallelepiped on the forward part of its upper side there is a vortex, therefore on the upper surface of parallelepiped there is the zone of high-power recirculation. Length of this zone is approximately equal to two altitudes of forward side of parallelepiped. The confirmation of this phenomenon can be seen in Fig.7 where the pattern of flowing of building by a flow directed from the side of machine hall $\beta=90^\circ$ is shown. It is visible, that the centre of recirculation zone locates from the forward edge on distance approximately equal to altitude of the building. In case, when stream is flowing from the side of annex, as it is visible from visualization pictures shown in Fig.8 ($\beta=175^\circ$), the recirculation zone is closed directly on the protective shell. As consequence the significant rarefaction appears in the field of input slot of collector of the third group of shafts.

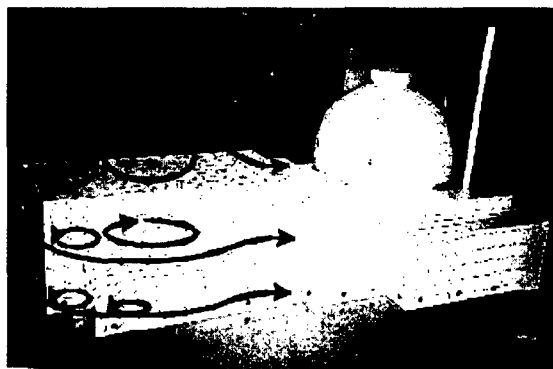


Fig.7.

The fourth group of shafts is most protected from effect of wind by NPS buildings. The entrance in lower collector of this group is located below than level of machine hall cover (see Fig.5). This, from the one hand, descends energy of flow and at wind action from the side of

shafts ($\beta = -165^\circ \dots -120^\circ$) significant increase of air massflow through shaft is not observed (see Fig.4). From the other hand, this weakens also negative influence of wind; therefore both values of air massflows and dimension less pressure differences (see Fig.6) are varying on the angle β considerably less than for other groups of shafts.



Fig.8.

CONCLUSIONS

1. The analysis of wind influence on PHRS shaft work in condition typical for NV NPS-2 shows the significant influence of vortex flow appeared at annex airflowing on pressure difference on shafts.

2. Minimal value of additional pressure difference generated by the wind is observed at flow angle $\beta = 165^\circ, 175^\circ$, when wind acts from the side of annex. In this case the minimal sum massflow through the shafts is realized, furthermore weak return flow appears in the windward side shafts.

3. Suggested construction design of PHRS air duct protection in form of lower collector and deflector fully eliminates negative influence of wind on air flow in PHRS shafts.

REFERENCES

1. E.I.Retter. Architectural - building aerodynamics. - Moscow: Building Edition, 1984. (In Russian)

OH EMISSION REGISTRATION AT HYDROGEN JET BURNING INSIDE ON-WAY SUPERSONIC FLOW IN THE SCRAMJET COMBUSTOR MODEL

V.Yu.Alexandrov, Yu.S.Mnatsakanyan, A.N.Prokhorov, V.L.Relin

Central Institute of Aviation Motors, Moscow, Russia

A.A.Shutov, V.P.Yurin

Research Test Center of Central Institute of Aviation Motors,

Lytkarino, Moscow region, Russia

In CIAM for several last years the researches of mixing and burning of supersonic jets with reference to the combustion chamber (CC) of Scramjet are carried out. The computational researches of supersonic jets mixing by the numerical solution of Navier-Stokes parabolized equations carried out some time back had shown improvement of mixing and burning processes at use of injector nozzles with elliptical exit cross-section instead of nozzles with circular exit cross-section [1,2]. The experimental researches, which have been carried out in CIAM Research Test Center, have confirmed improvement of mixing of supersonic jet outflowing from the injector with the elliptical shape of the nozzle with co-current supersonic flow [3]. It is defined, that the improvement of injected jet mixing with co-current flow occurs at the expense of jet split effect at use of the injector with the elliptical shape of the nozzle.

In the given work the experimental research of burning of supersonic jet of hydrogen in a co-current supersonic stream was conducted. Co-current stream is the oxidizing mixture simulating heated air. The researches were carried out in model Scramjet CC for injectors with circular and elliptical nozzles.

The comparative research of influence of the following parameters was carried out:

- Ellipticity of the injector nozzle ε ($\varepsilon=a/b$, where a and b - large and small axis of ellipse in nozzle exit cross-section accordingly);
- The ratio of pressures (unisobaricity of jet) n ($n=P_i/P_e$, where P_i - static pressure in injected jet at exit cross-section, P_e - static pressure in on-way flow).

The experimental researches were conducted on the installation of supersonic burning (SSB) (fig.1) of II-16 test cell of CIAM Research Test Center [4]. Into the Scramjet model CC with rectangular cross section ($H=45\text{mm}$ and $S=30\text{mm}$) the pylons with rectangular back face ($h=30\text{mm}$ and $s=10\text{mm}$), supplied by the injector with the various shape of the nozzle (fig.2) were placed. Diameter of injector nozzle critic cross-section was equal 3mm.

The experiments were conducted with two types of injectors: with circular exit cross-section of the nozzle ($\varepsilon=1$) and elliptical ($\varepsilon=\varepsilon^*$, $\varepsilon^*=1/q(M_i)$, where $q(M_i)$ - gas-dynamic function, M_i - Mach number of injected gas at the nozzle exit), that corresponds to equality of critic diameter and small axis of ellipse of the nozzle exit cross-section. Through the pylon into the chamber the hydrogen with temperature of an environment was injected. The Mach number of injected gas at the injector nozzle exit is identical for all injectors and equals $M_i=2.5$.

The parameters of on-way flow at the combustor entrance are chosen with the purpose of modeling of flight conditions of Hypersonic Flight Vehicle in standard trajectory corridor [5] with Mach number $M_F=6$:

- Total pressure $P^* = 3 \text{ MPa}$;
- Total temperature $T^* = 1650 \text{ K}$.

The combination scheme of air heating is applied for modeling conditions at combustor entrance. Previously air is heated up to 1000K in electric heater, then up to temperature 1650 in the fire heater with compensation of oxygen mass fraction in oxidizing mixture.

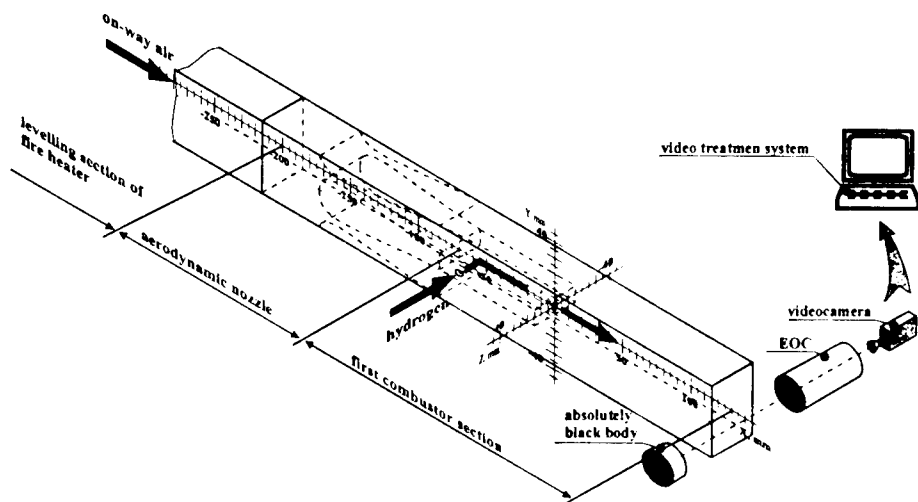


Fig. 1. The scheme of the SSB installation.

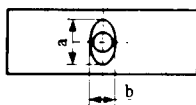


Fig. 2. Back face of pylon.

The comparative researches of combustion processes in model CC of Scramjet were fulfilled by observation of the plume behind the outlet of the chamber (see fig.1). Visual observations by the video camera and determination of chemical reaction zones at burning on emission of OH^- radicals with the help of the electron-optical converter (EOC) installed in the plane of combustor exit were carried out.

The research of processes in gas flow on radical emission is based on principle of formation of the image of this flow on properties of its radiation. The location of chemical reaction areas (areas with presence of OH^- radicals radiating on wavelength of 306 nm) in a gas flow is performed with the aid of narrow spectral area filtration from an integral radiant flux. The radiation zone intensity is transformed to the television image with use of the electron-optical converter. Specially created television registration system consists of the electron-optical converter and integrated to it semi-conductor tele-camera. The recording of the image is executed by the video-recorder with the subsequent input and processing on PC.

The use of the method of OH⁻ emission registration has allowed to realize visualization of operational regime of model CC. The burning zones at combustor exit have the various forms on sub- and super-sonic regimes (fig.3).

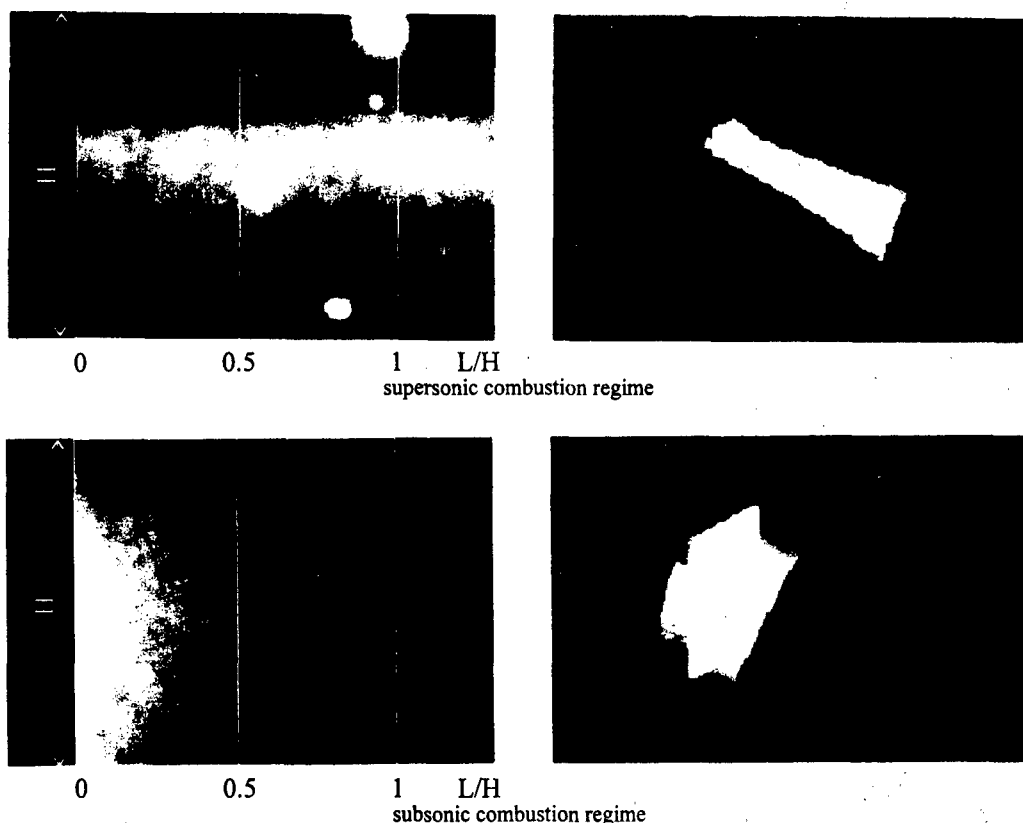


Fig. 3. OH⁻ radical emission registered by EOC at CC exit (left) and visual form of gas jet outflowing from CC (right) for various combustion regimes.

The results of comparative researches of supersonic combustion in model CC carried out with various types of injectors were presented in work [6]. In fig.4 the main results of these researches are shown. Width of combustion zone and radiation intensity in it show, that the process of combustion in model Scramjet CC is more effective at use of the elliptical injector. For the elliptical injector ($\varepsilon = \varepsilon^*$) the confirmation of jet split effect is obtained also. At the combustor exit the two flows with increased intensity of OH⁻ radical emission are clearly distinguished. In visible spectrum difference of the plume form for circular $\varepsilon = 1$ and elliptical $\varepsilon = \varepsilon^*$ of injectors also are observed.

The increase of unisobaricity n of injected jet leads to increase of the size and emission intensity of zones of chemical reactions, but does not change qualitatively their form.

Obtained results show that the jet of high-temperature gas jet keeps visual spectrum emission properties along the whole way length between CC outlet and exhaust duct inlet ($L \approx 8H$) (fig.4, right). OH⁻ radical emission intensity behind the CC exit decreases, that is the result of chemical reaction decay at hydrogen burning (fig.4, left).

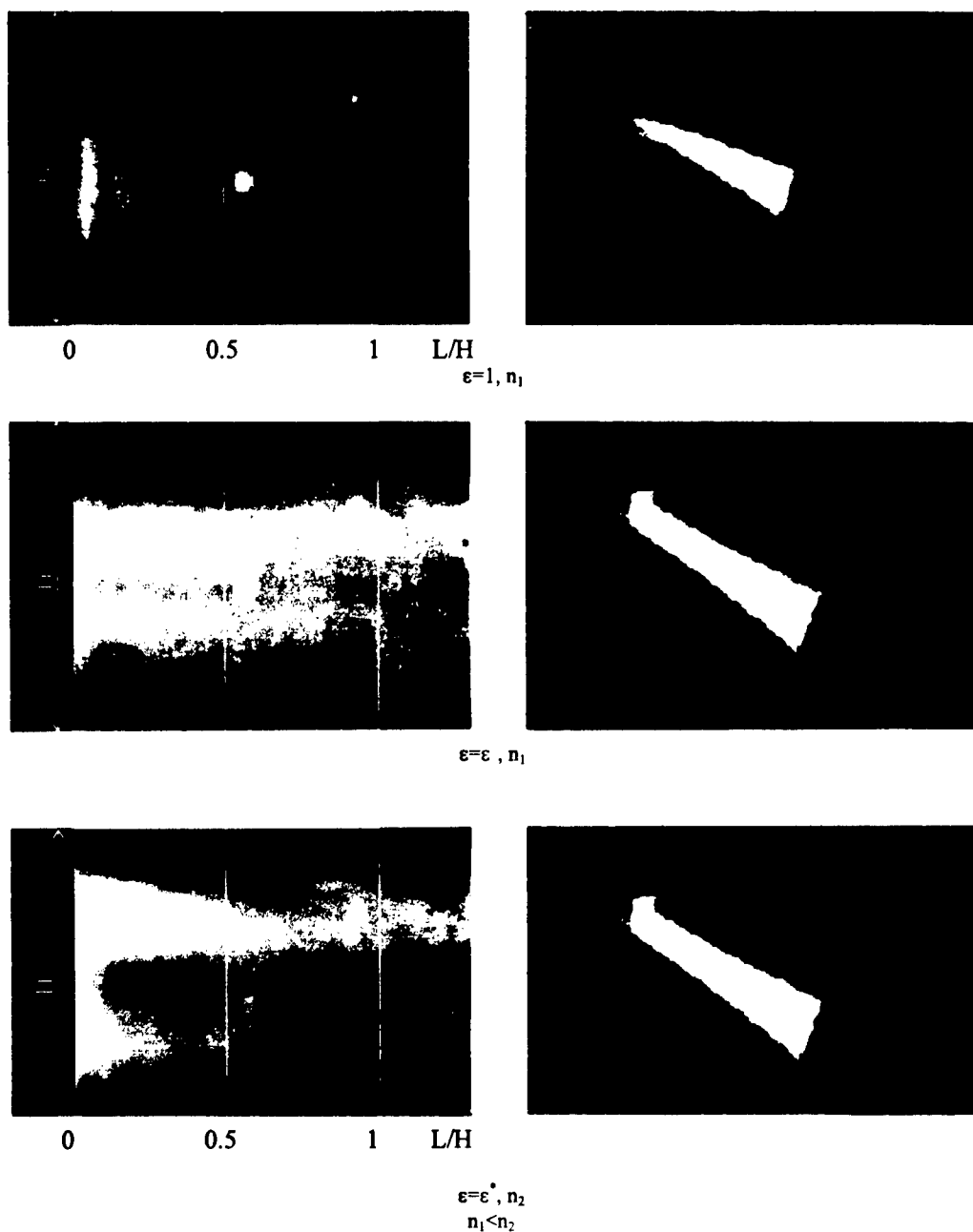


Fig. 4. OH^- radical emission registered by EOC at CC exit (left) and visual form of gas jet outflowing from CC (right) at supersonic combustion.

It is necessary to note, that during all experiments the stable self-ignition of hydrogen in co-current supersonic flow and realization of supersonic combustion regime in model Scramjet CC is observed.

The results of experimental researches described above allow to make conclusion, that the processes of supersonic jet mixing of and hydrogen burning in supersonic stream at use of elliptical injectors proceed more effectively, than with circular injectors, that confirms the results of calculations obtained earlier. The positive results of application of elliptical injectors are connected with injected jet split effect.

REFERENCES

1. V.Kopchenov, K.Lomkov. The Enhancement of Mixing and Combustion Processes Applied to Scramjet Engine. AIAA paper, 92-3428, 1992.
2. V.Kopchenov, K.Lomkov, S.Zaitsev, S.Borisov. AGARD LECTURE SERIES 194. Researches and Development Ram/Scramjet ant Turbojets in Russia, 1993.
3. V.Alexandrov, Yu. Mnatsakanyan, A.Panin, A.Prokhorov, A.Shutov. Experimental Investigation of Supersonic Jet Mixing by Using of Optical Methods in Appliance to Scramjet Combustor//Proceedings of Eighth International Conference on the Methods of Aerophysical Research, Novosibirsk, Sep.2-6, 1996- Novosibirsk,1996.- Pt. III., pp. 5-10.
4. V.Alexandrov, S.Belykh, G.Vedeshkin, A.Prokhorov. Investigation Laboratory of CIAM Research Test Centre to Test Large-Scale Propulsion System Models and Their Components for Aerospace Systems// Proceedings of Seventh International Conference on the Methods of Aerophysical Research, Novosibirsk, Aug.22-26, 1994-Novosibirsk 1994.- Pt. II., pp. 35-40.
5. R.Kurziner. Jet engines for large supersonic speeds of flight. Moscow, Engineering, 1989.
6. V.Alexandrov, M.Lepelletier, Yu. Mnatsakanyan, A.Prokhorov, M.Rene-Corail, A.Shutov. Experimental Investigation of Supersonic Elliptical Injectors in Appliance to Scramjet Combustor//Second International Aerospace Congress, Moscow, Russia, Sep. 1-5, 1997.

SUPPORT AND REALIZATION OF TESTS OF AXISYMMETRIC SCRAMJET ON TEST CELL C16VK CIAM RTC

V.Yu.Alexandrov, A.N.Prokhorov, A.S.Roudakov
Central Institute of Aviation Motors, Moscow, Russia

S.A.Belykh, G.K.Vedeshkin, A.A.Shutov, V.P.Yurin
Research Test Center of Central Institute of Aviation Motors, Moscow, Russia

J.Hicks
NASA Dryden Flight Research Center, Edwards, California

ABSTRACT

The questions of support and realization of tests of hydrogenous axisymmetric Scramjet in ground conditions are considered. The basic relations for calculation of component mass flowrates for fire heater work are presented. On the base of measurements of pressure and temperature the calculations of flow parameters at the aero-dynamic nozzle exit cross-section and along the duct of the engine are carried out. Calculations are conducted with taking into account the actual properties of gas (in view of reactions of dissociation and recombination) on the basis of simple methods.

1. INTRODUCTION

Activities on creation of Scramjet in CIAM are conducted already for more than 20 years [1]. One from priority places in these activities is occupied by experimental researches. The experimental researches are carried out as on small-size so on large-scale models, as in flight so in ground conditions. Under the contract between NASA and CIAM the fourth flight test of dual-mode axisymmetric Scramjet carried by Hypersonic Flying Laboratory (HFL) "Kholod" (CIAM) have successfully conducted in February, 1998[2]. As before, so after flight Scramjet tests the realization of ground Scramjet tests is necessary for confirmation of its characteristics, workability and for the better understanding of work process in the engine at Mach numbers corresponding to flight conditions. Therefore along with the flight tests, the ground tests of similar full-scale axisymmetric Scramjet were conducted on the C16VK test cell of CIAM RTC [3]. The analysis of the flight trajectory of HFL shows that the most critical parameter of simulation on ground benches is the total enthalpy (stagnation enthalpy) or total temperature (stagnation temperature) of flow depending on which of these parameters is simulated. At the testing of experimental object - axisymmetric Scramjet - on the C16VK test cell the fire heating of air is used. This allows to conduct tests with duration about 30 seconds. Total temperature of oxidizing mixture simulating hot air can be up to 2000K and total pressure (stagnation pressure) can be more than 6.0MPa. For realization of the fire heating on the C16VK test cell the methane is used which is burnt in oxygen-air mixture. In the oxidizing mixture simulating hot air the mass fraction of oxygen is kept equaled to mass fraction of oxygen in the air.

© V.Yu.Alexandrov, S.A.Belykh, J.W.Hicks, A.N.Prokhorov, A.S.Roudakov, A.A.Shutov, G.K.Vedeshkin, V.P.Yurin, 1998

Heater construction allows to apply hydrogen instead methane after new injectors and some other component manufacturing.

At the test cell working without experimental object Mach number at the aerodynamic nozzle exit cross-section equals to 5.96 in the flow core and the ram equals to 56.6 kPa.

During last years in CIAM the successful steps on the way of Scramjet experimental research are made. Solution of complex and many-sided problems of support and test of large-scale model engines have been found. One of the most significant lines is creation and initiation of high-power and well-equipped stand for test of Scramjet.

2. SUPPORT OF TESTS

2.1. TEST CELL

In CIAM the tests of Scramjet mainly are carried out on the CIAM RTC C16 complex of test cells [3]. This complex includes number of compactly located beds and experimental installations having the unified supply system of energy and working resources (Fig.1). The beds contain the installations for realization of researches in various fields of study of processes in engines of space systems. A series of small installations allow to operatively solve problems in research of working processes in combustion chambers of engines with the help of use small-size models of engines and their elements. Large beds are developed for researches of working processes in combustion chambers of large-scale experimental objects.

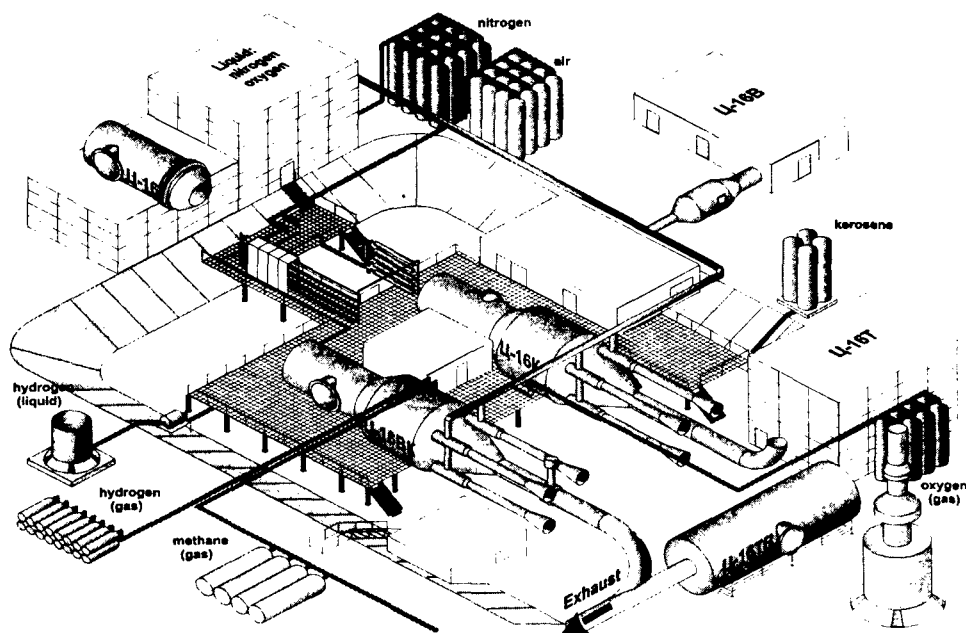


Fig.1. The scheme of C16 experimental complex.

The C16VK test cell is specialized for experimental researches of the characteristics of large-scale models of Scramjet and their elements in free jet with simulation of flight Mach numbers $M_F=4\div7$. The test cell represents pressurized thermo-baro-chamber (TBC) with the

built in gas-air contour (GAC), consisting of the aerodynamic nozzle ($D_{\text{exit}}=500\text{mm}$) and diffuser ($D_{\text{dif}}=700\text{mm}$). The C16VK test cell is equipped by the following systems:

- Supply of high pressure air ($P \leq 8\text{Mpa}$, $G \leq 15\text{kg/s}$);
- Combination of air heating - electrical heating ($T \leq 1000\text{K}$) and fire heating ($T \leq 2300\text{K}$);
- Exhaust system ($P \sim 1\text{kPa}$, $V \leq 600\text{m}^3/\text{s}$);
- Supply of gaseous combustible into an object ($P \leq 8\text{MPa}$, $G \leq 1.5\text{kg/s}$);
- Cryogenic cooling of object (consumption of a cooling agent $G \leq 3\text{kg/s}$);
- Automated system of control of technological process and regime of object test;
- Automated system of acquisition and processing of experimental data;
- Thrust measurement system ($F \leq 10\text{kN}$);
- Visualization of a flow at an inlet of object;
- System of passivation and fire extinguishing in TBC.

Before the initiation of tests of experimental object - axisymmetric Scramjet - the computational and experimental researches of test cell work with and without loading of the test cell diffuser by experimental object had been carried out on the reduced model of test cell.

Then activation of C16VK test cell without loading of the diffuser by Scramjet was performed. Simultaneously distributions of stagnation temperature and stagnation pressure behind a direct shock wave in the flow core at the exit cross-section of aerodynamic nozzle have been obtained (Fig 2). On the base of measurement data by the computational way with technique described below the distribution of Mach number M_c at nozzle exit was estimated. After the analysis of results the start-up of test cell with loading of its working part by axisymmetric Scramjet was realized.

2.2. TECHNIQUE OF MACH NUMBER ESTIMATION AT NOZZLE EXIT CROSS-SECTION

It is assumed that the structures (the contents in substance of mass fraction of elements: hydrogen, oxygen, nitrogen, carbon and argon) of components supplied into the fire heater are known. Temperature, pressure and mass flowrates of oxidizer and fuel are measured, so their enthalpies H_o^* and H_f^* , stoichiometry factor L_{fh} and oxidizer excess factor α_{fh} in the fire heater are consequently known. Assuming that heat leakage in the fire heater are negligible and combustion efficiency factor is $\eta \approx 1$, it is possible to record for a total enthalpy of a hot oxidizing mix which simulates hot air:

$$H_{mix}^* = \frac{\alpha_{fh} L_{fh}}{1 + \alpha_{fh} L_{fh}} H_o^* + \frac{1}{1 + \alpha_{fh} L_{fh}} H_f^*.$$

Measuring static pressure in the fire heater and calculating total pressure P^* from above equation total thermodynamic temperature of an oxidizing mixture in the fire heater T^* can be calculated.

For determination of flow parameter fields at the exit cross section of nozzle the measurements of total temperature $T^{*'}$ and total pressure $P^{*'}$ by combs behind a direct shock wave formed before probes were performed. For parameters of a flow before a direct shock wave (symbols without a stroke) and behind it (symbols with a stroke) the equations of conservation of mass flow, momentum, enthalpy and entropy are correct and have to solve

with taking into account actual properties of gas (i.e. reactions of a dissociation and recombination):

$$\begin{aligned} \frac{P}{RT} w &= \frac{P'}{R'T'} w', \\ P + \frac{P}{RT} w^2 &= P' + \frac{P'}{R'T'} w'^2, \\ H_{mix}^*(P^*, T^*) &= H_{mix}(P, T) + \frac{w^2}{2}, \\ S_{mix}^*(P^*, T^*) &= S_{mix}(P, T), \\ H_{mix}^*(P'^*, T'^*) &= H_{mix}(P', T') + \frac{w'^2}{2}, \\ S_{mix}^*(P'^*, T'^*) &= S_{mix}(P', T'). \end{aligned}$$

Solving equations of mass flow and momentum for speeds:

$$\begin{aligned} w^2 &= \frac{P' - P}{\frac{P}{RT} \left(1 - \frac{PR'T'}{P'RT} \right)}, \\ w'^2 &= \frac{P - P'}{\frac{P'}{R'T'} \left(1 - \frac{P'RT}{PR'T'} \right)} \end{aligned}$$

we obtain four equations of conservation of enthalpy and entropy for four unknown static parameters P, T, P', T' . As the results of calculations the distributions of Mach number M_c at the exit cross section of nozzle were resolved (Fig.2).

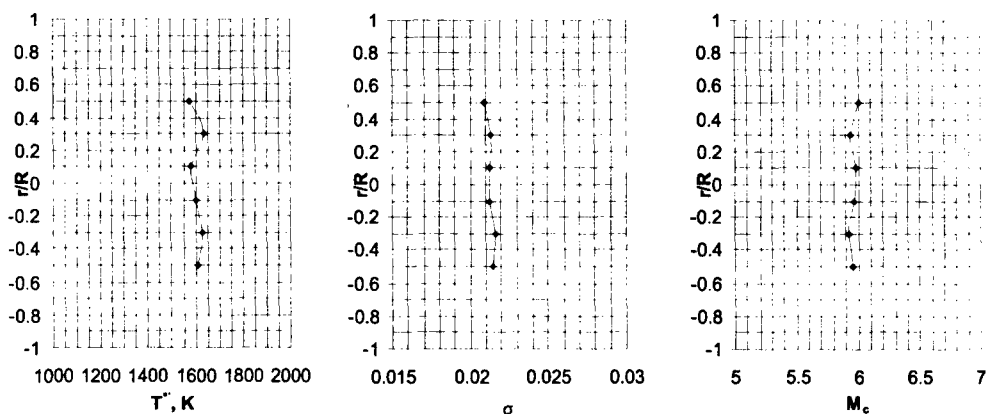


Fig.2. Distributions of Mach number M_c , total temperature T^* and pressure recovery factor $\sigma = \frac{P'^*}{P^*}$ in flow core at the exit cross section of aerodynamic nozzle ($R = D_{exit}/2 = 0.25\text{m}$).

In the same figure the distributions of total temperature $T^{*'}_0$ and pressure recovery factor $\sigma = P^{*'}_0 / P^*$ behind a direct shock wave are shown.

2.3. BASIC EXPRESSIONS FOR CALCULATION OF THE MASS FLOW OF COMPONENTS OF THE FIRE HEATER

At realization of Scramjet researches on ground beds it is necessary to simulate a flow of air with high total temperature. For providing high total temperature in flow core at testing of experimental object on C16VK test cell the fire heating of air was used. For estimation the fire heater operation regime to simulate hot air it is necessary to keep mass fraction of oxygen in oxidizing mixture replacing air equaled to mass fraction of oxygen in the air. For this purpose it is necessary to enrich oxidizing mixture by pure oxygen.

The elementary mass fraction composition of the air was admitted as follows:

- Mass share of oxygen: $G_O = 0.23174$;
- Mass share of nitrogen: $G_N = 0.75534$;
- Mass share of carbon: $G_C = 0.00012$;
- Mass share of argon: $G_{Ar} = 0.001280$.

If to designate the mass flowrates as:

- Air: G_{air} ;
- Oxygen: G_O ;
- Fuel: G_f ;

then the oxidizer excess factor in the fire heater will by definition be equal:

$$\alpha_{fh} = \frac{G_O + G_{air}}{L_{fh} G_f}$$

Where L_{fh} - stoichiometry coefficient for components in the fire heater. The factor L_{fh} can be expressed through stoichiometry factors for air L_{airf} and oxygen L_{of} in the fire heater for given combustible as follows:

$$L_{fh} = \frac{\frac{G_{air}}{L_{airf}} + \frac{G_O}{L_{of}}}{\frac{G_{air}}{L_{airf}} + \frac{G_O}{L_{of}}}$$

Substituting this expression into the formula for α_{fh} we receive:

$$\alpha_{fh} = \alpha_{of} + \frac{G_{air}}{G_f L_{airf}}$$

where

$$\alpha_{of} = \frac{G_o}{G_f L_{of}}$$

is the oxygen excess factor relating to combustible in the fire heater (or by other words - the factor of oxygen enrichment of oxidizing mixture simulating hot air).

Fuel supplied into the fire heater burns down as with oxygen contained in the air so with pure oxygen supplied for enrichment. For simplicity it is possible to assume that all fuel burns down only with pure oxygen. Thus the oxygen contained in the air does not participate in the burning. So the contents of oxygen in oxidizing mixture at the fire heater outlet g_{ofh} will be equal to the contents of oxygen in air g_o if at fuel burning down with pure oxygen in the formed products of combustion the contents of the remained oxygen g_{ores} will be equal to the contents of oxygen in the air (intermix of mixtures with an identical mass fraction of oxygen does not change this fraction in the formed mixture):

$$g_{ores} = \frac{G_{ores}}{G_f + G_o}$$

where G_{ores} - not burned down part of pure oxygen equaled:

$$G_{ores} = \alpha_{of} L_{of} G_f - L_{of} G_f$$

or

$$G_{ores} = G_o \frac{\alpha_{of} - 1}{\alpha_{of}} .$$

On the other hand the following ratio is obvious:

$$G_f + G_o = G_o \frac{\alpha_{of} L_{of} + 1}{\alpha_{of} L_{of}} .$$

Thus

$$g_{ores} = L_{of} \frac{\alpha_{of} - 1}{\alpha_{of} L_{of} + 1} .$$

Equating mass fractions of oxygen:

$$g_{ores} = g_o$$

we obtain

$$\alpha_{of} = \frac{L_{of} + g_o}{L_{of} (1 - g_o)} .$$

From last expression it is possible to conclude that for each particular kind of combustible there is certain value of factor α_{of} or, that is the same, certain ratio between the massflow of pure oxygen and combustible. In the table № 1 mentioned below the values of

stoichiometry factor L_{of} and oxygen excess factor in relation to combustible in the fire heater α_{of} for some characteristic types of combustibles are presented:

Table № 1

Type of combustible	Stoichiometry factor L_{of}	Factor α_{of}
Hydrogen	7.937	1.340
Methane	3.989	1.377
Kerosene	3.408	1.390

From above-stated it follows that stoichiometry factor L_{om} for oxidizing mixture prepared in the fire heater to simulate hot air, and stoichiometry factor L_{airp} for air in relation to combustible in the combustion chamber of tested object will be equaled (with accuracy determined by presence of carbon) if to maintain the appropriate values α_{of} .

$$L_{om} \approx L_{airp}$$

So the structure of an oxidizing mixture is governed by factor α_{of} , and temperature - by factor α_{fh} .

2.4. LAYOUT OF WORKING PART OF TEST CELL

Axisymmetric Scramjet was fixed to thrust measurement platform on special sting (Fig.3).

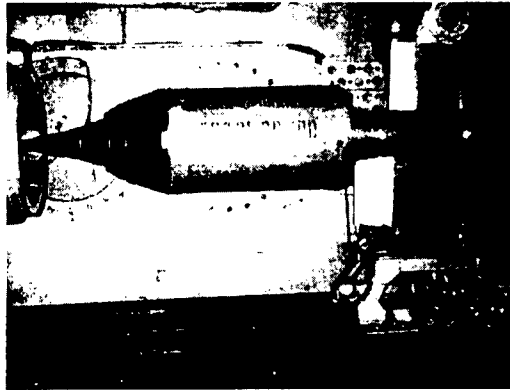


Fig.3. Sting of experimental object.

Sting is made as hollow pylon diametrically crossing GAC. Through the lower part of pylon combustible (gaseous hydrogen), gaseous nitrogen for passivation of cavities and cooling agent are supplied. Through the top of pylon the thermocouples, cable of power supply of ignition plug and pulse tubes are output. In the input part of the diffuser four pylons are made for prevention of essential deviation of the object from axis of the diffuser and destruction of sting. The layout scheme of GAC of test cell with the object placed into the working part is shown in Fig.4.

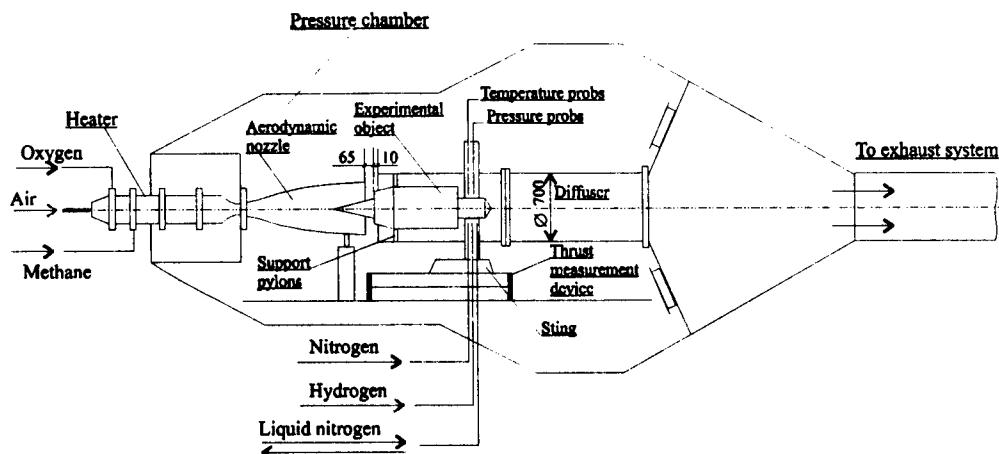


Fig.4. Layout of the working part of C16VK test cell.

3. REALIZATION OF TESTS

Test of axisymmetric Scramjet was conducted in two stages:

- First stage - without fuel (hydrogen) supply into the combustion chamber of the engine;

- Second stage - with fuel supply into the combustion chamber of the engine.

The parameters of flow core for both stages are approximately identical and equal:

- Total temperature $T^* = 1605K$;

- Total pressure $P^* = 5.1 MPa$;

- Mach number $M_e = 5.96$.

Such methodology of experiment realization has enabled, for the best understanding of working process in the engine, to determine and to compare the characteristics of the duct of axisymmetric Scramjet without the burning of hydrogen in the combustion chamber and with burning.

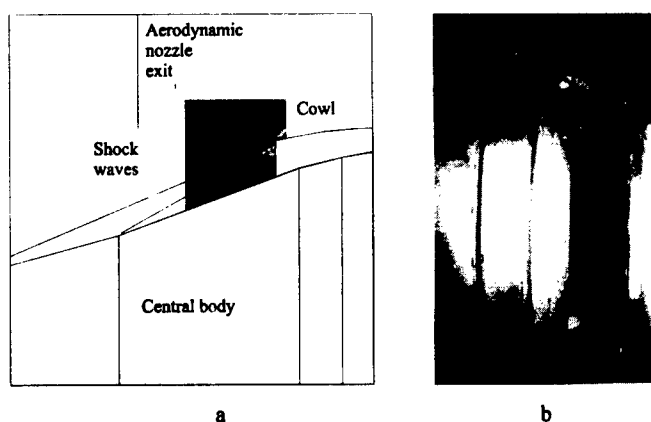


Fig.5. Position of shock waves at inlet of object (a), and outer view of object between nozzle exit and diffuser entrance

As on first, so on second stages of test the experimental object was cooled by nitrogen of low temperature 125 K.

The position of shock waves at inlet of object was observed with the help of schlieren device (Fig.5a). The outer view of object between nozzle exit and diffuser entrance was observed with the help of television camera (Fig.5b).

Control and synchronization of systems operation during realization of test were implemented under the test cell work cyclogramme. The registration of parameters during experiment was carried out by the automated measuring system.

At both test stages the pressures (Fig.6a) and temperatures along the duct walls and channels of cooling, force with which the object sting acts on the thrust measurement system are measured.

For understanding of processes taking place in the duct of the engine by use of pressure and temperature measurements the simple integral method of flow parameter calculation was applied with taking into account actual properties of gas (in view of reactions of a dissociation and recombination).

In each cross-section of the duct the equations of conservation of massflow and enthalpy (accounting heat runaway) were solved for static parameters of flow:

$$G_z = \frac{P w F}{RT},$$

$$H_m^* - Q = H(P, T) + \frac{w^2}{2}$$

where the values of:

G_z - total massflow through the engine,

F - cross-sectional area of the engine,

H_m^* - enthalpy of an entering flow,

Q - heat runaway into walls of cooling channels,

P - static pressure in cross-section,

assumed to be known in each cross-section under calculation. Expressing speed w through temperature T one equation for one unknown in each computational cross-section of the engine duct is obtained. The stagnation parameters in this cross-section were determined from equations of conservation of an enthalpy and entropy:

$$H_m^* - Q = H(P^*, T^*),$$

$$S(P, T) = S(P^*, T^*).$$

The control of correctness of obtained results was conducted in accordance with condition of decreasing of total pressure along the object duct or, by other words, in accordance with condition of entropy increase.

These calculations have allowed to estimate values of a pressure recovery factor σ (Fig.6b), current value of Mach number M_c (Fig.6c), and combustion efficiency factor η (Fig.6d).

The integral assessments have shown, that at both stages of tests the mode of supersonic flow in the intake of the object was realized. In the throat cross-section of the intake Mach number $M_{th}=2.6$ and value of recovery factor $\sigma=0.21$ were achieved.

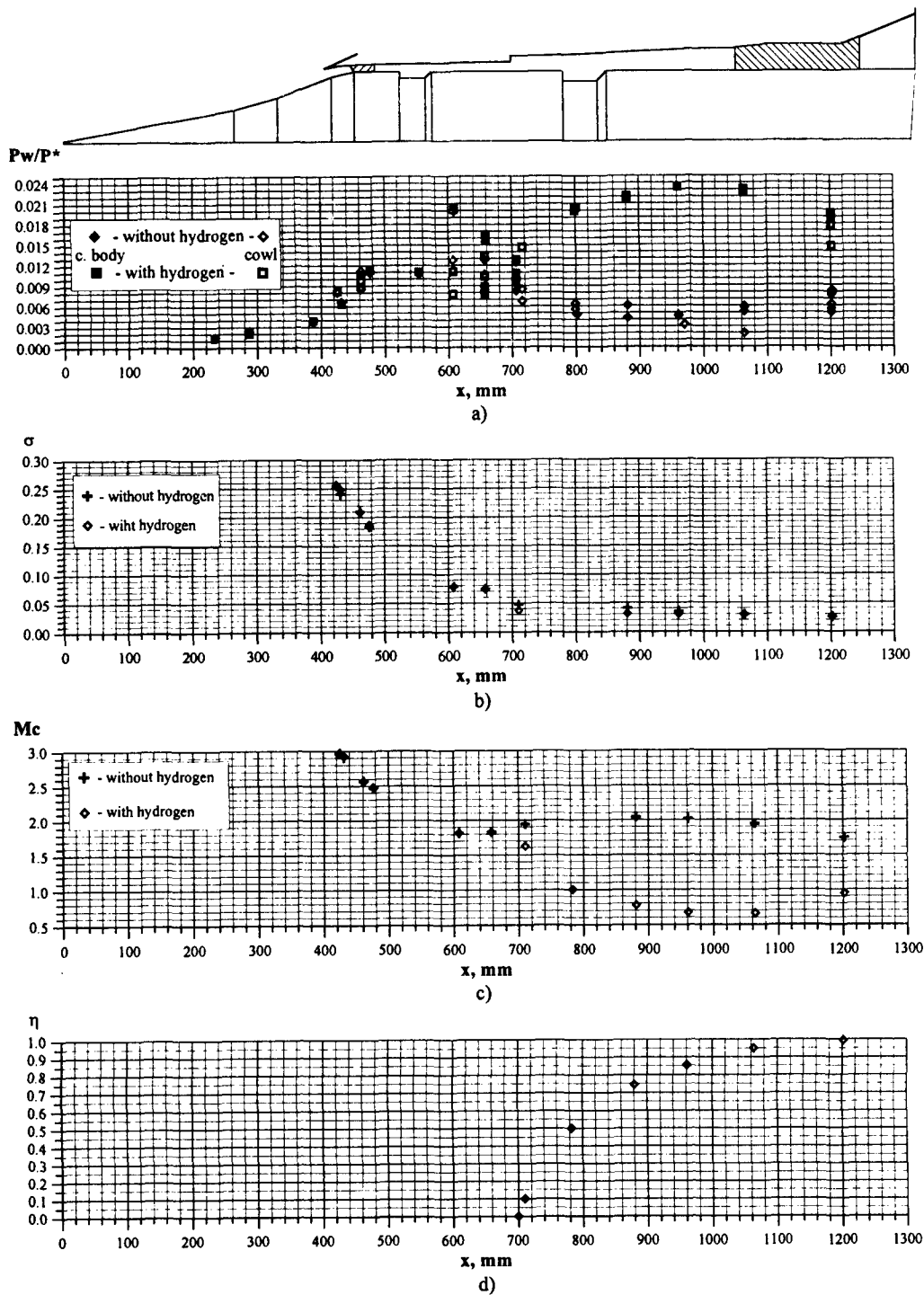


Fig.6. Pressure ratio on the duct walls (a), pressure recovery factor (b), Mach number (c), combustion efficiency factor (d) along the object duct.

At the second stage of tests at supply of the identical massflow of hydrogen in the second and third supply zone (Fig.6) the regime of supersonic combustion was realized from second up to third supply zone. Behind the third zone the flow, in average, became subsonic and the subsonic combustion was realized. At the entrance of the engine nozzle the flow reaches sound speed and Mach number $M_c > 1$ everywhere downstream of the nozzle. The oxidizer excess factor after the second zone was equaled $\alpha = 3.234$ and after third $\alpha = 1.617$. The combustion efficiency factor at supersonic combustion between the second and third zones by assessments is equal $\eta \approx 0.96$. It means that 0.96 part of hydrogen supplied into the second zone burns down before the third zone. The total combustion efficiency factor is equal by estimations $\eta \approx 0.99$. Such high value of combustion efficiency factor seems to be reached because of presence of subsonic combustion region.

It is necessary to note that the conducted analysis of experimental engine work is very rough and does not pretend on revelation of distinctive features of mixing and burning processes in the complicated supersonic spatial flow with subsonic regions.

4. CONCLUSION

The process of extrapolation of results of Scramjet ground tests on its flight characteristics is not simple as it is necessary to take into account differences of bed flow from real. To simulate all necessary parameters appropriate to flight conditions is impossible on a ground beds, nevertheless realization of tests on ground beds allows to receive a plenty of the valuable information. Under the contract between NASA and CIAM the support of ground tests of pilot sample of experimental object (Scramjet) was carried out. On C16VK test cell of CIAM RTC the tests of full-scale axisymmetric Scramjet with simulation of flight Mach number $M \approx 6$ were carried out. The results of researches shown that along the channel of the combustion chamber of experimental object the burning are realized as in supersonic so in subsonic flow. At this the combustion efficiency factor in experimental object reaches rather high value as in the zone of subsonic combustion $\eta \approx 0.99$, so in the zone of supersonic combustion $\eta \approx 0.96$.

It is planed to continue tests of axisymmetric Scramjet at various values of air excess factor in combustor and Mach numbers at intake inlet.

REFERENCES

1. A.S.Roudakov. Some Problems of Scramjet Propulsion for Aerospace Planes. Part II - Scramjet: Development and Test Problems. AGARD-LS-194, 1993.
2. J.W.Hicks, A.S.Roudakov, V.L.Semenov. Recent Flight Test Results of the Joint CIAM-NASA Mach 6.5 Scramjet Flight Program. NASA/TP-1998-206548, April 1998.
3. V.Yu.Alexandrov, S.A.Belykh, A.N.Prokhorov, G.K.Vedeshkin. Investigation Laboratory of CIAM Research Test Center to Test Large-Scale Propulsion System Models and Their Components for Aerospace Systems// Proceedings of Seventh International Conference on the Methods of Aerophysical Research, Novosibirsk, Aug. 22-26, 1994.-Novosibirsk 1994. - Pt. II, pp. 35-40.
4. V.Yu.Alexandrov, A.N.Prokhorov, A.S.Roudakov. Capabilities of Flight Conditions Simulation on Ground Test Facilities//Proceedings of Seventh International Conference on the Methods of Aerophysical Research, Novosibirsk, Aug. 22-26, 1994.-Novosibirsk 1994. - Pt. I, pp. 9-17.

A STUDY OF SUPERSONIC AIR JETS EXHAUSTED FROM A RECTANGULAR NOZZLE

A.P. Alkhimov, S.V. Klinkov, and V.F. Kosarev

Institute of Theoretical and Applied Mechanics SB RAS,
630090, Novosibirsk, Russia

Unusual nozzle shapes used in cold gasdynamic spraying is the reason for formation of jets that differ considerably from well-known axisymmetric or plane jets with a uniform distribution of gas parameters at the nozzle exit. In practice, it is often necessary to evaluate a possible use of this or that nozzle for successful spraying. One of the comparative aspects for these nozzles is a set of characteristics of the jets exhausted from a certain nozzle. Thus, we performed experiments with jets whose characteristics were similar to those of jets used for spraying.

Since the axial velocity of the gas rapidly decreases behind the potential core, the initial supersonic portion of the jet is of major interest for spraying practice. In a number of practical applications it is necessary to vary the spraying distance, and a question then arises in what limits we can do this without substantial distortion of the spraying process and changes in coating properties. To answer this question, we had to study the supersonic portion of the jets.

It is known from [1 - 3] that the profiles of velocity (v) and dynamic pressure ($p v^2$) are self-similar at the initial and basic portions of the jet. It is convenient to represent the dynamic pressure in the form $\gamma p M^2$, which leads to self-similarity of M^2 profiles in an isobaric flow. Note that we can find approximation formulas for velocity profiles in the literature, whereas there are certain difficulties in finding formulas for M^2 profiles. Meanwhile, it is more convenient to use the Mach number as an experimental parameter, because to determine it we have to know only the pressure field, but not the temperature. Besides, it is more convenient to write the conservation law for momentum difference in terms of the Mach number. Thus, one of the objectives of the present study was to verify self-similarity of M^2 profiles and find an approximating function for them.

The M^2 profiles were reconstructed from experimentally obtained profiles of static (p) and dynamic (p_0') pressures. The data obtained when studying the jets with different initial (denoted by *) parameters ($h = 1 - 4.5$ mm; $H/h = 2.7 - 8$; $M_* = 1.85 - 3.1$; $T_{0*} = 300 - 600$ K, where h and H are the small and large transverse dimensions of the jet at the nozzle exit) and plotted in coordinates $(M/M_m)^2$, x/δ_M fit a single curve. With an insignificant scatter, this curve can be represented by the function of the form

$$\varphi_M = \exp\left(-\left(0.83 \frac{x}{\delta_M}\right)^2\right)$$

(see Fig. 1) where δ_M is the jet thickness along its smaller size (in the x -direction) determined as the distance from the jet axis to the point where $M^2(\delta_M) = 0.5 M_m^2$.

It is worth noting that the stagnation temperature (T_0) and the jet pressure ratio (n) in the examined ranges ($T_0 = 300 - 600$ K, $n = 0.5 - 1$) do not exert a substantial effect on the M^2 profile.

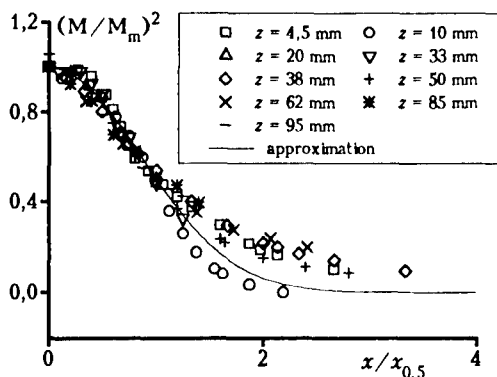


Fig. 1. Normalized M^2 profiles for an overexpanded jet exhausted from the nozzle with $h = 4.5$, $H/h = 2.7$, $M_* = 3.1$.

It is known from the jet theory that the profiles of stagnation temperature difference ($\Delta T_0 = T_0 - T_a$) are also self-similar allowing for the relationship

$$(T_0 - T_a) / (T_{0m} - T_a) = \Delta T_0 / \Delta T_{0m} = (v/v_m)^\sigma,$$

where $\sigma = 0.5$ for plane jets, $\sigma = 0.75$ for axisymmetric jets, v is the gas velocity, T_a is the ambient temperature. Assuming the profiles to be described by functions of the same form, we can obtain the relation between the velocity profile thickness (δ_v) and the temperature profile thickness (δ_T)

$$\delta_v = \delta_T \sqrt{\sigma}.$$

We performed a series of experiments to verify self-similarity, obtain an approximating function for the profiles of stagnation temperature difference, and find the relation between the thicknesses of M^2 and ΔT_0 profiles. Stagnation temperature was measured by a hot-wire probe on the basis of thermocouple. The profiles constructed in coordinates $\Delta T_0 / \Delta T_{0m}$, x / δ_T fit the curve

$$\varphi_T = \exp\left(-\left(0.83 \frac{x}{\delta_T}\right)^2\right)$$

with a small scatter (see Fig. 2).

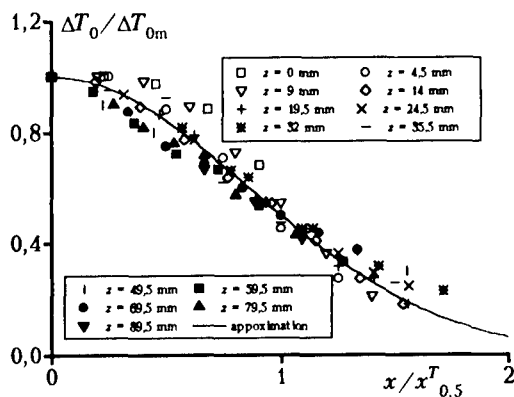


Fig. 2. Normalized profiles of stagnation temperature difference in an overexpanded jet exhausted from the nozzle with $h = 4.5$, $H/h = 2.7$, $M = 3.1$.

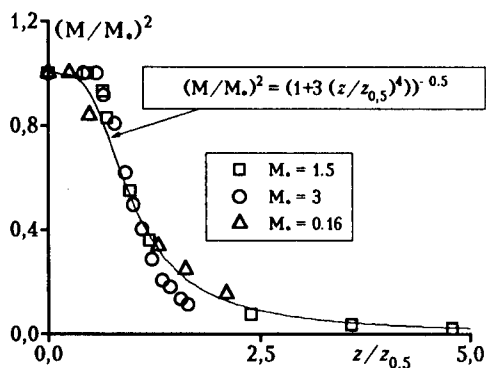


Fig. 3. Generalized dependence for distribution of axial values of M^2 versus the longitudinal coordinate from [2].

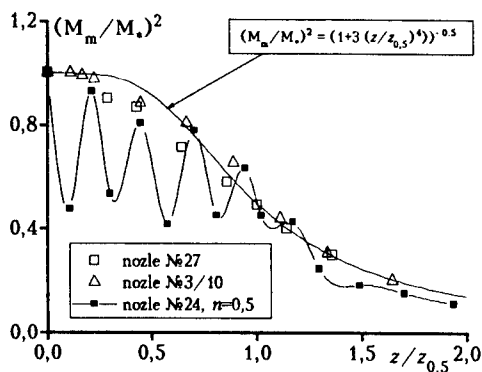


Fig. 4. Generalized dependence for distribution of axial values of M^2 versus the longitudinal coordinate.

The experimentally found ratio δ_T/δ_M for the examined range of parameters is close to 2.

One of the problems of jet theory is the finding of the axial values of parameters denoted here by the subscript m . The patching of two solutions for the initial and basic parts of the jet is used in [1], an inflection being observed at the point of patching (transitional region of the jet), which was not obtained in our experiments. We made an attempt to find a smooth approximating function in the transitional region. Figure 3 shows the data borrowed from [2], and similar data obtained in our experiments are presented in Fig. 4.

It is seen that all data lie on a single curve of the form

$$\left(\frac{M_m}{M_*}\right)^2 = \left(1 + 3\left(\frac{z}{z_{0.5}^M}\right)^4\right)^{-0.5},$$

where z is the longitudinal coordinate in the jet, $z_{0.5}^M$ is the coordinate where $M_m^2(z_{0.5}^M) = 0.5M_*^2$.

The largest deviation from the above curve is observed for data obtained for an overexpanded jet, though even in this case the upper peaks lie on this curve, whereas the lower peaks for $z/z_{0.5}^M < 1$ lie approximately at the same level. It should be noted that this function is also asymptotically valid, since according to the momentum conservation equation for axisymmetric jets (as at large distances all jets can be treated as axisymmetric) $M_m^2 \sim 1/z^2$.

It can be shown that for moderate heating of jets the relation between the axial stagnation temperature difference and the axial value of M^2 should be close to the form

$$\Delta T_{0m}/\Delta T_{0*} = (M_m^2/M_*^2)^{0.25}.$$

We used it to find the distribution function of the axial values of stagnation temperature difference. A comparison with experimental data allows us to write it in the form (Fig. 5)

$$\Delta T_{0m} = \Delta T_{0*} / \left(1 + (2^8 - 1)\bar{z}^4\right)^{1/8}$$

$$\bar{z} = z/z_{0.5}^T, \quad z_{0.5}^T \approx 2z_{0.5}^M.$$

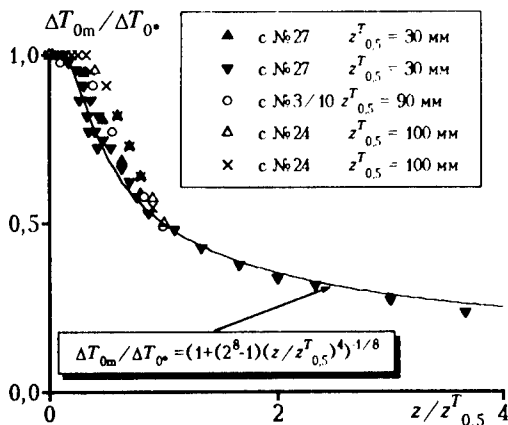


Fig. 5 Generalized dependence of normalized stagnation temperature difference versus the longitudinal coordinate.

The relation $z_{0.5}^T / z_{0.5}^M$ obtained experimentally for three jets is roughly equal to 2.

One of important problems of jet theory is the determination of the jet thickness as a function of the longitudinal coordinate. It is known from the literature that a linear increase in thickness is observed both in the initial and basic regions of the jet, though with different proportionality coefficients [2]. Thus, there is a transitional region in which the thickness growth is determined by a nonlinear function. Since we study the jets exhausted with a nonuniform initial profile because of a noticeable boundary layer on the nozzle walls, it should be expected that the potential core region is weakly expressed, thus, the entire region under study can be treated as a transitional one, and the jet thickness can be approximated by a nonlinear function. Assuming the jet to be plane, i.e., ignoring its expansion in the larger size direction, we can find the relationship between the jet thickness and the axial value of M^2 from the momentum conservation equation and obtain the formula

$$\delta_x = h \left(1 + 3 \left(z / z_{0.5}^M \right)^4 \right)^{0.5}.$$

If we assume that the jet expansion along the larger size is exactly the same as along the smaller size (quasi-axisymmetric case), i.e., $\delta_y / \delta_x = H / h$ (δ_y is the jet thickness along the larger size), and use the relation

$$\left(M / M_m \right)^2 = \exp \left(- \left(0.83 x / \delta_x \right)^2 \right) \exp \left(- \left(0.83 y / \delta_y \right)^2 \right),$$

we obtain

$$\delta_x = h \left(1 + 3 \left(z / z_{0.5}^M \right)^4 \right)^{0.25}.$$

Experimental data permit obtaining a more accurate curve (Fig. 6)

$$\delta_x = 0.75h \left(1 + 3 \left(z / z_{0.5}^M \right)^4 \right)^{0.4}$$

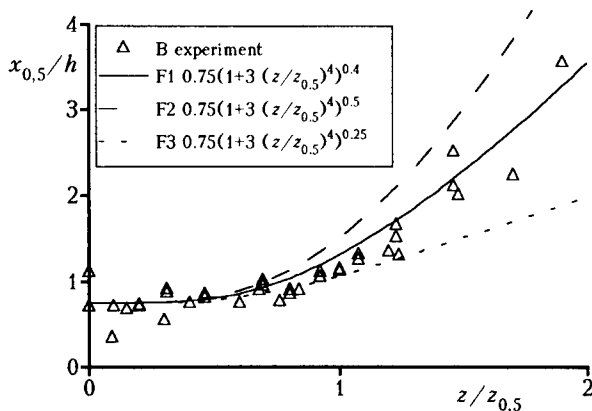


Fig. 6. Generalized dependence of jet thickness versus the longitudinal coordinate.

Thus, as it should be expected, the examined jets cannot be classified as either plane or quasi-axisymmetric.

Of certain interest is the consideration of the periodic structure of an off-design jet as a function of the jet pressure ratio. It is convenient to use the distance between the nozzle exit and the shock wave as a characteristic length. According to the literature, this distance at large pressure ratios ($n \gg 1$) is proportional to $n^{0.5}$. Schlieren pictures of the jet were obtained. An example is shown in Fig. 7 for a jet exhausted from the nozzle with $h = 3$ mm, $H/h = 3.3$, $M_* = 1.5$ for different jet pressure ratios.

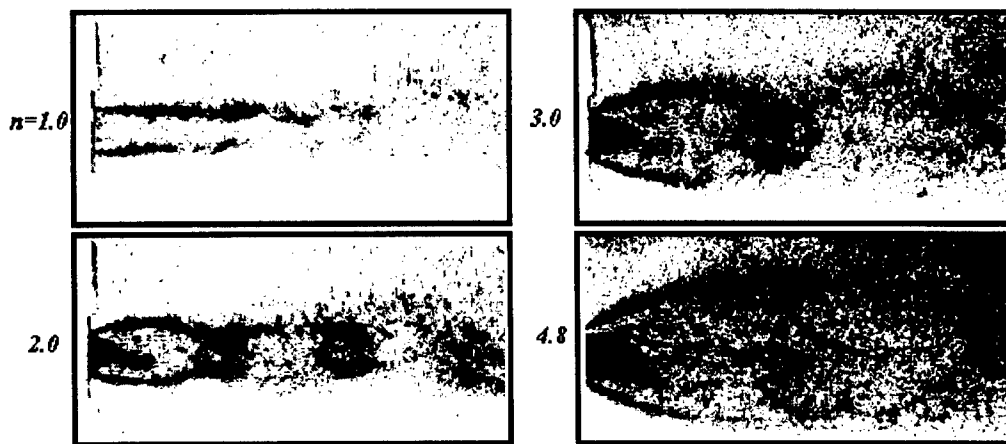


Fig. 7. Schlieren pictures of the jet exhausted from the nozzle with $h = 3$ mm, $H/h = 3.3$, $M_* = 1.5$ for different jet pressure ratios.

An analysis of obtained photos confirmed the proportionality to $n^{0.5}$. It is seen that a parabolic shock originates at $n \sim 2.5$, which becomes normal at $n \sim 4.5 - 4.8$. The absence of barrel shocks typical of the triple Mach configuration is also evident. It should be noted that the normal shock arises at considerably higher jet pressure ratios than in the case of axisymmetric jets ($n \approx 1.5$ [5]).

It is known that the number of jet barrels decreases as the jet pressure ratio increases, which is due to faster equalization of pressure. Therefore, it was necessary to find the jet pressure ratio influence on gas parameters far from the initial region, when the pressure already

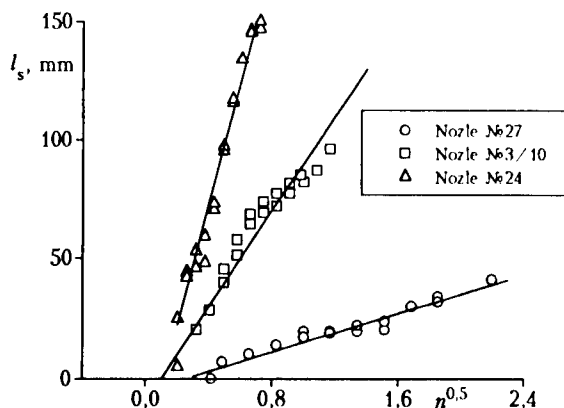


Fig. 8. The length of the supersonic region of the jet versus the jet pressure ratio $n^{0.5}$.

equals the ambient value. This can be done by studying the length of the supersonic part of the jet (l_s), since it was experimentally found that the jet flow achieves the speed of sound already in regions where the atmospheric pressure prevails. It is seen from Fig. 8, which illustrates this fact, that the same law of proportionality to $n^{0.5}$ holds true within a reasonable error.

The performed study verified the self-similarity of the profiles of M^2 , ΔT_0 , and v . The region of self-similarity begins at a certain distance from the nozzle exit and extends downstream without any limitations. The transition through the sonic lines does not have any effect on the profiles of parameters. Because of a considerable thickness of the boundary layer formed at the nozzle walls, the initial profiles can be hardly distinguished from self-similar ones. On these grounds, the region of self-similarity can be extended to the entire jet beginning from the nozzle exit.

It was found in the present study that the initial nonuniformity of gas parameters at the nozzle exit leads to a more smooth transition from initial to basic region of the jet in the longitudinal distribution of M^2 . The measurements of the jet thickness growth showed that the growth observed in experiments is smaller than the growth predicted for a plane jet, which is apparently explained by tip effects arising in jets with a finite ratio of dimensions. The length of an element of the periodic structure of the jet and the length of the supersonic portion of the jet were found to depend on the jet pressure ratio as \sqrt{n} , which was experimentally validated for examined jets.

REFERENCES

1. A.S.Ginevsky. Turbulent Jet and Wake Theory. Integral Methods of Calculation. Moscow: Mashinostroenie, 1969.
2. G.N.Abramovich. Turbulent Jet Theory. Moscow: Nauka, 1984.
3. L.A.Vulis and V.P.Kashkarov. Viscous Jet Theory. Moscow: Nauka, 1965.
4. G.N.Abramovich. Applied Gas Dynamics: Moscow: Nauka, 1991.
5. V.S.Avduevsky, E.A.Ashratov, A.V.Ivanov, and U.G.Pirumov. Supersonic Nonisobaric Gas Jets. Moscow: Mashinostroenie, 1985.

AERODYNAMICS AND HEAT TRANSFER IN A DISK ROTOR MACHINE WITH TANGENTIAL INPUT AND OUTPUT OF THE WORKING BODY

V.K. Baev, A.V. Nikulinskih, A.V. Potapkin, A.D. Frolov, and V.N. Yakovlev

Institute of Theoretical and Applied Mechanics SB RAS,
630090, Novosibirsk, Russia

INTRODUCTION

Disk rotor machines with tangential input and output of the working body are friction machines. They have attractive constructive and exploitation features, such as low noise and arrangement convenience. Besides, they allow for simple combining of two and more functions in one machines, which finally makes the use of such machines effective and rational.

To determine the areas of their rational use, it is necessary to study and describe the characteristics of friction machines from the viewpoint of processes that determine their functional purpose.

The results of the study of aerodynamic characteristics and heat transfer in the simplest machine, disk fan, are presented in the paper.

FLOW PATTERNS

New knowledge of the qualitative features of the flow was obtained on the basis of experimental research of the simplest disk fan models (Figs. 1 and 2) by the methods of flow visualization and velocity measurements in the channel with varied geometric parameters.

Among the most typical features, the following effects should be noted:

- low-frequency oscillations of the flow near the free rotor;
- asymmetry of flow distribution with symmetric geometry in the counter-stream pattern;
- possibility of changing the direction of this asymmetry under a certain action with preserved stability of the new flow regime (the "trigger" character of the flow) in geometrically symmetric configurations.

The features related to flow stability are of interest by themselves and, apparently, required special study.

Experimental results presented below were obtained for stable flow patterns around the configuration shown in Fig. 2.

AERODYNAMICAL CHARACTERISTICS

Analytical functions for the input-output characteristics of the fan were obtained by considering the system of conservation equations using the following assumptions:

1. the driving force is the gas friction force between the disks, which is determined as friction in a plane channel from the relative velocity;
2. the flow reconstruction occurs at the disk rotor entrance: a uniform flow with velocity U becomes nonuniform, and a circulation zone is formed, the static pressure at the front boundary of this zone being equal to the pressure in the frozen entrance flow.

To make the illustration clearer, the notation of characteristic quantities is shown in Figs. 1a and 2 for a counter-stream pattern.

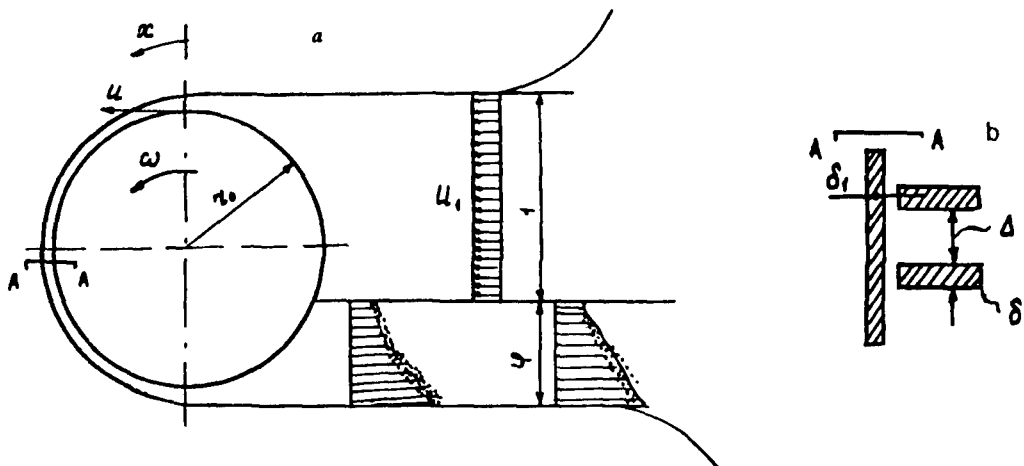


Fig. 1

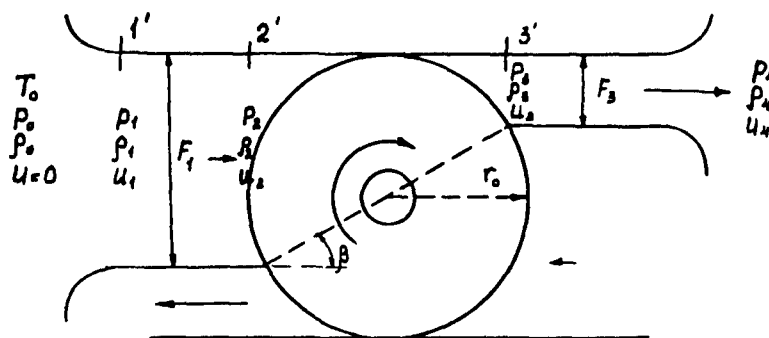


Fig. 2

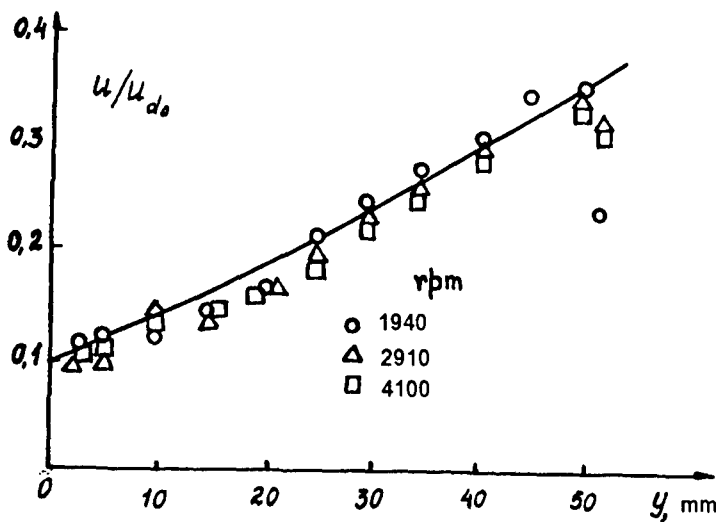


Fig. 3

As a result, a relation for velocity distribution along the radius in the exit cross-section was obtained for this physical model:

$$\bar{u} = \frac{\bar{r}}{1 + \sqrt{\frac{2\Delta}{\lambda\Omega\bar{r}}}} \quad (1)$$

where \bar{r} is the ratio of radius to the disk radius r_0 , $\bar{\Delta}$ – is the ratio of the distance between the disks to r_0 , λ – is the friction coefficient in the channel, Ω – is the flow turning angle in the fan, \bar{u} – is the ratio of velocity at the radius r to the maximum tangential velocity of the disk U_d .

Equation (1) denotes the existence of a universal law of velocity distribution at the exit, irrespective of partition position, i.e., φ .

This allows us to derive from (1) an equation for the mean relative flow velocity at the exit versus the geometric parameter φ and obtain an equation for the relative flow rate.

Internal losses due to friction on the side walls and cowl, losses at the rotor entrance and exit due to variation of its cross-section, and additional losses in the network are taken into account by introducing appropriate friction coefficients related to the mean velocity at the exit.

As a result, the formula for the relative flow rate has the following form:

$$\bar{G} = \frac{1}{1+k} \frac{\varphi_1}{\sqrt{1 + \frac{\xi_{BH} + \xi_c}{1+\varphi}}} \sqrt{\frac{\varphi}{r}} \quad (2)$$

Here $k = \sqrt{\frac{2\bar{\Delta}}{\lambda\Omega}}$, $\varphi_1 = \Delta/(\Delta + \delta)$, ξ_c is the friction coefficient of the network, \bar{G} is the ratio of the real flow rate to $G_0 = \rho_0 u_0$.

The internal friction coefficient can be determined by considering the conditions of relative motion of the disks, gas, and cowl (see Fig. 1a). It can be presented in the following form:

$$\xi_{BH} = \left\{ 1,5(1-\varphi_1) + \frac{\lambda_c}{\lambda} \frac{3,34\bar{\Delta}}{k^2} \frac{1}{1-6,7\delta_1} \left[\frac{1-\varphi_1}{\varphi_1} (1-k)^2 + 1 \right] \right\} \frac{\varphi_1^2}{2\varphi} \quad (3)$$

In (3), λ_c – is the friction coefficient on the wall, λ – is the friction coefficient on the disks.

Experimental studies were performed in the range of parameters: $r_0 = 80 - 100 \text{ mm}$, $n = 1940 - 4100$, $\varphi = 0,12 - 0,31$, $\bar{\Delta} = 0,03 - 0,08$, $\delta = 0,006 - 0,006$.

Figure 3 shows qualitatively the topology of experimental points with respect to the curve calculated from (1). As an example, a comparison of experimental data for $\bar{\Delta} = 0,0425$ with the data calculated from (2) and (3) for $\lambda_c/\lambda = 1-3$ is presented in Fig. 4.

Obviously, the best agreement is observed for $\lambda_c/\lambda = 2,5$, which testifies to a particular flow character near the cowl, with an elevated friction coefficient and, hence, heat-transfer coefficient.

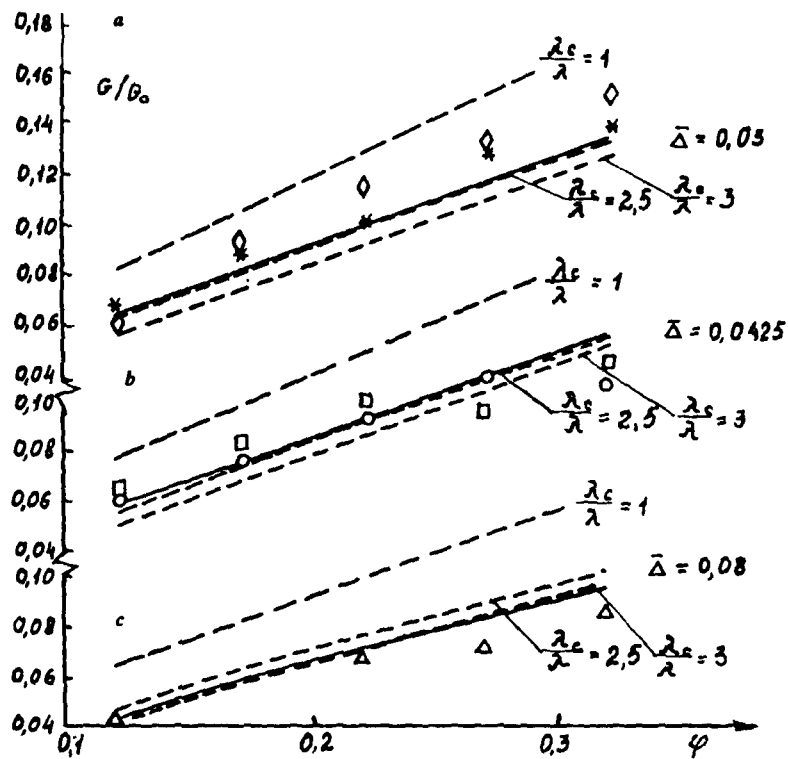


Fig. 4

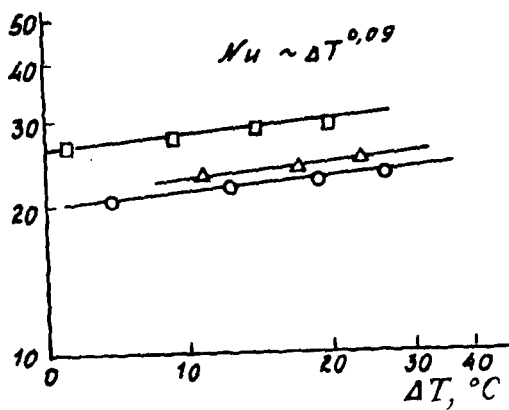


Fig. 5

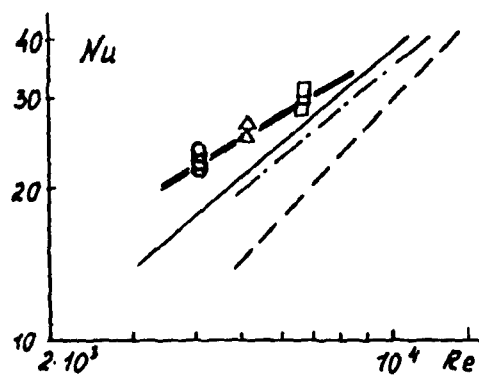


Fig. 6

— $Nu = 0.023 Re$
 — Data from [1]

HEAT TRANSFER ON THE EXTERNAL COWL

The latter circumstance, noted above, stimulated an experimental study of heat transfer on the cowl and constructing of the physical picture of the process.

The basic idea was an assumption about the emergence of secondary flows in the form of vortex structures arising because of velocity difference between the disk and the gas, and between the gas and the cowl. The curvature of averaged streamlines gives rise to centrifugal acceleration. Because of density difference due to heat exchange with the wall, this, in turn, should lead to additional amplification of heat transfer phenomena in the radial direction.

The results of the study of local and mean heat-transfer coefficients over the cowl surface validated the expected effects.

The experiments were performed using ribbon-type copper electric heaters, acting simultaneously as friction thermometers. The heaters were fabricated using the technology of manufacturing the printed circuit boards on foiled glass-cloth-based laminate.

The results are presented in Figs. 5 and 6.

Figure 5 illustrates the distribution of the heat-transfer coefficient along the x coordinate (see Fig. 2) for two values of temperature difference between the wall and the air.

The heat-transfer coefficient depends on the temperature difference approximately to the power 0.1, which corresponds to the value for natural convection [2].

Figure 6 shows the criterially-treated data in comparison with similar dependences for various regenerator packings, which are borrowed from [1].

The data presented show that the heat exchanger on the basis of disk fan has obvious advantages for $Re < 8000$.

Thus, the conducted analytical simulation of aerodynamics, internal losses and flow rate characteristics of disk fans and experimental studies that validated the credibility of the model and parameters calculated on its basis show that it is possible to develop effective multi-functional devices on the basis of disk rotor friction machines.

REFERENCES

1. Kutateladze S.S. and Boreshansky V.N. Handbook on Heat Transfer / Ed. S.I. Mochan. — Leningrad – Moscow: Gosenergoizdat, 1968.
2. Kutateladze S.S. Fundamentals of Heat Transfer Theory. — Moscow: Mashgiz, 1962.

CREATION OF CONTROL FORCES ON THE VEHICLE SURFACE BY THE EXTERNAL BURNING

V.K. Baev, A.F. Garanin, P.K. Tretyakov
Institute of Theoretical and Applied Mechanics SB RAS
630090, Novosibirsk, Russia

Attractiveness of the external burning schemes for the creation of lifting force and the vehicles thrust is the relative simplicity of the constructive realization and the possibility of eliminating of the thermal flame influence at the vehicle surface.

Effectiveness of the external burning for the control moments and forces creation was estimated in the series of the theoretical and experimental investigations (for example [1]).

W.C. Strahle in [2] showed theoretically, that by the method of the heat addition zone influence, realized in the inviscous flow, on the base region it is possibly the base pressure increase to the value, exceeding the free stream static pressure.

A.G. Prudnicov offered the idea of the burning organization above the vehicle surface and showed, that this process could be more effective, than the burning process directly in the boundary layer of the vehicle surface. V.K. Baev estimated the maximum impulses values from the external burning, supposing, that the burning is the instant combustion and then it is the adiabatic expansion in the transverse direction [3]. It is showed, that than the greater the flow mass is subjected to the influence, the greater the specific impulse.

The principal feature of the external burning organization with the fuel injection from a surface, how it is noted in [1], is that the supposed maximum normal pressure coefficient shall be equal nearly to the pressure coefficient in the boundary layer separation region. In ITAM Siberian Branch RAS were realized the tunnel experiments about the influence of the burning process, realized out the boundary layer, at the pressure distribution on the plate surface. In those experiments the hydrogen was used in the capacity of the fuel.

Investigation was realized in the wind tunnel with the working section size $200 \times 200 \text{ mm}^2$ at the free stream Mach number $M_\infty = 2.05$, the total pressure $P_0 = 320 \text{ kPa}$, the stagnation temperature $T_0 = (280-300) \text{ K}$ and the Reynolds number $Re = 38.6 \times 10^6$ with the characteristic size $L = 1 \text{ m}$.

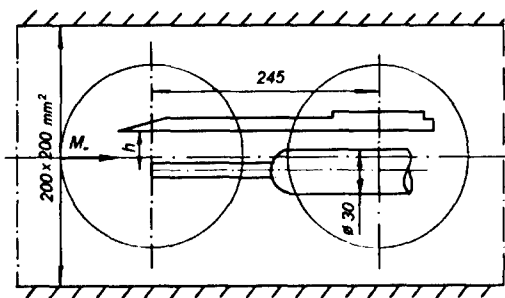


Fig.1. Scheme of the model installation in the tunnel with the hydrogen burning above the plate.

The model was the plate with the sharp front edge and the burner arrangement placed over it. The plate of the size $200 \times 310 \text{ mm}^2$ supported at the lateral side of the tunnel and was installed at the zero angle of a slope. The burner arrangement was the body with advancing from it tube with diameter 61 mm, from which the hydrogen is injected towards the free stream air. This arrangement was supported at the coordinate device (Fig.1). For the pressure measurement

on the plate surface there were 15 drain orifices on the plate length and 8 orifices in the transverse direction. The ignition of hydrogen was made with the special sparking plug.

Schlieren photograph, illustrating the stream picture and the interaction structure of the flame with the plate surface is showed in Fig. 2. It should be noted, that the flame stabilized by the separated zone, arising at the contrary hydrogen jet interaction with the free stream air. The flame expansion halfangle is the value $\beta = (14-15)^\circ$. The head conic shock, reflecting from the plate surface, interferences with the flame, and its configuration changes. The flame does not contacts the plate surface and its heating is possible only by the radiant heat stream. The flame interaction with the plate surface conforms to the pressure distribution (Fig. 3). The maximum pressure value ($P_{\max} = 2.5P_\infty$) does not depend practically from the location height of the hydrogen ejecting arrangement above the plate surface (in the range heights that took place in the experiment). The smooth pressure increasing, possibly, is the reason of the absence of the boundary layer separation on the surface and the pressure exceeding the value of the critic separate pressure, that equals approximately $P_{cr} = 2.0P_\infty$. The second pressure increase on the surface, possibly, was caused by the geometric forms of the hydrogen ejecting arrangement. It should be noted, that the stable burning was realized in the narrow range of the hydrogen flow rates, restricted by the flame-out ($G = 3.4$ g/s), on the one hand, and the heat chocking of the tunnel ($G > 4$ g/s), on the other hand. Therefore, the influence of the tunnel walls at the burning intensity is possible. Specially realized investigation [4] of the external disturbances influence at the burning process of the contrary hydrogen jet showed, that the flame expansion angle and, consequently, the burning intensity depends on the wave influences. In the transverse plate direction the increased pressure region is restricted by the intersection line of the head shock surface with the plate (Fig. 4).



Fig. 2. Schlieren photograph of the stream structure above the plate with the hydrogen burning above it: $M = 2.05$, $h = 45$ mm, $G = 3.8$ g/s (1.3%).

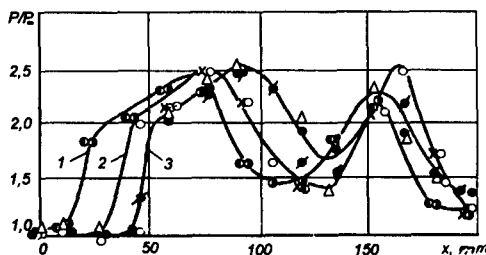


Fig. 3. Pressure distribution over the plate length with the hydrogen burning above it ($G = 3.8$ g/s) with different distance from its surface: 1- $h = 45$ mm, 2- $h = 54$ mm, 3- $h = 62$ mm.

In this direction the pressure reduces from the axis pressure to the free stream static pressure at the intersection line of the shock surface with the plate. The pressure distribution over the plate width was used for the estimation force, arising at the surface. The estimation was made for the variant: $h = 45$ mm, $G = 3.8$ g/s. The force value equals $P = 70$ kg approximately, that responds to the impulse $I = 18500$ s. The average value of normal force coefficient equals $C_{PN} = 0.26$.

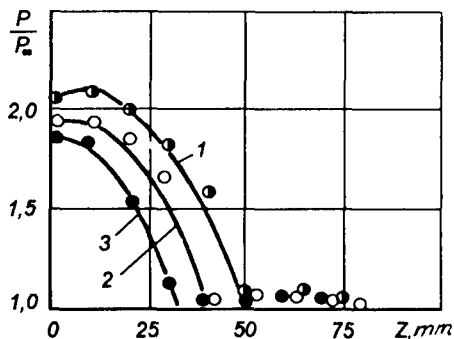


Fig. 4. Pressure distribution on the plate in the transverse direction with the flame distance from the plate ($G = 3.8$ g/s): 1 - $h = 45$ mm, 2 - $h = 54$ mm, 3 - $h = 62$ mm.

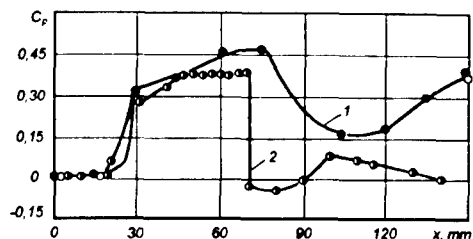


Fig. 5. Pressure coefficient change over the plate length: 1 - burning over the plate ($G = 3.8$ g/s, $h = 45$ mm); 2 - data [5], $G = 8.6$ g/s, $M = 2.25$).

For the comparison of the received results with the published data in Fig. 5 were showed the pressure coefficient magnitudes, received in [5], when the burning organization on the plate surface immediately. Here were showed the experimental results of the hydrogen burning at the Mach number $M_x = 2.25$. Hydrogen was ejected through the hole array normally to the plate surface at the rate $G = 8.6$ g/s. In addition air was ejected at the distance 30 mm from the ejection hydrogen place.

The pressure coefficient distribution showed, that in this case the pressure drops sharply behind the air ejection place.

Thus, the realized investigation of the external hydrogen burning in the supersonic flow showed two advantages of the burning process organization out the boundary layer in comparison with the surface burning:

- the heat influence absence on the surface;
- the higher values of the normal pressure coefficients.

REFERENCES

1. Billig F.S. External burning in supersonic streams. "The Johns Hopkins University-Applied Physics Laboratory Technical Memorandum", 1967, TG-912.-109 p.
2. Strahle W.C. Theoretical consideration of combustion effects on base pressure in supersonic flight // Twelfth Symp. (International) on Combustion. - Pittsburg, Pa.: The Combustion Institute, 1969. P.1163.
3. Baev V.K., Golovichev V.I., Tretyakov P.K., et al. Combustion in Supersonic Flow.- Novosibirsk: Nauka, 1984.-304 p. (in Russian).
4. Garanin A.F., Krainev V.L., Tretyakov P.K. Shock influence on the burning intensity in the separation zone with the contrary hydrogen ejection // Fizika Goreniya i Vzryva. 1984, № 2, - P.33-37.
5. Krause E., Maurer F., Pfeiffer H. Some results of investigation of problems relating to supersonic and hypersonic combustion. - ICAS Paper, 1972, № 72-21, DFVLR PORZ-Wahn (Germany).

The influence of acoustic resonator on the air-breathing combustor operation under pulsation burning of hydrogen

V.K.Baev, D.Yu.Moskvichev, A.V.Potapkin

**Institute of Theoretical and Applied Mechanics SB RAS,
630090, Novosibirsk, Russia**

The results on hydrogen combustion in an air-breathing ejector combustion chamber with constant area are described in [1]. It was found that there exists a range of parameters (hydrogen flow rate, injector position) wherein intense acoustic oscillations are observed, their frequency is in good correspondence with the characteristic times of hydrogen combustion (~ 2000 Hz) for an acoustic pressure level within 120-130 dB measured at a distance of 0.075 m upstream of the combustor.

For describing the vibrational burning, we will use the terminology from [2] wherein two stages of vibrational burning are distinguished: the initial stage characterized by a moderate level of acoustic pressure with oscillation frequency corresponding to the gas eigenfrequency in the combustion chamber, and the second stage, transition to which is accompanied by a dramatic growth of pulsation amplitude and by changes in pulsation frequency. Mathematical and physical models of this transition are discussed in [2, 3] and are not included into the present paper.

It was found in experiments that contrary to the initial stage of vibrational burning when the acoustic pressure level is no more than 120 dB and the measurements reveal the drag force (i.e., the force applied to the combustion chamber and directed towards the combustion products exhaust), the transition to the second stage of combustion is accompanied by the development of intense pulsations and thrust if there is a confuser at the combustor entrance (the force is applied to the combustion chamber and directed opposite to the exhausted jet of combustion products). The specific momentum is about ~ 200 s. Based on the assumption that oscillations originate as a result of critical phenomena from the viewpoint of flame existence, it was supposed that the effects can be amplified by the presence of a cavity closed to the ambient atmosphere but opened to the combustion region. The characteristic time of filling (dumping) of the cavity corresponds to the characteristic frequency of pulsations in the combustion chamber. The experiments were performed with the resonator which was a cylindrical pipe with a piston located inside. The piston position was varied during the experiment. The resonator position in the combustor was also varied. the resonator was placed near the combustor entrance, in the middle of the chamber, or near the combustor exit.

The setup scheme and the combustor with resonator are shown in Fig. 1a) and 1b), respectively.

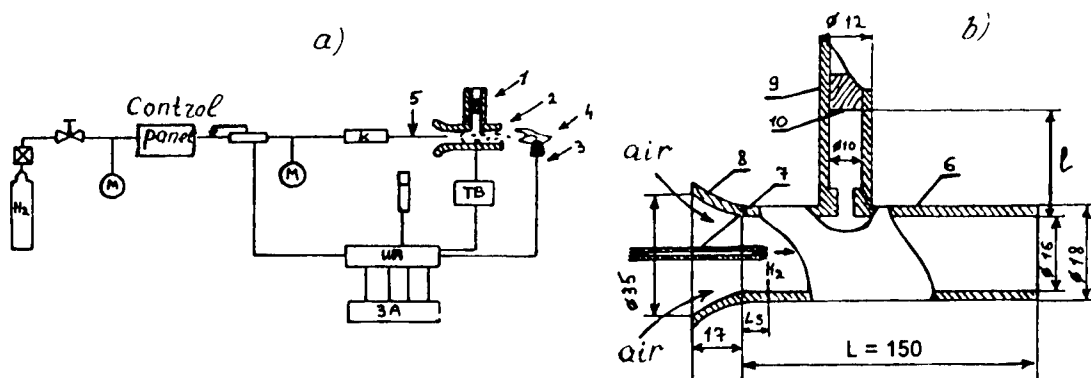


Fig. 1. Setup scheme. Combustion chamber.

Setup scheme: - valve, - pressure regulator, - manometer, - flowmeter, - traversing gear, microphone - , - strain-gage balance, 1- resonator, 2 - combustion chamber, 3 - thermocouple, - measurement instruments, - recording equipment, 4 - hydrogen-air plume, 5 - hydrogen injector.

Combustion chamber: 6 - combustion chamber, 7 - hydrogen injector, 8 - probe, 9 - resonator, 10 - piston

The combustor with resonator was fixed at a pantograph so that it could move only in the longitudinal direction. The longitudinal force (thrust or drag) F was registered by the strain-gage balance. A latch fixed in the combustion chamber was put through a slot of the strain-gage balance bar. The free travel of the latch in the slot was tenths of millimeter. The temperature of combustion products was measured by a chromel-alumel thermocouple placed in the plume at a distance of 20 mm from the combustor exit. Acoustic measurements were performed by a capacitor microphone. The hydrogen flow rate was determined from the pressure difference on a hydroresistance. The hydrogen was supplied to the combustion chamber through an injector spike which was placed in the chamber at a depth L_s . All signals from the gages were put out and recorded on a mirror-galvanometer oscillograph.

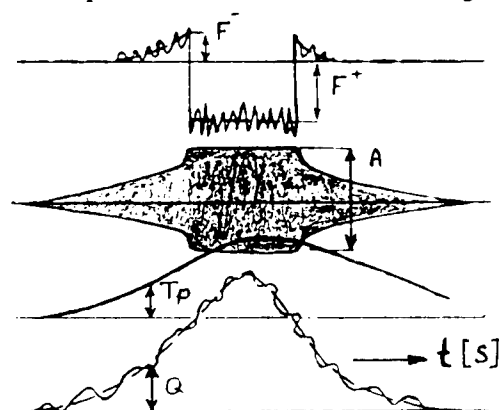


Fig. 2. Registrogram.

A typical registrogram is shown in Fig. 2. The solid lines show the recordings of parameter variations in experiment, the dashed line is the averaging used for experimental data processing. The shaded region is the recording of the amplitude A of acoustic

oscillations. F^- , F^+ are the recordings of the drag and thrust forces, respectively, T_p is the plume temperature, Q is the hydrogen flow rate, t is the time variation during the recording.

The results obtained from registogram processing are presented in Figs. 3, 4. Figure 3a) shows the force F in grams as a function of the volume flow rate of hydrogen Q (liters per second for hydrogen temperature within 16-20 C and normal atmospheric pressure). Figure 3b) shows the levels of measured acoustic pressure (in dBs). The data presented correspond to injector position $L_s/2L=0.183$ and piston position in the resonator $l/2L=0.36$.

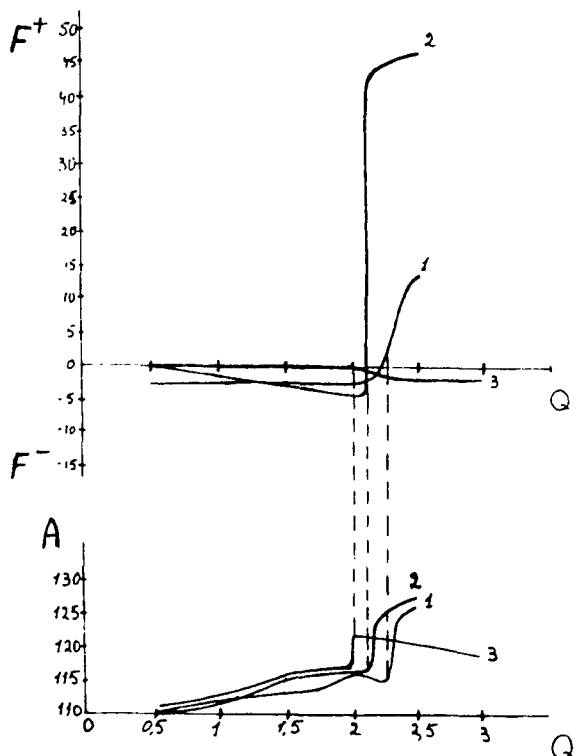


Fig. 3. The influence of resonator size and position on the thrust and acoustic characteristics of combustion chamber

Curve 1 is the resonator position near the combustor entrance, curve 2 corresponds to resonator position in the middle of the chamber, curve 3 - the resonator was placed near the combustor exit. On the curves of acoustic pressure level one can see the transition from the initial stage of vibrational burning to the second stage, which manifests itself as an instantaneous growth of A with increasing Q . The resonator shift from the combustor entrance to its exit led to lower hydrogen flow rate for which this transition was observed. At the initial stage of vibrational burning, the resonator shift from the combustor entrance to its exit increased the acoustic pressure with a constant flow rate and decreased the drag. Two processes were observed at this stage. On one hand, the resonator shift from the combustor entrance to its exit was accompanied by a decrease in drag F^- , on the other hand, for an unchanged resonator position, an increase of the flow rate Q led to drag increase as

the acoustic pressure grows. The opposite picture was observed behind the transition point to the second stage. The maximum level of oscillations was achieved at the middle resonator position, and this regime led to a three-fold increase of thrust F^+ when the resonator was placed near the combustor entrance (curves 1 and 2, respectively). When the resonator was positioned near the combustor exit, the drag force F^- arose (curve 3), and the resonator worked as a muffler, since an increase of the flow rate Q was accompanied by a decrease of acoustic pressure. It is seen from these results that the most beneficial regime from the viewpoint of obtaining the maximum thrust is the second regime of vibrational burning near the transition point and when the resonator is placed in the middle of the combustion chamber. Though accompanied by the growth of pulsation amplitude, an increase in hydrogen injection during the second regime still leads to a slow increase in thrust F^+ .

The influence of resonator size and position on the thrust and acoustic characteristics of combustion chamber are presented in Fig. 4a) and 4b), respectively.

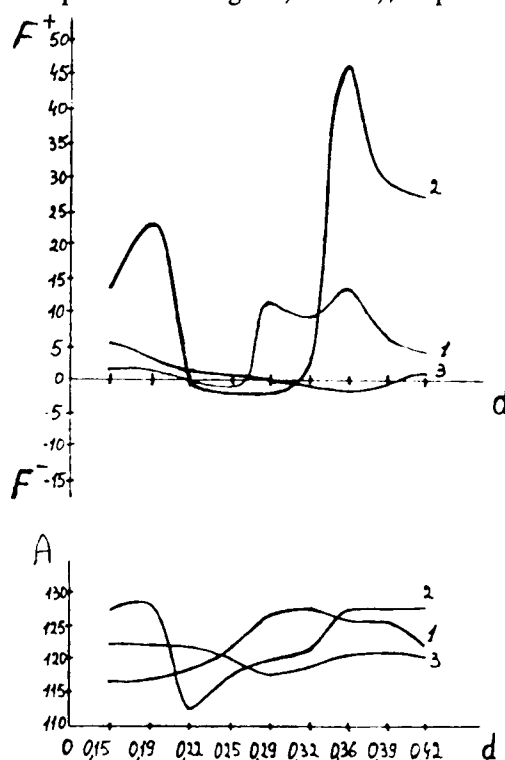


Fig. 4. The influence of resonator size and position on the thrust and acoustic characteristics of combustion chamber.

Curves 1-3 in this figure show the resonator position in the combustion chamber as described above, $d=l/2L$ is the relative resonator length, the injector penetrated to a depth L_s in the combustion chamber, and $L_s/2L=0.183$. The data are presented for a constant hydrogen flow rate $Q=2.5$ l/s.

When the resonator was placed near the combustor entrance (curve 1), the changes in resonator size induced a gradual change from thrust F^+ to drag F^- . As d was further increased from 0.26 to 0.39, the thrust growth up to 15 g was observed, which corresponds to the maximum pulsation amplitudes. For $d>0.39$ a decrease of pulsation amplitudes was

accompanied by a decrease in thrust $F+$. When the resonator was positioned in the middle of the combustion chamber, a similar picture was observed with more dramatic changes from drag to thrust, the thrust and drag values being approximately three times larger than in the previous case. The thrust maximum was observed for $d=0.35-0.37$, which was also in agreement with the pulsation amplitude maximum. The opposite picture of the force behavior was observed when the resonator was positioned near the combustor entrance. For d values lower than 0.27, an increase of pulsation amplitude was accompanied by a negligible growth of thrust, but in the region with d larger than 0.32 the growth of pulsations increased the drag $F-$. The vibrational burning regimes with intense oscillations, for which the maximum thrust was obtained, were usually accompanied by a $\sim 15\%$ decrease of the temperature of combustion products.

The results presented show that the thrust of an air-breathing combustion chamber can be controlled by changing the resonator position, its linear size, and fuel flow rate. Extreme values of specific momenta $I=F+/G$, where G is the weight flow rate per second, observed in experiments amounted to approximately 200 s without the resonator and to 300 s with the resonator. On the whole, these data are in contradiction with the statement forwarded, for example, in [4] that it is not possible to achieve thrust in air-breathing engines with low free-stream velocity. The data obtained testify that it is possible to transform a part of thermal energy produced during combustion into mechanical work and transport it through waves.

References

1. V.K.Baev, A.V.Potapkin, and D.V.Chusov, The influence of thermoacoustic processes on the force characteristics of the combustion chamber // Mathematical Modeling, Aerodynamics and Physical Gas Dynamics, Novosibirsk, 1995, P. 187-188.
2. A.M.Avvakumov, I.A.Chuchkalov, and Ya.M.Shchelokov. Unsteady Burning in Power Plants, Nedra, Leningrad, 1987.
3. B.V.Raushenbakh. Vibrational Burning. Gos. izd-vo fiz.-mat. lit-ry, Moscow, 1961.
4. R.I.Kurziner, Jet Engines for High Supersonic Flight Speeds, Mashinostroenie, Moscow, 1977.

UNSTEADY PROCESSES IN A COMBUSTION CHAMBER WITH SUPERSONIC FLOW VELOCITY

V.K. Baev, P.K. Tretyakov, V.V. Shumsky

Institute of Theoretical and Applied Mechanics SB RAS,
630090, Novosibirsk, Russia

Unsteady phenomena arising in combustion chambers (CCs) of various types of engines and furnaces caused by the burning processes are known in practice. Experimental results presented below point to a possibility of existence of anomalous combustion regimes, which are accompanied by changes in the flow structure due to flow unsteadiness and resonance phenomena.

1. Combustion in ducts with abrupt expansion (attached pipeline)

1.1. Homogeneous combustion of hydrogen-air mixtures at transonic flow velocities at the duct entrance

The combustion of a homogeneous hydrogen-air mixture was studied in a plane duct with a 40×62 mm cross-section and length of 765 and 260 mm [1]. It is seen from the plume photos that despite the subsonic velocity at the duct entrance (beginning from 224 m/s) the fore front of the plume has a geometry that points to emergence of wave structures typical of the off-design effusion. Strong oscillations leading to destruction of glasses and impossibility of steady-state regime were observed in experiments with a long duct. Combustion regimes in a short duct were also accompanied by oscillations, but their intensity was much smaller than in the case of long duct. A decrease in the air-to-fuel ratio α in the short duct led to a dramatic increase of noise intensity and combustion process unsteadiness. The estimate showed that the mean flow velocity in the cross-section behind the combustion zone in these regimes is close to the speed of sound.

1.2. Diffusion burning of hydrogen

Diffusion burning of hydrogen was studied in various ducts with sudden expansion, which had different geometric shapes of inlet devices [2]. The plume was stabilized by a step 40 mm high.

The flow in such a duct is substantially nonuniform and has a two-layered character. The combustion front is clearly seen in Schlieren pictures, the flow being supersonic above the front and subsonic beneath it. The distributions of flow parameters measured in various cross-sections along the duct confirm this conclusion. The analysis of flow filming showed that the combustion front performs crossflow oscillations with an amplitude 3 – 4 times as large as its thickness. A criterion determining the flow character in the duct is the relative heat supply θ .

The limiting heat supply regimes in the duct are of particular interest. The sonic velocity at the duct exit is realized with $\alpha = 4.2 - 4.4$. This combustion regime is accompanied by a sharp increase in pressure behind the step and by the emergence of low-frequency oscillations. One of the reasons for flow unsteadiness in this case can be the attainment of local sonic flow velocity simultaneously in several cross-sections of the duct. Besides, a pseudoshock combustion regime is observed for supersonic velocities at the constant-area duct entrance on regimes close to thermal choking [3]. An unsteady flow can arise on these regimes: it is known that the pseudoshock position in the duct is not fixed even without combustion, and the pseudoshock performs low-frequency oscillations along the duct.

For $M = 2.66$ and $\alpha = 3.62 - 4.21$ the behavior of parameters at the exit cross-section is anomalous. The flow structure is changed, which is accompanied by redistribution of temperature and pressure. The high-temperature region shifts towards the flow core, and the total pressure towards the flow behind the step (Fig. 1). The energy estimate based on the wave mechanism of energy transfer between the layers is in reasonable correlation with the measurements.

2. Wind tunnel study with air-breathing engine models (scramjets)

The wind tunnel studies were performed with models fully immersed into a super- or hypersonic air flow with the Mach number $M_\infty = 3 - 7.9$. The models were combinations of an inlet, combustion chamber, and nozzle. The CC operation with a strongly nonuniform flow structure at its entrance was modeled. The same phenomena related to the two-layered structure of the flow and oscillatory processes, as in an attached pipeline (Section 1), were observed in these experiments. Besides, a number of phenomena were noticed, which are only typical of operation of an inlet-combustor system and, therefore, could not be observed in experiments with an attached pipeline.

2.1. Two-layered flow

A two-layered flow structure is formed in combustion chambers when burning the hydrogen or liquid fuels. A comparison of data for the models tested in wind tunnels with those obtained for an attached pipeline reveals not only the qualitative but also, to a large extent, the quantitative agreement, though the test conditions were appreciably different (absolute lengths and heights of combustion chambers, flow fields at the CC entrance, method of hydrogen injection behind the step, and other absolute geometric and physical characteristics of the flow).

This shows that the main factors determining the CC operation regime were the same in experiments with an attached pipeline and in wind tunnel experiments with the models. The following factors can be mentioned here.

1. The presence of a step that occupies a considerable portion of the CC height (up to $2/3$ of its height). This allowed for flow stabilization, but at the same time, the CC length was insufficient for combustion products from the lower layer to mix with the main air flow.
2. Extremely low mixing of cocurrent supersonic and subsonic layers.
3. A large CC expansion.

It should be noted that the reversal of the maximum values of stagnation temperature and pressure from the combustion zone to the flow core, which was observed in an attached pipeline, was not obtained in wind tunnel experiments.

2.2. Transition of the two-layered combustion regime to the pseudoshock regime

In one of the plane models tested in a blowdown wind tunnel at $M_\infty = 3$ the hydrogen plume was stabilized by a cavity.

The flow structure in the combustion chamber had an explicit two-layered character. Upon hydrogen injection through the cavity and, in addition, through nine orifices on the lower wall (Fig. 2), the CC flow structure becomes different. For a total hydrogen flow rate corresponding to $\alpha \approx 5$, a narrow highlighted zone appears at the beginning of CC expansion, the combustion ending behind this zone. As the hydrogen flow rate increases, this highlighted band moves upstream, but the combustion goes on behind it in a narrow band along the upper wall. This pattern is observed up to the maximum possible flow rate $G_{H_2} \sim 3 \text{ g/s}$, $\alpha \approx 2.5$, ensured by the injection system. The following mechanism of heat supply to the CC was used. As the hydrogen flow rate increases and $\alpha \approx 5$ is attained, the combustion products exhausted from the cavity ignite the hydrogen injected from the orifices. The flow restructuring with the formation of pseudoshock burning regime takes place.

The conducted experiments showed that under certain conditions the two-layered combustion regime is transformed into a stable pseudoshock burning regime without flow stall even in ducts with a very small expansion, as it was in the present model.

2.3. Oscillatory processes in the CC

It was shown in [4] that an increase of the relative heating of the test gas shifts the bow part of the pseudoshock towards the CC entrance up to the inlet throat. The pressure probes located at the initial CC section register a pressure-unsteady process. It can be also noted that for $\alpha < 0.5$ this process is not only unsteady, but also oscillatory. At the same time the pressure probes located on the inlet surfaces and at the CC exit do not register this oscillatory process. This means that the pressure oscillations are concentrated at the CC beginning. The frequency of pressure oscillations was 200 – 350 Hz. They do not lead to oscillations of the overall gas column enclosed in the model duct and are related to fluctuations of local gas dynamic structures, possibly, separation regions. The oscillatory processes of this type can be very useful for organization of combustion in scramjet combustion chambers, since the pressure oscillations improve the fuel mixing and burning in high-speed air flows.

2.4. Interaction between the inlet and combustion chamber

Experiments conducted in a hot-shot wind tunnel with $M_\infty = 5 - 7.3$ show that the states of model starting / nonstarting can be altered during the regimes with fuel burning in scramjet models.

The mechanism of alternation of the starting/nonstarting states is associated not with the classical concept of inlet flow stall, but with the

separation region behind the inlet corner point, which is pressed out to the external compression surface. Outside this region, the duct flow remains supersonic. The expulsion occurs due to flow upthrust by the heat release in the CC. An oscillatory process of this type is similar to low-frequency oscillations in liquid rocket engines related to flow rate fluctuations in the injector-combustor system.

An oscillatory process in the gas column can occur not only due to heat supply in the inlet-combustor system, but also without combustion when the relative inlet throat area f_2 is reduced to the minimum possible value. The reason for the oscillatory process in this case is the shift of separation to compression surfaces due to throat choking/opening under the condition of its limiting capacity. A slight increase of f_2 from this minimum value eliminates the oscillatory process: the inlet starting is stable during the entire regime. A slight decrease of f_2 from the minimum value again eliminates the oscillatory process: the inlet remains nonstarted from the beginning to the end of the test.

Thus, the heat supply due to fuel combustion leads sometimes to low-frequency oscillations of the gas column enclosed in the model duct because of heat supply effect on the flow gas dynamics, which, in turn, affects the heat release intensity. The main responsibility for this oscillatory process lies on separation regions moving along the CC beginning and passing to external compression surfaces as the thermal upthrust increases.

2.5. High-frequency oscillations in the inlet-combustor system

It was shown above that oscillatory processes, both localized inside the duct and passing to external compression surfaces of the inlet, arise in the combustion chamber under certain conditions. In either case, these oscillatory processes are low-frequency ones.

When a scramjet model operating on liquid fuel with $\alpha \approx 1$, was tested in a high-enthalpy hot-shot facility, the cowl was destroyed, whereas the model was used in several experiments without any damage of material. The cowl strength could survive the pressure, which is by an order of magnitude higher than the maximum estimated pressure in the model with the extreme adverse combination of gas-thermodynamic parameters. The type and duration of the destruction, the fracture character are typical of the fracture caused by high-frequency oscillations.

The fact that not only low-frequency oscillations but also high-frequency ones are possible in the inlet-combustor system revives the problem of heat-loaded CCs: in experiments in high-enthalpy hot-shot facilities the combustor heat load was as high as in CCs of forced liquid rocket engines, for which the problem of the onset of high-frequency oscillations is fairly urgent.

3. Anomalous pressure distribution along the duct

The above results point that the flow structure with diffuse combustion in the CC with supersonic flow velocity at the entrance is complicated and ambiguous. If the flow structure did not affect the integral CC characteristics, the interest would be purely idle. However, the distribution of time-averaged pressures at the opposite walls of the duct show that it is important to know the flow structure and the role of unsteady processes in energy transformation and propagation in the CC.

It was found in experiments with an attached pipeline (see Section 1) that the difference of forces acting upon the upper (above the step) and lower (below the step) walls can vary from +200 kg to -60 kg depending on α , i.e., the transverse projection of the force vector applied to CC surfaces depends principally on the CC operation regime. Assuming a layered flow (in one case $\alpha = 1$, in the other one $\rightarrow \infty$), an idealized scheme yields a qualitative agreement with experimental ratio of mean pressures on the upper and lower walls, which allows one to take into account the basic features of a two-layered flow in a combustion chamber with a step.

The presented material can be regarded as the source information for creating a block to be included into the physical flow model for high-speed combustion chambers.

REFERENCES

1. Baev V.K., Serov Yu.V., and Tretyakov P.K. On oscillation frequency of the turbulent plume front// Combustion, Explosion, and Shock Waves. - 1970. - Vol. 6. - No. 2. - P. 246 - 248.
2. Baev B.K., Tretyakov P.K., Konstantinovsky V.A. The study of hydrogen combustion in a ducted supersonic flow with a sudden expansion// Archiven combustions. - 1981. - Vol. 1. - N 3/4. - P. 251 - 259.
3. Tretyakov P.K. Pseudoshock combustion regime// Combustion, Explosion, and Shock Waves. - 1993. - Vol. 29. - No. 6. - P. 33 - 39.
4. Baev V.K., Shumsky V.V., Yaroslavtsev M.I. Some methodical aspects of examining gas dynamic models with heat-and-mass supply in a hot-shot wind tunnel// Combustion, Explosion, and Shock Waves. - 1987. - Vol. 23. - No. 5. - P. 45 - 54.

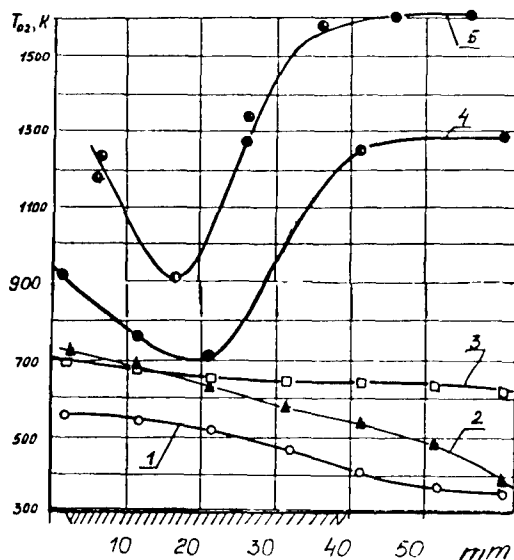


Fig. 1. Temperature at the duct exit.

1 — $\alpha = 14,6$; 2 — $\alpha = 8,92$; 3 — $\alpha = 6,38$; 4 — $\alpha = 4,21$;
5 — $\alpha = 3,62$.

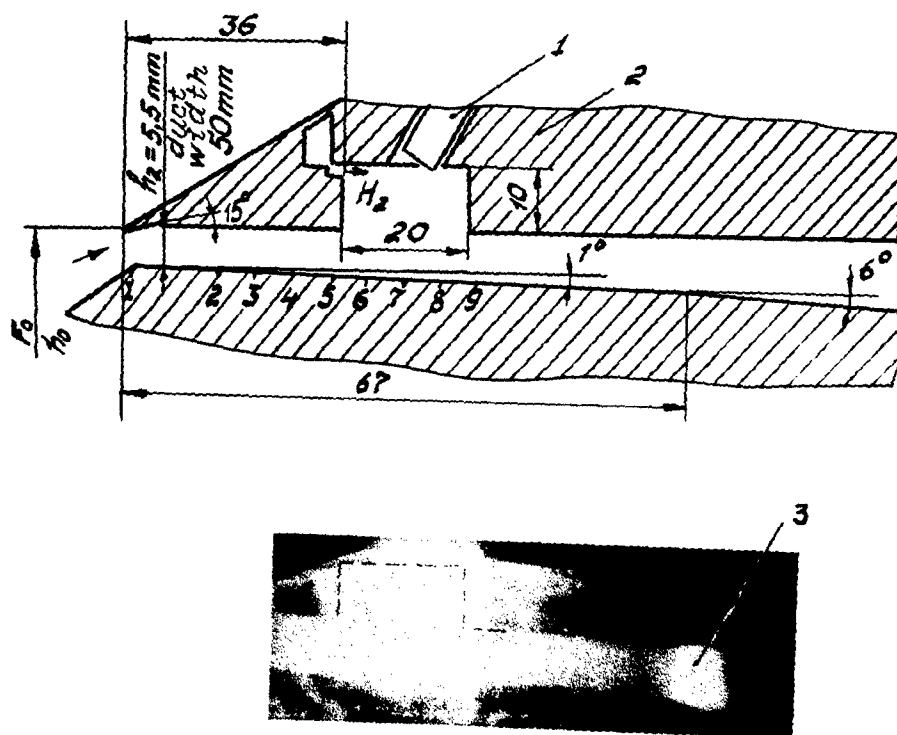


Fig. 2. Plane model with a cavity, $M_\infty = 3$.
 1 — torch; 2 — cavity; 3 — combustion in the pseudoshock
 (behind the normal shock).

SPECIFIC FEATURES OF THE FLOW IN GAS DYNAMIC SHORT-DURATION FACILITIES

V.K.Baev and V.V.Shumsky

Institute of Theoretical and Applied Mechanics SB RAS,
630090, Novosibirsk, Russia

Unsteadiness effects in high-enthalpy short-duration facilities with the working body parameters varied in time are analyzed in the paper by the example of a hot-shot wind tunnel with constant volume of the plenum chamber and two sequentially positioned throats (Fig. 1). Prior to experiments, the test section of the wind tunnel was evacuated. The diaphragm was located in section 1. The analysis is confined to regimes with supercritical pressure differences on the both nozzles. Volume V_2 could be filled with hydrogen, after hydrogen self-ignition volume V_2 worked as a combustion chamber (CC) with supersonic velocity at the entrance. Without hydrogen injection, the facility operates as a wind tunnel with a double plenum chamber (PC).

The following unsteadiness effects were observed.

1. If the pressure at the initial moment of effusion is used as a reference scale, the variation of the relative pressure in the first PC does not correspond to that calculated on the assumption of effusion quasi-steadiness.
2. The ratio of the pressure in the first PC to that in the second PC does not correspond to a constant value for steady effusion and increases during the entire run time.
3. The ratio of the pressure in the second nozzle to that in the second PC does not correspond to the critical value and increases in time.
4. The hydrogen combustion efficiency calculated from the measured pressure on the assumption of constant flow rate in the throats increases in time and can be higher than unity.

The reasons for unsteadiness effects are the unsteadiness of distribution of parameters inside each volume because of wave motion and the change in the gas mass because of different amount of incoming and outgoing substance.

The analysis is based on the assumption that it is possible to distinguish between these two effects in such a way that the effusion processes could be described by appropriate relations for steady flow using the volume-averaged values of density, while the wave and other unsteady processes in the volume could be taken into account by the method of averaging of proper parameters [1].

Effusion from the first plenum chamber

For each time instant τ , the variation of density ρ_1 in volume V_1 of the first PC is

© V.K.Baev and V.V.Shumsky, 1998

$$V_1 \frac{d\rho_1}{d\tau} = -G_1. \quad (1)$$

Introducing the time scale

$$\tau_0 = \frac{V_1}{F_1' a_1(0)},$$

equation (1) can be presented in the nondimensional form

$$\frac{d\bar{\rho}_1}{d\bar{\tau}} = -\bar{\rho}_1 \bar{a}_1 \left(\frac{\rho_1'}{\rho_1} \right)^{\frac{\kappa+1}{2}}, \quad (2)$$

Hereinafter the bar over the gas parameters denotes the quantity related to its value in the first PC at the moment $\tau = 0$, for example, $\bar{\rho} = \rho/\rho_1(0)$, $\bar{a}_2 = a_2/a_1(0)$, the prime indicates the parameters in the throat, the superscript * indicates the stagnation parameters in the throat, the subscripts 1 and 2 denote the parameters in the first and second plenum chambers, respectively, (0) indicates the parameters at the moment $\tau = 0$, G is the mass flow rate, a is the speed of sound, F is the area, $\bar{\tau} = \tau/\tau_0$. Integrating (2), we obtain for the ratio of specific heats $\kappa = 1.4$

$$\bar{\rho}_1 = \frac{1}{[1 + 0.116\bar{\tau}]^5}, \quad \bar{p}_1 = \frac{1}{[1 + 0.116\bar{\tau}]^7}. \quad (3)$$

The arrival time of the wave reflected on the front PC face at the throat and the pressure in the PC at this moment are [2]

$$\bar{\tau}_\kappa = \left(\frac{\kappa+1}{2} \right)^{\frac{\kappa+1}{2(\kappa-1)}}, \quad \bar{p}_\kappa = \left(\frac{2}{\kappa+1} \right)^{\frac{2\kappa}{\kappa-1}}.$$

For $\kappa = 1.4$

$$\bar{\tau}_\kappa = 1.728, \quad \bar{p}_\kappa = 0.279.$$

The calculation of \bar{p}_1 from (3) yields 0.278, i.e., the values almost coincide. This means that the total amount of gas leaving the PC, irrespective of its shape, is roughly equal during the time $\bar{\tau}_\kappa$.

The pressure variation in the PC can be represented as

$$\frac{d\bar{p}_1}{d\bar{\tau}} = -c \cdot \bar{p}_1, \quad (4)$$

where c is determined from the effusion from the PC which is a constant-area pipe, at $\bar{\tau} < \bar{\tau}_\kappa$, i.e., when the effusion occurs with a constant flow rate.

Integrating (4) and bearing in mind that for $\bar{\tau} = \bar{\tau}_\kappa$ and $\kappa = 1.4$ $\bar{p}_{1\kappa} = 0.402$, we obtain

$$\bar{p}_1 = e^{-0.739\bar{\tau}}. \quad (5)$$

The both functions (3) and (5) are reasonable approximations of experimental data with a noticeable deviation at $\tau \simeq 0$, which testifies to the presence of transitional processes at $\tau \rightarrow 0$. On the whole, equation (3) is in better agreement with experimental data at large times, while (5) is more convenient for analytical processes.

A good agreement with experiment begins from $\tau \approx 0,3$ for formula (3) and from $\tau \approx 0,6$ for formula (5), i.e., irrespective of the way the curve $p_1 = f(\tau)$ is described, the effusion process can be considered quasi-steady for $\tau > 0,3 - 0,6$. For $\tau < 0,3 - 0,6$ the effusion is affected by unsteady transitional processes inside the PC.

Pressure measurements in the second plenum chamber

1. Let us assume at first that the values of stagnation parameters of the gas in the second PC for each τ are the same in all points of volume V_2 . The density and pressure in volume V_2 enclosed between two throats F'_1 and F'_2 is determined by the gas mass accumulated due to flow rate difference in these throats:

$$V_2 \frac{d\rho_2}{d\tau} = G_1 \left(1 - \frac{G_2}{G_1} \right). \quad (6)$$

Denoting the bracket in the right-hand part by Δ , we obtain the nondimensional equation

$$\bar{\rho}_2 = - \int_1^{\bar{\rho}_1} \frac{\Delta}{\bar{V}_2} d\bar{\rho}, \quad (7)$$

where $\bar{V}_2 = V_2/V_1$.

After integrating (7) with regard for (5), assuming $T_2 \approx T_1$, we obtain

$$\frac{\bar{p}_2}{\bar{p}_1} = \frac{1}{\bar{F}'_2 + \bar{V}_2 \frac{1}{\epsilon^{0,528\tau} - 1}}. \quad (8)$$

It is seen that for the used assumption about the constant ratio of flow rates in the throats $\bar{p}_2/\bar{p}_1 \rightarrow 0$ as $\bar{\tau} \rightarrow 0$. This is typical of the initial period when volume V_2 is filled.

2. To explain the experimentally observed pressure growth $\frac{\bar{p}_2}{\bar{p}_1} > \frac{1}{\bar{F}'_2}$, we supplement our analysis with the process nonisothermality in the presence of heat transfer and (or) combustion when $T_2 > T_1$, as well as possible unsteadiness effects related to the character of heat supply.

Therefore, instead of (6), we write

$$V_2 \frac{d\rho_{2c}}{d\tau} = -V_1 \frac{d\rho_1}{d\tau} - \rho'_2 a'_2 F'_2.$$

The necessity of introducing the mean density ρ_{2c} is caused by the fact that even assuming a constant pressure p_2 over volume V_2 , the temperature distribution in volume V_2 , for example, during combustion, can be nonuniform and unsteady.

After transformations and integration we obtain (for $\kappa = 1,4$)

$$\frac{\bar{p}_2}{\bar{p}_1} = \frac{0,912}{\bar{F}'_2} \sqrt{\theta_0} \cdot \epsilon^{0,106\tau} \frac{1}{1 - \frac{\bar{V}_2}{\bar{F}'_2} \cdot \frac{\theta_c}{\sqrt{\theta_0}} 1,73 \epsilon^{0,106\tau} \left[0,422 - \frac{d \ln \theta_c}{d\bar{\tau}} \right]}, \quad (9)$$

where

$$\theta_c = \frac{T_2^*}{V_2} \int_{V_2} \frac{dV_2}{T_2}, \quad \theta_0 = T_2^*/T_1$$

Physically, θ_c denotes a nonuniform distribution of stagnation temperature along volume V_2 from section 1' to section 2', and θ_0 denotes the gas heating over the length from section 1' to section 2'. For constant temperature $\theta_c = 1$.

The structure of (9) shows clearly the influence of temperature distribution in the volume (the difference between θ_c and θ_0) and unsteadiness (the logarithmic derivative of θ_c with respect to time).

Figure 2 shows a comparison of the measured values of p_2/p_1 and the calculation using (9) with $\theta_0 = 1$ for the process without combustion in the second PC. The curve with regard for the volume filling process, calculated from (8), is also plotted there. The symbols indicate various geometries of the subsonic part of the second nozzle. It is seen that the agreement with (9) is fairly reasonable, and the deviation of experimental data towards smaller values does not contradict the heat removal from the hot gas to the walls, which certainly took place in experiment.

Figure 3 shows the results of θ_0 calculated on the basis of experimental data for the case of hydrogen combustion under the conditions of its self-ignition on injection into the second PC. The calculation was performed in accordance to (9) for $\theta_c = 1$ (complete burning in section 1' at the entrance to volume V_2 , curve 5) and for $\theta_c = \sqrt{\theta_0}$ (curve 4). The same figure shows the curves $\theta_0(\tau)$ for complete burning ($\eta = 1$) and for $\eta = 0,5$. For comparison, the curve $\theta_0(\bar{\tau})$, is shown, which is obtained from experimental data assuming $p_2/p_1 = \frac{1}{F_2'}$ without combustion, i.e., like in the case of steady regime (curve 1).

Figure 3 explicitly illustrates the importance of taking into account various unsteadiness effects when using the pressure measurements for interpretation of combustion data in facilities with flow parameters varied in time.

Pressure ratio in the second nozzle

Another unsteadiness effect is the experimentally found disagreement of the pressure difference with the critical value in the second nozzle. The measurements in the nozzle with a cylindrical throat yield a downstream pressure decrease in it. This gives grounds to consider the nozzle flow as a subsonic flow in the channel with $F = \text{const}$, which reaches the speed of sound at the end of this channel with the corresponding pressure drop. Then

$$\rho_2' a_2' = \rho_2'' U,$$

where ρ_2'' is the subsonic flow density with velocity U in an arbitrary cross-section of the channel $F_2' = \text{const}$.

Transforming this equation with the help of gas dynamic relations, obtain for $\kappa = 1,4$ [1].

$$\frac{p_2''}{p_2'} = \left\{ 1 - \frac{0,167 \cdot \left(\frac{p_1 \sqrt{\theta_0}}{p_2 F_2'} \right)^2}{\left[1,2 - 0,2 \left(\frac{p_1 \sqrt{\theta_0}}{p_2 F_2'} \right)^2 \right]^5} \right\}^{3,5} \quad (10)$$

Figure 4 shows the experimental data and the calculation (10) for the case $\theta_0 = 1$. Two curves, 1 and 2, in this figure correspond to the calculated curves 1 and 2 in Fig. 2 for p_2/p_1 . It is seen again that the results of approximate analytical function and experimental data are in reasonable agreement.

Thus, the method for describing unsteady flows in gas dynamic facilities, which was used in the present work and based on representation of these facilities as a set of sequentially nested volumes with uniformly distributed parameters inside them, yields analytical functions that are in satisfactory agreement with experiment. This gives grounds to believe that the unsteadiness effects observed experimentally in hot-shot facilities can be taken into account, which will increase their accuracy and informativeness as the means of physical modeling.

REFERENCES

1. V.K.Baev, A.V.Potapkin, and V.V.Shumsky. Unsteadiness effects in the study of combustion processes.— Novosibirsk, 1997.— 43 p.— (Preprint / ITAM SB RAS; No. 6-97).
2. Explosion Physics (ed. I.P.Stanyukovich).— M.: Nauka, 1975.

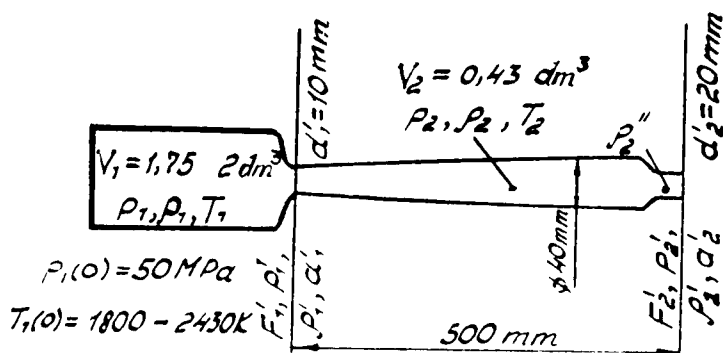


Fig. 1. A sketch of the facility.

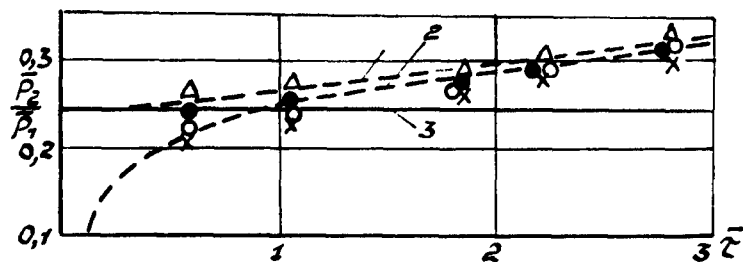


Fig. 2. Variation of the pressure ratio in plenum chambers without combustion.

1 — calculation (9) for $\theta_0 = 1$; 2 — calculation (8); 3 — $p_2/p_1 = \frac{1}{F_2}$.

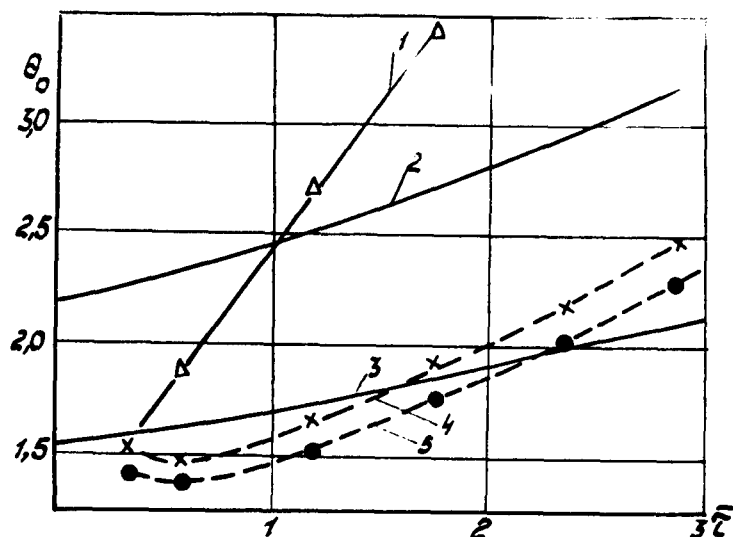


Fig. 3. Variation of relative heating during combustion.

1 — calculated values of θ_0 from experimental data assuming quasi-steadiness; 2 — calculation for complete combustion ($\eta = 1$); 3 — calculation for $\eta = 0.5$; 4, 5 — calculation (9) of θ_0 from experimental data for $\theta_0 = \sqrt{\theta_0}$, 5 — $\theta_0 = 1$.

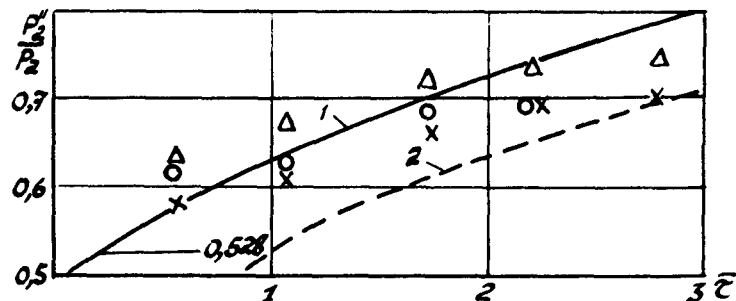


Fig. 4. Ratio of the pressure in the second nozzle throat to the pressure in the second plenum chamber without combustion.

SOME RESULTS OF DETONATION COMBUSTION REGIMES INVESTIGATION

L.V.Bezgin, A.N.Ganzhelo, V.I.Kopchenov

Central Institute of Aviation Motors
2, Aviamotornaya St., Moscow, 111250, Russia

Abstract

The shock-induced combustion problem is the focus of attention in connection with possible using of this process in some hypersonic facilities. Three problems were considered in this paper: flow structure investigation at the shock-induced combustion in uniform premixed flow; the estimation of the possibility to realize shock-induced combustion ramjet (shcramjet) taking into account the fuel-air mixing upstream engine entry; flow simulation in the ram accelerator. The flow structure is very complicated and it is the result of gasdynamic and chemical processes interaction. The SUPNEF computer code based on the parabolized Navier-Stokes equations (PNS) and detailed scheme of chemical kinetics is developed in CIAM to simulate and to investigate combustion process in supersonic and hypersonic flow, including detonation waves. This tool is used for the numerical solution of three aforementioned problems.

Introduction

The air-breathing hydrogen-burning engines with combustion in supersonic flow (scramjet) are considered as promising propulsion system for hypersonic flight. One promising concept for igniting and stabilizing a flame is an oblique shock wave [1-4]. This concept of the engine is based on the premixing of the fuel and air before combustor, for example, in the inlet. The main questions which must be analyzed in this concept are concerned with the efficiency of premixing process, the premature ignition of the mixture before the combustor, the influence of the non-ideal mixing on the engine efficiency. The using of ideal scheme of detonation wave at the engine performances estimation requires additional investigations [5, 6]. The feasibility of premixing of fuel and air at the fuel injection upstream from the engine entry as well as mixture ignition and flame stabilization by the shock in the engine duct taking into account real fuel-air mixture composition are the main goals of this research.

The next problem is concerned with the ram accelerator [7-9]. The projectile is injected into the launch tube which is filled with premixed fuel, oxidizer and diluent. Thrust is generated due to combustion realized between the tube wall and projectile. Combustion is initiated and stabilized by the interaction of the shock waves from the projectile nose with barrel walls. The important problem is the ability to initiate and stabilize the combustion front in such position that positive thrust can be generated. Therefore the proper simulation of the flow through the duct must be performed taking into account the gasdynamics and chemistry interaction over all range of projectile velocities.

Computational models and computer codes

The SUPNEF code [10] developed in CIAM is used for the numerical solution of these problems. The averaged parabolized Navier-Stokes equations (PNS) for multispecies mixture with real gas effects at high temperature are solved. The one-equation differential turbulence model [11] is employed. The wall boundary layers were not taken into account at this preliminary stage of investigation. The numerical solution of this equations system is obtained using method, which is based on the explicit higher order accuracy monotone Godunov [12] finite volume predictor - corrector scheme for the steady supersonic flows with implicit approximation of chemical sources terms. The calculations were performed on the adapted grid [13]. The detailed chemical kinetic scheme [14], including 30 reactions for 8 reacting species was used.

Some investigations of shock induced combustion in uniform premixed flow

The following model problem [15] was considered. The compression ramp flameholder is installed in the duct (see fig.1). The homogeneous premixed hydrogen and air enter the duct at Mach number 2.75, pressure 10^5 Pa. Three series of calculations were performed. The entry temperature influence on flow field was considered in detail [16] when the wedge angle θ was equal to 10° . The value α which is defined as air-to-fuel ratio divided by the stoichiometric air-to-fuel ratio is equal to 10. The angle of the wedge θ was varied in the second series of calculations. The value α was varied in the third series for specially chosen angle of wedge. The goal of this work is to study the steady flow structure especially shock-chemical reactions zone interaction. The detailed analysis of computational results was performed to identify the obtained flow picture with existing theoretical models [17-20] for waves and shocks with heat release.

The influence of the wedge angle θ on the flow structure is illustrated in fig.1-5. Temperature in this case is equal to 875 K and $\alpha=10$. At the wedge angle $\theta=9^\circ$, the mixture is not ignited by the shock and the combustion is not observed (fig.1). The ignition takes place when $\theta=10^\circ$ (fig.2). The typical flow structures obtained for the angles 12° , 14° and 16° are shown correspondingly in fig.3-5. The wedge angle increase provides the more strong adiabatic shock with temperature rise. Therefore, the flow structure changes, which are obtained at the angle increase, are qualitatively similar to these ones observed at the entry temperature rise. The total structure including region, where shock - chemical reactions take place, for angles $\theta \geq 11^\circ$ can be treated as the overdriven detonation.

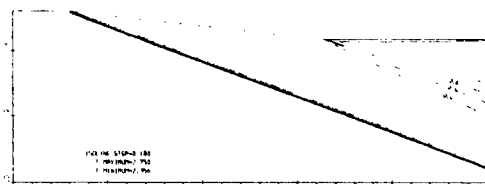


Fig.1 Mach number field, $\theta=9^\circ$

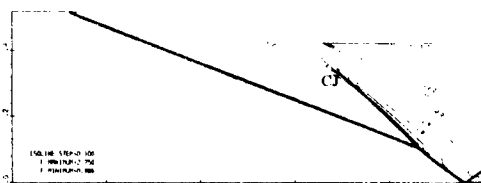


Fig.2 Mach number field, $\theta=10^\circ$

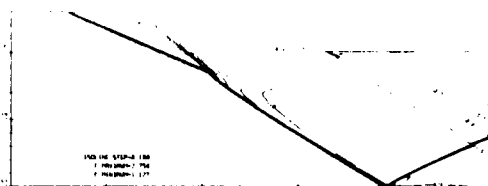


Fig.3a Mach number field, $\theta=12^\circ$

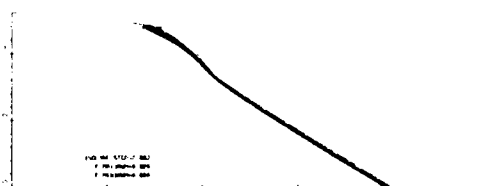


Fig.3b H_2O mass fraction field, $\theta=12^\circ$

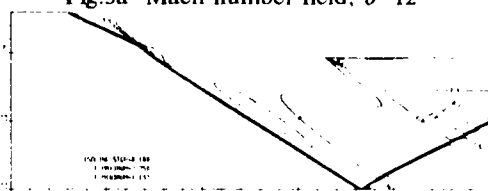


Fig.4 Mach number field, $\theta=14^\circ$

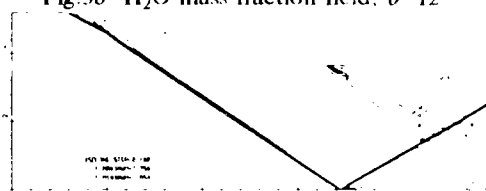


Fig.5 Mach number field, $\theta=16^\circ$

The third series of calculations was performed to investigate the influence of the heat release controlled by the value α on the flow structure. In accordance with theory of oblique shocks with heat release [18], it is possible to mark on the detonation shock polar diagram point CJ corresponding to Chapman-Jouquet conditions and point MD corresponding to maximal flow deflection angle in the attached shock. If the heat release increases, CJ point on detonation shock polar diagram approaches to the point MD. However, the angle corresponding to MD point is greater than angle corresponding to CJ point. The maximal deflection angle decreases as the heat release increases. At the same time, for given free stream conditions, it is possible to define, at some value of heat release, the maximal flow deflection angle corresponding to CJ point. Finally, at some maximal heat release the detonation shock polar diagram is subtended into the single point and two considered points CJ and MD coincide in this case. For entry Mach number 2.75 and temperature 875 K the maximal flow deflection angle in CJ point approximately is equal to 12.36° for $\alpha=3.44$. Therefore the heat release influence investigations were performed at wedge angle $\theta=12^\circ$.

The solution for $\alpha=10$ was obtained in previous series and results are presented in fig.3. The whole formation including both shock and reaction zone can be treated in correspondence to the aforementioned as the overdriven detonation. The solutions for $\alpha=7.5$ and 5.0 are presented correspondingly in fig.6 and 7. If to compare fig.3, 6, 7, it is possible to note that the decrease of α (this corresponds to heat release increase) is followed by the decrease of dimensions of the region near the upper wall where the adiabatic shock and reaction zone are separated one from another. This behavior is similar to the case of temperature rise or wedge angle rise. The analysis of the whole formation including shock - chemical reactions zone shows that for $\alpha=7.5$ the exit parameters correspond to the overdriven detonation, and for $\alpha=5.0$ - to the Chapman- Jouquet regime.



Fig.6 Mach number field, $\alpha=7.5$

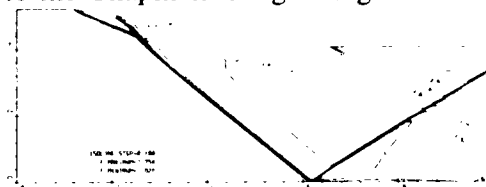


Fig.7 Mach number field, $\alpha=5.0$

The preliminary estimation of possibility to realize ODWE

It was supposed that the hydrogen jet is injected upstream of the engine entry to prepare the fuel - air mixture at the duct entry. The following questions were considered: the possibility to mix hydrogen with air and the evaluation of the mixing efficiency at the engine duct entry; the possibility to ignite the nonuniform hydrogen - air mixture in the engine duct by the shock generated on the leading edge of the engine cowl; the peculiarities of the combustion process in the engine duct and an estimation of the combustion efficiency. Some of the aforementioned questions were partially discussed in [4, 21].

The configuration of the lower surface of the small scale vehicle and the engine duct are presented in fig.8a. The calculation region includes the forebody - inlet - engine duct - nozzle and afterbody. The free stream conditions correspond to the flight Mach number 12, flight altitude 36.2 km and the angle of attack 10° . The hydrogen is injected downstream the shock, generated by the second wedge, on some distance from the wall. The hydrogen jet parameters are given as follows: $M_j=2.45$, $P_j=0.5$ atm, $T_j=450$ K.

The results are presented in fig.8a-8c by static pressure, water and hydrogen mass fraction fields. It is shown that combustion is initiated on some distance downstream the shock generated by the engine cowl. The usual diffusion combustion regime takes place in the down part of the engine duct near the cowl. The intensive combustion process with water formation in small region downstream the shock is observed in central part of the duct. In upper part of the duct, the intensive combustion takes place downstream the shock generated on the wall at the reflection of the shock arising at the leading edge of the cowl. The hydrogen jet is deflected to upper wall at the interaction with cowl shock.

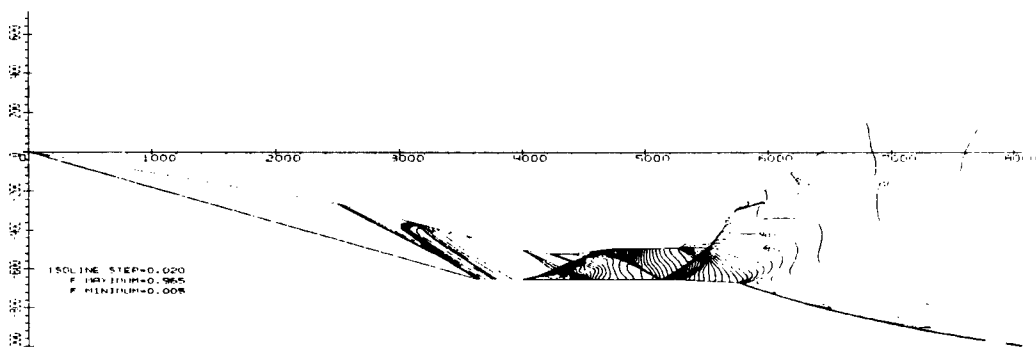


Fig.8a Static pressure field (atm)

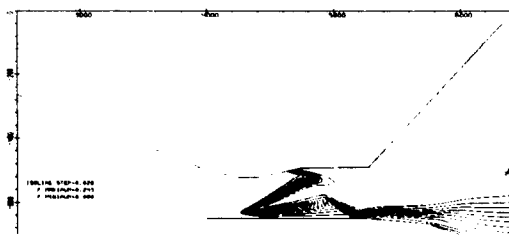


Fig.8b H₂O mass fraction field (fragment)

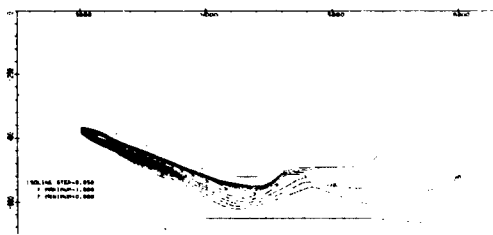


Fig.8c H₂ mass fraction field (fragment)

The performances estimation shows that the mixing efficiency at the duct entry is approximately 0.41. The combustion efficiency (estimated on the energy release) at the engine exit is approximately 0.52 at the mixing efficiency 0.85.

Shock induced combustion in ram accelerator projectiles duct

The tube of 19 mm radius is filled by homogeneous stoichiometric hydrogen-air mixture at the temperature 300 K and pressure 25 atm [9]. The fast code SUPNEF allows for the calculations of the whole region including conical part of projectile and the gap between cylindrical segment of a projectile and surface of the duct. The main attention is focused on the influence of entry Mach number on the flow structure.

The minimal value of free stream Mach number, at which the ignition occurs, is higher than 6. At $M=7$, the ignition occurs in the annular gap. The bow shock wave reflects from the duct wall, passes through expansion wave and reflects from a cylindrical segment of projectile. The ignition of mixture is observed downstream this reflected shock with appreciable delay near the surface of projectile.

The results for $M=9$ are shown in fig.9. In this case, ignition occurs downstream bow shock reflection from duct wall. The combustion zone near the duct wall is formed with small delay downstream reflected shock.

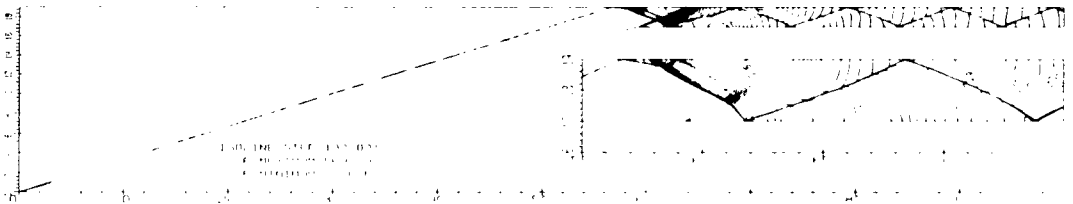


Fig.9a Static pressure field (atm), $M=9$

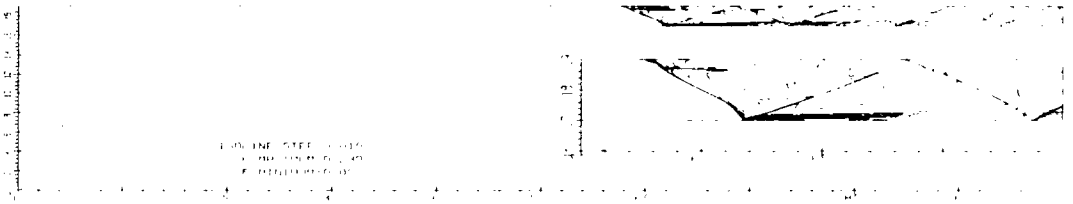


Fig.9b H_2O mass fraction field, $M=9$

The flow fields for $M=11$ are similar to previous ones for $M=9$. However, the ignition delay is practically absent near the duct wall downstream the reflection of bow shock. At $M=13$, the ignition occurs near the cone surface with some delay from the cone vertex. The detonation wave propagating to duct wall is formed in this case.

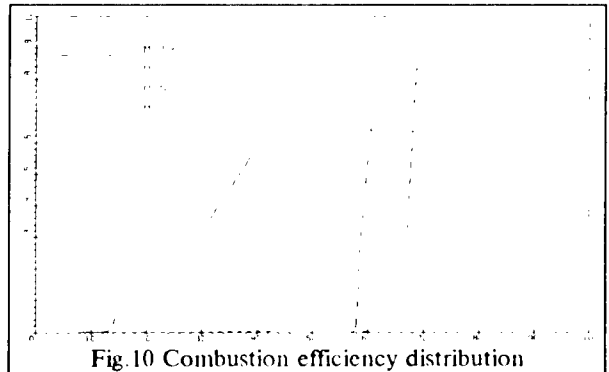


Fig.10 Combustion efficiency distribution

The distribution of combustion efficiency with duct length for the considered free stream Mach numbers is demonstrated by fig.10. Both the ignition delay and combustion efficiency in the cross-section corresponding to the gap exit are reduced if the free stream Mach number is increased. As projectile Mach number increases, the temperature behind shocks increases also and the system approaches to equilibrium with large values of radicals concentration at the expense of a dissociation reactions. Therefore, the combustion efficiency estimated by the released energy decreases. Thus, the mixture ignition, the flow structure and combustion efficiency strongly depend upon free stream Mach number.

References

1. Sislian J.P., Atamanchuk T.M. Aerodynamic and propulsive performance of hypersonic detonation wave ramjets // ISABE 89-7109, 1989.-P.1026-1035.
2. Atamanchuk T., Sislian J. On-and off design performance analysis of hypersonic detonation wave ramjets.-AIAA Paper 90-2473, 1990.
3. Kuznetsov M.M., Neyland V.Ja., Sayapin G.N. Efficiency investigation of scramjet with detonation and shockless supersonic combustion // Utchenye Zapisky TsAGI - 1992.-Vol.23, No.2.-P.30-37.
4. Sislian J.P., Dubebout R., Schumacher J., Oppitz R. Inviscid propulsive characteristics of hypersonic shcranjets.-AIAA Paper 96-4535, 1996.
5. Gonzalez D.E. Computational study of inlet injection for premixed shock-induced combustion.-AIAA Paper 96-4560, 1996.
6. Chinitz, W. On the use of shock-induced combustion in hypersonic engines.-AIAA Paper 96-4536, 1996.
7. Humphrey Joseph W. Parametric study of an ODW scramaccelerator for hypersonic test facilities.-AIAA Paper 90-2470, 1990.
8. Yungster S., Eberhardt S., Bruckner A.P. Numerical simulation of hypervelocity projectiles in detonable gases // AIAA Journal - 1991.-Vol.29, No.2.-P.187-199.
9. Chiping Li, K. Kailasanath, Elaine S. Oran Detonation structures generated by multiple shocks on ram-accelerator projectiles // Combustion and Flame - 1997.-Vol.108.-P.173-186.
10. Bezgin L., Ganzhelo A., Gouskov O., Kopchenov V., Laskin I. Numerical simulation of supersonic flows applied to scramjet duct // ISABE-95-7082, 1995.-P.895-905.
11. Kozlov V.E., Secundov A.N., Smirnova I.P. The turbulence models for compressible gas flows jets // Mechanica Jidcosti I Gasa - 1986.-No.6-P.38-44.
12. Godunov S.K., Zabrodin A.V., Ivanov M.Ja., Kraiko A.N., Prokopov G.P.-Numerical solution of multidimensional gas dynamics problems.-Moscow: Nauka, 1976.
13. Baruzzi G. Structured mesh grid adapting based on spring analogy // Proceedings of the CFD Society of Canada Conference, Montreal, June 14-15, 1993.
14. Dimitrow V.I. The maximum kinetic mechanism and rate constants in the $H_2 - O_2$ system // React. Kinetic Catal. Lett. - 1977.-Vol.7, No.1.-P.81-86.
15. Bussing T.R.A., Murman E.M. Numerical investigation of two-dimensional H_2 -Air flameholding over ramps and rearward-facing steps // Journal of Propulsion and Power - 1987.-Vol.3, No.5.-P.448-454.
16. Bezgin L., Ganzhelo A., Gouskov O., Kopchenov V. Numerical simulation of viscous non-equilibrium flows in scramjet elements // ISABE 97-7131, 1997.-P.976-986.
17. Courant R., Friedrichs K.O. Supersonic flow shock waves.-Interscience, 1948.
18. Chernyi G.G. Supersonic flow around bodies with detonation and deflagration fronts // Astronautica Acta - 1968.-Vol.13, No.5&6.-P.467-480.
19. Zeldovich Ja.B. Theory of combustion and detonation.-In: Chemical Physics and Hydrodynamics-Moscow: Nauka, 1984, P.143-198
20. Bartlma F. Gasdynamic der verbrennung.-Wien: Springer-Verlag, 1975.
21. Cambier J.L., Adelman H., Mences G.P. Numerical simulation of an oblique detonation wave engine // Journal of Propulsion and Power - 1990.-Vol.6, No.3.-P.315-323.

SOFTWARE COMPLEX FOR VELOCITY FIELD MEASUREMENT ON THE BASIS OF MULTIFRAME SHADOW PICTURES OF TWO-PHASE FLOW

V.M. Boiko, V.M. Giljov, S.G. Ocheretny, S.V. Poplavsky

Institute of Theoretical and Applied Mechanics SB RAS, Novosibirsk, Russia

INTRODUCTION

Various optical methods that yield a qualitative flow pattern (shadowgraphy, schlieren technique, laser sheet method) have gained a good reputation in studying two-dimensional flow pictures. When creating the «quantitative» methods, it is natural to use the existing optical methods with their light sources and registration techniques as a basis. One of the panoramic methods of flow velocity measurement is the track anemometry based on two- or multi-frame photoregistration using one of the above techniques and measurement of displacement of the medium inhomogeneity during a known time interval between the frames. The reconstruction of velocity field is the second stage of the measurement cycle, which can be performed by different means with an arbitrary accuracy, using arbitrary mathematical procedures, statistical methods, etc. However, this method of obtaining a large amount of quantitative information, its processing and mapping is a labor-consuming process.

Personal computers offer new possibilities of processing shadow pictures, namely, a photoscanner transforms the pictures into graphical files, which can be processed afterwards by graphical editors. Thus, images can be edited and data arrays for label displacements can be obtained using the systems Photofinish, Adobe Photoshop, etc., and the data arrays can be processed using electronic tables, for example, those of the Origin system. However, the abundance of incompatible file formats, the necessity of exchanging the files in the course of data processing, and because of standard programs surplus made it necessary to develop a single software complex including both the elements of graphical editors and the means of mathematical processing of resultant arrays.

The present paper deals with a software complex for processing multiframe shadow pictures of a two-phase flow for velocity field reconstruction. The code is written in the Visual C++ language for the operation system Windows 95 [1].

BASIC PRINCIPLES OF CODE OPERATION

BMP file processing

The goal of BMP file processing is to edit the initial image: contrast changing, particle mapping [2,3], reducing of all BMP files to the same size, and transforming a graphical file into a MAP file where each particle is described only by coordinates and size. At this stage the code works with a series of half-tone images in the form of BMP files, and each frame corresponds to its own BMP file, and then - with a MAP file or a group of MAP files. When forming the MAP files, the code automatically finds the particle coordinates and replaces the particle images by labels. The code operates in an automatic mode with files in which the internal function reduces the «contrast» to two colors: black and white.

The code can also operate in a manual mode, which allows the user to work with the initial image. All subsequent work is performed with MAP files which, in fact, are the desired array of coordinates of the chosen particles - labels.

MAP file processing

PIV processing of two MAP files is a statistical method of finding the label displacement vector in two neighboring frames, based on determining the maximum of the correlation function of displacement. This method is effective when there is a large number of single-size particles in the frame.

PTV processing of two MAP files is based on automatic identification of the same particles in different frames (Fig. 1). The identification criteria include individual parameters of a particle (size, transverse coordinate) and the signs of physical reliability of particle motion – «smoothness» of particle displacement trajectory. An advantage of this method over the PIV technique is that it allows for processing the images with a small number of particles, and the particle monodispersity is not necessary.

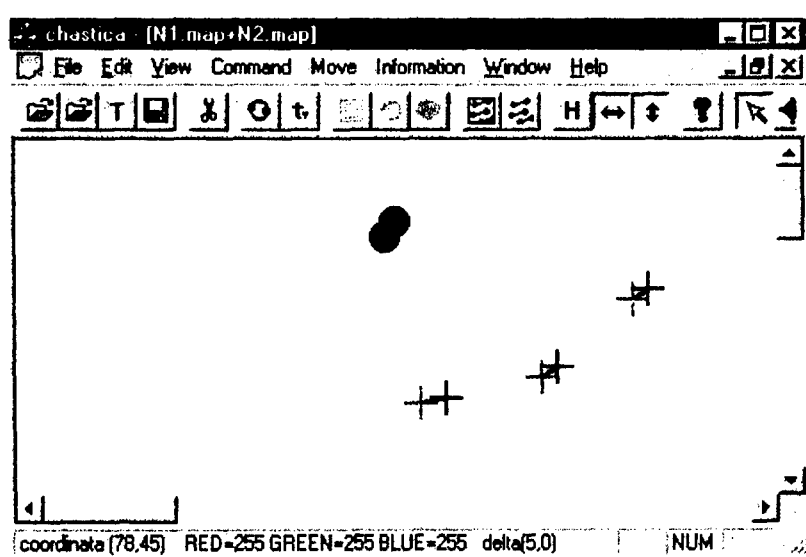


Fig. 1. Result of PTV processing.

The track for all labels in all frames is constructed by the method of superposition of several files in the output window, as if it were transparent slides with a contrasted image of particles-labels. To construct the overall track during the observation time, all MAP files of a given series, which contain an arbitrary number of labels, are summed. Labels with the same number (identified particles) are automatically joined by displacement vectors (Fig. 2).

Obviously, these vectors with proper normalization can be regarded as velocity vectors, since there are equal time intervals between the frames in the stroboscopic method of registration.

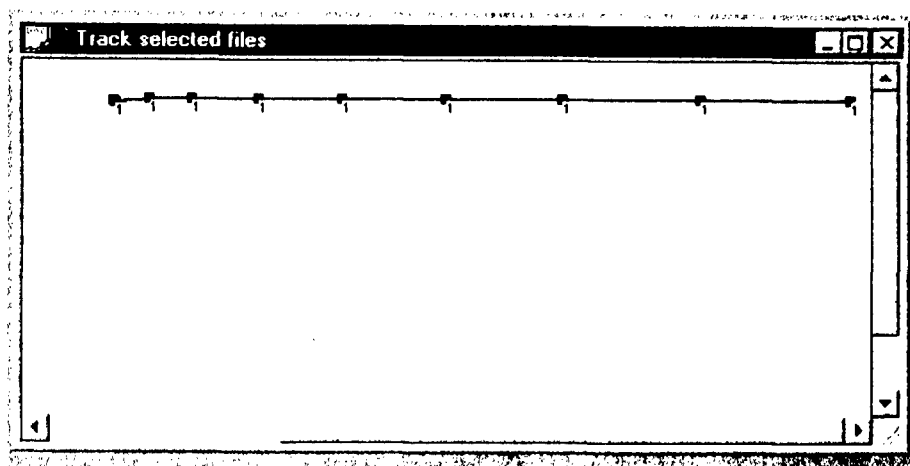


Fig. 2. Result of track construction

A POSSIBILITY OF GAS VELOCITY CALCULATION ON THE BASIS OF PARTICLE DISPLACEMENT DYNAMICS

The code can determine the gas velocity in a two-phase flow on the basis of particle displacement dynamics at an early stage of velocity relaxation of the phases. Let us emphasize that this is done without a priori knowledge of the particle and gas properties. The proposed approach is based on a possibility of grouping all undetermined parameters into a single aggregate – a certain parameter of velocity relaxation. Unfortunately, it has to be also calculated along with the flow velocity, but only two unknowns are left. Indeed, from the equation of particle motion in the flow behind the shock wave

$$m \frac{dV'}{dt} = s C_D \frac{\rho(u - V')^2}{2} \quad (1)$$

substituting $m = \rho_p \pi d^3 / 6$ and $s = \pi d^2 / 4$, we obtain the equation of motion in the form

$$\frac{d\left(\frac{V'}{u}\right)}{d\left(\frac{t}{\tau}\right)} = \left(1 - \frac{V'}{u}\right)^2, \quad \tau = \frac{4}{3} \frac{\rho_p}{\rho} \frac{d}{C_D u} \quad (2)$$

The parameter τ is the time constant of gas/particle velocity relaxation and contains all the unknown characteristics of the process. The solution of equation (2)

$$\frac{V'}{u} = 1 - \frac{1}{1 + t/\tau}$$

after integration yields the particle displacement against the duration of its residence in the flow

$$S(t) = u \tau \left[\frac{t}{\tau} - \ln \left(1 + \frac{t}{\tau} \right) \right] \quad (3)$$

which should be considered as a function of time and two desired parameters: $S(t; u, \tau)$. Formally, u and τ are not independent quantities, and another relaxation parameter characterizing the velocity relaxation length can be useful. Introducing

$$\sigma = u\tau = \frac{4 \rho_p d}{3 \rho C_D} \quad (4)$$

we obtain the particle displacement as a function of time and two independent parameters

$$S(t, u, \sigma) = ut - \sigma \ln \left(1 + \frac{ut}{\sigma} \right) \quad (5)$$

Numerical values of the parameters u and σ are found from the condition that the theoretical curve $S(t; u, \sigma)$ is «inscribed» into experimental points $S_i(t_i)$ in the best possible way ($i=1, \dots, n$ is the frame number). In this code the problem is solved using the least-squares technique [4,5], namely, if the function of time and two parameters $S(t; u, \sigma)$ is known, the desired quantities u and σ are the roots of the system of two equations

$$\begin{aligned} \sum_i^n [S_i - S(t_i)] \frac{\partial S(t_i)}{\partial u} &= 0 \\ \sum_i^n [S_i - S(t_i)] \frac{\partial S(t_i)}{\partial \sigma} &= 0. \end{aligned} \quad (6)$$

Solving these systems of equations for each particle, we obtain a set of paired values of u and σ which compose the gas flow field. Each pair should be considered as the averaging during the observation time t_n and in space: the shorter the particle track, the more local the measurement. Though the number of experimental points in a sample for determining two parameters can be reduced to *three*, the statistics is not representative with a small number of points. Some uncertainty is obvious: the higher the spatial resolution of the method, the lower its accuracy. For function (5) the initial system of equations has the form

$$\begin{aligned} \sum_i \left\{ S_i - \left[ut_i - \sigma \ln \left(1 + \frac{ut_i}{\sigma} \right) \right] \right\} \frac{t_i^2}{1 + \frac{u}{\sigma} t_i} &= 0 \\ \sum_i \left\{ S_i - \left[ut_i - \sigma \ln \left(1 + \frac{u}{\sigma} t_i \right) \right] \right\} \left[\frac{t_i \frac{u}{\sigma}}{1 + \frac{u}{\sigma} t_i} - \ln \left(1 + \frac{u}{\sigma} t_i \right) \right] &= 0. \end{aligned} \quad (7)$$

Unfortunately, there are more than one pair (u, σ) that satisfy this system. To identify the true values among all roots, it is necessary to reduce the regions of solutions by means of some preliminary evaluation, for example, by solving an approximate but linear system. Since an early stage of velocity relaxation is considered ($t/\tau < 1$), the following expansion is valid:

$$\ln \left(1 + \frac{t}{\tau} \right) \cong \frac{t}{\tau} - \frac{1}{2} \left(\frac{t}{\tau} \right)^2 + \frac{1}{3} \left(\frac{t}{\tau} \right)^3 - \dots$$

Then the displacement function (5) can be replaced by an approximate one:

$$S(t; u, \tau) \cong \frac{1}{2} \frac{u}{\tau} t^2 - \frac{1}{3} \frac{u}{\tau^2} t^3 + \frac{1}{4} \frac{u}{\tau^3} t^4 - \dots$$

Introducing new parameters $x_1 = u/2\tau$, $x_2 = u/3\tau^2$, $x_3 = u/4\tau^3 \dots$, and substituting into (6) a new fitting function

$$S^*(t; x_1, x_2, x_3, \dots, x_m) = x_1 t^2 - x_2 t^3 + \dots \pm x_m t^{m+1}$$

("+" - for odd m ; "-" for even; $m < n$ are the numbers of points in the array), we obtain a system of m linear equations. Since the general form is cumbersome, we shall confine ourselves to the two-parametric case:

$$x_1 \sum_i^n t_i^4 - x_2 \sum_i^n t_i^5 = \sum_i^n S_i t_i^2$$

$$x_1 \sum_i^n t_i^5 - x_2 \sum_i^n t_i^6 = \sum_i^n S_i t_i^3$$

Solving this system with respect to x_1, x_2 , we obtain approximate values of gas velocity and relaxation parameters of the process

$$u^* = \frac{4}{3} \frac{x_1^2}{x_2}, \quad \tau^* = \frac{2}{3} \frac{x_1}{x_2}, \quad \sigma^* = \frac{8}{9} \frac{x_1^3}{x_2^2}.$$

These quantities determine the region of convergence for solving the exact system of equations (7), or can be used as the final result if $t/\tau \ll 1$.

An example of determining the flow velocity behind the shock wave.

Below we present an example of processing a multiframe series of shadow pictures which registers the shock wave interaction with a rarefied dusty cloud. The shock wave Mach number is $M_s = 4.5$, the expected flow velocity is $u = 1200$ m/s. The displacement field for 10 particles (Fig. 3) was obtained by their «manual» selection from 12 frames, and the vectors connecting the labels after proper normalization can be considered as the mean particle velocity during the time between the frames ($20 \mu s$). The data arrays with particle displacements, which were obtained during track formation, are then used to calculate the gas velocity along a chosen trajectory.

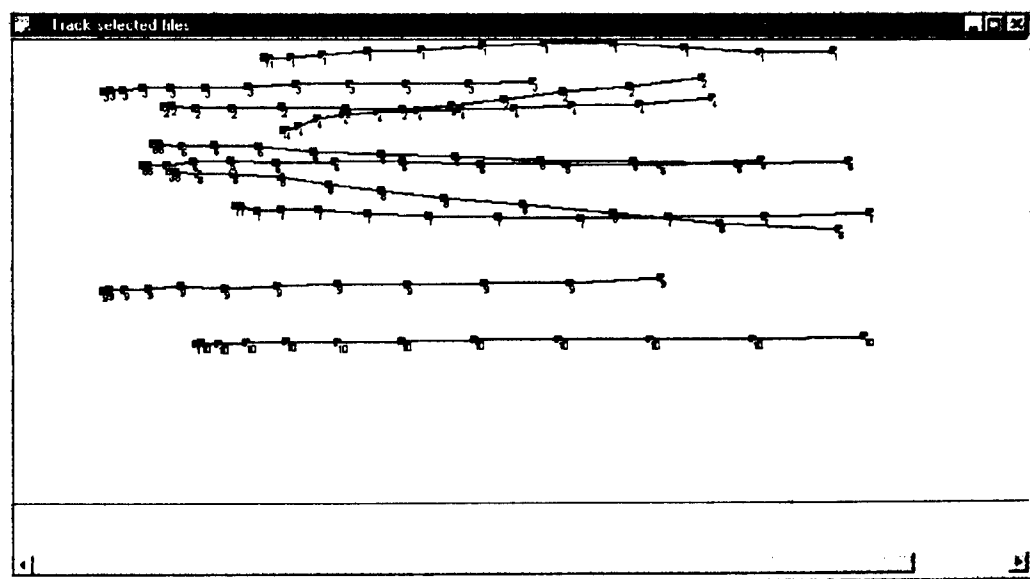


Fig. 3. Particle displacement field in the flow behind the shock wave at an early stage of relaxation.

The Table presents the output files of track processing for two particles: №3 and №9 from Fig. 3. The files contain the code-formed data arrays for particle displacements during the particle residence in the flow ($t[i], s1[i]$) and the results obtained by fitting with approximate and exact methods of calculation

Table

Calculation of track 3		Calculation of track 9	
t[i]	sl[i]	t[i]	sl[i]
0.000000e+000	0.000000	0.000000e+000	0.000000
1.900574e-005	0.000283	1.904398e-005	0.000283
3.900574e-005	0.000850	3.904397e-005	0.000963
5.900574e-005	0.001757	5.904397e-005	0.002040
7.900574e-005	0.003004	7.904397e-005	0.003514
9.900574e-005	0.004590	9.904397e-005	0.005497
1.190057e-004	0.006517	1.190440e-004	0.007877
1.390057e-004	0.008671	1.390440e-004	0.010597
1.590057e-004	0.011107	1.590440e-004	0.013771
1.790057e-004	0.013657	1.790440e-004	0.017228
1.990057e-004	0.016491	1.990440e-004	0.021081
2.190057e-004	0.019381	2.190440e-004	0.025218

Fitting of experimental points with a cubic interpolation function

$$S(t)=a*t^2-b*t^3$$

$$alf=2.000000$$

$$beta=3.000000$$

$$a=5.278072e+005$$

$$b=5.636285e+008$$

$$u1=659.016663 \text{ (m/c)}$$

$$tau1=6.242968e-004 \text{ (c)}$$

$$sigma1=0.411422 \text{ (m)}$$

$$S(t)=a*t^2-b*t^3$$

$$alf=2.000000$$

$$beta=3.000000$$

$$a=5.911203e+005$$

$$b=2.985056e+008$$

$$u1=1560.766357 \text{ (m/c)}$$

$$tau1=1.320177e-003 \text{ (c)}$$

$$sigma1=2.060487 \text{ (m)}$$

Fitting of experimental points with an exact displacement function

$$u2=626.304749 \text{ (m/c)}$$

$$tau2=6.206468e-004 \text{ (c)}$$

$$sigma2=0.388714 \text{ (m)}$$

$$u2=1536.000122 \text{ (m/c)}$$

$$tau2=1.312059e-003 \text{ (c)}$$

$$sigma2=2.015323 \text{ (m)}$$

The results of calculation (approximate $u1$, $tau1$, $sigma1$ and exact $u2$, etc.) point to a substantial difference in gas parameters in the flow core (track №9) and near the channel wall (track №3). In the given case, the particle trajectories are close to the gas streamlines, and the particle acceleration dynamics reflects the averaged velocity and flow relaxation parameters along chosen lines.

Thus, a software complex has been developed. It has the following features: operates on personal computers IBM PC in the interactive regime with various file formats; has a set of methods for editing the initial graphical files and forming the data arrays for the displacement of a large number of labels as a function of time; has internal mathematical means for data array processing for obtaining quantitative information on the parameters of two-phase flows.

The work was supported by the Russian Foundation for Basic Research (grant No 96-01-00322.)

REFERENCES

1. Billing V.A., Musikaev I.Kh. Visual C++ Programmer's Handbook. – Izdatelsky otdel «Russkaya Redaktsiya», Moscow, 1996. –352 p.
2. Pratt W. Digit Images Processing. – Wiley, New York, 1978.
3. Janishin V.V., Kalinin G.A. Image Processing in «C» language for IBM PC: Algorithms and Programs. – Mir, Moscow, 1994.
4. Kassandrova O.N., Lebedev V.V. Processing of Observation Results. – Nauka, Moscow, 1970. –104 p.
5. Slabky L.I. Methods and Devices of Limiting Measurements in Experimental Physics. – Nauka, Moscow, 1973. –272 p.
6. Bakhvalov N.S. Numerical Methods (Analysis, Algebra, Ordinary Differential Equations) . –Nauka, Moscow, 1975. –631 p.

HIGH-SPEED CINEMATOGRAPHY STUDY OF AN IMPULSE HIGH-PRESSURE GAS-LIQUID JET

A.A. Buzukov

Institute of Theoretical and Applied Mechanics SB RAS,
630090, Novosibirsk, Russia

An adequate physical and mathematical modeling of flows arising under the conditions of evolution of impulse high-speed jets is an important fundamental problem with a large number of engineering applications. The difficulties arising here are especially severe if the interacting media have extraordinary physical and chemical properties. One of the examples of these complicated events is the evolution of a fuel-air jet formed by high-pressure impulse injection of liquid fuel into compressed and heated air. The defining and solving of this problem are important because exactly this mixture is an unseparable constituent of the operating process of most internal combustion engines and determines to a large extent their efficiency, ecological safety, and other performance features. The mechanism of evolution of an impulse high-pressure jet of the fuel-air mixture, which is formed in the combustion chamber of a Diesel engine, is described in the present paper. A scheme for calculating the basic quantitative characteristics of the mixing process under these conditions is suggested.

Complex experimental researches were performed using the methods of high-speed cinematography [1, 2], microphotography with impulse laser lighting [3], impulse X-ray photography [4, 5]. These studies showed that the process under consideration can be conventionally split into four sequential stages, each of them having a specific character of the flow established in the jet and around it. Before analyzing these flows, one important circumstance should be noted, which has a determining effect on the overall process of jet evolution. Immediately after leaving the nozzle ($Re=10^3-10^6$), the fuel becomes sprayed due to cavitation destruction by unloading. The jet should be considered, therefore, from the very beginning as a flow of small particles ($10-100\ \mu m$) independent of each other but packed near the nozzle up to density of undispersed liquid (Fig. 1). Being injected from the nozzle, these particles acquire not only the longitudinal velocity ($U_0=150-350\ m/s$) but also the radial velocity ($U_r=20-50\ m/s$). Thus, such a jet can be characterized by a certain expansion angle β , which depends on injection pressure, ratio of liquid and gas densities, and dynamic rupture strength of the liquid under sudden unloading [6].

At the first stage the fore part of this compacted jet moving in gas acquires the shape of a "turned-out stocking" (Fig. 2), i.e., the interaction between the media follows a cumulative mechanism [3]. Until a certain time moment (until the jet length exceeds $30-60\ d_0$ where d_0 is the sprayer nozzle diameter) the liquid state is close to monolithic. Correspondingly, the liquid sheet moved apart from the motion direction is also continuous.

The second, transitional stage of jet evolution begins when its fore part becomes porous because of divergence of the axial flow (Fig. 3), it becomes perforated, and a large number of particles begin to interact with the medium. This process is defined as quasi-cumulative [1, 3, 5]. It is characterized by the fact that liquid bunches of various scales, entering the region of direct contact with the medium (both their additional crushing and coagulation occur here), are entrained to periphery, where they hang in the ambient space. It is essential that this gas-drop mass returns partly to the axial flow under the action of

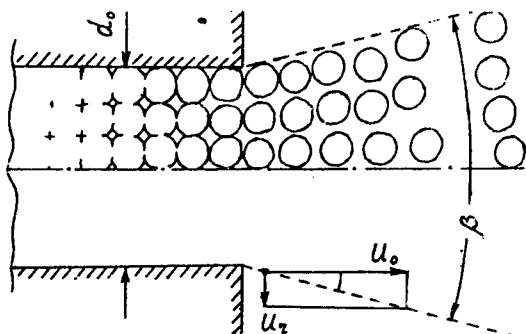


Fig. 1.

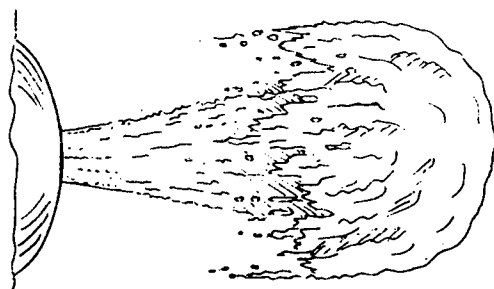


Fig. 2.



Fig. 3.

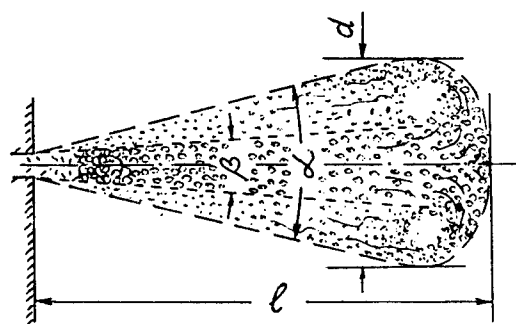


Fig. 4.

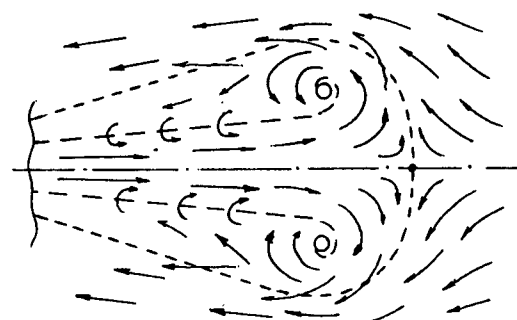


Fig. 5.

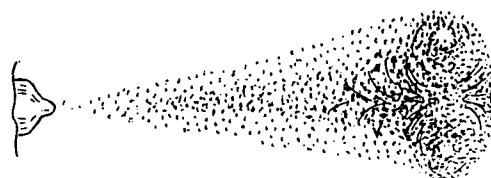


Fig. 6.

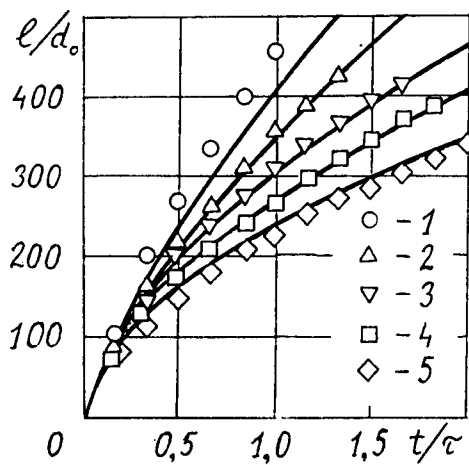


Fig. 7.

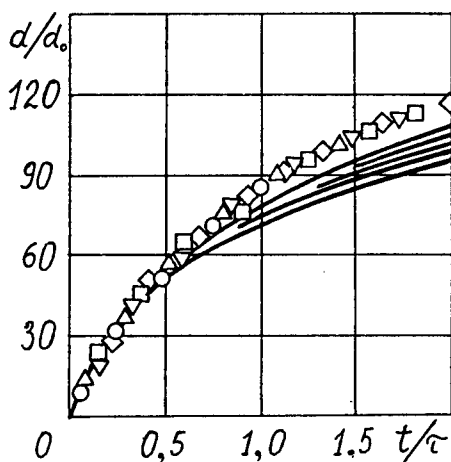


Fig. 8.

cocurrent gas flow. Thus, a closed recirculation flow forms in the fore part of the jet at this stage ($l=50-100 d_0$).

The third stage of the process can be considered as the basic one, because its duration is quite long, and heat release usually occurs exactly during this stage. The third stage is characterized by a stable hydrodynamic flow formed in the fore part of the jet. The structure of this flow corresponds to that observed in an annular vortex (Fig. 4). Contrary to the classical annular vortex, this hydrodynamic structure is constantly replenished by the flow of new gas-liquid mixture entering the rear zone of the vortex. On the other hand, the loss of mixture and its hanging in the ambient space take place at the side surface of this quasi-vortex. Thus, the jet is composed of an axial high-speed quasi-steady flow, its fore part where the mixture rotation occurs and a layer with comparatively low fuel content which encircles concentrically this complex [2, 6]. The presence of such a layer determines the external contours of the jet, which are observed in the frames of high-speed filming [1, 2] and are usually characterized by the common (root) expansion angle α . A scheme of this flow observed from the coordinate system moving with the frontal jet surface is shown in Fig. 5.

Finally, the fourth stage of jet evolution begins after the fuel injection is terminated (cyclic injection $q=20-100$ mg, duration $\tau=2-10$ ms). At this stage the replenishment of the vortex formation comes to an end, and it degenerates into an autonomous annular vortex independently moving in the medium (Fig. 6).

The body of this vortex is filled with a part of fuel-air mixture formed during injection, the other part of the mixture remains in the jet wake. Most frequently, however, the mixing process does not reach the fourth stage, since evaporation, ignition and combustion of the fuel-air mixture take place earlier, at the third stage.

On the basis of above concepts of jet evolution, which were mainly developed for mixing conditions in the combustion chamber of a diesel engine, a three-stage scheme for calculating the main characteristics of this process was suggested. The first stage covers a quasi-steady motion of a gas-liquid flow in the gaseous medium, independent of the processes in its fore part. The knowledge of liquid dispersion dynamics under the conditions of its high-pressure exhaustion from the nozzle and semi-empirical functions for jet expansion angle β are used.

At the second stage of calculations, the problem of cumulative penetration of the "projectile" (axial gas-liquid jet) into the "target" (ambient gaseous medium) is solved. Using the classical relations that describe this process and taking into account the lengthwise variation of jet parameters, it is possible to determine the main characteristic of the mixing process - the jet length l versus the time t .

The third stage of calculations includes determination of other important parameters of the jet: the root expansion angle α and the diameter d in the maximum cross-section. The formulas are used that relate the geometric parameters of such a canonical hydrodynamic structure as an autonomous annular vortex with the character of exhaustion of liquid, which forms this vortex, from the vortex generator nozzle. The condition of self-similarity of this flow allows one to extend these formulas to the case of the formation of annular quasi-vortex in the fore part of the jet.

Figures 7 and 8 show the calculated values of l and d (solid lines) in comparison with experimental data [2], in which the gaseous medium density ρ (kg/m^3) was 10 (1), 20 (2), 30

(3), 40 (4), and 50 (5). The presented plots show that the calculated and experimental values of jet parameters are in good qualitative and quantitative agreement. Some discrepancies are explained within the framework of the constructed physical model.

REFERENCES

1. V.K.Baev, A.N.Bazhaikin, A.A.Buzukov, and B.P.Timoshenko, On the cumulative mechanism of high-pressure fuel jet development//*Dvigatelsestroenie*. 1981. No. 2. P. 5-8.
2. A.A.Buzukov, Peculiarities of the pulsed high-velocity air-fuel jet evolution in the Diesel combustion chamber//*Thermophysics and Aeromechanics*. 1996. Vol. 3, No. 4. P. 347-356.
3. V.K.Baev, A.N.Bazhaikin, I.V.Boldyrev, A.A.Buzukov, V.A.Terent'ev, and B.P.Timoshenko, The initial stage of evolution of the fuel plume exhausted from a funnel with high pressure//*Combustion, Explosion, and Shock Waves*. 1979. Vol. 15, No. 1. P. 26-32.
4. V.K.Baev, A.N.Bazhaikin, E.I.Bichenkov, A.A.Buzukov, R.L.Rabinovich, and B.P.Timoshenko, X-ray momentum method of radiation of the internal structure of a fuel plume//*J. Appl. Mech. Tech. Phys.* 1980. Vol. 21, No. 1. P. 105-111.
5. V.K.Baev, A.N.Bazhaikin, A.A.Buzukov, and B.P.Timoshenko, Qualitative features of plume evolution during fuel injection into a medium with backpressure up to 10 atm//*J. Appl. Mech. Tech. Phys.* 1981. Vol. 22, No. 2. P. 66-70.
6. A.A.Buzukov and B.P.Timoshenko, Dispersion of a high-pressure jet of water-fuel emulsion//*J. Appl. Mech. Tech. Phys.* 1995. Vol. 36, No. 1. P. 106-111.

MAXIMUM ENTROPY BASED TOMOGRAPHY OF GAS FLOWS

N. V. Denisova

Institute of Theoretical and Applied Mechanics SB RAS,
630090, Novosibirsk, Russia

INTRODUCTION

Computer tomography is receiving increasing attention in the field of fluid mechanics research [1] – [3]. In most experiments the reconstructions were carried out in a subsequent series of 2-D planes located perpendicular to the flow direction. Supersonic jet was studied in [1] by the beam-deflection method. The convolution back-projection algorithm was employed to reconstruct the nitrogen gas density. Turbulent flow was considered in [2]. Measurements were made by multi-angular viewing of the holographic interferograms. A back-projection type algorithm was used for reconstruction of the unsteady flow field. Supersonic free jets were studied in [3] by interferometric tomography. A modified algebraic reconstruction technique algorithm was used for the reconstruction of density distribution of weakly perturbed jets from a deformed Laval nozzle.

Viewing access in most tomographic experiments is strongly limited, leading to a highly underdetermined inversion problem. Unfortunately, in ART and back-projection types algorithms streaking artifacts are a severe problem when the number of views is limited.

A promising approach to tomography problems is the maximum entropy (ME) method which seems ideally suitable for tomographic investigations of gas flows [4]. Numerical calculations showed that, with a small number of views, ME algorithms allow one to obtain good results of reconstruction relatively free from artifacts [4]–[6]. This quality of ME algorithm is especially important for the researches of unsteady processes.

An application of the ME approach to the problems of gas flow is considered in this paper. The problem of reconstruction with an opaque body is analyzed. Numerical examples are given of two-dimensional reconstruction with input data chosen to test the algorithm.

MAXIMUM ENTROPY APPROACH IN COMPUTER TOMOGRAPHY

The problem of reconstruction of a source function can be formulated as the inversion of Radon transform. Two-dimensional reconstruction problem can be presented as follows:

$$f(p, \theta) = \int_{-\infty}^{\infty} g(x, y) dl_{p, \theta} \quad (1)$$

where $f(p, \theta)$ are the projection data, $g(x, y)$ is the unknown source function, integrated along the line $l_{p, \theta}$, θ_i is the projection angle, p and θ are the normal coordinates of the line l . We assume that the unknown source function $g(x, y)$ satisfies

$$g(x, y) \geq 0 \quad (2)$$

Reconstruction from a finite set of projection data is known to be an indeterminate problem. The maximum entropy approach is a way to overcome the indeterminacy. The derivation of the ME criterion is well known [7]. The entropy equation is defined as

$$\psi(g) = - \int dx \int dy g(x, y) \ln[g(x, y)]. \quad (3)$$

Maximizing $\psi(g)$ we obtain the constrained optimization problem that allows us to select a unique solution. A detailed consideration was performed in [4]–[6] for different types of reconstruction geometry.

The resulting expression for the source function in the case of parallel beam geometry was obtained in [5] as

$$g(x, y) = \prod_j H_j(x \cos \theta_j + y \sin \theta_j) \quad (4)$$

The iteration formula for H_j was determined

$$H_j^{i+1} = f_j / \int dt \prod_{k \neq j} H_k^i(s \cos \theta_{jk} - t \sin \theta_{jk}) \quad (5)$$

where $\theta_{jk} = \theta_j - \theta_k$; θ_j, θ_k are the projection angles, (s, t) is a Cartesian coordinate system rotated at an angle θ_j relative to the basic system (x, y) . The expression for $g(x, y)$ and the coefficients H_j in the case of fan geometry were obtained in [6]. Gauss-Seidel method was used to solve the nonlinear system of equations (5).

The ME method yields a solution which is most probable in the sense of combinatorial theorem and for which given data would have been sufficient statistics. Usually a researcher wants to know how close this solution to the original source is. This question can probably only be answered by numerical simulation, which will test the reconstruction algorithm in the conditions close to real experiment.

NUMERICAL EXAMPLES

The numerical calculations were performed with computer-generated input data with realistic levels of noise. The reconstruction error was defined as the mean-square norm of deviation of the reconstruction solution $g(x, y)$ from the exact one g_0 :

$$\Delta = \frac{(\sum_i \sum_j (g(x_i, y_j) - g_0(x_i, y_j))^2)^{\frac{1}{2}}}{(\sum_i \sum_j (g_0(x_i, y_j))^2)^{\frac{1}{2}}} \cdot 100\%. \quad (6)$$

A test Model was chosen to examine the convergence characteristics of the ME algorithm. The Model is a superposition of five parabolic functions:

$$g(x, y) = \sum_{i=1}^5 c_i \left[1 - \frac{(x - x_{0i})^2}{a_i^2} - \frac{(y - y_{0i})^2}{b_i^2} \right] \quad (7)$$

with parameters

$$\begin{aligned} c_1 &= 1; a_1 = b_1 = 0.3; x_{01} = 0.5; y_{01} = 0.5; \\ c_2 &= 1; a_2 = b_2 = 0.3; x_{02} = -0.5; y_{02} = 0.5; \\ c_3 &= 1; a_3 = b_3 = 0.3; x_{03} = -0.5; y_{03} = -0.5; \\ c_4 &= 1; a_4 = b_4 = 0.3; x_{04} = 0.5; y_{04} = -0.5 \\ c_5 &= 1; a_5 = b_5 = 0.3; x_{05} = 0.; y_{05} = 0.; \end{aligned}$$

This model can simulate a cluster of five free jets exhausted from a sievelike nozzle. Figure 1 shows the results of reconstruction of the Model. $M = 33$ equally spaced rays in each view were used, and the tomogram had a dimension $K = 33 * 33$. The set of projection angles was defined by the relation

$$\varphi_j = \frac{\pi}{J} (j - 1) \quad (8)$$

where J is the total number of views.

A 3% noise was added to the exact data. The numerical calculations showed that the ME algorithm is stable against the noise error. One can see a good agreement with the exact image when the number of views is $J = 4$. It is a very promising result which demonstrates that the ME is suitable for reconstructing inhomogeneous distributions of parameters.

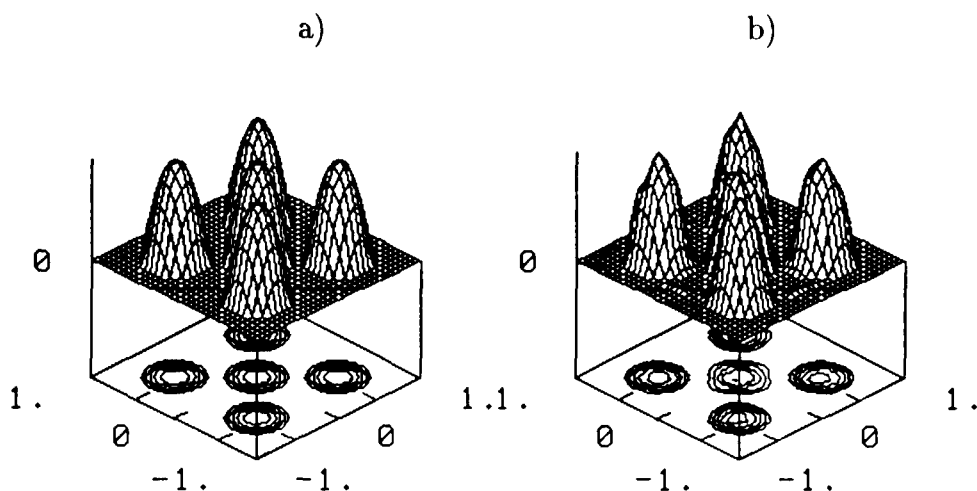


Figure 1: a) - original source , b) - reconstruction with 3% noise from 4 views.

Numerical calculations showed that the errors of reconstruction decrease very rapidly with increasing the number of views and in the presence of 3% noise reach a plateau at a level of about 9% for $J \geq 8$.

The problem of tomography reconstruction with an opaque body was also analyzed in this paper. Projection data are presented in this case as "information pieces". An interpolation of coefficients H_j was used to solve these problems. The interpolation was fulfilled into the region where projection data were lacking. It is assumed that we do not have any prior knowledge about the source function in this region. Figure 2 shows an example of reconstruction with an opaque body. To test the algorithm, a singularity as a peak of the source function was added. The magnitude and location of the singularity were varied. A good reconstruction quality was obtained on condition that the singularity must be observed at least from three views at rather different angles. We observed here a good agreement with the exact image for the number of views $J \geq 6$.

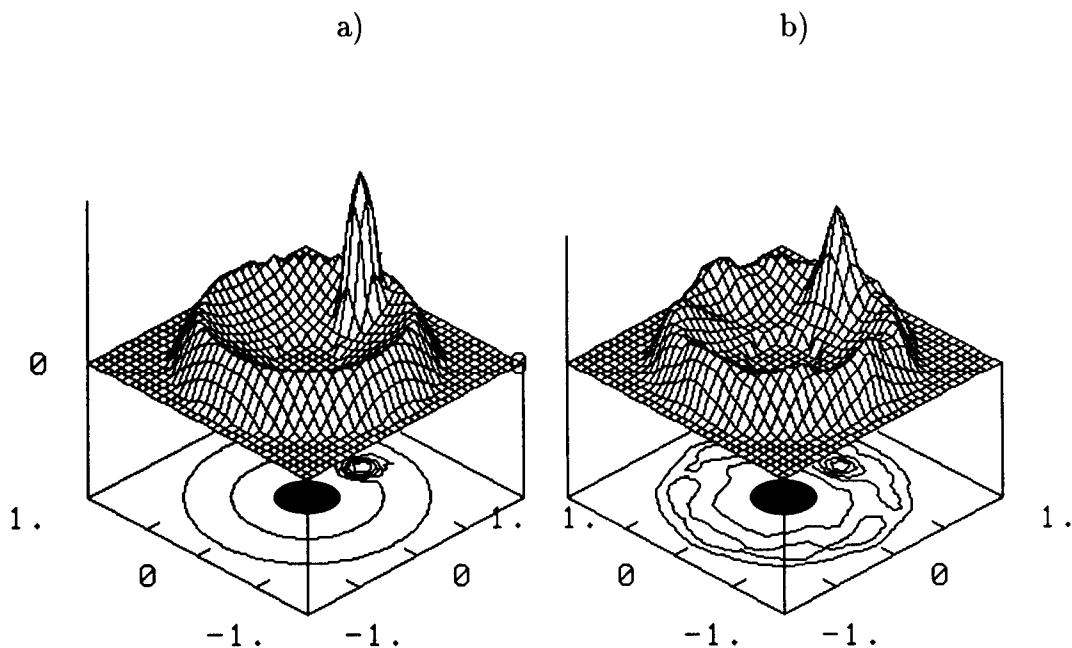


Figure 2: a) - original source, b) - reconstruction from 6 views.

CONCLUSION

The maximum entropy concept is a powerful tool for tomographic investigations of gas flows. The ME method rather confidently leads to the exact solution with increasing the number of views. This is in accordance with the general ME concept to choose the most probable solution among all possible variants. Good results of reconstruction were obtained in the situation with an opaque body when the projection data were presented as "information pieces".

References

- [1] Faris G.W., Byer R.L. Three-dimensional beam-deflection optical tomography of a supersonic jet// Appl. Opt.-1988.- Vol.27.-P.5202.
- [2] Watt D.W., Vest C.M. Turbulent flow visualization by interferometric integral imaging and computed tomography// Exper.in Fluids.-1990.-Vol.8.- P.301.
- [3] Soller C., Wenskus R., Middendorf P., Meier G.E.A., Obermeier F. Interferometric tomography for flow visualization of density fields in supersonic jets and convective flow// Applied Optics.- 1994. - Vol.33.- P.2921.

- [4] Minerbo G. MENT: A maximum entropy algorithm for reconstructing a source from projection data// Computer graph. and image proces.- 1979.- Vol.10.- P.48.
- [5] Denisova N.V.,Pickalov V.V.,Balandin A.L. Modified maximum entropy method in plasma tomography// Optics and Spectrosc.- 1996. - Vol.81.- P.35.
- [6] Denisova N.V. Fan tomography of gases and plasmas based on the maximum entropy method// Optics and Spectrosc.- 1997. -Vol.83.- P.1019.
- [7] Frieden B.R. Restoring with maximum likelihood and maximum entropy// J. Opt. Soc. Amer.- 1972.-Vol.62.- P.511.

NUMERICAL INVESTIGATION OF CROSSFLOW INSTABILITY ON 39°-SWEEPED WING

N.D.Dikovskaya, G.I.Klinkova, V.Y.Levchenko
ITAM SB RAS, Novosibirsk, Russia

A number of instabilities, connected with secondary flows, were observed in boundary layer flows over swept wings. Carried out calculations gave different results in definition of the most amplifying disturbances [1-4]. According to one data [2, 3], they were zero frequency stationary waves who demonstrated the highest amplification, according to others [1, 4]- travelling waves propagating in secondary flow direction. The goal of this work was to calculate the stability characteristics of a three-dimensional boundary layer over 39°-swept profile in a subsonic flow and to compare numerical results with experimental data [5] obtained under the same flow conditions.

The processing of experimental data [5] was carried out under the assumption of the "local parallelism" of inviscid flow. The used up reference systems for the flow on the external edge of the boundary layer are shown in Fig.1. Mean flow velocity V_e at the boundary layer edge (Fig.2, curve 1) was calculated using Bernoulli equation on the basis of static pressure experimental distribution along the X axis [6]. Chordwise component of mean flow velocity U_e (Fig.2, curve 3) was obtained from hot-wire measurements [5]. The approximation of $U_e(x)$ and $V_e(x)$ data was performed by the third order polynomials. Chordwise distributions of

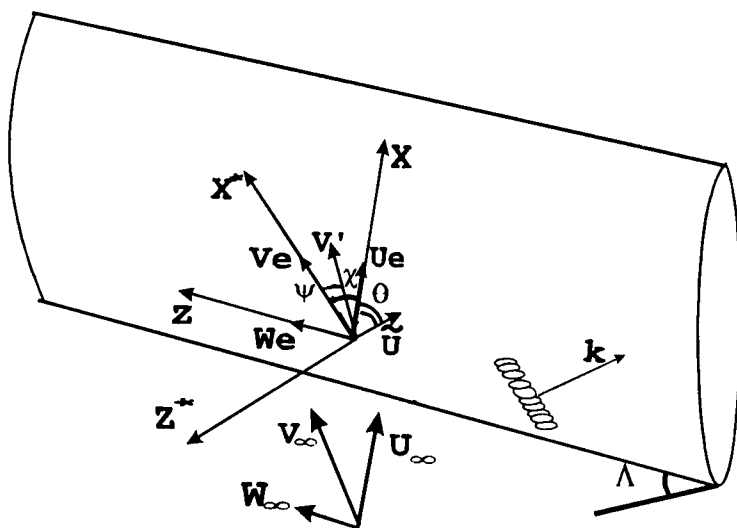


Fig.1. Using reference systems

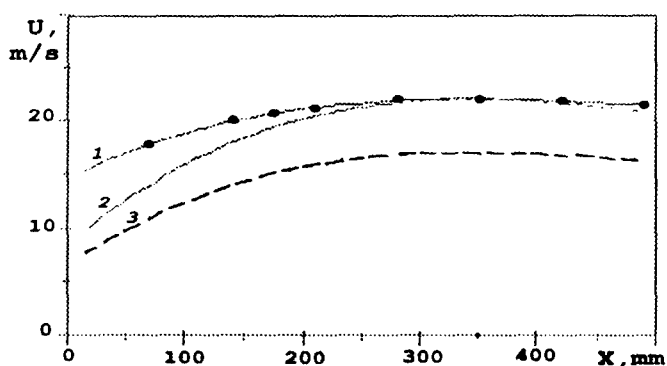


Fig. 2. Mean flow velocity: 1- V_e experimental data, approximated by polynomial; 2-component V' in the undisturbing freestream direction; 3-component U_e in a chordwise direction.

potential flow velocity component in free stream direction V' (Fig.2, curve 2) and of the angle ψ between potential streamline direction and undisturbed freestream direction were obtained from the following expressions:

$$V' = U_e / \cos \Lambda$$

$$\psi = \arccos(U_e / V_e) - \Lambda, \quad \text{where } \Lambda = 39^\circ.$$

The velocity profiles were obtained from the solution of Falkner-Skan-Cook equations system [6] with parameter $m = 0,345$. Falkner-Skan-Cook parameter m was determined from the condition of the best potential flow velocity approximation by the function $U_e(x) = Cx^m$. The equations were solved by shooting method using the IV-th order accuracy Runge-Kutte method. Then using Squire transformation, the three-dimensional equation system was reduced to a single quasi two-dimensional disturbance equation in the wave propagation direction $(\theta-\chi)$ [3]. Thus mean flow velocity profiles and all eigenfunctions were projected on this direction (Fig.1). Then the characteristics of three-dimensional disturbances in a spatial boundary layer were found by the solution of an well-known Orr-Sommerfeld equation [6,7].

As a result of swept wing crossflow stability calculations, the spatial growth rates $-\alpha_i$ and wave numbers $|k|$ were obtained as a functions of frequency. The calculations were carried out in the angle range $(\theta-\chi) = 87^\circ - 92^\circ$. As the occasion required step in angle was varied from $0,05^\circ$ up to $0,4^\circ$. For each direction the most amplifying disturbance frequencies were found. Besides, for angles values $88.7^\circ, 90^\circ, 91.2^\circ$ dependencies of $-\alpha_i$ and $|k|$ on frequency were calculated in the frequency range from zero up to 408 Hz (this covers the whole area of unstable

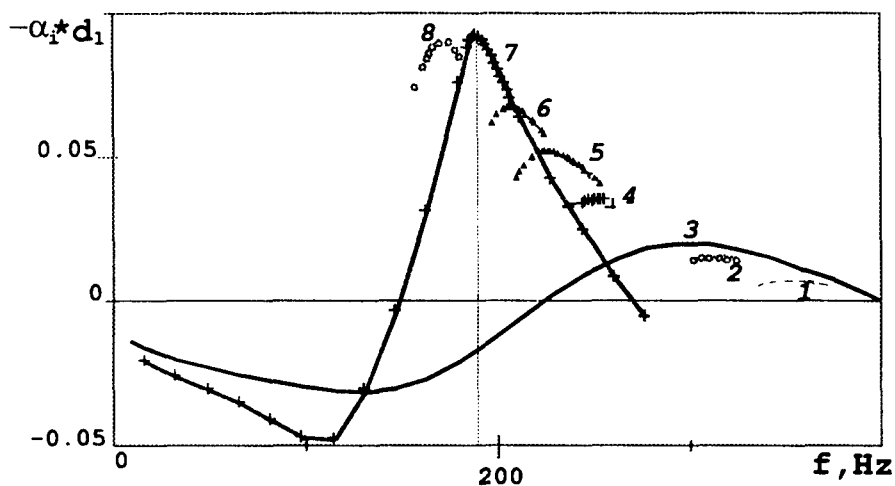


Fig. 3. Frequency variation of increments for various propagation angles: 1-89.3°; 2-89.8°; 3-90°; 4-90.6°; 5-90.8°; 6-91.0°; 7-91.4°; 8-91.6°

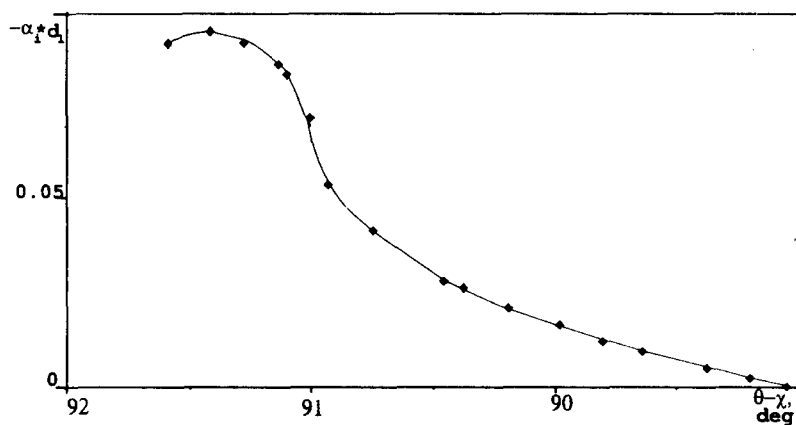


Fig. 4. Increments of the most amplifying disturbances as a function of propagation angles

frequencies). In all figures the displayed wave number and increment distributions were nondimensionlized by displacement thickness d_1 , calculated using velocity component V , tangential to the external flow streamline. In Fig.3 the frequency variation of increments $-\alpha_i$ for different propagation angles of disturbances is shown. As it can be seen, the frequency region of unstable modes lies below 400 Hz. At low frequencies ($f < 25$ Hz) the increments corresponding to different

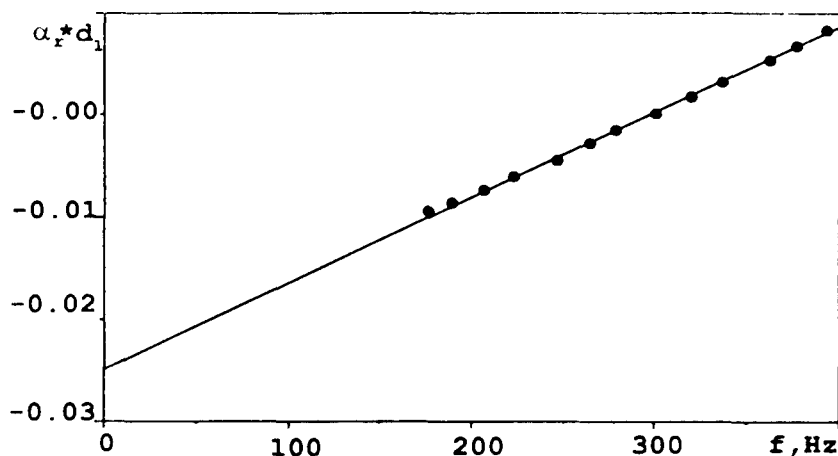


Fig 5. Frequency variation of longitudinal wave number for the most amplifying disturbances

angles differ weakly. The most unstable mode is a disturbance with frequency 180 Hz. At zero frequency the maximal increment is equal -0.007 that indicates weak attenuation of stationary modes.

Variation of the most amplifying disturbance increment $-\alpha_1$ with their propagation angles is shown on Fig.4. As it can be seen, the most amplifying disturbances correspond to the angle 91.4° . Experiment has shown that in accelerating flow, (which was under consideration in this work), an unstable mode with frequency 178 Hz and propagation angle 91.8° was selected. The second wave packet with frequencies from 0 up to 30 Hz just in the given area had small attenuation of amplitude. Thus the computations are in good agreement with experiments.

The projections of vector k on an axes X^* and Z^* (see. Fig. 1), connected with the direction of a potential flow in the given point, can be obtained using Fig.4:

$$\alpha_r = k_{X^*} = k \cos(\theta - \chi),$$

$$\beta = k_{Z^*} = k \sin(\theta - \chi),$$

Here α_1 is a longitudinal wave number, β -cross-sectional wave number. Value of βd_1 calculated for the most possible amplifying disturbances is equal to 0.45. It should be mentioned that at various flows and disturbances parameters, experimentally obtained values of βd_1 for the most amplified disturbances were very close to the theoretical ones and varied in the range 0.4...0.6 [4].

Variation of longitudinal wave numbers α_1 and propagation angles (in reference to potential flow direction) with frequency f for the most unstable spectral modes are shown in Figs. 5, 6.

In both cases the calculated points are well approximated by lines, that enables us to extrapolate the obtained data. Extrapolation gives the value of

propagation angle $(\theta-\chi)$ for disturbances with zero frequency approximately 93° (in reference to external streamline direction). At this a longitudinal dimensionless wave number kd_1 being determined from relationship $kd_1 = \alpha_r d_1/\cos 93^\circ$, is equal to 0,48. Under given flow conditions such estimation gives approximate value of stationary wavelength $\lambda = 2\pi/\alpha_r$ equal to 5 mm, that is from 2 to 3 times less then previously obtained values [3, 5], but at the same time this value coincides with the results of some experiments [2].

Frequency dependence of the phase velocities $C_k = 2\pi f d_1 / |k| V_e$ for the most unstable disturbance is shown in Fig.7. It can be seen, that as frequency decreases, the phase velocity tends to zero and coincides the exact value obtained for stationary modes ($C_k = 0$), that is inherent for large angles of

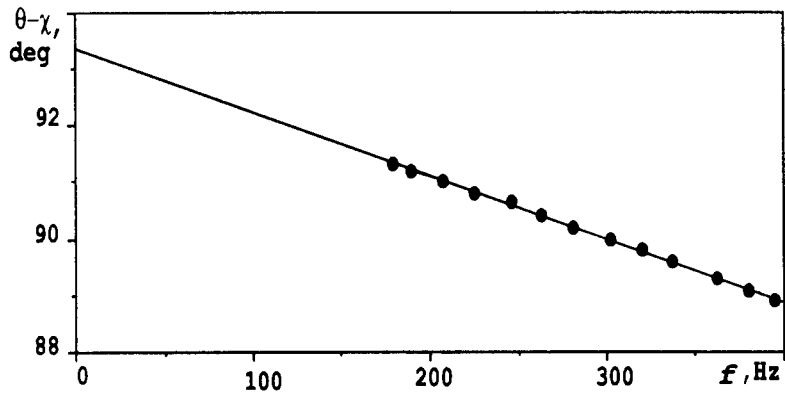


Fig.6. Frequency variation of propagation angles for the most amplifying disturbances

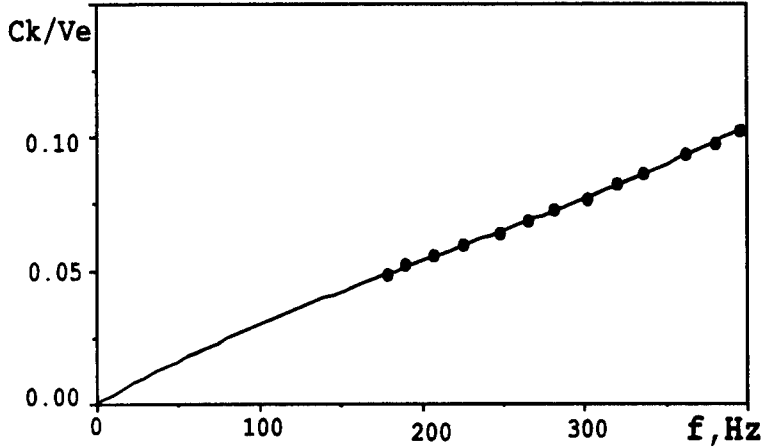


Fig.7. Frequency variation of phase velocity for the most amplifying disturbances

disturbance propagation. For frequency 180 Hz, calculated phase velocity C_k is equal to 1.1 m/s which is in good quantitative agreement with experimental data.

By this means comparison with experiment has shown that frequency, propagation angle and phase velocity of the most amplifying disturbances calculated using linear stability theory, are close to experimental data. Development of low-frequency disturbances (0-40 Hz) and stationary vortexes orientation relatively the mean flow can be predicted satisfactorily. But at the same time, a discrepancy up to 2-3 times in determination of preferential stationary disturbance wavelength is observed. The reason of this discrepancy is unclear now. May be it is because of flow nonparallelism influence was not included into consideration.

The authors would like to thank Irina Maslennikova for useful discussion. This work is supported under Russian Foundation of Basic Research (grant N.96-01-01778).

REFERENCES

1. Kachanov Yu.S. Generation, development and interaction of instability modes in swept-wing boundary layer // *Nonlinear Instability and transition in Three-Dimensional Boundary Layers*. (P.W.Duck, P.Hall eds).-Kluwer Academic publisher. Dordrecht-Boston-London, 1995. pp. 115-132.
2. Reed H.L., Saric W.S. Stability of three-dimensional boundary layer. // *Ann.Rev.Fluid Mech.* 1989.V.21.P.235-284.
3. J.P.Dagenhart. Amplified crossflow disturbances in the laminar boundary layer on swept wings with suction. // *NASA Technical Paper 81-1902.-1981*.
4. V.P.Gaponenko, A.V.Ivanov, Yu.S.Kachanov. Experimental investigation of the boundary layer stability on the swept wing with respect to nonstationary disturbances // *Teplofizika i aeromehanika*. 1995.V.2, N.4.P.333-359. (in Russian).
5. V.Y.Levthenko, V.A.Scherbakov. On the instability of 3-D boundary layer on the swept wing // *PMTF.- 1997.V.38, N.3.P.32-38* (in Russian).
6. Loytsyansky L.G. Fluid end gas mechanics.-M:Nauka,1970 (in Russian).
7. N.D.Dikovskaya, B.Yu.Zanin. Verification of the stability calculation of the wind profile // *International Conference on Methods of Aerophysical Research. Proceedings. Part 2. -Novosibirsk: Inst. Theor.& Appl. Mech., 1996, p.58-63.*

MODIFICATION OF THE METHOD OF SPECTRAL LINE INVERSION FOR PANORAMIC TEMPERATURE MEASUREMENTS IN GAS FLOW

V.P.Fomichev, G.A.Pozdniakov, and S.S.Pravdin

Institute of Theoretical and Applied Mechanics SB RAS
630090, Novosibirsk, Russia

The generalized inversion method was modified for panoramic measurements of gas flow temperature. The method was tested in a hydrogen plume.

The study of gas flows with chemical reactions often requires gas temperature measurements. There are no contact temperature probes for flows of chemically active media with stagnation temperature of 2000 K and higher. In these conditions, only the optical methods of temperature measurement are applicable.

INVERSION METHODS

Among many optical methods of temperature measurement, the methods of inversion of spectral lines is widely used, which is preferred for its simplicity and reliability [1]. Being correctly implemented, it is a more accurate method of temperature measurements in gas media with combustion and low-temperature plasma than other techniques. However, there are certain difficulties in its application, since it is necessary to have a source for comparison - a black-body with known controlled temperature. It should be emphasized that the object studied should be optically thick within the line.

The generalized method of inversion [2,3], in contrary to its prototype, does not require the equalization of temperatures of the etalon T_e (the same black-body) and the object. Besides, it is not necessary for the object to be optically thick within the line it is only necessary that a sufficiently strong absorption of etalon radiation by the medium is observed. Within the framework of this method, the temperature of the object T is calculated from an instant measurement in the line of intensities of object radiation I_f , etalon radiation I_l with known temperature T_e and its radiation transmitted through the object I_{fl} :

$$T = T_e / (1 - C \cdot T_e \cdot \ln(I_f / (I_f + I_l - I_{fl}))), \quad C = k/h\nu \quad (1)$$

An implementation of this method used for temperature measurements in a steady flow in a MHD channel is known [4]. The measurements were taken in the resonance line of NaI atoms. Here I_f , I_{fl} and I_l entering into formula (1) were successively measured by one probe. A successive measurement of these quantities leads to low temporal resolution; therefor this scheme cannot be used in practice to measure the spatial distribution of temperature in fast processes.

MODIFICATION OF THE GENERALIZED METHOD OF INVERSION

To measure the temperature distribution in unsteady objects, it is suggested to modify the generalized method of inversion. It is proposed to replace a successive

measurement of I_f and I_n in one point by simultaneous measurement of these quantities in the neighboring points, that will increase the temporal resolution, though decrease the spatial one.

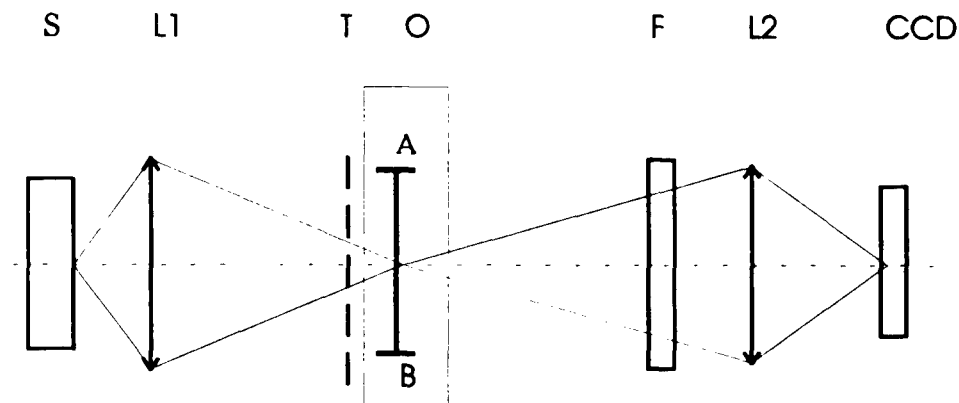


Fig. 1. S - etalon source, L1, L2 - lenses, T -transparent, O -object, F - filter, CCD - photodetector

Let us explain the essence of the proposed modification by a simple example (Fig. 1). For the sake of definiteness, let us assume that it is necessary to measure the temperature distribution in the object O at a certain section AB. For this purpose, we construct the image of etalon S on section AB. Using a transparent mask T we split the etalon image into fragments. Then we construct the image of section AB on the photodetector (here, a CCD linear array). This image consists of alternating sections illuminated only by the object (I_f) and those illuminated both by the etalon and object (I_n).

Assuming the temperature to change only weakly during one period (at the neighboring sections), contiguous values of I_f and I_n can be used in formula (1). The values of I_i can be obtained directly before the experiment.

The proposed method was used for temperature measurements in a pulse hydrogen plume (with burning time less than 0.1 s). In this case, the transparent divided the etalon image into two fragments. A 64-element CCD linear array TSL-124 was used as a detector. The data reading was performed with an interval of about 3 ms.

Two signals are shown in Fig. 2. Signal 1 was obtained directly before the flash and corresponds to the distribution of I_i . Signal 2 was obtained in the course of combustion. The numeral 3 indicates the interpolated values of I_f .

Figure 3 shows the temperature versus time in two points. Curves 1 and 2 refer to the left and right fragments of the etalon, respectively.

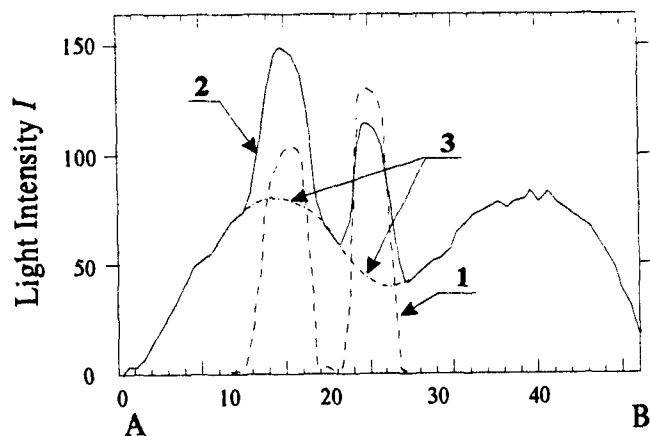


Fig. 2. Source signals.

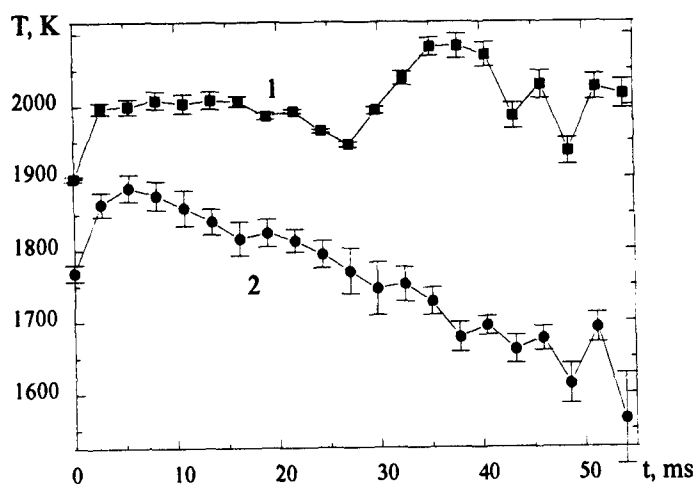


Fig. 3. Temporal dependence of plume temperature in two points

CONCLUSIONS

A method of panoramic temperature measurement is suggested and implemented. It is based on the generalized method of inversion of the spectral line. The method modification consists in replacing the temporal modulation of the etalon signal by the spatial modulation.

The method has a high temporal resolution. It is designed for panoramic measurements of temperature in fast processes. The spatial resolution is determined by the period of "etalon grid", the temporal resolution is determined by resolution of the detector.

REFERENCES

1. Lochte-Holtgreven W. (ed.) *Plasma Diagnostics*. — Amsterdam, 1968.
2. Sobolev N.N. Optical methods of temperature measurement // *Trudy FIAN*, —1953. — Vol. 7, — P.159.
3. Sviridov A.G., Sobolev N.N. On plume temperature measurement by the method of inversion of spectral lines// *ZhETF*.—1953,—Vol. 24, Iss. 1,—P.93.
4. Petrick M., Shumatsky B.A. (eds.) *Open-Cycle Magnetohydrodynamic Electrical Power Generation*. — Argonne National Laboratory, Argonne, Illinois, 1979.

DISTURBANCE EXCITATION IN SUPERSONIC BOUNDARY LAYER BY ACOUSTICS

S.A.Gaponov, B.V.Smorodsky

Institute of Theoretical and Applied Mechanics SB RAS
Novosibirsk, 630090 Russia

Problem of excitation of oscillations in boundary layer (BL) by a streamwise acoustic wave at Mach number $M = 2.0$ is considered. It was found that the ratio of amplitudes of mass flux perturbations inside BL and at its outer edge can reach significant values. Conclusion about existence of critical values of Reynolds number and an angle of orientation of acoustic wave, at which efficiency of excitation is highest, is confirmed. An approximate method for computation of disturbance level inside BL is offered. Interpretation of experimental data about supersonic BL receptivity is given.

1. The research submitted in the present paper is concerned the problem of supersonic BL receptivity to external non-stationary disturbances, leading to earlier flow transition from laminar to turbulent one. Problem of receptivity for the first time was discussed in [1]. On the basis of numerous wind tunnels experiments it was established [2], that the structure of disturbances in supersonic flow is defined basically by acoustic waves. Detailed review of early researches on this problem was given in [3]. The linear theory of interaction of acoustic wave falling at finite angle to surface of model with BL was applied in [4]. In [5, 6] interaction of streamwise acoustic wave (whose wave-vector is parallel to the surface) with BL was studied. Unfortunately, in these papers there were no data about amplitudes of disturbances inside BL. Such data for the first time were received in [7], however they were determined by an indirect way, based on extrapolation of results, received for acoustic waves with finite incident angles. The mathematical formulation of problem, taking into account displacement action of near-wall viscous flow at the outer edge of BL was also given in [7]. In the present paper on the basis of such formulation new data on excitation of oscillations in BL by streamwise acoustic wave were obtained.

2. We treat the problem of harmonic acoustic wave interaction with BL in the linear approximation that is valid at infinitesimal amplitudes of sound wave. Then disturbances outside the BL are described by the real part of complex function

$$\vec{Q}(x_1, y, z_1, t) = \vec{q}_0 \exp(i(\alpha_1 x_1 + \beta_1 z_1 - \omega_1 t)) , \quad (1)$$

where x_1 is a streamwise coordinate, y is normal to plate, z_1 in a spanwise direction (normal to x_1 and y).

Inside BL and in the adjacent diffraction region the disturbance flow field can be accepted as $\vec{Q} = Q_0(x)\vec{q}_0(y)$. Since flow in BL weakly varies in streamwise direction (excepting small area near the leading edge), one can suppose, that Q_0 also slowly varies in x_1 -direction. So $\vec{Q}(x, y) = Q_0(\varepsilon x)\vec{q}_0(y)$, where the small parameter $\varepsilon = R^{-1}$ is a measure of flow nonparallelism, R is the Reynolds number. Substituting \vec{Q} into equations of motion of viscous heat-conducting gas in the main approximation after usual linearisation procedure one can obtain that elements of vector $\vec{q}(y)$ satisfy to system of eighth

order ordinary differential equations depending on streamwise and spanwise wave numbers α_1 , β_1 , frequency ω_1 and mean flow velocity and temperature $U(y)$, $T(y)$. Taking into consideration the angle $\chi = \arctan(\alpha_1/\beta_1)$ and replacing variables from x_1 , z_1 to $x = x_1 \cos \chi - z_1 \sin \chi$, $z = x_1 \sin \chi + z_1 \cos \chi$, we obtain that disturbances are independent of z and the eighth order system can be reduced to the sixth order one similar to Dunn-Lin system [8]:

$$\frac{dq_i}{dy} = a_{ij}q_j, \quad i, j = 1, \dots, 6. \quad (2)$$

The following designations are here used: q_1 , q_3 - are perturbation velocities in x - and y - directions, $\gamma M_1^2 \cos \chi$ q_4 , q_5 are perturbations of pressure and temperature; $q_2 = dq_1/dy$, $q_6 = dq_5/dy$; γ is specific heat ratio, $M_1 = U_e/a$ is Mach number, $R_1 = U_e \delta / \nu_e$ is Reynolds number, $\alpha = \sqrt{\alpha_1^2 + \beta_1^2}$, $\omega = \alpha c$, $R = R_1 \cos \chi$, $M = M_1 \cos \chi$, a is velocity of sound, subscript e stands here for values at BL outer edge. The nonzero elements a_{ij} are determined in [3]. On flat insulated surface we impose boundary conditions

$$q_1(0) = q_3(0) = q_5(0) = 0. \quad (3)$$

The question concerning boundary conditions at $y = \delta$ requires the special analysis. It is well known [3], that at BL outer edge, where coefficients of (2) are constant, the amplitude of fluctuations is described by three exponential solutions with parameters

$$\lambda_1 \approx \lambda_2 / \sqrt{\sigma} \approx -\sqrt{i\alpha R(1-c)}, \quad \lambda_3 \approx -\alpha \sqrt{1 - M^2(1-c)^2}.$$

For acoustic wave falling to BL at finite incident angle λ_3 is a purely imaginary number [3] and solution is constructed by two standard vector functions with λ_1 , λ_2 and by two others with λ_3 , $\lambda_4 = -\lambda_3$.

As the incident angle comes to zero the phase speed $c \rightarrow 1 - 1/M$ and $\lambda_3 = -\lambda_4 \rightarrow 0$. Now we consider in more details the eigen-solutions for $\lambda_3 = \lambda_4 = 0$. Stability equations are in this case reduced to

$$(1-c)q_1^{(3,4)} + q_4^{(3,4)} = 0, \quad Q_5^{(3,4)} - (\gamma-1)M^2q_4^{(3,4)} = 0, \quad (4)$$

$$\frac{dq_4^{(3,4)}}{dy} = i\alpha(1-c)q_3^{(3,4)}, \quad \frac{dq_1^{(3,4)}}{dy} = q_2^{(3,4)}, \quad \frac{dq_5^{(3,4)}}{dy} = q_6^{(3,4)}.$$

One can easily see from (4) that at BL outer edge for $\lambda_3 = \lambda_4 = 0$ there are two linearly independent eigen vectors:

$$\vec{q}^{(3)}(\delta) = (1, 0, 0, -i(1-c), -(\gamma-1)M^2(1-c), 0), \quad (5)$$

$$\vec{q}^{(4)}(\delta) = (0, i\alpha, 1, 0, 0, -i\alpha(\gamma-1)M^2(1-c)). \quad (6)$$

Thus, at BL outer edge general solution to equations (2) could be written as $\vec{q}(\delta) = \sum_{i=1}^4 c_i \vec{q}^{(i)}(\delta)$.

Vector \vec{q} depends on four unknown constants. Three of them can be determined through the fourth from the wall boundary conditions. Consequently solution \vec{q} is determined to within an arbitrary multiplier. Taking into account that coefficients of stability equations vary slowly in streamwise direction, the factors c_i are also dependent on (εx) . Therefore solution inside BL can be written as

$$\vec{Q} = A(\varepsilon x) \vec{q}^0(\varepsilon x, y).$$

Here $A(\varepsilon x)$ – is an unknown amplitude subject to determination and \vec{q}^0 – is vector-function satisfying to system (2,3). We accepted the normalization condition $q_1^0(\varepsilon x, \delta) = 1$. Then $A(\varepsilon x) \approx c_3$ and parameters c_1/c_3 , c_2/c_3 , $c_4/c_3 = k(\varepsilon x)$ are determined as result of solution procedure. Thus, it is required to determine the connection of $A(\varepsilon x)$ with amplitude of the undisturbed by BL external acoustic wave q_0 .

3. In order to define $A(\varepsilon x)$ we shall consider in more details the behavior of disturbance outside BL, where the approximation of locally parallel flow is not valid. Indeed, at derivation of the stability equations it was implicitly supposed, that disturbance amplitude logarithmic derivative with respect to y exceeds $O(\varepsilon)$. However solution (1) does not satisfy to this condition at $y \gg \delta$ because of linear growth with y . Therefore outside the BL disturbances are described by other equations (for more details see [10].) Notice that for $y > \delta$, in case of weak influence of viscosity, the disturbed flow is close to non-rotational, that is

$$\frac{\partial u}{\partial y} \approx \frac{\partial v}{\partial x}, \quad \frac{\partial w}{\partial y} \approx \frac{\partial v}{\partial z}. \quad (7)$$

For harmonic with respect to z disturbance $\partial/\partial z = i\beta_1$. Multiplying the first equation of (7) on α_1 , and the second one on β_1 for $\alpha\tilde{u} = \alpha_1 u + \beta_1 w$, where $\alpha = \sqrt{\alpha_1 + \beta_1}$ one can obtain

$$\frac{\partial \tilde{u}}{\partial y} = \frac{\alpha_1}{\alpha} \frac{\partial v}{\partial x} + i \frac{\beta_1^2}{\alpha} v = F(x, y) \exp(i(\beta_1 z - \omega_1 t)). \quad (8)$$

Integrating this expression with respect of y from δ to ∞ and taking into account, that \tilde{u} at $y = \infty$ matches to undisturbed sound wave, and at $y = \delta$ should be matched with the solution of stability equations $A(\varepsilon x) \vec{q}^0(y) \exp(i(\alpha_1 x + \beta_1 z - \omega_1 t))$, we obtain

$$1 - A(\varepsilon x) = e^{-i\alpha_1 x} \int_{\delta}^{\infty} F(x, y) dy. \quad (9)$$

Using Fourier expansions by analogy with [11] we shall write down $F(x, y)$ as

$$F(x, \delta + y) = F(x - k, \delta) e^{i\alpha_0 k} - \int_k^{\infty} \frac{F(x - \bar{x}, \delta) e^{i\alpha_0 \bar{x}}}{\sqrt{\bar{x}^2 - k^2}} \alpha k J_1(a\sqrt{\bar{x}^2 - k^2}) d\bar{x}, \quad (10)$$

where $k = y\sqrt{M^2 - 1}$, $\alpha_0 = M^2 \omega_1 / (M^2 - 1)$, $a^2 = a_0^2 + \beta_1^2 / (M^2 - 1)$, $a_0^2 = M^2 \omega_1^2 / (M^2 - 1)^2$ and J_1 is Bessel function. Substituting (9,10) into (8) and taking into account, that $F(x) = 0$ for $x < 0$, we obtain

$$1 - A(\varepsilon x) = \frac{e^{-i\alpha_1 x}}{\sqrt{M^2 - 1}} \int_0^x F(x - \bar{x}, \delta) e^{i\alpha_0 \bar{x}} J_1(a\bar{x}) d\bar{x}. \quad (11)$$

Thus amplitude of streamwise velocity perturbation is determined by function $F(x, \delta)$, determined through solution of stability equations. We can adopt $F(x, y) \approx i\alpha k(\varepsilon x) \exp(i\alpha_1 x)$. Substituting this $F(x, y)$ in (11) and replacing variable $\bar{x} = x - z$ we derive the Volterra equation of the second kind:

$$A(\varepsilon x) = 1 - \frac{1}{\sqrt{M^2 - 1}} \int_0^x i\alpha A(\varepsilon z) k(\varepsilon z) e^{i(\alpha_0 - \alpha_1)(x - z)} J_1(a(x - z)) dz. \quad (12)$$

Integral equation (12) is derived in physical dimensional variables, while solution of stability equations is nondimensionalized by BL thickness. The dependence of solution from streamwise coordinate is expressed through variable $R = \sqrt{U_e x^* / \nu}$, where x^* is dimensional distance from plate leading edge. Therefore integral equation (12) can be written in nondimensional variables as:

$$A(R) = 1 - \frac{2}{\sqrt{M^2 - 1}} \int_0^R i \bar{\alpha}_1 R_1 A(R_1) k(R_1) e^{i(\bar{\alpha}_0 - \bar{\alpha}_1)(R^2 - R_1^2)} J_1(a(R^2 - R_1^2)) dR_1, \quad (13)$$

where $\bar{\alpha} = \alpha(\nu_e / U_\infty)$, $\bar{a} = a(\nu_\infty / U_\infty) = \sqrt{M^2 F_1^2 / (M^2 - 1)^2 + \bar{\beta}^2 / (M^2 - 1)}$, $\bar{\alpha}_0 = M^2 F_1 / (M^2 - 1)$, $\bar{\alpha} = \alpha(\nu_\infty / U_\infty)$, and F_1 is known reduced frequency. In order to solve the integral equation (13) at given values of reduced frequency and unit Reynolds number $Re_1 = U_e / \nu_\infty$ it is necessary at first to compute \bar{a} , $\bar{\alpha}$, $\bar{\alpha}_0$. Values $k(R_1)$ are determined through solution of stability equations.

The results of computations are represented below in the form of dependence of absolute values of streamwise component of mass flux perturbation normalized to its value at $x = R = 0$:

$$B = \left| \frac{A(R)}{T} \left(U \left(\gamma M_1^2 \cos \chi q_4 - \frac{q_5 / \cos \chi}{T} \right) + q_1 \right) \right|$$

from wall normal coordinate y or its highest in y value $B_{\max} = \max_y B(y)$ from angle χ and R at a given reduced frequency F .

4. We investigate the interaction of streamwise acoustic wave propagating at angle χ relatively to main flow direction at BL outer edge. All computations were carried out for a flat plate flowing around by supersonic flow with Mach number $M = 2.0$ in wide range of Reynolds numbers, angles χ and various values of reduced frequency F . Mean flow was computed by Sutherland's formula for the dependence of viscosity from temperature, for Prandtl number $\sigma = 0.72$ and specific heat ratio $\gamma = 1.4$ (details of mean flow computation are in [3]). Stability equations (2,3,5,6) were computed numerically by means of orthonormalization techniques. Volterra equation (13) was computed by standard method for this equation [12].

Fig.1 shows the distribution of mass flux perturbation, excited by streamwise acoustic wave, and normalized to its value at BL outer edge. It can be seen that inside BL there are intensive pulsations. This is similar to the case of acoustic wave with finite incident angle [4]. However the intensity of oscillations in streamwise acoustic wave can be much higher, than in the case of finite incident angles.

Curves on Fig.2 represent dependencies of $B_{\max} = B_{\max}(\chi)$ for $F = 91 \cdot 10^{-6}$ for Reynolds numbers $R=250, 320, 410, 520$ (lines 1-4). Our computations have confirmed conclusion [7] about excitation of intense oscillations inside BL by streamwise acoustic wave and about existence of critical values of χ_{cr} , where efficiency of excitation become highest. However there are some quantitative differences in values of B_{\max} and χ_{cr} . Fig.3 shows results of computations of the dependency $B_{\max} = B_{\max}(R)$. Like in the previous case ($B_{\max} = B_{\max}(\chi)$) the appearance of critical value R_{cr} where interaction is especially strong (intensity of oscillations in BL is maximal) is observed.

The analysis of data shows, that there is the combination of χ and R , at a given value F when the disturbances of the mass flux inside BL can greatly exceed their values at

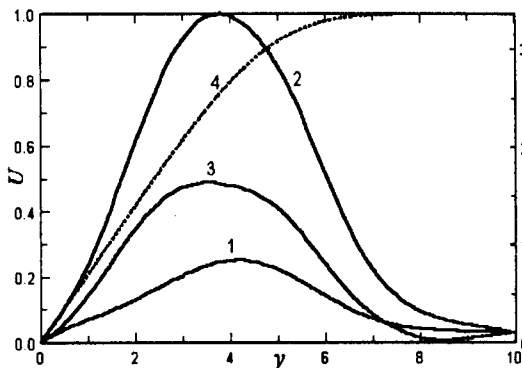


Fig.1 Mass flux perturbation $B(y)$ for $M_1 = 2.0$; $R = 320$; $F = 91 \cdot 10^{-6}$; $\chi = 0^\circ(1), 30^\circ(2), 37.5^\circ(3)$ and mean velocity $U(y)(4)$.

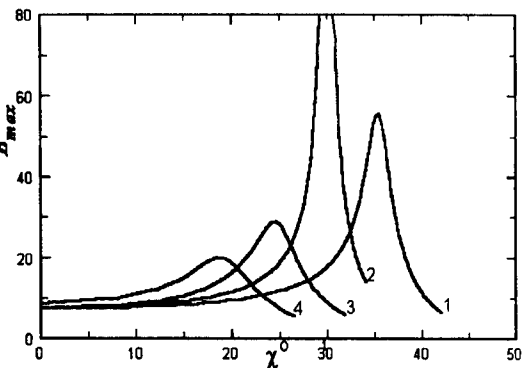


Fig.2 Mass flux perturbation maxima B_{\max} versus angle χ for $M_1 = 2.0$; $F = 91 \cdot 10^{-6}$; $R = 250(1), 320(2), 410(3), 520(4)$.

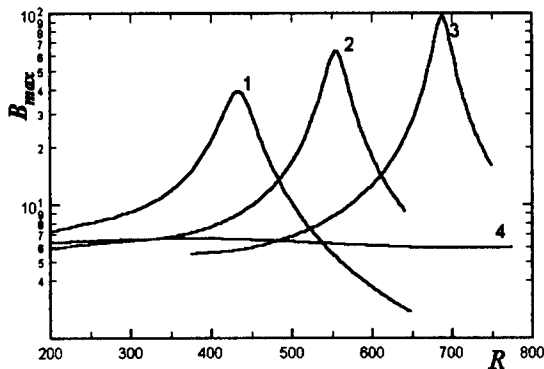


Fig.3 Mass flux perturbation maxima B_{\max} versus Reynolds number R for $M_1 = 2.0$; $\chi = 0^\circ$; $F \cdot 10^6 = 120(1), 91(2), 70(3), 37.6(4)$.

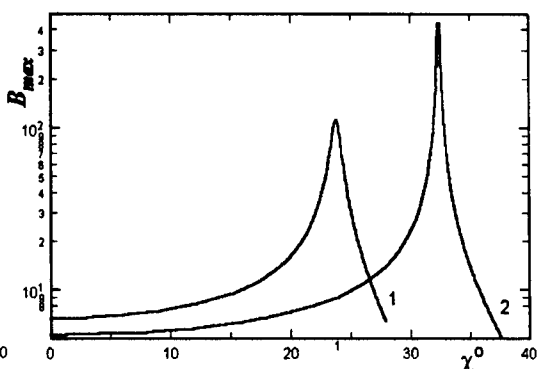


Fig.4 Mass flux perturbation maxima B_{\max} versus angle χ under conditions of experiment [9]: $M_1 = 2.0$; $F = 37.6 \cdot 10^{-6}$; $R = 575(1), 514(2)$.

BL outer edge. The explanation to this phenomenon can be given by the theory of eigen oscillations and resonant external forcing [13]. Other important circumstance is connected to excitation of eigen unstable oscillations in BL. From stability theory [3] it is well known, that at the lower branch of first mode neutral stability curve the phase velocity of unstable wave approaches to streamwise acoustic wave phase velocity $c = 1 - 1/M$. Therefore in the vicinity of lower branch waves of two types become indistinguishable. The level of disturbances inside BL can be defined approximately as follows. At $R < R_{cr}$, where R_{cr} belongs to the lower branch of neutral stability curve, the intensity of disturbances determines on the basis of described above interaction of streamwise acoustic wave with BL. Close to $R = R_{cr}$ we can adopt that amplitude of neutral Tollmien-Schlichting wave is equal to $B_{\max}(R_{cr})$, and at $R > R_{cr}$ $B^{TS} = B_{\max}(R_{cr}) \exp(-\int_{R_{cr}}^R \alpha_i dR)$, where $-\alpha_i$ is a growth rate of unstable wave. For more exact calculation of B^{TS} one can use the theory of unstable wave excitation by acoustics described in [6, 11].

Direct comparison of our theoretical data with experiments [9], as was mentioned in [13] is still impossible because of lack of experimental information. However Fig.4 presents dependency $B_{\max} = B_{\max}(\chi)$ for experimental conditions: $R = 575$ and 514 for $F = 37.6 \cdot 10^{-6}$. The main difference of experimental data and theoretical ones consists in the presence of two peaks at experimental curves $B_{\max}(\chi)$ [9]. This can't be explained theoretically now. It should be mentioned that external to BL acoustic wave is generated not only by the edge of a plate but also by whole disturbed area before it. Therefore for correct inspection of the theory the complete information about disturbances of the mass flux not only inside but also on BL outer edge is necessary.

This work was partly supported by Russian Foundation for Fundamental Research under Grant N96-01-01580 and by SB RAS under Grant for young scientists in 1998.

REFERENCES

1. **Morkovin M.V.** On transition experiments at moderate supersonic speeds// J. Aeronaut. Sci. 1957. V.24. N7. P.480-486.
2. **Lauffer J.** Some statistical properties of the pressure field radiated by a turbulent boundary layer// Phys. Fluids. 1964. V.7. N8. P.1191-1197.
3. **Gaponov S.A., Maslov A.A.** Propagation of disturbances in compressible flows. Novosibirsk: Science, 1980, 144 p. (in Russian)
4. **Gaponov S.A.** Interaction of supersonic boundary layer with acoustic disturbances// Mech. Zhidk. Gaza. 1977. N6. P.51-56. (in Russian)
5. **Duck P.W.** The response of a laminar boundary layer in supersonic flow to small amplitude progressive waves// J. Fluid Mech. 1990. V.219. P.423-448.
6. **Fedorov A.V., Khokhlov A.P.** Excitation of unstable modes in supersonic boundary layer by acoustic waves// Mech. Zhidk. Gaza. 1991. N4. P.67-71. (in Russian)
7. **Gaponov S.A.** On the interaction of supersonic boundary layer with acoustic disturbances// Thermophysics and Aeromechanics. 1993. V.2. N3. P.209-217.
8. **Dunn D.W., Lin C.C.** On the stability of the laminar boundary layer in a compressible fluid// J. Aeronaut. Sci. 1955. V.22. N7. P.455-477.
9. **Semionov N.V., Kosinov A.D., Maslov A.A.** Experimental investigation of supersonic boundary layer receptivity// Transitional Boundary Layers in Aeronautics. Eds. R.A.W.M.Henks & J.L. van Ingen. Amsterdam: North-Holland, 1996. P.413-420.
10. **Gaponov S.A.** On the mathematical simulation of disturbance propagation in the compressible flows near walls// Thermophysics and Aeromechanics. 1994. V.1. N1. P.75-88.
11. **Gaponov S.A.** Excitation of instability waves in the supersonic boundary layer by sound// Non-linear Instability of Nonparallel Flows: Proc. of IUTAM Symposium. Potsdam, N.Y., USA. 1993. P.206-212.
12. **Press W.H., Teukolsky S.A., Vetterling W.T., Flannery B.P.** Numerical Recipes in FORTRAN-77: The Art of Scientific Computing. Cambridge University Press. 1992. - 963 p.
13. **Gaponov S.A., Smorodsky B.V.** Supersonic boundary layer interaction with streamwise acoustics// Proc. of Int. Conference on Methods of Aerophysical Research. Part II. - Novosibirsk: Inst. Theor. & Appl. Mech., 1996, P.70-75.

EFFECT OF VARIOUS METHODS OF ORGANIZATION OF GASEOUS AND SOLID FUEL BURNING FOR BASE DRAG REDUCTION

A.F. Garanin, A.I. Glagolev

Institute of Theoretical and Applied Mechanics,

630090 Novosibirsk, Russia.

Institute of Mechanics MGU, 117234 Moscow, Russia.

Base drag reduction of various vehicles by the method of heat-and-mass addition in the base region is actual at present. The effectiveness of the method is demonstrated in [1,2].

In view of the rarefaction arising in the near wake of various vehicles, the base drag is equal to 25-30%, and sometimes 60-70% of the total aerodynamic drag.

Base drag reduction by the method of heat-and-mass addition in the base region is also attractive for the hypersonic vehicles with a large base area when they overcome the transonic and low supersonic velocities.

The level of the base pressure increase achieved due to heat-and-mass addition depends on the flow rate and thermophysical characteristics of the injected fuel, body geometry, free-stream Mach Reynolds numbers, etc.

Because of complicated flow structure arising in the base region of axisymmetric bodies in a supersonic flow, simple and reliable methods of determining the base pressure increase in the near wake by the heat addition in the base region could not be proposed. The free-stream static pressure is supposed to be the maximum value of the base pressure increase due to heat addition in the base region.

For relatively small heat addition values and low velocities of injected fuels, Tret'yakov [3] suggested a dependence determining the value of base drag reduction as a function of heat addition.

Therefore, an experimental determination of base drag reduction due to heat-and-mass addition is of interest both for practice and for creating analytical methods of calculating such flows.

The changes of the base pressure of cone-cylinder body was studied in [4] for the free-stream Mach number $M=2.14$. The hydrogen burning in the base region was injected from the lateral surface and through an annular slot upstream of the base cross-section. The base pressure increase obtained was higher than the free-stream static pressure by 3-4%.

It is shown in [5] that the hydrogen burning in the base region of an axisymmetric body 35mm in diameter with a blunt base involves the base pressure increase exceeding by (5-8)% the free-stream static pressure. The investigation was performed in the wind tunnel at the Mach number $M=2.0$ and hydrogen injection to the base region through a porous base and a set of orifices in the base section.

It is shown in [6] for the Mach number $M=3.0$ and total temperature $T=280-253$ K that the hydrogen burning in the base region in the flow rate range $\bar{G}=0.02-0.13\%$ leads to the maximum base pressure $P_b = 0.95P_\infty$. The hydrogen was injected in the free stream either in the radial direction upstream of the base or in the axial direction through a porous base wall.

A dependence of the relative base pressure increase of an axisymmetric body on the flow rate of incomplete combustion products of pyrotechnical compounds, which burn completely in the base region was determined in [7] for the free-stream Mach numbers $M=1.2-3.0$.

Fig. 1. Experimental model and its installation in the wind tunnel (a); forebody shapes (b, c), base section schemes (d, e): 1 - porous tube, 2 - pressure tubes, 3 - strut and optical window.

For the purpose of investigating the effect of the fuel injection method on the base drag reduction effectiveness with fuel burning in the base region, the hydrogen burning in the base region of an axisymmetric body was studied, the hydrogen being injected through a single orifice in the base cross-section and through a porous tube attached to the base. The effect of addition of a small amount of air through the forebody was also studied. The investigation was

performed in a supersonic wind tunnel with the test section size of $200 \times 200 \text{ mm}^2$ for the Mach number $M=2.5$, stagnation pressure $P_0=4 \text{ kPa}$, stagnation temperature $T=270\text{--}280 \text{ K}$. A sketch of the model and its installation in the wind tunnel is shown in Fig. 1a. The forebody was manufactured in two variants: 1) blind nose without air flow, Fig. 1b; 2) with an orifice along the body axis, Fig. 1c.

The base section had either an orifice with diameter $d=0.3D$ (D is the model diameter) or a porous tube installed on the base. The tube of diameter $14 \times 2 \text{ mm}$ had the length $L=1.5D$ with a plug at the end. The hydrogen was injected in the base region through the lateral surface of the tube.

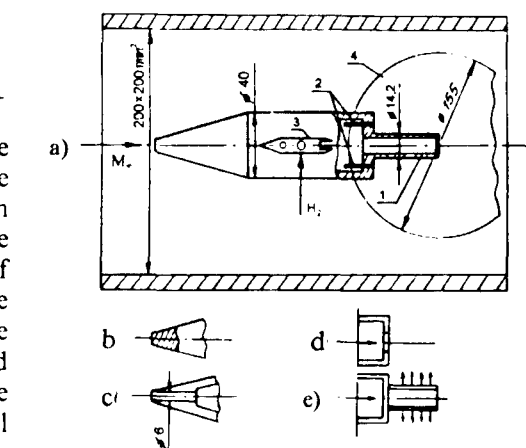
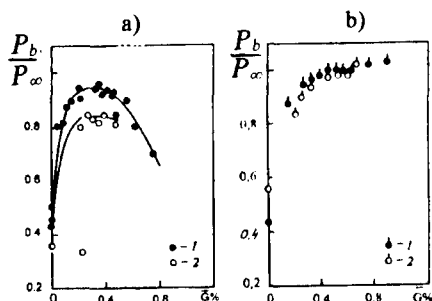
The base had two orifices for base pressure measurement. The base pressure was measured by fast-response pressure gages DMI-0.6 and strain-gage equipment 4ANCH-22 with continuous data recording by automatic potentiometers.

The obtained base pressure dependence on the relative hydrogen rate

$$\bar{G} = \frac{G \cdot 100}{\rho_\infty u_\infty F_m} \%, \quad (\text{where } G \text{ is the hydrogen flow rate, kg/s, } \rho_\infty, u_\infty \text{ are the free-stream density and velocity, kg/m}^3, \text{ m/s; } F_m \text{ is the model cross-section area, m}^2)$$

is shown in Fig. 2a for the body with an orifice in the base and in Fig. 2b for the body with a porous tube.

With increasing the hydrogen flow rate from $\bar{G}=0.06\%$ up to $\bar{G}=0.2\text{--}0.35\%$, the hydrogen burning with injection through the orifice resulted in the base pressure increase up to a constant maximum equal to $P_b=(0.95\text{--}0.96)P_\infty$, where P_∞ is the free-stream static pressure upstream of the model. A further increase of the hydrogen rate resulted in pressure decrease to $P_b=0.7P_\infty$ for



the hydrogen flow rate $\bar{G}=0.75\%$. This base pressure decrease is the result of the ejecting effect of the hydrogen stream and downstream displacement from the base of the maximum heat release observed on the basis of plume

Fig. 2. Base pressure versus hydrogen flow rate: a) base section with orifice, b) base section with porous tube.

1 - forebody without orifice, 2 - forebody with orifice.

luminescence. The base pressure of the investigated model without burning was $P_{b0}=(0.46-0.5)P_{\infty}$.

Hydrogen burning with additional air supply through the forebody results in a smaller base pressure increase equal to $P_b=(0.8-0.85)P_{\infty}$ for the hydrogen flow rate $\bar{G}=(0.2-0.45)\%$.

The air mass flow passing to the base region through the nose orifice equals $\bar{G}=3\%$. This corresponds to the air-to-hydrogen ratio $\alpha=(0.4-0.16)$ for the hydrogen flow rates $\bar{G}=(0.2-0.75)\%$. The air jet passing through the base orifice developed the exit velocity corresponding the Mach number $M_j=0.5$. Because of ejecting effect of one air jet the initial base pressure decreased to $P_{b0}=(0.36-0.42)P_{\infty}$. Hydrogen addition at the rate $\bar{G}=(0.22)\%$ increased the ejecting jet effect and resulted in a further base pressure decrease to $P_{b0}=(0.28-0.36)P_{\infty}$ (Fig. 2a).

Hydrogen injection through the lateral surface of the porous tube permitted to remove the ejecting jet effect and to improve the hydrogen mixing in the base region. In this case the hydrogen burning within the flow rate range $\bar{G}=(0.5-0.9)\%$ increases the base pressure up to a constant level exceeding by 2-3% the free-stream static pressure and by 9-10% the maximum pressure value achieved by hydrogen injection through the axial orifice.

Presenting the obtained results of various fuel burning in the base region as the increment of the base pressure difference $\frac{\Delta P_b}{P_{\infty}} = \frac{P_b - P_{b0}}{P_{\infty}}$, it is shown (Fig. 3) that for

equal Mach number and $\bar{G}=\text{const}$ the largest base drag reduction was achieved by hydrogen injection through the porous tube. A comparison of the base pressure difference achieved in afterburning of pyrotechnical fuels (curve I) with the pressure difference obtained in hydrogen burning shows that the greatest effect was obtained for the hydrogen burning with the greatest calorific value.

The change of the base drag coefficient $C_{xb} = -\frac{(P_b - P_{\infty})}{q_{\infty}} \cdot \frac{F_b}{F_m}$ calculated on the

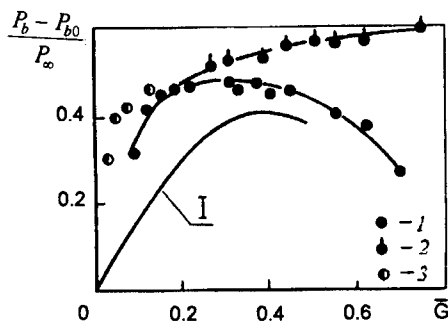
basis of obtained results versus the hydrogen flow rate shows that the hydrogen burning in the base region, being injected through the orifice without air flow, results in a reduction of the base drag coefficient from $C_{xb}=0.12$ with $\bar{G}=0$ to $C_{xb}=0.01$ (Fig. 4). This corresponds to a 90% base drag reduction. A further increase of the hydrogen flow rate results in a smaller base drag reduction.

Hydrogen burning with additional

air supply with the flow rate $\bar{G}=3\%$ resulted in a smaller base drag

Fig. 3. Base pressure increment with combustion of various fuels in the base region.

1 - $M=2.5$, hydrogen burning without air flow, injection through the axial orifice, 2 - $M=2.5$, hydrogen burning without air flow, injection through the porous tube, 3 - $M=3.0$, hydrogen burning, injection through orifices in the lateral surface [6], I - $M=3.0$, pyrotechnical fuel burning, $Q=10.8-22.8$ MJ/kg.



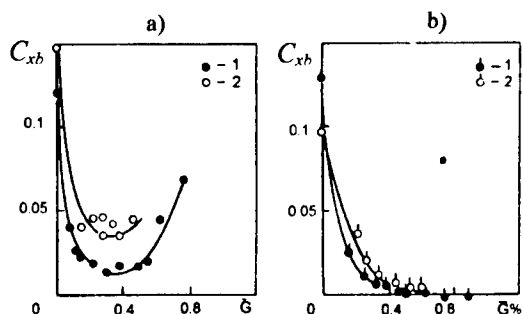


Fig. 4. Base pressure coefficient behavior with hydrogen burning: a) base section with orifice, b) base pressure with porous tube. 1 - forebody without orifice, 2 - forebody with orifice.

reduction. Because of the ejecting effect of the air jet the value of the base drag coefficient increased by 8-16% without hydrogen burning and reached the value $C_{xb}=0.13-0.14$. Hydrogen burning with the flow rate $\bar{G}=(0.2-0.4)$ in this variant results in the base drag reduction by 75%. In this case the base drag coefficient acquires the value $C_{xb}=0.03-0.04$ (Fig. 4a).

Hydrogen burning with the porous tube results in the total base drag reduction when the hydrogen flow rate is $\bar{G}>0.45\%$ (Fig. 4b). For hydrogen flow rates $\bar{G}>0.6\%$, the base thrust exceeding the base drag by (2-3)% is achieved.

Estimating the effectiveness of the base region burning in terms of specific momentum $I = \frac{(P_b - P_{bo})}{G} F_b$ (where F_b is the base area, m; G is the hydrogen flow rate, kg/s; P_b, P_{bo} are the base pressures with and without burning, kPa), it is seen (Fig. 5) that the greatest effect is achieved when the hydrogen is supplied through the porous tube (Fig. 4). In this case, as the hydrogen flow rate increases from $\bar{G}=0.15\%$ up to $\bar{G}=0.78\%$, the specific momentum decreases from 16000 ns/kg up to 5000 ns/kg. When the hydrogen is injected through the axial orifice within the same flow rate range, the specific momentum decreases from 16000 ns/kg to 2000 ns/kg.

Schlieren photographs illustrating the flow structure changes in the base region with and without burning are shown in Fig. 6. For the body with a blunt base without burning the external flow turning angle near the corner point is $\alpha=8^\circ$, and the wake throat is located at a distance $L=1.6D$ from base (Fig. 6a). For the hydrogen burning with the flow rate $\bar{G}>0.2\%$ the wake throat disappears, and the burning zone diameter equals the model diameter (Fig. 6b).

In the flow around the base with the porous tube, the external flow turning angle in the base corner decreases to $\alpha=5^\circ$, and the wake throat shifts downstream at a distance $L=3D$ (Fig. 5b). For hydrogen burning with the flow rate $\bar{G}>0.6\%$ the burning zone boundaries expand from the base, and a weak

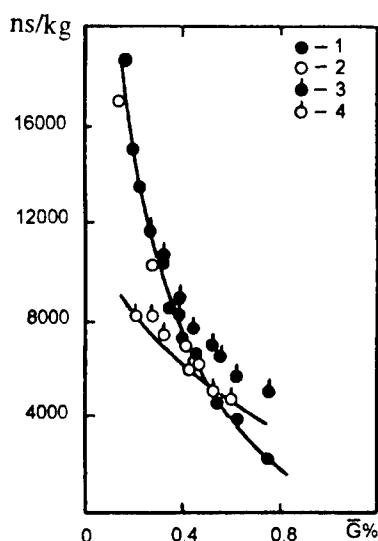


Fig. 5. Specific momentum for hydrogen burning in the baseregion.

1 - base without tube, without air flow, 2 - base without tube, with air flow, 3 - base with tube, without air flow, 4 - base with tube, with air flow.

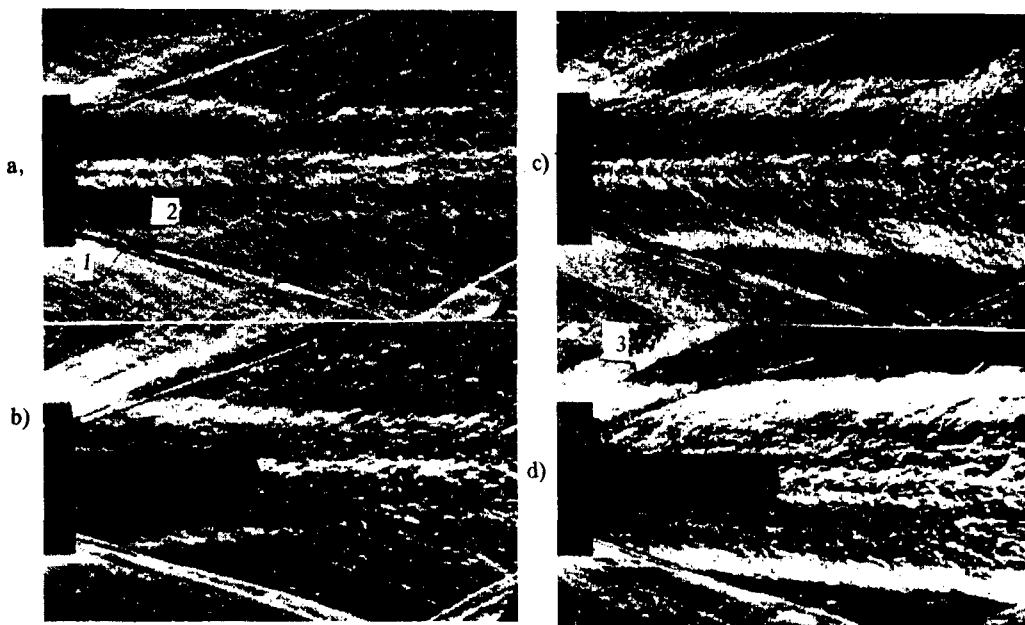


Fig. 6. Shadow pictures of the base flow structure: a, b) without burning, c) hydrogen burning without additional air stream, $G=0.2\%$, d) hydrogen burning, base section with porous tube, $G=0.7\%$.
1 – tail shock wave from the strut, 2 – vortex wake from the strut, 3 – shock wave from the flame.

shock wave 2 forms in the corner point, which indicates that the pressure in the burning zone exceeds the free-stream static pressure.

Thus, the conducted study showed that the greatest effect of increasing the base pressure with hydrogen burning in the base region is achieved with hydrogen injection through the lateral surface of a porous tube attached to the base section.

The presented results of hydrogen and pyrotechnical fuel burning show that for equal fuel rates the greatest base drag reduction is obtained by the burning of hydrogen with the largest calorific value.

REFERENCES

1. Progress in astronautics and aeronautics. Vol.40. Aerodynamics of base combustion / Ed. S.N.B.Murthy. – New York: AIAA. 1976.
2. Baev V.K., Golovichev V.I., Tretyakov P.K. Combustion in Supersonic Flow. – Novosibirsk: Nauka, 1984. – 304 p. (in Russian).
3. Tretyakov P.K. Generalization of data on injection and burning effectiveness on the base pressure. // Trudy TsIAM. – 1985. – № 1140. – P.177-192.
4. Townend L.H., Reid I. Some effect of stable combustion in wakes formed in a supersonic stream // Supersonic Flow, Chemical Processes and Radiative Transfer. – N. Y. et al., 1964. – P.137-155.
5. Baev V.K., Garanin A.F., Tretyakov P.K. Investigation of stream structuring behind an axisymmetric body exposed to a supersonic flow by inert and reacting gases // Combustion, Explosion, and Shock Waves. – 1975, № 6. – P.859-863.
6. Hubburt I.E., Strahle W.C., Neale D.H. Mach 3 Hydrogen external/base burning // AIAA J. – 1981. – Vol.19, June. – P.745-749.
7. Strahle W.C., Hubburt I.E., Walteric R. Base burning performance at Mach 3 // AIAA J. – 1982. – Vol.20, № 7. – P. 986-991
8. Glagolev A I., Zubkov A.I., Garanin A.F., Tretyakov P.K. Heat addition effect on the base pressure of bodies of revolution at supersonic velocities // Combustion, Explosion, and Shock Waves. – 1996. – Vol.32. – P.107-114.

CONTROL OF SHOCK WAVE PARAMETERS BY MEANS OF MASS AND ENERGY SUPPLY

A.F. Garanin, P.K. Tretyakov, V.F. Chirkashenko, Yu. N. Yudintsev

Institute of Theoretical and Applied Mechanics SB RAS 630090 Novosibirsk, Russia

Many theoretical and experimental papers are devoted to controlling the parameters of a shock wave (SW) generated by a body moving with supersonic speed. The body shape effect on the formation and propagation of shock waves has been most intensively studied, for example in [1, 2]. At the same time, of great interest is the possibility of controlling the SW parameters by supplying additional energy in the disturbed stream near the body.

In the present paper we study the possibility of controlling the SW parameters (intensity

$\Delta \bar{P}_{ck} = \frac{P_{ck} - P_{\infty}}{P_{\infty}}$ and momentum of the positive SW phase $\bar{J}^+ = \int_{\bar{x}_A}^{\bar{x}_B} \Delta \bar{P}(\bar{x}) d\bar{x}$) by means of

injection of gas mass in the form of air jets exhausted from the model and thermal energy supplied behind the SW due to hydrogen combustion near the model.

The research method is based on the measurement of excess static pressure profiles near the model immersed in the flow with subsequent recalculation of the profiles for larger distances using the quasi-linear theory [3]. The experiments were performed in the supersonic wind tunnel T-313 (ITAM SB RAS) for the Mach number $M_{\infty}=2.04$ and Reynolds number $Re_1=25 \times 10^6$ [1/m]. The profiles of excess static pressure behind the SW were measured on a perforated reflection plate mounted on the floor of the test section at a distance of 200 mm

from the model axis, which corresponds to four model diameters $\bar{K}=H/d_m=4$. To obtain

reliable estimates of the energy supply effect on the SW parameters, all experiments were conducted on a basic model, which was a half-cone with an angle $\beta_h = 20^\circ$ on a cylinder with diameter $d_m=50$ mm. Sketches of the models are shown in Fig. 1. The first group of models was used to study the influence of air injection into the disturbed flow in the region of expansion wave formation on the body. For this purpose, some variants of slotted sonic nozzles were organized using replaceable inserts on the cylindrical surface of the model near the corner point in order to form expansion fans in a 90° sector. The nozzle axes were inclined to the model axis by $\varphi = 30^\circ$ and 90° . A hydrogen injection pipe and an

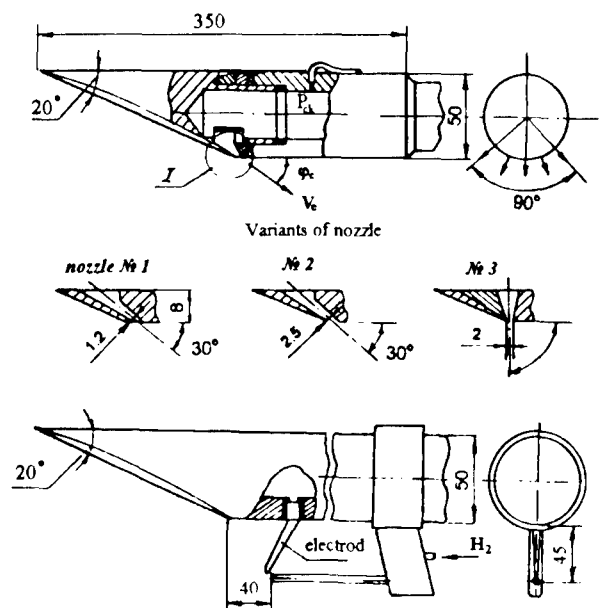


Fig. 1. Sketches of the models.

ignition electrode for hydrogen ignition were placed near the model to study the thermal energy supply in the flow region behind the expansion wave.

The air pressure in the model volume upstream of the nozzle and the flow rate of injected hydrogen were measured in experiments. The total pressure in the jets was measured within the range $P_{0j} = 0-4$ MPa, and the hydrogen flow rate during its combustion was 13.7 g/s. The experiments were performed for equal temperatures of the free-stream air and exhausted jets $T_{0\infty} = T_{0j} = 300$ K.

The influence of the jet with changing total pressure on the flow formation near the model is shown in Fig. 2 by the example of the model with nozzle 2. An underexpanded jet exhausted almost from the corner point of the half-cone with the initial axis inclination angle

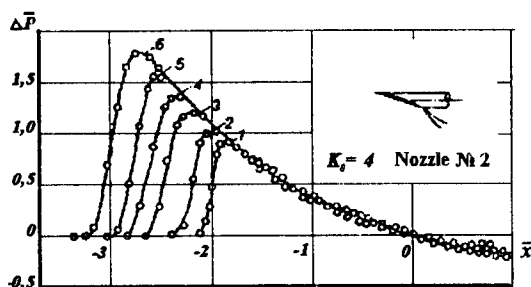


Fig. 2. Effect of the total pressure in the plenum chamber of the nozzle on the shape of the excess static pressure profile behind the shock wave. 1 - $P_{0j} = 0$, 2 - 0.35 MPa, 3 - 1 MPa, 4 - 1.5 MPa, 5 - 2.05 MPa, 6 - 3.1 MPa.

larger by 10° than the cone generatrix angle, does not affect the position of the expansion wave formation on the model surface, which corresponds to the conditions with $P_{0j} = 0$. With jet injection, this expansion wave is formed downstream of the nozzle and retains its pressure profile in the influence region irrespective of the jet pressure ratio. An increase in SW intensity and momentum with increasing the jet pressure ratio is due to interaction of the disturbed incoming stream with the exhausted jet, which results in an attached shock wave on the windward side of the jet.

This SW induces the flow stall from the model surface upstream of the nozzle with a shock wave formed ahead of the separation region. This wave system interacts with the bow shock wave from the half-cone. As a result, the bow shock wave moves upstream, its intensity and momentum increase with a fixed position of zero characteristic with respect to the model. The pressure decrease behind the bow SW in this case is caused by an expansion wave formed in the flow past a slip surface separating the exhausted jet from the incoming stream. The expansion wave intensity substantially increases as the jet pressure ratio increases. An increase of jet inclination angle up to 90° (nozzle 3) does not change qualitatively the interaction process, but in this case equal values of the SW parameters are achieved with lower pressure values in the jet, i.e., the influence of jet attitude relative to the SW is revealed. Being plotted as functions of the parameter complex $C_R \sin \varphi$ in Fig. 3a, the

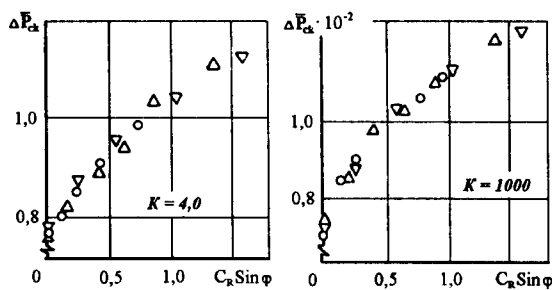


Fig. 3. Shock wave intensity versus the the nozzle thrust and orientation. \circ - nozzle 1, Δ - nozzle 2, ∇ - nozzle 3.

shock wave parameters ($\Delta \bar{P}_{ck}^+, \bar{J}^+$) show that with this control method the changes in the SW parameters are determined by the component of the

nozzle thrust coefficient normal to the model axis. The nozzle thrust coefficient is defined as

$$C_R = \frac{R}{q_\infty S_m} \quad \text{where } R \text{ is the nozzle thrust, } q_\infty = \frac{\chi}{2} P_\infty M_\infty^2 \text{ is the dynamic pressure,}$$

$$S_m = \frac{\pi d_m^2}{4} \text{ is the mid-section area of the model. This generalization is retained as the shock}$$

wave propagates at large distances (Fig. 3b). An increase of the normal component of the nozzle thrust coefficient up to $C_R = 1.6$ leads in the near field to an increase in SW intensity and momentum by 2 and 2.5 times, respectively. In the far field ($\bar{K} = 1000$) this increase is 1.6 and 2.2, respectively.

Figure 4 shows the pressure profile behind the SW, which were measured near the model equipped with a system for hydrogen combustion under the conditions without hydrogen injection, with hydrogen injection, and with hydrogen combustion.

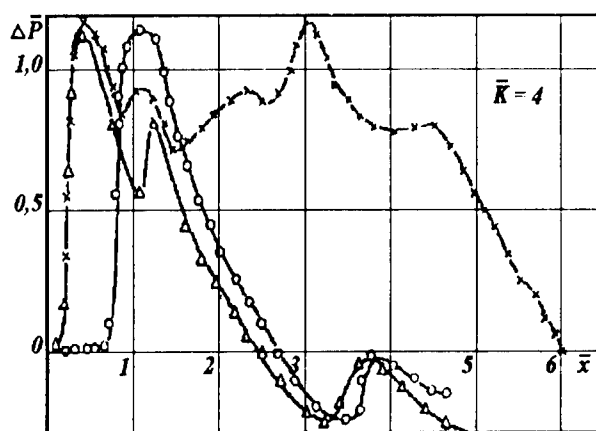


Fig. 4. Pressure profiles behind the shock wave. O – initial model, Δ – with hydrogen injection, x – with hydrogen combustion.

An upstream injection of hydrogen behind the expansion wave on the initial body near the model shifts the bow shock wave from the model upstream practically without changing its intensity and with a small (~30%) increase of momentum.

In the pressure profiles, an intermediate step appears which gives rise to the momentum change. Behind the bow SW, there arises a drop in the pressure caused by the rarefaction wave forming when the flow moves around the contract surface which separates the hydrogen jet and the air flow.

The heat addition due to the hydrogen combustion exerts practically no effect upon the flow pattern near the SW formed by the hydrogen jet without

combustion. Only a small increase in the pressure level at the intermediate step and displacement of the latter upstream take place.

The flow pattern changes dramatically in the influence region of the hydrogen plume extended downstream from the intermediate shock wave. A strong compression wave is formed in the expansion region corresponding to the initial body, which substantially increases the excess pressure momentum near the model. The expansion wave with intensity, corresponding to the expansion wave on the initial body without hydrogen injection, is shifted downstream from the bow shock wave at a distance of more than four model diameters. Affected by these factors, the momentum of the positive SW phase near the model increases by approximately four times in comparison with the momentum of the SW from the initial body. According to recalculation shown in Figs. 5 and 6, the effect of momentum increase is retained as the SW propagates at larger distances.

The bow SW intensity decreases with the distance from the model, as it takes place on the initial body under the action of expansion wave non-shaded by the plume. An intermediate shock wave is formed on the front of compression wave propagating behind the expansion wave. At a distance

$\bar{K} = 10$ this intermediate shock wave interacts with the bow shock wave and induces a jump-like increase in its intensity. As the bow SW propagates further, due to increased momentum and downstream shift of the influence region of expansion wave from the corner point of the model, the process of its decay extends to larger distances in comparison with the initial body and hydrogen injection without combustion. This results in a twice larger SW intensity provided by the model variant with heat supply at a given distance for practically equal initial SW intensities, as the SW moves away from the body. This effect is observed at large distances. A comparison of the examined methods for controlling the SW parameters (Figs. 5, 6) shows that the thermal energy supply increases the SW momentum

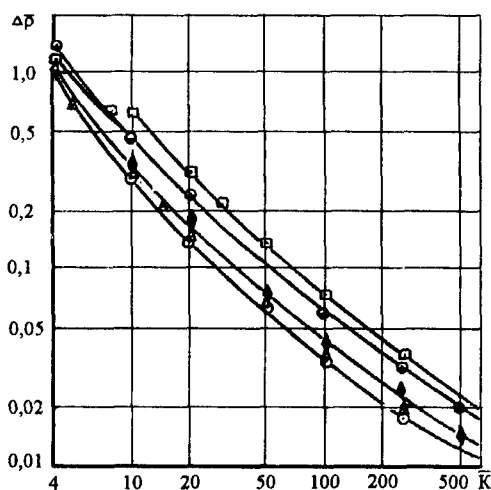


Fig. 5. Shock wave intensity versus the distance from the model. O – initial model, Δ – with hydrogen injection, □ – with hydrogen combustion, ◆ – model with nozzle 1 ($P_{0j} = 0.7$ MPa), ● – model with nozzle 1 ($P_{0j} = 3.7$ MPa).

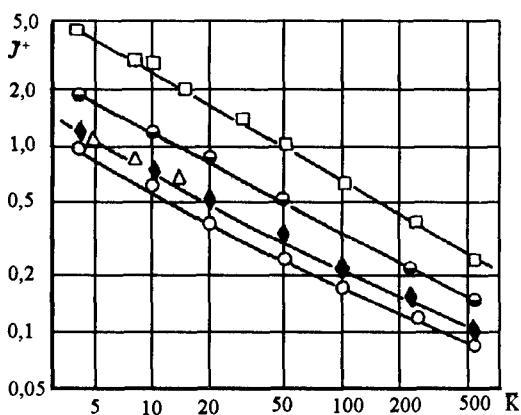


Fig. 6. Momentum of the positive SW phase versus the distance from the model. O – initial model, Δ – with hydrogen injection, □ – with hydrogen combustion, ◆ – model with nozzle 1 ($P_{0j} = 0.7$ MPa), ● – model with nozzle 1 ($P_{0j} = 3.7$ MPa).

and intensity (for $\bar{K} \geq 10$) by 100 and 25%, respectively, as compared with the corresponding parameters of the SW generated by the model with nozzle 1 for $P_{0j} = 3.7$ MPa.

In conclusion we can say that the gas mass supply in the form of an underexpanded jet exhausted from the model increases the SW momentum by increasing its intensity and length of the positive SW phase with a constant position of zero excess pressure, which leads to a faster decay of the shock wave in the process of its propagation. The changes in the SW parameters are determined by the nozzle thrust vector component normal to the model axis.

The thermal energy supply increases the SW momentum without changing its initial intensity due to the formation of compression wave behind it, which shifts the characteristic of zero excess pressure

downstream. As a result, the process of SW intensity decay extends to larger distances in comparison with the initial body.

Note also that the efficiency of controlling the SW parameters using the energy supply should also depend on its organization, i.e., the place of energy sources and the distribution of their power.

The authors are thankful to Dr. V.F.Volkov for his assistance in processing the experimental results.

References

1. Hague D.S., Jones R.T. Application of multivariable search techniques of the design of sonic boom overpressure body shapes // NASA. – SP-255. – 1970.
2. Chirkashenko V.F., Yudin Yu.N. Parameters of shock waves from bodies of revolution in a homogeneous atmosphere // Izv. SO AN SSSR, Ser. tekhn. nauk. – 1984. – Iss. 3. – . 16.
3. Whitham G.B. The flow pattern of a supersonic projectile // Commun. Pure Appl. Math. – 1952. – Vol. 5.

INLET PERFORMANCES MEASUREMENT IN SHORT-DURATION AERODYNAMIC FACILITY

B.N. Giljazetdinov, V.I. Zvegintsev

Institute of Theoretical and Applied Mechanics SB RAS,
630090, Novosibirsk, Russia

The development of short-duration aerodynamic wind tunnels requires perfection of an experimental technique for such facilities. When scramjet models are tested the measurement of the mass flow rate through the engine inlet is an important and reasonably labour-consuming operation. The standard way for the flow rate measurement implies that specific inter-model volume for the flow distortions improvement and the aft sonic nozzle with an uniform field of parameters are involved [1].

Another method of flow rate measurement suitable for short-duration facilities could involve the outside placed volume which is attached to inlet exit and it swallows the whole air flow from the inlet. The pressure growth within the volume indicates the current value of incoming flow rate. Such technique was suggested and tested in [2] in a Ludwig tube wind tunnel and in adiabatic shock tunnel with constant parameters of a flow. In the present work a mass flow rate measurements on a technique similar [2] are discussed, but executed experiments were performed in an impulse wind tunnel where flow parameters have decreased during the run time.

The inlet model investigation was conducted in a short-duration wind tunnel named "Tranzit" (ITAM SB RAS) at flow Mach number $M = 3$ and $M = 4$ without heating of working gas (air) in the settling chamber. The layout of an experimental facility is shown in Fig.1.

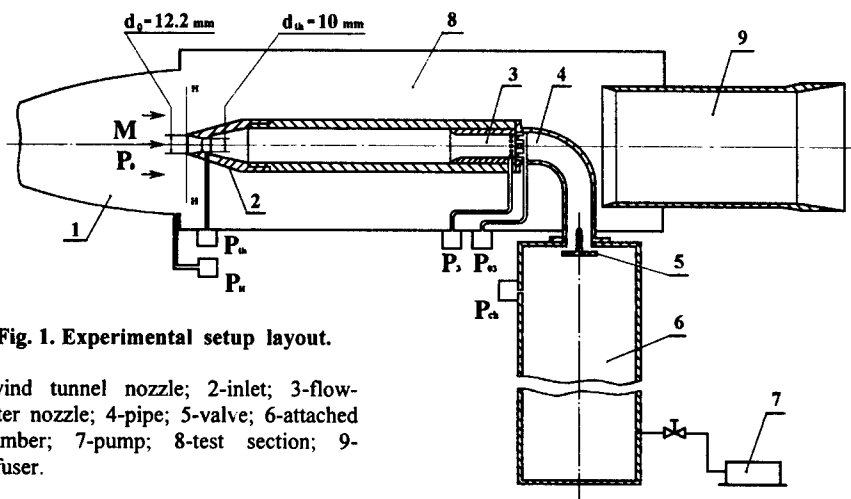


Fig. 1. Experimental setup layout.

1-wind tunnel nozzle; 2-inlet; 3-flow-meter nozzle; 4-pipe; 5-valve; 6-attached chamber; 7-pump; 8-test section; 9-diffuser.

The tested model represents a supersonic axisymmetrical frontal inlet of completely internal compression, which is described in [1]. Such inlet has well defined significance of specified mass flow rate (practically strictly equal to 1 when the angle of attack is zero), thus permits to check accuracy of measurements. The model contains an internal volume, which is ended with a flow-meter sonic nozzle 3 at the model exit. The total and static pressure in the exit plane of the nozzle were measured with the help of averaging rakes. Further the whole air flow leaving from the model could be directed to the special outside placed chamber 6 with volume 32,3 dm³ through a small length channel 4. At the end of the channel 4 before the chamber 6 the controlled fast-acting valve 5 is located with a passage diameter of 30 mm.

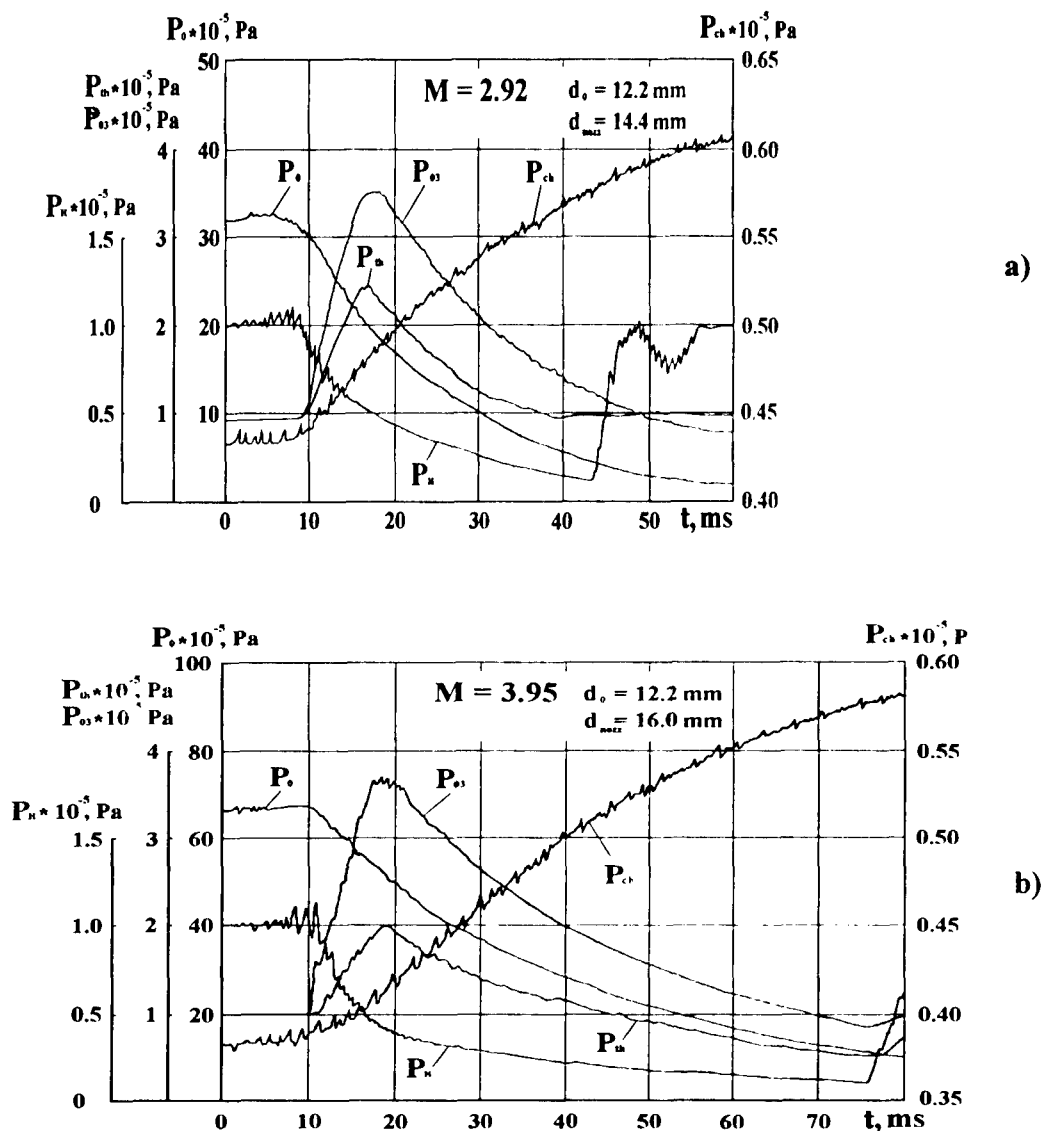


Fig. 2. Typical experimental pressure records

Prior to a tunnel run the chamber 6 is evacuated by the pump 7 up to pressure 0.3 - 0.4 atm. After the tunnel start and working flow establishment (it took approximately 10 ms) the controlled valve 5 was activated and air flow arrived into the chamber. The processes of the wind tunnel operation, a fast-acting valve 5 opening and the digital data acquisition system start were synchronized with the help of a special electronic system. High-frequency pressure gauges give the values of pressure within the settling chamber and test section 8 of the tunnel, in different points of inlet and attached chamber. The record of parameters during the run was made with the help of a high-speed digital registration system in CAMAC standard.

Typical records of pressure measurement during the experiment are shown in Fig. 2a, 2b. At data processing of these records a procedure of experimental data smoothing through the approximation them by polinomial of degree 6 was applied. In Fig. 3a and 3b the ratio of pressure within the inlet throat and at the flow-meter sonic nozzle exit, as well as, a attached chamber pressure are indicated.

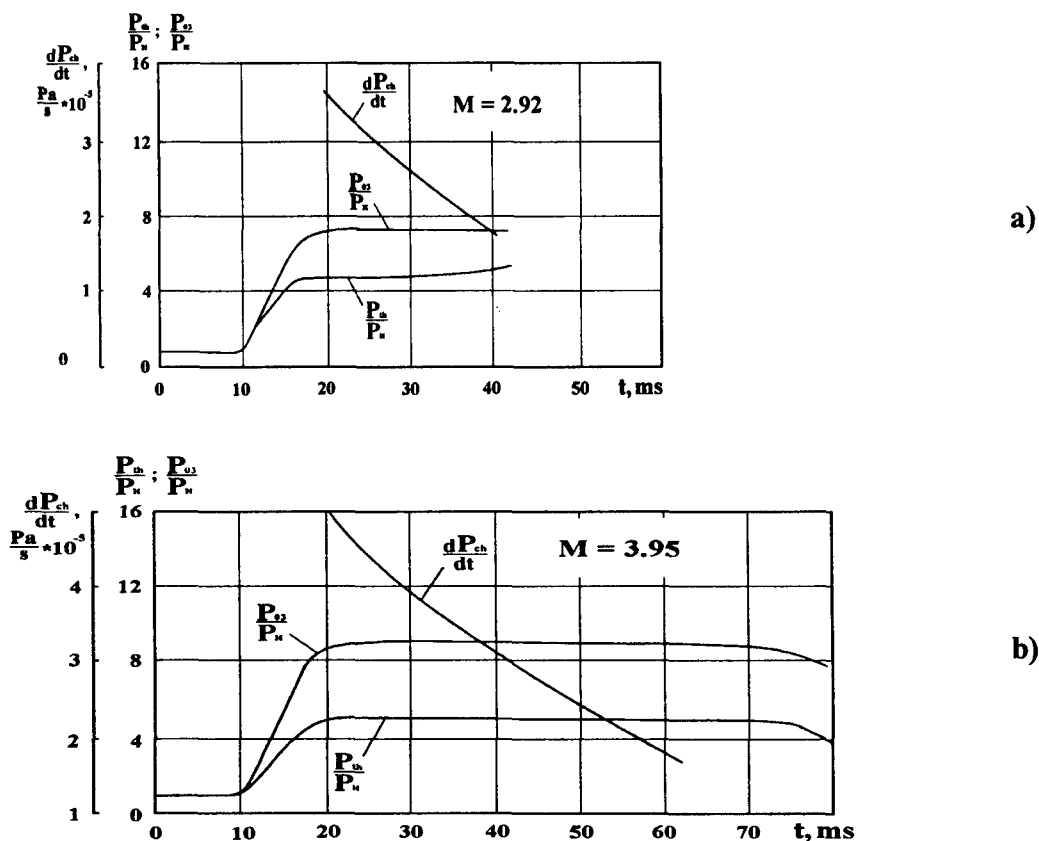


Fig. 3. Typical data processing results

From figures 2,3 it is visible, since 15-20 ms a quasi-steady flow field in the wind tunnel and the model is established, that is characterized by practically constant value of Mach number in combination with a smooth decrease of flow dynamic pressure, as well as

flow Reynolds number. Useful running time is depending on initial storage mass of a test gas within the settling chamber and varied from 25 ms at $M = 3$ to 50 ms at $M = 4$ in executed experiments.

During the running time the specified pressures P_{th} / P_H and P_{03} / P_H are remained practically constant, that characterizes quasi-steadyness of the flow pattern in the model. The pressure within an attached chamber is growing continuously, however the rate of this increase is monotonically slows down, that is in agreement with reduction of the mass flow rate through the inlet. For casual errors reduction the main variants of described tests were repeated 3 - 4 times.

The received data permit to determine significance of the mass flow rate by two independent methods simultaneously: a) on flow parameters on sonic nozzle exit and b) on the rate of pressure increase within the attached chamber. It is known, that at supersonic ratio of the pressure in the flow-meter sonic nozzle 3 of tested inlet model (see Fig.1) the flow with sound speed is generated. The efficient area of a flow exit section was defined in view of the boundary layer thickness in a kind of an area coefficient β changing at mass flow rate calculations on measuremental values of total pressure and temperature:

$$G = \beta \cdot m \cdot \frac{P_{03} \cdot F_{nozz} \cdot q(M_{nozz})}{\sqrt{T_{03}}}$$

here: β - area coefficient for used flow-meter nozzle; $m, q(M)$ - gasdynamic relations; F_{nozz} - area of nozzle exit; P_{03}, T_{03} - total pressure and temperature of the nozzle output flow.

As it is indicated in [3] when short-duration facilities even with constant parameters of a flow are used a specific dynamic error of mass flow rate measurement comes into being which manifests itself as a difference in mass flow rates measured at the inlet entrance and inlet exit section. This error is stipulated by inertness of inner model volume filling process. The technique of the correction of this dynamic error was given in [4] and was used here.

Simultaneously the same flow mass rate was defined on the basis of the pressure growth rate in an attached chamber. Previously the used chamber filling process was investigated in detail. Obtained experimental data have confirmed, that in future short-duration wind tunnel testing the process of chamber filling will be correspond to adiabatic law and thus the incoming air flow rate can be determined in accordance with adiabatic relationship:

$$G = \frac{V_{ch}}{\alpha \cdot R \cdot T_{03}} \cdot \frac{dP_{ch}}{dt}$$

here V_{ch} - volume of a chamber; P_{ch}, T_{03} - current significances of air pressure and temperature in a chamber.

The results of the flow mass rate based on two independent measuremental techniques are shown on Fig.4 for two investigated cases ($M = 3$ and $M = 4$). It is evident that reads dispersion does not exceed 5 %. The same level of accuracy is achieved in [2].

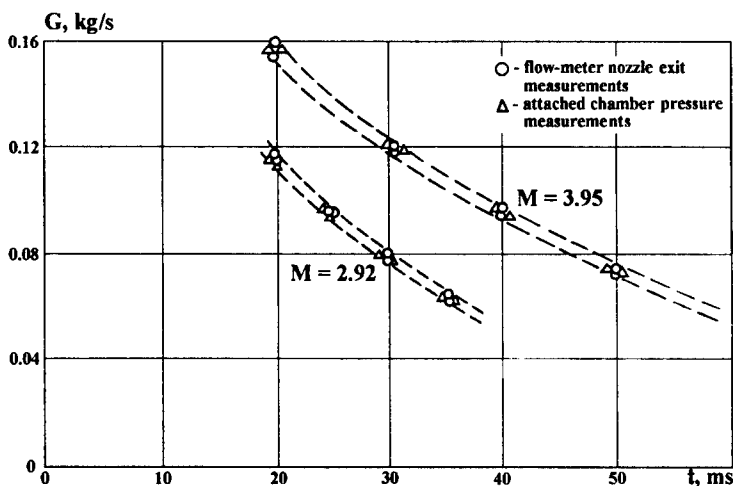


Fig. 4. Mass flow rates obtained data

Except absolute significance of the mass flow rate measurement at different conditions, the large attention at inlet testing is given to determination of the inlet throttling performance, that means interrelation determinate between the specified flow rate $\varphi = G_{th}/G_0$ of captured flow and total flow pressure losses (pressure recovery factor $\nu = P_{03}/P_0$) during the compression process.

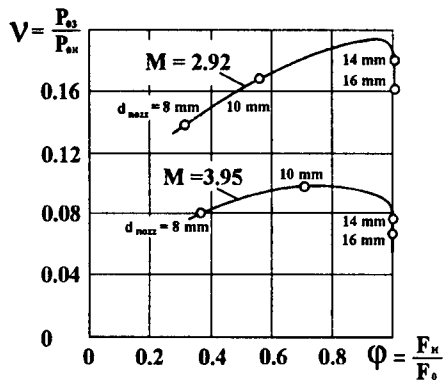


Fig. 5. Throttling inlet performance

While the described experiments, in parallel with the mass flow rate measurements, a new technique of throttling performance reception have been sampled. For this purpose, tests with different areas of sonic nozzle, up to so small significances which resulted in inlet unstart (normal supersonic input was destroyed), were conducted. The pressure recovery factor $\nu = P_{03}/P_0$ at the flow-meter nozzle exit was measured with the help of total pressure rake or it was determined on the data of pressure measurements in the attached to inlet chamber.

The throttling inlet performances that received for the model with flow compression area contraction ratio $F_0/F_{th} = 1.49$ are indicated in Fig. 5. It is visible, if a diameter of the flow-meter nozzle is equal to 16 or 14 mm, the value of specified flow mass rate φ fits to expected value ($\varphi = 1$) fairly well. As the area of sonic nozzle exit section is decreased the progressive input flow transformation takes place, which results in increase of the total pressure. Simultaneously the flow density is raised too, thus the mass flow rate through the sonic nozzle is saved. When a nozzle with diameter less than 14 mm was mounted the

specified mass flow rate ϕ decreased sharply, that signifies normal supersonic flow at the inlet entrance was destroyed and bow-shock configuration occurred.

As a whole, conducted tests and the received results have confirmed the rather accurate measurements of mass flow rate and throttling performance are possible when inlet model with attached chamber is tested in short-duration wind tunnels with time-dependent flow parameters.

REFERENCES

1. Zvegintsev V.I., Kisel G.A. Measurement of the inlet mass flow rate in impulse wind tunnel. - Novosibirsk, "Modelling in the mechanics", V.7 (24), N4, 1993. - P.90-99. (In Russian).
2. Wie D.V., Corpening G., Mattes L., Carpenter D., Molder S., McGregor R. An experimental technique for the measurement of mass flow of scramjet inlets tested in hypersonic pulse facilities. AIAA Paper 2331-89, 1989. - 15 P.
3. Williams R. Application of pulse facilities to inlet testing // Journal of Aircraft. N5, 1964. - P.236-241.
4. Zvegintsev V.I., Sedelnikov A.I. The account of nonstationary effects during inlet testing in the impulse wind tunnels. - Reports of SB RAS, technical sciences section. Issue 4, N15, 1988. - P.63-69. (In Russian).

THE USE OF NETWORK TECHNOLOGIES IN AEROPHYSICAL RESEARCH AT ITAM SB RAS

V.M. Giljov, V.F. Kurmell, O.N. Mosseichuk, S.G. Ocheretny

Institute of Theoretical and Applied Mechanics SB RAS,
630090, Novosibirsk, Russia.

In the Institute of Theoretical and Applied Mechanics (ITAM), SB RAS, from the very beginning network technologies gained wide application when conducting aerophysical studies. At the first step (early 80-ths), to the basis of constructing the automated system for scientific research (ASSR) of ITAM, a three-level computerized system was laid [1]. Computers of the first (objective) level were allocated immediately at the experimental setups of the Institute. They were connected to central communicative minicomputer [2] via communication channels, and through it, to a large electronic computer BESM-6 which was used for the accumulation and computing of experimental data as well as for performing their comparison with the results of theoretical modelling [3].

In view of the change-over to personal computers, an impetus was given to further development of the Institute's computer network. At the present time, the latter represents a well-developed network architecture designed in close analogy to Ethernet. All computers hooked up to the network are united in an integrated information space with free access to Internet. Up to date, as many as about a hundred of the Institute's computers are included into the computer network.

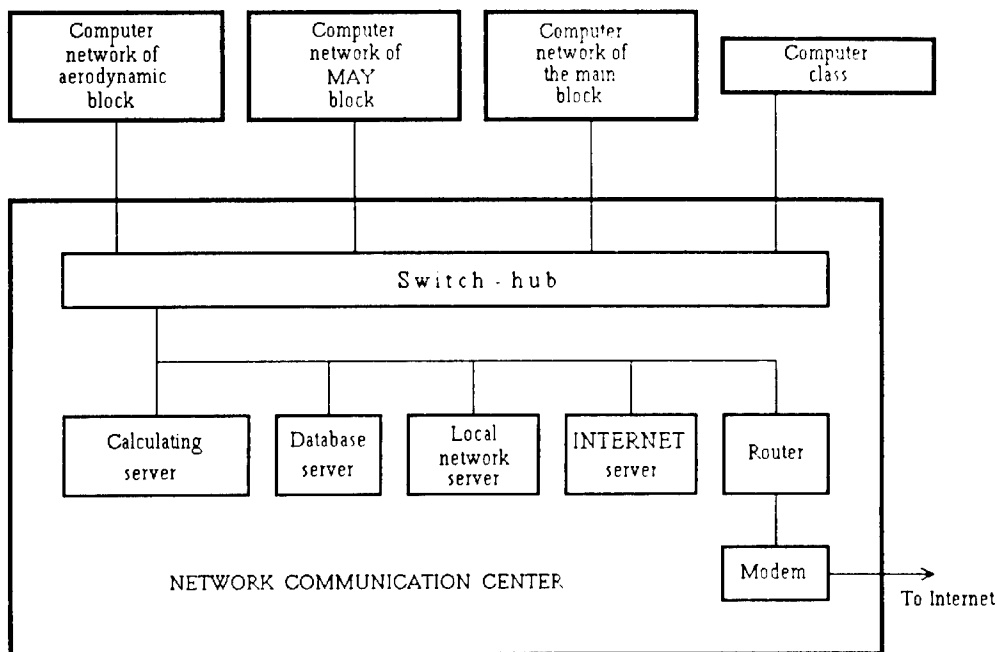
TOPOLOGY OF THE INSTITUTE'S COMPUTER NETWORK

Figure presents the topology of the computer network of the Institute of Theoretical and Applied Mechanics, SB RAS. To the computer network, stations are connected, which are located in three main blocks of the Institute (the computers in the main block are used for mathematical modelling, while the computers of the aerodynamic and MAY- blocks for carrying out both experimental and theoretical studies). In addition, a number of departments have their own local networks, the latter ones being connected to the integrated computer network of ITAM. As the protocols in the Institute network, TCP/IP, IPX ones and some others are used, which allow simultaneous work of several stations employing a great variety of software products without interfering with each other.

For segmentation of the network, the hooking up of net abonents situated in different blocks is organized through a switch-hub system. In the same manner, also a number of local departmental networks are connected to the main one as well as rather large groups of users sharing a common territory. The use of the above hardware facilities permits dividing of the Institute's network into eight independent segments, which prevents penetration of network packages intended for a given segment into other parts of the system. This substantially improves the performance and raises reliability of the network.

Inside each block, intercomputing connections are provided with the help of standard hardware facilities (coaxial-cable or twisted-pair lines, hooking up of subscribers to the network through hubs, etc.).

© V.M. Giljov, V.F. Kurmell, O.N. Mosseichuk, S.G. Ocheretny, 1998



Topology of the computer network of ITAM, SB RAS.

NETWORK COMMUNICATION CENTER

The network communication center is the central component of the system, by means of which telecommunications and network control are organized. In the center, network servers are located, each performing its definite functions:

- an Internet server providing an access to the Internet network, it functions also as mail and WWW-servers and operates under the operating system Linux;
- a local-network server intended for exerting control over the Institute's local network, the server working under the system Windows 95;
- a database server operating under Linux;
- a calculating server basing on a high-speed RISC-processor ALPHA and controlled by the multiple-user OS Linux, the server being available for all users of the Institute's computer network;
- a router providing an access for an individual user of the Institute's computer network to Internet, the data communication being ensured by a high-speed modem connected immediately to a prescribed Internet channel. The router is governed by a computer code written in its read-only memory.

COMPUTER CLASS

The computer class is a constituting component of the ITAM's network infrastructure. Staff-members of the Institute, as well as students and post-graduate students of higher educational institutions taking their training at the ITAM or doing their research work at the Institute are the users of the class.

The class is equipped with the modern-day computer facilities. At the present time, as the computer terminals, personal computers Pentium 166MMX are used. The calculating server is built on the 64-bit RISC-processor ALPHA operating at a frequency of 533 MHz. It is located in the network computer center.

The computers are connected together by means of Internet, and they share a common disk operating system, the loading being executed through the network as well. As the operating system, the Linux one is used offering an effective use of all available computational resources and allowing to organize both multi-user work with all levels of control over resources allowed to each user and multi-level data protection. Employing this operating system has allowed to avoid all problems caused by viruses as well as unauthorized use of software products. The presence in the network of a powerful server with an architecture quite different from the Intel one allows students to get to know various principles laid to the basis of scientific calculations.

In the class, a complete set of software products is installed required both for training students and for doing scientific work. It includes highly developed programming means, debugging aids and compilers for science-oriented languages C, C++, Fortran, Java, as well as powerful means for experimental data visualization. A certain part of the visualization means were developed in our Institute and were offered for free use, in particular, a code KAGR for plotting two-dimensional graphs and a package KAPIC permitting visualization of three-dimensional geometry and flow field patterns. Another part of the research engineering codes has been borrowed from the bank of freely distributed products, for example, VIGIE, a code for the visualization of aerodynamic data designed in Inria, France (the French National Institute for Research in Computer Science and Control), and some others. Other software products are also installed needed for preparation and designing various reports and scientific publications.

PARALLEL TECHNOLOGIES

During last several years, numerical algorithms for performing parallel calculations were under extensive development in the Institute [4,5]. The first parallel machine MP-3 installed in the ITAM was equipped with Intel-860 processors. Although it had insufficient computing power and reliability, the machine offered a real means for performing parallel calculations.

Another approach to conducting parallel calculations can be proposed when using personal computers of the terminal class. Being equipped with special software and united in a computational cluster by a fast-response network, these computers form, in fact, a multi-processor parallel computer with physically and logically distributed RAM. The means of parallelization is the Message-Passing Interface. This standard environment for parallel computations has gained application in a wide range of parallel machines, including supercomputers with thousands of processors. Implementation of such a computing complex at the Institute permitted devising top-level calculational methods and technologies. To the best of our knowledge, at present the above complex surpasses in computing power (6 Pentium-166MMX + Alpha 533 with a total memory of 448 MB) all computing facilities available in Novosibirsk. Involvement to the cluster of a machine basically different in architecture and computing power from standard personal computers provides a unique opportunity for parallel calculation studies in non-uniform mediums as well as for developing means of dynamic distribution of loading over all processors in use.

Thus, implementation of up-to-date computer technologies has allowed to organize in the Institute a powerful multi-purpose computing complex, which, on the one hand, represents a modern computer class, and, on the other, highly efficient parallel "supercomputer" which can be used for solving many challenging problems on numerical modelling.

FACILITIES ALLOWED TO NET ABONENTS

The use of network technologies while performing aerophysical studies offers a great variety of opportunities for abonents of the Institute's computer network.

Using the local network provides the following scope of opportunities:

- storage on the local-network server of user's data as well as various software products, which, in particular, can be used for installation of computer codes on users' computers;
- data communication between different computers joint by the local network;
- storage on the server of bibliographic as well as various scientific, technical and patent information used by the Institute's scientific workers and engineers in their work;
- storage on the server of experimental database having been obtained in the course of aerophysical studies as well as of computational data, performing comparison between results of numerical calculations and experimental studies with the help of this server;
- conducting on the calculating server of high-efficient calculations when performing numerical modelling in the field of mechanics.

When working in the Internet, the following opportunities are available:

- mail messages transeiving;
- searching for various required information over numerous WWW and FTP servers included into Internet;
- data communication with foreign partners;
- performing calculations on remoted high-efficient computers situated in a number of scientific centers both in Russia and abroad;
- work with remoted databases.

IMPLEMENTATION OF NETWORK TECHNOLOGIES

In the report, a number of particular examples of the utilization of network technologies when conducting aerophysical studies in the ITAM, SB RAS are presented.

Research groups of the Institute take active part in international research projects. Joint works are carried out in collaboration with scientists of other Akademgorodok's Institutes and other Russia's scientific centers as well as with foreign colleges. Staff-members of the Institute take active part in competitions for various international grants. Under this circumstances, reliable and stable operation of the computer network as well as extensive development of modern data-exchange technologies are of great importance.

Using computer facilities, numerical calculations are carried out on powerful supercomputers situated in different institutes in Russia and abroad.

Works are under way on the development of file storage's and databases with an access being available via the network. Laboratories participate in the creation and submitting of various scientific information to international aerodynamic databases. In

particular, a number of important results obtained lately in the ITAM, SB RAS, were presented to the Houston High-Speed Flow Database University of Houston, <http://hhsfd.math.uh.edu/>).

More recent attention was given to the adoption and development of the technologies related to the Internet. The Institute's server (<http://www.itam.nsc.ru>) has been created and it is developing extensively now, detailed information being stored about the Institute and the studies conducted by its staff-members.

REFERENCES

1. Bashurov V.V., Vasilenko E.L., Vyshenkov Yu.I., Pirogov A.I., Kharitonov A.M. Measurement – computational complex of the supersonic wind funnel T-313. // IV All Union School on the Methods of Aerophysical Research. – Novosibirsk, 1986. P.165 (in Russian).
2. Vyshenkov Yu.I., Glinsky A.N., Ivanov M.S. Software products for secondary processing of aerodynamic data // Ibid. P.173.
3. Vyshenkov Yu.I., Giljov V.M., Kirtok P.G. Software means for inter-computer linkage of a two-level system for automation of aerophysical studies // Ibid. P.174.
4. Ivanov M.S., Antonov S.G., Markelov G.N. Parallel DSMC algorithm for 3D chemically reacting rarefied flows // Parallel CFD' 95: Abstracts. – Pasadena, 1995.
5. Ivanov M., Markelov G., Taylor S., Watts J. Parallel DSMC strategies for 3D computations // Proc. Parallel CFD' 96 / Eds. P.Schiano et al. Amsterdam: North Holland, 1997. P. 485-492.

PRELIMINARY INVESTIGATIONS of SCRAMJET MODULE

M.A.Goldfeld, A.V.Starov

Institute of Theoretical and Applied Mechanics SB RAS, Novosibirsk, Russia

V.A.Vinogradov

Central Institute of Aviation Motors, Moscow, Russia

INTRODUCTION

Creation of hypersonic flying vehicles with air-breathing propulsion is an urgent problem because these vehicles are promising from the viewpoint of their use for various practical purposes. An inlet is one of the basic parts of such an engine.

ITAM SB RAS together with CIAM has performed theoretical and experimental researches of two models of three-dimensional inlets [1]. The first model had an adjustable strut, which allowed for inlet throat variation from 0.126 to 0.316. The side walls and the strut had a sweepback angle of 45° . It was found that this inlet has comparatively low flow rate coefficient ($f(M)$) and a smaller starting range[1].

The second model did not have this strut, and the inlet operation was adjusted by discrete longitudinal motion of the cowl. Symmetric side walls of the model has a sweep forward angle of 45° with the relative throat area of 0.358. The testing of this model allowed one to obtain satisfactory characteristics of the inlet in experiments in the flow core ($\delta=0$), but a dramatic reduction of the flow rate and total pressure recovery coefficients was observed if there was a thick boundary layer at the inlet duct entrance [1].

On the basis of results for these models, an engine module was developed. The inlet of this engine had swept forward side walls and the central strut with sweepback. It was supposed to use the favorable influence of sweep on the inlet starting and flow rate characteristics.

The following objectives were pursued in testing the engine module:

- obtaining of flow rate characteristics on the basis of flow parameters at the combustion chamber exit;
- determining the total pressure recovery coefficient and flow Mach number in the inlet throat;
- determining the inlet starting conditions and flow formed in the duct using the Schlieren pictures and oil-film visualization;
- determining the influence of a thick boundary layer at the inlet entrance on the inlet starting and integral characteristics;
- determining the pressure fields in the inlet and combustor.

MODEL AND EXPERIMENTAL TECHNIQUE

A scheme and basic dimensions of the developed scramjet model are shown in Fig. 1. To approach the full-scale size and taking into account the model symmetry about the strut, the inlet was made as a half-model. The bluntness radius of all leading edges was 1 mm.

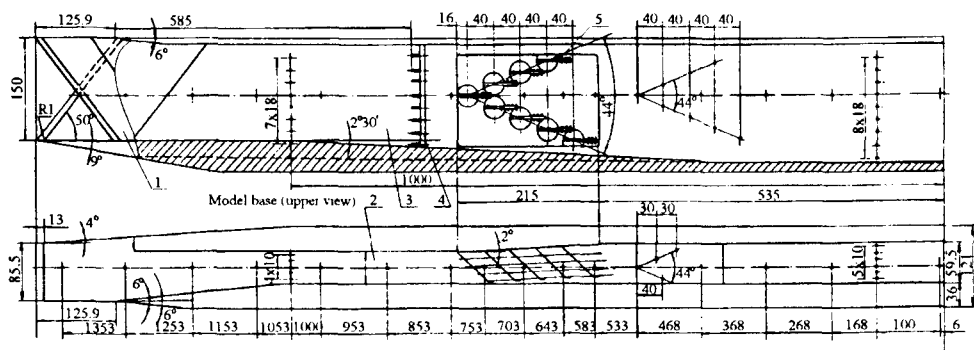


Fig. 1. Scramjet module. 1-left wall, 2-model base, 3-strut (right wall), 4-total pressure rake, 5-injectors.

The model construction allows for fuel injection into the combustor during combustion tests in a hot-shot wind tunnel. The fuel is injected through a group of injectors mounted on an insert which is placed in a rectangular window on the strut (experimental studies were performed without injectors on a smooth wall). To make injection more uniform and to avoid the duct blockage, the injectors are located in two bearings with respect to the horizontal plane passing approximately through the middle of inlet height. Each injector has four orifices for fuel injection. They are located on a swept strut along the model duct width. It is also possible to install windows in the strut and side wall for visualization of the flow and fuel combustion.

For the sake of static pressure measurements on internal stagnation surfaces and on the cowl, the model had 149 static pressure taps. The largest number of static pressure taps was positioned in the inlet throat and combustion chamber, which are most important from the viewpoint of inlet starting control and stable combustion.

The total pressure in the inlet throat for determining the total pressure recovery coefficient was measured by a rake that had eight pressure probes positioned uniformly over the throat height. For determining the air flow rate at the model exit, there was a rake with 32 pressure probes located uniformly over the height and width of the exit cross-section of the model. Four static pressure probes were located on internal surfaces of the model in close vicinity of the rake.

The main set of tests was performed in the blowdown wind tunnel T-313 of ITAM SB RAS with test section size 600×600×2000 mm at Mach numbers from 2 to 4 and unit Reynolds numbers from 25 to 54 million. Experiments at $M=6$ were conducted for unit Reynolds number of about 9 million, the flow being heated up to 450K [2].

The tests were performed for two variants of model mounting in the test section. In the first case, it was mounted on a strut in the flow core of the wind tunnel, and there was no boundary layer at the inlet entrance ($\delta=0$). In the second case, the model was mounted on the wind tunnel wall with a special transitional plate, which allowed for diverting a thick boundary layer of the wind tunnel to the inlet entrance to simulate the boundary layer on the aircraft fuselage upstream of the engine duct entrance ($\delta>0$). The boundary layer thickness on the wind tunnel wall was about 40 mm, which amounted to 27% of the model duct height.

The Schlieren visualization of the flow over the model entrance and the oil-film visualization of the limiting streamlines at the entrance were also performed.

The experiments for $M=6$ and 7.2 were conducted in the hot-shot wind tunnel IT-302M of ITAM SB RAS with nozzle exit diameter of 300 mm and test section length

of 1000 mm. The test conditions are presented in the table, the range of flow parameters being as is shown for wind tunnel operation without pressure multipliers.

Mach number	6	6	7.2	7.2
Total pressure, MPa	12.14-1.60	12.43-1.70	44.52-7.79	38.22-7.65
Temperature, K	2566-1706	2159-1475	2382-1591	1847-1259
$Re_1 \times 10^6$, 1/m	5.19-1.41	7.04-2.03	13.77-5.20	19.76-8.09

EXPERIMENTAL RESULTS

An analysis of pressure distribution shows that it is highly nonuniform. An example of static pressure distribution over the inlet throat perimeter at $M=6$ is shown in Fig. 2. It is seen that especially strong nonuniformity is observed on the strut. This can be related to the boundary layer separation caused by the action of a more intense shock wave, since the inclination angle of the side wall surface is larger than the corresponding angle of strut inclination by a factor of 1.5. This conclusion is also supported by a considerable pressure nonuniformity in the presence of a thick boundary layer at the inlet duct entrance. Similar results were obtained for all Mach numbers when the inlet was started. For subsonic flow regimes in the throat, the pressure field was more uniform.

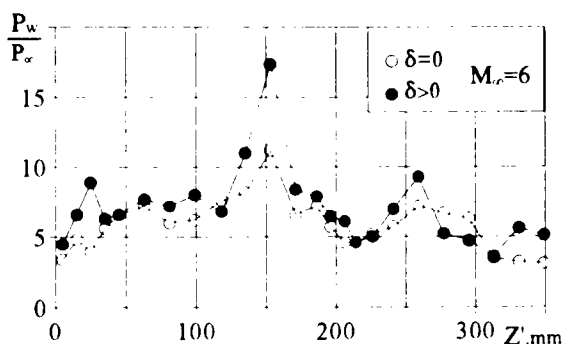


Fig. 2. Static pressure over the inlet throat perimeter. (Base, strut, cowl, side wall).

When analyzing the pressure distribution along the model (Figs. 3, 4), we can see an alternation of pressure peaks typical of supersonic duct flow, which is due to alternation of shock waves and expansion waves. This nonuniformity is also observed when decreasing the Mach number, but retaining a supersonic flow in the model duct. If the inlet was not started, the pressure equalizes both along the duct and over the inlet throat perimeter. For $M<2.5$, the inlet was started neither in the flow core, nor on the tunnel wall. This was confirmed by the Schlieren pictures of the flow over the model duct entrance. For $M \geq 3$, a thick boundary layer had a strong effect on the character of static pressure distribution and pressure level in the duct. Because of model asymmetry, this effect was different at the opposite compression surfaces. Thus, the pressure equalization and reduction of the overall pressure level along the duct were observed at $M=6$ on the strut (Fig. 3). A typical saw-tooth

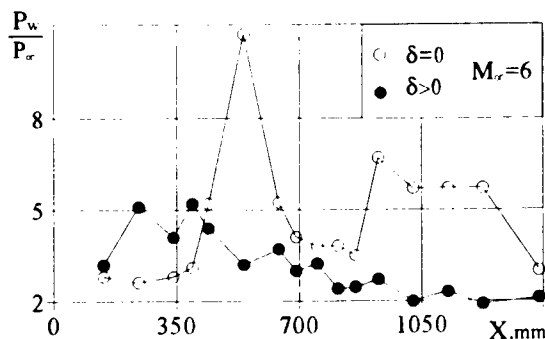


Fig. 3. Static pressure distribution along the strut.

distribution of static pressure was observed on the side wall (Fig. 4), though there was some shift along the model and some increase of peak pressure values. This is probably due to the appearance and growth of local separation regions.

An example of total pressure distribution in the inlet throat for $M=4$ and 6 is shown in Fig. 5. A strong pressure nonuniformity over the duct height can be noted, as well as a step-like character of pressure distribution in a supersonic duct flow, especially in the lower part of the throat approximately up to half of its height. The flow stall changes qualitatively the pressure distribution. This is manifested in smoothing the pressure peaks at $M=3$, and the character of pressure distribution approaches that typical of the near-wall turbulent layer (for $M<3$). This result is apparently determined to a large extent by the boundary layer separation at the model base. The presence of separation is also supported by the static pressure distribution at the base along the model duct. Figure 5 shows also the influence of a thick boundary layer upstream of the model on the total pressure variation in the inlet model throat (black markers), which leads to total pressure reduction, mainly at the model base. Besides, the pressure profile equalization is observed (for $\delta>0$), which is most pronounced when decreasing the free-stream Mach number.

As noted above, this model is an engine module which has an inlet and combustion chamber with a system for fuel injection. This allows one to perform combustion tests in a hot-shot facility. since there is always the problem of

identification of measurement results in different wind tunnels, moreover, in principally different wind tunnels such as T-313 and IT-302M, the experiments were performed for the Mach number 6 and similar Reynolds numbers. The results obtained in wind tunnels with blowdown and hot-shot operation regimes are in fairly good agreement with each other [2]. An example of total pressure distribution in the model throat for Mach numbers 6 and 7.2 in the hot-shot wind tunnel IT-302M is presented in Fig. 6. For comparison,

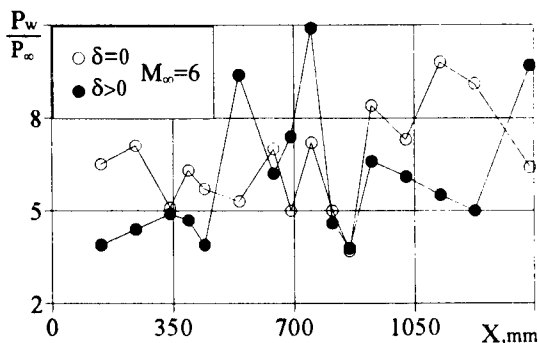


Fig. 4. Static pressure distribution along the side wall.

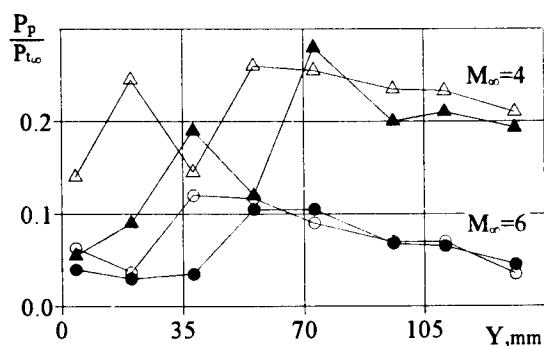


Fig. 5. The Pito pressure in the inlet throat.

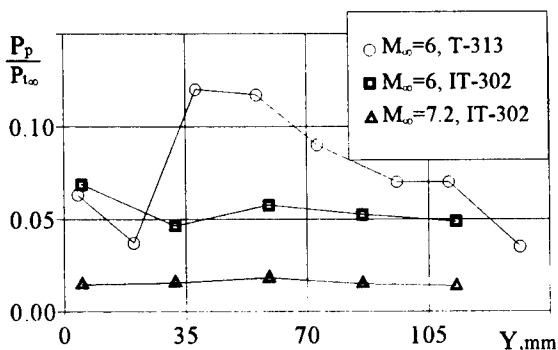


Fig. 6. The Pito pressure in the inlet throat in different wind tunnels.

the same picture shows the total pressure profile in the throat for $M=6$ obtained in the main set of tests in the blowdown wind tunnel T-313. A certain difference in pressure profiles obtained in these two wind tunnels is apparently caused by substantially different temperature regimes of the model surface and, hence, by different states of the boundary layer [3].

The results of static and total pressure measurements made it possible to estimate the mean Mach number in the inlet throat as a function of the free-stream velocity (Fig. 7). These calculations were based on averaging of the total and static pressure over the model cross-section. Since the fields of total and static pressures are strongly nonuniform, one has to bear in mind a possible uncertainty of determining the Mach number in the duct. This could be the reason for

obtaining an underestimated Mach number in the throat for $M=3$ ($\delta=0$). This follows from the analysis of pressure distribution and schlieren pictures. These data testify that the inlet is started at $M=3$ in the flow core and in the presence of a thick boundary layer at the model entrance.

Figure 7 shows the Mach numbers in the throat of a 3D inlet with adjustable central strut [1]. It can be concluded on the basis of these data that for smaller stagnation parameters of the flow a double-swept configuration allows for supersonic combustion in the combustion chamber beginning from comparatively low free-stream Mach numbers, i.e., the flow velocity at the duct exit of such an inlet allows one to supply the maximum possible energy with minimum total pressure losses.

On the basis of measurements performed in the throat the pressure recovery coefficient was determined (Fig. 8). It is seen that the pressure recovery coefficient in a double-swept inlet remains rather high up to $M=6$, even in the presence of the boundary layer at the entrance it is twice as high as the pressure recovery coefficient of an adjustable inlet in the flow core.

When the total pressure fields at the exit were measured, it was established that the pressure was strongly nonuniform both in the vertical and horizontal directions. It was retained for all Mach numbers and both variants of model mounting in the wind tunnel. It is known that this nonuniformity in pressure distribution can lead to considerable errors in determining the air flow rate through the inlet. By increasing the number of total pressure probes up to 7-10 and more, however, it is possible to reach the accuracy of flow rate determination better than 3%. The averaging of total and static pressures over the areas was used. On the

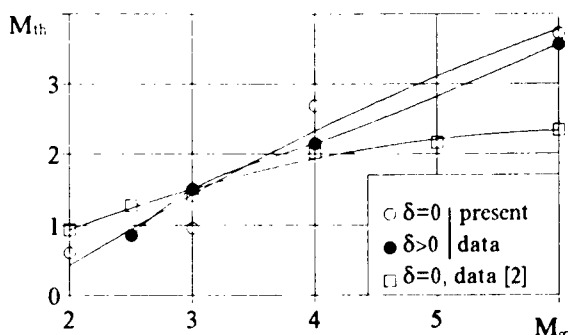


Fig. 7. Throat Mach numbers.

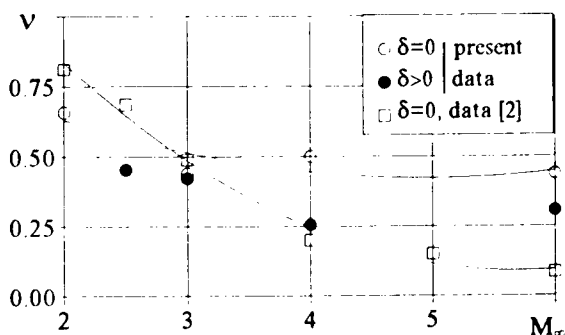


Fig. 8. The pressure recovery coefficient

basis of these data, the flow rate coefficient versus the Mach number was determined (Fig. 9). Beginning from $M=4$, the flow rate coefficient of the inlet of given configuration is slightly lower than that of previously tested inlets; however, its value is quite acceptable and practically independent of the presence of boundary layer, similar to a swept forward inlet.

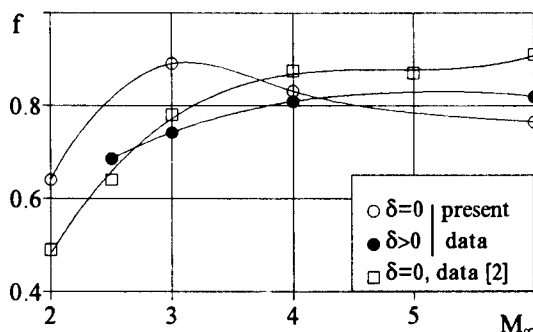


Fig. 9. The flow rate coefficient.

CONCLUSION

The conducted tests of a three-dimensional inlet model resulted in obtaining integral characteristics of the inlet, including the thick boundary layer effect on the inlet starting and duct flow. It was established that such an inlet ensures a supersonic flow in the duct for $M>2.5$ with a sufficiently high level of flow rate. At the same time, it was shown that additional efforts are needed to increase the total pressure recovery coefficient and the overall compression in order to ensure combustion.

Together with the data of [1], these results can be considered as the first stage of studying a 3D inlet for scramjet. The testing of this model will be continued with extending the Mach number range and combustion experiments to study the ignition and combustion conditions for hydrogen and (or) hydrocarbon fuel.

REFERENCES

1. Goldfeld M.A., Stepanov V.A., Vinogradov V.A. Experimental and numerical investigation of two concepts of the hypersonic inlet. — AIAA Paper N95-2721, San Diego, CA, 11p, 1995.
2. Goldfeld M.A. Experimental study of 3D inlets for high supersonic flight velocities. — Proceedings of ICAR ITAM, Novosibirsk, 5-94, 41p, 1994.
3. Goldfeld M.A. An experimental investigation of 3D intakes for high supersonic flight speeds. — Proceedings of conference Engine-Airframe Integration, Bristol, UK, 13p., 1996.

A NUMERICAL STUDY ON REDUCING THE INTERNAL NONUNIFORM SHOCKED FLOWS TO EQUIVALENT ONE-DIMENSIONAL STREAMS

Yu.P. Goon'ko, A.N. Kudryavtsev, R.D. Rakhimov

Institute of Theoretical and Applied Mechanics SB RAS, Russia

INTRODUCTION

Reducing the non-uniform gas flows to equivalent one-dimensional streams in inlet and engine ducts is of practical importance for scramjet performance analysis because one-dimensional approaches are still widely used for calculating the flows in the scramjet channels [1]. Various methods of flow averaging are used in these cases depending on particular objectives and features of the posed problem [2]. A comparative analysis of several averaging methods is performed in the present work on the basis of numerical data for a scramjet inlet shocked flow. In every method either total pressure, or momentum, or flow entropy is conserved, apart from the flow rate and total enthalpy.

DEFINITION OF A GENERIC EXAMPLE

The analysis of averaging methods is performed by the example of a two-dimensional inviscid flow inside the simplest ramp inlet with a long constant-area duct.

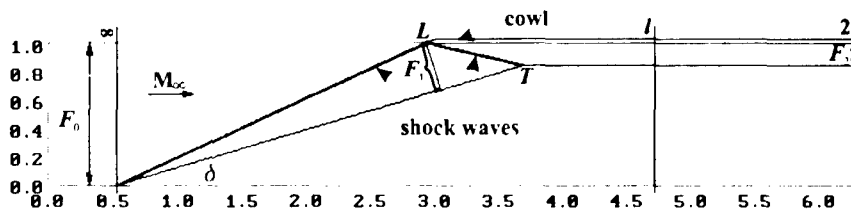


Fig. 1a Isobars: $M_\infty = 6 = M_D$; $\varphi = 1$

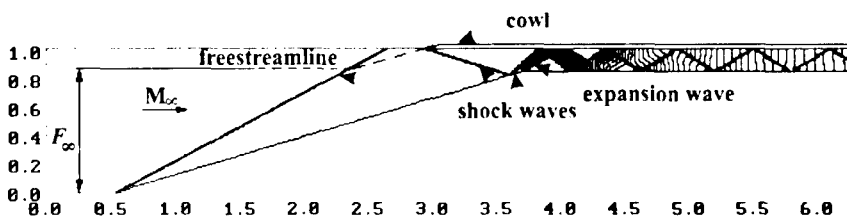


Fig. 1b Isobars: $M_\infty = 4.5 < M_D$; $\varphi < 1$

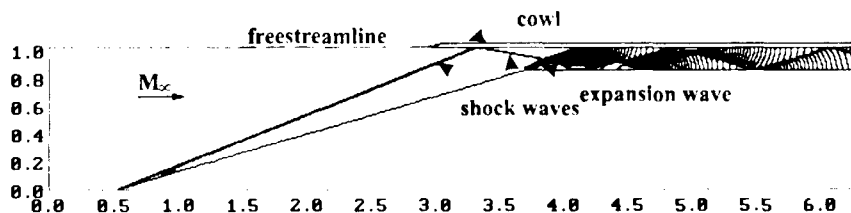


Fig. 1c Isobars: $M_\infty = 10 > M_D$; $\varphi = 1$

The equation of state for a perfect gas is assumed valid, and the ratio of specific heats is assumed constant. The inlet geometry (Fig. 1) is determined for a so-called design regime when at a given free-stream Mach number $M_\infty = M_D$ and ramp wedge angle δ the oblique shock wave from the wedge is incident onto the leading edge of the cowl lip (point L) and the reflected shock wave falls onto the compression center-body at the corner point (point T , Fig. 1a). The design parameters for data presented below are the Mach number $M_D = 6$ and the wedge angle $\delta = 15^\circ$.

In the design regime the flow in the duct is uniform (Fig. 1a). The duct flow non-uniformity in off-design regimes (Fig. 1b, c) is generated by shifting the oblique shock waves from the wedge or cowl lip and by the expansion fan from the body inflection. A uniform flow realizes at the entry with cross-section area F_1 for Mach numbers $M_\infty \leq M_D$, the entry flow parameters corresponding to those behind the wedge shock wave and the flow rate coefficient is $\varphi = F_\infty / F_0 \leq 1$ (here F_0 is the inlet reference area). For Mach numbers $M_\infty > M_D$ the flow at the inlet entrance is piecewise and includes the free stream and the stream behind the wedge shock wave (Fig. 1c), in this case $\varphi = 1$.

NUMERICAL SOLUTION

The two-dimensional steady Euler equations are solved numerically to investigate the supersonic flow within the inlet. We used the space-marching method based on the MUSCL-type TVD scheme [3] along with the third-order Runge-Kutta stepping in the streamwise direction. The numerical fluxes on cell faces are calculated by solving the Riemann problem [4] with the approximate HLLE (Harten-Lax-van Leer-Einfeldt) method. The cell face values of primitive variables are reconstructed from the cell averaged ones using the third-order formula and the van Albada's slope limiter [5]. The flow structure for various regimes could be seen from the pressure flowfield (Fig. 1). It should be noted that both the shock slopes and flow parameters behind the shock waves for the design regime coincide with the exact solution within 0.05%. The error in determining the integral flow characteristics is less than 0.1%. The axial component of the total momentum in each marching cross-section l inside the duct was determined in a normalized form

$$\bar{I}_{tx} = \sum_i [\bar{p}_i (\gamma M_i^2 \cos^2 \theta_i + 1)] \bar{F}_i, \quad (1)$$

where $\gamma = 1.4$, i is the cell number, $\bar{F}_i = F_i / F_0$ is relative cross-sectional area of the cell, $\bar{p}_i = p_i / p_\infty$, M_i , θ_i are the relative static pressure, the Mach number, and the flow angle in the cell, respectively. The relative total flow rate and the flow rate through the i -th cell of the computational domain are determined as

$$\bar{G}_i = \sum_i \Delta \bar{G}_i \bar{F}_i, \quad \Delta \bar{G}_i = \bar{p}_i M_i \cos \theta_i / (M_\infty \sqrt{\bar{T}_i}), \quad (2)$$

and the relative temperature $\bar{T}_i = T_i / T_\infty$ is determined from the known gas dynamic relations [2].

THE METHODS OF REDUCING THE INTERNAL NONUNIFORM FLOWS WITH SHOCK WAVES TO EQUIVALENT ONE-DIMENSIONAL STREAMS

It should be noted that for all considered reducing-averaging methods the direction of an equivalent one-dimensional stream in some cross-section of the duct is assumed coincident with the duct axis. Let us consider the following methods.

1. Analytical approach. This approach is based on determination of the reduced stream parameters with the use of integral equations of energy, flow rate, and momentum

conservation for the fraction of the inlet-captured stream from the free-stream cross-section to the duct exit cross-section 2 (Fig. 1a). To solve the momentum equation in this case an exact or approximate value of the force acting upon the inlet ramp is to be determined. The relative supersonic flow velocity at the duct exit is determined by a quadratic equation [6], the Mach number and other flow parameters are then determined from the known velocity. In the simplest case under consideration, the force acting upon the inlet ramp can be exactly determined, and this approach for an inviscid flow yields an exact limiting estimate for the stream parameters at the inlet exit as the duct length $L \rightarrow \infty$. Thus, the considered reducing-averaging methods were compared with respect to the present approach.

2. The method with averaging of the total pressure over the flow mass. The relative total pressure of an averaged flow in the l -th cross-section is determined as

$$\bar{p}_{0l} = \left[\sum_i \bar{p}_{0i} \Delta \bar{G}_i \bar{F}_i \right] / \bar{G}_l, \quad (3)$$

where the relative value of the local total pressure p_{0i} is related to the static pressure p_i by the known gas dynamic function $\pi(M_i) = p_i/p_{0i}$ [2].

The averaged Mach number \bar{M}_l and relative static pressure \bar{p}_l for a known total pressure \bar{p}_{0l} are determined from appropriate relations [2]. The momentum of the averaged flow is

$$\bar{I}_l = (\gamma \bar{M}_l^2 + 1) \bar{p}_l \bar{F}_l. \quad (4)$$

3. The method with averaging of the total pressure over the entropy. This method is reasonable for estimation of the engine losses or efficiency [2]. The averaged total pressure is determined as

$$\ln \bar{p}_{0l} = \left[\sum_i \ln \bar{p}_{0i} \Delta \bar{G}_i \bar{F}_i \right] / \bar{G}_l, \quad (5)$$

where all parameters are defined above, and the averaged parameters \bar{M}_l and \bar{p}_l are found in a way similar to method 2.

4. The averaging method based on the momentum equation. This method is preferable for estimating the force characteristics [2], various its variants are possible.

4.1. Firstly, the averaging is performed at *flow rate conservation*

$$\bar{G}_l = \bar{p}_l \bar{M}_l \bar{F}_l / (M_\infty \sqrt{\bar{T}}) \quad (6)$$

and the relation for determining the averaged Mach number \bar{M}_l has the form

$$\frac{\gamma \bar{M}_l^2 + 1}{\bar{M}_l \sqrt{\gamma / (\gamma - 1) + \gamma \bar{M}_l^2 / 2}} = \frac{\bar{I}_l}{\bar{G}_l M_\infty \sqrt{\gamma / (\gamma - 1) + \gamma M_\infty^2 / 2}}. \quad (7)$$

From the known Mach number \bar{M}_l , the static pressure of an equivalent one-dimensional flow is

$$\bar{p}_l = \bar{I}_l / [(\gamma \bar{M}_l^2 + 1) \bar{F}_l] \quad (8)$$

and the total pressure is determined from the function $\pi(\bar{M}_l)$.

4.2. Secondly, as it is often done in practice, *the static pressure is averaged over the cross-section area*

$$\bar{p}_l = \left[\sum_i \bar{p}_i \bar{F}_i \right] / \bar{F}_l, \quad (9)$$

the averaged Mach number is

$$\tilde{M}_l = \sqrt{[(\tilde{I}_x / \tilde{p}_l F_l) - 1] / \gamma}, \quad (10)$$

and the total pressure \tilde{p}_0 is determined from the function $\pi(\tilde{M}_l)$.

TOTAL CHARACTERISTICS OF A SCRAMJET ENGINE

To estimate the differences due to various approximate determination of the flow parameters at the inlet exit and, hence, approximate determination of the engine performance, we calculated the thrust characteristics of a scramjet engine with the examined inlet. A simplified approach [7] was used. It is based on one-dimensional relations for calculating the gas dynamics of an internal supersonic flow in the combustor and nozzle. The thrust characteristics of an ideal scramjet with the same nonadjustable geometry of the engine channel were calculated for each variant of determination of inlet duct averaged airstream. The losses in the engine channel are neglected, the fuel supply corresponds to the stoichiometric air-to-fuel ratio $\alpha=1.0$. The flight conditions correspond to the dynamic pressure $q_\infty = 5 \cdot 10^4$ N/m². The fuel efficiency was assumed $H_u = 1.3 \cdot 10^8$ J/kg, the stoichiometric mass coefficient was $L_0 = 34.25$, the heat capacity of combustion products was assumed constant and characterized by the mean (effective) ratio of specific heats $\gamma_c = 1.26$. An engine combustion chamber with fuel supply in the initial constant-area section $F_c = F_2 = \text{const}$ and in a subsequent expanding section with keeping the Mach number $M_c = \text{const}$ was considered. It should be noted that in reducing a non-uniform flow to an equivalent one-dimensional one determined by three independent gas dynamic parameters it is possible to satisfy only three integral conservation laws. When determining the air-breathing engine performance, it is obviously necessary to conserve the flow rate and the total enthalpy of the inlet-captured airstream. In reducing with method 4.2 when the momentum equation is used as the third condition of conservation, the force characteristics of the stream are conserved, and, hence, the thrust characteristics of the engine are correctly estimated. Averaging of the total pressure over entropy with method 3 implies a correct estimate of the losses in the engine duct. The calculation results show that the mass averaging of the total pressure yields almost the same effect. However, the force balance in determining the thrust characteristics of the engine is violated in the last cases. Let us consider total characteristics of the inlet and engine. The inlet drag coefficient is determined from the changes in airstream momentum as

$$c_{D(inl)} = c_{D(lq)} + 2\varphi - [\tilde{p}_2(\gamma_2 \tilde{M}_2^2 + 1) - p_\infty] \bar{F}_2. \quad (11)$$

Here $c_{D(inl)} = D/(F_0 q_\infty)$ is the inlet drag coefficient and $c_{D(lq)}$ is the drag coefficient over the liquid contour of the inlet-captured airstream.

For method 4.1 which conserves the axial component of the stream momentum in the duct, the coefficient $c_{D(inl)}$ equals to the exact value determined by method 1. In all other cases, this is an approximate value of the inlet drag coefficient.

The effective thrust coefficient of the engine is determined as

$$c_{T(eff)} = c_{T(eng)} - c_{D(inl)} - c_{D(ext)}. \quad (12)$$

The internal thrust is a force of the engine between the inlet exit cross-section and the nozzle exit cross-section

$$c_{T(eng)} = (J_e - \tilde{J}_2) F_0 / q_\infty, \quad (13)$$

where $\tilde{J}_2 = (\tilde{p}_2(\gamma_2 \tilde{M}_2^2 + 1) - p_\infty) F_2$, $J_e = [p_e(\gamma_e M_e^2 + 1) - p_\infty] \bar{F}_e$. The external drag coefficient $c_{D(ext)}$ of the scramjet was determined for a cowl with the surface inclination angle $\delta_{cowl} = 5^\circ$.

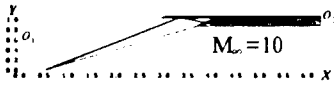


Fig. 2a Isobars

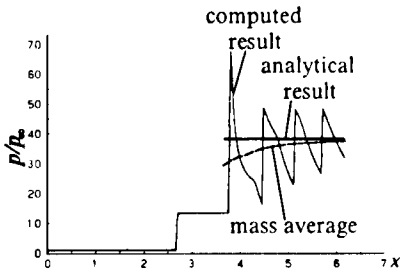


Fig. 2b Pressure distribution along the axis $O_1 O_2$

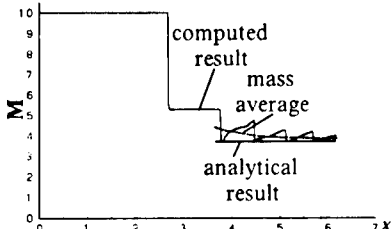


Fig. 2c Mach number distribution along the axis $O_1 O_2$

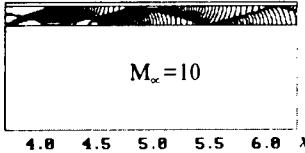


Fig. 4a Isobars

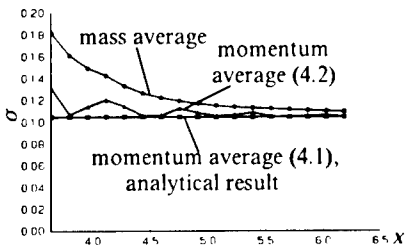


Fig. 4b Relative total pressure of the one-dimensional equivalent flow

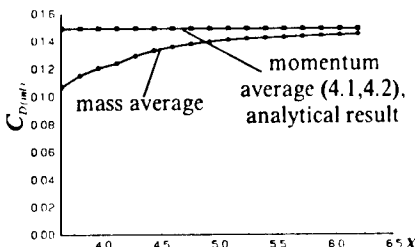


Fig. 4c Inlet drag coefficient corresponding to the equivalent one-dimensional flow

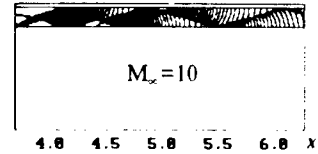


Fig. 3a Isobars

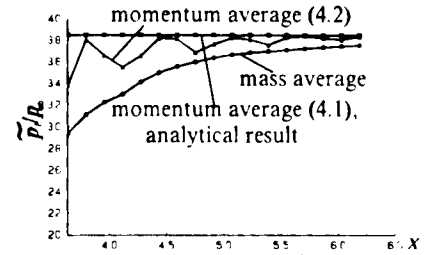


Fig. 3b Pressure of the equivalent one-dimensional flow

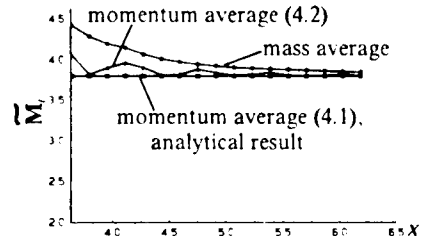


Fig. 3c Mach number of the equivalent one-dimensional flow

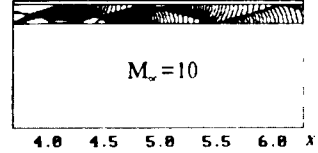


Fig. 5a Isobars

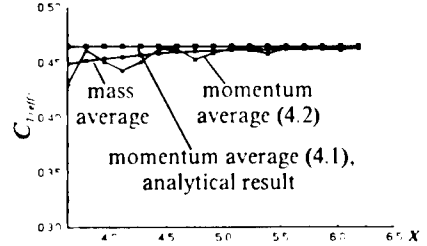


Fig. 5b Effective thrust coefficient

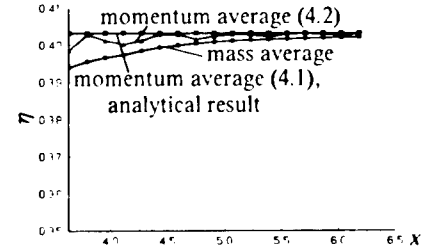


Fig. 5c Scramjet net efficiency

To estimate the characteristics due to the losses in the engine duct, we used the total pressure recovery factor of the inlet $\sigma = \tilde{p}_{02} / p_{0\infty}$ and the net efficiency coefficient of the engine

$$\eta = \left[V_\infty^2 \left(\beta \frac{V_e}{V_\infty} - 1 \right) - (\beta - 1) \frac{V_\infty^2}{2} \right] / \left[(\beta - 1) \left(H_u + \frac{V_\infty^2}{2} \right) \right], \quad (14)$$

where V_∞ is the free-stream velocity, V_e is the exhaust jet velocity, $\beta = 1/(\alpha L_0)$ is the coefficient of increasing gas mass passing through the engine.

RESULTS AND CONCLUSIONS

The calculations covered the Mach number range $M_\infty = 4.5-10$. These results are illustrated in Figs.2-5 by the example of an inlet with the duct length $\bar{L} = L / F_2 = 16$ for the off-design flow pattern at $M_\infty = 10$. The distributions of local static pressure and Mach number along the duct axis O_1O_2 are shown in Fig.2b,c. There are waveforms in this distributions attributed to multiple reflections of shock waves in the duct, their amplitude decreases along the duct length. Deviations of averaged parameters of the equivalent one-dimensional flow from the exact analytical solution decreases correspondingly, Figs.2b,c and 3b,c. Examples of force and efficiency characteristics of the inlet and engine determined are shown in Figs.4,5, respectfully. For the reducing method 4.1 the flow parameters are constant over the length and coincide, in the case under consideration, with parameters determined analytically. Method 4.2 with stream momentum conservation and static pressure averaging over the duct area yields rather small deviations. This agrees with a result obtained in [2], where it is shown that, for non-uniform streams with high supersonic velocities and total temperature constant over the cross-section, four rather than three conservation laws are satisfied simultaneously with a good accuracy: those for total enthalpy, flow rate, momentum, and entropy. Method 2 with averaging of the total pressure over the flow mass leads to significant deviations in determining the force characteristics, i.e., to an underprediction of the inlet drag coefficient by 10-28% (Fig. 4c) and about 7% deviation in thrust value (Fig.5b). The engine efficiency is also underpredicted by about 3% (Fig.5c). Method 3 essentially produces the same results as method 2. All considered reducing methods yield the engine characteristics which are little different from each other (no more than by 1-2%) when the averaging is performed in duct cross-sections lying at a distance of more than 10 throat heights from the duct entrance. Thus, reducing methods using the momentum equation conservation seem to be preferable for estimating the scramjet characteristics.

REFERENCES

1. Weissman D. Representation of Two-Dimensional Hypersonic Inlet Flows for One-Dimensional Scramjet Cycle Analysis. – AIAA Paper 90-0527, 1990.
2. Cherkez A.Ya. One-Dimensional Gas Flows // Abramovich G.N. Applied Gas Dynamics. Moscow: Nauka, 1969, P.250-257.
3. Yee H.C., Warming R.F., Harten A., Implicit Total Variation Diminishing Schemes for Steady-State Calculations // Journal of Computational Physics. – 1985. – Vol.57. – P.327-360.
4. Godunov S.K., Zabrodin A.V., Ivanov M.Ya., Kraiko A.N. Numerical Solution of Multidimensional Problems of Gas Dynamics. – Moscow: Nauka, 1976.
5. Sweby P.K. High Resolution Schemes Using Flux Limiters for Hyperbolic Conservation Laws // J. Numer. Anal. – 1984. – Vol.21. – N.5. – P.995-1011.
6. Goonko Yu.P., Mazhul I.I. Limiting estimates of aerodynamic characteristics of flat inlets at large Mach numbers $M_\infty \rightarrow \infty$ // Thermophysics and Aeromechanics. – 1994. – Vol.1. – N.3. – P.231-236.
7. Goonko Yu.P., Mazhul I.I. Estimation on integral aerogasdynamics of hypersonic scramjet-powered aircraft // Thermophysics and Aeromechanics. – 1995. – Vol.2. – N.3. – P.203-214.

LIQUID CRYSTAL THERMOGRAPHY AND PIV METHOD IN INVESTIGATIONS OF UNSTATIONARY PROCESSES IN FLUIDS

C.Greated

Edinburgh University, UK

V.I.Kornilov, V.N.Kovrizhina, V.M. Khachatryan, A.A. Pavlov, G.M. Zharkova

Institute of Theoretical & Applied Mechanics of SB RAS,

4/1, Institutskaya Str., 630090, Novosibirsk, RUSSIA

INTRODUCTION

Combined measurements of velocity and temperature in turbulent flows are subjects of fundamental and practical interest. Optical measuring techniques, yielding integral information or providing local temperature and velocity measurements, offer new prospects in air- and hydromechanics. The measurement of velocity and temperature fluctuations is important for the study of micro- and macrophenomena that occur in stratified flows, at a free water surface and at a water/air interface. Spatial distribution of temperature and its variation with height and time in the surface layer are rather relevant for the heat exchange mechanism and ocean/atmosphere interaction. Liquid-Crystal Thermography (LCT) and Particle Image Velocimetry (PIV) techniques show promise in their use for such measurements [1,3]. The aim of this investigation was to combine LCT and PIV methods for study of unstationary processes in hydrodynamic flow.

EXPERIMENTAL SETUP

The set-up [Fig.1] is a water channel made of acrylic plastic with a total length of 900 mm with a cross-section $80 \times 80 \text{ mm}^2$.

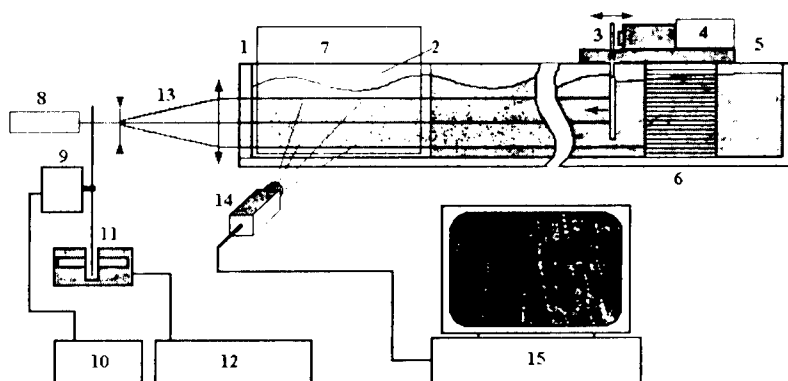


Fig.1. Water channel for testing the LC and PIV technique. 1-the end face of the channel; 2- window; 3-wave generator; 4-electron generator; 5 - nonoperating section; 6- honeycomb; 7-LC sensor; 8-laser; 9-disk modulator; 10-power source; 11-photon-coupled pair; 12-frequency meter; 13-optical block; 14-CCD camera; 15-PC.

© C. Greated, V.I.Kornilov, V.N.Kovrizhina, V.M. Khachatryan, A.A. Pavlov, G.M. Zharkova, 1998

One of the end faces of the channel 1 is a parallel plane plate made of optical glass and serves to introduce the probing radiation into the examined medium (for PIV method). A part of the side wall adjacent to this face 2 is also made of optical glass and works as a window for lighting the LC sensor and image registration. Closer to the opposite end of the channel there is a wave generator 3, its oscillation frequency being set by an electron generator 4. To reduce the intensity of the wave reflected on the end face of a nonoperating section 5, honeycomb 6 is placed between the wave generator and this face. The wave generator can be moved along the channel within 60 mm. Together with generator frequency adjustment, this allows one to obtain a resonance standing wave in the measurement section. The LC sensor 7 was flat plates-frames made of metal 200 μm thick, with a rectangular window. Copper foil (30 μm thickness) was glued to the window with a heat-insulating glue. The selective reflection bandwidth of LC being used was 2.2°C, the thickness of LC layer was not greater 20 μm . The sensor was placed in water so that the LC coating was partially outside the water, at least at a distance equal to the wave amplitude. The water in the channel and the sensor were at room temperature. Then, a slow jet of hot water in the vicinity of the sensor created a temperature stratified (from top to bottom) profile displayed with LC as colour response, and oscillations of a fixed frequency were initiated. The colour images were transferred to a computer with a frequency of 50 frames per second and processed.

LIQUID-CRYSTAL THERMOMETRY

Information about the temperature fields can be found from the spectral characteristic of the reflection radiation. As a rule, it is difficult to measure directly the selective reflection wave length under the conditions of aerodynamic or thermophysical experiment with LC indicators. As a consequence, all algorithms of temperature measurement using LC are indirect [3-8]. When it is necessary to determine localisation of the peak values of heat loads, it is reasonable to use the methods with a high spatial resolution, including full information about the colour. A non-linear colour solid (colour space) was used in the present work for a quantitative description of colour information. The colour is expressed there in terms of intensity, hue, and saturation (abbreviations HSI, HIS, or IHS in different publications). A point-by-point conversion from one solid to another is carried out using the formulas

$$I = (R + G + B)/3; \quad S = 1 - (\min(R, G, B)/I)$$

$$H = 90 - \text{Arctg}(F/\sqrt{3}) * 360/(2\pi), \text{ if } G > B \text{ or } 270 - \text{Arctg}(F/\sqrt{3}) * 360/(2\pi), \text{ if } G < B;$$

$$\text{or } 180, \text{ if } G > 0; G = B; \text{ and } 0, \text{ if } G = B,$$

$$\text{where } R, G, B \text{ is red, green and blue primaries; } F = (2R - G - B)/(G - B)$$

The results of preceding researches [1-3] showed that the 'hue' versus 'temperature' relationship obtained is described by a non-linear monotonic function which can be used for measurement purposes. The HSI system has some advantageous properties such as possibility of independent operation with individual components (only the parameter H is used for temperature calibration); invariance of H (contrary to R, G, B signals) with respect to lighting non-uniformity; no necessity of reaching the temperature of the peak values of intensity in experiment, which sometimes simplifies the choice of the operating temperature range. Taking this into account, the HSI system was chosen in the present work for a further LCT development and increasing the measurement accuracy. For temperature measurement it

is required to execute hue versus temperature $H - f(T)$ calibration. The calibration procedure can be performed by different methods under closely controlled conditions (for example lighting, angle position and camera settings). At present our calibrating procedure work has been incorporated into a software package based on true colour image processing. From a JVC video camera the surface image was transferred into a computer for digital processing by means of the software. In present experiments a copper disk 40 mm in diameter was used for calibration, its polished surface being covered with a temperature-sensitive coating. It was a thin-film coating on the basis of polymer-encapsulated cholesteric LC with the selective reflection bandwidth of 2.2°C . The beginning of the calibration region (red colour) had a temperature of 27.8°C . The disk temperature was set by means of a water thermostat and was measured with an accuracy of 0.1° . The study of the calibration curve for various disk point positions (effect of the angular dependence of LC selective reflection) showed that experimental data obtained in the working range of a given LC are approximated by a polynomial.

EXPERIMENTAL RESULTS AND DISCUSSION

LCT and PIV techniques were applied to register the temperature and velocity in a standing resonance wave generated artificially in a water channel [Fig.1]. The results of measurements are presented in Fig.2 as spatial and time dependencies of temperature for various values of the x and y co-ordinates.

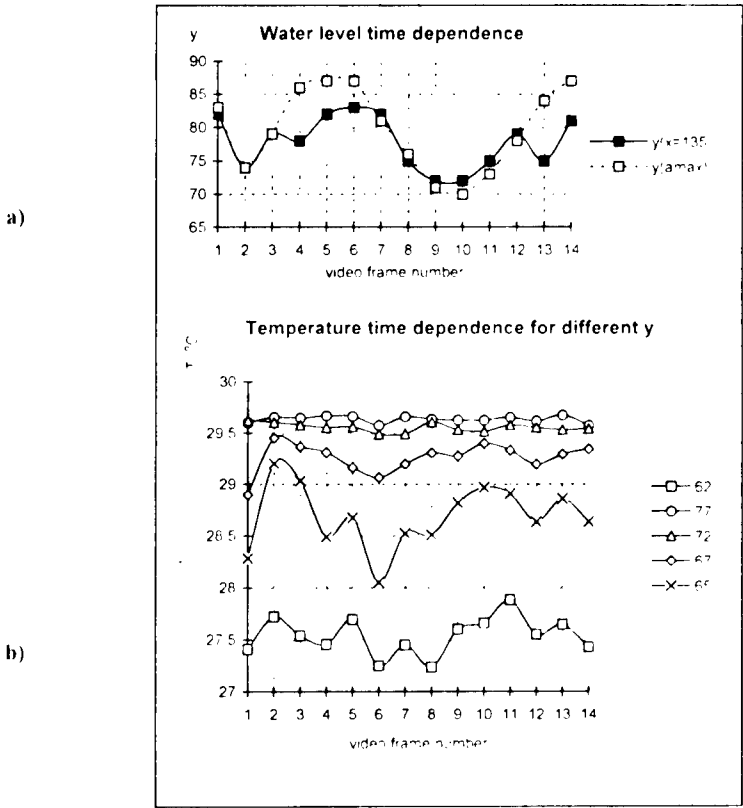


Fig. 2.

Above there are the curves for changes of the local (corresponding to the co-ordinate $x=135$) water level in the channel and the water level in the point of peak amplitude value (Fig. 2a). The number of frames is shown as the abscissa. It is seen that in this experiment the period of oscillations in the region of the peak value of the amplitude is 0.18 s (frequency 5.5 Hz). In the region $x=135$ the character of oscillations of the water level is slightly different. In the region $y = 60-77$ there is a change of colour from red to blue, which corresponds to a temperature difference of about 2.2°C. Figure 2b shows the temperature variation at the point $x=135$ as a function of time. An analysis of these plots shows that, as expected, the character of temperature variation is different at different depths. Indirectly, this is indicative of changes in the flow structure with height. The most high-frequency oscillations are observed at the height $y=62$ and correspond to a period of 0.04 s or frequency of 25 Hz. The scale of temperature oscillations varied from 1 to 0.3°C, which is much higher than the fluctuation noise of the TV signal. Thus, a conclusion can be drawn that the LC sensor permits the study of processes with unsteadiness times of about 0.02-0.04 s. Unfortunately, the instrument used, namely, a camera with a speed of 50 frames per second, does not allow the observation of more high-frequency processes. In future, the authors are planning to carry out a more detailed study of dynamic characteristics of LC coatings and to optimise the sensor construction on the basis of this study.

A traditional optical scheme [Fig. 1] was used for velocity fields registration. The radiation of a He-Ne laser ($P=10$ mW) **8** is modulated by a disk modulator **9**. The velocity of disk rotation is controlled by the voltage from a power source **10**, the modulation frequency is registered using a photon-coupled pair **11** and frequency meter **12**. By means of the optical block **13**, laser radiation is formed into a flat beam (laser sheet) and directed to the water medium region under study that contains specially inserted light-scattering particles. Images of the tracks of moving particles in a chosen cross-section is registered by video-camera **14** and transferred to an IBM PC **15**. The image is registered with a time of exposure including two or more pulses of the probing radiation. A CCD camera CV-M10 with a progressive sweep and a resolution of 659x494 pixels was used. Figure 3a shows a typical image obtained in this case. Knowing the modulation frequency of the probing radiation and the image scale, the velocity of a given particle can be calculated from the distance between the images of the same particle for different pulses. Not only the absolute value of velocity vector is found, but also its direction in a chosen plane. However, as seen from the character of images obtained, the velocity vector direction is determined with an accuracy 180°. Digital processing of obtained images is one of the most relevant components in PIV techniques. The processing includes several stages. The first one can include improving of the contrast of initial image, setting to zero the image portions with brightness lower than a certain sets level. The image obtained after the primary processing is shown on Fig. 3b. The first stage is not an obligatory one and is used only if the source information is of poor quality.

At the second stage, some part of the image is separated. In what follows, this image part is called a spot. A correlation function of the following form is found for this spot:

$$G(\xi, \eta) = \int_{-S}^S F(x, y) \cdot F(x - \xi, y - \eta) \cdot dx \cdot dy$$

Zero co-ordinates x and y correspond to the central pixel of the spot, and the velocity vector calculated for this spot corresponds exactly to this point. The limits of integration $(-S, S)$

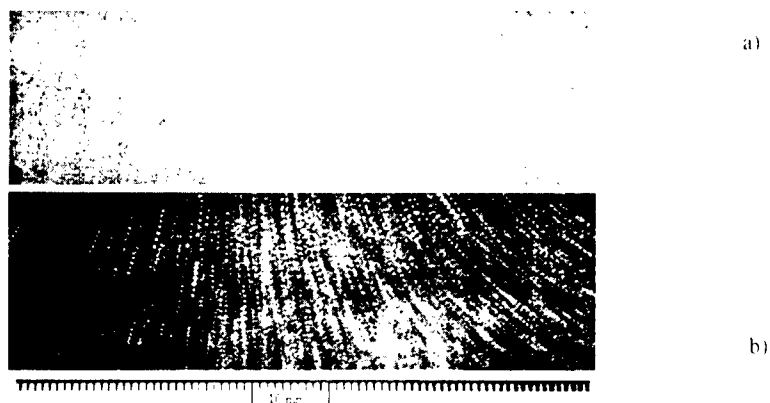


Fig3. Initial particle track image and particle track image obtained after the primary processing of initial image.

determine the spot size. On one hand, this size must be rather large to include the images of tracks of several light-scattering particles. On the other hand, the spot dimensions define the spatial resolution of the method and cannot be arbitrarily large. Some techniques make it possible to reduce the level of spurious signal of the correlation function. For instance, in our case, due to the useful signal symmetry, an averaging of the type $G(\xi, \eta)$ is possible. The last stage includes the determination of the co-ordinates of information maxima and the calculation of velocity vector.

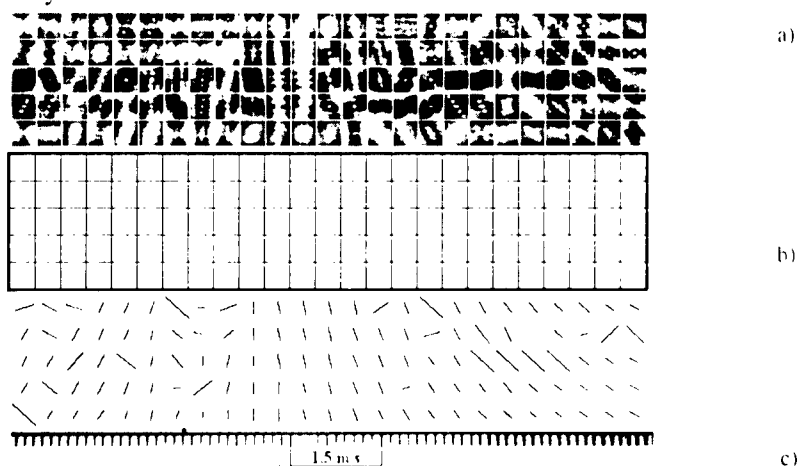


Fig.4. Symmetrised correlation functions, selected maxima of correlation functions and velocity vector field, obtained for initial particle track image (fig. 3a).

Figure 4a shows the functions $G(\xi, \eta)$ calculated for the initial image of Fig. 3a that were made symmetric and normalised over the range 0-255. It is seen that $G(\xi, \eta)$ has typical maxima symmetric about the central point. Figure 4b shows the positions of the maxima calculated from these functions. The co-ordinates of these maxima correspond to a spot-averaged shift of light-scattering particles between the pulses of probing radiation. Knowing the image scale and the modulation frequency of probing radiation, velocity is calculated from

positions of these maxima (Fig. 4c). A large amount of errors is observed because of bad quality of the initial image.

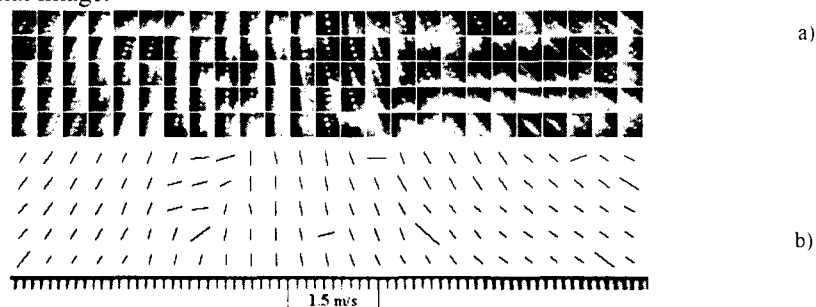


Fig. 5. Non symmetrised correlation functions and velocity vector field for particle track image (fig. 3b), obtained after the primary processing of initial image..

Non symmetrised correlation functions and velocity vectors calculated for a filtered image (fig. 3b) are presented in Fig. 5. Figure 6 shows the same information for asymmetric correlation functions. One can see a considerable reduction of errors in velocity field calculations, as compared with the initial image, and an increase in their number if the operation of symmetrisation is excluded.

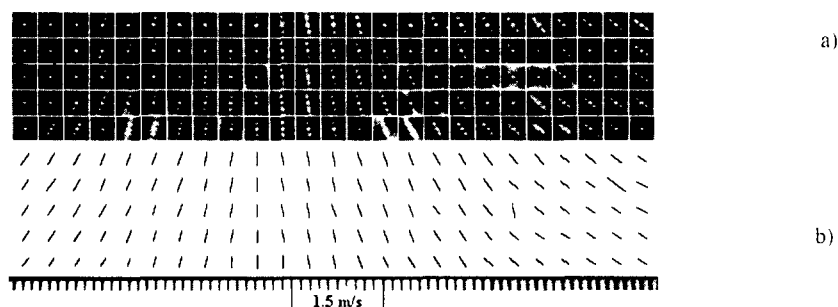


Fig.6. Symmetrised correlation functions and velocity vectors field, obtained for particle track image (fig. 3b).

ACKNOWLEDGMENTS

The authors wish to acknowledge the support of the INTAS for funding this work under grant No. 93344. We would like to thank Prof. C. Greated and Dr. Hann (Edinburgh University, UK) for helpful discussions.

REFERENCES

1. Dabiri D. Charib M. Digital Particle Image Thermometry and Velocimetry// Proc. of the VII Int. Symp. on Flow Visualisation, Sept. 11-14, 1995, Seattle, Washington, p. 558-566.
2. Ozawa M., Muller U., Kimura I., Takamory T. Flow and Temperature Measurement of natural Convection in a Hele-Shaw Cell using a Thermo-sensitive Liquid Crystal Tracer// Exp. in Fluids, 12, 1992, p. 213-222.
3. Wang Z., Ireland P.T., Jones T. V. An Advanced Method of Processing Liquid Crystal Video Signal from Transient Heat Transfer Experiments. ASME Paper, 93-GT-282.1993.

SIMULATION OF HYPERSONIC FLIGHT CONDITION FOR SCRAMJET-POWERED VEHICLES AT WIND TUNNEL WITH ADIABATIC COMPRESSION

**A.M. Kharitonov, V.I. Shyshov, Ju.I. Vyshenkov,
V.I. Zvegintsev, ITAM SB RAS
V.N. Rychkov, M.E. Topchiyan, LIH SB RAS
A.A. Mescherjakov, V.I. Pinakov, DTI HRH SB RAS
Novosibirsk, Russia**

Introduction

The requirements for ground test facilities based on the performance capabilities and goals of advanced hypersonic vehicles are discussed in the number of papers [1-7]. A typical approach looks like that [7]. From the analysis of promising hypersonic air-breathing vehicles flight trajectories, the field of flow parameters required for flight simulation can be defined. Along these trajectories the flow enthalpy values up to 32 MJ/kg might be achieved, which corresponds to stagnation temperature of about $T_0 = 8000$ K or 10000 K and exceeds that of the total air dissociation into atoms takes place. Keeping in mind the fact of strong influence of real gas effects one has arrived at conclusion about the obligatory necessity to reproduce real enthalpy and chemistry of air flow during ground testing. But it is impossible due to two principal reasons. Firstly, because of the enormous energy (hundreds MW) associated with the vehicles and trajectories of interest even at the meter-scale of the models. Secondly, a high stagnation temperature in the settling chamber of the ground facility alters the chemical composition of the working gas. Already at $T_0 = 3000$ K the air contains up to 5% of dissociated oxygen. During the expansion process through the hypersonic nozzle, the gas composition tends to freeze, so the model interacts with a noticeable amount of high-energy active free radicals. From that a pessimistic conclusion can be drawn: hypersonic vehicle ground testing possibilities are limited to Mach numbers of about $M = 8$ [8].

Existing facilities

At present, the consensus regarding the ground testing possibilities appears to be as follows: there are no facilities existing or in development for large-scale propulsion testing above Mach 8 except for very few short-duration facilities [9]. The basic parameters of several hypersonic wind tunnels, most suitable for free-jet propulsion tests are presented in the Table. The greater part of these facilities refers to large-size conventional reflected-shock shock tunnels that were constructed to study real gas effects, mixing and combustion under high-enthalpy conditions. Shock tunnels have been in operation for many years, vast experience of their exploitation has been accumulated and results obtained there have been published. Among them, the LENS (Large Energy National Shock tunnel) is a representative example [11].

© A.M. Kharitonov, V.I. Shyshov, Ju.I. Vyshenkov, V.I. Zvegintsev, V.N. Rychkov,
M.E. Topchiyan, A.A. Mescherjakov, V.I. Pinakov, 1998

Table

Facility	Country	Po, atm	To, K	Dc, mm	M	t, mc	Test gas	Re *10 ⁻⁶ 1/m	Ref.
Longshot	Belgium	4000	2350	360	15-20	5-15	N2	16	[7]
U-11	Russia	2000	2600	800	10-20	500	air	4.5-70	[6]
F-4	France	1000	5500	430-930	6-20	200	air	1.5	[10]
IT-302M	Russia	500	3000	300	5-15	120	air	2	[1]
LENS	USA	1200	5500	1220	6-18	3-18	air	1 - 100	[11]
TH2	Germany	630	4600	586-2000	12	2-9	air	4.5	[7]
U-12	Russia	200	3200	1400	2-10	1-25	air	1-40	[6]
HEG	Germany	1800	10000	800	7-10	1-2	air	1	[12]

The following restrictions are inherent in the shock tunnels: low level of Reynolds number, the working gas contamination with dissociation products due to high stagnation temperature and very short test time duration (typically 1 - 2 ms and up to 18 ms for LENS). These features confine the shock tunnel application area to studies of high temperature surface heating, erosion, ablation, etc.

In Longshot and U-11 a combination of the free heavy piston with a check valve is harnessed for adiabatic compression of test gas [6,7]. By this means the pressure and run duration have been significantly increased. But the problems related to valve design restrict the tunnel simulation possibilities to nitrogen and carbon dioxide as a test gas.

In 1959 R.J.Stalker suggested a 'free heavy piston shock tunnel' concept, that was later taken up all around the world. A typical kind of such facilities is the HEG in Goettingen [12]. These facilities hold the greatest promise for high temperatures up to 10000 K. However, the high temperature reduces considerably the possible Re number level (by 1-2 orders less than necessary) even if the pressure is raised to 2000 atm. Short run duration (1-2 ms) is not sufficient for aerothermodynamic processes stabilization.

The hot-shot wind tunnels represent another type of short-duration facilities for hypersonic testing. An electric discharge is used as the energy source here. One of the modern facilities of this kind is F-4 [10]. Hot-shot tunnels have the P₀ range of also no more than 2000 atm. These facilities offer fairly good chances for hypersonic tests up to M = 11 - 12. Further pressure increase for this type wind tunnels is very difficult because of energy supply limitations and settling chamber strength problems. The main hot-shot wind tunnel drawbacks remain the flow contamination with dissociation products and with the electrode erosion products; the flow temperature inhomogeneity and the flow parameters drop during the test time.

The gap between the necessary flow parameters and those achieved in reality makes the designers and scientists search for new unconventional methods for obtaining a hypersonic gas flow [13].

Our concept

We suggest, first of all, the full-scale Reynolds number reproduction in a way of maximal increasing of the working gas pressure. It is well known that the maximum value of Re at a fixed value of M is achieved under the conditions of the minimum possible static temperature and maximum possible static pressure of the flow. A natural lower limit for

static temperature is the test gas condensation. High flow density allows one to get more complete simulation of supersonic combustion in accordance with binary reaction parameter ($\rho_0 L$) responsible for ignition delay and with triple reaction parameter ($\rho_0^2 L$) determining the rate of the chemical energy release at the scramjet combustor and nozzle.

Gas sources with a complete adiabatic cycle of gas preparation can be used for high pressure facility designing. In particular in SB RAS the long-time experience on high-pressure gas source development is accumulated. The pressure multipliers have been used for the first time in the gasdynamic facility A - 1 there. The pressure value up to 10000 atm with nitrogen as a test gas and 6000 atm with air has been achieved in this unique facility [14].

The pressure multipliers provide high stagnation pressure generation and the running time can be increased by a factor of 10-20 with nearly steady flow parameters during the run time. Relatively low temperature in the settling chamber combined with high pressure allows for complete reproduction of M and Re within the entire range of flight conditions. High purity of the test gas allows for verification of numerical methods and transition to numerical description of combustion process in actual flight conditions if the information on chemical-kinetic properties of the air-fuel mixture is available.

Hypersonic wind tunnel AT-303

These original decisions were used while designing the newly created hypersonic wind tunnel AT-303 at the Institute of Theoretical and Applied Mechanics SB RAS. The facility is based on adiabatic cycle of test gas compression with the help of pressure multipliers and it can ensure very high values of Reynolds number in the hypersonic range of velocities due to high pressure of the test gas in the settling chamber. Wind tunnel AT-303 is dedicated for the study of fundamental and applied problems related to a long-time flight of promising scramjet powered hypersonic vehicles. It will provide scramjet system design data and criteria for airframe-propulsion integration, as well as overall configuration aerodynamic characteristics. The participants of this program are: ITAM, LIH, Design Technology Institute of High-Rate Hydrodynamics (DTI HRH) and TsAGI (Moscow). A sketch of this hypersonic adiabatic compression wind tunnel AT-303 with pressure multipliers is presented in Figure 1.

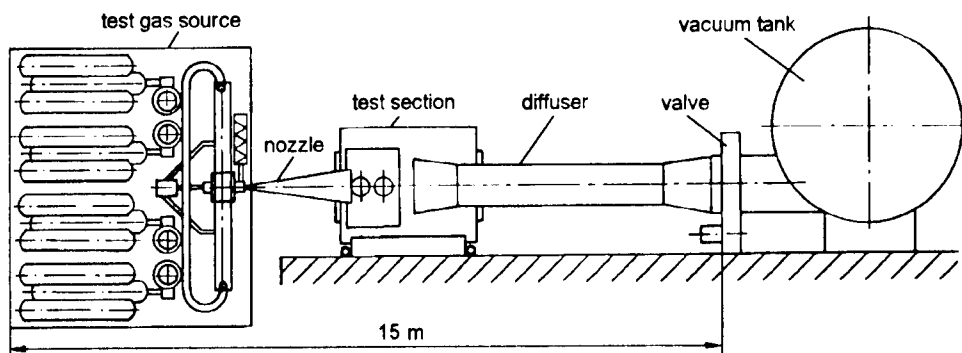


Fig. 1. Sketch of hypersonic wind tunnel AT - 303

The basis of the wind tunnel is the test gas source. The remaining elements of the wind tunnel are typical of hypersonic wind tunnels: conical nozzle with total angle of 16° , test section, exhaust diffuser, large-scale vacuum valve, and vacuum tank.

The principal scheme of the gas source is shown in Figure 2. Prior to the run, the valve in the settling chamber 4 is closed, and the pistons in high pressure section 3 are in a start position. The settling chamber is filled with the test gas through a special electric storage heater 7. At this moment the initial pressure of test gas is no more than 200 bar and the temperature is no more than 1000 K.

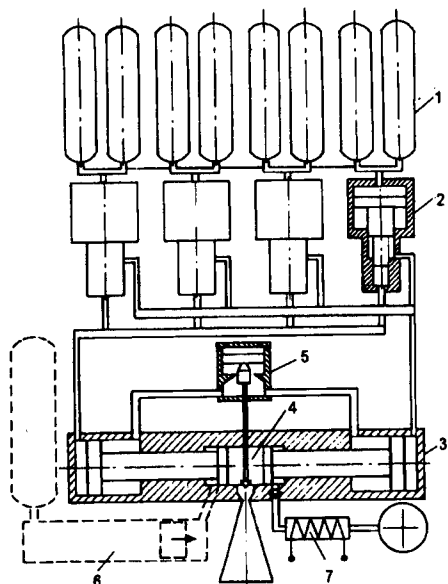


Fig. 2. Principal scheme of the test gas source.

1 - high-pressure barrels; 2 - hydraulic multiplier; 3 - high pressure section; 4 - settling chamber; 5 - control device; 6 - diabolic compression system; 7 - electric storage heater.

To start the wind tunnel, the driver gas with pressure up to 200 atm is supplied from barrels 1 to hydraulic high-pressure multipliers 2, and the pressure within the liquid system increases up to 1400 atm affecting the pistons. The pistons begin to move compressing adiabatically the test gas in the settling chamber up to pressure of 3000 atm with temperature of up to 2500 K. The speed of piston motion is about 5 m/s and it is controlled by liquid flow through the throttling device 5. This device keeps also a constant pressure in the settling chamber during the operation time.

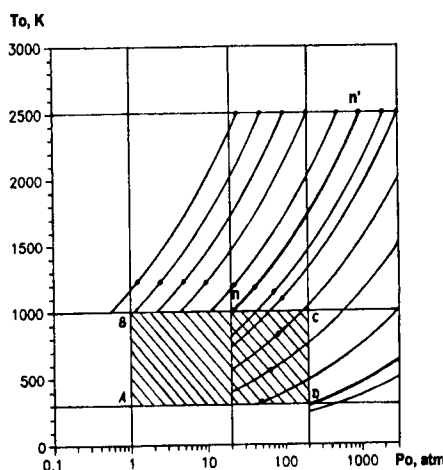


Fig. 3. AT-303 performance map

In Figure 3 the working gas parameters achievable at the first turn of facility are shown in the $P_0 - T_0$ plane. The initial state points lie inside the rectangle ABCD. The line BC represents the boundary of initial temperature (1000 K) achievable with the help of electric heater. The line CD is the maximum of initial pressure (200 atm), which is limited by the heater strength. Note, the initial gas volume between the pistons is of about 6 dm^3 . The relation between the initial and the final conditions in the settling chamber is connected by isentropes since the gas compression cycle is adiabatic.

In Figure 3 the inclined lines nn' represent the isentropes for real air and the gas state is changing along these lines during an adiabatic compression process. The path covered along the isentrope is associated with the final volume of working gas. The volume reduction from 6 to 11 times is required for extreme final parameters ($P_0=3000$ atm, $T_0=2500$ K) generation.

The first turn of this facility with electric storage heater will provide from 1 to 3.6 dm³ of pressurized air, which will be sufficient for run duration of more than 40 ms with the conical nozzle exit diameter 300 and 600 mm when the flow Mach number lies between $M = 7$ and $M = 20$.

The second turn of the facility (named AT-303M) implies the wind tunnel modification, which consists in the first adiabatic precompression stage with free heavy self-wedged pistons installation instead of the electric storage heater, as it is illustrated by the dotted lines in Figure 2. The first stage consists of two gun tubes with inner diameter 200 mm fitted to the second stage pressure multipliers and settling chamber. The total distance covered by each of two self-wedged pistons moving towards each other is about 10 m. The initial settling chamber volume will consist of 15 dm³. The second turn AT-303M will allow to increase stagnation temperature up to 3000 K and to have the settling chamber volume between 8 and 15 dm³. Running time will be increased up to 1 s with the nozzle exit diameter 800 mm.

Technical parameters of new wind tunnel

Nozzle diameter D , mm
Settling chamber volume, dm³
Stagnation pressure P_0 , atm
Stagnation temperature T_0 , K
Mach number M
Reynolds number Re_D
Run duration t , s
Test gases

First turn AT-303

300 – 600
6
3000
2500
7 – 20
 $10^8 - 10^6$
0.04 – 0.5

Second turn AT-303M

300 – 800
8
3000
3000
7 – 20
 $10^8 - 3 \cdot 10^6$
0.05 – 1.0

Air, nitrogen

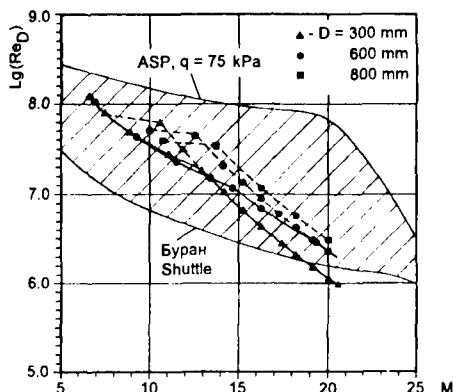
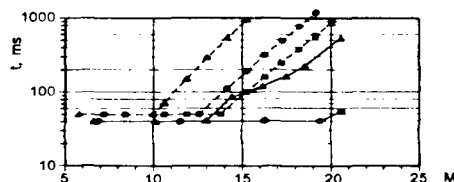


Fig. 4. Achievable Reynolds number range in the new wind tunnel

Fig. 5. Achievable run duration in the new wind tunnel



The range of possible M and Re numbers for such advanced facility is shown in Figure 4. The upper line corresponds to the typical trajectory of scramjet-powered hypersonic vehicle at dynamic pressure $q=75$ kPa, the lower line corresponds to Space Shuttle or Buran reentry trajectory. The solid marked lines characterize the range of Reynolds number and Mach number reproduced in the new wind tunnel AT-303 for the nozzle exit diameter of 300 and 600 mm. The Reynolds number is based on this diameter too. The dashed lines show the same characteristics that will be reproduced in the second turn of the facility AT-303M for the nozzle exit diameter of 300, 600 and 800 mm. In the Figure 5 the expected running time with the same nozzle exit diameters is presented. The running time was calculated in consideration of the boundary layer thickness for the mentioned nozzles.

As it is seen from Figures 4, 5 the wind tunnel AT-303 will ensure full-scale simulation of the Mach and Reynolds numbers of real hypersonic flight with the running time from 40 ms to 1000 ms and more. High purity of the test gas, long test time duration and rather large-scale nozzle in that facility are sufficient for ground testing of scramjet-powered hypersonic vehicles models.

REFERENCES

1. Kharitonov A.M. and Topchian M.E. Wind tunnels for hypersonic study (achievements, problems, outlook). - Novosibirsk: Thermophysics and Aeromechanics. - 1994, Vol.1, No.1. - P. 89-103.
2. Harsha P. and Waldman B. The NASP challenge: testing for validation. - AIAA-89-5005, AIAA 1st National Aero-Space Plane Conf., Dayton, OH, July 20-21, 1989.
3. Scott R.Thomas and R.Wayne Guy. Scramjet testing from Mach 4 to 20, present capability and needs for the nineties. - AIAA-90-1388, AIAA 16th Aerodynamic Ground Testing Conf., Seattle, WA, June 18-20, 1990.
4. Guy de Richemont. Existing and new hypersonic facilities required for HERMES spacecraft testing. - JCAS-90-6.5.1.
5. Chevalier A., Falempin F. Review of new French facilities for PREPHA program. - AIAA-95-6128, AIAA 6th Intern. Aerospace Planes and Hypersonic Technologies Conf., Chattanooga, TN, Apr.3-7, 1995.
6. Anfimov N. TsNIIMash capabilities for aerogasdynamic and thermal testing of hypersonic vehicles. - AIAA-92-3962, AIAA 17th Aerospace Ground Testing Conf., Nashville, TN, July 6-8, 1992.
7. Muvlart J., Spel M., Walpot L., and Cano J.L. European high enthalpy testing capabilities and its use for design // Int. Conf. Methods Aerophys. Research: Proc. Pt 3. - Novosibirsk, 1996. P.227 - 244.
8. Bogdonoff S.M. Hypersonic testing and the Princeton radiatively driven hypersonic wind tunnel // Int. Conf. Methods Aerophys. Research: Proc. Pt 3. Novosibirsk, 1996. P.16 - 26.
9. Smith V.K., Keel L.C., and Boudreau A.H. Ground testing facilities requirements for hypersonic propulsion development. - AIAA-87-1884, AIAA/SAE/ASME/ASME 23rd Joint Propulsion Conf., San Diego, CA, June 29-July 2, 1987.
10. Bugeau A. and Castan E. Hermes first force measurement in ONERA-F4 wind tunnel // Proc. of European Symp. of ESTEC, Noordwijk, Nov.22-25, 1994. - 8 p.
11. Holden M., Kolly J., Chadwick K. Calibration, validation and evaluation studies in the LENS facility. - AIAA 95-0291, 33rd Aerospace Sciences Meeting and Exhibit, Reno, NV, Jan. 9-12, 1995.
12. Eitelberg G. Calibration of the HEG and its use for verification of real gas effects in high enthalpy flows. - AIAA-93-5170, AIAA/DGLR 5th Intern. Aerospace Planes and Hypersonic Technologies Conf., Munich, Germany, Nov.30-Dec.3, 1993.
13. Miles R.B., Brown G.L., Lempert W.P., Yetter R., Williams G.J.Jr., Bogdonoff S.M., Natelson D., Guest J.R. Radiatively driven hypersonic wind tunnel // AIAA J., Vol.33, No.8, Aug.1995. - P.1463-1470.
14. Pinakov V.I., Rychkov V.N., Topchian M.E. Possibilities of hypersonic flow simulation in high-pressure gasdynamic facilities. - Novosibirsk: PMTF (Journal of Applied Mechanics and Technical Physics), No.1, 1981. (in Russian).

DETERMINATION OF THE DYNAMIC CHARACTERISTIC OF AN ASPIRATING PROBE USING A SHOCK TUBE

A.Ya.Konkin, V.A.Lebiga, V.N.Zinoviev
Institute of Theoretical and Applied Mechanics RAS
630090, Novosibirsk, Russia

Introduction

The probes of special design, so-called an aspirating probe, were proposed for measurements of concentration of one gas in a mixture [1]. Problem of calibration, requirements to probe design, peculiarities of application details etc. have been studied before [1...5]. An estimation of dynamic characteristics of an aspirating probe is required when the measurements are carried out in unsteady flows, at scanning at high gradients of the flow parameters for continuous measurements, and when it is necessary to determine fluctuations of concentration.

The problem of experimental determination of the time delay and frequency limit according to the response characteristics of a probe are the subject of the present paper.

Experimental Equipment

The general design of the aspiration probe have been described earlier [1...3]. A sensitive to flow parameters element is placed in a channel jointed to a vacuum pump. There is a sonic nozzle at the outlet of the channel. Therefore the Mach number M at the sensor location is fixed and determined by internal probe's geometry ($M = 0.12$ for the probe used in present study [2, 3]). Thus, the sensor output depends on flow temperature, density etc. A tungsten wire (6 micron in diameter 1.2 mm length) has been used as a sensitive element. It was shown that since the Mach number is constant inside the probe it is necessary to know the voltage e across the wire, total pressure p_0 and total temperature T_0 at the point of flow being investigated to determine the concentration c of gas components: $e = e(c, p_0, T_0)$.

A shock tube ~2 m length and 3 cm in diameter was used for probe calibrations. A stainless steel tank 0.04 m³ has been used to prepare required composition of the air-helium mixture. The concentration has been fixed by partial pressures of the components. The tank was joined to the shock tube and was used as a damping volume.

Dynamic Characteristics of Aspirating Probe

In order to determine the frequency response of an aspirating probe, one should provide controllable disturbances and measure the probe's response on these disturbances. It was described a few methods to get a controlled unsteady flow. In one of them pressure pulsations have been produced by a compressor to determine the frequency characteristic of an aspirating probe with two wires [4]. From frequency spectrum analysis it was concluded that the frequency range of this aspirating probe is up to 19 kHz. A pulsating flow has been provided by rotating disk with holes at another experiments [5]. It was obtained that the frequency range corresponds to the first harmonic and has an order of 1 kHz in this case. Contradictoriness of known data leads to necessity to investigate the aspirating probe frequency responses carefully.

There are three elements tending to lag in the aspirating probe used for the present investigations, namely: wire, internal probe volume, and pressure pipeline, therefore it is necessary to estimate the time lag of each element. Theoretical results on estimation of a time lag of each element are presented in [3]. Probably, the most difficult problem is to determine and reduce the time lag of the aspirating probe itself, because it is possible to avoid the influence of the pressure pipeline by use of a miniature pressure transducers mounted just in the aspirating probe, the anemometer sensor (a wire or a film) has, as a rule, comparatively high frequency range which can be determined easily.

Time lag due to internal probe's volume depends on the relaxation time of parameters inside the probe. To estimate the value of the time lag a technique proposed in [6] has been used. There is an undisturbed flow with free stream conditions at the probe inlet and those corresponding to $M = 1$ at the probe outlet. The flow is assumed one-dimensional, the density is constant over the volume. Equation of continuity for the volume under consideration can be written as:

$$G_{in}(t) - G_*(t) = V \frac{d\rho}{dt}, \quad (1)$$

where V is internal volume of the probe, ρ is density, subscripts (in) and (*) correspond to the probe inlet and the outlet at $M=1$,

$$G = \beta \frac{p_o q(M) S}{\sqrt{T_o}}, \quad \text{where} \quad \beta = \sqrt{\frac{\gamma}{R} \left(\frac{2}{\gamma+1} \right)^{\frac{\gamma+1}{\gamma-1}}},$$

S is the channel cross-section, γ is specific heat ratio, R is the gas constant,

$$q(M) = \left(\frac{\gamma+1}{2} \right)^{\frac{\gamma+1}{2(\gamma-1)}} \frac{M}{\sqrt{1 + \frac{\gamma-1}{2} M^2}} \times \left(1 + \frac{\gamma-1}{2} \frac{M^2}{1 + \frac{\gamma-1}{2} M^2} \right)^{\frac{1}{\gamma-1}}$$

is a function of the Mach number.

Using the equation of state for the perfect gas (assuming that the total temperature is constant over the volume and the heat transfer through the probe walls is negligibly small) Eq.(1) can be transformed into

$$\frac{d}{dt}(p_o)_* + a_* \cdot (p_o)_* = a_{in} \cdot (p_o)_{in}, \quad (2)$$

where

$$a_* = \beta \frac{R \sqrt{T_o} q(1) S}{V} \quad \text{and}$$

$$a_{in} = \beta \frac{R \sqrt{T_o} q(M_{in}) S_{in}}{V}.$$

Equation (2) corresponds to equation of flow parameter relaxation in the internal channel of an aspirating probe. An equation of

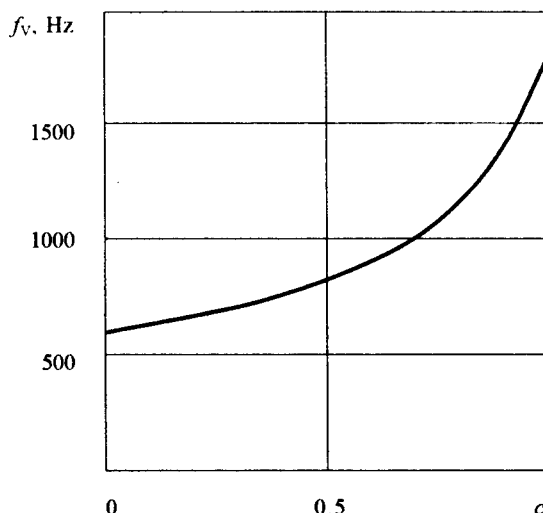


Fig. 1. The dependence of $f_v(c)$ on air-helium mixture concentration

pressure change in the probe channel versus time can be obtained for various disturbance types solving Eq. (2) for different types of the right-hand side. The relaxation time of the flow inside the probe is determined by the value of parameter α , which is of frequency dimension.

Parameter α increases with temperature slowly and has a very strong dependence on concentration c . An example of $f_L(c)$ for air-helium mixture is shown in Fig. 1. Limit frequency f_L due to the internal volume of the probe was calculated as value inversely proportional to α .

It is very important to note that the minimum value of f_L corresponds to zero concentration of helium. Consequently, to determine the dynamic characteristic of an aspirating probe at measurements in flows with variable concentration c it is sufficient to do this only for air.

Determination of the Frequency Response of Aspirating Probe by a Pressure Step

As noted above, in order to obtain the frequency response of an aspirating probe, one should generate controllable disturbances and determine a response of the probe's sensitive element on these disturbances. To do it, experimental scheme shown in Fig. 2 was used. The aspirating probe 1 and the surface wire probe 2, connected to the constant temperature anemometers CTA, were installed at the end of the shock tube 3. A membrane 4 was located at a small distance from the end. The other end of the shock tube was open. An excess pressure was produced in the cavity, and, after destroying the membrane 4, an expansion wave W starts propagating towards the tube end A (see Fig. 2). Its arrival at the end A is detected by the surface probe 2, which triggered a single sweep of an oscilloscope 5, to record a change of the aspirating probe 1 output.

The period of time Δt , which corresponds to the expansion wave refraction from the tube end, depends on the shock tube section length L , see Fig. 2, and the pressure ratio p_2/p_1 . To be sure that time difference Δt is small enough to consider the pressure change as a step one, the value of p_2/p_1 was restricted in present experiments. For air as the pushing gas and $p_2/p_1 = 3$ $\Delta t \approx 0.00023$ ms; for helium as the pushing gas and $p_2/p_1 = 9$ $\Delta t \approx 0.00015$ ms. Thus, the change in pressure at the end of the shock tube can be considered as a step one because the time of this change is much less than the time expected from theoretical estimations for the aspirating probe [3].

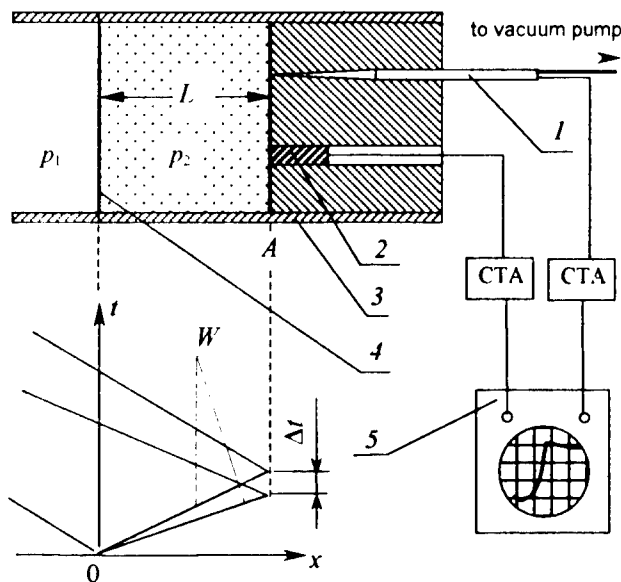


Fig. 2. A scheme illustrating determination of the dynamic characteristic of the aspirating probe, and x vs t diagram for the shock tube

Determination of the Frequency Response of Aspirating by a Contact Surface

To measure fluctuations of the concentration it is necessary to know the aspiration probe frequency response on the controllable concentration changes. That changes can be obtained at a contact surface in a shock tube. The following scheme can be used to determine the frequency response of aspirating probe by a contact surface, Fig. 3.

Inside the shock tube 1 opened at one of its ends, both the surface probe 2 and the aspirating probe 3 were installed. An excess pressure was provided to the left of the membrane 4. After the breakdown of membrane, both the shock S and the contact C surfaces move towards the probes. Arriving to the surface probe the shock triggers a single sweep of the oscilloscope. To make the effects due to the shock and due to the contact surface be distinguishable, the probes were installed at such distance to the membrane that an interval Δt was ensured at least as 1 ms. A damping tank 5 was jointed to the high-pressure part of the shock tube to diminish the effect of the reflected waves W .

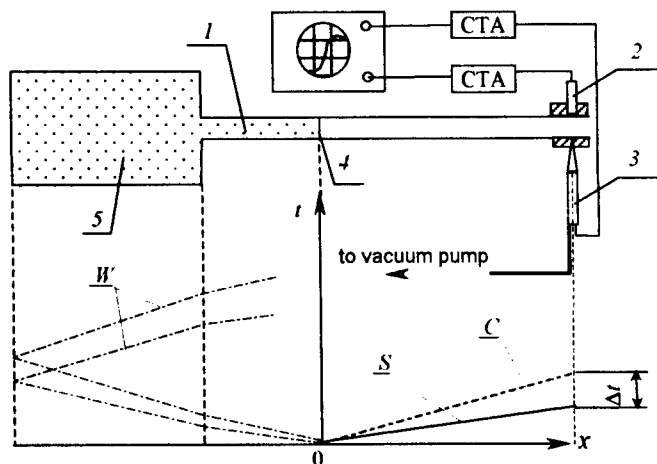


Fig. 3. An experimental scheme for determination of dynamic characteristic of the aspirating probe with a step of concentration

Experimental Results

The frequency response of the probe was determined at different p_2/p_1 ratios for both air and helium as the working gas. The technique described above has been used to obtain dynamic characteristics of aspirating probes both by pressure and by concentration steps. However, it was established that the use of the pressure step gives more explicable and, therefore, more reliable data.

Some examples of results are presented in Fig. 4.

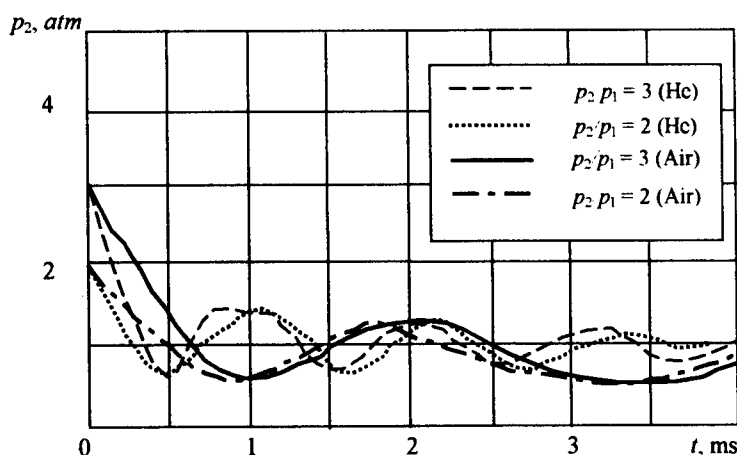


Fig. 4. Dynamic characteristic of the aspirating probe for different p_2/p_1 ratios.

From the results obtained, it follows that, as the expansion wave arrives to the tube end, the pressure in the probe falls down to the atmospheric one, oscillating during 10 - 15 ms. The frequency response of the aspirating probe is determined by the time Δt during which the pressure in probe approaches the atmospheric pressure, see Fig. 4. For air and helium being the pushing gas, the time lag is of order 1 and 0.5 ms respectively, which agree with theoretical estimations of the probe frequency response shown in Fig. 1.

Conclusions

The technique of determining the frequency response of an aspirating probe by the stepwise changing of pressure or concentration has been developed. Different configurations of shock tubes are used in this case.

An aspirating probe has the largest time lag when the concentration of a lighter component tends to zero. Therefore, the limiting time lag of aspirating probe could be estimated only for a heavier gas in the mixture, for example, for air in an air-helium mixture.

Upon using the procedure for the determination of the frequency response of the probe affected by a back pressure step in the form of an expansion wave, the experiments should be performed at the restricted pressure ratios to ensure small enough time difference corresponding to the pressure change.

References

1. W.F.Ng, F.T.Kwok, T.A.Ninnemann. A Concentration Probe for the Study of Mixing in Supersonic Shear Flows. AIAA Pap. 89-2459, 1989, p.6.
2. V.N.Zinoviev, A.Ya.Konkin, V.A.Lebiga. An Application of Aspiration Probe in Supersonic Mixing Flows // Proceedings of ICMAR'94, Part 2, 1994, Novosibirsk, Russia, pp.248-253.
3. A.Ya.Konkin, V.A.Lebiga, V.N.Zinoviev, Determination of an Aspirating Probe Frequency Response // Proceedings of ICMAR'96, Part 2, 1996, Novosibirsk, Russia, pp.108-113.
4. W.F.Ng, A.H.Epstein. High-Frequency Temperature and Pressure Probe for Unsteady Compressible Flows // Rev. Sci. Instrum., Vol. 54, No.12., 1983, pp.1678-1683.
5. Chen Yuhui, Sun Xijiu, Development of Dual Hot-Wire Aspirating Probe, Modern Tech. & Measurements in Fluid Flows // Proceedings of the 2nd ICFDMA - Oct. 19-22, 1994 -China. Intern. Acad. Publish, 1994, Beijing.
6. V.I.Zvegintsev, A.I.Sedel'nikov, Correction of Unsteady Effects at Inlet Testing in Hot Shot Wind Tunnel // Izvestiya Sibirskogo Otdeleniya AN SSSR, Ser. Tekhn. Nauk, Issue No. 15, 1988, Novosibirsk (In Russian).

EXPERIMENTAL STUDY OF MEAN AND PULSATONAL FEATURES IN SUPERSONIC BOUNDARY LAYER ON BLUNTED FLAT PLATE

A.D. Kosinov, N.V. Semionov, A.I. Semisynov, M.B. Bessonov

Institute of Theoretical and Applied Mechanics SB RAS,

630090 Novosibirsk, Russia

INTRODUCTION

Known that the leading edge bluntness leads to formation of an entropy layer above the model and laminar-turbulent transition depends on values of the nose bluntness. Experiments have shown that increasing of the nose bluntness of models stabilize a flow at first, but then can bring destabilization ones [1-3]. However there are not yet sufficient understanding of transition reverse phenomenas in the flow, excepting remarks made in [4]. The influence of small bluntness of leading edge on linear stability of the flat plate boundary layer at Mach number 2 was studied in [5]. It was obtained that amplification rates of three-dimensional controlled disturbances have a nonmonotone dependence versus the bluntness radius. Similar results were obtained by theoretically in [6]. The investigations of linear development of controlled disturbances in the boundary layer of blunted flat plate were presented in [7].

In the paper the experiments are presented at the radius 2.5 mm of leading edge bluntness. Mean flow and nonlinear development of controlled disturbances in the boundary layer of this plate was tested.

EXPERIMENTAL EQUIPMENT

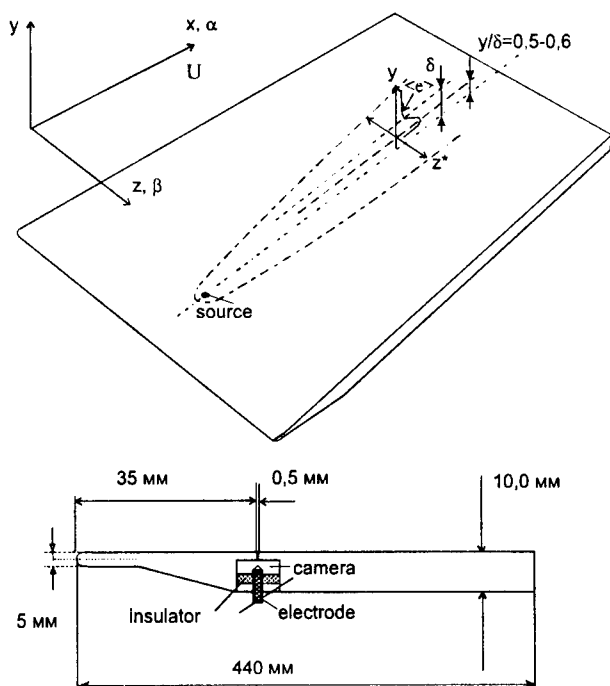


Fig. 1. Scheme of the model

The experiments were performed in the T-325 supersonic wind tunnel of the ITAM of the SB RAS with test section dimensions $200 \times 200 \times 600$ mm. Free stream Mach number was $M=2.0$ and unit Reynolds number was $Re_l = (U/\nu) = (6.4 \pm 0.1) \times 10^6 \text{ m}^{-1}$.

The experimental set-up was the same as in [5, 8]. As the model have been used a flat steel plate of the length 440 mm, width 200 mm and thickness 10 mm. Cylindrical leading edge had the radius 2.5 mm. The model was horizontally mounted in the centre plane of the test section under a zero angle of attack. The local source of controlled disturbances was triggered by the high frequency glow discharge in chamber and was similar to the ones described in [5, 8]. Artificial

disturbances were entered into supersonic flow through an aperture by diameter of 0.5 mm in working surface of the plate. The model is presented in Fig 1. Co-ordinates of the disturbances source were $x=35$ mm downstream from the leading edge and $z=0$ that means the model centre in transversal direction. To measure of mean value and pulsations of flow the hot-wire anemometer have been used. As the hot-wire the tungsten wire by diameter of 5 μ m and 0.76 mm length was used

The probe was moved along three co-ordinates with the help of a traversing gear of an accuracy of 0.1 mm for downstream and spanwise direction (x, z) and of 0.01 mm for normal co-ordinate (y). The hot-wire signal was written in the computer by using of 10-bit 1 MHz A/D converter. To improve the signal to noise ratio we have used a synchronous summation of up to 500 digital oscillograms in the experiments. Length of the each oscillogram was 400 microseconds. To define the frequency-wave spectra of the controlled pulsations the discrete Fourier-transform was used. The technique of the experiments and procedure of data processing was in details described in [8].

RESULTS

Behind the shock wave Mach number was equal $M=1.93\pm 0.2$ in weakly gradient area. Measurements in transversal directions showed that flow is nongradient within the range of ± 25 mm from a symmetry line of the model and 30 mm downstream from the leading edge. It was obtained that dependencies of total and static pressure over normal co-ordinate are close to the constant values. The mean velocity and temperature profiles of shear layer were measured with the help of the hot-wire anemometer in a nongradient area. An example of Mach and temperature profiles are shown in Fig 2. Experimental data were compared with theoretical results obtained by Mr. Guido Dietz from Aachen University (Germany). These data were in a good agreement.

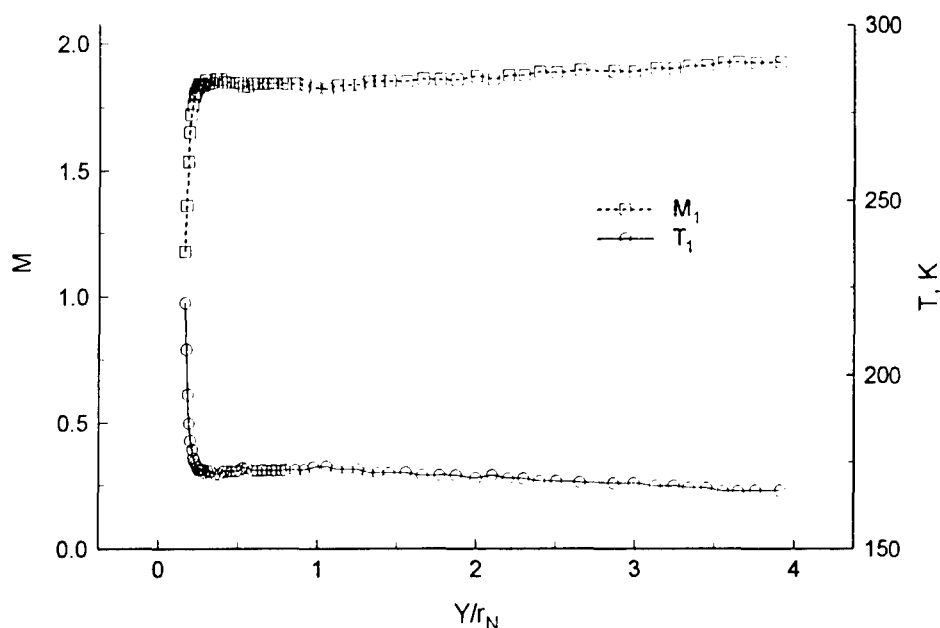


Fig.2. Mach and temperature profiles at $x=35$ mm, $r_s=2.5$ mm

As note in [5] the linear development of disturbances in the supersonic boundary layer of blunted plate is similar to the ones of the plate with the sharp leading edge. However the disturbances amplification in the boundary layer of blunted plate more slowly. Hence an experimental study of wave train development of artificial disturbances in the boundary layer of the blunted plate was carried out in the same way as in [9]. Electric discharge was ignited at a frequency of 2×10^4 sparks per second. Periodic disturbances was excited in the boundary layer. The measurements were carried out at the pulsations maximum in the boundary layer. Oscillograms distributions over x, z was measured. After data processing the amplitude and phase distributions $A_f(x, z)$ and $\Phi_f(x, z)$ of controlled disturbances were obtained for several sections $x = \text{const}$ from $x = 60$ mm up to $x = 130$ mm. Using discrete Fourier-transformation the wave spectra over β for the mentioned above sections were defined.

The nonlinearity actually began from $x > 100$ mm at this initial amplitude of disturbances. As an example the amplitude β -spectra of the fundamental and subharmonic waves are shown in Fig.3 and 4 at $x = 120$ and $x = 130$ mm respectively. The subharmonic amplitude β -spectra are different to observed ones at $x = 70$ mm for linear evolution of wave train. There are many peaks in the amplitude β -spectra. Consider five of them as it was made in [9]. The maximum at $\beta = 0$ and four maxima at $\beta = \pm(0.5-0.6)$ rad/mm and $\beta = \pm(1.3-1.5)$ rad/mm. How follows from this data, the fundamental and subharmonic disturbances have amplitude-wave spectra, similar to the ones for the case of the plate with sharp leading edge [9]. If maxima at $\beta = \pm(0.5-0.6)$ rad/mm are usual to the eigen waves of the supersonic boundary layer at $f = 10$ kHz, then the appearance of increasing waves with wave number $\beta > 1$ rad/mm is connected with the subharmonic resonance. The maximum at $\beta = 0$ is possibly related with the sound radiation of the supersonic boundary layer.

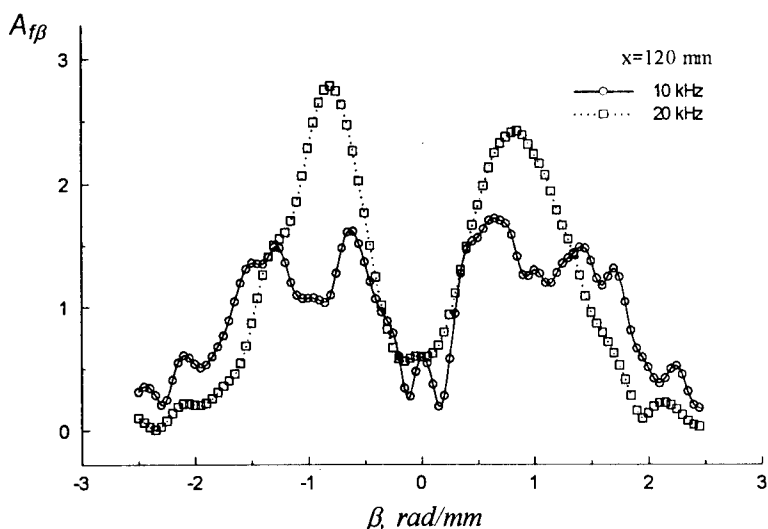


Fig.3. Amplitude β - spectra of controlled disturbances

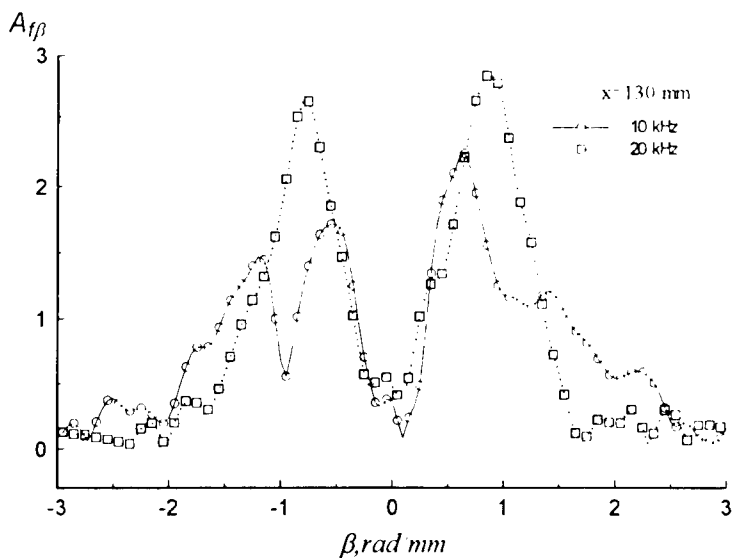


Fig.4. Amplitude β - spectra of controlled disturbances

Dependencies of longitudinal wave number $\alpha_r(\beta)$ over transversal wave number β for fundamental and subharmonic waves are presented in Fig. 5.

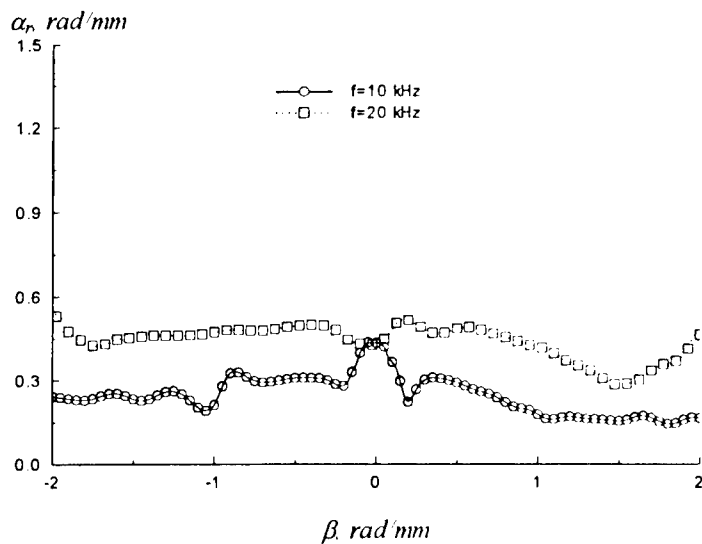


Fig.5. Dispersion dependencies

Estimations of $\alpha_r(\beta)$ were made for the verification of implementation of subharmonic resonance conditions:

$$\begin{aligned}\omega_1 &= \omega_2 + \omega_3, \\ \alpha_{r1} &= \alpha_{r2} + \alpha_{r3}, \\ \beta_1 &= \beta_2 + \beta_3.\end{aligned}$$

This conditions are realised for asymmetrical wave triplets selected on maxima in amplitude β -spectra. Results of this check for pair of asymmetrical wave triplets are presented in tables 1, 2 and in the manner of the vector diagram in Fig.6 for the data shown in Fig.3 and 4. Therefore the process of the subharmonic resonance take place on the blunted plate too

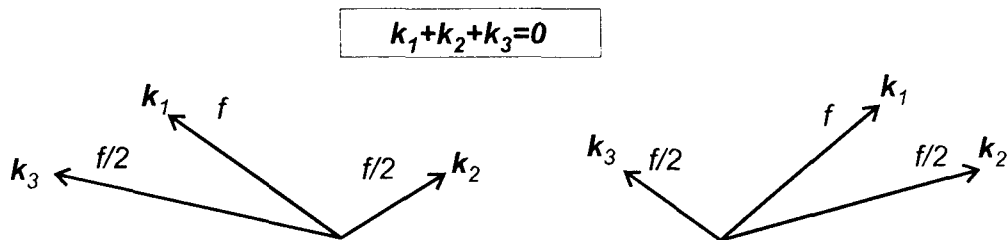


Fig.6 View of asymmetrical wave triplets

Table 1

n	f , kHz	β , rad/mm	α_r , rad/mm	χ , degrees
1	20	-0.8	0.49	-58.5°
2	10	-1.5	0.23	-81.3°
3	10	0.7	0.25	70.3°

Table 2

n	f , kHz	β , rad/mm	α_r , rad/mm	χ , degrees
1	20	0.9	0.44	64°
2	10	1.5	0.17	83.5°
3	10	-0.6	0.28	-65°

Any distinctions of the case of the blunted plate and the case of the sharp leading edge plate are obtained. About ten percent reduction of the phase velocities for the blunted plate was observed that is similar to [7].

CONCLUSIONS

The experiments on the wave train nonlinear development in the boundary layer of the blunted plate was carried out for the first time. It was obtained that the subharmonic resonance take place on the blunted plate. It was shown that the process is the similar as for the plate with sharp leading edge, but parametric amplification of disturbances is slowly. Wave triads are asymmetrical like [9]. The measurements of mean flow profiles using constant temperature anemometers have shown a correspondence of the data with one presented in [7].

ACKNOWLEDGMENT

This research has been supported by Russian Fundamental Research Foundation grant No 96-01-01881.

REFERENCES

1. Struminskiy V.V., Kharitonov A.M., Chernykh V.V. Experimental investigation of laminar-turbulent transition of boundary layer at supersonic speeds// Izv. Akad. Sci. USSR. Zh. Mech. Zhid. G. 1972. - V.3. - P.30-34 (in Russian).
2. Muir J.F., Trujillo A.A. Experimental investigation of the effect of nose bluntness, free-stream unit Reynolds number, and angle of attack on cone boundary layer transition at a Mach number of 6// AIAA Paper 72-216, 1972.
3. Stetson K.F. Effect of bluntness and angle of attack on boundary layer transition on a cone and biconic configuration// AIAA Paper 79-0269, 1979.
4. Khan M.M.S., Reshotko E. Stability of the laminar boundary layer a blunted plate in supersonic flows// FTAS TR-79-142, 1979.
5. Kosinov A.D., Maslov A.A., Shevelkov S.G. Experiments on the stability of supersonic laminar boundary layers// J. Fluid Mech. - 1990. - V.219. - P.621-633.
6. Malik M.R., Spall R.E., Chang C.L. Effect of nose bluntness on boundary layer stability and transition// AIAA Paper 90-0112, 1990.
7. Kosinov A.D., Semionov N.V., Shevelkov S.G. Special features of generation and development of a harmonical wave in supersonic boundary layer// Recent Advances in Experimental Fluid Mechanics. - Beijing: International Academic Publishers. 1992. P.53-58.
8. Kosinov A.D., Semionov N.V., Shevelkov S.G. Investigation of supersonic boundary layer stability and transition using controlled disturbances// Int. Conf. on the Methods of Aerophys. Research. Proc. Pt.2. - Novosibirsk, 1991. P.159-166.
9. Kosinov A.D., Semionov N.V., Shevellov S.G., Zinin O.I. Experiments on the nonlinear instability of supersonic boundary layers// Nonlinear Nonparallel Flows. - Potsdam, N.Y., Springer-Verlag. 1994. P.196-205.

A NUMERICAL METHOD FOR SIMULATION OF UNSTEADY PHENOMENA IN HIGH SPEED SHEAR FLOWS

A.N.Kudryavtsev and D.V.Khotyanovsky

Institute of Theoretical and Applied Mechanics SB RAS,
Novosibirsk 630090, Russia

INTRODUCTION

The numerical simulation of the transition to turbulence in high-speed shear flows is a problem which is a great challenge to modern computational fluid dynamics. The computations of the development of instability waves in real supersonic flows require using numerical techniques which are of high accuracy for smoothly varying, wavelike solutions and capable of capturing shock waves without oscillations and other numerical artifacts. The objective of our paper is an assessment of the recently proposed weighted essentially non-oscillatory (WENO) schemes as a numerical tool for similar problems.

We simulate a spatial development of both subsonic and supersonic instabilities in a free shear layer formed by mixing of two parallel supersonic streams. In addition, we give examples of shear layer instability in more complex situations which include the interaction of instability waves with an impinging shock wave, and the initial stages of evolution of underexpanded supersonic plane jet exhausting into the co-flowing stream.

NUMERICAL TECHNIQUES

We solve numerically two-dimensional compressible Navier-Stokes equations

$$\frac{\partial Q}{\partial t} + \frac{\partial F}{\partial x} + \frac{\partial G}{\partial y} - \frac{1}{Re} \left(\frac{\partial R}{\partial x} + \frac{\partial S}{\partial y} \right) = 0$$
$$Q = \begin{pmatrix} \rho \\ \rho u \\ \rho v \\ e \end{pmatrix}, F = \begin{pmatrix} \rho u \\ \rho u^2 + p \\ \rho uv \\ (e + p)u \end{pmatrix}, G = \begin{pmatrix} \rho v \\ \rho uv \\ \rho v^2 + p \\ (e + p)v \end{pmatrix}, R = \begin{pmatrix} 0 \\ \tau_{xx} \\ \tau_{xy} \\ r_4 \end{pmatrix}, S = \begin{pmatrix} 0 \\ \tau_{xy} \\ \tau_{yy} \\ s_4 \end{pmatrix}$$

Here ρ is the density, E is the total energy per unit mass, u and v are the velocity components in the x and y directions, respectively. The constitutive equation for the pressure p is given by

$$p = (\gamma - 1) \left(E - \rho \frac{u^2 + v^2}{2} \right)$$

where γ is the adiabatic gas constant, $\gamma = 1.4$.

Assuming the Stokes hypothesis, the viscous terms can be written as

©A.N.Kudryavtsev, D.V.Khotyanovsky, 1998

$$\tau_{xx} = \frac{2}{3}\mu \left(2\frac{\partial u}{\partial x} - \frac{\partial v}{\partial y} \right), \quad \tau_{xy} = \mu \left(\frac{\partial u}{\partial y} + \frac{\partial v}{\partial x} \right), \quad \tau_{yy} = \frac{2}{3}\mu \left(2\frac{\partial v}{\partial y} - \frac{\partial u}{\partial x} \right)$$

$$r_4 = u\tau_{xx} + v\tau_{xy} + \frac{\mu}{(\gamma-1)\text{Pr}} \frac{\partial c^2}{\partial x}, \quad s_4 = u\tau_{xy} + v\tau_{yy} + \frac{\mu}{(\gamma-1)\text{Pr}} \frac{\partial c^2}{\partial y}$$

Here c is the speed of sound, $\text{Pr} = 0.72$ is the Prandtl number, and μ is the viscosity which is assumed to be a linear function of temperature.

The approximation of inviscid terms is the most important part of any numerical scheme for the compressible Navier-Stokes equations. The central difference and spectral approximations suffer from non-physical oscillations near flow discontinuities. The upwind total variation diminishing (TVD) schemes provide robust capturing of shock waves and other discontinuities, but they necessarily reduce the accuracy to the first order near smooth extrema. Another class of upwind schemes which is more attractive to simulate the transition and turbulence in high-speed flows is the ENO (essentially non-oscillatory) [1], [2] and weighted ENO schemes [3], [4]. The ENO schemes use an adaptive "smoothest" substencil chosen within a larger, fixed stencil to construct high-order approximation of the solution avoiding the interpolation across discontinuities and preserving uniformly high order of accuracy at all points where the solution is smooth. The main idea of the WENO schemes is to use a superposition of several substencils with adaptive coefficients to increase the order of approximation even more.

In this paper we adopt the finite-difference, flux-based, fifth order WENO scheme [4]. We use Roe splitting when calculating the numerical fluxes at cell interfaces. In Fig.1 we give comparison of dispersion and dissipation properties of first derivatives approximations obtained with various schemes.

The diffusive terms of the Navier-Stokes equations are approximated with the central difference formulas of 4-th order, for instance

$$\left(\frac{\partial \mathbf{R}}{\partial x} \right)_{ij} = \frac{\mathbf{R}_{i-2,j} - 8\mathbf{R}_{i-1,j} + 8\mathbf{R}_{i+1,j} - \mathbf{R}_{i+2,j}}{12\Delta x}$$

The components of \mathbf{R} contain the derivatives like $\partial u/\partial x$ and $\partial u/\partial y$. For calculating $\partial u/\partial y$, we use a central difference formula. If the same purely central differencing is used for calculating $\partial u/\partial x$, it leads to a very wide, 9-point along x , stencil for viscous terms. The Fourier analysis (assuming a constant μ) reveals that the corresponding formula for the second derivative has unsatisfactory dissipative properties for large wavenumbers α (Fig.2). The dissipation vanishes as α approaches its maximum value $\pi/\Delta x$ which can be represented on the grid. Therefore, we use another way. The x -derivatives with different subscripts are approximated by differently biased 5-point formulas of 4-th order whose leftmost point is always $i-2$:

$$\begin{aligned} (\partial u/\partial x)_{i-2} &= (-25u_{i-2} + 48u_{i-1} - 36u_i + 16u_{i+1} - 3u_{i+2})/12\Delta x \\ (\partial u/\partial x)_{i-1} &= (-3u_{i-2} - 10u_{i-1} + 18u_i - 6u_{i+1} + u_{i+2})/12\Delta x \\ (\partial u/\partial x)_i &= (u_{i-2} - 8u_{i-1} + 8u_{i+1} - u_{i+2})/12\Delta x \\ (\partial u/\partial x)_{i+1} &= (-u_{i-2} + 6u_{i-1} - 18u_i + 10u_{i+1} + 3u_{i+2})/12\Delta x \\ (\partial u/\partial x)_{i+2} &= (3u_{i-2} - 16u_{i-1} + 36u_i - 48u_{i+1} + 25u_{i+2})/12\Delta x \end{aligned}$$

Here we omit the subscript j . Applying these formulas gives a compact, 5-point approximation which at a constant μ coincides with the standard, 4-th order expression for the second derivative. Though our approach is more expensive, the total computation time increases only slightly since a great bulk of time is spent when calculating the convective terms.

Time stepping is performed by the explicit, Runge-Kutta-Gill scheme of fourth order because of its high-order accuracy and low storage requirements. For investigated high-Reynolds-number flows the time increment is mainly restricted by the inviscid CFL condition. The CFL number used in all our computations was of the order of $0.7 \div 0.8$.

EXAMPLES OF NUMERICAL SIMULATIONS

To justify our numerical method, we obtained the Navier-Stokes solution for the profile of the shock wave and compared it with the analytical solution (Fig.3). This problem does not have any essential spatial scale, therefore the only characteristic scale is the computational cell size. It is evident, that even in the case of relatively high cell Reynolds number $Re = 10$, our method robustly resolve the shock wave without oscillations.

The results of Euler computations for the acoustic wave propagating in a channel are given in Fig.4. Acoustic disturbance is imposed at the inflow on the uniform supersonic stream in such a way that we have a stationary wave confined by the channel walls in normal direction, and travelling wave in streamwise direction. The amplitude of the wave was set small enough $A = 0.01$ to discard nonlinear effects. It is clear that the sine wave advects in space without any distortions although the space resolution is not so high.

The simulations of spatial development of a compressible shear layer formed by mixing of two parallel streams with Mach numbers M_1 and M_2 are conducted in a rectangular computational domain. The flow at the inflow boundary is supersonic, and the most unstable linear wave and its subharmonic with the amplitudes $A_1 = 0.1$, $A_{1/2} = 0.01$ are introduced here as a forcing. The non-reflecting boundary conditions [5] are imposed on the outflow and far-field boundaries. The Reynolds number Re based on the velocity of faster stream and the vorticity thickness of the shear layer $\delta_\omega = (U_1 - U_2)/(dU/dy)_{\max}$ at the inflow boundary is equal to 1000. U_1, U_2 denote here the streamwise velocities of the faster and slower streams respectively. The number of grid points used is 800×150 . The grid was stretched in normal direction to enhance resolution near the center of shear layer.

The typical flowfields are presented in Fig.5 and Fig.6 for two different values of the convective Mach number, $M_c = 0.5$ and $M_c = 1.5$. The convective Mach number M_c defined as $M_c = (U_1 - U_2)/(c_1 + c_2)$, where c_1, c_2 are the speeds of sound in the corresponding streams, is the most appropriate parameter to characterize the compressibility effects.

It is evident that the flow patterns are completely different in the subsonic and supersonic cases. At the subsonic convective Mach number (Fig.5), the Kelvin-Helmholtz instability produces roll-up of the shear layer into large-scale vortex structures. Farther downstream, the pairing of vortices takes place. When M_c is supersonic (Fig.6) the development of supersonic (acoustic) instability results in the emergence of oblique

shock waves in the free streams. We could not see the merging of large scale structures in the case of $M_c = 1.5$ up to the outflow boundary of the computational domain.

The interaction of the shock wave with the shear layer has been proposed in [6] as a mechanism for enhancing the mixing at high speeds. It has been investigated in some experimental works, for instance, in recent paper [7]. The shock with an angle of 22° impinges on the shear layer between two streams with $M_1 = 3$ (the upper one) and $M_2 = 2$ (the lower one). The shear layer at the inflow is forced by the most unstable wave with the amplitude $A_1 = 0.01$. The computed Euler flowfield is shown in Fig.7. As a result of the interaction, the shock wave refracts and the shear layer deflects. The vortex intensity seems slightly increasing behind the shock wave.

We also performed the simulations of the underexpanded plane jet exhausting into coflowing stream. The pressure mismatch at the inflow was $P_{jet}/P_\infty = 1.1$. Although we have undisturbed inflow in this case, multiple shock wave and expansion fan interactions with the jet shear layers appear to be the source of the disturbances which lead to the formation of the vortices similar to Kelvin-Helmholtz ones (Fig.8).

CONCLUSIONS

The high-order WENO schemes have been successfully used to investigate the development of compressible shear layers in various situations. They seem capable of capturing strong shock waves and reproducing accurately the behaviour of smooth portion of the solution. The Navier-Stokes and Euler computations have been performed to simulate both subsonic and supersonic instabilities of a spatially developing shear layer, the impingement of the shock wave on the shear layer, and the underexpanded jet exhausting into the co-flowing stream.

ACKNOWLEDGEMENT

This work was supported by the Russian Foundation for Basic Research (RFBR) under the grant No. 98-01-00723.

REFERENCES

1. Harten A., Engquist B., Osher S., Chakravarthy S. Uniformly high order essentially non-oscillatory schemes, III // J. Comput. Phys. - 1987. - Vol.71. - P.231-301.
2. Shu C.-W., Osher S. Efficient implementation of essentially non-oscillatory shock capturing schemes // J. Comput. Phys. - 1989. - Vol.83. - P.32-78.
3. Liu X.-D., Osher S., Chan T. Weighted essentially non-oscillatory schemes // J. Comput. Phys. - 1994. - Vol.115. - P.200-212.
4. Jiang G., Shu C.-W. (1996) Efficient implementation of weighted ENO schemes // J. Comput. Phys. - 1996. - Vol.126. - P.202-228.
5. Thompson K.W. Time-Dependent Boundary Conditions for Hyperbolic Systems // J. Comput. Phys. - 1987. - Vol.68. - No.1. - P.1-24.
6. Kumar A.S., Bushnell D.M., Hussaini M.Y. A mixing augmentation technique for hypervelocity scramjets. - AIAA Paper 87-1882, 1987.
7. Ramaswamy M., Loth E., Dutton J.G. Free shear layer interaction with an expansion-compression wave pair // AIAA Journal. - 1996. - Vol.34. - P.565-571.

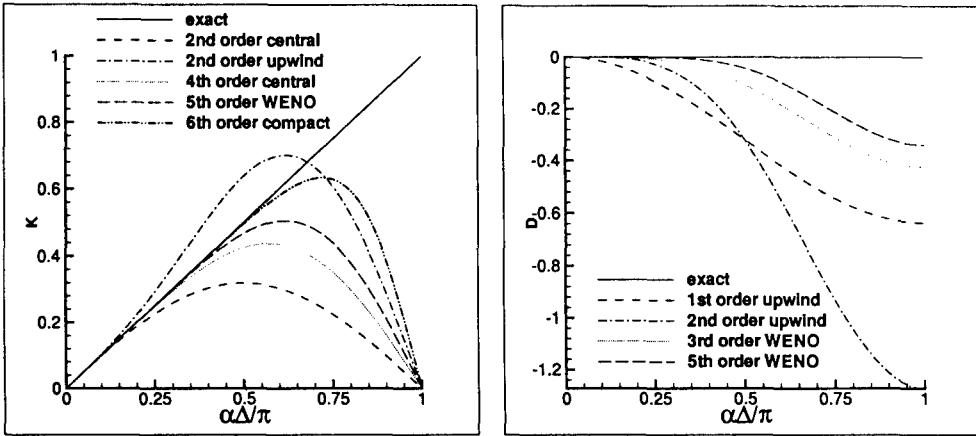


Fig.1. Dispersion (left) and dissipation (right) properties of first derivatives approximations.

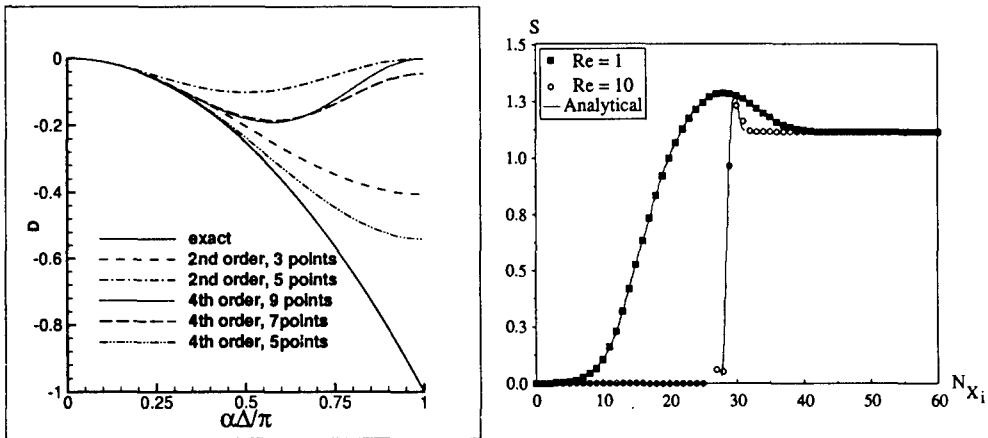


Fig.2. Dissipation properties of second derivatives approximations

Fig.3. Entropy profiles of the shock wave for two cell Reynolds numbers compared with analytical solution.

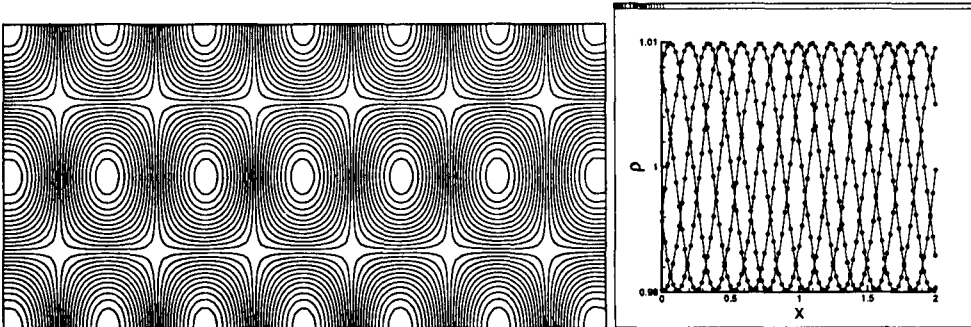


Fig.4. Acoustic wave in a channel. Density contours snapshot and density distribution along the centerline at different times.



Fig.5. Vorticity contours at $M_1 = 2.5$, $M_2 = 1.5$, $Re = 1000$.

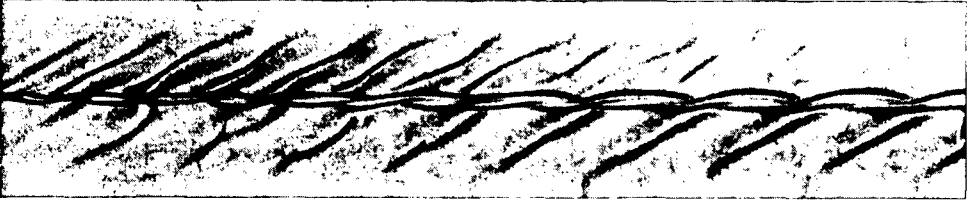


Fig.6. Density gradient flowfield at $M_1 = 1.5$, $M_2 = 1.5$, $Re = 1000$.



Fig.7. Interaction of the shear layer with the shock wave. Density gradient.

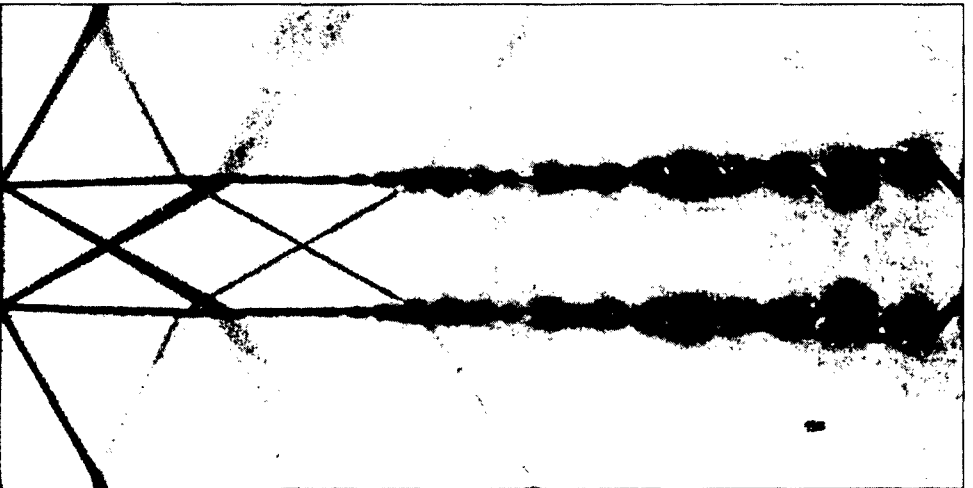


Fig.8. Underexpanded plane jet. Density gradient.

NONLINEAR EVOLUTION OF SHEAR LAYER DISTURBANCES IN A SUPERSONIC PLANE JET

A.N.Kudryavtsev and D.V.Khotyanovsky

Institute of Theoretical and Applied Mechanics SB RAS,
Novosibirsk 630090, Russia

INTRODUCTION

Numerical simulation of the nonlinear evolution of the unstable disturbances in a plane supersonic jet exhausting into the co-flowing stream has been carried out. This kind of flow is of interest due to its practical importance in such problems of jet propulsion as mixing, supersonic combustion, and jet noise generation.

Linear stability analysis reveals multiple-mode character of the jet instability. Linear stability studies of an incompressible jet [1] show the existence of two instability modes in case of a plane jet, one of those has symmetrical normal velocity eigenfunction, which we will refer to as a sinuous mode, and another is antisymmetrical one (varicose mode).

It is well known that the compressibility greatly influences the stability properties of the jet flow. The top-hat jet analysis using the vortex sheet model of the jet shear layers [2] reveals a number of unstable modes in supersonic case, which is made possible by the transfer of energy across the jet by sound waves.

In this study we are primarily concerned with nonlinear stages of the jet instability at subsonic as well as supersonic relative speeds. Weighted essentially non-oscillatory scheme of the fifth order [3] was applied for the discretization of the Navier-Stokes equations convective terms. Results of computations show essentially distinct patterns of the jet instability in subsonic and supersonic cases, and for different instability modes.

NUMERICAL PROCEDURE

To simulate spatial evolution of the instability waves in supersonic plane jet we solve numerically two-dimensional Navier-Stokes equations of compressible gas. The viscosity is assumed to be linearly proportional to temperature. The Prandtl number is unity.

For the spatial discretization of convective terms of Navier-Stokes equations weighted essentially non-oscillatory (WENO) scheme of the 5th order [3] is used. This scheme represents a new generation of high-order shock-capturing schemes providing high accuracy at smooth solutions, which is necessary when modelling wave processes, and capture shock waves inherent in high-speed flows without oscillations. Unlike more common total variation diminishing (TVD) schemes, ENO schemes do not reduce the order of accuracy at local extrema of the solution.

©A.N.Kudryavtsev, D.V.Khotyanovsky, 1998

In this paper we use Roe splitting technique when computing numerical fluxes at cell interfaces.

Diffusive terms in Navier-Stokes equations were approximated with the central differences of the 4th order.

Time integration was made with low-storage Runge-Kutta-Gill scheme of the fourth order. For investigated high-Reynolds-number flows the time increment is mainly restricted by the inviscid CFL condition. The CFL number used in all our computations was of the order of $0.7 \div 0.8$.

All calculations were performed in the rectangular computation domain. The size of the domain was typically 50×10 jet widths. Number of grid nodes used was 800×160 . The grid was uniform in streamwise direction, and stretched along the normal coordinate according to algebraic mapping in order to enhance resolution in the jet shear layers.

At the top and bottom boundaries, and at the outflow we impose non-reflecting characteristic boundary conditions [4] to prevent undesired reflections which could affect the flow. The inflow conditions were imposed in the following way. At the first stage of the computations we have at the inflow co-flowing supersonic top-hat jet and the ambient supersonic stream of smaller velocity. The pressures in the jet and in the ambient streams are equal. The computed Navier-Stokes stationary profiles of streamwise velocity and temperature in some downstream location were then used in the linear stability analysis. The computed linear stability eigenfunctions were imposed on the stationary mean flow as the inflow forcing.

RESULTS

We consider here two cases with different relative velocities of the jet and the ambient stream. We will characterize the influence of the compressibility on the stability characteristics by so-called convective Mach number:

$$M_c = \frac{U_{\text{jet}} - U_{\text{ambient}}}{a_{\text{jet}} + a_{\text{ambient}}}$$

where $U_{\text{jet}}, U_{\text{ambient}}$ are streamwise velocities, $a_{\text{jet}}, a_{\text{ambient}}$ are speeds of sound in the corresponding stream.

First case corresponds to subsonic relative speeds, and the Mach numbers of the jet and the ambient stream are $M_{\text{jet}} = 2.5$, $M_{\text{ambient}} = 1.5$. Temperatures of the jet and the ambient stream were chosen to be equal, and the convective Mach number determined across the jet shear layer is in this case $M_c = 0.5$.

In the second considered case we increase the velocity difference between the jet and the ambient stream. The corresponding Mach numbers are $M_{\text{jet}} = 4.5$, $M_{\text{ambient}} = 1.5$, and the convective Mach number is $M_c = 1.5$. Reynolds number based on the width of the jet and the velocity difference is $Re = 5000$ in our computations.

The computed steady basic flow profiles of streamwise velocity and temperature at $x = 10$ are given in Fig.1 for two considered convective Mach numbers. Normal velocity eigenfunctions for two instability modes obtained by linear stability analysis in subsonic case are shown in Fig.2. Linear stability eigenfunctions of the most unstable sinuous and varicose modes in supersonic case are given in Fig.3. In comparison with the

subsonic eigenfunctions which quickly vanish outside the jet shear layer the supersonic ones oscillate either in the ambient stream or in the jet. It is associated with the Mach wave emission from the jet shear layers in the latter supersonic case.

The obtained linear stability eigenfunctions were used as the inflow forcing in Navier-Stokes computations. Usually we impose at the inflow the most unstable linear wave with the amplitude $A_1 = 0.1$, and its subharmonic with the amplitude $A_{1/2} = 0.01$.

The results of computations for subsonic sinuous mode are shown in Fig.4. In early stages of the evolution the instability waves in two shear layers develop independently and are quite similar to the well-known Kelvin-Helmholtz vortices. Farther downstream the neighboring vortices in each shear layer start merging and gradually expand over the whole jet width. Beyond this point the instability structures in two shear layers are no longer independent and interact in a complex way.

Flow visualizations in case of higher Mach number of the jet (Fig.5, 6) show the essentially different instability evolution. Vortical structures in the shear layer are very slender and flattened. In case of supersonic sinuous mode (Fig.5) Mach waves are emitted by the jet into the ambient stream. The appearance of the Mach waves is not something unexpected and was observed experimentally [5]. Farther downstream these Mach waves transform into weak inclined shock waves. As the instability grows, the shock waves and expansions appear in the jet core, and the jet breaks up.

On the contrary, the varicose instability mode (Fig.6) seems to remain confined in the jet core up to the outflow. The flow evolves as a sequence of complex periodic patterns containing shock and expansions. These patterns are somewhat similar to steady cell structure typical for non-isobaric jets. This is not surprising because the pressure in the jet core at the inflow is changing in time due to the forcing, and this could correspond to the situation when the jet becomes locally overexpanded or underexpanded at different moments. Of course, in our simulations we have travelling waves, not steady state structure.

In Fig.7 we gave a comparison of the variation of kinetic energy of a harmonic with downstream distance obtained by linear stability analysis and Navier-Stokes computations with small inflow amplitude.

Kinetic energies of harmonics are determined as follows:

$$E_k = \int |(\sqrt{\rho}u)_k|^2 + |(\sqrt{\rho}v)_k|^2 dy$$

where $q_k(x, y)$ denotes k-th coefficient in Fourier expansion of $q(x, y, t)$.

Linear stability analysis was made in some downstream locations in locally parallel assumption using computed Navier-Stokes profiles. This approach enables us to take into consideration the spreading of the jet shear layers. Linear growth rate is connected with the kinetic energy of a harmonic as

$$-(\alpha_k)_i = \frac{1}{2E_k} \frac{dE_k}{dx}$$

where $(\alpha_k)_i$ denotes the imaginary part of the wavenumber of the k-th harmonic obtained by linear stability analysis.

This comparison was made only for the subsonic instability of both modes. It is clear that the disturbance of the given frequency becomes less unstable downstream due to the spreading of the shear layers, and in some downstream location ($x \approx 11$ for varicose, and $x \approx 19$ for sinuous), where the energy stops growing, becomes neutral. At the same time, as it is expected, the frequency of the most unstable wave moves to the lower values.

The growth of the energy of small amplitude disturbance in Navier-Stokes computations is close to its linear stability values, but it is slightly lower because of the viscosity influence on the disturbances, which is not taken into account in our inviscid linear stability analysis.

CONCLUSIONS

Numerical simulation of the nonlinear evolution of the instabilities in a plane supersonic jet has been performed. WENO scheme of the 5th order was applied for the numerical solution of Navier-Stokes equations. In order to trigger the instability in the jet shear layers, the inflow forcing based on linear stability eigenfunctions was applied.

The results of Navier-Stokes computations demonstrate the essential difference between the flow patterns for two considered Mach numbers of the jet and for the different modes of instability.

When the velocity difference between the jet and the ambient stream is high enough, i.e. at supersonic convective Mach numbers, the instability evolution incorporates the emission of the Mach waves, formation of weak shock waves in the ambient stream in case of sinuous mode, and the occurrence of periodic cell structure in the jet core in case of varicose mode. Sinuous mode of the instability seems to be mainly responsible for the break-up of the jet.

ACKNOWLEDGEMENT

This work was supported by the Russian Foundation for Basic Research (RFBR) under the grant No. 98-01-00723.

REFERENCES

1. Betchov R, Criminale Jr. W.O. Spatial instability of the inviscid jet and wake // *Phys. Fluids*. - 1966. - Vol.9. - No.2. - P.359-362.
2. Gill A.E. Instabilities of "Top-Hat" jets and wakes in compressible fluid // *Phys. Fluids*. - 1965. - Vol.8. - No.8. - P.1428-1430.
3. Jiang G., Shu C.-W. Efficient implementation of weighted ENO schemes // *J. Comput. Phys.* - 1996. - Vol.126. - P.202-228.
4. Thompson K.W. Time-Dependent Boundary Conditions for Hyperbolic Systems // *J. Comput. Phys.* - 1987. - Vol.68. - No.1. - P.1-24.
5. Goldstein M.E. *Aeroacoustics*. - McGraw-Hill, 1976.

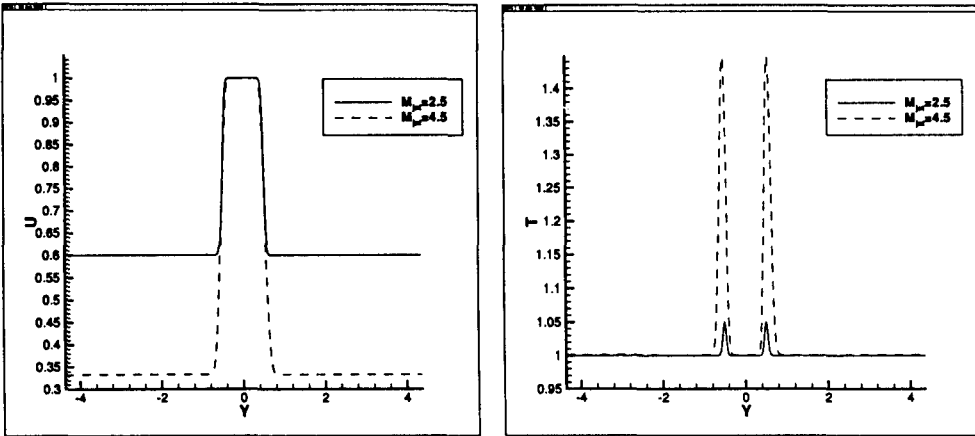


Fig.1. Profiles of streamwise velocity (left) and temperature (right) of the steady basic flow for two convective Mach numbers.

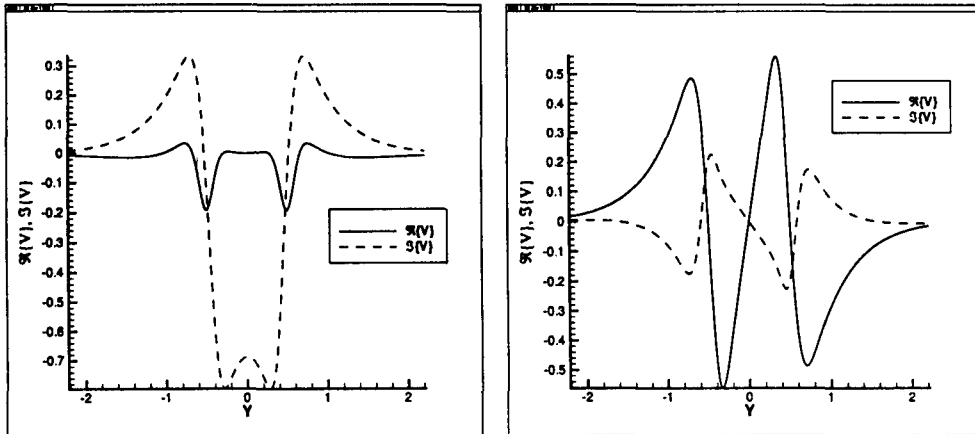


Fig.2. Normal velocity eigenfunction. Sinuous (left) and varicose (right) modes.

$M_{jet} = 2.5, M_{ambient} = 1.5$

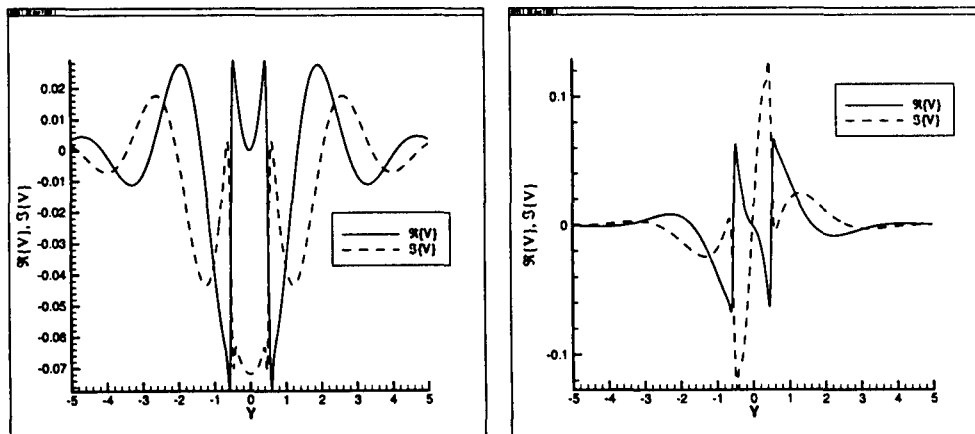


Fig.3. Normal velocity eigenfunction. Supersonic sinuous (left) and varicose (right) modes. $M_{jet} = 4.5, M_{ambient} = 1.5$.

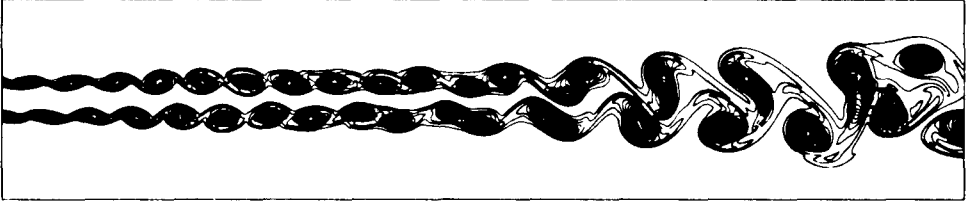


Fig.4. Subsonic sinuous mode. Entropy contours. $M_{jet} = 2.5$, $M_{ambient} = 1.5$, $Re = 5000$.



Fig.5. Supersonic sinuous mode. Density gradient. $M_{jet} = 4.5$, $M_{ambient} = 1.5$, $Re = 5000$.



Fig.6. Supersonic varicose mode. Density gradient. $M_{jet} = 4.5$, $M_{ambient} = 1.5$, $Re = 5000$.

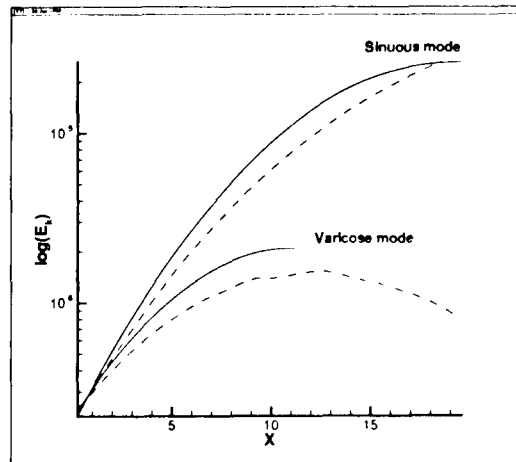


Fig.7. Energy of a harmonic vs downstream distance for linear stability with locally parallel assumption (solid lines) and Navier-Stokes computations (dashed lines). Sinuous and varicose modes. $M_{jet} = 2.5$, $M_{ambient} = 1.5$, $Re = 5000$.

AN AERODYNAMIC STUDY OF COLUMN-TYPE HEADFRAMES

V. V. Larichkin

Novosibirsk State Technical University, 20 K. Marx Prospekt,
630092, Novosibirsk, Russia.

INTRODUCTION

In recent years aerodynamics has found a wide utility in designing surface engineering structures. The latter is caused by stringent requirements imposed upon reliability of such structures, by their complex shape, application of new materials, etc. Since, when solving the above problems, one has to deal with a full-scale air stream, the use of aerodynamics is restricted to physical processes taking place, for the main part, in low-speed incompressible gas or fluid streams. A main peculiarity of this type of problems is taking account of the interrelation between aerodynamics and meteorology.

The motion of atmospheric air in the ground boundary layer is always turbulent. For an engineer, the following aspects of the flow are of primary interest:

- mean velocity of wind and its variation with height, needed for performing a calculation of the stationary level of wind load;
- level and scale of turbulence of the full-scale wind both being required for calculating the wind-load dynamic component;
- local and near-wall turbulence generated by the structure under design, required for evaluating the cross-coupling and making allowance for vortex excitation (vortex resonance).

Since most of surface constructions in their shape are bluff bodies for wind, they share common aerodynamic properties of geometrically simple bluff bodies such as cylinder, parallelepiped, etc. At the same time, they have their own aerodynamic features resulting, first of all, from their being three-dimensional objects [1-5].

The most promising among novel tendencies in developing high-performance headframes are the constructions including a combination of a few cylindrical columns rigidly connected together with lintels-galleries. Large overall dimensions of the constructions (height of over 100 m) and involvement of a combination of complex-shaped elements necessitate a detailed investigation of the aerodynamics of such constructions both from the viewpoint of well-substantiated wind-load estimation and from that of choosing the most favourable location of the object on the building site to meet both operational and ecological requirements.

As is known, in order to determine the wind load, one should know not only the total force exerted by the wind stream, but also the distribution of its pressure over the entire surface of the construction. For making a good choice for the object's location, it is of extreme importance to know parameters of the wake stream past the construction.

The present work was aimed at a detailed study of the interaction of a headframe with modified shape with a wind stream through physical modelling in a wind tunnel.

EXPERIMENTAL PROCEDURE

The one-five hundredth model was a construction made of three smooth console round cylinders arranged according to equilateral-triangle scheme and rigidly joint together in their upper parts with lintels imitating transport galleries. In order to take off the surface wind pressure in the midship section of one of the cylinders, which could revolve round its own axis, there has been made a drainage hole 0.6 mm in diameter. The model was installed on a plate (screen) with a turntable and a built-in three-component balance. The tests were carried out in the wind tunnel of the Novosibirsk State Technical University with the open working section of 1,2 m diameter and 2,0 m length at subcritical Reynolds numbers $Re > 2.0 \times 10^4$ under conditions of either a uniform flow at the longitudinal-velocity turbulence level $\varepsilon = 1,5\%$ or a shear one modelling the ground boundary layer. In the latter case, different distributions over height of mean and pulsational velocities of wind were modelled with the help of stationary vortex generator or different-type reliefs of the screen imitating a ground surface. The part tests were carried out in the wind tunnel of the Novosibirsk State Technical University with the open working section elliptical section of (600 800) and 1200-mm length a uniform flow at the longitudinal-velocity turbulence level $\varepsilon = 1,7\%$. The general view of the model and scheme of the experimental setup are shown in Fig 1

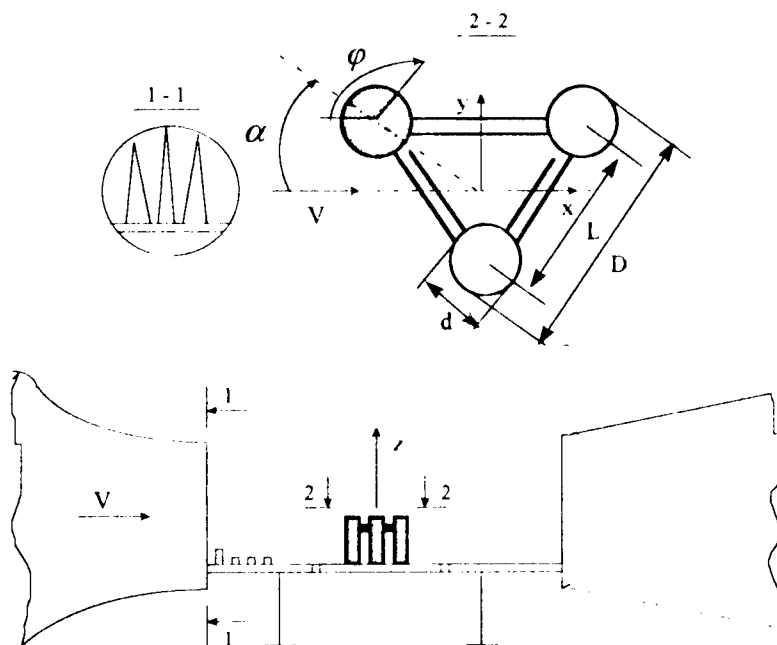


Fig 1

EXPERIMENTAL RESULTS

The flowpattern of the cross-flow around the three round console cylinders arranged according to the triangle scheme is extremely involved, the flow around each cylinder differing substantially from that around one isolated cylinder. Depending on the spacing between the lengthwise axes of the cylinders (L), angle of attack (α), Reynolds number, either presence or absence of approach-stream velocity gradient, the distribution of pressure over their surfaces underwent dramatic changes. As an example, Figure 2 presents for different angles of attack under conditions of a uniform flow the dependence of dimensionless pressure coefficient C_p on the angle which determines position of the point of interest. As is seen, the distribution of pressure over the surface of the cylinder under study (shaded circle in Fig. 1) is determined in the main by orientation of the cylinder with respect to the approach-stream velocity vector. In the variants where the cylinder under study was located ahead of the two other cylinders ($0 < \alpha < 60^\circ$), the presence of the latter ones resulted in an increased pressure on its lee side and in a shift of the flow separation point towards high angles. Positioning of the cylinder under study in the aerodynamic shadow of the two other cylinders ($60 < \alpha < 240^\circ$) was found to bring about a redistribution between the positive- and negative-pressure zones with a substantial fall in its aerodynamic resistance.

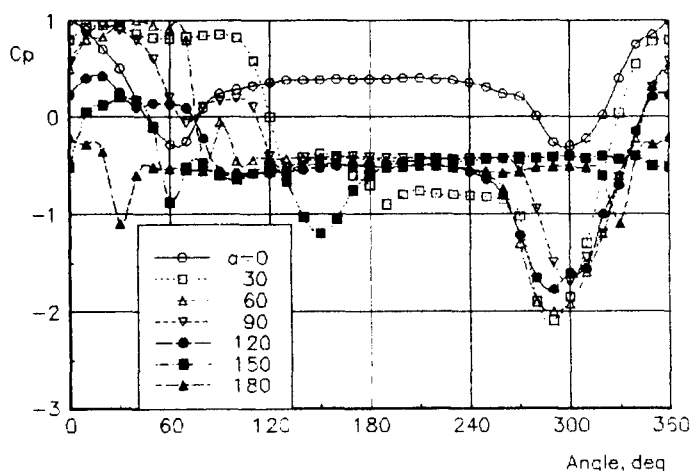
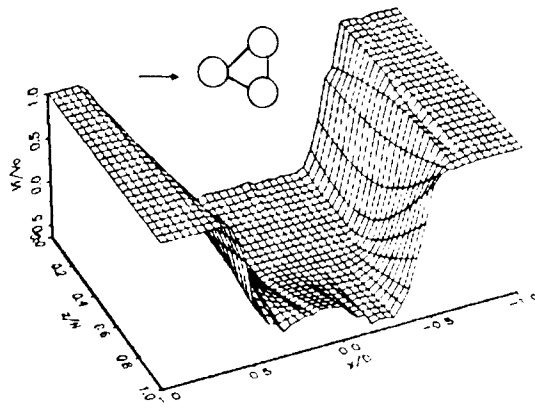


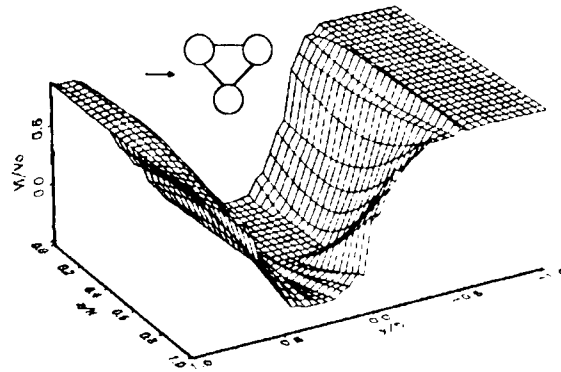
Fig. 2

As a hot-wire anemometer probing of the near model wake shows, for the majority of values of determining parameter, the wake flow exhibits an asymmetric shape. The latter changes the direction of the total aerodynamic force, its components in all three directions appearing with the lengthwise and transverse ones being the largest. At the chosen ratio $H/d = 10$, the main influence on the wake flow is exerted by the relative separation between cylinders (H/D) and by the inflow angle. Figure 3 exemplifies 3D splines of mean-velocity profiles for different angles of attack ($0, 30^\circ, 60^\circ$) at the same distance from the model $x/D = 1$.

a



b



c

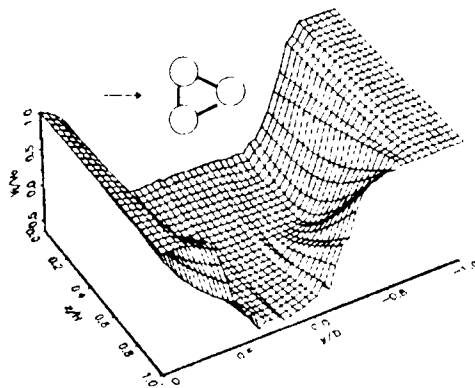


Fig. 3

The effect of the approach-stream velocity upon the evolution of flow in the model wake is illustrated by Fig.4. The differences in the mean-velocity losses of the wake stream in these cases are seen to be relatively small, the distributions of the pulsational velocity along the direction of stream and throughout the model's height, however, being drastically different (Figs. 5 and 6).

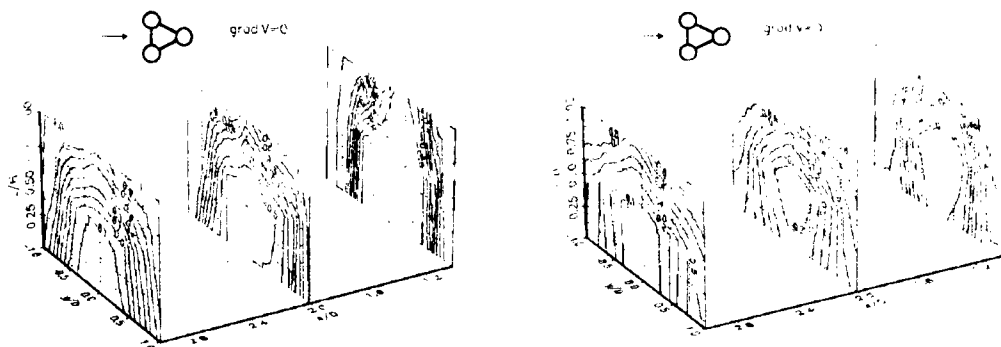


Fig. 4

Analysis of the vortex formation process throughout the height of the construction under study has shown that under the conditions of a uniform flow around the object, there can be realized three indistinctly pronounced sets of vortex streets with different frequencies. For example, at $\alpha = 0$, at the middle part of the construction, the vortex formation frequency corresponds to the Strouhal number ($Sh = f * d / v$) which turns out to be roughly equal to the value of the criterion for the case of infinitely long round cylinder, while at the top and at the bottom parts of the construction, the Strouhal number drops in value markedly, which can be explained by screen and end effects. The latter is confirmed also by the data reported in [6].

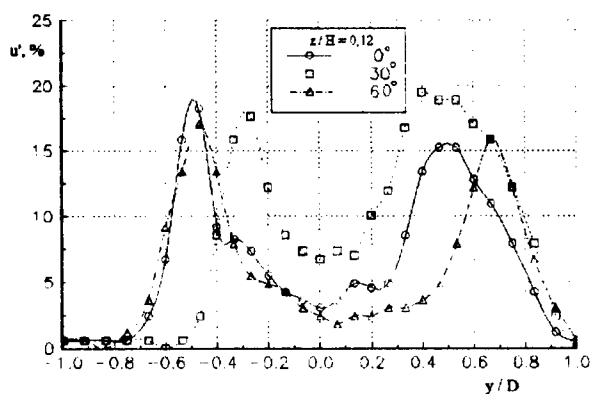


Fig. 5

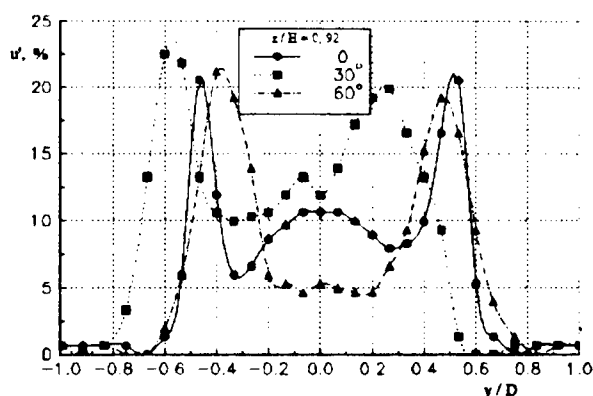


Fig. 6

It was found that, depending on the separation between columns and on the orientation of the construction with respect to the wind stream, there could be realized either stable or unstable regimes of flow resulting in substantially differing values of the dynamic component of wind load. The most unfavourable inflow angles were found to lie within the 30° to 40° interval. Recommendations are offered as to the most optimum mutual arrangement of columns as well as to that of headframes on mine territories with different type of terrains.

REFERENCES

1. D'Asdia P., Noe S. Vortex induced vibration of reinforced concrete chimneys: in situ experimentation and numerical previsions // 2nd European & African Conf. on Wind Engineering: Proc. Pt 2. - Genova, Italy, June 22-26, 1997, P. 1329 - 1336.
2. Matsumoto M., Kobayashi Y., and Shirato H. The influence of aerodynamic derivatives on flutter // J. Wind Engng. and Industrial Aerodynamics, 60:227-239, 1996.
3. Maruta E., Kanda M., and Sato J. Effects on surface roughness for wind pressure on glass and cladding of buildings // 2nd European & African Conf. on Wind Engineering: Proc. Pt 2. - Genova, Italy, June 22-26, 1997, P.1033 - 1042.
4. Tamura T., Miyagi T. and Kitagishi T. Numerical prediction of unsteady pressures on a square cylinder with various corner shapes // 2nd European & African Conf. on Wind Engineering: Proc. Pt 1. - Genova, Italy, June 22-26, 1997, P. 815 - 822.
5. Launder B. E. and Kato M. Modeling flow-induced oscillations in turbulent flow around a square cylinder // ASME Fluid. Eng. Conf. Jun. 1993.
6. Bardakhanov S. P., Larichkin V. V. Change structure near wake of two cantilever cylinders // J. Izvestiya SO AN SSSR, ser. tekhn. Nauk, vol. 6. - 1989 (In Russian).

AN EXPERIMENTAL STUDY OF ARTIFICIAL DISTURBANCES IN THE SHOCK LAYER ON THE FLAT PLATE

A.A.Maslov and S.G.Mironov

Institute of Theoretical and Applied Mechanics SB RAS, 630090,
Novosibirsk, Russia

INTRODUCTION

The use of the method of artificial wave trains in the study of boundary layer stability allows one to obtain reliable information about the evolution of wave of particular frequency and amplitude in the boundary layer, and eliminates the dependence of obtained results on the free-stream disturbance characteristics in the test section of the wind tunnel. This method has been successfully used to study subsonic, supersonic, and hypersonic boundary layer flows. There are no publications about the use of the method of artificial wave trains for free-stream Mach numbers higher than 6. For supersonic and hypersonic flows this method is used as a method of electric discharge. Under the conditions of low free-stream densities observed in hypersonic wind tunnels of continuous operation at high hypersonic Mach numbers ($M_\infty > 10$), the energy contribution of the discharge into the flow decreases, and the discharge loses its locality. Under these conditions, certain advantages are offered by devices generating the disturbances due to unsteady periodic hypersonic flow around a body with a cavity, like an oblique-cut gasdynamic whistle [1]. Proper relative positions of the whistle and the plate [2] makes it possible to introduce disturbances with controlled frequency and amplitude into the shock layer from the leading edge.

The objective of the present work is to study the characteristics of artificial density disturbances in a hypersonic shock layer on a plate, which are introduced from the leading edge using the technique described in [2], and their evolution in the shock layer.

EXPERIMENTAL SETUP AND MEASUREMENT METHOD

The experiments were conducted in the hypersonic wind tunnel T-327 based at ITAM SB RAS for the Mach number $M_\infty=21$ and Reynolds number calculated from the free-stream parameters, $Re_1=6 \cdot 10^5 \text{ m}^{-1}$. The stagnation pressure in the plenum chamber of the nozzle was $P_0=8 \text{ MPa}$, the stagnation temperature was $T_0=1100 \text{ K}$.

The characteristics of density fluctuations were measured in the shock layer on a flat plate model, which was a trapezium with 0.1 m leading edge width, 0.08 m trailing edge width, 0.35 m length, and 0.008 m thickness. The model was made of blackened aluminum. The leading edge angle was 7° , the bluntness radius was about 0.05 mm. The plate sides were made as wedges with an angle of 20° .

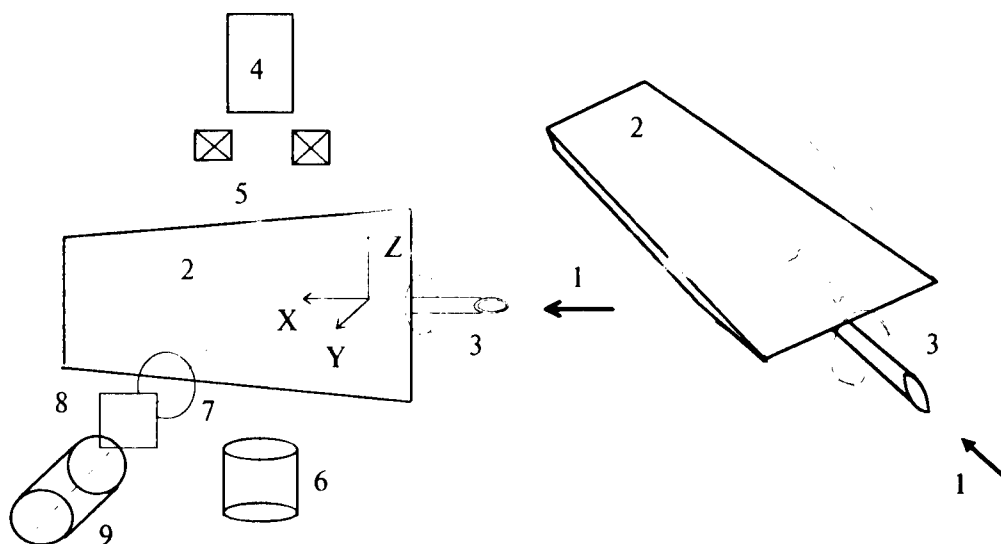


Fig.1. 1 - hypersonic flow, 2 - plate, 3 - oblique-cut gasdynamic whistle, 4 - electron gun, 5 - electron beam, 6 - collector of electrons, 7 - lens, 8 - optical filter, 9 - photomultiplier.

The experimental layout is shown in Fig. 1. The measurements were performed by the method of electron-beam fluorescence using the technology described in [3]. The measurement point was scanned along the X coordinate by moving the plate along the flow axis within the range of $-5...+210$ mm with respect to the leading edge of the plate. The scanning along the Y coordinate normal to the shock layer was performed by moving the plate across the flow within the range of $-15...+15$ mm with respect to the flow axis. The scanning along the transverse coordinate Z was performed by moving the optical system of fluorescence registration (observation point) along the electron beam axis within the range of $-20...+50$ mm with respect to the symmetry plane of the plate.

The construction and operation principle of the source of disturbances are described in [1, 2]. The source tube with 0.008 m outer diameter and 0.006 m inner diameter was located under the plate and had an inflection to ensure the optimum angle of 8.5° between the tube axis and the free-stream direction, which ensured the pressure pulsation intensity close to its maximum value in a wide range of frequencies [1]. The distance between the source tip and the leading edge of the plate was 40 mm along the stream direction. The intensity of introduced disturbances could be varied by changing the distance between the tube and the leading edge in the crossflow direction.

All measurements were performed for a fixed frequency $f=8.3$ kHz and harmonic, which for these experimental conditions corresponded to the frequency parameter $F=0.6 \cdot 10^{-4}$ and $1.2 \cdot 10^{-4}$. To eliminate the influence of appreciable nonparallelism of the mean flow field in the shock layer, the measurements were

conducted in the region of the maxima of the density pulsation distribution along the Y coordinate across the shock layer. The measurements showed that the positions of pulsation maxima coincide with the line $Y=0.75\Delta$ (Δ - is the shock wave position obtained by electron-beam visualization of the flow on the plate). Within a 10% accuracy, the positions of pulsation maxima corresponded to the line of equal mean density in the shock layer on the plate.

The data processing included the calculation of relative amplitude and phase spectra between the fluorescence intensity fluctuations and pressure fluctuations in the source of disturbances. The density fluctuations in the shock layer penetrating from the free stream were excluded. The pulsation intensity and the mean signal were normalized by the electron beam current. The influence of the beam current variation on the measurement results was eliminated. The level of density fluctuations was additionally normalized by the root of the root-mean-square intensity of pressure fluctuations in the whistle cavity in order to eliminate the reference signal variation.

When the measurement point is scanned along the transverse coordinate Z (along the electron beam), the level of the constant and variable components of the signal of the optical registration system changes. This is because the electron beam becomes wider when passing through the flow due to its scattering on gas molecules. Therefore, the measured data were additionally normalized by the dependence of the mean signal on Z higher along the beam, far from the centerline, where the flow on the plate is not disturbed. The obtained approximating functions were close to those found previously in [4]. The amplitude and phase spectra were then calculated on the basis of wavenumbers with respect to the transverse coordinate Z using the Hamming's spectral window. After that, using the obtained spectra, we found the amplitude and phase dependences versus the longitudinal coordinate X, increments, longitudinal phase velocities, and propagation angles of density wave in the shock layer.

MODEL OF DISTURBANCE GENERATION

To understand the mechanism of disturbance generation in the shock layer and the results of investigation, let us consider a simplified physical models of disturbance generation using the proposed scheme. When the shock wave from the whistle passes periodically during a pulsation cycle through the plate edge (unsteady interaction) in the phase of its position beneath the plate edge, the plate edge interacts with the free stream. The angle of shock wave inclination to the flow at the leading edge is 14° , the density jump is 5, the Mach number is 8.3. When the plate edge crosses the shock wave from the source whose inclination angle is 16° at a distance of 40 mm, the Mach number behind the shock is 7.4. In this case, however, this region of the plate edge experiences the action of the flow at an angle of 13° from under the plate due to turning of streamlines behind the shock wave. According to numerical calculations performed by Dr. T.V. Poplavskaya within the framework of the full viscous shock layer equations for a two-dimensional flow, the static pressure in the wake behind the intersection line is three times lower than in the undisturbed peripheral region. This nonequilibrium causes the gas overflow from the periphery to the center, which leads to the flow

ascending from the surface and formation of a pair of counter-rotating vortices. In this case, naturally, the vortices are clearly unsteady and synchronized with the shock wave oscillations.

When the plate edge is not very deeply immersed into the shock layer of the whistle (quasi-steady interaction), the shock wave oscillations change only the depth of its penetration into the shock layer and, hence, the contact region width. All earlier considerations and estimations are valid, with an exception that there is a steady vortex pair whose transverse size oscillates with the pulsation frequency of the shock layer from the source.

The measurements revealed a deformation of transverse distributions on the mean density when the density decreases at the plate axis and increases at the "valley" boundaries, which corresponds to the influence of a vortex pair entraining the low-density gas from the plate surface to the shock layer boundary and descending more dense layers of gas to the plate surface. The distributed intensities of density fluctuations correspond to the pattern of mean density deformation and experience a 180° phase jump when the measurement point passes from the region of decreasing mean density to that of increasing mean density, which verifies the presence of ascending and descending gas flows.

RESULTS

Two types of interaction between the plate edge and the shock layer on the whistle were observed in the course of measurements: generation of unsteady vortices (a) and formation of a steady pair of vortices with superimposed pulsations (b).

(a). In the first case, the maximum deformation of the mean density field lies within 5%. The transverse distributions of density pulsations have one maximum at the plate axis and expand weakly from one cross-section to another in a wide range of X values. The relative value of density pulsations $\langle n \rangle / n$, varied from 0.1% to 0.15% within the X range of 60-210 mm. The estimate of the half-width of the disturbed region corresponds to the plate edge penetration by 0.1 mm into the shock layer on the whistle, the shock wave oscillations being 0.2 mm (the corresponding amplitude of pressure fluctuations in the whistle cavity is 140 dB).

The analysis of obtained amplitude and phase β - spectra with respect to the transverse coordinate for the fundamental frequency and harmonic showed that there is a fairly wide maximum of the amplitude near the zero value of β , wherein the phase is constant. The spectral character corresponds to the propagation of a plane front of waves with different inclination angles (up to 70° - 80°). The longitudinal phase velocity C_x for the fundamental frequency and for the harmonic versus the propagation angle χ are shown in Fig.2 (curves 2,3). There is a region of faster phase variation at the plate tip, which corresponds to a smaller phase velocity. This agrees with the data of [2] where the near field of the interaction region was studied. The resultant phase velocity is smaller than $1/M_c \cos \chi$ (curve 1, Fig.2), which indicates the acoustic nature of developing disturbances. The disturbances increments for the fundamental frequency and the harmonic are shown in Fig.3 (curves 1,2). For the harmonic the disturbances are decaying.

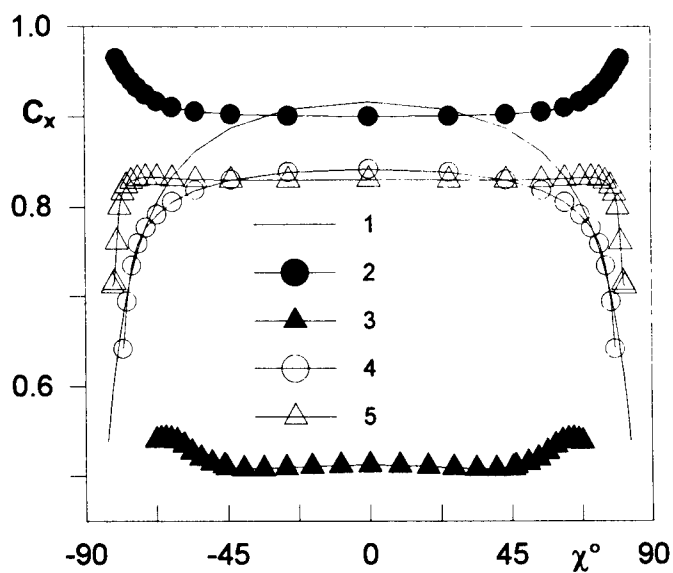


Fig.2. Longitudinal phase velocity versus propagation angle

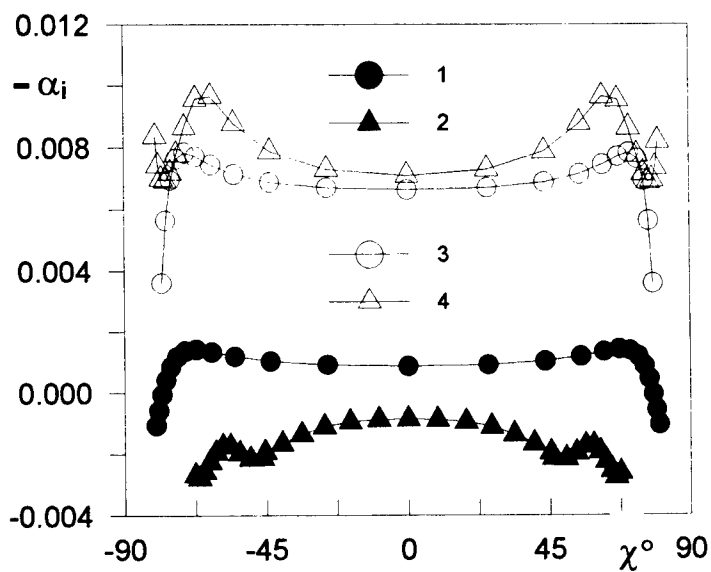


Fig.3. Disturbances increment versus propagation angle

(b). In the second case, the plate edge was introduced into the shock layer of the source by 1.6 mm. A steady pair of vortices was formed in the shock layer of the plate, and a 40% deformation of the mean density field was observed. The range of variation of the maximum intensity of density fluctuations along the plate $\langle n \rangle / n_\infty$ was 0.5-6%. The amplitude and phase β - spectra with respect to the transverse coordinate Z for the fundamental frequency and harmonic were similar to the first case. The disturbances propagated with an approximately equal longitudinal phase velocity $C_x \approx 0.84$ (curves 4,5, Fig.2). Their increments are shown in Fig.3 (curves 3,4). An exception was only the region near the plate edge where the phase velocity was close to $C_x \approx 0.3$ obtained in [2]. Low values of phase velocity testify to an acoustic nature of developing disturbances. On the other hand, high values of pulsation increment were obtained, as compared with the previous case and the data for natural disturbances in the shock layer of the plate.

CONCLUSIONS

Experimental study of the characteristics of artificial disturbances in a hypersonic shock layer on a flat plate is carried out at unsteady and quasi-steady interaction of a conic shock wave with a leading edge of a plate. The dependences of longitudinal phase velocity and increment of artificial disturbances versus the propagation angles of density waves are obtained. Essential dependence these characteristics from the conditions of disturbances generation is shown. Probably, it is connected to development of secondary instability on the pair of counter-rotating vortices, arising in a shock layer in the case of quasi-steady interaction.

ACKNOWLEDGEMENT

This research has been supported by Russian Foundation for Fundamental Research, Grant No. 98-01-00462.

REFERENCES

1. Maslov A.A. and Mironov S.G. Experimental investigation of the hypersonic low-density flow past a half-closed cylindrical cavity // *Fluid Dynamics* - 1996. - Vol. 31. - N. 6. - P. 928 - 932.
2. Maslov A.A., Mironov S.G. and Shplyuk A.N., An experimental electron-beam study of perturbations in a hypersonic shock layer on a plate // *Int. Conf. on the Methods of Aerophysical Research: Proc. Pt. 3.* - Novosibirsk, 1996, P. 212 - 215.
3. Maslov A.A., Mironov S.G. and Shplyuk A.N. An experimental study of density fluctuations in a hypersonic shock layer on a flat plate // *J.Appl.Mech.Tech.Phys.* - 1996. - Vol. 37. - N. 6. - P. 51 - 60.
4. Vetlutsky V.N., Maslov A.A., Mironov S.G., Poplavskaya T.V. and Shplyuk A.N. Hypersonic flow on a flat plate. Experimental results and numerical simulation // *J.Appl.Mech.Tech.Phys.* - 1995. - Vol. 36. - N. 6. - P. 60 - 67.

AN EXPERIMENTAL STUDY OF VORTEX STRUCTURES IN GAS DYNAMIC DUCT WITH SWIVELLING NOZZLE

B.M.Melamed, V.N.Zaikovskii

Institute of Theoretical and Applied Mechanics SB RAS,
630090 Novosibirsk, Russia

It is important to study the swirl jet flows because they are abundant in various natural phenomena and used in practice in many branches of industry. It is known that the intensification of heat and mass transfer processes depends significantly on the degree of flow swirl [1]. When studying the swirl flows, various research techniques are used: probing of the flow structure, pneumometric measurements of the internal duct surface, and flow visualization in the near-wall layer [2].

Proceeding from specific features of organization of the internal structure, the swirl flows can be classified into forced flows in vortex chambers and free flows propagating in a co-current stream. The local and integral characteristics of the former are fairly well studied due to prescribed swirl law and known boundary conditions [3]. The study of the free swirl flows requires the knowledge of detailed flow structure, especially for vortex jets generated in the separation region.

A typical example of such a flow is streamwise paired vortex structures arising on the end face of a propellant charge in solid-propellant rocket engines with star-like ducts [4]. A sketch of the model is presented in Fig. 1, where 1 is the simulator of the propellant charge with circular of star-like duct, 2 is a submerged swivelling nozzle.

The results of the flow pattern for a star-like charge duct are presented in [5] for the case when the duct symmetry axis coincides with the nozzle axis, i.e., when the nozzle is not deflected. Paired vortices are formed on the ledges (L) between the rays of a star-like duct, the streamwise separation line lies in the symmetry plane of a star ray (R), and the reattachment line lies in the symmetry plane of the ledge. The number of paired structures is equal to the number of ledges in the duct. The vortices are uniformly located over the perimeter of the nozzle duct cross-section (see Fig. 1).

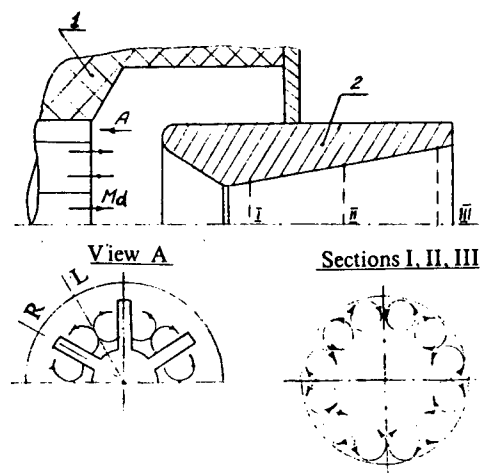


Fig. 1. The general layout of the facility.

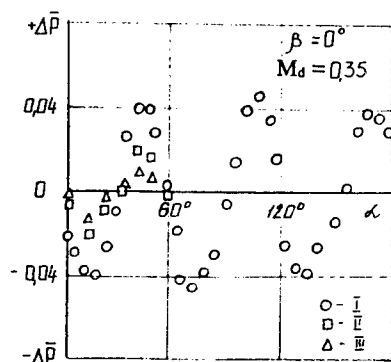


Fig.2. The distribution of the relative pressure $\pm \Delta p$

Some results on the evolution of vortex structures in the engine duct for a six-ray star-like shape of the charge duct with the nozzle deflected with respect to the axis are presented in [6].

The streamwise swirl jets significantly intensify the thermal erosion in the nozzle behind the throat. Equally spaced streamwise recesses are formed on the inner surface of a supersonic bell. Their number corresponds to the number of rays of a star-like duct. Reliable prediction of gas dynamic and thermal processes in the nozzles of considered type is necessary to ensure strength and reliable operation of supersonic bells.

For this purpose, an engineering technique for calculating the static pressure distribution on the inner surface of a swivelling nozzle was proposed in [7]. This technique is based on parametric experimental studies conducted in a wide range of governing parameters (velocity at the exit of a circular charge duct, turning angle of the nozzle with respect to its axis, geometry of sub- and supersonic sections of the nozzle). The pneumometric data for the nozzle surface in the present work were processed similar to [7]: a nondimensional relative parameter $\pm\Delta P$ was used, which characterizes the value of pressure deviation over the cross-sectional perimeter of a supersonic nozzle bell in the presence of vortices from the pressure values at the corresponding point without vortices, related to the pressure at this point in the absence of vortices ($+\Delta P$ corresponds to reattachment of vortices to the surface, $-\Delta P$ to their separation):

$$\pm\Delta P = (P - P_0)/P_0,$$

where P is the local pressure on the inner surface of the nozzle with a star-like duct, P_0 is the local pressure at the corresponding point of a circular duct (without vortices). The results of such treatment are shown in Fig. 2 for a half of the first cross-section $0^\circ < \alpha < 180^\circ$ (circles) where α is the angular coordinate of points over the nozzle cross-section perimeter. The level of the relative parameter are compared in the interval $0^\circ < \alpha < 60^\circ$ with those of other cross-sections (squares for the second cross-section and triangles for the third one). The flow velocity at the duct exit was varied in experiments by changing the area of the simulator duct cross-section. For a star-like duct the velocity at the ray exit was $M_d=0.25$ and $M_d=0.35$.

An empirical dependence is a curve with clear periodic alternation of minima and maxima. The deviations of extreme values of the relative pressure from the values in a circular duct are about 4% in the first cross-section, 2% in the second one, and about 1% in the third cross-section. The measurement accuracy of experimental data is determined by pressure gages with a $\pm 0.3\%$ error used in experiments.

The number of maxima and minima over the entire perimeter of the cross-section, in accordance with the model of interaction of swirl structures with the wall, determines the number of streamwise vortices (it was 12 in our case). The maximum corresponds to vortex separation region, and the minimum corresponds to vortex reattachment to the inner surface of the bell. The magnitude of extremes decreases downstream in accordance with increasing cross-section of the local vortex structure and decreasing tangential component of velocity at the periphery according to the law of quasipotential rotation ($V_\tau \cdot R = \text{const}$). The maxima of relative pressure decrease also when decreasing the flow Mach number at the exit of a star-like duct. At the moment of vortex incipience, the maximum of tangential velocity $V_{\tau\text{max}}$ at the boundary of the central region of quasisolid rotation ($V_\tau / R = \text{const}$) is apparently determined by the mean velocity at the duct exit. The presented experimental data testify to existence of a system of steady streamwise paired vortex structures at the flow periphery in a supersonic bell.

Let us consider the evolution of a system of vortices arising in a supersonic part of the duct in a deflected nozzle. As is shown in [7], the nozzle rotation violates the symmetry of the test gas entrance, and the flow in the internal volume of the deflected nozzle becomes three-dimensional. The pressure distribution over the internal nozzle

surface loses the axial symmetry. The pressure level decreases on the leeward surface of the sub- and supersonic parts of the nozzle ($\alpha = 180^\circ$), and increases on the windward surface of the supersonic part ($\alpha = 0^\circ$).

The maximum deviations of the relative pressure $\pm \Delta P$ are proportional to the angles of flow deflection in the corresponding region of the duct. Thus, when the nozzle is deflected, the paired swirl structures in the transonic region, which propagate in a co-current flow, experience the action of additional streamwise pressure gradient ($\pm \Delta P$) and considerable curvature of the streamlines. Thus processed pressure distributions measured over the perimeter of the first cross-section of a supersonic bell for the governing parameters $M_d = 0.35$, $\beta = 20^\circ$ and simulator duct in the form of a six-ray star are presented in Fig. 3,a. The experimental dependence is a periodic curve with two uniformly located maxima and minima. Together with the previously considered model of interaction of swirl structures with the wall, this experimental fact allows one to draw a conclusion about the presence of four vortices in this cross-section.

The system of six paired vortex structure, existing at the entrance to a deflected nozzle, transforms in the extreme region of pressure deviation from the axial symmetry into a system consisting of two pairs of large vortices (Fig. 3,b). The maximum values of relative pressure deviation from the mean level were about 4% for the primary vortices and 12% for the secondary ones. Approximately a three-fold increase of the relative pressure deviation is observed with approximately three-fold decrease of the total number of vortices.

The pattern of the relative pressure distribution in a given cross-section for a lower angle of nozzle deflection $\beta = 10^\circ$ favors a better understanding of the vortex evolution process behind the throat (Fig. 4,a). In this case, an intermediate state of transition from the primary vortex system to a system with large vortices is observed. The primary streamwise vortex structure are still retained on the windward surface of a supersonic bell ($\alpha = 0^\circ$) in the high-pressure region, while their destruction and formation of an enlarged paired vortex structure takes place on the leeward side ($\alpha = 180^\circ$) in the low-pressure region (Fig. 4,b).

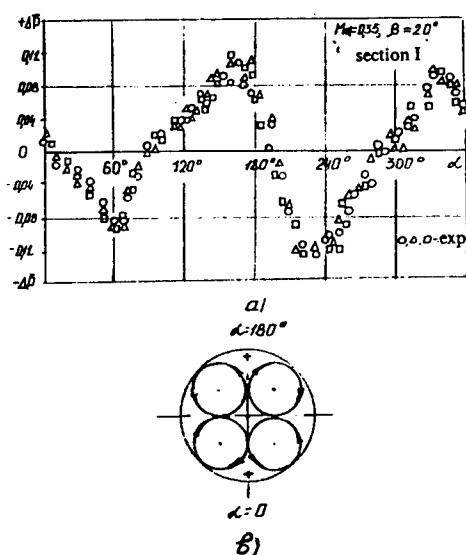


Fig. 3. The distribution of the relative pressure $\pm \Delta P$

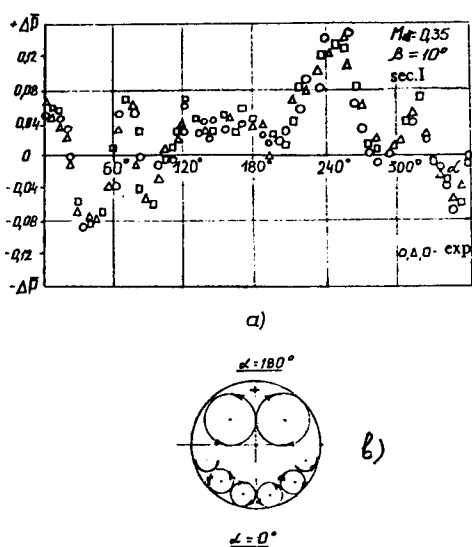


Fig. 4. The distribution of the relative pressure $\pm \Delta P$

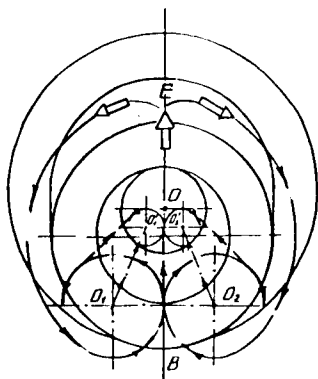


Fig. 5. The plot of vortex pattern

A similar result was also obtained for an angle of nozzle deflection 20° , but for the Mach number of the incoming flow reduced to $M_d = 0.25$. Thus, the transformation of the initial vortex structure into an enlarged one is characterized by a combination of two governing parameters: Mach number of the incoming flow and deflection angle of a submerged nozzle, which form a pattern of nonaxisymmetric pressure distribution and curved streamlines in the transonic region.

The obtained experimental data show that for a six-ray star-like duct in a deflected supersonic bell the system of twelve primary vortices is transformed into a symmetric system of four secondary vortices, each of them being

formed by merging of three streamwise structures swirled in the same direction.

We suggest the following mechanism of evolution of vortex structures. The streamwise vortex structure propagating in a co-current flow behind the star-like duct exit interacts with the deflected outer surface (E) of the submerged nozzle (Fig. 5). This results in a symmetric division of the incoming flow into two parts with subsequent turning on the end face of the model and exhaust towards the leeward subsonic nozzle region (B). Two symmetric swirl flows, O_1 and O_2 , are formed at the interaction of these divided counterstreams, each containing three pairs of the primary streamwise vortices. Under the subsequent action of external turning load increasing towards the throat, additional streamwise pressure gradient, and bending of streamlines, the pairs are broken, and then the vortices with the same swirl direction merge. Since in each outer swirl flow O_1O_1' and O_2O_2' there are three vortices with this and that swirl, their merging behind the throat forms again a paired symmetric system of four enlarged vortices (see Fig. 3,b).

The obtained experimental data on the evolution of a steady vortex structure for a star-like shape of the charge duct in a swivelling nozzle allow one to draw the following conclusions:

1. Paired swirl structures arise at the exit of a star-like duct under the action of a transverse velocity gradient, their number is equal to the number of rays of the simulator duct, and their diameter changes proportionally to the size of duct elements.

2. The merging of streamwise swirl structures takes place if the incoming flow turns in a supersonic nozzle deflected by an angle $\beta = 10^\circ$ with the flow Mach number at the star-like duct exit $M_d > 0.25$.

3. The process of destruction of the primary vortex structure and merging into large-scale vortices begins at the leeward surface of the supersonic bell.

REFERENCES

1. Volchkov E.P. Near-Wall Gas Screens. — Novosibirsk: Nauka, 1983. — 239 p.
2. Gupta A.K., Lilley D.G., Syred N. Swirl Flows. Abacus Press, England, 1984.
3. Khalatov A.A. Theory and Practice of Swirl Flows. — Kiev: Naukova Dumka, 1989. — 192 p.
4. Shishkov A.A., Panin S.D. Operation Processes in Solid-Propellant Rocket Engines. — Moscow: Mashinostroenie, 1988. — 240 p.
5. Kuraev A.A., Kuraeva A.D., Petrova B.N. Emergence of shock waves in nozzles with vortices passing through the throat // Gas Dynamics and Physical Kinetics. — Novosibirsk, 1974. — P. 90-91.
6. Zaikovskiy V.N., Melamed B.M. Evolution of vortex structures in engine duct with swivelling nozzle // XIV All-Russia Workshop "Jet and Unsteady Flows in Gas Dynamics": Abstract. Novosibirsk, 1995.
7. Zaikovskiy V.N. An engineering method of pressure calculation at the internal surface of a swivelling nozzle // Thermophysics and Aeromechanics. — 1997. — Vol. 4. — No. 4. — P. 401-406.

THE DEVELOPMENT OF A DATABASE OF AERODYNAMIC EXPERIMENTS AND COMPUTATIONS PERFORMED AT ITAM

O.N. Mosseichuk

Institute of Theoretical and Applied Mechanics SB RAS, Novosibirsk, Russia

1 Introduction

A large amount of computational and experimental studies has been performed at ITAM SB RAS during the last decades for solving fundamental and applied problems of aerogasdynamics related to the development of supersonic and hypersonic flying vehicles. The problem of storage and systematization of vast amounts of information obtained in these studies is very urgent.

The processing and analysis of great amounts of data, systematization and storage of numerical and experimental results, comparison of results presented in versatile form, from multidimensional numerical arrays to the filming of wind tunnel experiments, – this list of problems that require an effective solution in the nearest future is far from being complete.

“The database of aerodynamic experiments and computations performed at ITAM” has been created within the framework of the research work on the development of an all-Institute database of aerodynamic experiments and computations. It is designed for informational support of fundamental and applied researches in the field of aerodynamics.

The database is designed for improving the efficiency of scientific work, providing the scientists with powerful tools for processing, analysis and visualization of the results of a scientific experiment. The solutions on the basis of advanced software ensure a high reliability of the centralized storage of the data and a flexible authorized access to the results. The system can be used as a tool for scientific researches and as a database of experimental data for CFD validation.

2 History of database evolution

The importance of the posed problem has been known for a long time. Our Institute has known a rich story of the development of automated systems for processing and

storage of the results of aerodynamic experiments. These works have been performed since the time the first really available and working computers appeared, and that was BESM-6.[1].[2].[3] The peak of this activity was observed in late 80s when the SNAOD system (a system for accumulation, analysis and processing of the data of aerodynamic researches) was put into operation and started to work at the Institute. [4] This was an operating, fairly advanced for that time system that allowed one, to a certain extent, to automate many stages of an aerophysical experiment. The era of large Soviet computing machines came to an end rather quickly. Unfortunately, all developments, data and codes were irretrievably lost when these machines went out of operation. The era of personal computers led to personal storage of data, however strange this can seem. Almost each laboratory started to develop its own processing systems and databases. Practically all of them had the same merits and drawbacks. These systems worked under the MS DOS operation system, they have no means of controlling the access to them, no possibilities of remote access, and no possibilities of multiple access. In fact, they had no prospects of gradual evolution with gradual and planned accumulation of data, algorithms and means of their processing, which is a necessary condition for creating a database. Subsequent frequent change of PC generations with almost impossible transfer of the developed software to new versions demonstrated that these efforts had no future. At the same time, an analysis of these developments can offer valuable experience, since it clearly shows the users' demands and possible ways for meeting them.

Having created a database called the "Atlas of Aerodynamic Characteristics" in 1992, a group scientists from our laboratory came to a conclusion that it is necessary to change the basis and ideology of operation of this kind of systems. In the next years, a number of systems have been created, which automate the numerical aerodynamic experiment. These integrated packages include a complete cycle of preparation, starting and controlling the state of a computation, preliminary analysis of results, accumulation of results, their visualization, analysis, comparison, etc. [5] The systems have a developed graphical interface and use databases. Feeling the need in creating an all-Institute database, we carefully examined and accumulated the experience obtained during the development of integrated systems. In 1997 the critical mass was surpassed and the development of a new system began.

3 Ideology of constructing the system

When creating such a system, it is very important to define clearly the main principles of constructing the database and the ideology of users' work. As already noted, an aerodynamic experiment is characterized by a large set of extremely versatile data, whose relations are rather sophisticated. We are experienced in creating and using both databases with clearly defined and rigidly fixed structure and those with arbitrary methods of creation with user-defined links. Both concepts have advantages and drawbacks. The arbitrary creation is more flexible, it allows for storage of arbitrary data in the database and for organization of extremely complicated links between them. The exploitation of such a database has shown, however, that it can be used only by

people that created it, in fact, its administrators. The probability of losing some links and, correspondingly, some data is very high. A constant support of the workability of such a database is complicated and expensive. A database with fixed structure is free of these drawbacks, but its functional capabilities are more limited from the very beginning, the extension and adding of new types of data are labor-consuming or sometimes impossible. To find a compromise between these types and to create an extendable database with a flexible logical structure – this is the main problem to be solved.

The main idea of solving this problem is to create a particular structure for data storage of each set of data. For example, a set of runs in one wind tunnel have one set of data, and a special structure for their storage is organized. We call it a class of data and understand it actually as the description of the database fields and tables and the links between them. The data for these real experiments are stored in the database, in their own class. When a numerical experiment simulating the real one is performed, the results contain a lot of data that characterize the computation itself, and they cannot be stored in the same class of data; hence, a new class is organized. The classes are created in accordance with specific stencils and system ideology, they contain mandatory service fields that ensure their integrity and integration into the system. It is quite logical that the descriptions of classes are also stored in the database in special tables.

The logic of the database operation is fixed and determined by the structure of data storage. All data manipulations can be divided into three levels.

At the first level, the user works with the names assigned to experimental results, names of geometric models, classes of data and catalogs. It should be noted that a catalog system with an arbitrary level of nesting defined by the user is supported. Having chosen the data of interest, the user passes to the next level.

The most important and frequently encountered data are available for the second-level work. Usually these are the initial data and integral characteristics of results chosen at the first level. Viewing and editing in a tabular form, constructing graphs, viewing the images of various formats, comparison between various experiments and computations are possible.

At the third level, the data characterized by a large numerical volume are presented for viewing and editing. These are usually the values of characteristics distributed over the surface, flowfields, etc. The user's interface and possibilities are the same as at the second level plus special visualization methods.

4 Visualization

The next important feature of the aerodynamic database is the means of visualization. Obviously there is no sense to view in a tabular form the data which are often represented as arrays containing tens or even hundreds of thousand values. Therefore, though the tabular representation is realized in the database, special attention is paid to the development of a flexible tool for building the graphs and visualization of 2D and 3D flowfields. The developed structure of data storage allows for simultaneous storage

of data and methods of their visualization. The visualization itself is performed by means of external programs. The database authors tried to ensure the closest integration of individual visualization codes and the database. The Kagr and Kapić software systems developed at ITAM are currently used, it is also possible to work with Gnuplot, Tecplot, and Vigie systems.

5 Realization

Special attention in the database development is paid to its scalability, possibility of further development and increasing efficiency. An SQL server of databases operating under a UNIX family systems is the core of the system that ensure the required characteristics and possibilities of increasing the resources. The system is constructed on a client-server principle, and all data can be accessed through a local Institute network. It should be noted that all software used is licensed and belongs to the freeware category.

A personal computer with the Linux operation system [6] and a PostgreSQL server [7] are used as a server. This configuration demonstrated a high reliability and acceptable speed of operation. The client part was written in the C++ language, it also works under the Linux operation system. When this program was under development, it was also made possible to transfer this software to the Windows operation system. However, this work has not been yet performed, the main difficulty is the transfer of visualization means, which is rather problematic. Probably, we will have to use less advanced software, such as Gnuplot, or some commercial software.

Besides, a variant of the client part is made in the Java language. It works slightly slower, is to work under all operation systems, but there are still problems with visualization means on platforms other than UNIX. Nevertheless, some methods are available, in particular, the drawing of simple graphs and 3D geometric model without visualization of distributed characteristics.

6 Some examples of using the system

One of the main advantages of the suggested system is a close integration of the database and visualization methods. Already now several types of data representation are available to the user, in future it is planned to increase their number and offer a possibility of using various graphical packages. Once the data are prepared and loaded into the database, there is no need to prepare them in formats required by different visualization systems, the user can compare the data with all previously loaded data accessible for him. The links between various data obtained in the course of one experiment allow the user to realize easily complex visualizations. Figure 1, for example, shows the screen for the user working with the characteristics distributed over the surface of an aerodynamic model. The top left window is the main working window, the user can see there all available data and indicates those he would like to see in the tabular form. These data are shown in the bottom left window. Having

chosen the argument, parameters and intervals, the user can plot the needed functions in the bottom right window. Besides, an additional window can be opened, which shows a 3D geometric model with visualization of points for building the graph.

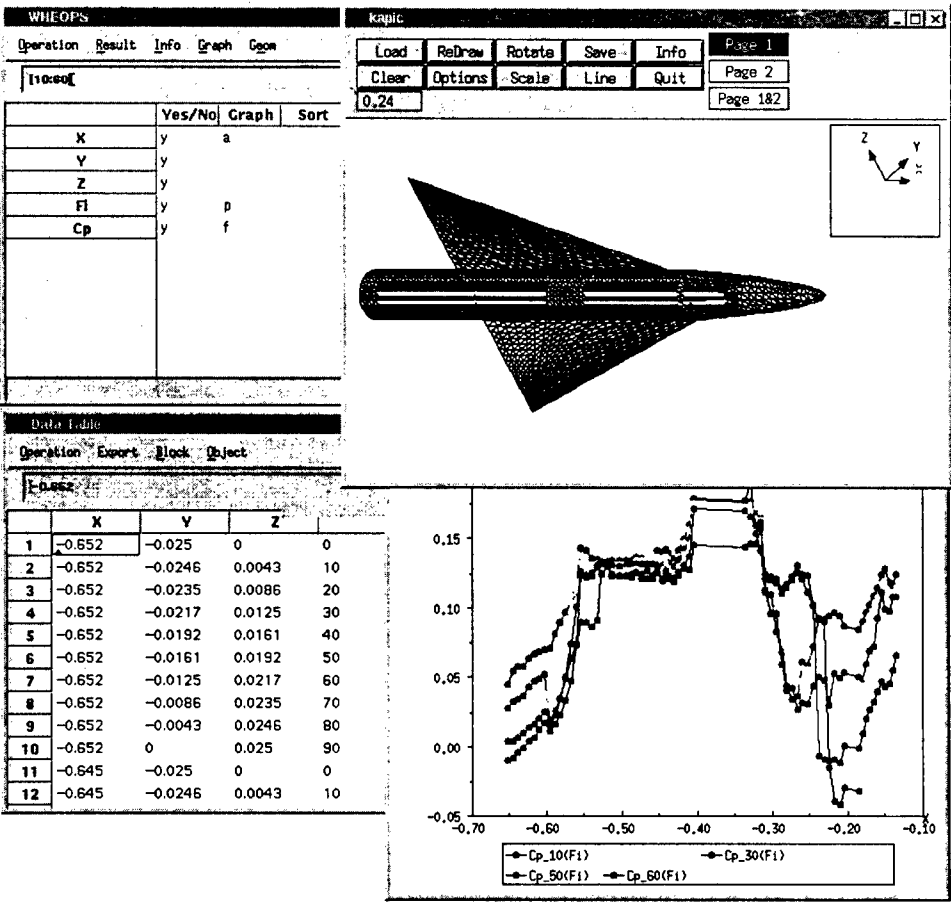


Figure 1: Screen for the user working with the characteristics distributed over the surface of an aerodynamic model.

The graphs and the corresponding lines on the model have the same color. Changing the argument, parameters and intervals (Fig. 2)), various parts of the model can be easily studied, certainly, if a sufficient amount of experimental data is available.

This example illustrates which possibilities are offered by a distinctly structured storage of data, and how simple it is to perform rather complex visualizations that sometimes require a long-time and careful preparation of data.

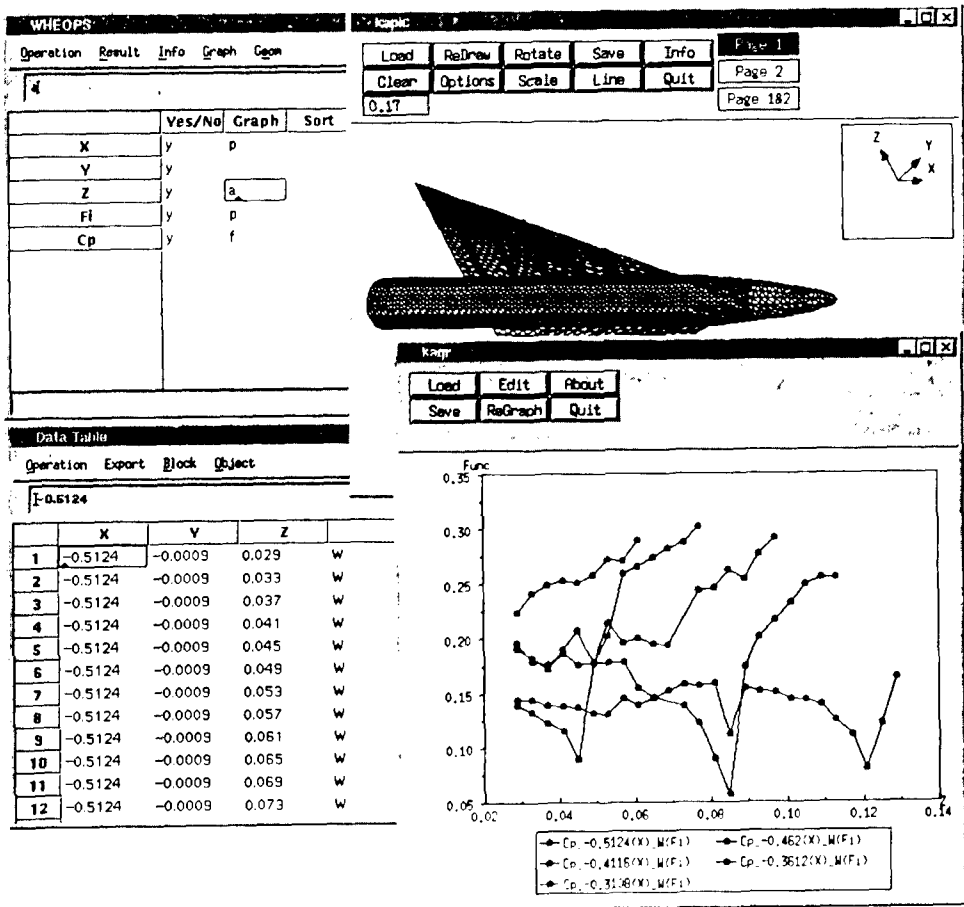


Figure 2: Another example of characteristics shown on the screen .

7 Prospects of development

The current state of the information system under development can be estimated as a performed pilot project. The system is workable and has passed limited testing. The wide-scale implementation involved both technical and organizational problems. The main problem seems to be the education of the users, preparation of documentation, and the overcoming of a psychological barrier. Scientists are not used to working with centralized resources, it is difficult for many of them to trust the control over their results to somebody else. At the same time, all people acquainted with the system believe its utilization and further development are useful.

When designing the system, it was planned that its exploitation would be combined with adding new material, improving the visualization mechanisms, adding new methods of data processing. The work on database integration into the Internet and presenting a limited access to data through WWW browsers is currently performed.

Counting on advance technologies of collective working with data, the development initially oriented to a specific area such as aerodynamics, long-term studies in the field of integrated aerodynamic systems allowed for creating the optimal structure of data storage and effective mechanisms of their visualization and comparison. Such a system can significantly improve the effectiveness of aerodynamic experiment and surely has good prospects.

References

- [1] Vyshenkov Yu.I., Kharitonov A.M. A system of collecting and processing of the data of aerophysical measurements of ITAM SB USSR Acad. Sci. // Principles of Organization of Applied Software. - Novosibirsk: ITAM SB USSR Acad. Sci., 1981.
- [2] Vyshenkov Yu.I., Glinsky A.N., Ivanov M.S. Software for the automated system of scientific information of ITAM. A system for data acquisition, analysis and processing// Automation of Aerodynamic Experiment. - Novosibirsk: ITAM SB USSR Acad. Sci., 1985.
- [3] Vyshenkov Yu.I., Gilyov V.M., Tikhomirova T.P. Software for acquisition and accumulation of experimental data. Novosibirsk, 1990.
(Preprint/ ITAM SB USSR Acad. Sci.; No.3 -90).
- [4] Glinsky A.N., Ivanov M.S., Zhukova G.A. SNAOD – a system for accumulation, analysis and processing of the data of aerodynamic researches // Abstr. “ Dialogue “Man – Computer” Conference. Pt 3 Databases and Information Retrieval Systems, Problem-oriented. -Sverdlovsk: USSR UrB Acad. Sci., 1989.
- [5] Zhukova G.A., Kashkovsky A.V., Mosseichuk O.N. RAMSES - Rarefied Aerodynamics Modeling System for Earth Satellites. Novosibirsk, 1995.
(Preprint/ ITAM SB RAS; No.4 -95).
- [6] Yu A., Chen J. The POSTGRES95 SQL-server User Manual, Version 1.0 . Computer Science Div., Dept. of EECS, University of California at Berkeley, 1995
- [7] Husain K., Parker T., Linux unleashed. Indianapolis: SAMS Publishing, 1996

THE RESULTS OF NUMERICAL INVESTIGATION OF A GAS FLOW IN HYPERSONIC NOZZLES AT HIGH REYNOLDS NUMBERS

M.I.Mutchnaja

Institute of Theoretical and Applied Mechanics SB RAS
630090, Novosibirsk, Russia

The problem of viscous gas flow in a hypersonic axisymmetrical nozzle of given geometry is considered for stagnation pressure values of about thousands atmospheres. This work is initiated by urgent practice, and the problem is not new in formulation. The flow is described by the system of simplified Navier-Stokes equations including vibrational nonequilibrium within the scope of the theory of two-temperature relaxation [1,2]. The difference of the present work is that the gas is not ideal in thermodynamic sense at high pressure values. This is taken into account here by the advent of the compressibility factor $p=Z(p,T)\rho RT$ into the equation of state. The value of $Z(p,T)$ is found in the tables [3] by means of two-dimensional linear interpolation.

The algorithm of the solution and the program of calculation remained practically the same as in [1]. The system of equations is solved by the marching method along the axial coordinate x using the implicit finite-difference scheme, with the application of regularization in the form of "sub-layer approximation" for suppression of upstream disturbances in the subsonic wall region. The entry conditions are set in the supersonic part of the nozzle. They are taken from the calculation of sub- and transonic flow regions using the "slender channel" model. The calculations are performed on a nonuniform difference grid refined near the wall following a logarithmic law. The boundary layer near the nozzle wall is turbulent at high stagnation parameters. In the calculation this is taken into account by using effective viscosity (the Cebeci-Smith algebraical turbulence model is used).

Modern hardware has now allowed one to obtain the results which had been inaccessible in principle when the author began similar calculations. Particularly, the operation of the work program on БЭСМ-6 permitted to set a maximum of 80 grid nodes in the radial direction. Now it is possible to set up to 1000 nodes and more on PC/AT-486. Since the step along the marching coordinate x is chosen automatically in the program and depends on the step along the radial coordinate r , then Δx is also smaller by an order of magnitude. The program for a nozzle designed for Mach numbers $M=15\div 25$ can be computed for 2-3 days on the personal computer PC/AT-486 on this small-sized grid. On the БЭСМ-6 the same program would compute during a few months, even assuming there were some capabilities of memory extension.

Figure 1 illustrates a comparison of the calculations on different grids. Here the results are shown for a conical nozzle with cone half-angle $\theta = 8^\circ$, throat section radius $r_* = 1\text{mm}$ and exit section radius $r = 300\text{mm}$. The stagnation temperature was set $T_0 = 3000\text{K}$, the stagnation pressure was $p_0 = 3000\text{atm}$, the wall temperature was $T_w = 295\text{K}$. The characteristic Reynolds number based on the throat section radius and parameters in the plenum chamber, $Re_o = \rho_o r_* (2C_{p_o} T_0)^{1/2} / \mu_o$ is equal to 7.3×10^6 , which corresponds to the unit Reynolds number $Re \approx 2 \times 10^6$ in the test section. This nozzle is intended for the high-enthalpy hypersonic wind tunnel AT- 303 created at ITAM SB RAS [4].

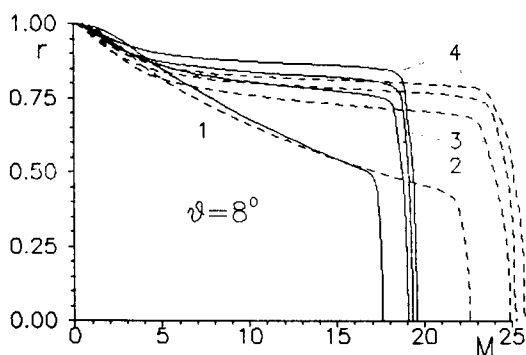


Fig. 1

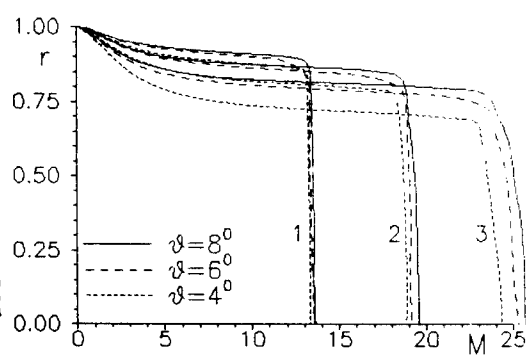


Fig. 2

The Mach number profiles are presented in Fig. 1 in two cross-sections with radii 150mm (solid lines) and 300mm (dashed lines). The distance from the axis of symmetry of the nozzle normalized by the radius of local cross-section r_w is plotted as an ordinate; $r = 0$ corresponds to the nozzle axis, $r = 1$ corresponds to the wall. Calculations were performed with the number of nodes along the radius $N = 81, 301, 501$ and 1001 (curves 1-4, respectively). The single calculation with $N = 2001$ was performed on Pentium-Pro/180, since the memory of PC/AT-486 was not sufficient for this purpose. The results of calculations with $N = 2001$ practically coincide with the version $N = 1001$ and they are not presented on the plot. The comparison shows that it is necessary to set 1000 grid nodes in the radial direction. The use of a coarser grid does not ensure sufficient accuracy of the calculation in the region of large gradients in the boundary layer, which results in overestimation of its thickness and underestimation of Mach number in the flow core. It is seen from the plot that the calculation with $N = 81$ gives completely unacceptable results. It should be noted that the calculation time of the variant with $N = 81$ on PC/AT-486/DX2/66 is 25 minutes, this time is equal to 17 hours for $N = 501$ and is about 3 days for $N = 1001$. The variant with $N = 2001$ was computed for 2.5 days on Pentium-Pro/180.

The purpose of the present work is to investigate the flow uniformity at the exit of hypersonic nozzles. Under the initial and boundary conditions mentioned above the calculations were performed for comparison of the flow characteristics in three conical nozzles with cone half-angles $\theta = 4^\circ, 6^\circ$ and 8° . The exit section radius is $r = 300\text{mm}$ for all nozzles. Hence, the length of the nozzles differs substantially, and the nozzle with $\theta = 4^\circ$ is almost twice as long as the nozzle with $\theta = 8^\circ$. The profiles of Mach number in three sections are presented in Fig. 2. The sections are such that their radii are equal for all three nozzles, while the distances from the throat section are certainly different. The numeral 1 refers to the section with radius $r_w = 60\text{mm}$, 2 - $r_w = 150\text{mm}$, 3 - $r_w = 300\text{mm}$. It is seen from the plot that the flow with a large isentropic core is realized in all nozzles. The core radius at the exit is about 0.7 of the cross-section radius for $\theta = 4^\circ$ and 0.8 - for $\theta = 8^\circ$. Besides, the larger is the cone half-angle, the thinner is the boundary layer in the sections of identical diameter and the larger is the value of Mach number. The flow in the core is practically one-dimensional for all nozzles in the section with $r = 60\text{mm}$. The radial character of the core flow manifests itself more clearly as the distance from the throat section is extended. The distributions of Mach number on the axis M_o are shown by solid lines in Fig. 3. The numeral 1 corresponds to the nozzle with $\theta = 8^\circ$, 2 - $\theta = 6^\circ$, 3 - $\theta = 4^\circ$.

The plot demonstrates decreasing of the longitudinal gradient M_o with decreasing the cone half-angle. The preference should be given to the nozzle with the cone half-angle 4° from the point of view of flow quality at the exit (the uniformity both in the longitudinal and cross-sectional directions is implied).

For the nozzle with $\theta = 4^\circ$ the flow with stagnation pressure $p_o = 1000 \text{ atm}$ was calculated for the same values $T_o = 3000 \text{ K}$ and $T_w = 295 \text{ K}$. Figure 3 shows the distribution of Mach number at the axis for this variant (small-sized dashed line). The profiles of Mach number for $p_o = 1000 \text{ atm}$ (small-sized dashed lines) and $p_o = 3000 \text{ atm}$ (solid lines) are compared in Fig. 4. It is seen how the pressure decrease (and hence, the Reynolds number decrease) affects the boundary layer growth.

For comparison the results of calculations without regard for the compressibility factor are presented, i.e., with $Z \equiv 1$ (Figs. 3-4, dashed lines). It is possible to see that the account of compressibility factor renders appreciable influence on results of calculations, especially for the nozzle with $\theta = 4^\circ$. The difference in Mach number values in the flow core is 2 % for $\theta = 8^\circ$ and 4,5 % for $\theta = 4^\circ$.

Here it is necessary to pose a question on reliability of results obtained earlier on БЭСМ-6, including the results published by the author in [2]. The following situation was revealed at repeated calculation on the personal computer of the variants submitted in [2].

The grid refinement did not lead to essential changes in results on the isentropic flow core when the calculation was performed for conical nozzles. The profiles of Mach number are shown in Fig. 5 for the conical nozzle with $\theta = 10^\circ$, experimental data for which are presented in [5]. Numerals 1 and 2 refer to the variant with $p_o = 192 \text{ atm}$ and $Re_o \approx 10^6$, the numeral 1 designates the section $x/r_* = 500$, 2 - the exit section $x/r_* = 1085$. The numeral 3 designates the section $x/r_* = 1085$ for the variant with $p_o = 50 \text{ atm}$ and $Re_o \approx 2.5 \times 10^5$. It is seen that the increase in the number of mesh nodes refines the flow pattern in the boundary layer. The border between isentropic core and boundary layer becomes less blurred, and the profiles of parameters in the core are more filled and closer to experimental data. It can be noted that the results of calculations practically coincide among themselves in the core at $N > 100$.

In these variants the characteristic Reynolds number is $Re_o \approx 10^5 \div 10^6$, therefore, the boundary layer is laminar, and just this circumstance distinguishes these calculations from those considered above. This means that in the calculations of flows with the laminar boundary layer on a coarse grid a sufficient number of nodes is ensured inside the boundary

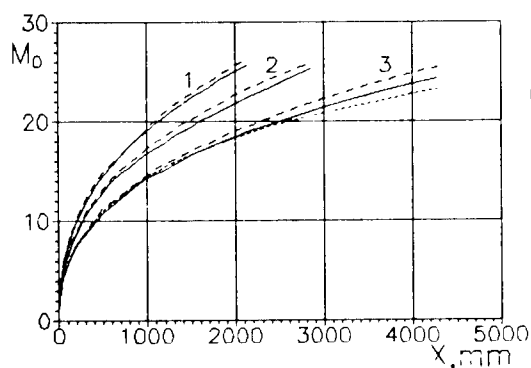


Fig.3

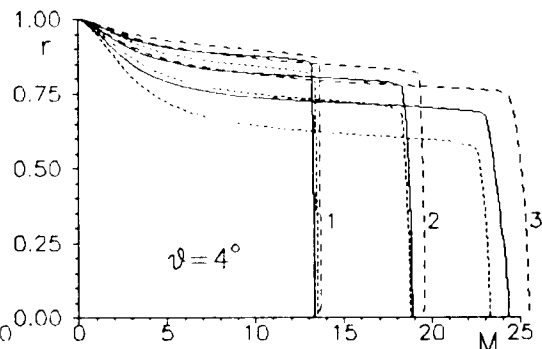


Fig.4

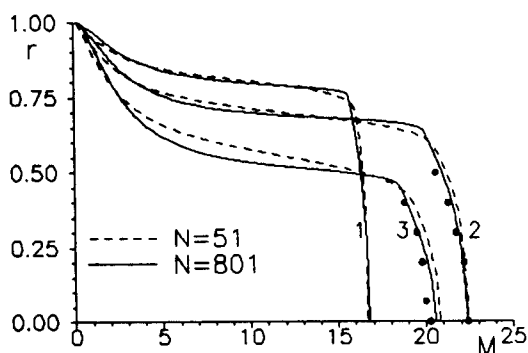


Fig. 5

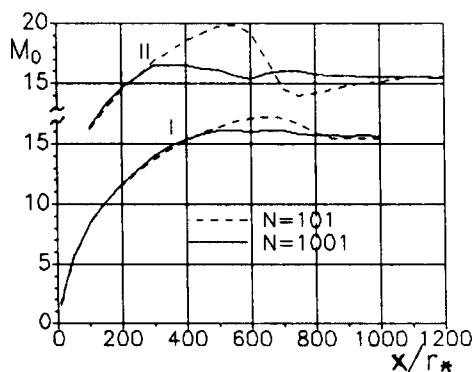


Fig. 6

layer if the grid is close to the wall. The same refinement turns out to be insufficient for the turbulent boundary layer with its much larger gradients in the wall region. This results in overestimation of the boundary layer thickness even at the first steps (see Fig. 1). Correspondingly, the size of isentropic core and the value of Mach number in the core are underestimated.

It turned out that the grid splitting results in essential changes in the core in the calculations of a laminar flow in long contoured nozzles, contrary to conical nozzles. It is illustrated in Figs. 6 and 7 which show the results of the calculations for two nozzles: I) - $\theta_{\max} = 11^\circ$, $p_o = 43 \text{ atm}$, $Re_o \approx 4 \times 10^5$; II) - $\theta_{\max} = 18^\circ$, $p_o = 100 \text{ atm}$, $Re_o \approx 6 \times 10^5$. The data for the first nozzle are presented in [6], the second nozzle is available on the wind tunnel T-326 ITAM SB RAS. Both nozzles were designed for obtaining a uniform flow with Mach number $M=15$ at their exit. The results of calculations on two computational grids are presented for each nozzle. The distribution of Mach number on the axis is shown in Fig. 6. The profiles of Mach number in several sections are shown in Fig. 7. The letters *a* and *b* refer to nozzle I, the numerals 1-3 designate the sections $x/r_* = 650, 750, 1000$. The letters *c* and *d* refer to nozzle II, the numerals 1-4 designate the sections $x/r_* = 200, 500, 700, 1030$. It should be noted that the results of the calculations of these variants with $N=501$ and $N=1001$ practically coincide.

It is seen from the plots that the flow overexpansion in the flow core which was discussed in [2] is preserved as the computational grid is refined, but to a much smaller degree than on a coarse grid. The analysis showed that in this case the reason for appreciable divergence of the results obtained on different grids is as follows. Due to contouring of the nozzle wall, the region of viscous - inviscid interaction influences strongly the flow core formation. Thus, in calculation on a coarse grid, the number of nodes on the interface between the boundary layer and isentropic core is proved to be insufficient, which results in distortion of the flow pattern.

The results of the calculations on a refined grid show that the flow in the core at the nozzle exit is fairly close to uniform. But the Mach number value proved to be slightly higher than the designed one. The longitudinal gradient of Mach number in the core is close to zero at a large distance before the exit. Thus, though the hypersonic contoured nozzle designed on the basis of the solution of an inverse problem (when the isentropic core is calculated separately and the boundary layer displacement thickness is added to it) does not fully reproduce the designed flow, but still it is not so bad as the author claims in [2].

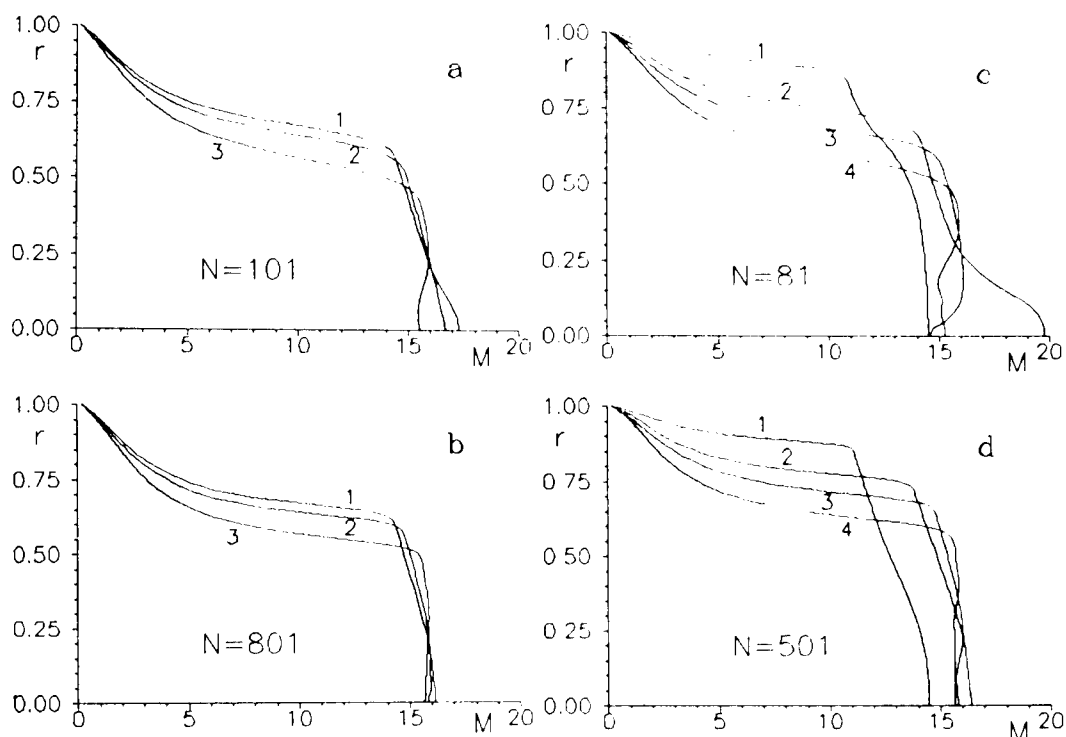


Fig.7

The author thanks V.N.Vetlutsky for the useful discussion.

REFERENCES

1. Mutchajaja M.I. The use of simplified equations of Navier-Stokes for calculation of a flow in hypersonic nozzle. - Novosibirsk, 1981. - 22 p. - (Preprint ITAM SB USSR; - N.17-81). (in Russian)
2. Mutchajaja M.I. The research of flows in hypersonic nozzles within the scope of simplified equations of Navier-Stokes // Izv. AN USSR, MZhG. - 1986. - N. 6. - P. 20-26. (in Russian).
3. Zykov N.A., Sevastjanov P.M. The matters to the calculation of gasodynamic installations with high parameters of stagnation of nitrogen // Trudy TsAGI. - 1971. - 1329. - P. 21-51. (in Russian).
4. Kharitonov A.M., Gilyazetdinov B.N., Zvegintsev V.I., Topchiyan M.E. The simulation of hypersonic flight using adiabatic compression facilities with pressure multipliers // Int. Conf. on Method of Aerophys. Research: Proc. Pt 2. - Novosibirsk, 1994. - P. 137 - 142.
5. Koppenwallner G. Der Hypersonische Vakuumwindkanal der Aerodynamischen Versuchsanstalt // Gottingen DGRR/WGLR - Jahrestagung Bad Godesberg, 1966. - X. - N. 66-113.
6. Mezhirov I.I. The research of flows in hypersonic nozzles of aerodynamic wind tunnels // Trudy TsAGI. - 1981. - 2119. - 60 p. (in Russian).

OVERVIEW OF ESA AEROTHERMODYNAMIC RESEARCH AND PROJECT ACTIVITIES (1996-1999)

**by J. Muylaert and W. Berry
ESA/ESTEC, P.O. Box 299, 2200AG Noordwijk, The Netherlands**

INTRODUCTION

At ESA, a specialist section for Aerothermodynamics was created in 1988. Over this ten year period, as the technical capabilities of the Section have increased, inevitably more demanding space missions have emerged, comprising launchers, re-entry vehicles, planetary landers and space station crew transfer and rescue vehicles. These new missions have imposed demanding aerothermodynamic requirements and challenges. These are reviewed in this paper.

Aerothermodynamics at ESTEC has now evolved into a wide field of applications encompassing all the major fluid dynamic aspects:

- External aerodynamics of aerospace vehicles, covering their complete flight regime: subsonic, transonic, supersonic and hypersonic speed. The outputs of this work are aerodynamic loads and kinetic heating rates, used for the structural design, thermal design and flight control design of the vehicles;
- External aerodynamics of aerospace vehicles to cover the transition from high altitude free molecular flow to continuum flow as vehicles enter planetary atmospheres. Flight control of vehicles during this phase require a combination of reaction control from small rocket engines and aerodynamic control from vehicle control surfaces;
- Aerodynamics of parachute and parafoil landing systems;
- Internal aerodynamics of aerospace vehicles covering the design of propulsion engine inlets, propulsive exhaust nozzles, engine flow control valves, manifolds and vents;
- Microaerodynamics which encompasses the assessment of local flow effects in gaps between thermal protection tiles; at steps between structural elements and at corners, such as those occurring at aerodynamic control surface hinges;
- Unsteady flow effects due to aerodynamic buffeting and flutter of structural elements;
- Chemically reacting flows in combustion chambers and in the shock layer of aerospace vehicle during entry into planetary atmospheres;
- Two and three phase flows in nonequilibrium, chemically frozen or equilibrium conditions where contamination or debris are concerns;
- Rocket engine exhaust plume flow impingement effects on spacecraft surfaces: forces moments, heating and contamination;
- Flow analysis of liquid-in-tube nutation dampers.

AEROTHERMODYNAMIC ACTIVITIES AT ESA

ESA is faced with challenging aerothermodynamic problems in several of its manned space flight, science, application satellite and launcher programmes. The Aerothermodynamic Section has given technical support to all these programmes and in parallel has prepared and implemented coherent TRP and GSTP research programmes to improve industrial design tools and to strengthen the co-operation between universities, research establishments and industry.

The MANNED SPACE FLIGHT PROGRAMME

Over the ten year period, this programme has been the main initiator and stimulus for a large number of aerothermodynamic activities. Its needs have resulted in the current high level of European technical expertise in experimental facilities and techniques and CFD codes for space vehicle design. The current programmes are:

ARD

The Atmospheric Re-entry Demonstrator (ARD) is a guided re-entry vehicle of the Apollo type, (Figure 1) which will be launched on the third Ariane 5 flight in October 1998. This mission will be a major achievement for Europe as the ARD will be the first ESA vehicle to perform a complete re-entry. Throughout its re-entry and descent, flight measurements will be taken to evaluate heating, transition, reaction control system interaction, ionisation (black out) and parachute deployment. The post flight analysis will give industry invaluable experience, allowing them to validate and improve their design tools.

XCRV

The Experimental Crew Rescue Vehicle (XCRV), also called the X38, is being designed as an experimental vehicle for the emergency return of crew from the International Space Station (ISS). It is a joint ESA/NASA project scheduled to have its maiden flight in late 2000. Europe plays an important role in the aerodynamic design of this vehicle. The aerothermodynamic challenges are:

- control and stability of the vehicle through its complete re-entry flight regime;
- efficiency estimates of the body flap and rudder effects of boundary layer transition;
- microaerothermodynamic effects like local heating in hinges and gaps;
- heating rates on the nose and heating effects of windward boundary layer transition;
- integration of flight instrumentation into the vehicle in a non obtrusive manner.

Figure 2 shows a multiblock surface mesh used for Navier-Stokes computations.

ATV

The Automated Transfer Vehicle (ATV) is an expendable supply vehicle for the transport of equipment and propellant to the International Space Station. During rendezvous and docking operations using small rocket engines on the vehicle, exhaust plume interaction effects will arise and these must be well understood and quantified during the design of the vehicle. The ATV must be destroyed during re-entry. Aerothermodynamic calculations must guarantee that the burn-up of the vehicle in the atmosphere takes place completely so that no parts of this large vehicle fall to Earth.

MSTP TECHNOLOGY PROGRAMME

The Manned Space Technology Programme was created to continue the development of technologies in re-entry aerothermodynamics after the cancellation of the Hermes Space Plane programme. The emphasis was on: ground test facilities; re-entry capsule critical issues; industrial CFD code improvements including code validation workshops; a parafoil technology programme; the creation of an engineering data base for design. This work was completed by the end of 1997 when the programme was terminated. Figure 3 shows the test cases for CFD validation used for the aerothermodynamic workshops and the extrapolation-to-flight approach used for design.

Plasmatron

An induction heated plasma facility (plasmatron), was designed and developed at the Von Karman Institute (VKI) in Belgium, for the study of gas surface interactions such as catalycity and ablation in a contaminant free environment.

Scirocco

The 70 MW Scirocco arc heated plasma facility is under design and construction at CIRA in Capua, Italy. It will be used for materials testing under the high temperature conditions experienced by re-entry vehicles. It will be ready for operational use by the end of 1999.

The SCIENCE PROGRAMME

Spacecraft for science programmes have to deal with plume impingement problems caused by the exhaust gases from attitude and orbit control rocket engines. Additionally, those spacecraft which must enter planetary atmospheres face critical aerothermodynamic problems.

Intermarsnet and Venus Return Mission

The ESA-NASA Intermarsnet mission will place three instrumentation stations on the surface of Mars and an Orbiter around Mars for data relay purposes. The launch is scheduled for 2003 using an Ariane 5 launcher. The stack of three stations must perform a ballistic entry into the Martian atmosphere using a heat shield to progressively reduce the vehicle's speed by aerodynamic drag. A parachute landing system will then be used to place the vehicle on the Mars surface. The aerothermodynamic issues are entry heating and vehicle stability, heat shield separation and parachute deployment.

One of the most challenging ESA scientific missions under study is the Venus Sample Return. It aims to return soil and atmospheric samples from Venus. Two Ariane 5 launchers will be required; one to launch an Orbiter composed of the Venus Orbital Module and Earth Return Module and the other to launch a Venus Lander which will enter the Venus atmosphere and descend using aerodynamic braking and parachute landing systems. For the return to Earth of rock and soil samples the Lander will use a balloon to lift the vehicle off the Venus surface. A multistage solid rocket system will then propel the vehicle to a Venus parking orbit to rendezvous and dock with the Orbiter vehicle. The Earth Return Module will then be propelled back to Earth and will enter the Earth's atmosphere and descend to a soft landing using aerobraking and parachute descent systems. The critical aerothermodynamics issues are:

- Venus aerocapture and aerobraking;
- Venus and Earth atmospheric entry and descent;
- ascent of the balloon;
- ascent of the solid rocket propelled stage.

XMM

XMM is a large spacecraft, which makes plume impingement effects from the attitude control rocket engines into a critical issue. To illustrate the work that has been done to minimise impingement effects, Figure 4 shows the thruster nozzle pressure contours, the location of the thruster and the numerical calculation grids used. A combination of Navier-Stokes codes for the nozzle flow field calculation, with a Monte Carlo analysis for the plume near field in combination with free molecular flow calculations for the thruster far field were used to address this problem.

THE SATELLITE TELECOMMUNICATION AND EARTH OBSERVATION PROGRAMME

The major aerothermodynamic problem for these spacecraft is plume impingement effects from rocket engines used for attitude and orbit control. The impingement effects from chemical rocket engines is now well understood and advanced analysis tools are available. Electric propulsion is now being introduced on these spacecraft for orbit control purposes. This will pose a new problem of impingement of ionised propellant species and this problem is now being addressed at the level of the basic physics of the phenomena.

THE LAUNCHERS PROGRAMME:

Ariane 5

Experimental and numerical studies have been carried out to assess the contamination from unused propellant as it is vented to space from the Second Stage Propulsion System (EPS) and the Attitude Control System (SCA). Another activity was the design, construction and transonic windtunnel testing of the unsteady base flow buffeting loads on the Ariane 5 vehicle. Windtunnel models were constructed for transonic and supersonic windtunnel testing. The particularity of some models are that they also simulate the plume flows, using cold nitrogen gas, from the Vulcain main engine and from the Solid Rocket Boosters. Figure 5 shows a Schlieren photograph of the flow. The compression and expansion waves are clearly visible. Activities are continuing for the study of the influence of hot plume on steady and unsteady base pressure.

FESTIP PROGRAMME

ESA's Future Space Transportation Investigation Programme (FESTIP) has been implemented to examine future reusable launcher concepts that could be of interest for Europe. For FESTIP,

aerodynamic activities were concentrated on generating aerodynamic and aerothermodynamic databases for each of the single-stage-to-orbit (SSTO) and two-stage-to-orbit (TSTO) configurations and on the definition and follow up of the FESTIP technology programme in aerothermodynamics. The technology programme focussed mainly on the following critical points: roughness induced boundary layer transition; turbulence modelling for shock wave- boundary layer interactions; flap efficiencies and heating; base flow plume interaction; flight measurement techniques; air data systems. As an example of this work, Figure 6 shows the European Experimental Test Vehicle (EXTV) studied in the context of Festip. This version is designed for vertical take-off and horizontal landing.

FLTP Programme

ESA's Future Launcher Technology Programme (FLTP) is now being prepared to continue the work undertaken in the FESTIP Technology Programme. It is expected that this programme will be started in 1999. Major aerothermodynamic activities which need to be pursued within the FLTP are:

- Improvement of measurement techniques such as pressure sensitive paint, infra red and, phosphor paint techniques for heating analysis; stereo lithography for rapid model prototyping; standardised force balances for rapid testing in transonic, supersonic and hypersonic facilities; numerical and engineering tools for aero database generation;
- Simulation of hot plumes for base plume interaction for steady and unsteady loads;
- Stage separation loads, plume interaction loads, local microaerothermodynamic loads, buffeting on protuberances and base flows;
- Transition and turbulence modelling for shock-boundary layer interactions;
- Interaction effects between aerothermodynamics, propulsion, structures and thermal protection;
- Propulsion system improvements: nozzle flow separation control; advanced nozzle concepts and integration.

TECHNOLOGY RESEARCH AND DEVELOPMENT ACTIVITIES AT ESA ON AEROTHERMODYNAMICS

A series of technology research activities have been initiated to prepare the technology needs for Europe's space programme. Some of these important programmes are:

- Development and validation of three dimensional nonequilibrium Navier-Stokes codes combined with research on parallel processing to investigate cost and time savings of executing aerodynamic codes on massively parallel computers;
- Validation experiments in hypersonic windtunnels for the study of different types of boundary layer transition mechanisms and turbulence modelling improvements for shock boundary layer interactions including the influence of hot wall effects;
- Scaling and extrapolation to flight conditions using NASA Shuttle Orbiter data for the study of the influence of real gas effects on trimming and flap efficiency. Testing in the F4 facility at ONERA and the shock tube HEG at DLR, to allow the comparison of wind tunnel data with flight data using CFD;
- Testing instrumented tiles as flown on Japan's Hyflex re-entry vehicle in the DLR plasma facilities for the study of micro-aerothermodynamic phenomena such as tile gap filler heating and local boundary layer transition;
- Improving Direct Simulation Monte Carlo codes for the study of satellite thruster plume interactions which cause forces, moments, heating and contamination;
- Optimising force balances for dynamic-derivative testing using free and forced oscillation techniques for blunt body configurations such as the Huygens probe, the ARD and the X38;
- Experimental study of base flow buffeting on simple and complex configurations such as the Ariane 5 launcher, including cold plume effects at transonic flow;
- Experimental and numerical studies of external expansion nozzles (plug nozzles) and nozzle flow separation control mechanisms for improved propulsion performance at sea level;

- Aerothermochemistry database creation and standardisation including multi-phase flows;
- Aerodynamic analysis tool development for preliminary design.

INTERNATIONAL COLLABORATION

Collaboration with partners outside Europe on specific items such as the Shuttle Orbiter and X38 with the USA, the Hyflex re-entry vehicle with Japan and Plasmatron test facilities with Russia have been very useful. An improved understanding has been obtained on critical hypersonic design problems such as the influence of real gas effects on vehicle pitch trim and flap efficiency; tile gap heating and determination of the catalytic effects of thermal protection system tile coatings.

- In co-operation with the USA, NASA Shuttle Orbiter models were tested in the ONERA and DLR High Enthalpy facilities in exchange for NASA Langley wind tunnel and flight data. This resulted in a good understanding on the use of these real gas facilities in the design process. Figure 7 shows the pitching moment versus reduced enthalpy (Ho/RT_o) as measured in some hypersonic facilities S4, F4 and comparison with flight.
- In co-operation with Japan, as part of an ESA/Japan exchange agreement; a combined experimental and numerical activity is underway in the DLR LBK facility to study the heating between tiles flown on Japan's Hyflex re-entry vehicle. The objective is to compare plasma wind tunnel data with flight data and to analyse scaling and wind tunnel-to-flight extrapolation issues. CFD plays an important role in these wind tunnel and flight re-building activities.
- In co-operation with Russia, a series of very useful activities were performed such as: lessons learned from the Russian re-entry vehicle Bor and Buran; use of Russian facilities for database creation for validation especially for thermal protection system testing. Of particular importance is the Russian expertise in plasmatron design, manufacture and testing for gas surface interaction effects: ablation; oxidation; ageing; coating catalytic behaviour. A strong collaboration is now engaged with the VKI (Belgium) where the Agency has funded a completely new 2 MW plasmatron, which is the world's largest. Figure 8 shows the VKI plasmatron performance envelope.

CONCLUSION

This paper has presented the wide scope of aerothermodynamics for aerospace vehicles and has traced ESA's activities in this field over the last 10 years since August 1988 when the Aerothermodynamics Section was first implemented at ESTEC. Aerothermodynamics has emerged as an important discipline, which is essential to enable the design of advanced launchers, re-entry vehicles and advanced propulsion systems.

The Agency is sponsoring European Industry and Research Laboratories to develop efficient numerical and improved experimental tools for aerothermodynamic design and verification. ESA's technology research programmes in aerothermodynamics have already helped European Industry to increase its competence in this field. ESA has set up a coherent research programme to meet the needs of space projects. However, in order to maintain European expertise in CFD and experimental techniques, a continuing investment is essential. For the future, ESA will continue to pursue its objective to strengthen European aerothermodynamic capabilities by co-ordinating European efforts and by promoting close collaboration between Universities, Research Establishments and Industries.

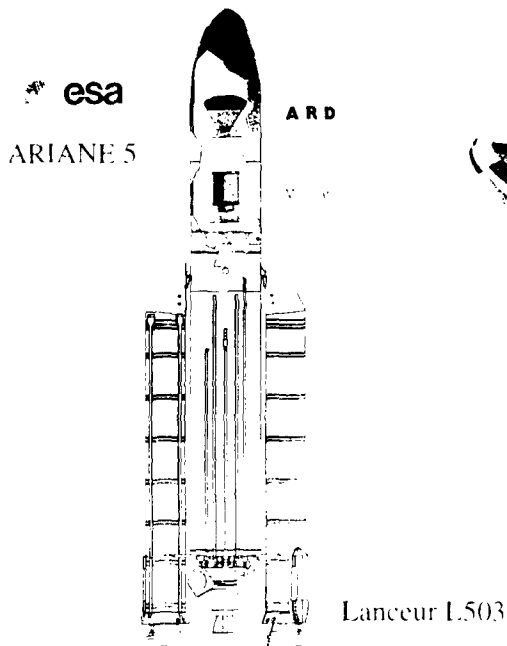


Figure 1: Atmospheric Re-entry Demonstrator

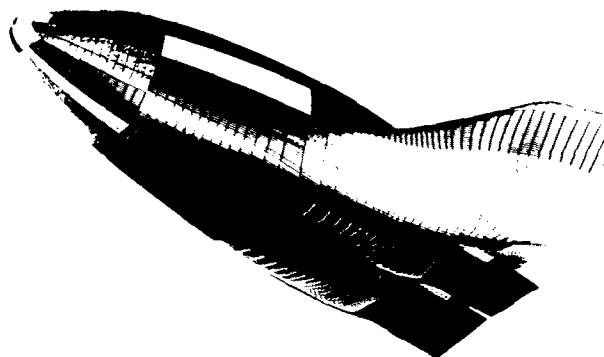


Figure 2: X38 Crew Return Vehicle
(Figure 5 and 7)

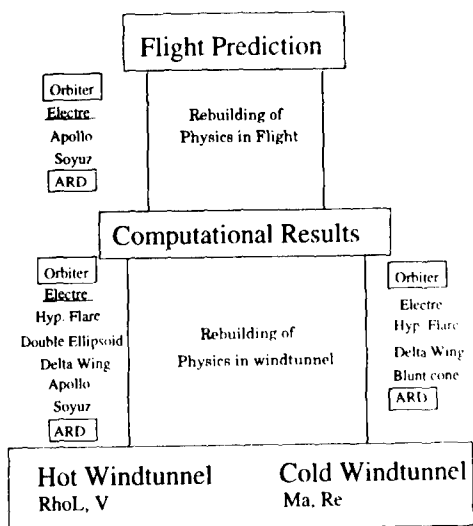


Figure 3: CFD Validation Workshop Tests Cases

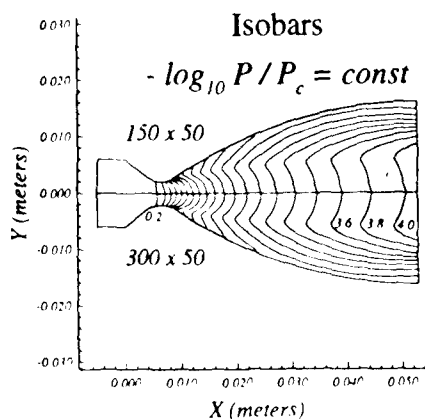
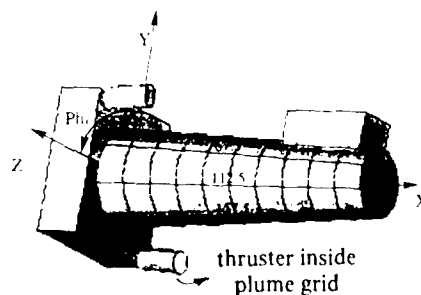


Figure 4: XMM Thruster Pressure Contour
and Surface Mesh

Figure 5: Schlieren Photo of Ariane 5 Transonic Testing at FFA with Plume Active

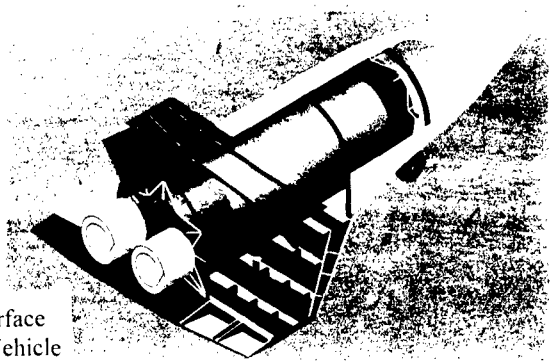


Figure 6: Proposed Layout of the EXTV Surface
the European Experimental Test Vehicle

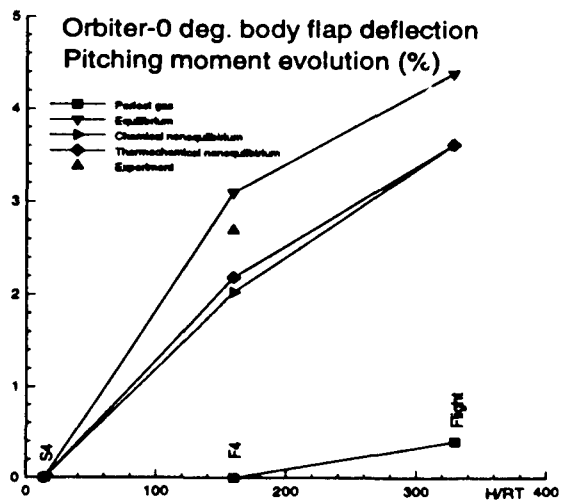


Figure 7: Orbiter Pitching Moment Evolution versus Reduced Enthalpy in S4, F4 and Flight

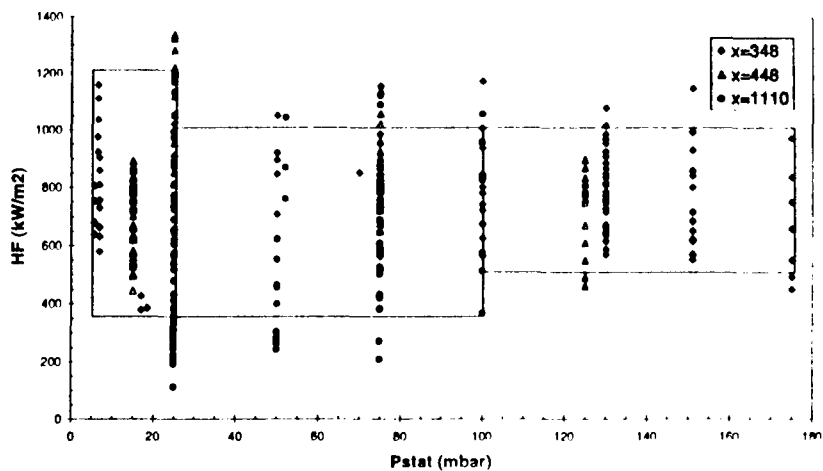


Figure 8: VKI Performance Envelope

LAMINAR-TURBULENT TRANSITION, RELAMINARIZATION, SEPARATED FLOWS, INTERACTION OF TRANSITION AND SEPARATION ON ROCKET NOSE CONES OF TWO TYPES IN A TRAJECTORY FLIGHT AT

$$\text{Re}_{L,\infty} \leq 10^8, M_\infty \leq 4.5, a \leq 32 g$$

A.M. Pavlyuchenko, O.A. Bragin, A.A. Tyutin, and A.N. Popkov

*Institute of Theoretical and Applied Mechanics SB RAS
630090 Novosibirsk, Russia*

INTRODUCTION AND PROBLEM FORMULATION

The derivation of reliable quantitative data on heat transfer and drag of bodies at $M_\infty \leq 5$ and length-based Reynolds numbers $\text{Re}_{L,\infty} \leq 10^8$ requires comprehensive studies based on ground and in-flight aerophysical experiments and on calculations employing numerical methods and computers [1]. Wind tunnels are an important tool in investigating complex aerophysical processes occurring in transonic, super- and hypersonic flows. Because of wind tunnel defects (flight Reynolds numbers are not simulated; Reynolds and Mach number, temperature factor and free-stream turbulence are not simulated simultaneously; there exists an acoustic field in wind tunnels at $M_\infty \geq 2$, etc.), the research flight experiments are becoming of great importance with the known limitation of numerical and integral calculation methods. For example, the acoustic field in wind tunnels at $M_\infty \geq 2$, generated by the turbulent boundary layers on the walls of the test sections, makes the study of transition in boundary layers on models difficult. According to Beckwith and Bertram [2], the transition Reynolds numbers for sharp-nosed cones in tunnels at $M_\infty \leq 5$ are significantly lower than under flight conditions. The length-based Reynolds number calculated for models in wind tunnels are several times smaller than those of flying craft [3]. But phenomena such as boundary layer separation, shock wave/boundary layer interaction, transition and others are a function of Re [4], so scientific flight experiments [2, 4-8] for the purpose of deriving aerophysical data over a range of variables that cannot be simulated in wind tunnels, as well as for testing calculations and comparison with wind-tunnel experiments are important.

We have previously [1, 5] proved the desirability of developing aerophysical research rockets, based on type M100 and "Oblako" ("Cloud") meteorological rockets with recoverable nose cones, designed to perform systematic studies of aeromechanics, heat transfer, turbulence, etc., at $M_\infty \leq 5$.

Figure 1 diagrams the aerophysical exploration rockets with recoverable nose cones, equipped with the standard measuring systems and multichannel telemetry described in [5]. Figure 1, *aI* shows the instrumented rocket based on the M100 meteorological rocket (1 is the spike, 2 - instrument compartment, 3 - intermediate compartment, 4 - parachute bay, 5 and 6 - 1st and 2nd stage engines). The maximum Mach and Reynolds numbers obtained with the M100 are $M_\infty \leq 4.5$ and $\text{Re}_{L,\infty} \leq 0.8 \cdot 10^8$. Figure 1, *aII* is the rocket developed on the basis of the "Cloud" meteorological rocket (1 - nose section with measuring and transmitting systems, 2 - engine, 3 - parachute bay). For the "Cloud", $M_\infty \leq 2$, $\text{Re}_{L,\infty} \leq 2 \cdot 10^7$ and $H \leq 8$ km.

The following objectives were to be attained using these two rockets

1. Obtaining quantitative data on heat transfer and pressure along the surface under real Reynolds and Mach numbers and flight conditions both in unseparated and separated flow.
2. Investigating the stability and transition in wall boundary layers with the "Cloud" rocket.
3. Investigating the effect of transient conditions on gas dynamics and heat transfer at rocket accelerations to $32g$.
4. Obtaining data on relaminarization of the compressible turbulent boundary layer on the M100.
5. Calculating the critical values of the gradient criterion of stability [9, 10] for the laminar boundary layer on a meteorological rocket of the "Cloud" type at $M_\infty \leq 2$ and for relaminarization on a meteorocket of the M100 at $M_\infty \leq 4.5$.

1. FLIGHT TEST DATA ON TRANSITION AND RELAMINARIZATION, COMPARISON BETWEEN CALCULATED AND NATURAL VALUES OF WALL TEMPERATURE

Reliable data on the Reynolds number at the onset of transition and over the length of the transition region at super- and hypersonic speeds can be currently obtained only in flight conditions. The corresponding results have been presented, for example, in [2, 3, 11-13]. The data of full-scale experiments on the transition Reynolds number in a supersonic boundary layer obtained on the forebody of a "Cloud"-type single-stage rocket aerophysical complex under the conditions of aerodynamic heating and operating engine at an acceleration $\alpha \leq 12g$ [3, 5] are of considerable practical interest, since the processes that take place under such conditions cannot be realized in wind-tunnel tests or simulated numerically. In this connection, of current interest is the problem of the laminar-turbulent transition zone, and of the model which would enable one to gain better insight into the boundary-layer turbulence on a full-scale flying object of the "Cloud" type.

Of practical interest here are the calculations of heat transfer in supersonic boundary layer reported in [14]. In this work, on the basis of both the Emmons turbulent-spot theory and the relationship between the turbulent-spot formation rate and the Reynolds number established when analyzing wind tunnel data, an expression for the intermittence factor has been obtained, which is valid for the flow around a thermally insulated surface. The known full-scale data on the laminar-turbulent transition (see, for example, [2]) were obtained on objects without operating engine. In this connection, it is interesting to compare the Re_{tr} values at three points of a "Cloud"-type complex forebody [3] in the on-power regime and on a freely flying conical body [2] for identical Mach numbers and unit Reynolds numbers. The values of Re_{tr} for $M_c=1.6$, $Re_{1,\infty}=28.6 \cdot 10^6 \text{ m}^{-1}$ turned out to be very much the same, while at $M_c=1.66$, $Re_{1,\infty}=30 \cdot 10^6 \text{ m}^{-1}$ and $M_c=1.45$, $Re_{1,\infty}=26.2 \cdot 10^6 \text{ m}^{-1}$ the Re_{tr} values for the "Cloud"-type object were found to be by 20 and 33% smaller than for the freely flying body in [2]. The latter points to a necessity to make an allowance for the effect of the operating engine of the complex upon the Reynolds number of the transition beginning.

Wall temperature distributions along nose cones of axisymmetric aerophysical missiles M100 ($Re_{1,\infty} \leq 10^8$, $M_\infty \leq 4.5$, $\alpha \leq 32g$) and "Cloud" ($Re_{1,\infty} \leq 2 \cdot 10^7$, $M_\infty \leq 2$, $\alpha \leq 12g$) were obtained by Pavlyuchenko et al. in flight tests [5]. The Reynolds numbers of transition beginning for the "Cloud" objects were found by Pavlyuchenko et al. [3, 15] under the conditions of operating engines, vibrations and deformations. The heat transfer in the boundary layer in the transition regime was calculated by means of Emmons turbulent-spot theory modified by Chen and

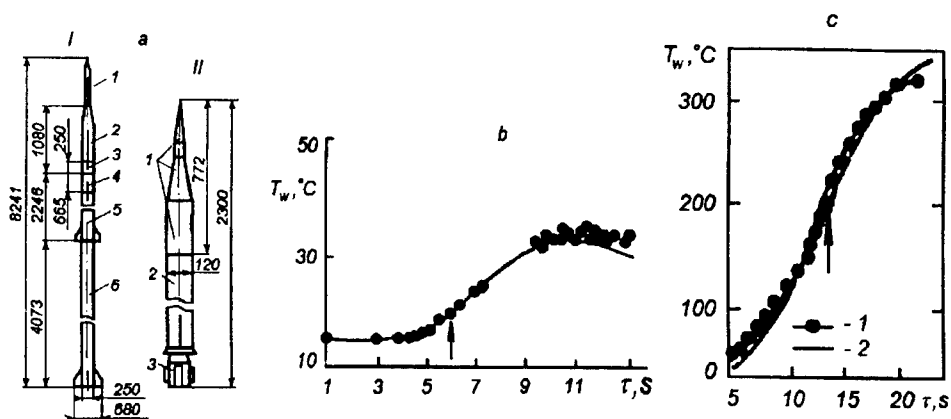


Fig. 1. Flight complexes M100 (aI), Cloud (aII) [4, 5] and dependences of the wall temperature Cloud (b) and the M100 (c) on time [3, 4, 15].

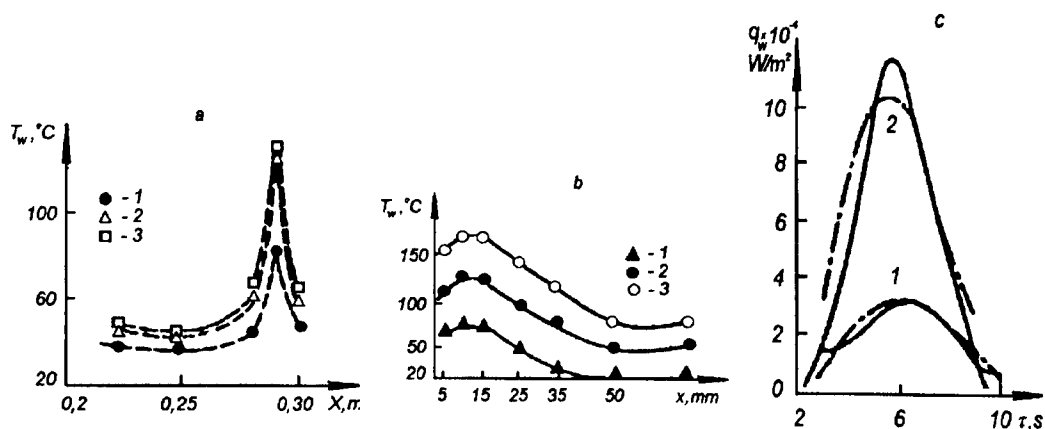


Fig. 2. Distribution of the wall temperature along the separation zones before steps on the Cloud ((a) $\tau = 6,24$ s; $7,8$ s; $9,36$ s), on M100 ((b) $\tau = 7$ s; 13 s; 17 s) and the heat flux on the Cloud ((c) 1 - before separation; 2 - in the separation zone) [6, 7]

Thyson [14], spot generation velocity being calculated on the basis of experimental transition data. Theoretical and experimental temperature values have demonstrated good agreement (Fig. 1), the arrow shows the transition beginning. The turbulent flow regime around the M100 missile formed after take-off and for flight time $\tau \approx 14-15$ s - quasilaminar one to be connected with relaminarization process. At $\tau = 87$ s boundary layer relaminarization on the Viking-10 rocket started at $Re_{x,c} = 0.9 \cdot 10^6$ [11], for $\tau \geq 87$ s an algorithm was used which contained expressions for the laminar boundary layer. Relaminarization also occurred on the M100. Numerical experiments show that it sets in at different points along the nose cone of the M100 at $Re_{x,c}$ between $3 \cdot 10^6$ and $4 \cdot 10^6$ [4]. It is seen from Fig. 1 that the in-flight and predicted wall temperature values are in rather satisfactory agreement. The arrow shows the relaminarization beginning.

2. HEAT TRANSFER ON "CLOUD" AND M100 WITH SEPARATED FLOWS

For the "Cloud" rocket we have also obtained data on the temperature distribution over the zone where there is flow separation, upstream of a step on the nose cone produced by a ring with $h = 6$ mm placed at $X = 312$ mm [6]. The boundary layer thickness was such that $\delta < h$. Prior to separation the boundary layer was laminar [3, 6]. Figure 2 presents the wall temperature distribution along the separation zones for times of 6.24, 7.8, and 9.36 s. The local temperature maximum is due to reattachment to the wall of the flow generated by interaction between secondary circulation flow and vortex in the lower corner of the step. The temperature peak in Fig. 2 is due to reattachment of the flow on the wall near the step when the flow in the separated boundary layer is transient [6]. In accordance with Fig. 2, for the "Cloud" the length of separation region was $L_{sep}/h = 15$. For M100, where the separating boundary layer was turbulent, $L_{sep}/h \leq 4.67$ (Fig. 2, [7]). The presence of the temperature peak on the "Cloud" (see Fig. 2), its value prior to separation [3, 6] and the length of the separation region show that the laminar flow in the separated boundary layer becomes unstable and the flow in it becomes transient or turbulent.

3. GRADIENT CRITERIA OF TRANSITION AND RELAMINARIZATION FOR FLIGHT CONDITIONS OF FLOW AROUND BODIES

Gradient criteria of stability suggested by Yanenko, Gaponov [9] and Van Driest, Blumer [10] seem to be promising for the problem of laminar-turbulent transition and relaminarization at natural conditions of flow around bodies in the presence of heat transfer. Yanenko et al criterion Re_{gr} is invariant for many regimes and types of flows. Van Driest et al number T_r is not invariant. Both of them take into account local properties and are approbated for flows to be idealized. Application of these to flight conditions demands some additional verification. Approbation of these two criteria for natural conditions has been realized on the basis of flight data and numerical simulation integration method suggested by Pavlyuchenko et al [16]. According to that, having solved the system of compressible boundary layer equations an experimentally measured wall temperature distribution is used in boundary conditions for the above mentioned system. Velocity profiles were approximated by a cubic spline which allows one to exclude additional errors in velocity derivatives. Figure 3 demonstrates the dependence of Yanenko, Gaponov [9] and Van Driest, Blumer [10] criterion on the vertical coordinate of laminar boundary layer for "Cloud" and M100 nose cones. Behavior of criteria under consideration is of great practical interest in the beginning of laminar-turbulent transition and

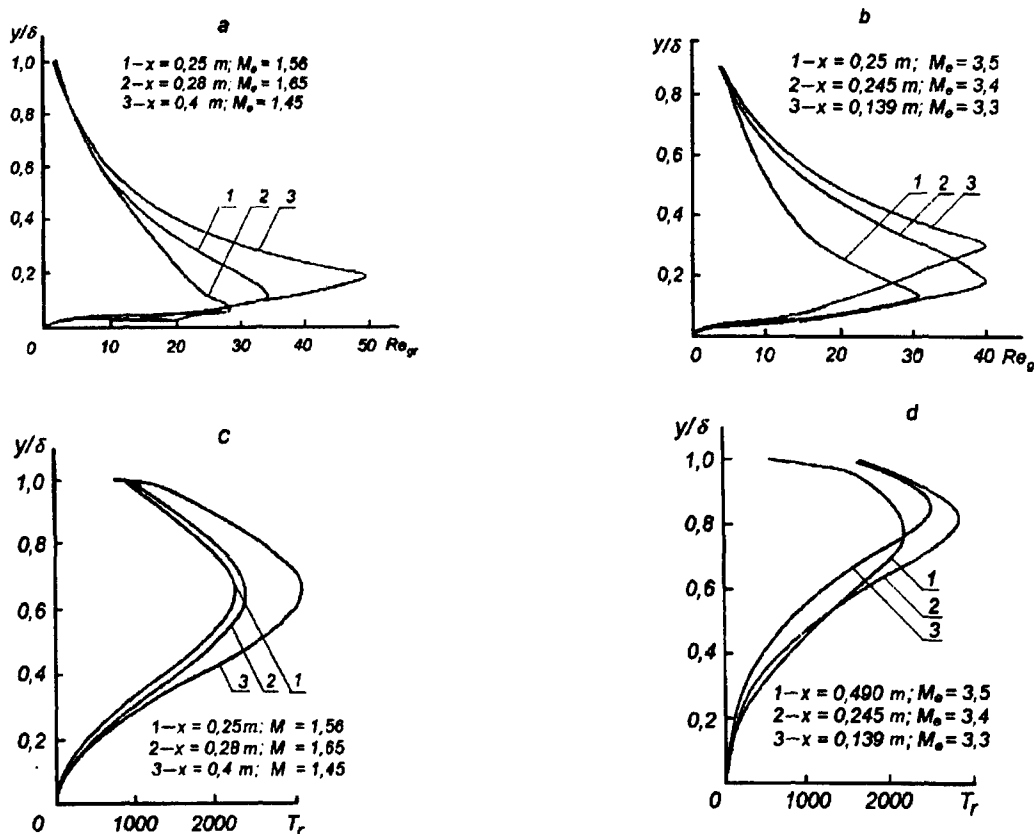


Fig. 3. Gradient stability criteria of N.N. Yanenko, S.A. Gaponov (a, b) and Van-Driest, Blumer (c, d) in the beginning of transition (a, c) and in the beginning of relaminarization (b, d) [16, 17].

relaminarization on nose cones of the "Cloud" and M100, respectively. The data for Re_{gr} are shown in Fig. 3. Distributions of Re_{gr} and T_r are obtained for the supersonic flow conditions. The distribution of Re_{gr} and T_r criteria in Fig. 3 in transition and relaminarization regions, respectively, differ considerably [16, 17]. The Re_{gr} criterion is more suitable for physical conditions of transition. The difference in Re_{gr} and T_r distributions in transition and relaminarization regions is both qualitative and quantitative.

Invariant criterion of Yanenko and Gaponov is more physically and mathematically grounded in comparison with Van Driest and Blumer one. Invariant criterion Re_{gr} may be recommended for analysis of stability, transitions and relaminarization in real flight conditions of supersonic flow around bodies.

The presented results have a scientific and practical significance and contribute to solving the scale effect problem in the high-speed aerodynamics.

REFERENCES

1. Zheltukhin N.A., Pavlyuchenko A.M. Scientific problems in designing an airborne for aerophysical studies // *Appl. Aerogas dynamics*. - Novosibirsk: ITAM SB RAS. 1980. - P. 3-22.
2. Beckwith I.E., Bertram M.H. A survey of NASA Langley studies on high-speed transition and the quiet tunnel. - NASA TM-X-2566. - 67 p.
3. Pavlyuchenko A.M., Maksimova E.M. Numerical method of processing of a flight thermal experiment on a meteorocket of a "Cloud" type with the theory of turbulent spots proposed by Emmons // *Izv. SO AN SSSR, Ser. tekhn. nauk*. - 1983. - Iss. 2. - No. 8. - P. 27-35.
4. Pavlyuchenko A.M. Heat transfer on axisymmetric rocket nose cones with separationless and separated flows // *Heat Transfer / Soviet Research*. - 1984. - Vol. 16. - No. 4. - P. 115-129.
5. Pavlyuchenko A.M., et al. Flight temperature and pressure measuring on the saved head part of meteorockets of M100 type and the "Cloud" // *Izv. SO AN SSSR, Ser. tekhn. nauk*. - 1983. - Iss. 1. - No. 3. - P. 46-54.
6. Pavlyuchenko A.M., Tyutin A.A., Korablev A.V. Heat transfer on an "Oblako" meteorological rocket with boundary layer separation // *Ibid.*, - 1984. - No. 4/1. - P. 52-63.
7. Pavlyuchenko A.M., Bragin O.A., et al. Aerophysical experiments at the meteorockets of M100 type with boundary layer separation // *Ibid.*, - 1987. - Iss. 2. - No. 7. - P. 71-79.
8. Pavlyuchenko A.M., Bragin O.A. Study of aerophysical and dynamical characteristics at the reusable flight axisymmetrical complex // *Sib. Fiziko-Tekhn. J.* - 1992. - Iss. 1. - P. 66-76.
9. Yanenko N.N., Gaponov S.A. Invariant criteria of stability of compressible fluid flows // *DAN SSSR*. - 1981. - Vol. 259. - No. 5. - P. 1056-1059.
10. Van Driest E.R., Blumer C.B. Boundary layer transition: freestream turbulence and pressure gradient effects // *AIAA J.* - 1963. - Vol. 1. - No. 6. - P. 1303-1306.
11. Snodgrass. Flight measurement of aerodynamic heating and boundary layer transition in the Viking10 nose cone // *Rocketry Problems*. - 1957. - No. 1. - P. 28-39.
12. Beckwith I.E., Greel T.R., Chen F.J. Free stream noise and transition measurement in a Mach 3.5 Pitot quiet tunnel // *AIAA-83, 21st Aerospace Science Meeting*. 1983. - P. 1-17.
13. Berkowitz A.M., Kyriss C.I., Martellucci A. Boundary layer transition flight test observations // *AIAA Paper* 77-125. - 1977. - 41 p.
14. Chen K.K., Thyson N.A. Extension of Emmons spot theory to flow on blunt bodies // *AIAA J.* - 1971. - Vol. 9. - No. 5. - P. 821-825.
15. Pavlyuchenko A.M., Tyutin A.A., Maksimova E.M., Bragin O.A. On the problem of transition of compressible laminar boundary layer into turbulent one under natural conditions // *Laminar-Turbulent Transition: Proc. IUTAM Symp.* - Berlin: Springer-Verlag. 1984. - P. 547-551.
16. Pavlyuchenko A.M., Maksimova E.M., Popkov A.N. Gradient criteria of stability, transition and relaminarization of supersonic near-wall boundary layers for flight conditions of the flow around nose cones of axisymmetric aerophysical complexes M100 and "Cloud". - Novosibirsk. - 1995. - 30 p. (Preprint / ITAM SB RAS; № 7-95).
17. Lentjev A.I., Pavlyuchenko A.M. Gradient criterion of transition, relaminarization and friction drag in supersonic boundary layers on flying objects at heat exchange // *Proc. 10th Int. Heat Transfer Conf.* Vol. 3. - Brighton., 1994. - P. 41-45.

WIDE APERTURE TOMOGRAPHY METHOD IN FLOW INVESTIGATION

V. V. Pickalov, N. V. Chugunova

Institute of Theoretical and Applied Mechanics SB RAS.

630090, Novosibirsk, Russia

Tomography methods which allow for determining the internal structure of an object on the basis of integral characteristics (projection data) have been known for a long time. The classical methods of reconstruction ignore the detector geometry, and tomography algorithms for image reconstruction are developed assuming the projection data to be obtained by integration along infinitely thin lines. In a real experiment, however, the detector accepting the signal has always a certain width and, in the general case, a nonzero angular aperture prescribed by the collimator.

An iteration algorithm capable of taking into account the geometry and position of an arbitrary detector is suggested and studied in the paper.

INTRODUCTION

The objective of emission tomography in a two-dimensional formulation is the reconstruction of the internal structure of an object in a plane cross-section on the basis of projections obtained by registering the radiation of this object in several directions [1].

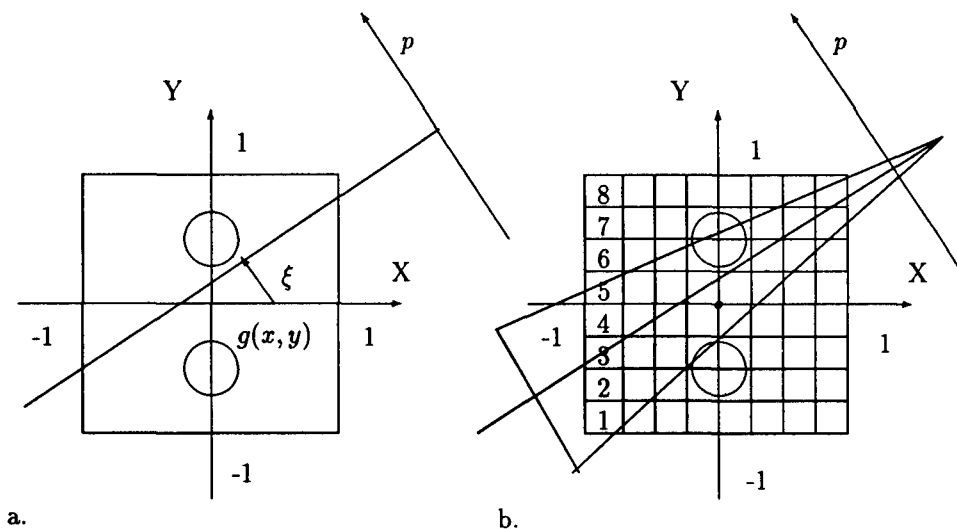


Figure 1: Schemes for obtaining projection data: a) classical scheme, b) scheme for a wide-aperture detector.

Let the function $g(x, y)$ describes a sought distribution (Fig. 1(a)), for example, spatial distribution of refractive index, density, etc. The projection of this function along a certain line $L_{\xi p}$ is the integral $f_{\xi p}^0 = \int_L g(x, y) dL_{\xi p}$, called the line integral, and a set of line integrals forms the projection. Thus, it is necessary to determine the function $g(x, y)$

on the basis of known projections $f^0(p, \xi)$. This problem refers to the class of ill-posed inverse problems of integral geometry, and there are many approaches to its solution [2].

It was shown in [3] that when integrals over a band determined by detector geometry are used instead of line integrals, the classical reconstruction algorithm yields a solution which is too smooth (Fig. 2(d)). This study was performed for a standard algorithm of filtered back projection (FBP). Two iteration algorithms taking into account the detector geometry were considered in the same paper. The first algorithm is the ART modification, the second one is based on expansion of the inverse operator with respect to direct operator powers into the Neumann series (ENS). The numerical experiment showed that both algorithms yield comparable results for narrow bands. If the detector determines a wider band, however, the ART reconstruction becomes too smooth. This effect was not observed for the second iteration algorithm, but the iteration process was unstable. The present paper is devoted to further development of the ENS iteration algorithm.

ITERATION PROCESS USING EXPANSION INTO THE NEUMANN SERIES

The inverse operator expansion with respect to direct operator powers has been known for a long time, though this approach is seldom used for tomography problems [5, 6].

Let us use the approximation - split the domain, in which the tomographic reconstruction is performed, into elementary cells - *pixels*. The value of emission coefficient is assumed constant in each pixel. As a result, we obtain a system of linear algebraic equations $Ag = f$ where A is the matrix of coefficients containing the areas of pixels in a diverging band determined by the detector (see Fig. 1(b)), $g(x, y)$ is the tomogram, and $f(p, \xi)$ is the projection obtained in this band.

Let $Ag = f$ is the operator representation of the problem, then $g = A^{-1}f$, however, the operator A^{-1} is unknown. The matrix approximation of the operator A usually leads to matrices with very large dimensions, and direct methods of obtaining the inverse matrix A^{-1} become inefficient. Let us represent A in the form $A = BA_0$, $B = AA_0^{-1}$ where A_0^{-1} is some known approximation to the operator B^{-1} (for example, the operator of solving the tomography problem in infinitely thin beams). The Neumann series for the operator B^{-1} can be then written as

$$g = A_0^{-1} \sum_{k=0}^{\infty} \lambda^k (E - B)^k f = A_0^{-1} B^{-1} f = A^{-1} f, \quad (1)$$

where E is the unit operator, λ is the real number called the relaxation parameter. The convergence condition for a unit sphere is $|\lambda| \|E - B\| \leq 1$.

Then the iteration ENS algorithm is described by the formula

$$g_{ij}^{l+1} = g_{ij}^l + \lambda^l A_0^{-1} r^l = g_{ij}^l + \lambda^l I_{SL} r^l, \quad (2)$$

here g_{ij}^{l+1} is the reconstruction result at the $(l+1)$ th iteration, λ^l is the relaxation parameter at the l th iteration, a_{ij} are the elements of the matrix A , $I_{SL} = A_0^{-1}$ is the operator of solving the problem in infinitely thin beams (the FBP algorithm with Shepp-Logan filter [4] was used in this case), f is the source projection, f_d^l is the pseudoprojection at a given iteration $f_d^l = Ag^l$, $r^l = f - f_d^l$ is the residual vector.

When working with the operator I_{SL} , scaling is needed to correlate the units. The mean band width determined by detector geometry was chosen for scaling. To suppress the influence of random experimental noise, regularized cubic splines were used [5]. The performance of this algorithm without normalization were partly studied earlier in [3].

In emission tomography, the examined function cannot take negative values. This a priori information about the object was taken into account in the numerical simulations. After each iteration the obtained negative values were set to zero.

NUMERICAL SIMULATIONS

A mathematical phantom modeling an emission object in the form of an asymmetric model composed of two gaussians was chosen for the study (Fig. 2(a)):

$$g(x, y) = C \exp \left\{ -\frac{4 \ln 2}{a^2} (x'' - x_0'')^2 - \frac{4 \ln 2}{b^2} (y'' - y_0'')^2 \right\}, \quad (3)$$

with parameters $a_1 = a_2 = b_1 = b_2 = 0.25$, $x_{01} = x_{02} = 0$, $y_{01} = 0.5, y_{02} = -0.5$, $C_1 = C_2 = 1$.

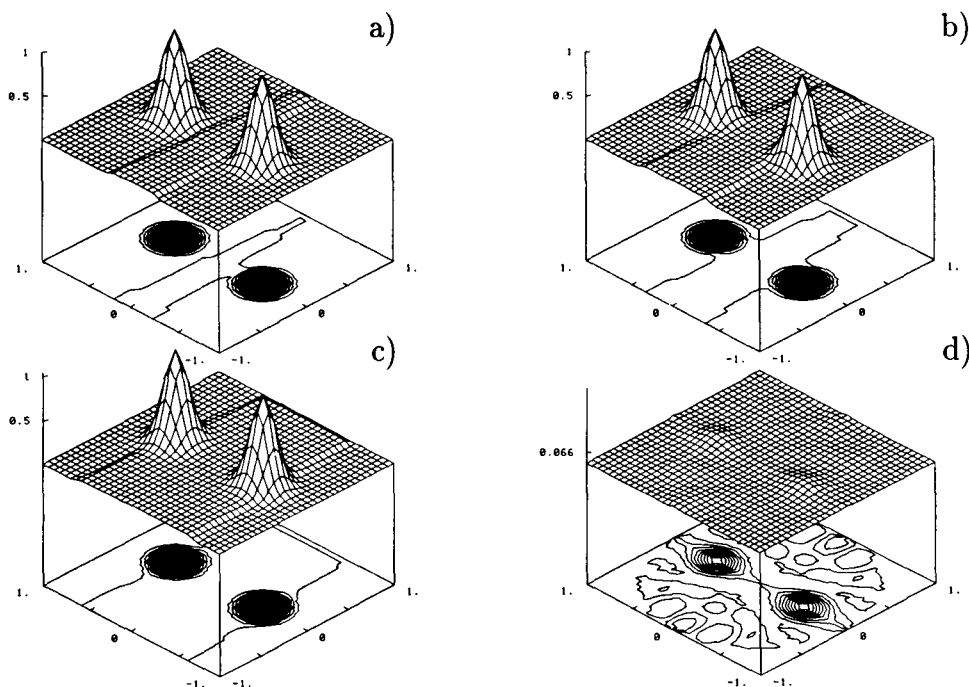


Figure 2: Detector trace of tomograms for the distance to the detector $R_q = 1.5$ (a), $R_q = 3$ (b), and $R_q = 6$ (c), Shepp-Logan reconstruction (d).

The reconstruction error was studied in the numerical experiment as a function of band configuration determined by various detector parameters. The reconstruction error (in percentage) was determined from the formula

$$\Delta_1^2 = \frac{\sum_i \sum_j (g_{ij} - g_{ij}^e)^2}{\sum_i \sum_j (g_{ij}^e)^2}. \quad (4)$$

Here g_{ij}^e is the exact model, g_{ij} is the reconstructed tomogram.

The modeling was performed with the number of observation angles $K=6$, the number of detectors for one view $N = 21$, tomogram size $N_x = N_y = 33$.

Figure 2 shows the tomograms with the traces of the "observation band" of one detector, the band width being varied. This detector had the following parameters: aperture angle $\alpha = 5^\circ$, detector width $R_d = 0.1$, distance between the detector line and the origin $R_q = 1.5$ (a), 3 (b), and 6 (c). Figure 2(d) shows the reconstruction result from 6 views by the classical method of filtered back projection (FBP) using the Shepp-Logan filter and ignoring the detector geometry ($R_q = 1.5$). It is seen in the figure that the reconstruction is too smooth, the reconstruction error is $\Delta_1 = 86\%$.

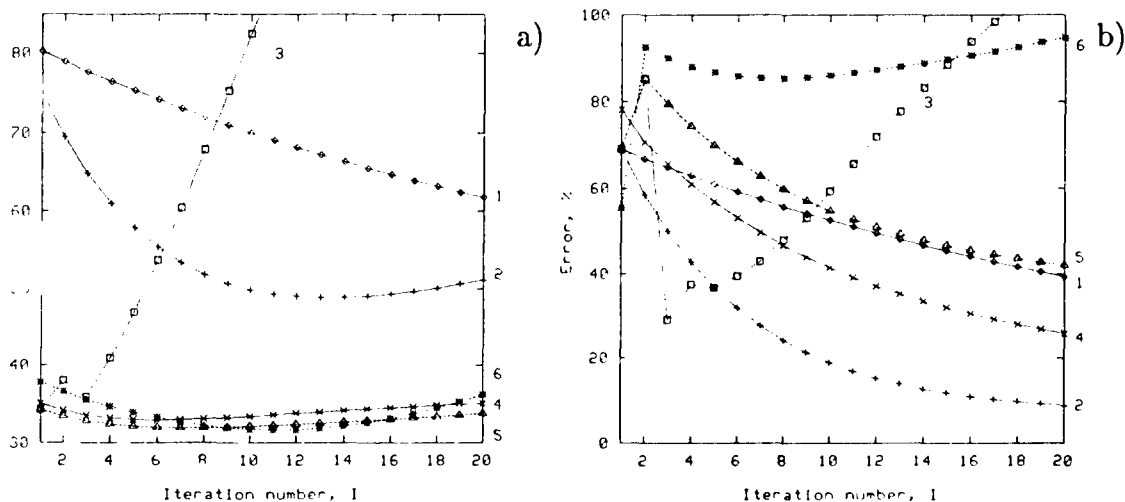


Figure 3: ENS algorithm: a) reconstruction error Δ_1 , (%), b) residual norm Δ_1 , (%).

Figure 3(a) shows the reconstruction error Δ_1 versus the relaxation parameter for the ENS algorithm.

Curves 1-3 here were obtained for $R_q = 3$, $\lambda = 0.1$ (1), $\lambda = 0.5$ (2), $\lambda = 1.5$ (3). Curves 4-6 were obtained for varied $\lambda = 1.5$ for the first iteration and 0.1 for the rest iterations, $R_q = 1.5$ (curve 4), $R_q = 3$ (curve 5), and $R_q = 6$ (curve 6). Figure 3(b) shows the corresponding residual norms.

For $\lambda = 0.1$ (Fig. 3(a), curve 1) the iteration process converges very slowly and reaches $\Delta_1 = 33\%$ (the number of iterations $I = 100$). Increasing λ , the iteration process starts to diverge, but the value of $(\Delta_1)_{\min}$ decreases. For $\lambda = 1.5$ (curve 3) we obtained the best values of Δ_1 for three first iterations with subsequent rapid divergence. Obviously, it is necessary to stabilize the iteration process to preserve the advantages of the first iterations for large λ and convergence for small λ . A modified approach was developed and studied. This approach is based on varying the relaxation parameter λ for each step of the iteration process. For example, for $R_q = 1.5$ the most successful combination was $\lambda = 1.5$ for the first step and 0.1 for all other steps of the iteration process $\Delta_1 = 32.9\%$ (Fig. 3(a), curve 4). The iteration process reaches the minimum error with a small number of iterations.

It should be noted that for varying R_q by a factor of 2-4, the modified algorithm yields good results, the reconstruction error changes only by 2-3% (curves 5 and 6).

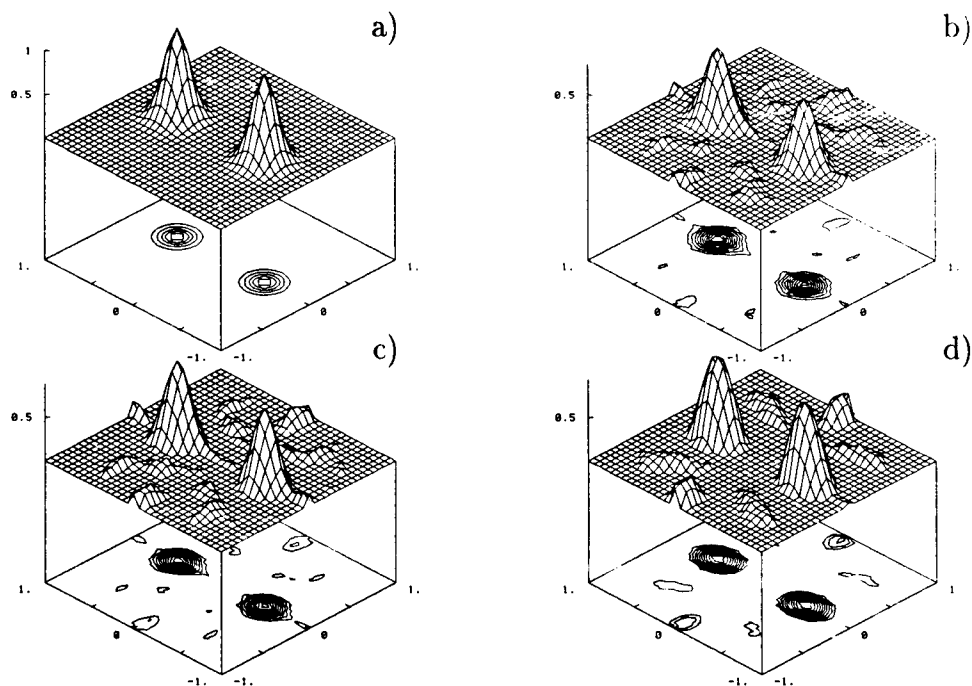


Figure 4: a) exact tomogram, b)-d) reconstruction by the ENS algorithm with varied λ , 20 iterations, $R_q=1.5$ (b), $R_q=3$ (c), $R_q=6$ (d).

Appropriate tomograms are shown in Fig.4. Let us note that an increase in band width affects to a certain extent the character of artifacts, but the overall pattern remains practically the same.

CONCLUSION

A modified algorithm has been developed and studied. This algorithm is based on expansion into the Neumann series, which allows one to take into account the detector geometry in the course of reconstruction. The modification is the relaxation parameter variation during the iteration process. It has been shown in numerical experiment that when the relaxation parameter increases, the iteration process based on the Neumann series with a constant λ diverges. The modified algorithm allows the user to stabilize the process and achieve a more stable result little dependent on the bandwidth changes ($R_q = 1.5-6$).

The authors are thankful for partial support by the Russian Foundation for Basic Research and the Netherlands Organization for Scientific Research (NWO).

References

- [1] Herman G.T. Image Reconstruction From Projections. The Fundamentals of Computerized Tomography. New York: Academic Press, 1980.
- [2] Natterer F. The Mathematics of Computerized Tomography. Stuttgart: Wiley, 1986.

- [3] Pickalov V.V., Shugurova N.V. The algebraic algorithms of optical tomography for wide apertures // IV Conf. "Optical methods of flow research": Abstr. Moscow: VALANG, 1997. P. 100-102. (in Russian)
- [4] Shepp L.A., Logan B.F. The Fourier reconstruction of a head section // IEEE Trans. 1974. NS-21. P.21-43.
- [5] Pickalov V.V., Melnikova T.S. Plasma Tomography. Novosibirsk: Nauka, 1995. (in Russian)
- [6] Likhachov A.V, Pickalov V.V. New algorithm of the emission 3D-tomography for optically thick plasma // Proc. of the 12th Int. Conf. on Gas Discharges and their Applications. Greifswald, 1997. Vol.2. P.484-487.

ON THE THEORY OF PARAMETRIC EQUATIONS OF TWO-DIMENSIONAL LAMINAR BOUNDARY LAYER

A.N. Popkov

Institute of Theoretical and Applied Mechanics SB RAS, 630090 Novosibirsk, Russia

1. **The present work** is a logical continuation of the paper [1]. To facilitate the understanding of the present paper, it is necessary to recall some facts and definitions from [1], wherein the equations of 2D steady laminar boundary layer of incompressible fluid in the presence of pressure gradient are reduced to the parametric form. After introducing the stream function Ψ and using the transformations of dependent and independent variables

$$\xi = \xi(x), \quad y = \delta(x) \cdot \eta, \quad \Psi = U_e \cdot \delta(x) \cdot \Phi[\xi(x), \eta],$$

these equations reduce to the known nondimensional formulations

$$L(\Phi, \chi, \beta_1) = \alpha \cdot [\Phi, \dot{\Phi}]_{(\eta, x)}(a), \quad L(\Phi, \chi, \bar{\beta}_1) = \bar{\alpha} \cdot [\Phi, \dot{\Phi}]_{(\eta, \xi)}(b), \quad (1)$$

with "standardized" boundary conditions

$$\eta = 0 : \Phi = 0, \quad \dot{\Phi} = 0; \quad \eta \rightarrow \infty : \dot{\Phi} \rightarrow 1; \quad (2)$$

with the operator

$$L(\Phi, \chi, \beta_1) = \ddot{\Phi} + \chi(x) \cdot \Phi \ddot{\Phi} + \beta_1(x) \cdot (1 - \dot{\Phi}^2).$$

The right-hand sides of (1a) and (1b) are the Poisson brackets, e.i.,

$$[\Phi, \dot{\Phi}]_{(\eta, x)} = \dot{\Phi} \frac{\partial \Phi}{\partial x} - \Phi \frac{\partial \dot{\Phi}}{\partial x},$$

whose specific features are that they contain derivatives with respect to x or to ξ . The functions $\chi(x)$, $\beta_1(x)$, $\delta(x)$ are determined by the relations

$$\chi(x) = 0.5(\alpha + \beta_1), \quad \beta_1(x) = \alpha \frac{\dot{U}_e}{U_e} = \bar{\beta}_1 = \frac{\bar{\alpha}}{U_e} \frac{dU_e}{d\xi},$$

$$\delta(x) = \sqrt{\alpha \nu / U_e}, \quad \alpha = 2\xi / \xi', \quad \bar{\alpha} = 2 \cdot \xi.$$

(The dot denotes the derivative with respect to η , the prime indicates the derivative with respect to x).

It should be noted that the transformation of the longitudinal coordinate $\xi(x)$ is an arbitrary function, and it is possible to impose the conditions of differentiability and continuity on it. The resultant nondimensional equations (1) can be considered as general. Particular equations are obtained by specifying the functions $\xi(x)$. This nondimensionalization of the boundary layer equations is a mandatory first stage of parametrization. The second stage is the introduction of a recurrent sequence of parameters following the general rule [1].

© A.N. Popkov, 1998

To form a sequence of parameters, it is necessary to raise the Poisson bracket factor α or $\bar{\alpha}$ to the recurrent power k and multiply it by the k th derivative with respect to x or ξ (depending on the parametrized nondimensional form of (1)) of the external flow velocity, and divide it by the value of this velocity.

Thus, for equations (1a) and (1b) the recurrent sequences of parameters are

$$\beta_k = \frac{\alpha^k}{U_\epsilon} \frac{d^k U_\epsilon}{dx^k}, \quad \bar{\beta}_k = \frac{\bar{\alpha}^k}{U_\epsilon} \frac{d^k U_\epsilon}{d\xi^k}, \quad k = 1, 2, 3, \dots \quad (3)$$

For parameters of (3) we have two parametric forms of boundary layer equations:

$$L(\Phi, \chi, \beta_1) = \sum_{k=1}^{\infty} [(2k\chi - (k+1)\beta_1)\beta_k + \beta_{k+1}] \cdot [\Phi, \dot{\Phi}]_{(\eta, \beta_k)}, \quad (4)$$

$$L(\Phi, \chi, \bar{\beta}_1) = \sum_{k=1}^{\infty} [(2k\chi - \bar{\beta}_1)\bar{\beta}_k + \bar{\beta}_{k+1}] \cdot [\Phi, \dot{\Phi}]_{(\eta, \bar{\beta}_k)}, \quad (5)$$

The boundary conditions for equations (4) and (5) coincide with (2). The initial conditions are determined when specifying the equations, i.e., when setting $\xi(x)$ in each particular case. The choice of the function $\xi(x)$ is determined by the conditions of full parametrization of (4) and (5). This means that the function $\chi(x)$ should depend only on the parameters

$$\chi(\beta_k) \quad \text{or} \quad \chi(\bar{\beta}_k). \quad (6)$$

It can be shown that there are such $\xi(x)$ for which equations (4) and (5) yield known parametric equations. Assuming $\xi = x^2$, (4) is transformed to the equation derived in [2]. For

$$\xi = \epsilon xp(2c^2 \int_0^x \frac{dx}{U_\epsilon Z^{**}}), \quad Z^{**} = \delta^{**}/\nu$$

equation (4) yields the 'universal' equation [3]. The use of the Gortler transformation allows one to obtain the parametric equation from [4]. Thus, the presented examples show that equations (4), (5) generalize the known parametric forms.

All above statements are a formal mathematical derivation of parametric equations. However, of principal importance is not the notation of this or that equation, but the information about the type of boundary condition $U_\epsilon(x)$, which is 'encoded' in a given equation, in its successive approximations.

The basic characteristic of a parametric equation is a class of functions $U_\epsilon(x)$ determined by the structure of parameters and, sometimes, by the notation of this equation.

If the conditions

$$\beta_k = 0 \quad \text{or} \quad \bar{\beta}_k = 0, \quad k = 1, 2, 3, \dots$$

are valid in the singular point of the parametric equations (4) and (5), the initial conditions for these equations are determined by the solution of the Blasius equation

$$\ddot{\Phi} + \chi_0 \cdot \Phi \ddot{\Phi} = 0, \quad \text{where} \quad \chi_0 = \text{const} \neq 0. \quad (7)$$

As shown in [1], equation (4) describes the boundary layer flow for the external flow velocity presented in the form of an arbitrary power series with respect to the physical coordinate x :

$$U_e = a_0 + a_1x + a_2x^2 + a_3x^3 + \dots + a_kx^k + \dots = a_0 + \sum_{k=1}^{\infty} a_kx^k. \quad (8)$$

Thus, (4) is a generalized equation for a wide class of external velocity distribution functions - a class of analytical functions.

Parametric equations with different notation and structure of parameters but determining the same class of distribution functions of external velocity $U_e(x)$ will be called **equivalent**. For example, the equations of [2] and [3] are equivalent since they describe the boundary layer flow with $U_e(x)$ (8), though the notation is substantially different.

Equation (5) is generalized for even wider class of functions $U_e(\xi)$

$$U_e = b_0 + b_1\xi + b_2\xi^2 + b_3\xi^3 + \dots + b_k\xi^k + \dots = b_0 + \sum_{k=1}^{\infty} b_k\xi^k.$$

If equations (4) are equivalent irrespective of the choice of $\xi(x)$, then equations (5) depending on $\xi(x)$ will describe the boundary layer flows with different distributions $U_e(\xi(x))$.

2. Equations (4) and (5) describe the boundary layer development on bodies either from the stagnation point or with a zero taper angle. This means that these equations do not contain initial singular points where we could obtain self-similar solutions for the Hartree parameter interval $0 < \beta_X < 1$, which is the initial condition for pointed bodies with the taper angle varied within $0 < \varphi < 2\pi$. To obtain such parametric equations, we present the parameter $\beta_1(x)$ in the form of the sum of a certain constant κ and a quantity $\gamma_1(x)$:

$$\beta_1(x) = 2\kappa + \gamma_1(x). \quad (9)$$

The function $\gamma_1(x)$ can be represented as the first parameter

$$\gamma_1(x) = \alpha z / z. \quad (10)$$

For the desired function $z(x)$, taking into account (9) and (10), we obtain the first-order ordinary differential equation. After its integration we determine $z(x)$

$$z = \text{const} \cdot U_e \cdot \xi^{-\kappa}, \quad (11)$$

After introducing a recurrent set of parameters related to the governing factor γ_1 (10)

$$\gamma_k = \frac{\alpha^k d^k z}{z d^k x}, \quad k = 1, 2, 3, \dots$$

and parametrization of, e.g., equation (1a), we obtain the following parametric form of equations of 2D laminar boundary layer:

$$L(\Phi, \chi, \gamma_1) = \sum_{k=1}^{\infty} \{ [2k(\chi - \kappa) - (k+1)\gamma_1] \gamma_k + \gamma_{k+1} \} \cdot [\Phi, \dot{\Phi}]_{(\eta, \gamma_k)}, \quad (12)$$

If $\xi = \int_0^x U_e dx$, i.e., the Gortler transform, here $\chi = 1$, the distribution of external velocity is

$$U_e = x^{c_1} \sum_{k=0}^{\infty} a_k x^{c_2 k}, \quad c_1 = \frac{\kappa}{1-\kappa}, \quad c_2 = \frac{k}{1-\kappa}, \quad \kappa \neq 1.$$

Thus, the external velocity is determined by a generalized power series. For $\xi = x^N$, $\chi = \frac{1}{N} + \kappa + 0.5 \cdot \gamma_1$ we have

$$U_e = x^{N\kappa} \sum_{k=0}^{\infty} a_k x^k.$$

A self-similar solution for the external flow velocity in the singular point $\gamma_k = 0$, $k = 1, 2, 3, \dots$, which determines the Cauchy problem for the parametric equation (12)

$$U_e = a_0 x^i, \quad i = \kappa / (\chi(\gamma_k = 0) - \kappa). \quad (13)$$

Thus, setting different values of the constant κ and transformation $\xi(x)$ from the class of allowable values, we can obtain versatile polynomials of the distribution of external flow velocity and the necessary boundary conditions (13).

Since the parameters γ_k contain sequential derivatives of a certain complex (11) containing both a specified boundary condition $U_e(x)$ and a transformation of the longitudinal coordinate $\xi(x)$, which was not defined a priori, these parameters can be called **mixed**. Obviously, the choice of complexes, such as (11), can be different and the presented derivation of (12) with mixed parameters should not be regarded as the only possible one. The use of mixed parameters extends the classes of functions of the boundary condition $U_e(x)$, for which the parametrization of the laminar boundary layer equations is possible.

3. The value of $z(x)$ is determined, as mentioned above, from a differential equation. If we multiply the both sides of this equation by α :

$$\alpha \frac{\dot{z}}{z} = \alpha \frac{\dot{U}_e}{U_e} - \kappa \alpha \frac{\dot{\xi}}{\xi}, \quad \text{or} \quad \gamma_1 = \beta_1 - \kappa \cdot \Gamma_1,$$

it is easy to notice that the quantity $\Gamma_1 = \alpha \dot{\xi} / \xi$ is the first parameter of the following set of parameters:

$$\Gamma_i = \alpha^i \frac{\xi^{(i)}}{\xi}, \quad \xi^{(i)} = \frac{d^i \xi}{dx^i}, \quad i = 1, 2, 3, \dots,$$

which is introduced following the general rule for an arbitrary function $\xi(x)$. The parameter Γ_1 is equal to 2 and always constant. If all $\Gamma_i = \text{const}$, $i = 2, 3, 4, \dots$, then the function $\xi(x)$ is only a power function $\xi = C_1 x^{C_2}$, where C_1 and C_2 are constant.

When we put into consideration the parameter Γ_1 , we expand the class of employed transformations of the longitudinal coordinate, this is the main idea of introducing Γ_i . Thus, for two independent functions $U_e(x)$ and $\xi(x)$, we write two sets of parameters:

$$\beta_k = \alpha^k \frac{U_e^{(k)}}{U_e}, \quad \Gamma_i = \alpha^i \frac{\xi^{(i)}}{\xi}; \quad k, i = 1, 2, 3, \dots, \quad (14)$$

Finally, the equation is written in the form

$$L(\Phi, \chi, \beta_1, \Gamma_2) = \sum_{k=1}^{\infty} \alpha_k [\Phi, \dot{\Phi}]_{(y, \beta_k)} + \sum_{i=2}^{\infty} \varepsilon_i [\Phi, \dot{\Phi}]_{(y, \Gamma_i)}, \quad (15)$$

the boundary conditions coincide with (2), the initial conditions are determined by integrating equation (7), to which (15) reduces for the values of parameters

$$\beta_k = 0, \quad k = 1, 2, 3, \dots; \quad \Gamma_i = 0, \quad i = 2, 3, 4, \dots \quad (16)$$

The initial conditions (16) determine the Cauchy problem for equation (15) at the singular point, and since this equation has no arbitrariness in quantities entering into it, there is no need to impose additional conditions of the type (6). The external velocity distribution, which satisfies (15), is written in the general case as

$$U_e = \sum_{k=0}^{\infty} a_k \left(\frac{\xi}{\xi} \right)^k \quad u \quad \xi = \sum_{i=1}^{\infty} b_i \cdot x^i. \quad (17)$$

Thus, we can see that the distribution $U_e(x)$ is described by the function of the type (8).

Comparison of the influence of the parameters β_1 and Γ_2 .

If all Γ_i are constant, then the transformation $\xi(x)$ is a power function. Let $\beta_1 \neq \text{const}$, $\beta_j = 0$, $j = 2, 3, 4, \dots$, but it follows from (17) that $U_e = a_0 + a_1 x$. It is shown in [1] that for this distribution of external velocity equation (15), wherein only one Poisson bracket with respect to β_1 is left, has two singular points, the solution at these points being described by the Falkner-Skan equation in the Hartree form

$$\ddot{\Phi} + \Phi \ddot{\Phi} + \beta_X (1 - \Phi^2) = 0. \quad (18)$$

The zeroth approximation corresponds to $\beta_X = 0$, the first approximation to $\beta_X = 1$. The difference in these approximations is rather significant, since the zeroth approximation describes a laminar boundary layer on a plate, whereas the first approximation describes the same in the vicinity of the stagnation point. Thus, the variation of the parameter β_1 involves a considerable change in the fluid flow in the boundary layer.

The influence of the parameter Γ_2 . Let us consider equation (15) whose right-hand part has only one Poisson bracket depending on the parameter Γ_2 , i.e. $\varepsilon_2 \neq 0$. All β_k are constant, then the external flow velocity is

$$U_e = a_m x^m \cdot \left(\frac{1 + b_2 x}{1 + 2 \cdot b_2 x} \right)^m; \quad (19)$$

The values of χ and β_1 are

$$\chi = 0.5 \cdot (m + 1)(2 - 0.5\Gamma_2), \quad \beta_1 = m \cdot (2 - 0.5\Gamma_2).$$

Equation (15) turns to the ordinary differential equation (18) for $\Gamma_2 = 0$, и $\Gamma_2 = 2$, ($b_2 = \pm\infty$), the solutions of the latter being dependent on the same value of the pressure gradient parameter in the Hartree form $\beta_X = 2m/(1+m)$, and the distribution of external velocity in these singular points is described by the known power function $U_e = a_m \cdot x^m$.

Despite the fact that in the general case we integrate the equation in partial derivatives, the difference of the resultant solution from the self-similar one is very weak. In other words, equation (15) in the considered one-parametric approximation with respect to Γ_2 described an almost self-similar solution, and, thus, the external velocity distribution (19) yields a laminar boundary layer flow close to the self-similar solution.

On the basis of the above said, the parameters β_k containing the derivatives of the boundary condition can be called **strong** parameters. The parameters γ_j , whose structure does not contain the boundary condition, are **weak** parameters. These notions are conventional, but they allow one to solve an important problem of fluid motion in the boundary layer, which is close to self-similar motion.

The parametric equation of the type (15) is called in [5] '2k-parametric'. Obviously, these equations can be obtained by different methods. In general, the introduction of the both systems of parameters can be performed by numerous different methods, the parameters of the both systems can be mixed, etc.

For example, let us introduce two systems of parameters, which turn the parametric equation into the Blasius equation when they equal zero at the singular point. For this purpose, the function $\chi(x)$ should be represented in the form

$$\chi = r + s\beta_1 + d\gamma_1,$$

where r , s and d are arbitrary constants. The recurrent sets of the parameters β_k and γ_j , ($k, j = 1, 2, 3, \dots$) are written similar to (14), the 2k-parametric equation has the form of equation (15), but the recurrent factors α_k and q_j in the right-hand parts differ from α_k and ε_j in (15). The parameters γ_j are mixed. It is possible to find the external flow velocity and the longitudinal coordinate transformation without deriving a parametric equation:

$$U_e = \sum_{k=0}^{\infty} a_k \left(\frac{\xi}{\zeta}\right)^k \quad u \quad \xi = \sum_{j=0}^{\infty} b_j \left[\left(-\frac{r}{2dj-1}\right) \cdot \int_0^x U_e^{\frac{2j-1}{2dj-1}} dx \right]^{-\frac{2dj-1}{r}}$$

The longitudinal coordinate transformation is a generalization of that suggested in [2], and also the Gortler transformation for particular values of the constants r , s , and d .

Thus, the presented theoretical study of the parametric equations of 2D laminar boundary layer of incompressible fluid with pressure gradient allows one to classify, order, and generalize the known forms of equations and longitudinal coordinate transformation, and also to obtain new results. This study can be also extended to the flows in 2D laminar boundary layers with heat-and-mass transfer.

References

- [1] Popkov A.N. Parametric equations of laminar boundary layer and computational methods based on their solutions//Izvestiya Vuzov, Aviatcionnaya Tekhnika, Kazan', 1979, No. 4, P. 63-69.
- [2] Shkadov V.Ya., On solving the boundary layer problem//Izv. AN SSSR OTN, Mekhanika i Mashinostroyeniye 1962, No. 3.
- [3] Loitsyansky L.G. A parametric method of integration of the laminar boundary layer equations//Technical gas dynamics, Trudy LPI, 1965, No. 248.
- [4] Salukov V.N. Generalization of the universal equation of the Loitsyansky's theory of laminar boundary layer//Publications de L'Institut mathematique, Nouvelle serie 13(27), 1972.
- [5] Loitsyansky L.G., Similarity methods in the theory of integration of the laminar boundary layer equations // Problems of mathematical physics, on 75th anniversary of the corresponding member of USSR Acad Sci. G.A.Grinberg, Nauka, Leningrad, 1976.

THE ACTION OF INJECTION OF INERT AND CHEMICALLY ACTIVE HIGH-TEMPERATURE GAS MASS ON DUCT FLOW GAS DYNAMICS

A.G. Prudnikov

Baranov Central Institute of Aviation Motorbuilding
Moscow, Russia

P.K. Tretyakov

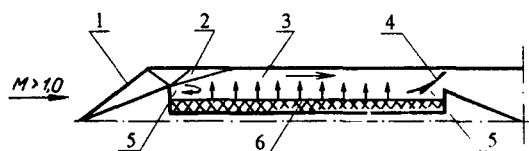
Institute of Theoretical and Applied Mechanics SB RAS,
Novosibirsk, Russia

The results of experimental study of gas dynamics of a flow in an axisymmetric duct with expanding cross-section under the action of distributed and local addition of inert or chemically active mass of propellant combustion products are presented.

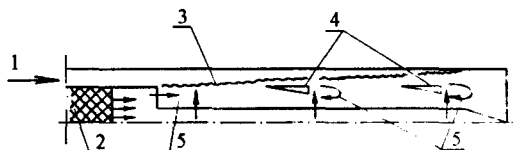
It is shown that for a subsonic flow velocity at the entrance ($M = 0.7$) and duct expansion larger than 3.0 the flow can be organized so that the transition through the critical speed of sound occurred without geometric throttling, i.e., a mass flow/thermal nozzle can be obtained.

The research goal was to verify experimentally the physical principles of organization of the combustor operation in an air-breathing engine (ramjet), which allow for organization of the flow with mass addition and combustion in such a way that the critical speed of sound in the flow was achieved without geometric throttling, as it takes place in traditional configurations. Theoretical possibility of obtaining a mass flow and thermal nozzle is well known, it follows from the action inversion equation derived by P.A. Wulis and I.F. Shebeko. However, the presence of a nozzle is necessary for practical realization of the operation process in an air-breathing engine.

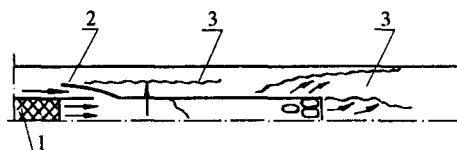
The construction of experimental models was based on the known configuration of two-contour



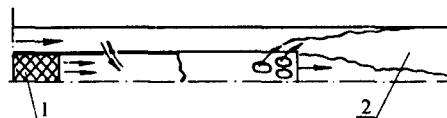
*Scheme 1: 1 - shock waves, 2 - expansion waves
3 - "cold" flow core, 4 - attached shock waves
5 - separation region, 6 - fuel charge*



*Scheme 2: 1 - homogeneous mixture, 2 - propellant gas generator,
3 - combustion front, 4 - stabilizers, 5 - separation regions*



*Scheme 3a: 1 - propellant gas generator, 2 - inlet,
3 - afterburning region*



*Scheme 3b: 1 - gas generator,
2 - afterburning region ("thermal" nozzle)*

Fig. 1. Schemes of organization of two-contour heat release.

organization of the combustion process. An example of its experimental implementation for a two-mode ramjet working on a hydrocarbon fuel (kerosene) is the study conducted in [1].

It is well known that the heat release in the scramjet duct is most effective in a pseudoshock combustion regime [2]. In this regime, the flow Mach number decreases to $M = 1.0$ due to heat addition from the chemical reactions of combustion. In the ramjet combustor with subsonic velocity the traditional principles of combustion organization do not allow one to maintain high pressure in the flow after the inlet compression; therefore, a converging section of the nozzle is needed.

Several possible constructive schemes of organization of two-contour heat release in a scramjet (Fig. 1) are presented below. It is necessary to note that it is preferable to use these schemes for small-size aircraft.

Scheme 1 is the simplest one. The afterburning of the products of open burning of the propellant takes place in several recirculation regions formed by steps. In the limiting case, when the propellant combustion products are chemically inert, the thrust increases due to mass addition and mixing process in the second contour.

Scheme 2 implies the combustion in the second contour flow of a uniform "quasihomogeneous" fuel-air mixture, which is stabilized by a longitudinal system of plumes of the first contour flow. These plumes are formed by a system of stabilizers, with high-temperature jets of propellant combustion products with negative oxygen balance being supplied to recirculation regions of these stabilizers.

In the third scheme the afterburning process of generator gas takes place in the subsonic air flow of the first contour forced to come from the second contour flow (scheme a) or naturally ejected (scheme b).

The experiments were conducted using an attached pipeline and ramjet models manufactured according to schemes shown in Fig. 1. All models had an axisymmetric body 50 mm in diameter, which was attached to the nozzle unit.

Tests with inert mass addition (combustion of ballistite fuel).

The combustion products of ballistite fuel have a zero oxidation balance. In this case, the operation process in the model duct is determined by gas injection from the fuel charge combustion and by the gas temperature. Figure 2 shows the base pressure, the static pressure profiles along the combustion chamber for various propellant flow rates. The air flow rate and the mass flow rate of propellant combustion are known from experiments. The pressure variation along the model duct follows the gas dynamic structure of the flow. The presence of a step at the entrance cross-section leads to flow expansion (pressure measurement point 2) to a level close to base pressure (pressure measurement point 0). An increase in pressure at the duct exit is caused by an emergence of a shock wave (see Fig. 1). As it follows from

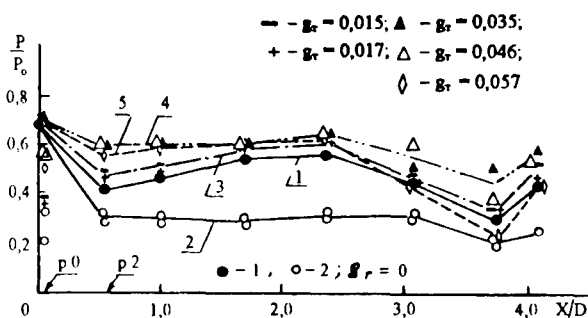


Fig. 2. Results of model testing with inert gas injection (scheme 1, Fig. 1)

without combustion: 1 - $\phi = 0.23$; 2 - $\phi = 0.04$;
with combustion: 3 - $\phi = 0.23$; 4 - $\phi = 0.285$; 5 - $\phi = 0.05$

the figure, an increase of the mass flow rate of propellant combustion ($g_f = G_f/G_a$) with decreasing the exit cross-section blockage ($\varphi = F_{\text{exit}}/F_{\text{duct}}$) allows one to preserve a high pressure level in the duct.

The estimate of flow velocity in the flow core for the case with fuel combustion showed that the flow velocity is close to transonic one ($M = 0.7-1.0$) up to cross-section located at a distance of approximately 2.5 diameters from the duct entrance. Then the flow is accelerated up to $M > 1.0$.

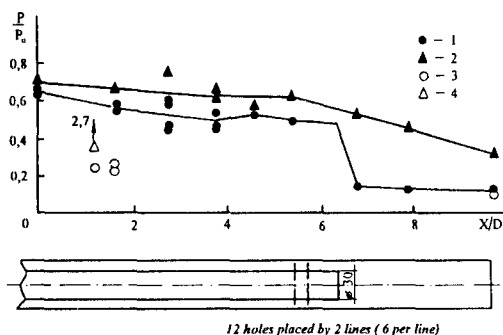


Fig. 3. Results of model testing with propellant gas generator (scheme 3b, Fig. 1).

1 – without combustion; 2 – with combustion, $g_f = 0.05$;

Pressure in gas generator: 3 – without combustion, 4 – with combustion.

in testing the combustor model made according to scheme 3b (see Fig. 1). Figure 3 shows a sketch of the model duct and the pressure distribution along the duct for two cases: without combustion and with solid propellant combustion. The generator gas was

Thus, we can conclude that it is possible to organize a mass flow nozzle due to injecting high-temperature chemically active mass.

Tests with chemically active mass addition.

The model testing according to scheme 2 (see Fig. 1) with the gas generator operating on solid propellant with oxidizer deficit and a system of separation of flame stabilizers proved a principal possibility of combustor flow control by means of redistribution of generator gas injection along the duct. The thermal choking in the exit cross-section could not be obtained, since the duct length was insufficient for completing the process of generator gas afterburning. This purpose was achieved

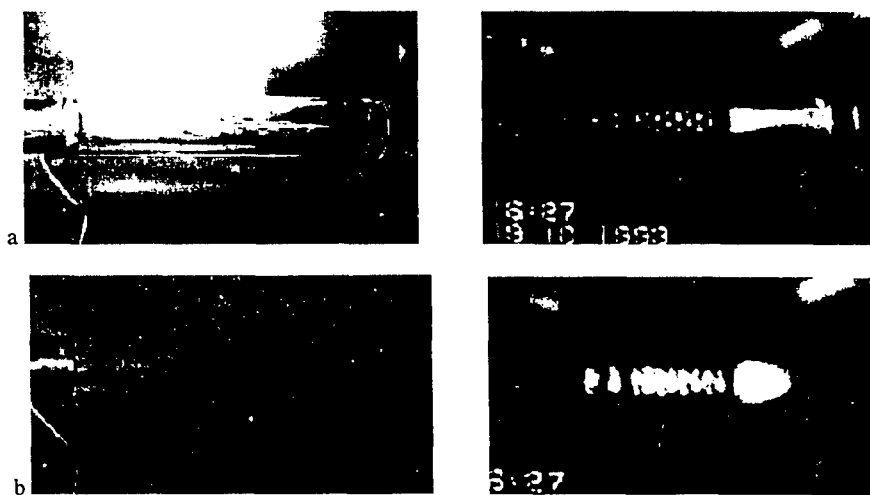


Fig. 4. Photographs of flow regimes with combustion. a – in a quartz tube, b – without a quartz tube.

supplied into a tube 30 mm in diameter with two rows of orifices. The gas temperature was approximately $T_g = 1500$ K, the stoichiometric coefficient was $L_0 = 6.0$. On the basis of this pressure distribution, the Mach number in the cold part of air flow was calculated. A transonic flow is formed in the annular duct. Without combustion, the amount of air supplied through two rows of orifices is sufficient to accelerate the flow behind the tube exit without the final shock wave, the flow being accelerated to $M = 1.8$. In the regime with propellant combustion, the sonic velocity is established in the cross-section $x/D = 7.9$, and the maximum flow velocity corresponds to the Mach number $M = 1.34$ in the exit cross-section of the duct. This regime can be called a local thermal nozzle regime. An illustration to this set of experiments is a qualitative experiment with visualization and registration of the combustion process. A quartz tube was mounted instead of the model body. The difference was that ten rows of orifices were made in the inner tube. Figure 4 shows photographs corresponding to different conditions of combustion. The model with quartz tube and propellant afterburning is shown in Fig. 4a. The plume shape is indicative of flow acceleration. The plume is more powerful in the case without the quartz tube (Fig. 4b). In the presence of a quartz tube, part of the air enters the inner tube from the annular channel. Without the tube, the generator gas comes through orifices and burns completely in the outer flow.

REFERENCES

1. Boloshchenko O.V., Meshcheryakov E.A., Ostras' V.N., Sermanov V.N. Analysis of specific features of gas generation and conversion of hydrocarbon fuels in a two-regime scramjet // *Trudy TsAGI*. – 1995. – Iss. 2572. – P. 3-19.
2. Tretyakov P.K. Pseudoshock combustion regime // *Combustion, Explosion and Shock Waves*. – 1993. – Vol. 29, №. 6. – P.33-39.

NUMERIC SIMULATION OF TRANSPORT PROCESSES IN SUSPENSIONS AND GAS SUSPENSIONS

V.Ya. Rudyak, A.A. Belkin, G.V. Harlamov

Novosibirsk State University of Civil Engineering
Novosibirsk, Russia

INTRODUCTION

Dispersed media are widely spread both in nature and in technical applications. They include gas suspensions, aerosols, suspensions, emulsions etc. Such systems flows are usually calculated in framework of multifluid hydrodynamic models in which interface interactions are taken into account. Expressions for interface forces and transport coefficients received from phenomenological theories or experimental data are used in such cases. Such an approach is not satisfactory in many cases because the conditions of phenomenological theories application are often broken and experimental data are not complete.

At the same time rigorous kinetic theories of such systems have been poorly developed and do not permit to calculate transport coefficients and interface forces even in case of high rarefied gas suspensions and suspensions. So the direct numerical simulation of transport processes in the heterogeneous media provides as the very valuable information as an experiment. The such simulation results give important information about equilibrium and nonequilibrium characteristics of the considered heterogeneous systems. In particular, it is possible to study fluid-solid state phase transitions, to calculate transport coefficients and interface forces, to determine relaxation times.

The present paper is the first work in the series devoted to direct numerical simulations of transport processes in dispersed media. Dispersed medium (suspension or gas suspension) is simulated by a system of hard spheres of different diameters and masses. Transport properties have been calculated by molecular dynamics method (the basic principles of this method were formulated in the pioneer work [1]). The results of our calculations of the velocity autocorrelation function, radial distribution function and dependence of medium pressure on density are presented.

MODEL DESCRIPTION

The simulated system presents a cube sell filled with layers of N molecules. The length of cubes rib is equal to L . For high-density regions they have the form of the rectangular parallelepiped. At the initial time the molecules velocity according to a certain law were assigned. The total momentum of the system is equal to zero and the kinetic energy $E_k = E_0 = \text{const}$. The conservation of these values during the systems evolution is the main physical criteria of the numerical experiment correctness.

Intermolecular forces in hard spheres model is equal to zero for all molecular pairs except colliding ones. This fact permits to use the following modification of the method offered in article [1]. Collision times are calculated for all particles and the minimum time is selected for each particle. These times are ranged as increasing. All the particles are

©V.Ya. Rudyak, A.A. Belkin, G.V. Harlamov, 1998.

moved along their trajectories for minimum time (till the nearest collision) and then the post-collision velocities and collision times are recomputed for collided particles and for the particles that might have collided with them. A separate part of the algorithm is realization of boundary conditions. In present paper the so named periodic boundary conditions were used: when a molecule reaches the boundary of the cell the same molecule is putted through the contrary boundary.

The object of our study is dispersed media. The binary mixture of light small hard spheres (gas molecules) and heavy large ones (dispersed particles) is simulated by method of molecular dynamics. The number of heavy hard spheres N_p , their masses m_p and radii R_p were varied on a wide range. After the system had been in equilibrium (the main criteria was equality of molecule energy and particle one) its properties were studied.

VELOCITY AUTOCORRELATION FUNCTION

Velocity autocorrelation function

$$Kr_v(t) = \frac{1}{N} \sum_{i=1}^N \mathbf{v}_i(0) \cdot \mathbf{v}_i(t)$$

is the most important characteristic of both equilibrium behaviour of the system and dissipative processes. The ergodic hypothesis

$$Kr_v(t) = \frac{1}{N} \frac{1}{K} \sum_{i=1}^N \sum_{k=1}^K \mathbf{v}_i(\tau_k) \cdot \mathbf{v}_i(\tau_k + t),$$

have been used for calculating of a function Kr_v . Here K is realization number. The curves Kr_v of one-phase fluid at various concentrations have been calculated for the testing of the program. The obtained curves coincided with the results of known works (in particular, of paper [2]).

Fluid density was characterized with the parameter $\alpha = V_m/V_0$, $V_0 = 8NR^3/\sqrt{2}$, where V_m is a cell volume and V_0 is the close packing volume, R is radius of a molecule (or particle).

Then mixtures of molecules and particles of the same radius and various ratio of masses m_p/m_0 at various α were calculated. The change of Kr_v of molecules and particles at the increasing share of particles in the system is illustrated in Fig. 1. The medium density is rather high, it is comparable to a solid by its properties. That's why the curves have typical negative region with minimum (for one-phase fluid it is located near $t = 8\tau_\lambda$, τ_λ is a mean free path time). At any ratio of concentrations n_p/n the function Kr_v of the particles is located to the right of the corresponding function of molecules.

When the particle concentration decreases (see the solid line in Fig. 1) the minimum of the velocity autocorrelation function of molecules goes down and moves to the right. The relaxation time of the particles velocity autocorrelation function increases considerably. The heavy particle lacks several collisions with molecules for a significant change of its velocity. On the other hand the relaxation time of the both components decreases when concentration of the particles (and the particle - particle collisions number) grows (see Fig. 1 for concentration $n_p/n = 1$). When particles prevails in the system their velocity autocorrelation function coincide practically with the function for the same spheres at the

corresponded density. In this situation the molecules turn out to be "squeezed" between the heavy spheres the properties of a solid are characteristic of them in the greatest degree.

Let us consider the heavy particles as the Brownian ones. Their motion along the x coordinate is described by the Langevin equation

$$m_p \frac{d^2 x}{dt^2} = -\gamma \frac{dx}{dt} + F_x(t), \quad \gamma = 6\pi \eta R_p, \quad (1)$$

where $F(t)$ is a stochastic force and η is a viscosity of a carrier fluid. It is easy to show that autocorrelation function which satisfy the equation (1) has an exponential form

$$Kr_v(t) = Kr_v(0) \exp(-t/\tau_{pv}) \quad , \quad \tau_{pv} = m_p/\gamma. \quad (2)$$

The curves in Fig. 1 show that autocorrelation functions have no exponential form at rather long times and high densities of the fluids. On the contrary, the function $Kr_v(t)$ has practically an exponential form in rarefied gases and gas mixtures. So, it is necessary to study a rather rarefied system when we want to simulate the system described by the law (2)¹. The molecule free path l must be rather long for this purpose but naturally it should be much less than the cell size L , $l \ll L$. In order to select a suitable from this point of view value of the parameter α the series of calculations have been provided. Two of the obtained results are given in Fig. 2. Here solid line corresponds to the density $\alpha = 2.0$ ($l = 0.21$, $L = 22.45$) and dashed line corresponds to the density $\alpha = 4.8$ ($l = 1.14$, $L = 30.2$). In both cases $n_p/n = 10$, $m_p/m_0 = 100$, distances are measured in units R . We see that velocity autocorrelation functions indeed dependences on the fluid density strongly. Analysing the figure one can see that at $\alpha = 4.8$ the function Kr_v does not have a negative part and approximates an exponential curve for rather long times. Henceforth in present paper a carrier medium with such a density will be used for the Brownian motion simulation.

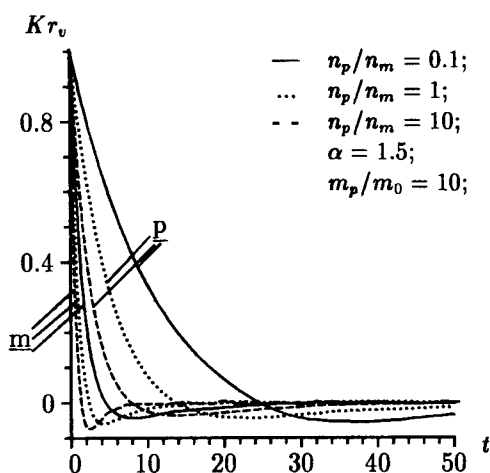


Fig. 1. Function Kr_v of the molecules and particles in a binary mixture.

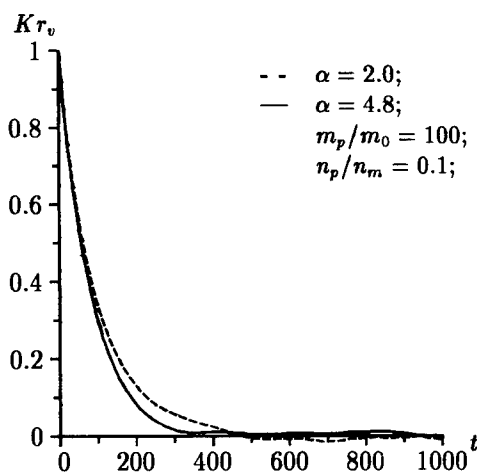


Fig. 2. Function Kr_v of the particles in a binary mixture.

¹Here we mean a rarefied system as compared with solid phase.

DIFFUSION COEFFICIENT AND RELAXATION TIME OF THE BROWNIAN PARTICLE

Let us consider evolution of one heavy particle (Brownian particle) in a molecular bath. One thousand molecules have been used in the latter for calculation. The ratio of the Brownian particle mass and the molecule mass was equal to $m_p/m_0 = 100$ and the ratio of their radii R_p/R was equal to 1, 2, 3 and 4. So the mass measured in units m_0 . The unit of time was equal to the time for which a molecule passed the half linear size of the cell.

In these units $kT = 74.925$ (k is the Boltzmann constant, T is the temperature). The ratio of the volume occupied by the molecules to the volume of close packing $V/V_0 = 4.8$. $V = V_m - V_p$, where V_p is the volume of the Brownian particle. Time dependence of the velocity autocorrelation function of the Brownian particle and the mean square distance of the particle during given time $\langle R^2(t) \rangle$ have been calculated

$$\langle R^2(t) \rangle = \lim_{K \rightarrow \infty} \frac{1}{K} \sum_{k=1}^K \{ [x(\tau_k + t) - x(\tau_k)]^2 + [y(\tau_k + t) - y(\tau_k)]^2 + [z(\tau_k + t) - z(\tau_k)]^2 \}.$$

Rather smooth curves for $\langle R^2(t) \rangle$ have been already obtained at $K \sim 10^4 \div 5 \cdot 10^4$. We limited our investigation with these values of K .

It should be noted that at the arbitrary initial data the average energy E_p of the Brownian particle did not reach the value of the molecules average energy for rather long

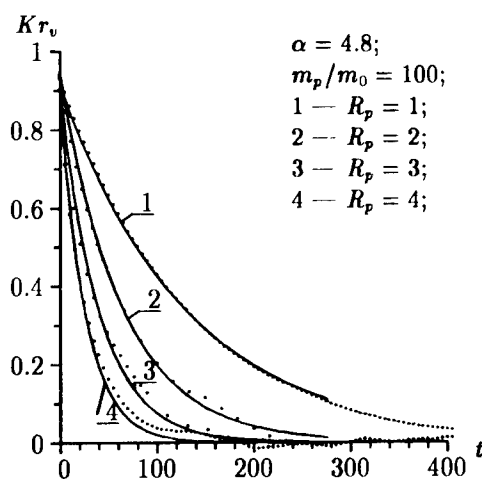


Fig. 3. Function Kr_v of brownian particles of various radii.
.... calculated data
— approximation of this data by exponential curve (2)

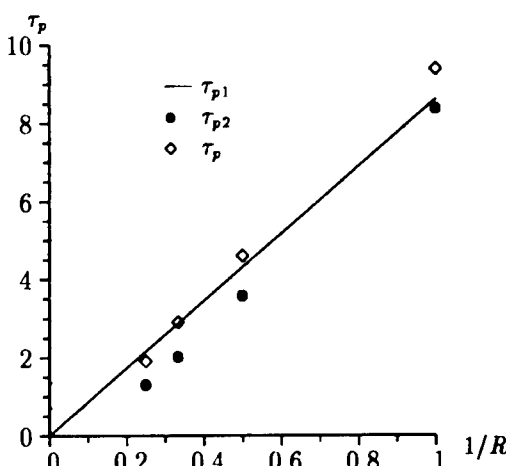


Fig. 4. Comparison of relaxation time τ_p with theoretical calculations

times and amounted to about $82 \div 94\%$ of this value. On the other hand, changing the initial configuration of the system it is possible to obtain in calculations the Brownian particle average energy approximating or even exceeding the average molecule energy. Apparently, it points to the fact that the quasistable states in which the average energy of the Brownian particle differs from that of a molecule is appeared in the studied system of finite number particles. The total energy and the total momentum of the system is conserved with great accuracy. The Brownian particle track has a complex chaotic character. Fig. 3 shows the time dependence of the velocity autocorrelation functions and their approximations by the exponential curves (2) with τ_{pv} given in the table.

Approximation of the calculated values $\langle R^2(t) \rangle$ by the solving of the Langevin equation (1)

$$\begin{aligned} \langle R^2(t) \rangle = 3 \langle x^2(t) \rangle = & \frac{2E_p \tau_{pR}^2}{m_p} [1 - \exp(-t/\tau_{pR})]^2 + \\ & + \frac{4E_p}{m_p} \left\{ t - 2\tau_{pR}[1 - \exp(-t/\tau_{pR})] + \frac{1}{2}\tau_{pR}[1 - \exp(-t/\tau_{pR})] \right\}, \end{aligned} \quad (3)$$

affords to define the relaxation time τ_{pR} . Comparing the relaxation times τ_{pv} and τ_{pR} given in table we see that they coincide with one another very well (see the table).

Table. Calculated and theoretical dependencies of velocity relaxation times and diffusion coefficients of the brownian particle from R_p (average molecule energy $E_{av} = 112.5$)

R_p	τ_{pv}	D_v	τ_{pR}	D_R	τ_{p1}	D_{12}	τ_{p2}	D_2	E_p
1	9.4	6.42	9.3	6.36	8.63	5.9	8.38	5.73	102.5
2	4.6	3.17	4.65	3.27	4.31	3.03	3.57	2.51	105.6
3	2.9	1.89	2.9	1.96	2.88	1.94	2.02	1.36	101.2
4	1.9	1.32	1.9	1.23	2.16	1.42	1.30	0.85	98.46

The following notations have been used in the table. D_v and D_R are the diffusion coefficients of the Brownian particle defined by the following expressions

$$D_v = \frac{1}{3} \int_0^\infty K \tau_v(t) dt, \quad D_R = \frac{kT}{m_p} \tau_{pR}.$$

D_1 and τ_{p1} are the diffusion coefficient and relaxation time calculated according to the Langevin theory

$$\tau_{p1} = \frac{m_p}{6\pi\eta R_p},$$

where η is a viscosity of the hard elastic spheres system calculated according to the Enskog theory ¹[3]

$$\eta = \eta_0 \left(\frac{1}{\chi} + 0.8b\rho + 0.7614(b\rho)^2\chi \right),$$

¹The calculations of the hard spheres pure gas viscosity [2] prove the correctness of this theory in our conditions.

$$\chi = 1 + 0.625b\rho + 0.2869(b\rho)^2 + 0.1115(b\rho)^3,$$

$$\rho = \frac{m_0 N}{V}, \quad b = \frac{2\pi\sigma^3}{m_0}, \quad \sigma = 2R_0, \quad \eta_0 = 1.016 \frac{5}{16\sigma^2} \sqrt{\frac{m_0 kT}{\pi}}.$$

τ_{p2} and D_{12} are the relaxation time and diffusion coefficient calculated according to the theory of molecular diffusion in dense gases of hard elastic spheres [4]

$$\tau_{p2} = \frac{m_p}{kT} D_{12},$$

$$D_{12} = [D_{12}]_1 / \chi_{12}, \quad [D_{12}]_1 = \frac{3}{8n\sigma_{12}} \sqrt{\frac{kT(m_p + m_0)}{2\pi m_p m_0}}, \quad \sigma_{12} = R_p + R,$$

$$\chi_{12} = 1 + \frac{\pi}{12} n_0 \sigma_0^3 (8 - 3\sigma_0/\sigma_{12}) + \frac{\pi}{12} n_p \sigma_p^3 (8 - 3\sigma_p/\sigma_{12}).$$

Here n_0 , σ_0 and n_p , σ_p are the concentration and diameter of the molecules and Brownian particles, respectively.

The dependence of the relaxation times τ_v , τ_R , τ_1 , τ_2 on $1/R_p$ are given in Fig. 4. It can be seen that calculated points are located close to the curve obtained on the basis of the Einstein and Langevin theories though one might expect confirmation of the molecular diffusion theory with so small radii of the particles and the elastic interaction between particles and molecules.

PHASE TRANSITION

The hard spheres potential permit to simulate the very subtle effects of the collective behavior of the particles system. Such an example is the step-wise change of the pressure in the state equation of a hard spheres system. This phenomenon is interpreted as the first-order phase transition "fluid-solid" [1]. In present paper the properties of one-component system near the point of phase transition were investigated.

It has been showed that the transition depends greatly on the initial configuration of molecules. In particular, there was no transition in cubic lattice even at a maximum density for such packing ($\alpha = 1.48$). In face centered lattice at $\alpha = 1.5$ the quasistable solid state is being observed for rather a long time. However then the system quickly turns into a liquid state. The structure change of the system in this situation was studied with the help of the radial distribution function. In a fluid the periodic structure relaxes but the first maximum increases (and hence the importance of nearest neighbors). The phase transition to the liquid state is not observed at the medium density $\alpha < 1.49$.

REFERENCES

1. Alder B.J., Wainwright T. Studies in Molecular Dynamics. I// J. Chem. Phys. — 1960. — Vol. 31. — P. 459.
2. Alder B.J., Gass D.M., Wainwright T.E. Studies in Molecular Dynamics. VIII// J. Chem. Phys. — 1970. — Vol. 53. — P. 3813.
3. Ferziger J.H., Kaper H.G. Mathematical Theory of Transport Processes in Gases. — Amsterdam: North-Holland. 1972.
4. Chapman S., Cowling T.G. The Mathematical Theory of Non-Uniform Gases. — Cambridge: Cambridge University Press, 1960.

PARAMETRIC INVESTIGATION OF THE MULTI-BEAM BRIDGES AEROELASTICITY

Salenko S.D., Obukhovskiy A.D.

Novosibirsk State Technical University,
630092, Novosibirsk, Russia

In the paper, aeroelastic vibrations of dynamically analogous models of two real three-beam span constructions of bridges across the Ob river (fig. 1) and across the Tom one are studied, as well as those of two- and three-beam sectional models. The experiments were carried out in the wind tunnel T-503 of the Novosibirsk State Technical University with the length of working section of 2 m, diameter of 1.2 m and stream velocity up to 60 m/s.

One-hundredth scale models were used as dynamically analogous ones. Their design peculiarities are described elsewhere [1]. The main distinctive feature of the Tom bridge as compared to the previously studied Ob one is the value of separation between beam axes.

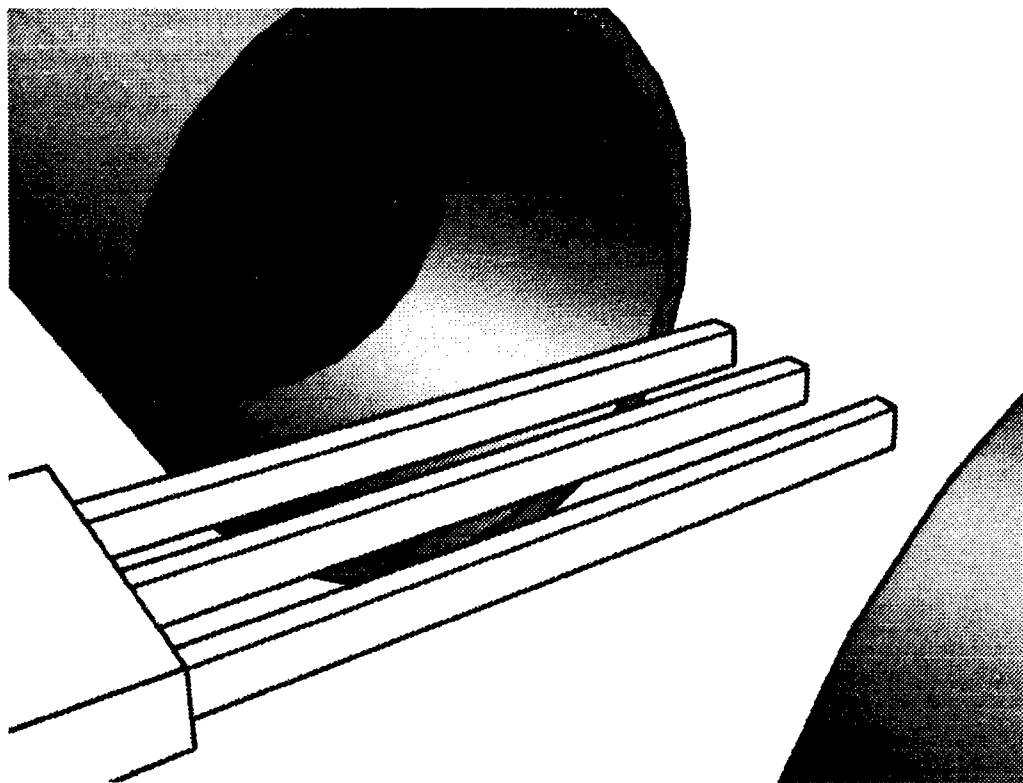


Fig. 1. Aeroelastic dynamically analogous model in wind tunnel.

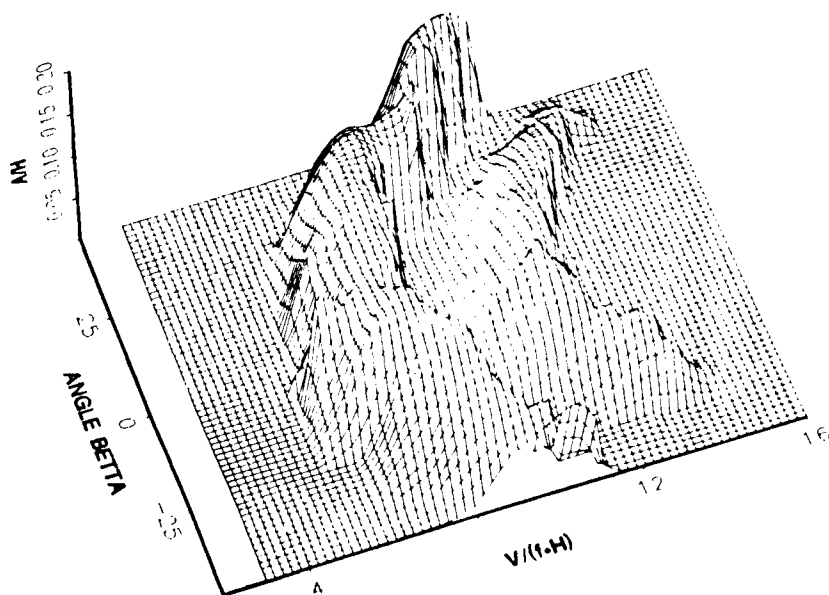


Fig. 2. Dimensionless amplitude of Ob bridge console end versus slip angle and reduced velocity.

Experiments on the dynamically analogous models have shown similar results, the main peculiarity being the presence of two regions of stream velocity, within which resonant vibrations were found to arise. Both the intensity of the vibrations and the conditions under which they were arising were found to depend strongly on model design. Experiments with blowing at an angle have shown that at sideslip angles exceeding 20 degrees the behaviour of amplitude-velocity characteristics (AVC) were dependent both upon model's geometry and upon the sign of sideslip angle (Fig 2). For each configuration of the model, there existed a certain most dangerous, from the viewpoint of the excitation of vibrations, sideslip angle, the observation being consistent with [2].

In view of the widespread application of multibeam constructions in engineering, an analysis was attempted of aerodynamic instability of such constructions in a wide range of their geometric parameters. These studies were performed under conditions of a plane-parallel flow on sectional models differing from one another both in the spacing between their beams and in the shape of beam cross-section. In all cases, the height of the cross-section was kept unchanged ($H=60\text{mm}=\text{const}$) and it was taken as the main characteristic linear size for determining similarity criteria (Re , Sh , Sc) as well as models' dimensionless geometric parameters. The width of the section B was chosen from the set $\{10, 20, 40\}$ mm, which corresponded to relative widths B/H of $1/6$, $1/3$, or $2/3$. The separation between beams was

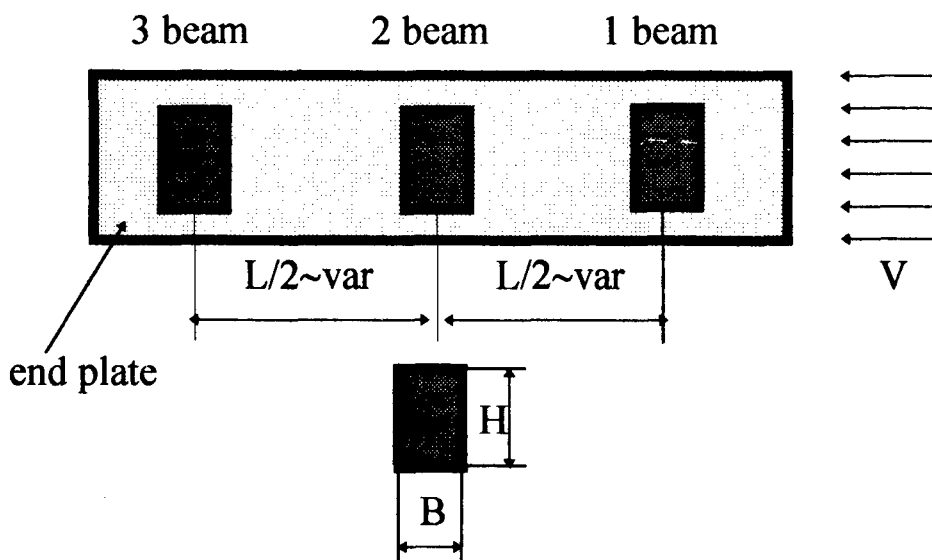


Fig. 3. Geometrical parameters of sectional models.

varied with the relative step $1/4$. The largest relative separation between the axes of end beams L/H amounted to 10 (Fig. 3). Normally, the models to be blown through were either three- or two-beam ones, the latter being the one with the eliminated central beam. For comparison purposes, aerodynamic behaviour of isolated beams was studied as well.

The tests were conducted on a setup which allowed the model under study to execute oscillations in vertical plane. The model was installed horizontally inside the working part of the wind tunnel at right angle to the approaching stream, being suspended on an elastic hanger consisting of eight steel wire tie-rods and eight springs. The hanger permitted an amplitude of oscillations to be realized exceeding a half of the beam cross-sectional height, such vibrations, however, being unattainable in practice. The frequency of the vibrations f was about 14 Hz and it was maintained constant for all variants of the constructions. The oscillations were recorded using a strain gauges fixed at an arm of the hanger. The registered signals were digitized to be processed subsequently by a computer.

The stream velocity was varied from 2 to 20 m/s in steps being smaller than 0.3 m/s.

The main results of the tests in the form of generalizing amplitude-velocity characteristics of some types of models are presented in Figs.4-5. From their analysis, the following main conclusions can be drawn:

- 1) Isolated beams with $B/H=1/3$ or $2/3$ possess a common region of resonant velocities, the maximum amplitude of oscillations corresponding to the reduced velocity $V/fH=8.5$ ($Sh=0.12$). The beam with $B/H=1/6$ exhibits no vibrations at all.

- 2) Two-beam models share, as a rule, the same region of resonant velocities which usually coincides with the corresponding region for isolated beams (if any does exist). The smaller the beam width, the lower values of reduced velocity are observed: at $B/H=1/6$ $-V/fH=6...8$, while at $B/H=1/3$ $-V/fH=8...10$. However, there are some exceptions to this generality. The most prominent among them is the AVC exhibited by the model with $B/H=2/3$ and $L/H=7$, which shows two peaks with near the same intensity at $V/fH=7$ and $V/fH=8.5$. The observation of two peaks in the AVC of the model with $B/H=2/3$ and $L/H=4$ agrees well with the results by

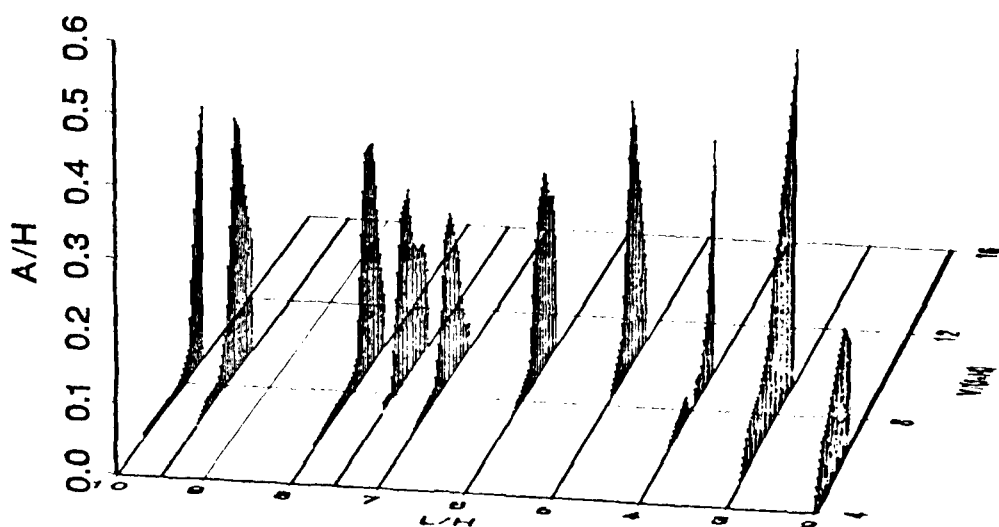


Fig. 4. Generalizing amplitude-velocity characteristics of two-beam models ($B/H = 2/3$).

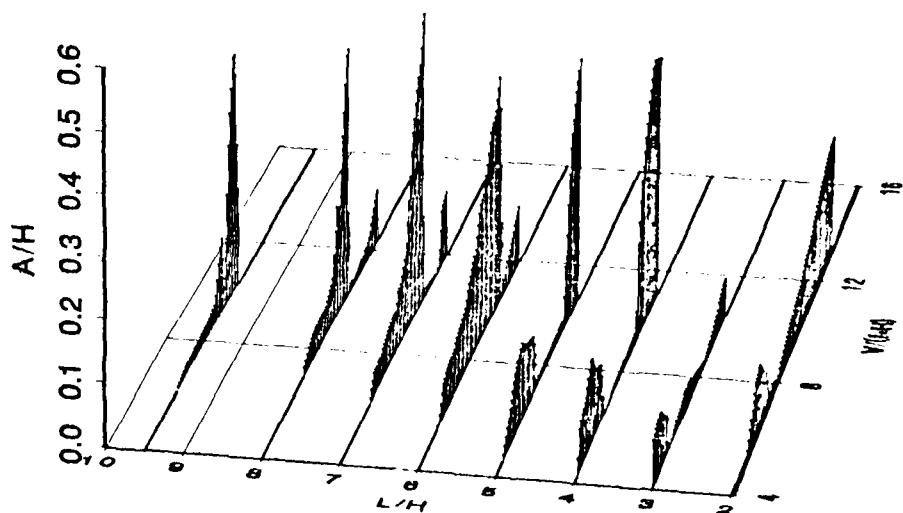


Fig. 5. Generalizing amplitude-velocity characteristics of three-beam models ($B/H = 2/3$).

Tackeuchi [3], which provide an evidence for the existence of two peaks in the spectra of pulsational velocity measured by hot-wire anemometer in the vicinity of motionless two-beam models similar to those described above (fig.6).

3) Three-beam models (excluding the models with the narrowest beams, $B/H=1/6$) show a few intervals of resonant velocities. Normally, one of them lies closely to the ranges where vibrations of corresponding two- or single-beam models are excited, which points to the same physical reason for the excitation of oscillations being likely connected with the classical vortex-resonance mechanism, when a coincidence of the natural frequency of model's vibrations with the frequency of vortex stall of one beam takes place.

For models with the separation between beams $L/H=2...5$, an additional resonant region is found lying in the interval $V/fH=4...7$. In this case, for each type of beams there is observed almost linear dependence of the values of reduced velocity, at which oscillations of the model take place, upon relative separation between beams. This dependence can be approximately represented by the formula

$$V/fH = L/H + 2 B/H.$$

Let us call the separation between neighbouring "humps" or "troughs" of the wake the wavelength of aerodynamic wake. In case of the classical vortex resonance, the latter will be the spacing between two neighbouring vortices of the same sign in the Karman street. It can be easily shown that the values of V/fh are equal to non-dimensional wavelength of the aerodynamic wake. The latter allows the conclusion to be made that the oscillations in this region resulted from beam interference, and, first of all, from the influence exerted by the first beam on the others located downstream.

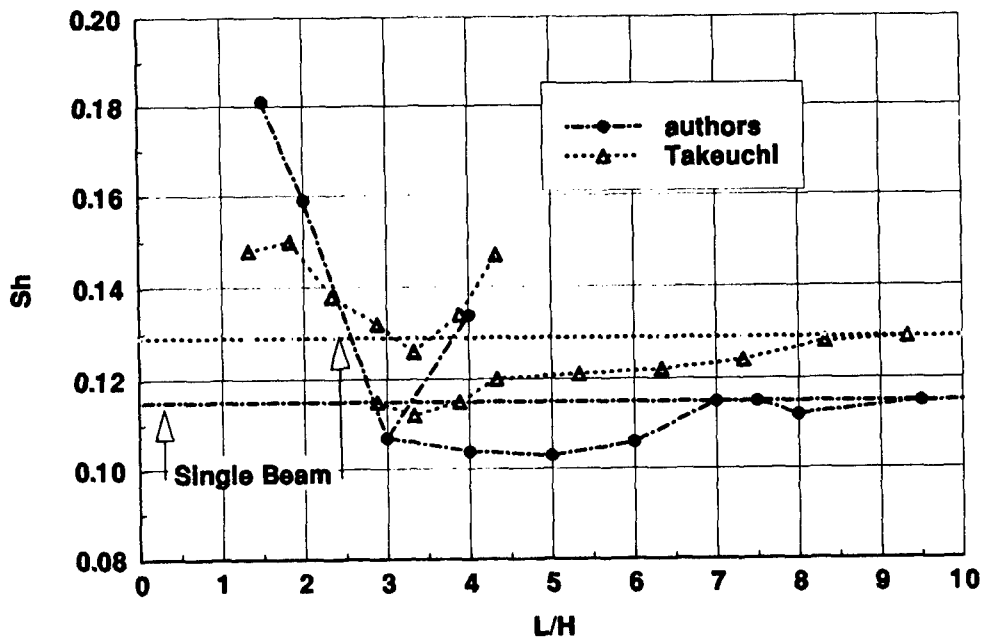


Fig. 6. Strouhal numbers of oscillated two-beam models ($B/H=2/3$).

As the separation between beams increases ($L/H=6...8$), the additional resonant zone shifts towards the high-velocity region. To middle-sized beams ($B/H=1/3$), resonant velocities around $V/fH=10$ correspond, while to wide ones those around $V/fH=12$.

In the case of large separations between beams ($L/H=9...10$), no additional resonance could be observed. The latter can be explained by that the aerodynamic wake had managed to get washed out before it reached the downstream beams.

Another evidence for the difference between the mechanisms of excitation of aerodynamic oscillations in the main and in the additional resonant-velocity regions is provided by different character of the development of oscillations from zero to maximum amplitudes at the stream velocity being kept constant. In the main region, a rapid growth up to the maximum amplitude is observed, while in the additional regions at small amplitudes the excitation occurs slowly, and very often a finite external disturbance is needed to trigger the oscillations. Our estimations show that under the full-scale conditions, it takes 5 to 10 minutes to reach maximum amplitude of bridge span oscillations.

The obtained results show that aeroelastic oscillations of multibeam constructions differ considerably from those of isolated beams.

REFERENCES

1. Salenko S.D., Obukhovskiy A.D., Aeroelastic oscillation specialities of multibeam consols // Proc. of 8th. International Conferences "Methods of Aerophys. Research"-Novosibirsk, 1996- Vol 2-P. 205-209.
2. Livesey F.M., Larose G.L. The Pont de Normandie During Construction. Aeroelastic Modelling of Behavior // Proc. of East European Conference on Wind Engineering //Warsaw, Poland, 1994 - Part 1- Vol.2- P. 223-232.
3. Takeuchi T. Effects of Geometrical Shape on Vortex-induced Oscillations of Bridge Tower / Journal of Wind Engineering and Industrial Aerodynamics-1990-Vol 33-P.359-368

PRESSURE OSCILLATIONS INVESTIGATIONS ON MULTI-BEAMS BRIDGES MODELS

S.D Salenko, A.D Obukhovsky.

Novosibirsk State Technical University,
630092, Novosibirsk, Russia.

In the paper, pulsational components of aerodynamic forces acting upon multibeam span bridge constructions at the stage of their assembling are studied in order to gain better insight into the excitation of aeroelastic oscillations of bridges. The presence of several ranges of Strouhal (Sh) number, in which intensive resonant phenomena take place, is a characteristic feature of these oscillations [1].

Experiments were carried out in the Laboratory of Industrial Aerodynamics of the Novosibirsk State Technical University on the wind tunnel T-503. A detailed description of the wind tunnel and of the aerodynamic bench was given elsewhere [2].

The general view of the models used in this study is shown in Fig. 1. The relative width of beams B/H in the experiments was $2/3$, the relative separation between the axes of end beams L/H varying in the range from 4.5 to 9.5. The oscillation frequency of the models ranged from 14 to 25 Hz. The Reynolds number determined from the beam height varied from $0.2 \cdot 10^5$ to $0.6 \cdot 10^5$.

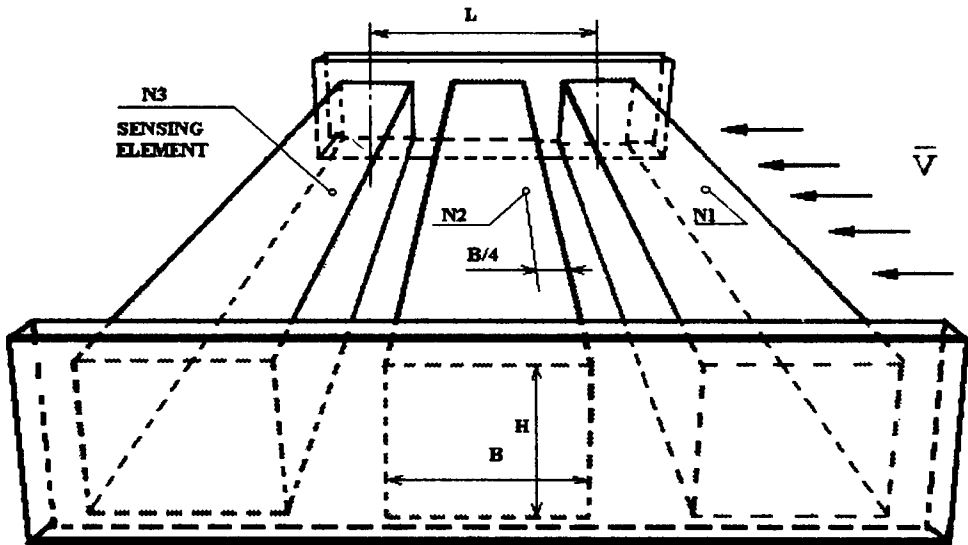


Fig. 1. General view of experimental model.

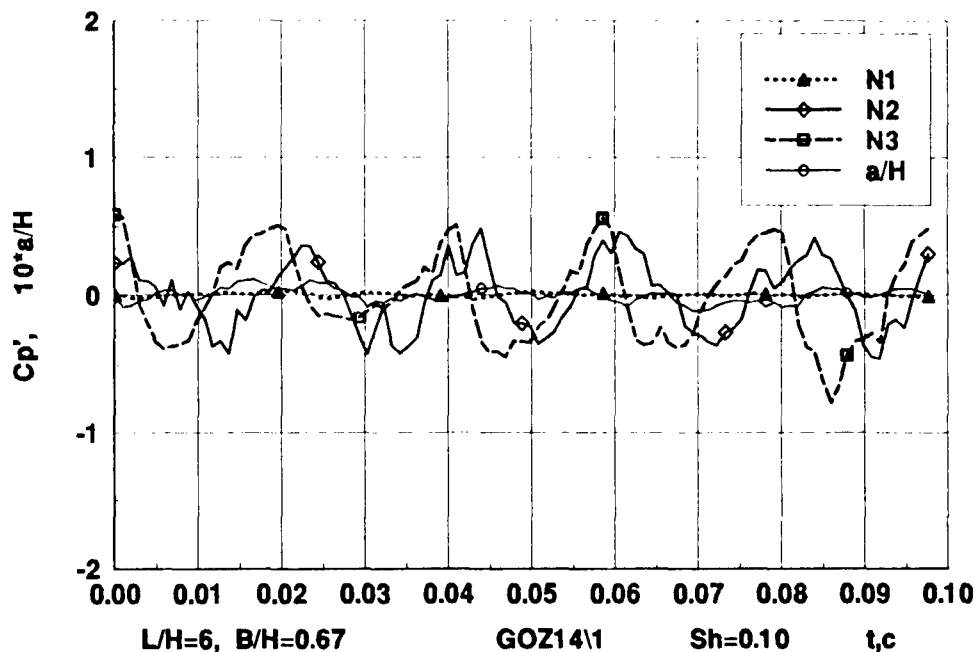


Fig. 2. Oscillogram of pressure pulsations on the beams of motionless model.

Pressure pulsations were measured with the help of semiconductor sensing elements, which were located inside each of model's beams and connected with drainage openings made on its surface. The openings were located in the symmetry plane of the model, one opening being made on each side faces (top and bottom ones) of the beams at a distance $1/4H$ from their front edge. Since, as was shown in [3], the pressure over the length of the side faces of oscillating prisms having a rectangular cross-section varies insignificantly, from measurement results obtained at one point of each face one can make an estimation of forces acting upon the whole surface.

Taking readings from sensing elements was performed at a frequency being 35...45 times higher than that of model's oscillations. The signals from elements were amplified, digitized and processed by a computer. Spectral analysis of pressure pulsations of beams was performed, as well as that of oscillograms of model's vibrations. Phase shifts between the pressure pulsations at different beams and the displacement of models were measured. Experimental dependences of characteristics of pulsational pressure components upon oscillation and approach-stream parameters for different geometric proportion of models were obtained.

At the first stage, pressure pulsations on motionless models were studied. For the considered geometric configurations, the amplitudes of the pulsations of pressure coefficient at the first beam were close to zero, and those at the second and at the third beams were the same order of magnitude, about 0.5 (Fig.2). The latter indicates that the first beam, giving rise to a Karman street, contributed insignificantly to the pulsational force component, but it formed a stream which, flowing around the next beams, brought about considerable pressure pulsations. Analysis of pressure pulsations has shown that at relative separation between beams $L/H > 5$, in the spectral characteristics there existed a clearly pronounced peak at a frequency

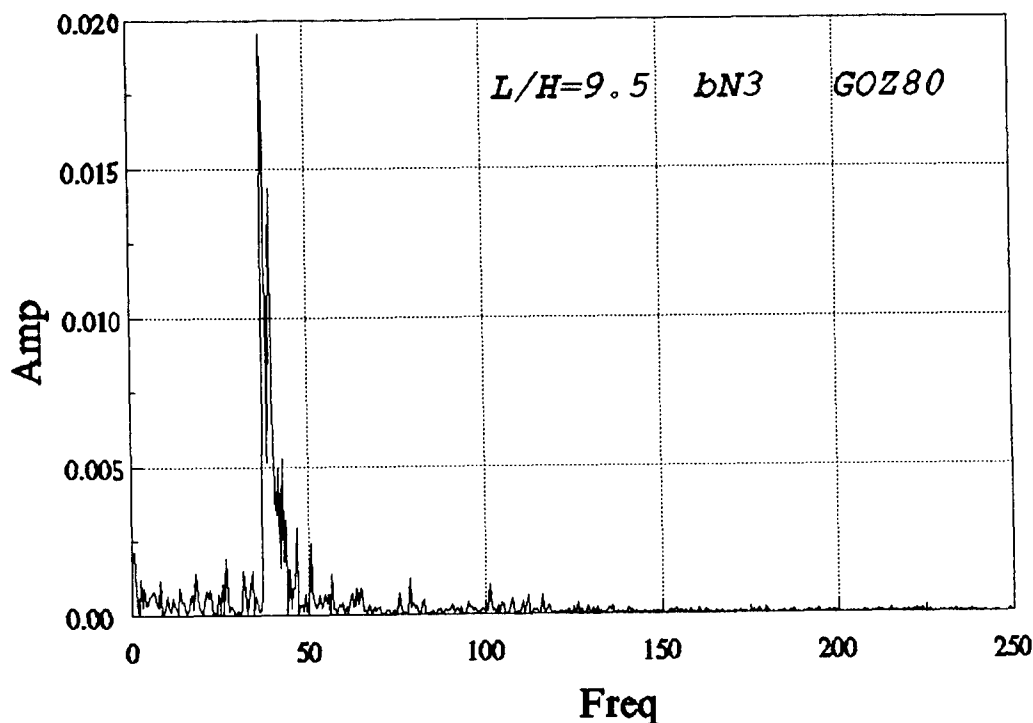


Fig. 3. The pressure pulsations spectral characteristics at large separation between beams

corresponding to the Strouhal number of the isolated beam (Fig.3). At $L/H < 5$, spectral characteristics revealed a broad frequency range of pressure pulsations covering in Strouhal number the both regions of aeroelastic vibrations (Fig.4). The latter is presumably due to that at small separations between beams the second and the third beams appeared to be situated in the stall region of the first beam, while at large separations a regular wavy flow pattern was formed with streamlining both the second and the third beams [3]. These results are consistent with those obtained by T.Takeuchi [4] on the pulsational velocity spectra in the vicinity of immobile two-beam models being similar to the models used in our study, which provide an indication that at large separations between beams only one peak is observed in the spectra, while at small separations two peaks are seen.

The distribution of pressure over the oscillating models were found to depend substantially upon the amplitude of model's oscillations. At small amplitudes, pressure pulsations at the first, second and third beams exhibited insignificant phase shift between them, each of the beams making a positive contribution to developing oscillations (Fig.5). As the amplitude rises, the difference between the phases increases, the second beam, as a rule, amplifying the oscillations, while the third damping them. At large amplitude of oscillations, the situation at the first beam changes drastically: the amplitude of the pulsating pressure increases three- or fourfold, the phase shift, however, growing in value as well, running into a value of about π . As a result, the contribution to the development of oscillations due to the marked aerodynamic forces at the first beam acting almost in antiphase to the displacement of model, remains the same order of magnitude with that of other beams. Noteworthy also is high value of the amplitude of

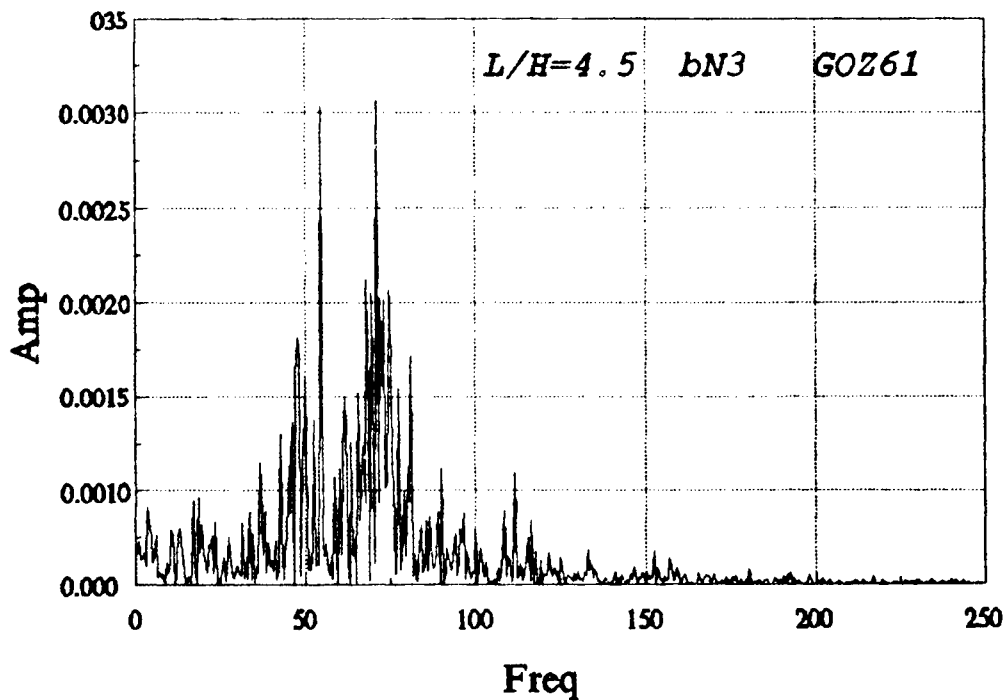


Fig. 4. The pressure pulsations spectral characteristics at little separation between beams

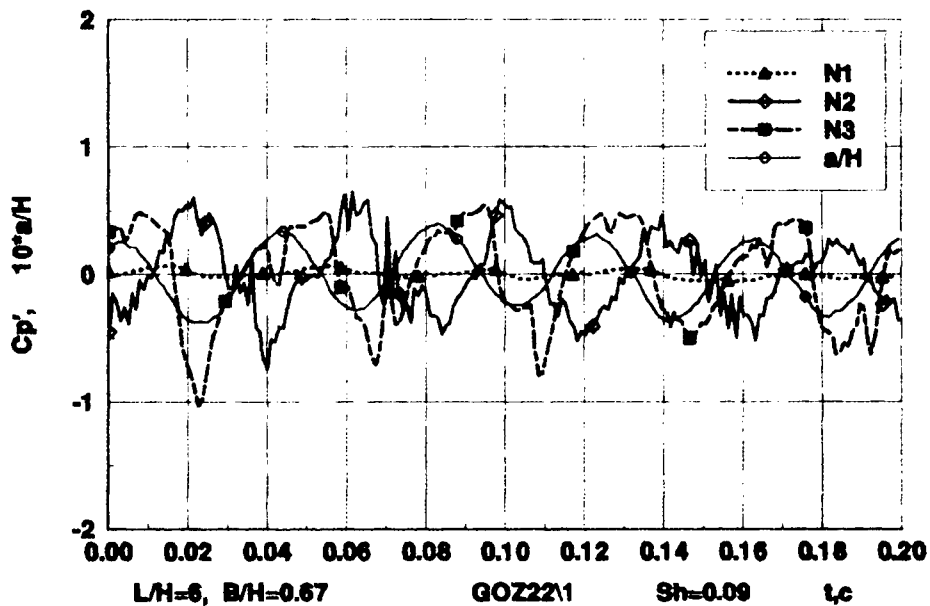


Fig. 5. Oscillogram of pressure pulsations on the beams at small amplitudes .

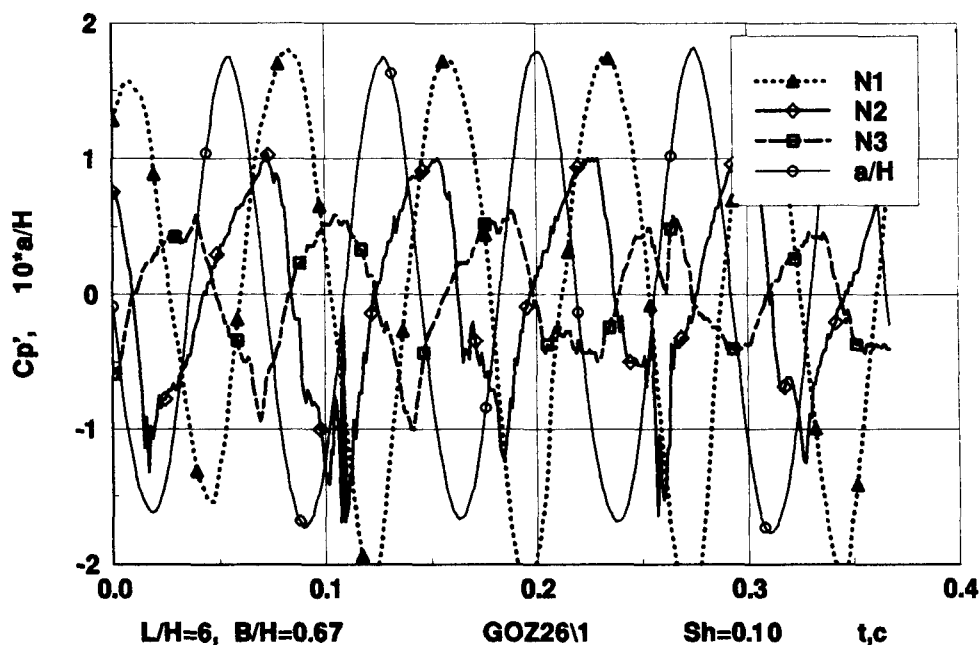


Fig. 6. Oscillogram of pressure pulsations on the beams at high value of the amplitude.

pressure pulsations at the first beam, which at strong oscillations of model was found to be in excess of 2(Fig.6).

The obtained results allow to gain better insight into the problem of the origin and damping of multiple-span bridge constructions.

REFERENCES

1. Salenko S.D., Obukhovskiy A.D. Aeroelastic oscillation specialties of multibeam consols.// Proc. of 8th. International Conferences "Methods of Aerophys. Research".- Novosibirsk, 1996.-Vol.2.- P. 205-209.
2. Salenko S.D., Obukhovskiy A.D. Parametric investigation of multi-beam bridges aeroelasticity // Int. Conf. Methods Aerophys. Research: Proc. Pt 3. - Novosibirsk, 1998.- P.241 - 246.
3. Севастьянова Е.В., Соловьева Е.В. Исследование структуры течения около свободно колеблющихся цилиндрических тел различного поперечного сечения // Промышленная аэродинамика, вып.36- Москва: Машиностроение, 1991. 206-220.
4. Takeuchi T. Effects of Geometrical Shape on Vortex-induced Oscillations of Bridge Tower // Journal of Wind Engineering and Industrial Aerodynamics.-1990- Vol. 33.-P.359-368.

CONVECTION AND HEAT TRANSFER IN ANGULAR MOMENTUM NONEQUILIBRIUM TURBULENT FLOWS

V.M. Trofimov

Institute of Theoretical and Applied Mechanics SB RAS
630090, Novosibirsk, Russia

INTRODUCTION

The evolution of aerospace technology, particularly, the aspect of heat protection, posed the problems closely related to the properties of turbulent motion in supersonic flows. Our previous experimental and numerical studies in supersonic flows with cavities and steps showed that the heat transfer behavior is qualitatively different from the static pressure behavior and can even have an opposite tendency [1]. The "memory effects" manifest themselves most clearly in the streamwise heat transfer distribution. The measurements of turbulence characteristics in the mixing layer ahead of the steps revealed their considerable deviation from the equilibrium distribution. The main problem is that there are no adequate turbulence models for conditions of these flows. Integral methods still play an important role. At the same time, the Kutateladze-Leontiev theory [2], which is widely and successfully used in supersonic flows, is invalid for these conditions. We also showed that an introduction of a new boundary layer does not yield any positive result. The conclusion is that it is necessary to study the mechanism of formation of the internal structure of developed turbulence, its influence on convection and heat transfer, and to develop methods for description of turbulent motion at high Reynolds numbers.

The challenge of the present work is to develop such an approach to investigating convection and heat transfer, including experimental studies of the influence of internal structure of turbulent flows on heat transfer, development and verification of model concepts of large-scale turbulence behavior in supersonic flows with high pressure gradient, construction of a model of angular momentum nonequilibrium turbulent flow and its application in the problems of heat convection in a fluid layer to reveal the mechanism of generation of large-scale structures in developed turbulence.

A review of literature was made on the problems of turbulent flows with internal structural processes and relaxation phenomena, and also the known approaches to their description, including asymmetrical mechanics. The analysis of publications showed that there are grounds for wider use of the concepts of moment media in the description of structural processes in turbulent flows, convection, and heat transfer. This primarily refers to flows with high Reynolds numbers and large pressure gradients.

EXPERIMENTS

The influence of the internal flow structure on the heat transfer processes in supersonic flows with high local pressure gradients was experimentally studied. The problem formulation included the study of three-dimensional flows behind flat steps, expanding steps, and also flows in a supersonic duct with flow turning. A complex of measurement methods included the electrocalorimetric method of the measurement of heat transfer coefficients

(the method of graphite film), the method of pneumometric measurements on the surface, the method of liquid crystalline thermoindicators, and also the visualization methods: optical, vane filament, and oil-film techniques.

The results of visualization of the limiting streamlines, the directions of the medium streamlines in the boundary layer (vane filaments), and temperature fields of the models confirmed the existence of quasisteady streamwise structures in the flows behind flat steps, and yielded new quantitative data about their behavior. More detailed data on the influence of these structures on heat transfer were obtained (Fig.1). On the basis of these data, a new scheme of secondary vortex motion, including at least two layers of vortex structures, was proposed (Fig.2). A similar tendency of scale hierarchy of streamwise structures was registered earlier in low-speed flows with obstacles. Thus, it is a common property of flows with high streamwise pressure gradients.

Experimental studies of turbulent heat transfer on the walls of a supersonic duct with the turning of its axis revealed a *different* kind of *structural effect* on heat transfer [3]. A specific feature of such flows is intense (up to 200 dB) discrete tones in the pressure pulsation spectrum in the frequency range of 1-5 kHz, which are excited upstream of the nozzle. The distribution of the heat transfer coefficient at zero angle of nozzle axis deflection is described well by the theory [2] (Fig.3 a). As the angle of nozzle axis

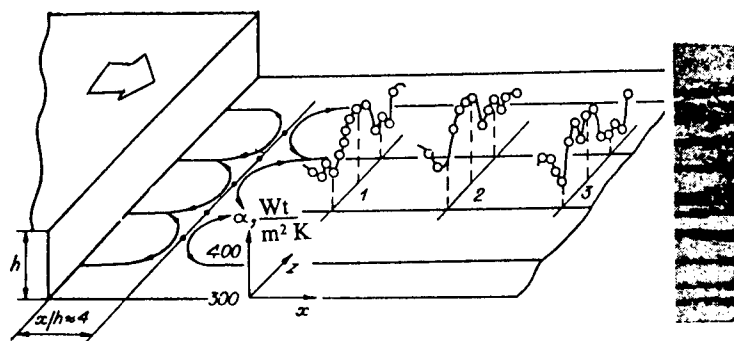


FIG. 1. Influence of the longitudinal structures on a heat transfer considerations near the backward step (the Mack number $M = 3.0$)

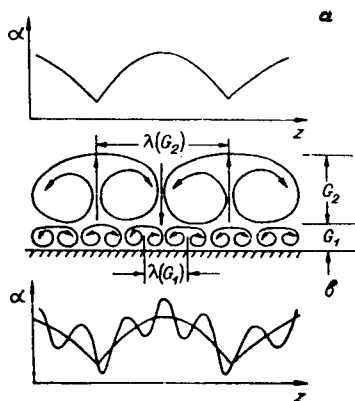


FIG. 2. Longitudinal vortices concept : a - old, b - new

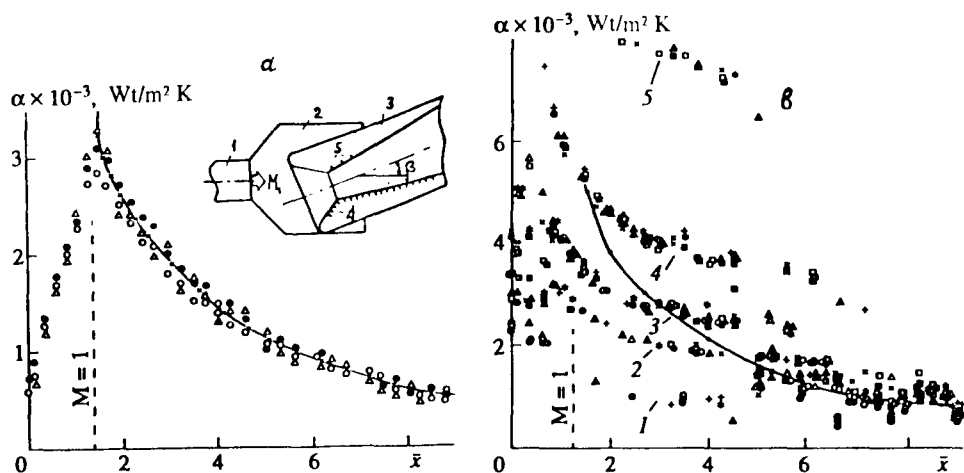


FIG. 3. Distribution of the heat-transfer intensity coefficients along the nozzle $x = X/R^*$ (R^* is radius of the nozzle throat): a — $\beta = 0^\circ$; the curve is a calculation from Ref. 2. b — $\beta = 20^\circ$; 1-5 — structural levels of heat transfer; curve — calculation (Ref. 2, $\beta = 0^\circ$)

increases, another qualitative behavior is clearly observed. The heat transfer coefficients are randomly stratified into 3-7 levels with different probability of falling into each level (Fig. 3 b). The probability is higher at the medium layers, but decreases as the axial angle increases. The analysis of experimental data revealed the multiplicity of the ratio of the squares of heat transfer coefficients that belong to different levels. Their relationship with the frequency characteristics of acoustic nature was established, and an empirical dependence was found, which is a power function of the ratio of the squares of heat transfer coefficients versus the level number $\alpha_n^2/\alpha_1^2 = 2^{n-1}$, $n = 1, 2, 3, \dots$. The relationship of the measured amplitudes of discrete components of the pressure pulsation spectrum has a similar form and corresponds to the pressure field of multipole sources. By analyzing the equation of aerodynamic noise of a turbulent jet, a source term was revealed, which can describe the interaction of radiation from vortices-multipoles with an external acoustic field, similar to acoustic resonance interaction in paramagnetic medium (APR). Such a possibility was confirmed by a comparison of real scales of the largest vortices in the boundary layer with the frequency observed on discrete tones of the acoustic field. Their complete correlation was found, which is necessary to invoke interaction similar to APR.

The main conclusion is that the character of interaction of vortices-multipoles as objects of internal structure with acoustic radiation testifies to the existence of internal angular momentum in the field medium, related to these objects. The consequence is important for us: the reorientation of the angular momentum of large vortices in the field of pressure gradients cannot occur instantly, but is accompanied by relaxation processes, which can be responsible for the "memory effects".

VERIFICATION OF MODEL CONCEPTS

To verify these model concepts, we constructed an approximate integral method for calculating the heat transfer in supersonic flows with large pressure gradients. It is based on the main propositions of the asymptotical theory [2]. A compressible boundary layer flow is considered. Using the integration with respect to the transverse coordinate, we pass to an integral energy equation containing an unknown Stanton number, which requires

the definition of the heat transfer law. Using the limiting heat transfer law within the framework of the asymptotical theory, we can calculate the heat transfer in many flows with moderate pressure gradients. Large local pressure gradients, however, do not allow one to use this theory. Contrary to the initial theory, the limiting heat transfer laws were obtained here in the form including the nonequilibrium influence function. This function is constructed assuming the absence of equilibrium in the motion of large vortices with the mean flow in the course of reorientation of their angular velocities in the field of pressure gradient. This function takes into account the contribution of all sections with different pressure gradients, prior to a given point, which reorient the turbulent vortices. The calculations of the distribution of heat transfer coefficients in the vicinity of steps in a supersonic flow (Fig.4) and on the walls of a supersonic diffuser (Fig.5), and their comparison with experimental data confirmed the effectiveness of model concepts.

METHOD OF ANGULAR MOMENTUM NONEQUILIBRIUM FLOWS

The experiments showed, and the verification of model concepts confirmed that it is necessary to take into account the property of preferable orientation of internal structural objects (vortices) in the medium when describing turbulent flows with high Reynolds

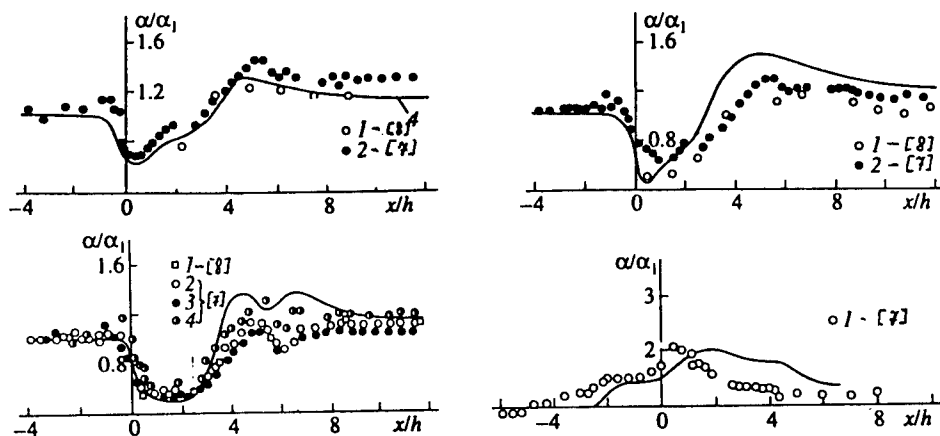


FIG. 4. Consideration of the heat transfer coefficients near the steps.

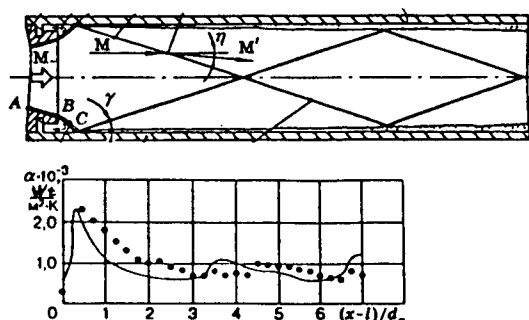


FIG. 5.

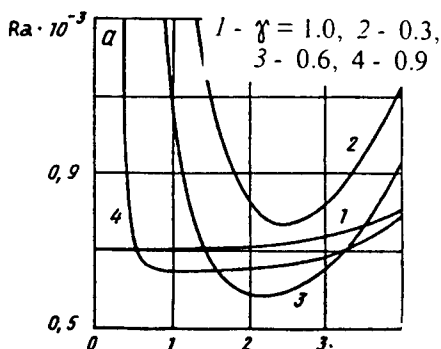


FIG. 6. Shifting of minimum of neutral curve.

numbers and large pressure gradients. The analysis of literature showed that the optimal method for that is to use a generic approach based on the concepts of a medium with internal angular momentum.

We use a model of medium with internal angular momentum and involve a body of mathematics for hydrodynamics with internal rotation. Performing the time averaging commonly used in hydromechanics, we obtain a system including the momentum equation, the angular momentum equation, and the continuity equation. Contrary to Boussinesq-closed Reynolds equations, the aforementioned equations contain additional terms with effective rotational viscosity, taking into account the internal angular momentum of oriented vortices, and also an additional independent vector equation for the full angular momentum. If the condition of angular momentum equilibrium is satisfied (zero internal angular momentum), we obtain the usual Reynolds equations.

What are the benefits of the new approach? First of all, it offers a theoretical justification for semi-empirical theories of Prandtl, Karman, and Hinze. It is shown that the main formula of Prandtl's theory for tangential stress follows from the condition of mean-time vanishing of the sum of the angular momentum of vortex mass carried through a certain area by right and left vortices of oscillatory motion ($M^+ + M^- = 0$). Hence, Prandtl's solution is a consequence of assuming the rotational isotropy of the mean motion and denotes the absence of any preferable spatial orientation of vortex motion. This solution immediately follows from the condition of angular momentum equilibrium as a specific case of equations of the proposed approach. The discrepancy between the known experimental data and Prandtl's solution for the mean velocity profile in the external part of turbulent boundary layer and in the turbulent core of duct flow at high Reynolds numbers is explained by violation of rotational isotropy and described by the new model. It is shown that Hinze's relaxation equation, obtained for the purpose of describing the inheritance phenomena in boundary layers, is a specific case of equations of the angular momentum in the proposed approach. It is important that the method of angular momentum nonequilibrium turbulent motion allowed us to find analytical solutions for a number of turbulent flows at high Reynolds numbers ($> 10^6$) in ducts and pipes. These solutions are almost as simple in form as Prandtl's solution, but, in contrast to the latter, they yield a good description of the turbulent flow core at high Re.

GENERATION OF STRUCTURES IN DEVELOPED TURBULENCE

On the basis of the developed approach we can consider the mechanism of generation of internal structures in developed turbulence. The classical methods based on the Reynolds equations do not give a clear idea about it. At the same time, the use of our approach directly for a very complicated object, such as turbulent motion in supersonic flows with steps and cavities, does not allow us to go far analytically, avoiding the development and justification of a complex computational algorithm. Therefore, retaining the high Reynolds numbers and angular momentum nonequilibrium which are important for us, the chosen object of investigation allowed us to perform strict analytical analysis from the beginning to the end, without using numerical or other approximate methods.

The general formulation of the problem consists in the following [4]. A large scale disturbance is assumed to be developed on a neutral profile of temperature stratified fluid rotating around a vertical axis with uniform angular velocity. The system of equations is linearized under the assumption of the initial stage of disturbance evolution. The boundary conditions for nondimensional amplitudes together with the system of amplitude equations allowed us to formulate boundary value problems with discrete spectrum. The main result was obtained by solving the boundary value problem with nonequilibrium at the upper boundary of a rotating layer.

The behavior of neutral curves of this problem is dramatically different from the classical case. For the values of angular momentum nonequilibrium parameters equal or larger than the critical value ($\gamma = 1$), there is no region of stable long-wave harmonics: all disturbances with all wavelengths become unstable when a certain value of the Raleigh number is reached. It is seen (Fig.6) from the behavior of neutral curves with $\gamma < 1$ that as the nonequilibrium parameter γ increases the scale of the most unstable disturbances increases (since the wavenumber decreases), which ends by the formation of one large-scale structure with a scale of the whole region, contrary to structures commonly used in the classical problem, in the form of Benard cells whose scale is equal to the convective layer thickness. A similar picture of generation of a large-scale structure is observed under the conditions of helical turbulence [5, 6].

For the conditions of development of tropical cyclones in the Earth's troposphere, the scale of energy-containing vortices is $\lambda = 12.5 m$, and the seed vortices have a scale of 5-8 km. The resultant large-scale structure (cyclone) has a scale of 200-1000 km.

Thus, convection and heat transfer in supersonic gas flows with high pressure gradients and the model of emergence of large-scale structures in rotating convective fluid layers have been experimentally and theoretically considered from a single viewpoint of angular momentum nonequilibrium turbulent motion. The results obtained clarify the physical mechanisms of the influence of turbulent motion on convection and heat transfer at high ($> 10^6$) Reynolds numbers and verify that the turbulent motion at high Reynolds numbers manifests itself as a medium with internal angular momentum.

The work was supported by the Russian Foundation for Basic Research (grants 96-02-19500, 96-01-01798, 98-02-17783).

REFERENCES

1. Trofimov V.M. Gas dynamics and heat transfer in separated turbulent flows : Ph.D. Theses. Novosibirsk, 1988 (in Russian).
2. Kutateladze S.S., Leontiev A.I. Heat and mass transfer in turbulent boundary layer. Moscow: Energoatomizdat, 1985 (in Russian).
3. Zaikovskiy V.N., Trofimov V.M. Mechanism of stratification of turbulent heat transfer in a sound field in the presence of rotational anisotropy of the flow//Pis'ma Zh. Eksp. Teor. Fiz. 1997, Vol. 65, Iss. 2, P. 145-149 (JETP Lett., Vol. 65, No. 2, 25 Jan. 1997, pp.154-159.).
4. Berezin Y.A., Trofimov V.M. A model of non-equilibrium turbulence with an asymmetric stress. Application to the problems of thermal convection//Continuum Mech. Thermodyn., 1995, Vol. 7, No. 4, pp.415-437.
5. Levich E., Shtilman L., Tur A.V. The origin of coherence in hydrodynamical turbulence//Physica A, 1991, Vol. 176, pp. 241-296.
6. Berezin Y.A., Hutter K., Zhukov V.P. Large-scale vortical structure supported by small-scale turbulent motions, Helicity as a cause for inverse energy cascade//Continuum Mech. Thermodyn., 1991, Vol. 3, pp. 127-146.
7. Zheltovodov A.A., Zaulichny E.G., Trofimov V.M. Development of turbulence models for computations of heat transfer at supersonic turbulent separated flows conditions (in Russian)//Zh.Prikl.Mech.Tekhn.Fiz., No. 4, 1990, pp.96-104.
8. Charwat A.F., Dewey C.F., Ross J.N., Hitz J.A. An investigation of separated flows: Part 2. Flow in the cavity and heat transfer// J.Aeronaut.Sci. 1961, V.28, No.7, pp.514-527.

ACOUSTIC TONES INVESTIGATION IN ZONE OF TURBULENT HEAT TRANSFER STRATIFICATION AT SUPERSONIC VELOCITIES

V.M. Trofimov, V.N. Zaikovskii

Institute of Theoretical and Applied Mechanics SB RAS
630090, Novosibirsk, Russia

INTRODUCTION

Acoustic interactions with developed turbulence under conditions of strong rotational anisotropy (losses of reflection symmetry) of the flow are of special interest, since the effect of the acoustics on momentum and heat transport processes is qualitatively different in the presence of asymmetry of the stressed state of such a medium.

Acoustic (vortex) flows and heat transport due to them near obstacles of different types are ordinarily not established immediately, but rather they develop gradually until the retardation due to the viscosity of the medium compensates the increase in their velocity under the action of the sound. The scale of the flow is determined by the thickness of the acoustic boundary layer $\delta = (\nu/\omega)^{1/2}$ (ν is the kinematic viscosity coefficient and ω is the angular frequency of the sound).

In [1] a stratification of heat transfer into discrete levels has been observed experimentally in an interaction of an acoustic field with a turbulent boundary layer in a supersonic channel. In [2] a new mechanism of stratification is investigated which corresponds to interactions between the sound fields of the turbulent vortices and the radiation from the discrete currents of the external flow which are such that the acoustic flows are established so quickly that several (3-7) vortex modes of acoustic origin, giving way to one another in a random manner, are realized near the heat transfer surface.

The basic arrangement of the experiment and the measurement procedure are presented in [1]. In the present work, we obtained new data which made it possible to determine the mechanism which results in the stratification of heat transport.

EXPERIMENTS

The experiments conducted on a gasdynamic RD (rocket engine) apparatus (Institute of Theoretical and Applied Mechanics, Siberian Branch of Russian Academy of Sciences) with air flow rates of up to 10 kg/s. The distributions of the heat transfer intensity coefficients, pressure, and pressure pulsations at the walls of a supersonic channel were measured as a function of the position of the channel axis with respect to the subsonic gas flow rate at the entrance. Characteristic acoustic oscillations were excited in the semiclosed volume of the gas flow and then interacted with the sound fields of the turbulent vortices in the boundary layer of the supersonic channel.

The gas (air), passing through the entrance channel 1 (Fig.1a), flows into the second channel 3, which is shaped like a conical Laval nozzle. The diameter of the throat (critical section) equals 38.4 mm. The position of the nozzle 3 was varied by changing the angle β , and the velocity of the flow at the entrance to the nozzle was varied by changing the Mach number M_1 of the jet flowing out of the channel 1. The measurements were performed along the generatrices of the nozzle 3 on the upstream and downstream sides; this was

achieved by rotating the nozzle relative to the axis by 180° .

Three heat transport regimes are observed on the generatrix of the nozzle 3 (temperature sensors 4), depending on the values of M_1 and β . The first regime (fig.1a) corresponds to an ordinary turbulent heat transport regime in a supersonic channel (here and below in the figures the curve was calculated according to [3]). The second type (Fig. 1b and 1c) reflects the effect of nonstationary processes due to the instability of large-scale secondary vortex flows, which in turn interact with the sound field of the entrance of the nozzle 3. This type of heat transport exhibits the typical nonstationary, irregular character expressed in the random variance, which increases with M_1 , in the values of the heat transfer coefficients. The third regime (Fig.1d), first observed in [1], is characterized by a clearly observed ordering of the heat transfer coefficients α_n , which are distributed with different probability in several levels n (Fig. 1b), and by ratio α_n^2/α_1^2 ($n = 1, 2, 3, \dots$) which takes on integer values.

Pressure pulsation measurements were performed on the wall of nozzle 3 at variation of angles β and γ , as well as the Mach number M_1 of the jet flowing out of the channel 1. A location of the sensor 1 corresponds to a region of clearly defined heat transfer stratification, the sensor 2 was located at the end of the region where the stratification was out.

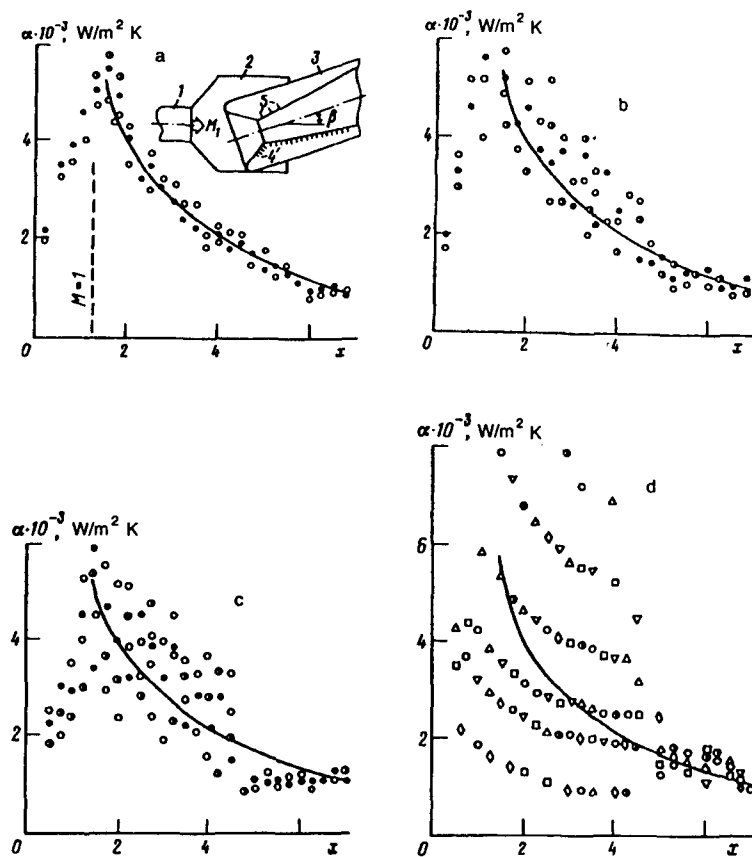


FIG. 1. Distribution of the heat transfer intensity coefficients along the generatrix of the nozzle $x = X/R^*$ (R^* is the radius of the nozzle throat): a — $M_1 \approx 0$, $\beta = 0^\circ$; b — $M_1 = 0.18$, $\beta = 0^\circ$; c — $M_1 = 0.35$, $\beta = 0^\circ$; d — $M_1 = 0.35$, $\beta = 20^\circ$.

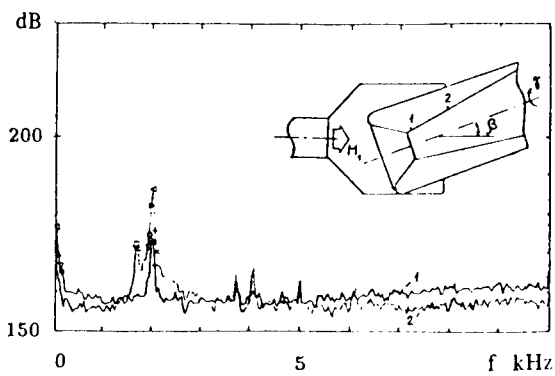


FIG. 2. $\beta = 0$, $M_1 = 0.05$

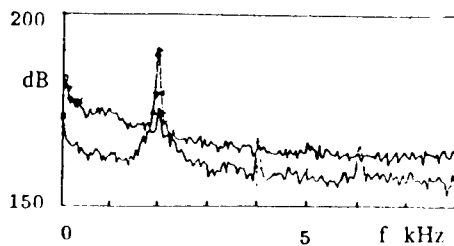


FIG. 4. $\beta = 0$, $M_1 = 0.20$

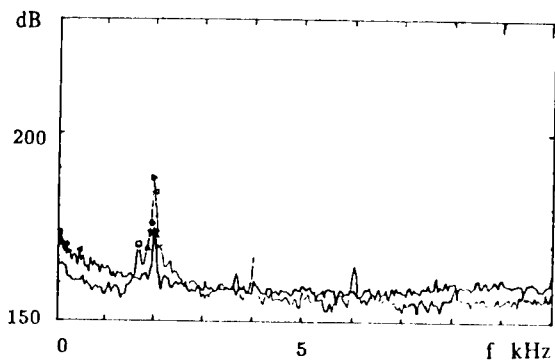


FIG. 3. $\beta = 0$, $M_1 = 0.10$

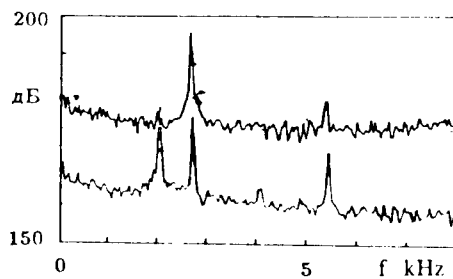


FIG. 5. $\beta = 0$, $M_1 = 0.72$

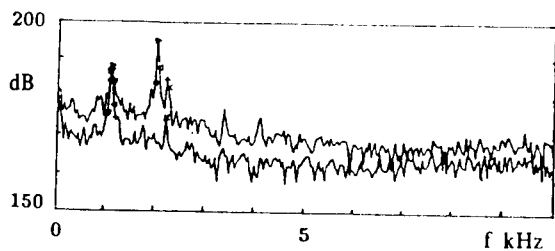


FIG. 6. $\beta = 0$, $M_1 = 0.35$

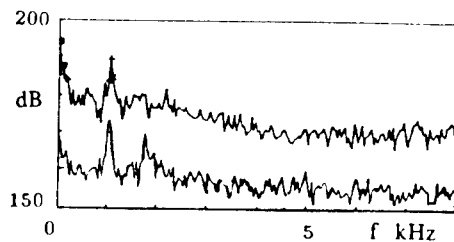


FIG. 7. $\beta = 20^\circ$, $\gamma = 0^\circ$, $M_1 = 0.35$

The pressure pulsation measuring and data processing method (discrete Fourier transformation with weigh functions - frequency spectrum windows) allowed present reliably data in frequency range 0-10 kHz. Actually the 0-5 kHz range concerned us since the discrete tones of pulsation spectrum were observed in that region.

The pressure pulsation spectrum (sensors 1 and 2) is presented in Fig.2-7. The ordinate is pressure pulsation level at the frequency f determined as $L_f = 20 \lg \frac{p}{p_{00}}$, where p is the pressure pulsation amplitude at the frequency f in band of $49Hz$, $p_{00} = 2 \cdot 10^{-5} \text{ Nt/m}^2$. All spectra are averaged over some samples with the aim to exlude the overshoots.

We can observe (Fig.2-6) that *i*) the pulsation level grows with the Mach number increasing, *ii*) the frequencies of the discrete tones are the same for all region of measurements, *iii*) the acoustic state in enter part of the nozzle is the governing factor.

The comparision of regime with $\beta = 0^0$ (Fig.6) and $\beta = 20^0$ (Fig.7) demonstrates the effect of the channel deflacon on the spectrum of pulsations. The discrete tones are a decrease in value.

These observations are indicative of the interaction between the discrete tones acoustic radiation and the turbulent vortices (of boundary layer flow) oriented in the gradient field of the main flow. On the basis of present knowledge, the physical mechanism of acoustic interaction [2] takes a new verification. Heat transfer stochastic stratification supports in our opinion the principal fact. It is as follows: the turbulent flow shows evidence of the moment medium (medium with the intrinsic angular momenta) in conditions such measurements, namely, in present of the high pressure gradient and the intensive acoustic radiation.

The work was supported by the Russian Foundation for Basic Research (grants 96-02-19500, 98-02-17783).

REFERENCES

1. Zaikovsky V.N., Trofimov V.M. Observation of structural levels of turbulent heat transfer // Pis'ma Zh. Eksp. Teor. Fiz. 1995. Vol. 61. Iss. 8. P. 627-630 (JETP Lett. Vol. 61, No. 8, 25 April 1995. P.645-649.).
2. Zaikovsky V.N., Trofimov V.M. Mechanism of stratification of turbulent heat transfer in a sound field in the presence of rotational anisotropy of the flow // Pis'ma Zh. Eksp. Teor. Fiz. 1997. Vol. 65. Iss. 2. P. 145-149 (JETP Lett. Vol. 65, No. 2, 25 Jan. 1997. P.154-159.).
3. Kutateladze S.S., Leontiev A.I. Heat and mass transfer in turbulent boundary layer. Moscow: Energoatomizdat, 1985 (in Russian).

NUMERICAL INVESTIGATION OF SUPERSONIC FLOW STRUCTURE IN THE DUCT AT THE PRESENCE OF MAGNETIC FIELD

A.B.Vatazhin, O.V.Gouskov, V.I.Kopchenov
CIAM, Moscow, Russia

Recently some proposals [1-5] to use the MHD-devices as flow control systems in hypersonic technology are discussed. It is necessary to estimate these proposals not only qualitatively, but quantitatively as well. At the same time, the qualitative arguments and simplified quantitative estimations are currently presented as a rule to justify these proposals. The flow field in the hypersonic propulsion system is too complex. The new physical models must be developed and included into the existing computational models of the flow in hypersonic propulsion system. Furthermore, it seems to be appropriate to solve some simplified model problems to understand main flow features and to estimate the efficiency of the supersonic and hypersonic flow control by MHD methods in the range of parameters typical for hypersonic propulsion systems.

The possibility of MHD flow control in the duct of hypersonic propulsion system and flow structure are investigated now in CIAM on the base of the combined mathematical model [6]. This combined model [6] includes as constituents the gasdynamics, turbulence and supersonic combustion models. This model is supplemented by the physical model for the description of MHD flow. The existing preceding experience in MHD flow investigation [7] is used and adapted to new applications.

Some model problems were solved to investigate the efficiency of hypersonic flow deceleration with the aid of magnetic field on the first stage. In this article there are presented some results on deceleration of axisymmetric supersonic flow in the magnetic field of single current loop or in the magnetic field of finite length solenoid for inviscid, laminar and turbulent flow regimes. The results of solution of the problem about the flow deceleration in 2-D channel in the regime of electric power generation with continuous electrodes installed on the channel walls are presented also.

Short description of mathematical and physical models

The governing equations for the present analysis are the unsteady compressible two-dimensional or axisymmetric full Navier-Stokes equations. The time dependency of the governing equations permits the solution to progress from an arbitrary initial guess to the steady state. The expressions for the volume densities of MHD force \mathbf{f} and electric power q supplied to the gas must be included into the right side of equations as follows $\mathbf{f} = \mathbf{j} \times \mathbf{B}$, $q = \mathbf{j} \cdot \mathbf{E}$. Here \mathbf{B} , \mathbf{E} and \mathbf{j} are vectors of magnetic field, electric field and electric current density. The volume electric charge density is neglected. When induced magnetic field is also neglected in comparison with the applied external magnetic field, the equations for \mathbf{E} , \mathbf{j} and \mathbf{B} determination are following [7,8]

$$\mathbf{j} = \sigma(-\nabla\varphi + \mathbf{v} \times \mathbf{B}) - \frac{\beta}{|\mathbf{B}|} \mathbf{j} \times \mathbf{B}, \quad \text{div } \mathbf{j} = 0,$$

$$\text{rot } \mathbf{B} = 0, \quad \text{div } \mathbf{B} = 0, \quad \mathbf{E} = -\nabla\varphi$$

Here φ is electric potential, σ is electric conductivity, β is the Hall parameter, and β , σ are known function of thermodynamic parameters. In these equations \mathbf{B} is applied magnetic field. The equations for \mathbf{B} are supposed to be satisfied in the regions where external electric circuits

are assumed to be absent. It is suggested that transport coefficients (viscosity, conductivity) did not dependent upon the magnetic field B .

In turbulent case the averaged full Navier-Stokes equations are used. The one equation differential model "v1-91" [9] for turbulent viscosity is employed in the code FNAS2D [6].

Flow deceleration in cylindrical duct by single current loop or solenoid magnetic fields

The axisymmetric flow in the circular tube with nonperforated and electrically nonconductive walls is investigated. For simplicity, it is assumed that the electric conductivity is isotropic and constant and Hall effects are negligible. It is supposed that external magnetic field is generated by circular current loop or by axisymmetric solenoid. Therefore external magnetic field is assumed to be axisymmetric. In such case the MHD source terms f and q in accordance with the velocity, magnetic and electric fields structure are following:

$$f_x = -\sigma B_y (u B_y - v B_x), \quad f_y = \sigma B_x (u B_y - v B_x), \quad q = 0.$$

Here x and y are axial and radial coordinates, u and v are axial and radial velocities. The axisymmetric magnetic field is presented according to [8].

The flow at the duct entry is supposed to be supersonic and uniform. All parameters distributions must be given for supersonic flow at the duct entry. The slip velocity conditions are posed on tube walls in inviscid case and no-slip conditions - in viscous case. For viscous and heat conducting gas, the wall temperature is supposed to be equal to free stream temperature in the entry cross-section. In supersonic inviscid flow on the exit computational boundary, the additional boundary conditions are not required. In viscous case, the so called drift boundary conditions with normal derivatives of all parameters being determined inside computational region are posed both in supersonic core region and in subsonic part of wall boundary layer.

The system of equations is used in dimensionless form. The main values used for reference are following: the duct radius R , the free stream velocity V_0 , density ρ_0 , gas constant \mathcal{R} , dynamic viscosity μ_0 , characteristic magnetic field B_* and electric conductivity σ_0 . Then the following dimensionless parameters appear in the system of equations

$$Re = \rho_0 V_0 R / \mu_0, \quad S = \sigma_0 B_*^2 R / \rho_0 V_0^2, \quad Pr, \quad Pr_t, \quad \gamma,$$

where Re is Reynolds number and S is MHD interaction parameter.

As the first example, the inviscid, laminar and turbulent flows in the cylindrical duct with magnetic field generated by current loop were investigated for the entry Mach number equal to 5. The cross-section $x=0$ is concerned with position of electric current loop. The radius H of current loop is equal to two duct radius. The exit duct section is located in position $x=5$.

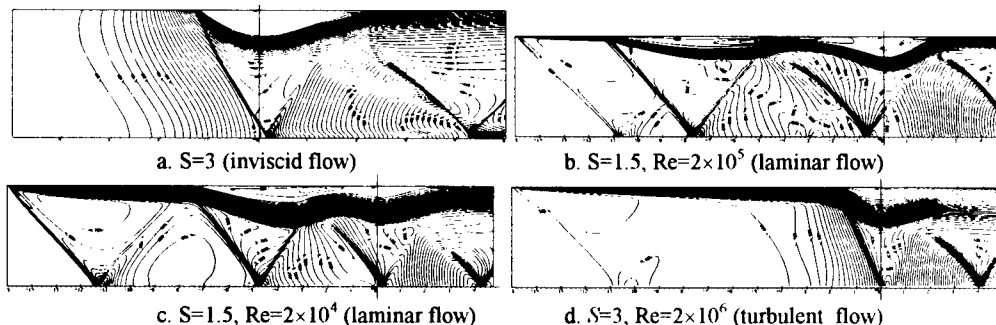


Fig.1. Mach number fields. Magnetic field generated by current loop

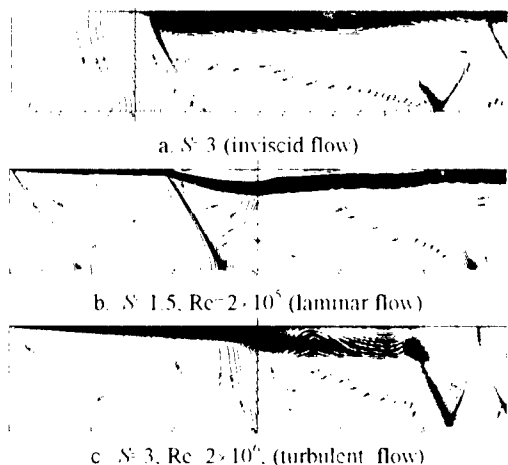


Fig. 2. Mach number fields. Magnetic field of solenoid

Further, the data for flow in cylindrical duct when the magnetic field is generated by solenoid are presented. The solenoid entry is located in the cross-section $x=0$. The solenoid exit cross-section is located at $x=10$ and the right boundary of calculation region is posed at $x=15$. The length of the duct from entry cross-section to entrance to solenoid is equal to 5 and 15 duct radius correspondingly in the cases of inviscid and viscous flows. The solenoid radius is twice greater than channel radius.

MHD interaction for inviscid flow (Euler equations) and for laminar and turbulent viscous flows at different Reynolds numbers (full Navier-Stokes equations) was analyzed. The Mach number contours for the solenoid are shown in Fig. 2. For turbulent case, it is necessary to note that visible turbulent boundary layer exists already at the solenoid inlet. The boundary layer thickness is increased appreciably at the entry to solenoid as the result of magnetic field influence. Then in solenoid the boundary layer thickness is almost constant up to exit from solenoid. The flow in this case did not contain the separation region.

Flow deceleration in 2-D channel in the regime of electric power generation

The 2-D flow in the tube of constant height with nonperforated walls is investigated. It is supposed that magnetic field \mathbf{B} is directed normally to the plane of the flow. The magnetic field is averaged over lateral coordinate z in the channel. The component B_z of the magnetic field is designated as B and it is the only nonzero component $\mathbf{B}=(0, 0, B(x))$. The 2-D electrodynamic equations can be formulated as follows:

$$\begin{aligned} j_x &= \sigma_\mu \left[-\frac{\partial \varphi}{\partial x} + vB + \beta \left(\frac{\partial \varphi}{\partial y} + uB \right) \right], \quad \frac{\partial j_x}{\partial x} + \frac{\partial j_y}{\partial y} = 0, \quad \sigma_\mu = \frac{\sigma}{1 + \beta^2}, \quad \beta = \alpha B \\ j_y &= \sigma_\mu \left[-\frac{\partial \varphi}{\partial y} - uB + \beta \left(-\frac{\partial \varphi}{\partial x} + vB \right) \right] \end{aligned}$$

Here α is supposed to be the known function of thermodynamic parameters. The components of MHD force f_x, f_y and electric power q supplied to gas are defined as

$$f_x = j_y B, \quad f_y = -j_x B, \quad q = -j_x \frac{\partial \varphi}{\partial x} - j_y \frac{\partial \varphi}{\partial y}$$

In the considered approximation [7], B is function of x only and is supposed to be given. The presented equations can be used for the determination of electric potential distribution if velocity components u and v are known. The solution of these equations requires

During these calculations influence of MHD interaction parameter on the flow field was estimated. In order to investigate the viscosity influence on the deceleration process some cases were considered. The calculations were performed for laminar viscous flow with $Re = 2 \cdot 10^5$ and $Re = 2 \cdot 10^6$. In order to provide the development of boundary layer in flow, the entry section of 15 radius length is positioned before cross-section where current loop is posed. For the turbulent flow, the Reynolds number is supposed to be equal to $2 \cdot 10^6$. The Mach number fields for the current loop are presented in Fig. 1.

the formulation of the boundary conditions on the duct wall and at the entry and exit duct cross-sections. The formulation of these boundary conditions depends upon the physical problem (see, for example, [7]). The following wall boundary conditions were considered in this article.

Walls are ideally sectioned electrodes. In this case the electric potential distribution along the upper and lower walls is supposed to be known. Some analytical solutions [7] can be used. The wall potential distribution of some real devices obtained from experiments can also be used [10]. Thus, it is given that $\varphi = \varphi_-(s)$ along the lower wall and $\varphi = \varphi_+(s)$ along the upper wall. Here s is coordinate along the wall.

It is necessary to note that the solution of the whole gasdynamic - electrodynamic problem can be obtained with the aid of iterative procedure when the electrodynamic subsystem is solved using known gasdynamic parameters and gasdynamic subsystem is solved taking into account known characteristics of electromagnetic field.

Simplified electrodynamic models are widely used in technical applications instead of 2-D models. Exact solution of electrodynamic equations exists if to suppose that the channel height h , magnetic field B and electric boundary conditions do not vary with x , but velocity components u , v , electric conductivity σ and value α are dependent on transverse coordinate only. It is possible to suppose that these solutions can be used also if the dependence of all aforementioned values upon the longitudinal coordinate is weak. Then the quasi 1-D approach is described by equations [7,11]:

$$E_y = -\frac{\partial\varphi}{\partial y} = \frac{j_y}{\sigma_\beta} + B(u - \beta v), \quad j_y = -\frac{B\langle u - \beta v \rangle - (\delta\varphi / h)}{\langle \sigma_\beta^{-1} \rangle},$$

$$j_x = \sigma v B - \beta j_y, \quad f_x = j_y B, \quad f_y = -j_x B, \quad q = j_y E_y.$$

Here $\delta\varphi = \varphi_- - \varphi_+$, and $\langle \xi \rangle = h^{-1} \int \xi(x, y) dy$.

The system of equations is written in dimensionless form. The main values used for reference are following: the duct height D_0 at the entry, the free stream velocity V_0 , density ρ_0 , gas constant \mathcal{H} , dynamic viscosity μ_0 , characteristic magnetic field B_* , the reference difference $\delta\varphi_0 = (\varphi_- - \varphi_+)_0$ of electric potential on the duct walls, electric conductivity σ_0 and value α_0 . Then the following dimensionless parameters appear in the system of equations

$$\text{Re} = \rho_0 V_0 D_0 / \mu_0, \quad S = \sigma_0 B_*^2 D_0 / \rho_0 V_0, \quad K_0 = \frac{\delta\varphi_0}{V_0 B_* D_0}, \quad \text{Pr}, \text{Pr}_t, \gamma, \beta_0 = \alpha_0 B_*,$$

where Re is Reynolds number, S is MHD interaction parameter, K_0 is the load parameter and β_0 is the Hall parameter.

The deceleration of supersonic flow of electrically conducting gas in the 2-D duct of constant height is investigated. The duct entry cross-section is located at coordinate $x=-6$ and the exit cross-section - at $x=5.5$. The flow deceleration is provided by crossed electric and magnetic fields in the central part of the duct. The magnetic field smoothly abates to the entry and exit cross-sections of the duct. The electric potential difference is supported between upper and lower duct walls in central part of the duct. The duct is operated in the regime of MHD generator when the upper and lower walls have correspondingly negative and positive electric potential in the central part of the duct. The electric potential on each wall approaches to zero in directions to the entry and exit cross-sections of the duct. The flow at the duct entry is supposed to be supersonic and uniform. The flow Mach number M at the duct entry is equal to 5.

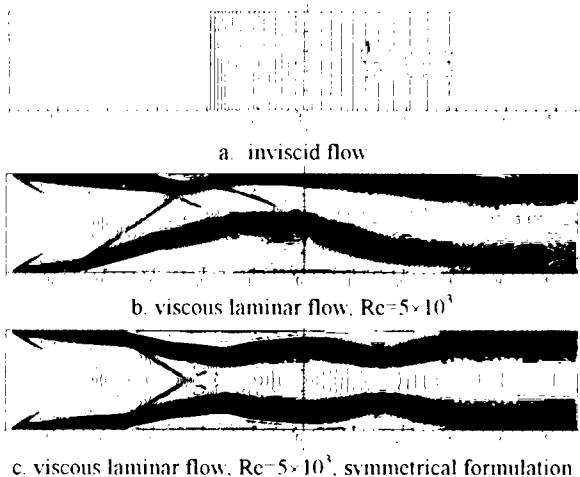


Fig.3. Mach number fields, $M_0=5$, $S=0.1$, $K_0=0.3$, $\beta_0=0$
quasi 1-D electrodynamics

are shown in fig.3. It is obvious that in the case of quasi 1-D electrodynamic the flow which is uniform at the duct entry remains uniform through all the duct for the inviscid flow (Fig 3a).

The next cases correspond to viscous laminar flow with the Reynolds number 5×10^3 . The distinctive peculiarity of obtained separation flow picture in the symmetric duct is the asymmetric flow field structure (Fig 3b). The asymmetric flow field is realized with large separation region on the lower wall. Only small separation region is realized on the upper wall of the duct. The results presented in Fig 3.c were calculated for the comparison with previous case when only one half of the duct was considered. In this case the symmetry condition on the duct symmetry plane is formulated. One can see the symmetric picture of flow pattern. It is possible to suppose that symmetrical flow with large separation region is unstable relative to small asymmetrical disturbances. The features of computational procedure can be the reason of such disturbances.

Further, some calculations were performed for this problem for 2-D flow using 2-D electrodynamic model. Both the gasdynamic parameters at the duct entry and magnetic field

This problem was solved using both quasi 1-D approach for electromagnetic field and accurate 2-D formulation of the electrodynamic problem. The perfect gas with adiabatic constant $\gamma=1.4$ is considered. The electric conductivity σ is assumed to be a constant isotropic value. The MHD interaction parameter S in performed calculations is equal to 0.1. The load parameter K_0 estimated by the value $\delta\varphi_0$ is equal to 0.3 and Hall effect is ignored.

The first series of calculations was performed for 2-D flow using quasi 1-D electrodynamic approach. The Mach number fields for this case

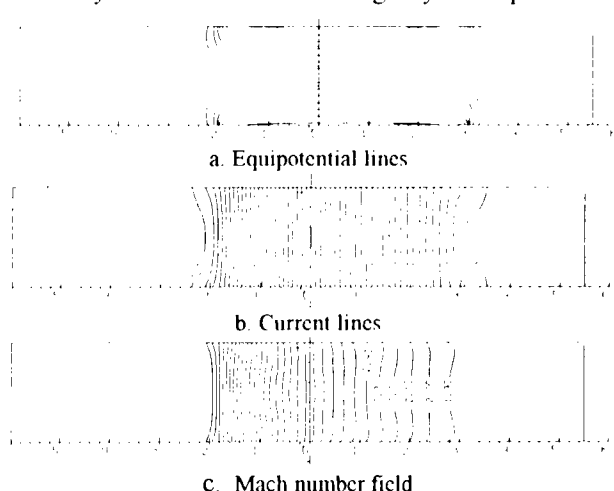


Fig.4. $S=0.1$, $K_0=0.3$, $\beta_0=0$, inviscid flow, 2-D electrodynamics

distribution are the same as in the case of quasi 1-D electrodynamics. Therefore it is possible to compare results obtained with quasi 1-D and 2-D electrodynamic solutions both for inviscid and viscous flows.

The following data are presented in 2-D case: the lines of equal electric potential (a), the "streamlines" of electric current (current lines) in (b) and Mach number fields (c). Mach number fields comparison for inviscid calculations (Fig 4) shows that the influence of 2-D electrodynamic effects on the deceleration is

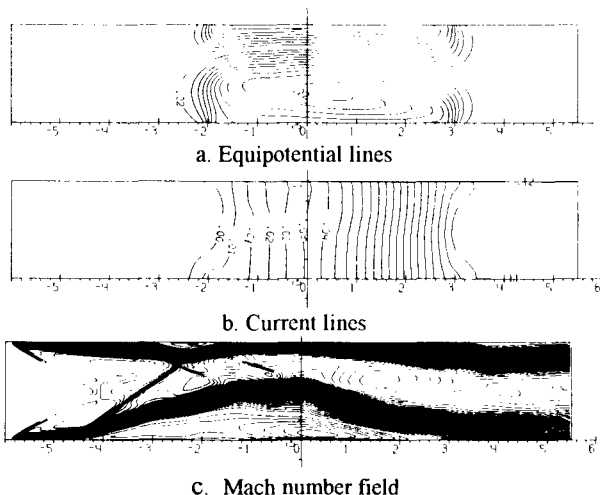


Fig.5. $S=0.1$, $K_0=0.3$, $\beta_0=0$, viscous laminar flow. $Re=5 \times 10^3$
2-D electrodynamics

negligible in comparison with quasi 1-D electrodynamics.

For the viscous laminar flow at the Reynolds number 5×10^3 , the electric potential, current and Mach number fields are shown in fig.5. In this case, the asymmetrical separated flow similar to this one in fig.3b is realized. The comparison of obtained results in 2-D case with those for 1-D electrodynamics shows that the difference in the flow fields is not appreciable. At the same time, the viscous and inviscid flow patterns differs significantly.

Thus, the presented examples testify to significant influence of the wall boundary layer on the structure of the hypersonic flow at its deceleration by magnetic field. This fact must be taken into account at the efficiency estimations of the MHD flow control applied to hypersonic propulsion system.

Acknowledgments

This work is partially supported by EOARD (Grant F61708-96-W0297) and by RFBR (project № 98-01-00923)

REFERENCES

1. Bityurin. V.A. Zeigarnik. A.L. Kuranov. On a Perspective of the MHD Technology in Aerospace Applications. - AIAA 96-2355. 1993.
2. Evgeniy P. Gurijanov, Philip T. Harsha. AJAX: New Directions in Hypersonic Technology. - AIAA 96-4609. 1996.
3. Kacnelson S.S. Zagorskiy A.V. Magneto hydrodynamic Flow Control in Scramjet Duct. // Thermophysics and Aeromechanics. - 1997. - V.4, N1. - P.41-46.
4. Brichkin D., Kuranov A., Sheikin E. MHD Control Technology for Hypersonic Vehicle. // 2-nd Weakly Ionized Gases Workshop. AIAA 8-th International Space Planes and Hypersonic Technologies Conference. - April 27-39, 1998. - P. 239-261.
5. Claudio Bruno, Paul A. Czysz. An Electro-Magnetic-Chemical Hypersonic Propulsion System. - AIAA 98-1582. 1998.
6. Bezgin L.V., Ganzhelo A.N., Gousskov O.V., Kopchenov V.I. Numerical Simulation of Viscous Non-Equilibrium Flows in SCRAMJET Elements // 13th ISABE 97-7131. - Chattanooga, Tennessee, USA. - September 7-12, 1997. - v.2, P.976-986.
7. Vatazhin A.B., Ljubimov G.A., Regirer S.A. Magneto hydrodynamic flows in channels. - Moscow: Nauka. 1970.
8. Vatazhin A.B., Isakova N.P. Deceleration of supersonic flow of conducting gas in strong magnetic field // Izv. AN USSR. - Fluid dynamics. - 1972. - N5. - P.145-155. (in Russia)
9. Gulyaev A.N., Kozlov V.E., Secundov A.N. A universal one-equation model for turbulent viscosity // Fluid dynamics. - 1993. - v.28, N4. - P.485-494.
10. Borghi C.A., Cristofolini A., Ribani P.L. A time-dependent two-dimensional analysis of transients in plasma MHD generators // 12th International Conference of magneto hydrodynamic electric power generation. - Yokohama, Japan. - Oct.15-18. 1996. - P.807-814.
11. Ivanov V.A., A method for calculation of MHD flow with boundary layer separation // High temperature. - 1994. - v.32, N5. P.909-912.

FORCE AND HEAT LOADS ON A POINTED BODY IN THE WAKE OF LOCAL ENERGY SOURCE

V.N.Vetlutsky, T.A.Korotaeva, and A.P.Shashkin
Institute of Theoretical and Applied Mechanics SB RAS
630090, Novosibirsk, Russia

The study of supersonic flow around an aircraft with a local energy source in front of it is of primary interest from the viewpoint of flow control. The flow is considered in the framework of the Prandtl model: an inviscid flow plus a thin boundary layer on the body surface. The external flow is calculated on the basis of three-dimensional Euler equations. The viscous flow calculation is performed on the basis of the boundary layer equations for a fully laminar case. The influence of energy supply on 3D effects in an inviscid flow and boundary layer is investigated. The study is performed by the example of a classical body (ogive). It is shown that the presence of a local energy source affects strongly the inviscid flow structure near the body and, hence, on the boundary layer flow. This can cause a significant redistribution of the force and heat loads on the body. It is shown in many papers, for example, [1-4], that the influence of local energy source on the total aerodynamic characteristics is rather substantial. The character of energy source action on the flow outside the boundary layer is analyzed in the present paper by the example of the flow around an ogive body, and the distributions of skin friction coefficient and Stanton number over the body surface are considered.

The gas outside the boundary layer is considered inviscid, compressible, and non-heat-conducting. The external flow near the ogive in the presence of an energy source is determined by solving 3D Euler equations by the finite volume method, which was described in detail and tested in the papers [3, 4]. The Cartesian coordinate system is used. The calculations are performed using the shock-capturing method. The following boundary conditions are applied:

- no-slip condition on the solid wall;
 - flow symmetry condition in the symmetry plane;
 - free-stream parameters at infinity;
 - «soft» boundary conditions at the exit boundary.
- The free-stream parameters are used as initial conditions.

The equations and boundary conditions are normalized: density by ρ_∞ , velocity by $|V_\infty|$, pressure by $\rho_\infty V_\infty^2$, entropy function by s_∞ , energy by V_∞^2 , where $p_\infty, \rho_\infty, V_\infty$ are the free-stream pressure, density, and velocity; f_{sx} is the entropy function, which in view of the perfect gas equation of state has the form $s = \ln(p/\rho^\kappa)$; κ is the ratio of specific heats.

The boundary layer is calculated using a code based on the solution of 3D compressible boundary layer equations. For this purpose, a non-orthogonal coordinate system (ξ, η, ζ) is introduced on the surface of a pointed body, where ξ is the distance from the body tip along the axis, η is the distance normal to the surface, and ζ is the meridional angle in cross-section perpendicular to the axis [5]. It is assumed that the body surface near the tip can be approximated by a conical surface and the boundary layer in this region is laminar.

Then the inviscid flow parameters are constant along generatrices in this region, and the boundary layer equations allow for a self-similar solution depending on the variables ζ , $\eta/\sqrt{\xi}$ [6]. It was used as initial data for solving the problem on the entire body surface. The flow parameters obtained by solving the problem of inviscid flow around this body are set at the boundary layer edge. Symmetry conditions are set in the plane $\zeta=0$ if it is a reattachment surface, otherwise no conditions are needed here. Another boundary $\zeta = \zeta_1$ either coincides with the outflow surface or chosen such that the gas flew out through it. Therefore, no conditions are defined there. Conventional slip conditions and surface temperature are set on the body surface $\eta=0$.

Three-dimensional boundary layer equations are solved numerically using an absolutely steady second-order difference scheme suggested in [7] for incompressible flow and tested in [8, 9] for a compressible one. The developed algorithm was used to calculate the boundary layer on ogive-cylindrical bodies in a supersonic uniform flow [8]. The resultant profiles of velocity and Mach number, the distributions of skin friction and Stanton numbers on the body surface are compared with multiple experimental data, and their reasonable agreement is demonstrated.

In the present work a volume-distributed energy source is used, for which the source power is assumed a known function of coordinates and time in particular, the energy can be supplied on the basis of Gaussian distribution, and the supplied energy is taken into account by an additional source term in the energy conservation equation.

The model borrowed from [1] is used as an energy source in the form

$$\frac{dQ}{dt} = q_0 \left(\frac{p_\infty}{\rho_\infty} \right)^{3/2} \frac{1}{R_s} \exp \left(-\frac{\Delta r^2}{R_s^2} \right),$$

Q , R_s are the energy released in the source and the effective heat spot radius, respectively, Δr is the distance between the current point in the flow field and the energy source center, p_∞ and ρ_∞ are the free-stream pressure and density, respectively. The value of q_0 , that characterized the source intensity, is assumed to equal 20 on the basis of estimates made in [1].

The influence of a local energy source positioned upstream of the body on the inviscid flow and the boundary layer parameters was studied for an ogive body with aspect ratio 2.5, free-stream Mach number 3.0, and zero incidence. Two variants were compared: 1) uniform flow around the body, and 2) flow around the body with an energy source present in the flow. The source center was located at a relative distance of 0.23 along the axis and at a distance of 0.05 away from it.

Calculation examples of external flow around an ogive body are shown in Figs. 1, 2. The pressure isolines along the considered body are presented here in the symmetry plane and in a cross-section ($\bar{x} = 0.4$) for the case of uniform flow around the ogive (Fig. 1) and with energy source (Fig. 2).

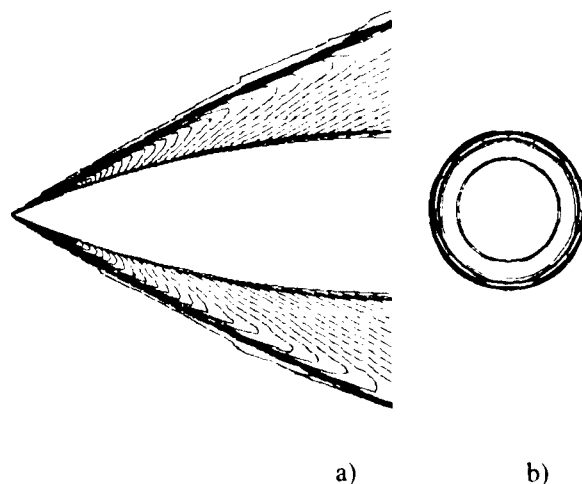


Fig. 1 Uniform flow around an ogive. Pressure isolines a) in the symmetry plane, b) in cross-section $x=\text{const}$

The calculations of external flow around the examined body showed that the inclination angle of velocity vector with respect to the free-stream direction is close to zero near the source axis. Moving away from the axis, this angle becomes rather large and decreases with the distance from the source (as the strength and inclination angle of the bow shock from the source decrease). This change of the local angle between the bow shock from the ogive and the free stream leads to significant restructuring of the bow shock shape. Besides, a high-entropy region is formed in the wake behind the source, which also has a large effect on the flow upstream of the ogive. The calculations also showed that a low-pressure region is formed in the wake behind the source, which transforms to a high-pressure region in its bow shock. This difference decreases when moving downstream from the energy source center.

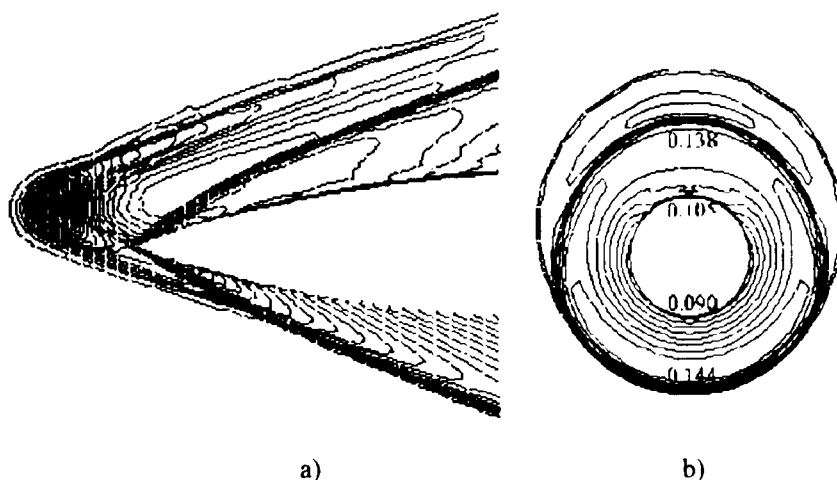


Fig. 2 Flow around an ogive in the wake of local energy source. Pressure isolines a) in the symmetry plane, b) in cross-section $x=\text{const}$

It is seen from Figs. 1-2 that the processes described lead to flow compression in the stream periphery behind the source and, hence, to rarefaction directly in the wake behind it. This, in

turn, causes a strong bulging of the bow shock ahead of the ogive in the wake behind the energy source and the shock compression at the wake periphery (Fig. 2a). Thus, at the section $\bar{x} = 0.4$ from the body tip is the distance between the bow shock and the ogive surface can differ by 40% from this distance in a uniform flow. As a result, a spatially nonuniform flow is formed in the field above the boundary layer. At the section $\bar{x} = 0.4$ from the ogive tip the pressure above the top part of the flow is lower than the pressure in its bottom part by $\sim 2\%$, which is seen in Fig. 2, while directly on the body surface the top pressure is higher than the bottom pressure by $\sim 16\%$. This occurs due to transverse overflow and interaction of compression and expansion waves that arise because of energy source effect on the flow.

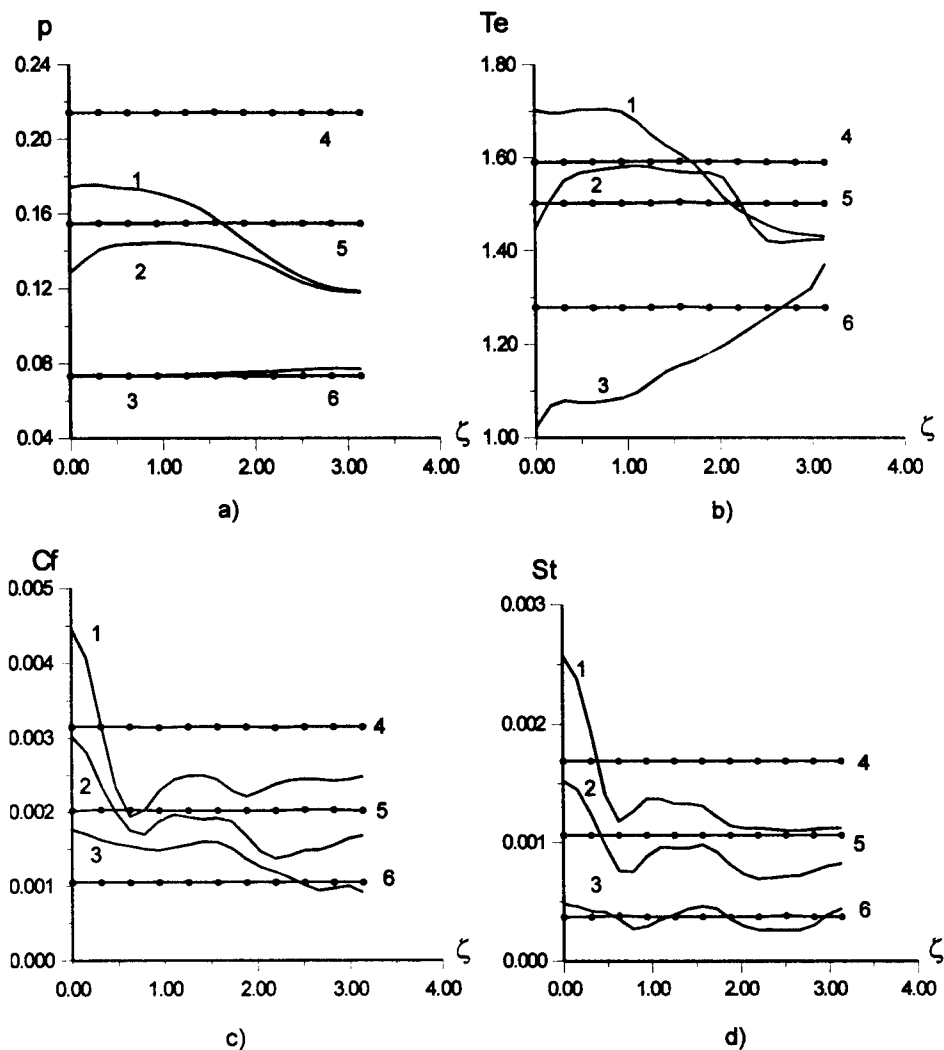


Fig. 3 Effect of local energy source on the boundary layer parameters. Solid lines – distribution of boundary layer parameters with energy source 1 – $\bar{x} = 0.2$; 2 – $\bar{x} = 0.4$; 3 – $\bar{x} = 0.9$; marked lines – the same without energy source 4 – $\bar{x} = 0.2$; 5 – $\bar{x} = 0.4$; 6 – $\bar{x} = 0.9$

Figure 3 shows the distributions of the boundary layer parameters in cross-sections $\bar{x} = 0.2, 0.4, 0.9$ versus the meridional angle ζ . The solid lines correspond to the variant with energy source, the results obtained without the source are also shown here for comparison by marked lines.

Heat emission upstream of the body decreases considerably the pressure in the boundary layer (Fig. 3a). However, this difference decreases when moving along the ogive and practically vanishes in the last cross-section. The temperature at the boundary layer edge (Fig. 3b) in the first cross-section is higher on the side where the energy source is located and lower on the opposite side than in a uniform flow. Then it decreases in the first region and becomes lower than without the energy source, while it decreases considerably more slowly on the opposite side.

The skin friction coefficient (Fig. 3c) is higher on the side of the heat source than without it and lower on lateral and shaded sides. The region of high skin friction coefficient extends towards the last cross-section, and almost reaches the corresponding value for uniform flow on the shaded side. A similar picture is observed in Stanton number distribution (Fig. 3d). The only difference is that its value in the last cross-section almost reaches the case without the source, with small fluctuations about the latter.

Thus, a local energy source affects significantly the boundary layer processes, which leads to an increase in skin friction and heat flux coefficients on the body surface.

References

1. Georgievsky P.Yu, Levin V.A. Supersonic flow around the body with heat supply upstream of it // Papers of Mathematical Institute USSR AS. Modern Problems in Mechanics and their Applications. -1989. -Vol.186. -P. 197-201.
2. Georgievsky P.Yu, Levin V.A. Supersonic flow around the body with external heat sources //Pis'ma v ZhTF. -1988. -Vol.14. -Iss.8. -P.684-687.
3. Korotaeva T.A., Fomin V.M., Shashkin A.P. Numerical study of the influence of a local energy source on 3D supersonic flow around pointed bodies. -Novosibirsk, 1996. -36 p. -(Preprint ITAM SB RAS; No. 1-96).
4. Korotaeva T.A. Numerical study of 3D nonuniform supersonic flow around bodies: Ph.D.Theses. -Novosibirsk, 1997. -168 p.
5. Vetlutsкая I.M., Vetlutsky V.N. Calculation of 3D compressible boundary layer on a pointed body// Ch.MMSS. -1986. -Vol. 17. -No 5. -P. 25-42.
6. Vetlutsky V.N., Ganimedov V.I. The investigation of a compressible laminar boundary layer past an elliptical cone// Computers and Fluids. -1982. -Vol. 10. -No. 3. -P. 173-179.
7. Vetlutsky V.N. Laminar boundary layer on a flat plate with rotating cylinder// Computers and Fluids. -1981. -Vol. 9. -No. 4. -P. 427-434.
8. Vetlutsky V.N., Krause E. Calculation of three-dimensional, compressible boundary layers on pointed bodies and comparison with experiments// ZFW. -1992. -Vol.16. -P. 308-316.
9. Vetlutsky V.N., Poplavskaya T.V. Numerical calculation of 3D compressible boundary layer on contoured triangular wings with supersonic leading edges// J. Appl. Mech. Tech. Phys. -1993. -No. 5. -P. 88-94.

FLOW GASDYNAMIC STRUCTURE SPACE-TIME SCALES IN AEROPHYSICAL EXPERIMENT WITH PULSATING LASER THERMAL SOURCE

V.I. Yakovlev

Institute of Theoretical and Applied Mechanics SB RAS,
Novosibirsk, Russia

The stabilization of an optical pulsating discharge in supersonic flow for the first time realized in work [1] created unique possibilities (contactless, low laser radiation power) to study experimentally gas flows at external energy supply. In order to solve the problems effectively and to make an adequate choice of the means and methods of aerophysical experiment it is necessary to know the characteristic space and time scales of studied phenomenon. It was shown in the experiments [2] with laser thermal source (optical discharge) ahead streamlining body that their interaction effect depends on pulse repetition frequency and results in the body's aerodynamic drag reduction because of the thermal wake formation behind energy supply region. The characteristic frequency (about 50 kHz) of transition from unstationary flow to quasystationary one, and also the wake's dimension (diameter no more 6 mm), feebly varied with growing distance from optical discharge, were determined. However, the correlation of these parameters with both gas flow and pulse-periodic laser radiation characteristics was not studied. It is necessary to analyze in detail the experimental data about gasdynamic structure forming near laser thermal source. The purpose of this work is to find out the correlation of space - time scales (configuration of the thermal wake and other wave structures, the characteristic frequency of transition to quasystationary flow) with both initial gas flow and laser radiation parameters. The gasdynamic aspect of the interaction (pulsating laser thermal source/supersonic flow) problem is taking into account only, therefore the experimental data has been analyzed in comparison with calculated ones, based on known models about gasdynamic processes while optical breakdown and local energy release.

The experiments were carried out using aerodynamic set-up [3] at working parameters: test gas (argon) stagnation pressure and temperature 0.45 MPa and 293 K, ensuring Mach number $M=2$. Laser beam passed plenum chamber and nozzle unit (exit diameter 20 mm) along flow axis and was focused inside working chamber behind unit's exit. The pulse-periodic laser radiation mean power ranged 1.4-1.8 kW, that was absorbed by optical discharge. Using these data and known laser impulse dynamic [4] it was estimated the impulse power mean values of about 110-20 kW at frequencies 12.5-100 kHz, accordingly. Nevertheless the real peak values were several times higher during 0.3 mcs while the full impulse duration was about 1.2 mcs.

Supersonic flow gasdynamic structure was visualized by schlieren - method, using pulsed light sources (laser at wavelength 308 nm, spark discharge) and stationary one (incandescence lamp). It allowed to get «momentary» (exposition time about 0.01 and 1 mcs) and «average» (0.01 s) flow pictures at different sensitivity and space resolution. Light filters transparent in spectral region 305-313 nm were used to suppress the own plasma radiation. But it was not so while the low power stationary light source was used and, consequently, another luminous regions were showed also in addition to the localized optical discharge zone. Such complex application of the traditional method allowed to reveal characteristic, but slightly marked wave structure peculiarities in addition to data obtained earlier [2,3].

The flow unstationary structure is characterized by generation of shock waves having configuration almost elliptical (especially so at early stage), later transforming into nearly spherical one. Showing small-scaled irregular fluctuation's background there are in flow large-scaled (diameter no more 5-6 mm) regions of density disturbance, following one after another down stream the optical discharge. Making frequency transition from 45 kHz to 100 kHz these regions merge and form characteristic structure - the thermal wake [2,3]. It's peculiarity is the existence of following one after another (at interval 0.8-1.8 mm) narrow zones of density perturbation with its planes perpendicular to the flow axis. When the distance increasing these zones and the wake's boundary becomes less distinguished. The «average» flow pictures show but homogeneous and slightly luminous the wake also, it's light emission decreasing down stream. Experimental data for the thermal wake's configuration (R -radius, Z -distance) are presented by dots 1 in fig.1 and corresponds to laser pulse repetition frequency 100 kHz.

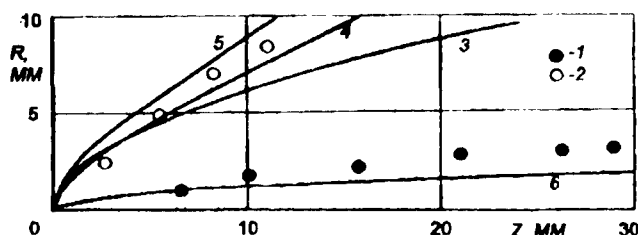


Figure 1. Wave's configuration (1 - thermal wake, 2 - density shock) caused by laser energy supply at $f=100$ kHz. 1,2 - experimental data, 3-6 - calculated ones at $\gamma=1.2$ (4, 6) and 1.67 (3, 5) where 3 - automodel solution

The flow visualization by long exposition time shows in addition slightly marked stationary structure - density shock (dots 2) near thermal source's head part as if it was streamlined body. Direct comparison of various shlieren -

pictures shows, that such configuration is the result of superposition of unstationary shock waves while moving away optical discharge region. It is confirmed by calculation of the density shock's configuration using known solution by point explosion model. Line 3 in fig.1 represents the automodel solution (cylindrical symmetry) by formula [5]: $R(Z) = (E/\alpha\rho)^{1/4} (Z/u)^{1/2}$, where R -the shock's radius, Z - distance from the thermal source's head part, E - mean value of energy per unit of length, that is $E=W\tau/ut$, W, τ - power and duration of the laser impulses, t - its time interval, ρ - initial gas density, α - some value, depending on specific heat capacities ratio γ , u - flow velocity. Parameter $W\tau/t$ is the laser radiation power mean value, measured in the experiments. It is worth to note that much the same result (up to $R \approx 6$ mm) and it slightly lowered at longer distance one can get using the spherical symmetry solution with the energetic parameter being equal to the laser impulse energy $E=W\tau$. Consequently, the question about what solution to be used hadn't special meaning (argon jet radius 10 mm). Increasing the distance the experimental and calculated data diverge, indicating the first increased. It is caused by relatively low energetic parameters, which don't meet the condition of hard explosion. Therefore in order to take into account opposite pressure's influence it was used approximate solution [6] of cylindrical symmetry. These results are represented in fig.1 and corresponds to various γ by lines 4 ($\gamma=1.2$) and 5 (1.67), that is practically all the range of its variation. The comparison of measured and calculated data shows their good agreement, especially taking into account possible systematic error of measured distance because of hard luminosity near $Z=0$.

The most characteristic peculiarity of gasdynamic structure - thermal wake behind the optical discharge in supersonic flow is caused by the light supported detonation wave [7], moving at high velocity with the laser radiation being absorbing locally behind it's front. In accordance with the results of numerical simulation [8] of stationary laser energy supply, there is forming jet stream in an immovable gas in a similar manner like sonic nozzle gas outflow into a co-

current hypersonic flow at the same wave's velocity. The heated gas under expansion forms high velocity jet upon long distance up to some hundreds nozzle's diameters (focal points). As verified in [8] the jet radius may be calculated using energetic parameter $E=W/V$, where wave velocity V is [7]: $V=[2(\gamma^2-1)W/s\rho]^{1/3}$ and s - focal point area. The automodel solution is: $R^*=F(\gamma)Z^{*1/2}$, where dimensionless (divided by focal point diameter) radius R^* and distance Z^* are used. Also $F(\gamma)=[(\gamma+1)/2(3\gamma-1)]^{1/4}$ using data [7].

Analyzing the pulse-periodic mode of energy supply it is necessary to take into account certain specification of processes in the gas flow. Practically «instantaneously» ($\tau \ll t$) formed extended plasma column (thermal source) moves down stream upon distance ut , before the next one appears. Measured extents of the thermal source are about 5-7 mm, which correspond to calculated ones by relations $L=\int v dt$ or $L=V\tau$. The recorded laser impulse's dynamics $W(t)$ or corresponding mean values W and τ were used in calculations of L . Characteristic scale of a medium's removal by the flow have almost the same value (4.2 mm and more, depending on pulse repetition frequency). Because of this removal effect the wave structure is supposed to be formed (under certain condition $L \approx ut$) in a similar manner like at stationary energy supply. Naturally, some peculiarities may be caused by transitional (for example, jet starting) processes. Possibly, the above-mentioned narrow zones of a density perturbation inside the thermal wake were the result of each optical breakdown's start process. Nevertheless the relation $L=u/f_1=ut_1$ can be useful to determine the threshold frequency f_1 of transition to quasistationary flow mode. So determined data, corresponding to laser radiation at the pulse repetition frequencies $f=12.5, 25, 45$ and 100 kHz are presented in

fig.2 as relative values ff_1-t_1/t . There were used $\gamma=1.2$ (line 2), also 1.25 (3) and 1.15 (4) in these calculations, because by estimation its correspond to argon plasma parameters at most. Furthermore this diapason of γ is near but don't exceed the bounds, which determine the stability of shock waves [9]. Presented data shows that $ff_1=1$ in frequency range 45-65 kHz. It corresponds to the generalized (line 1) experimental data [2], showing the achievement of steady effect (the relative aerodynamic drag C/C_0 reduction to practically constant value) at the same frequencies (more then 50 kHz).

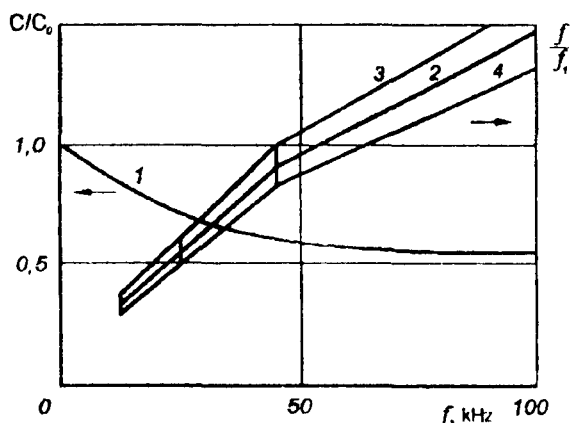


Fig.2. Characteristic frequency (time) relative scales ($ff_1=t_1/t$) and the experimental data ($C/C_0 \cdot J$) showing the transition to quasistationary flow ($ff_1=1$) in dependence on laser's pulse repetition frequency f .

Unlike the stationary energy supply, controlled by energetic parameter $E=W/V$, the pulse-periodic conditions stipulate it's dependence on thermal source extent and removal scale relation also. It may be supposed that approximately $E=(W/V)(L/ut)$, coinciding with early used mean value of energetic parameter $W\tau/ut$. It results in solution, with in contrast to stationary one has multiplier $\xi=(L/ut)^{1/4}$. However, it's application when deviates from unity considerably has no sense. If $\xi \ll 1$ it is necessary to use unstationary solutions for each originally isolated energy supply regions. In the case of $\xi \gg 1$ these region's removal by flow is negligible and,

consequently, the thermal conductivity as the principal mechanism of optical discharge stabilization becomes considerable. Having $\xi \gg 1$ it takes to correct parameter L , because each optical breakdown is realizing in heated gas already, which parameters considerably differ from initial ones. If $\xi \leq 1$ and it is increasing the energy supply region's space intervals decrease, resulting in formation of the quasistationary structure - thermal wake behind energy supply region. Consequently, in the case of $\xi \approx 1$ it's radius have to correspond to stationary solution at most. It is confirmed by correlation of the experimental (dots 1 in fig.1) and calculated (line 6) data, corresponding to energetic parameters of the impulse at 100 kHz, ($\xi \approx 1.3$). The experimental data excess at longer distance may be explained by γ increasing (as for example 4, 5 in fig.1) because of temperature decreasing. Infringement of the automodel (strong wave) conditions at radius less then 3 mm (for example 3, 5) has no significant importance.

The work was supported by the Russian Foundation of Basic Research (grant № 96-01-01947).

REFERENCES

1. Tretyakov P.K., Grachev G.N., Ivanchenko A.I. et al. The stabilization of the optical discharge in supersonic argon flow // *Physics-Doklady*. - 1994. - Vol.39. - №6. - P.466-467.
2. Tretyakov P.K., Garanin A.F., Grachev G.N. et al. Supersonic flow over bodies control by using a powerful optical pulsating discharge // *Physics-Doklady*. - 1996. - Vol.41. - №11. - P.339-340.
3. Tretyakov P.K., Garanin A.F., Kraynev V.L., Tupikin A.V., Yakovlev V.I. Investigation of local laser energy release influence on supersonic flow by methods of aerophysical experiments // *Proceedings of the Int. Conf. on the Methods of Aerophysical Research*: - Novosibirsk, 1996. - Pt.1. - P.200-204
4. Grachev G.N., Ponomarenko A.G., Smirnov A.L. et al. Producing of a powerful optical pulsating discharge by CO₂ pulse periodic laser radiation in supersonic gas flow // *Proceedings of the Int. Symp. on Modern Problems of Laser Physics*: - Novosibirsk, 1996. - P.650-656
5. Myrabo L.N., Raizer Y.P. Laser-Induced air spike for advanced transatmospheric vehicles // *25th AIAA Plasmadynamics and Lasers Conf.* - Colorado Springs, 1994. - AIAA 94-2451. - P.1-13.
6. Korobeinikov V.P. Problems of the theory of a point explosion - M.: Nauka, 1985 - 400 p, (in Russian)
7. Raizer Y.P. Gas Discharge Physics. - New York, Berlin Springer-Verlag, 1991.
8. Thomas P.D. Jet flowfield behind a laser supported detonation wave // *AIAA-Journal* - 1977. - Vol.15. - №10. - P.1405-1409.
9. Tarnavsky G.A., Fedosov V.P. About steadiness of the shock wave's flows of a gas at low adiabatic index // *Computational methods of the mechanics of continuous medium* - Novosibirsk, 1986 - Vol.17. - №4 - P.150-166, (in Russian).

NUMERICAL SIMULATION OF SUBSONIC FLOWS*

A.V. Zabrodin, A.E. Lutsky, I.S. Men'shov, I.L. Petrushchenkov, V.A. Cherkashin

The Keldysh Institute of Applied Mathematics
Russian Academy of Sciences, Moscow, 125047, RUSSIA

During the last two decades, a large amount of work has been performed in KIAM RAS on the development of algorithms and numerical methods for the aerodynamics problems. Various flows about different flying vehicles have been calculated with the purpose to improve the aerodynamical characteristics of the latter. Because of restrictions on the hardware performance and RAM size, the research was usually restricted to the super sonic steady-state flows (see [1]).

Creation of the Russian high-performance MBC-100 systems makes it possible to simulate subsonic flows, solving not only Euler, but Navier — Stokes equations as well. This paper considers the first results obtained in this field. Some results of the 3D subsonic flow around an aircraft model are presented, along with the related results for 2D flows around the airfoils. Implementation of the parallel algorithms on the distributed-memory multi-computer MBC-100 is discussed as well.

1. Numerical for time-dependent 3D Euler equations

The algorithm for numerical simulation of subsonic flows over complex shaped bodies (extending up to a complete aircraft) is based on time dependent inviscid Euler equations. Some of viscous effects can be taken into account afterwards by means of boundary-layer equations.

The time-stepping procedure is used to find steady-state solution (if it exists).

The 3D Euler equation can be written as follows:

$$\begin{aligned} Q_t + E_x + F_y + G_z &= 0 \\ Q &= (\rho, \rho u, \rho v, \rho w, e)^T \\ E &= (\rho u, \rho u^2 + p, \rho uv, \rho uw, (e + p)u)^T \\ F &= (\rho v, \rho uv, \rho v^2 + p, \rho vw, (e + p)v)^T \\ G &= (\rho w, \rho uw, \rho vw, \rho w^2 + p, (e + p)w)^T \end{aligned} \quad (1.1)$$

where $e = p / (\gamma - 1) + \rho(u^2 + v^2 + w^2) / 2$ — total energy; u, v, w — Cartesian velocity components, p — pressure, ρ — density.

The system (1.1) can be also written in the integral form (conservation law form):

$$\begin{aligned} \oint_{\partial\Omega} (U_i, n) ds &= 0 \quad i = 1, 2, \dots, 5 \\ U_i &= (Q_i, E_i, F_i, G_i), \\ \Omega &\subset \mathbb{R}^4 \quad n \in \mathbb{R}^4 \end{aligned} \quad (1.2)$$

where Ω is any bounded region in (t, x, y, z) space with the 3d boundary $\partial\Omega$.

* The work was supported by Russian Foundation for Basic Research (grants No. 96-01-00493, 97-01010)

The boundary conditions associated with the equations (1.1) are:

$(\vec{V}, \vec{n}) = 0$ on the body surface and

$$(\rho, u, v, w, p) \xrightarrow{r \rightarrow r^*} (\rho, u, v, w, p)^* \quad (1.3)$$

$$r = \sqrt{x^2 + y^2 + z^2}$$

Shock waves and contact discontinuities are automatically captured by the difference scheme, based on the conservation laws approximation.

Complex geometries may be difficult (or indeed impossible) to cover with single structured mesh. So a block structured mesh is employed. The total flowfield is divided into subdomanes (blocks) consisting of a structured mesh. The mesh blocks are required to match at the interfaces. The body-fitted grid surfaces are used. Algebraic transformations (interpolative techniques to distribute inner grid points from prescribed grid boundary points) are used to generate grids in each separate block independently, as long as interface grid points are the same.

The equation (1.2) are discretized using the finite volume method. The grid points $\vec{r}_{klm} = (x, y, z)_{klm}$ $k = 0, 1, \dots, kt; l = 0, 1, \dots, lt; m = 0, 1, \dots, mt$ in each block constitute three set of surfaces: $\{k = \text{const}\}$, $\{l = \text{const}\}$, $\{m = \text{const}\}$. The k, l, m orientation of the blocks is arbitrary. The values of flow variables (ρ, u, v, w, p) are stored in the cell centers. Each cell is bounded by 6 faces with 8 vertexes \vec{r}_i ($i = 0, 1, \dots, 7$). The coordinates of inner points on the face are given by 3-linear functions:

$$\begin{aligned} \vec{r} = & (1 - \alpha)(1 - \beta)(1 - \gamma)\vec{r}_0 + \alpha(1 - \beta)(1 - \gamma)\vec{r}_1 + (1 - \alpha)\beta(1 - \gamma)\vec{r}_3 + \\ & \alpha\beta(1 - \gamma)\vec{r}_2 + (1 - \alpha)(1 - \beta)\gamma\vec{r}_4 + \alpha(1 - \beta)\gamma\vec{r}_5 + (1 - \alpha)\beta\gamma\vec{r}_7 + \alpha\beta\gamma\vec{r}_6 \end{aligned}$$

The finfite-difference approximation of system (1.2) is given

$$\sum_{k=0}^5 (U_i^k N^k) = 0, \quad i = 1, \dots, 5 \quad (1.4)$$

The flowfield values for $k=0$ ($t=t_0$) are given. To evaluate data on the next time level $t_1=t_0+dt$ ($k=5$) the numerical fluxes on faces $k=1, 2, 3, 4$ are to be prescribed.

In the original Godunov [2] scheme the numerical flux function is taken to be the flux value arising at the tangent plane in the exact solution of the Riemann problem with the piecewise constant data taken from the cells adjoint to the interface.

To achieve higher accuracy the piecewise linear distributions are used [3]:

$$U(t, x, y, z) = U(t_0, x_0, y_0, z_0) + \Delta x U_x + \Delta y U_y + \Delta z U_z + \Delta t U_t \quad (1.5)$$

To prevent formation of spurious oscillations on shocks some flux limiter is usually introduced. First of all one sided differences are calculated:

$$U_\xi^+ = U_{k+1} - U_k, \quad U_\xi^- = U_k - U_{k-1}.$$

In the present work the approximate value of derivative is evaluated by **minmod** limiter:

$$U_\xi = \text{sign}(U^+) \min(|U^+|, |U^-|) \text{ if } U^+ U^- > 0; \quad U_\xi = 0. \text{ else.}$$

For subsonic flows without shocks the simple formulae: $U_{\xi} = 0.5(U^{+} + U^{-})$ can be valid also.

The U_i values are calculated according to equation systems (1.1). With equations (1.5) U^+ , U^- are calculated on the right and on the left of the corresponding face center. Then the Riemann problem with these initial data is solved.

2. The parallel implementation of the Euler solver on the multiprocessor system

The numerical simulation of complex 3D subsonic flows requires large computational resources both in processing speed and memory.

When approaching the subsonic flow case from the physical viewpoint, the body influence domain should be considered infinite in all directions. The computational region, nevertheless, has to be finite in size, but large enough, for the influence of the artificial external boundaries be sufficiently small (in fig.3 the shape of typical computational domain is shown).

The Russian multiprocessor system MBC-100 [4] to a considerable extent satisfies specified requirements on the speed and total size of memory.

The natural parallelism of computational fluid dynamics and explicit numerical scheme are exploited. Block structured meshes exhibit a coarse-grain parallelism at the block level and fine-grain parallelism at the mesh point level. Only first level of parallelism is used for presented calculations. The features that make the explicit finite difference scheme highly amenable for parallel processing are:

- 1) data communication is only between nearest neighbors;
- 2) the amount of data transmitted is proportional to the block bound area; the amount of computation is proportional to the block volume; thus the ratio of computations to communications is very favorable.

The spatial decomposition of computational domain is a natural method to divide the computational work among several concurrent processors. One or more blocks are mapped on a single processor. This partitioning should balance the load between processors and minimize the amount of required across block boundaries. The same program runs on each node. Each node program identifies its block numbers with an instance number. Interconnections to other blocks are given with grid data. Each processor analyses the interconnections and built up the communication requirements.

Interblock communications is performed in the following way. There exist one global coordinate system in physical space (x, y, z). To provide the needed geometrical flexibility, each block has its own coordinate system (k, l, m) in computational space. Any of the 8 orientations which are theoretically possible between local coordinate systems can be chosen. The exchanged messages are the (ρ, u, v, w, p) values on the faces of neighboring blocks. Some functions handle the communication. The first one scans the boundaries and create receive table. This table contains the information needed for communication, such as expected data from neighboring blocks and their correlation with the local block data. Accordingly the send table is created.

Under correct balancing of the processor loading it is possible to get practically linear speedup of system with increasing a number of used processors. However it may be difficult in some cases to obtain such balancing. It take place, for instance, if blocks are greatly distinguished on the amount of nodes. As an example consider the calculation of subsonic flow around aircraft models on the multiprocessor system MBC-100.

Total number of cells is 416768, number of blocks - 136, the most number of cells in the block is 9600, the least - 576. Table 1 presents the calculation time $T(p)$ of the same

number of steps for the different number of processors p used. The efficiency of the parallelization is usually estimated by comparing such values with the calculation time for 1 processor. In the present case this can not be done directly, as on 1 processor the task does not fit in memory. Instead, the values of the $pT(p)$ are presented. In the "ideal" case, this dependency should appear to be a constant: $pT(p)=T(1)$. The asterisk marks the 2 cases with strong disbalance of load between the processors. It is seen that for those cases the parallelization is much less effective. For the rest cases, the range between the upper and the lower values fall into the 26 % range.

Table 1

*p = 17	T(p) = 6036	pT(p) = 102612
p = 19	T(p) = 4735	pT(p) = 89965
p = 27	T(p) = 3580	pT(p) = 96660
p = 30	T(p) = 3109	pT(p) = 93270
*p = 34	T(p) = 4266	pT(p) = 145044
p = 40	T(p) = 2917	pT(p) = 116680
p = 44	T(p) = 2580	pT(p) = 113520

3. Grid generation for 3D flow calculations

Grid generation is the first step in numerical simulation process and the most labor intensive one. There are different types of continuous space disscretizations, i.e. grid generation, but among all the variety structured multiblock grids seem to be most suitable for parallel computing.

Grid generation process consists of three main steps:

1. Manipulations with initial geometry.
2. Continuous space subdivision into hexahedrons with curves and surfaces.
3. Grid generation inside blocks with optional global smoothing procedure.

There are some approaches for generating grid in a single global iterative process, but even in that case we nevertheless have to point out so called "topological map" or "connectivity" of the multiblock grid, i.e. describe block boundaries without assigning them physical coordinates. The problem of structured multiblock grid generation is that this process requires a lot of human resources. For instance typical grid around commercial airplane consists of few hundred blocks. It means that it takes to create about the same order of spatial curves and surfaces manually. Unfortunately we can't avoid this procedure, but there are some tricks to do it in a smart way. One trick is to use what is called "many-to-many connectivity" or "partial face interface", i.e. allow blocks to coincide with each other in arbitrary way, not only "one-to-one". If it's necessary, further splitting into one-to-one can be done automatically. Another trick is very important and is always referenced as "journaling" or "replay" capability. It means that if you once generated a grid for some typical geometry, you can use the same procedure for generating grid on the similar geometry automatically. As an example there is a problem of draft aerodynamical aircraft design, when different parts of construction are moving along each other. "Replay" capability implies the language for working with "journals" or "scenario" with corresponding interpreter. We accept initial data as a set of points with subsequent interpolation and surface-surface intersection. Experiments reveal that interpolation we use is pretty close to original and anyway sufficient for numerical simulation. While generating grids on initial geometry we are working in parametrical space for each element of geometry. Obviously unic non-singular parametrization of some surfaces may not exist, so the parametrization of surfaces with

multiple maps was implemented in code. Further steps are: cut initial geometry with curves on surfaces, then create curves in space - edges of future blocks. All faces based on four adjacent curves and blocks based on six adjacent faces could be generated automatically. Any time user can change the shape of some curves with subsequent modification of depended objects, change number of grid nodes and node distribution on edges. The presented code guarantees proper propagation of all alternations through the data structure.

The main steps of grid generation around aircraft model are shown in Figs. 1, 2.

In Fig. 1 the total surface of the model is shown. The details of grid generation by interpolation method are available in Fig. 2a. Several block near model surface are shown in Fig. 2b.

4. Numerical results

The results of numerical simulation of subsonic flow about aircraft model 906 are presented. The calculations were executed for Mach number $M = 0.15$ within the range of attack angle from 0 to 20 degrees under zero slide.

The flow under consideration possesses a plane of symmetry ($z = 0$), so it is sufficient to conduct a calculation in halfspace. The computational domain was divided into 136 blocks.

On the model surfaces and on the symmetry plane the conditions $V_n = 0$ were imposed. The number and type of conditions on external boundaries is defined from characteristic relations. In presented variant of algorithm this was realized by the calculation of Riemann problem with initial data from cells, adjoining to the external boundary and incident flow. The calculations of subsonic two-dimensional flows, executed earlier, have shown adequacy of such way of numerical realization of boundary condition (1.3).

Pressure distributions ($p = \text{const}$ lines) on the model surface for $\alpha = 0, 8, 16$ are shown in Figs. 4a, 4b, 4c. For the variant $\alpha = 0$, the pressure on the wing surfaces is practically constant. When increasing attack angle the rarefaction region on upper surfaces of wing near the front edge is formed.

The details of the pressure distribution mentioned above correlate with the location of the stream lines location. In the Figs. 5a, 5b, 5c for these values of attack angle the fragments of stream lines on upper surfaces of wing and fuselage are presented. For $\alpha = 0$, the stream line are almost parallel to the incident flow vector. For $\alpha = 8, 16$, there exist some singular lines on the wing surface. These curves separate the stream lines from fuselage and front edge.

The pressure distributions on $z = \text{const}$ plane crossing the wing and tail for $\alpha = 4-16$ are presented in Fig. 6.

The dependencies of drag, lift and pitching moment on attack angle were obtained from the flow calculations performed. The dependencies $C_y(\alpha)$, $m_z(\alpha)$ are presented at Fig. 7. The black curve presents the experimental data, and the squared line - the calculated ones. It can be seen that they correspond rather well. The non-linear behavior of the experimental dependencies (most easily seen for $m_z(\alpha)$ for large α) must be due to the flow separation. The numerical simulation of 2D problems carried out previously shows that a very fine grid is necessary to discover such an effect. Obviously, doing the same in 3D case would result in excessive time of calculation.

The dependence $C_y(C_x)$ is presented at Fig. 8. As well as in the previous figure, the solid line presents the experimental data. The numerically simulated data, again, generally corresponds with it.

5. Numerical results of calculation subsonic flow around a Jukovskii airfoil with the model of Navier — Stokes equations

In this chapter, numerical results of calculation subsonic flow around a 2D Jukovskii-type airfoil obtained with the model of viscous heat conducting compressible fluid are discussed. The system of governing differential equations are written in the conservation law form in the following way:

$$\partial_t \mathbf{q} + \partial_k \mathbf{f}_k = \partial_k \mathbf{g}_k \quad (5.1)$$

where \mathbf{q} is the solution vector of conservative parameters, \mathbf{f}_k ($k = 1, 2$) are the vectors of inviscid fluxes, and \mathbf{g}_k ($k = 1, 2$) are viscous or dissipative fluxes, which have the form:

$$\begin{aligned} \mathbf{q} &= (\rho, \rho u_1, \rho u_2, e)^T \\ \mathbf{f}_1 &= (\rho u_1, \rho u_1^2 + p, \rho u_1 u_2, (e + p)u_1)^T \\ \mathbf{f}_2 &= (\rho u_2, \rho u_1 u_2, \rho u_2^2 + p, (e + p)u_2)^T \\ \mathbf{g}_1 &= (0, \tau_{11}, \tau_{21}, q_1 + \tau_{11}u_1 + \tau_{21}u_2)^T \\ \mathbf{g}_2 &= (0, \tau_{12}, \tau_{22}, q_2 + \tau_{12}u_1 + \tau_{22}u_2)^T \end{aligned} \quad (5.2)$$

Here τ_{ij} are components of the viscous stress tensor,

$$\tau_{ij} = 2\mu(\partial_i u_j + \partial_j u_i) - \frac{2}{3}\mu\delta_{ij}(\partial_1 u_1 + \partial_2 u_2), \quad i, j = 1, 2$$

q_i are components of the heat flux:

$$q_i = \lambda \partial_i T, \quad i = 1, 2$$

The notations u_1, u_2 relate to Cartesian components of the velocity vector \mathbf{u} , μ is the viscosity coefficient, λ is the heat conductivity coefficient.

It is supposed that thermodynamic properties of the gas are described by the equation of state of a perfect ideal gas with parameters of air: the molecular weight is 28.97, the adiabatic factor is 1.4. The viscosity coefficient and the Prandtl number ($\mu c_p / \lambda$, c_p is specific heat capacity of the gas under constant pressure) are considered as constants and equal $1.713 \cdot 10^{-4}$ g/cm/sec and 0.7201, respectively.

The differential equations (5.1) are integrated in a domain out of the airfoil with boundary conditions $\mathbf{u} = 0$, $T = T_w$ (T_w — a fixed temperature) at the surface of the airfoil, $\mathbf{q} = \mathbf{q}_0$ at the outer boundary of the computational domain. The subscript 0 is used to denote inflow parameters, which have the following values in the present calculations: the density — $1.293 \cdot 10^{-3}$ g/cm³; the pressure — $1.013 \cdot 10^6$ dine/cm²; the temperature — 273 K; the Mach number — 0.25. The temperature at the airfoil surfaces taken equal to that in the inflow, $T_w = T_0$.

Taking into account viscosity and heat conductivity of the gas, the flow around the airfoil becomes no longer self-similar, that is inherent for the ideal model, and flow

parameters depend on a linear distance of the airfoil. As this distance, the airfoil span can be chosen, which is taken equal 200 cm in the calculations presented below. Along with this choice, the inflow Reynolds number is of $1.25E10^7$.

Numerical solution to the problem stated above is carried out in a C-type domain, the outer boundary of which is setting at the distance of 15 span halves from the sharp back edge of the airfoil in the afterbody zone.

Two non-uniform grids are used in this domain to do spatial discretization of the governing equations that are highly clustered in the boundary layer so that the ratio between the wall cell Reynolds number and the inflow Reynolds number is equal 10^{-5} . One grid is of 272 by 100 computational cells, where 100 cells are placed between the body surface and the outer boundary, and 128 cells on the surface. The other consists of 452×160 cells with 160 cells in the radial direction and 256 cells on the surface.

Heaving given spatial discretization of the computational domain, the system of differential equations (5.1) is approximated by finite-difference equations derived with the finite volume method and two-step implicit time integration scheme:

$$\omega_i \Delta \mathbf{q}_i = -\Delta t \sum_{\sigma} s_{\sigma} (T_{\sigma}^{-1} \mathbf{F}_{\sigma}^{n+1} - \mathbf{G}_{\sigma}^{n+1}) \quad (5.3)$$

where ω_i is a cell area, s_{σ} is an interface length, T_{σ} is the transforming matrix the components of which are defined by the coordinates of the outer orthonormal basis at the interface, \mathbf{F}_{σ} and \mathbf{G}_{σ} are inviscid and viscous numerical fluxes at the interface defined by the following formulas:

$$\mathbf{F} = \mathbf{f}_1(\mathbf{Q}), \quad \mathbf{Q} = T_{\sigma} \mathbf{q}, \quad \mathbf{G} = \mathbf{g}_k n_k. \quad (5.4)$$

Here n_k are coordinates of the unit normal vector outer to the interface.

The numerical fluxes at the upper (new) time level are approximately computed in the form:

$$\begin{aligned} \mathbf{F}_{\sigma}^{n+1} &= \mathbf{F}_{\sigma}^n + A_i^{+} \Delta \mathbf{Q}_i + A_{\sigma(i)}^{-} \Delta \mathbf{Q}_{\sigma(i)}, \\ A^{+} + A^{-} &= A = \partial_Q \mathbf{F}, \quad A^{+} \geq 0, \quad A^{-} \leq 0 \end{aligned} \quad (5.5)$$

where the Jacobian matrix splitting onto positive and negative parts (regarding the sign of eigenvalues) A^{+} and A^{-} is taken in the form of Jameson — Turkel [5]: $A^{\pm} = 0.5(A \pm r(A))$, where $r(A)$ is the spectral radius of the Jacobian matrix. The Jacobian matrix of the dissipative numerical flux is majored by the diagonal matrix D_{σ} of the form as follows:

$$D_{\sigma} = \text{diag}(0, \nu, \nu, \nu, \kappa) / h_{\sigma}, \quad (5.6)$$

where $h_{\sigma} = |\mathbf{n} \cdot (\mathbf{x}_{\sigma(i)} - \mathbf{x}_i)|$, and the indexes i and $\sigma(i)$ are referred to adjoin cells with the common interface σ ; ν and κ are dynamic coefficients of viscosity and heat conductivity. With account of (5.5), the system of equations (5.3) can be modified in the following system of linear algebraic equations with respect to the time increment of the solution vector $\Delta \mathbf{q}$:

$$\begin{aligned} (I + \sum_{\sigma} M_i^{+}) \Delta \mathbf{q}_i + \sum_{\sigma} M_{\sigma(i)}^{-} \Delta \mathbf{q}_{\sigma(i)} &= \Delta t \mathbf{R}_i \\ M^{\pm} &= \frac{\Delta t}{\omega_i} s_{\sigma} (T_{\sigma}^{-1} A^{\pm} T_{\sigma} \pm D_{\sigma} I) \end{aligned} \quad (5.7)$$

which is then solved with the method of Jameson — Yoon [6]. This method makes approximate factorization of the implicit left-hand side operator into two operators with

triangular matrices, which can be easily solved then with forward and backward sweeps over computational cells. To obtain the second order of accuracy for spatial operators, a piece-wise linear cell reconstruction of the solution vector \mathbf{q} with the minmod limiter for derivatives is implemented to extrapolate edge values required for the inviscid numerical fluxes calculation.

The algorithm for solving the Navier — Stokes equations described above can be also used for solution inviscid (Euler) equations, if viscosity and heat conductivity are vanished.

Calculations are presented in this paper for two flows with attack angles of 5° and 15° , respectively. These calculations have been carried out for both the Navier — Stokes and Euler equations in the uniform manner. Results are given by fields of isolines for pressure and entropy spatial distributions, and time distributions of dimensionless integral force characteristics C_{p_x} , C_{p_y} , F_{t_x} , F_{t_y} , which are defined in the following way:

$$\begin{aligned} C_{p_x} &= \frac{\int p n_1 ds}{\rho_0 U_0^2 L}, & C_{p_y} &= \frac{\int p n_2 ds}{\rho_0 U_0^2 L}, \\ F_{t_x} &= \frac{\int (\tau_{11} n_1 + \tau_{12} n_2) ds}{\rho_0 U_0^2 L}, & F_{t_y} &= \frac{\int (\tau_{21} n_1 + \tau_{22} n_2) ds}{\rho_0 U_0^2 L}, \end{aligned} \quad (5.8)$$

The entropy isolines and the pressure isolines for the viscous flow model are given in Fig. 9 for the case of the flow attack angle of 5° , and the grid of 272 by 100 cells. This figure clearly exhibits the main feature of the flow - formation of a vorticity wake coming from the upper part of the airfoil. This wake is created as a result of two instabilities in the flow. One of them is initiated at the back sharp edge of the airfoil where the flow goes away from the airfoil surface. The other is due to disattachment of the boundary layer from the body surface on its upper part. This disattachment leads to a developed vortex band, which propagates for a long distance from the airfoil (Fig. 9). This result is in line with results of [7], where the phenomenon of boundary layer disattachment is also numerically investigated. In [7] is noted that the disattachment is preceded by arising of a microvortex in the boundary layer, which moving forward with the fluid and developing leads to a macrovortex in the exterior flow beyond the boundary flow. Being repeated, this process forms a sequence of vortices going off and moving away from the airfoil, which is clearly seen in Fig. 9).

This vortex process is evidently nonstationary phenomenon, which has to lead to nonstationarity in time distributions of the force integral characteristics. These characteristics are given in Fig. 10 as functions of the dimensionless time, where a_0 is the inflow sound velocity, L_{prof} is the length of the airfoil span. It is seen that there is no any constant-wise limit in these distributions. Conversely, a quasiperiodic behavior is exhibited characterized by repeated maximal and minimal values in these distributions, which seemed to be caused by arising and coming away of a vortex in the boundary layer on the upper part of the airfoil.

Quite different flow pattern is exhibited when the same problem is solved with the model of inviscid Euler equations. The entropy and the pressure isolines for this case are shown in Figs. 11. The algorithm with zeroth viscosity and heat conductivity and the same grid of 272 by 100 cells are used to obtain this solution. As it is seen from these figures, no vortex wake is arisen while the ideal inviscid model is used, and the solution

comes to a completely steady limit when any parameters do not change with time during further calculations.

Numerical results for the angle of attack 15° are illustrated in Figs. 12-14 where the isolines are presented for both inviscid and viscous models for the grid 272 by 100 cells. To check the dependency of the numerical solution on grid, calculations have been also done with the grid twice finer, i.e. of 452 by 160 cells.

These figures clearly exhibit that no steady solution is obtained in these two cases. As viscous model as inviscid that gives separation of the flow on the upper part of the airfoil which causes a developed vortex sheet in the afterbody flow. These calculations show that stable steady flow seems to be not existed at the angle of attack of 15° even for the ideal (Euler) model. Non-stationary regime of the flow is also confirmed by time distributions of integral force characteristics which are given for the two grids and models in Fig. 14. These distributions have clear oscillating character; the period of these oscillations has approximately the same value as for viscous as for ideal models. So, the flow at the angle of 15° (and, probably, for greater angles) is mostly defined by separation of the flow and developing of vortex instabilities at the upper part of the body.

References

1. Blinov A.I., Gusev A.V., Lutsky A.E., Petrushchenko I.L. Numerical investigation of the influence on aerodynamical characteristics of supersonic aircraft. – Moscow, 1990. – (Preprint / KIAM RAS; No 105). (In Russian.)
2. Numerical solution of multidimensional gasdynamics problems / Ed. S.K. Godunov. – Moscow: Nauka, 1976. (In Russian.)
3. Anderson W.K., Thomas J.L., Van Leer B. Comparison of finite volume flux vector splitting for the Euler equation // AIAA J. – 1986. – Vol. 24, No. 9. – P. 1453-1460.
4. Zabrodin A.V., Levin V.K., Korneev V.V. The massively parallel computer system MBC-100 // Parallel Computing Technologies Third International Conference St.Petersburg, Russia, September 1995. Lecture Notes in Computing Science 964.
5. Jameson A. and Turkel E. Implicit Schemes and LU Decompositions // Mathematics of Computation. – 1981. – Vol. 37, No 156. – P. 385-397.
6. Yoon, S. and Jameson A. Lower-upper symmetric-gauss-seidel method for the Euler and Navier — Stokes equations // AIAA J. – Vol. 26, No 9. – 1025-1026.
7. Muti Lin J.C., Pauley Laura L. Low-Reynolds-number Separation on an Airfoil // AIAA J. – 1996. – Vol. 34, No 8. – P. 1570-1577.

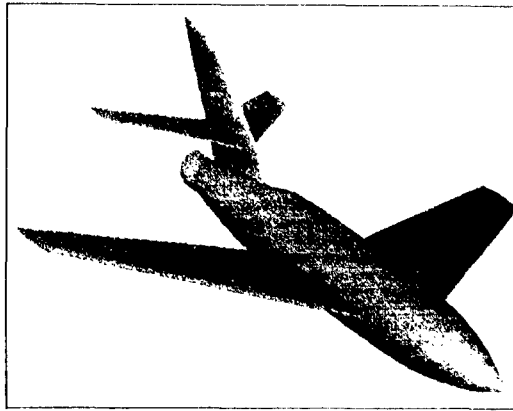
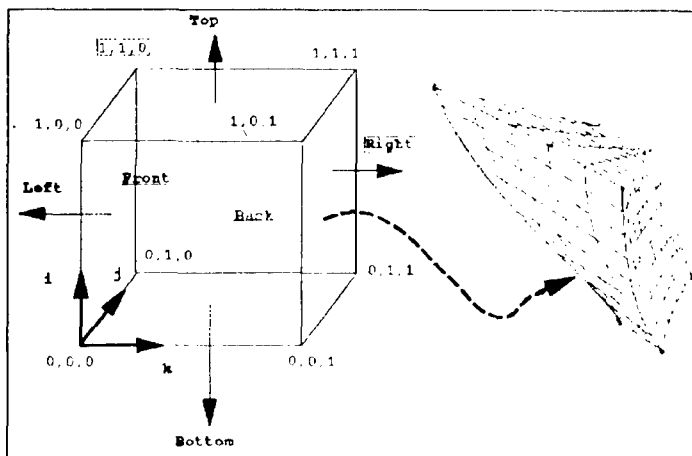
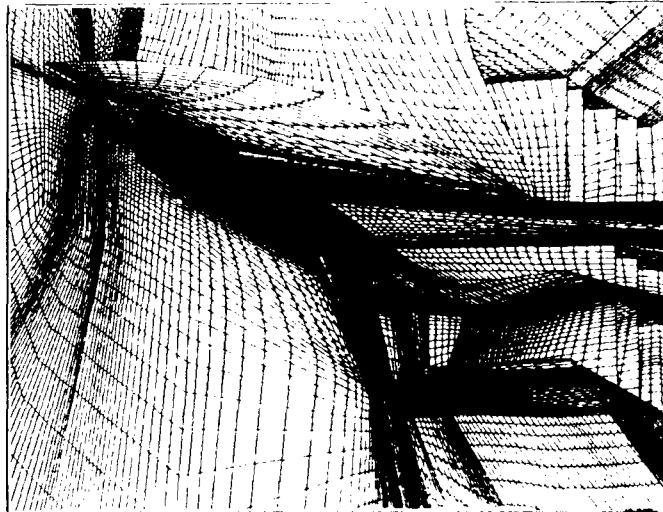


Fig. 1. Aircraft model.



a



b

Fig. 2. Algebraic technique for grid generation

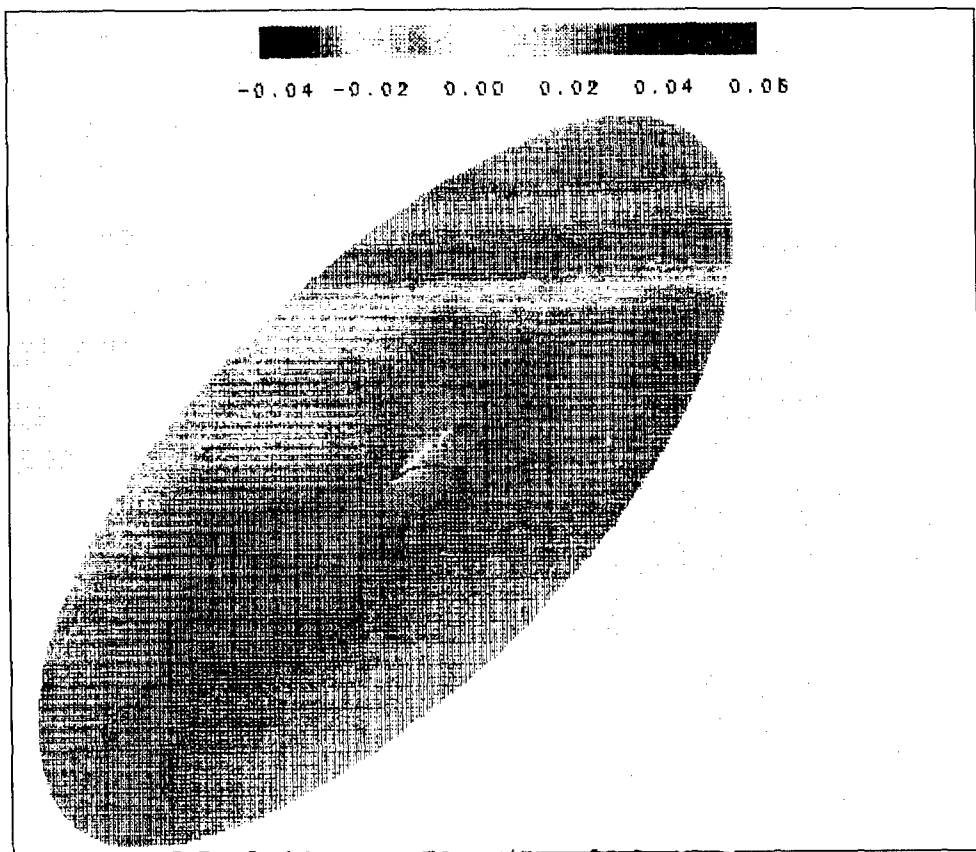
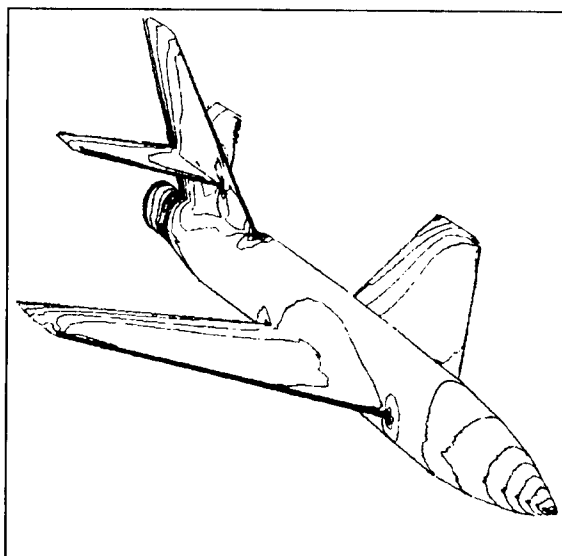
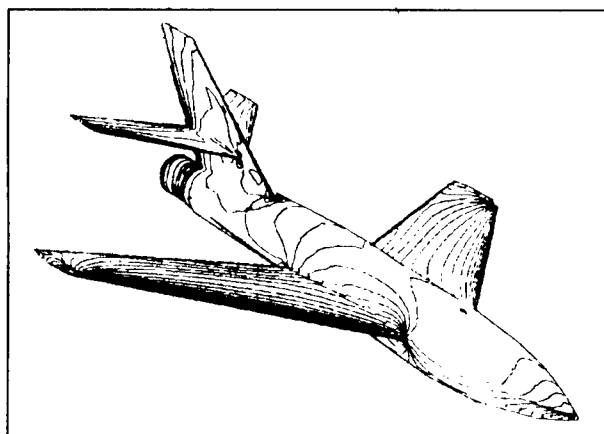


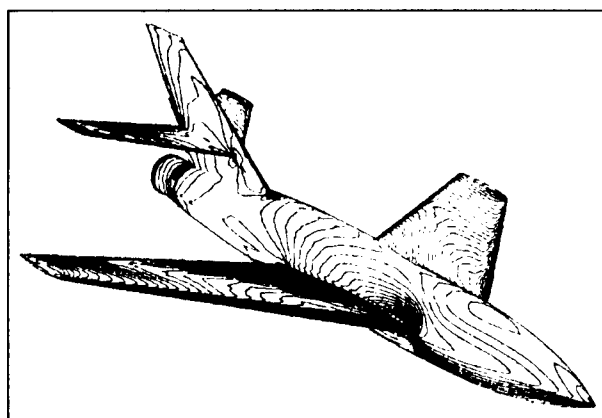
Fig. 3.
 $M = 0.15$, $\alpha = 8^\circ$, V_y distribution



a) $\alpha = 0^\circ$

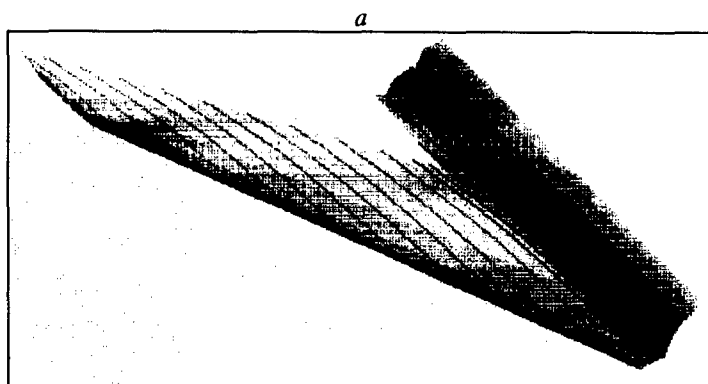


b) $\alpha = 8^\circ$

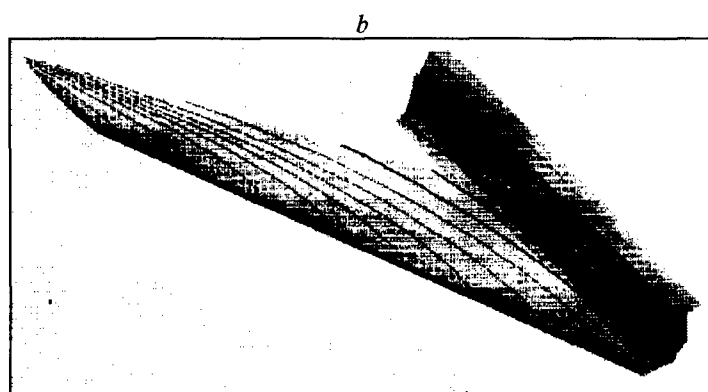


c) $\alpha = 16^\circ$

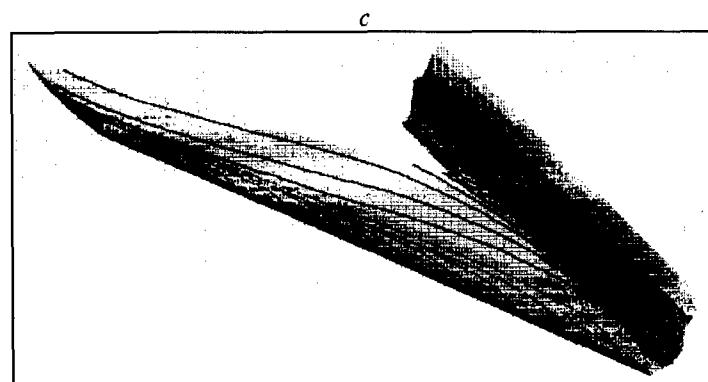
Fig. 4. Pressure isolines.



$\alpha = 0^\circ$

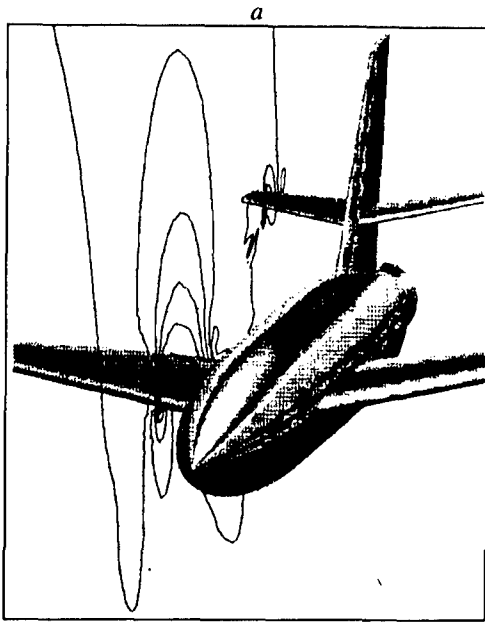


$\alpha = 8^\circ$

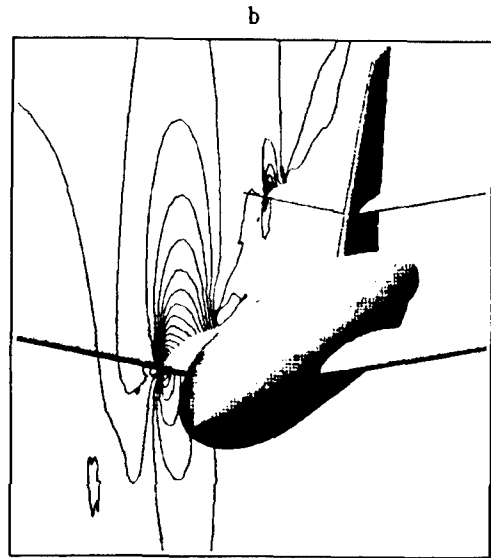


$\alpha = 16^\circ$

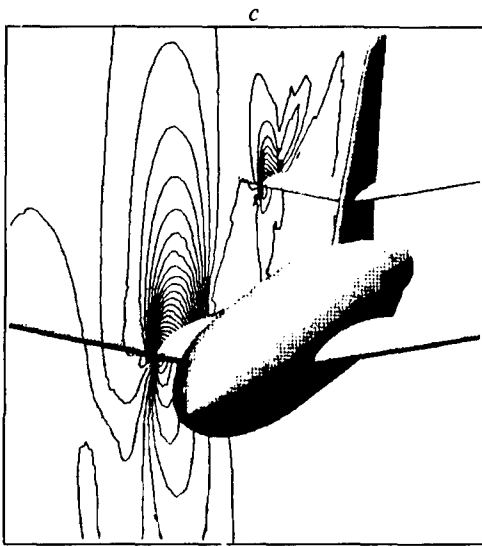
Fig. 5. Stream lines.



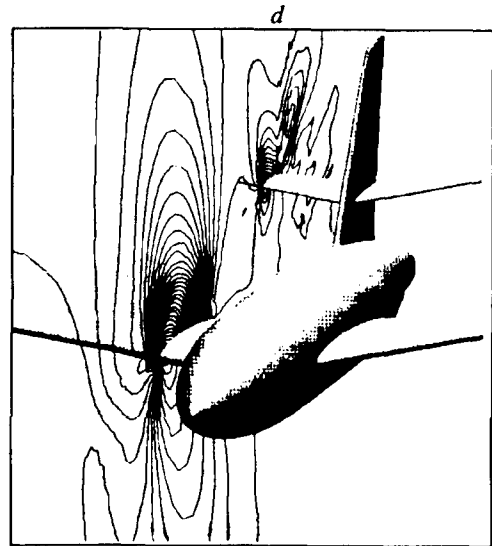
$\alpha = 4^\circ$



$\alpha = 8^\circ$



$\alpha = 12^\circ$



$\alpha = 16^\circ$

Fig. 6. Pressure isolines ($z = \text{const}$).

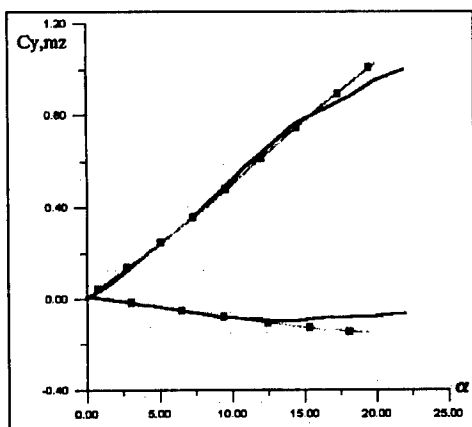


Fig. 7.

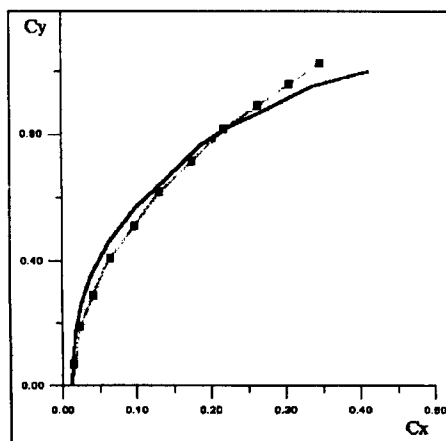


Fig. 8.

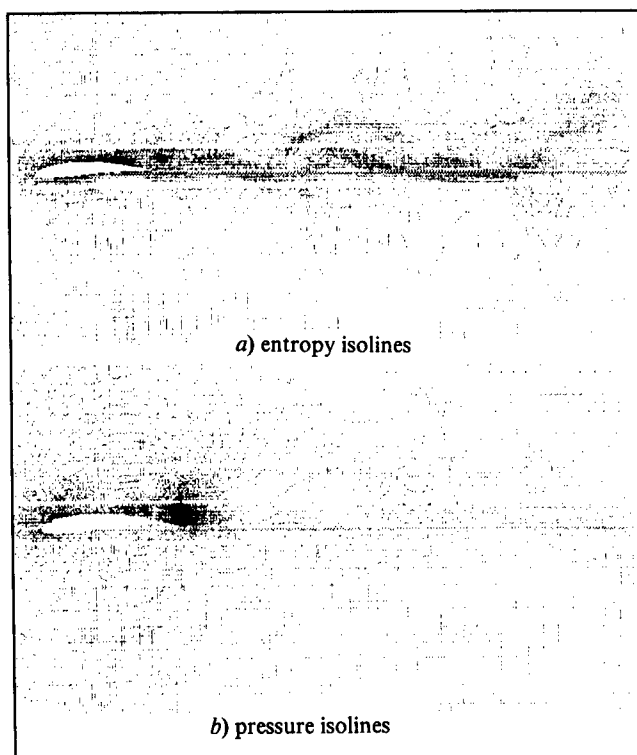


Fig. 9. Viscous flow, $\alpha = 5^\circ$.

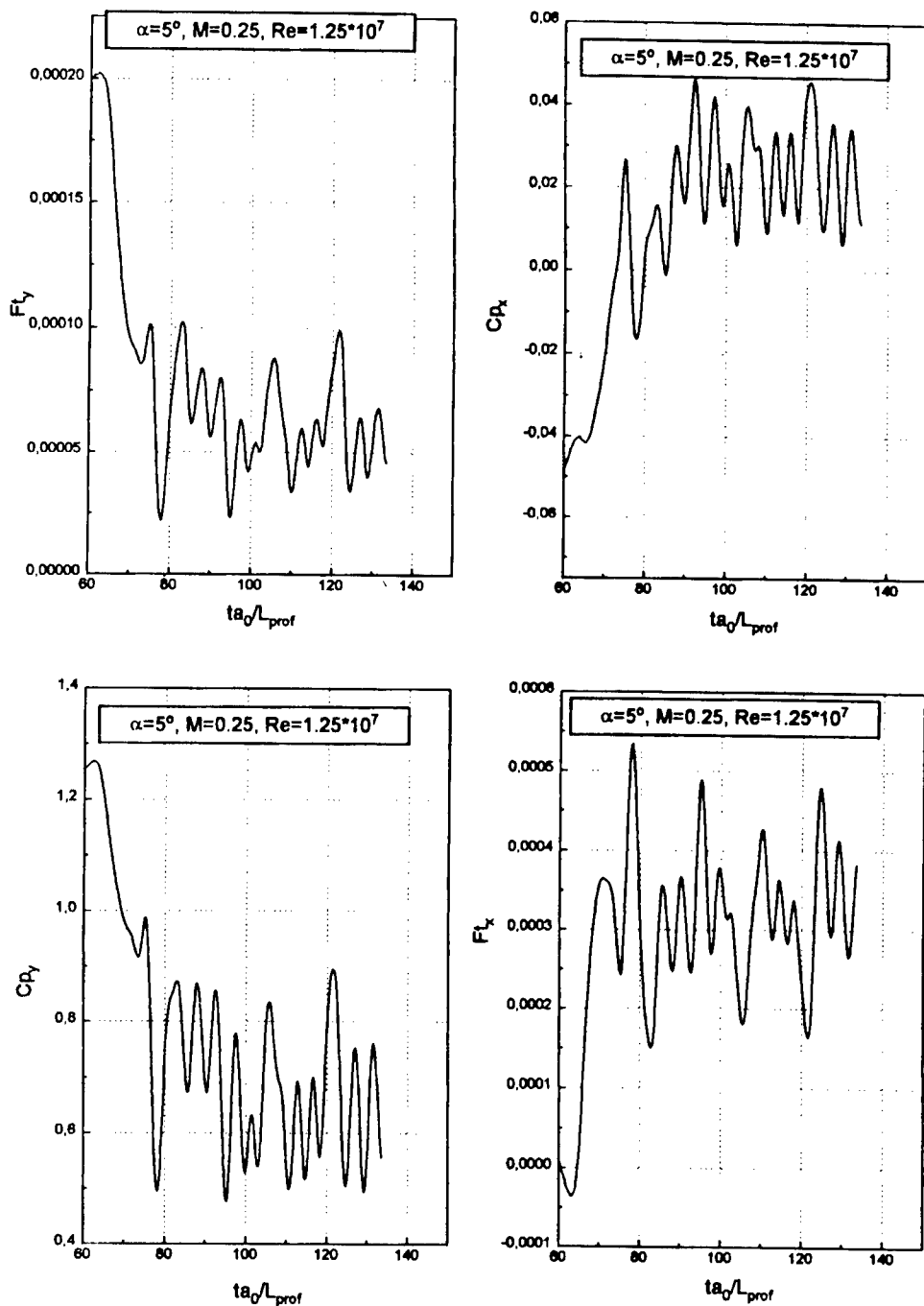


Fig. 10. Time distributions of integral force characteristics: viscous flow, the angle of attack 5° .

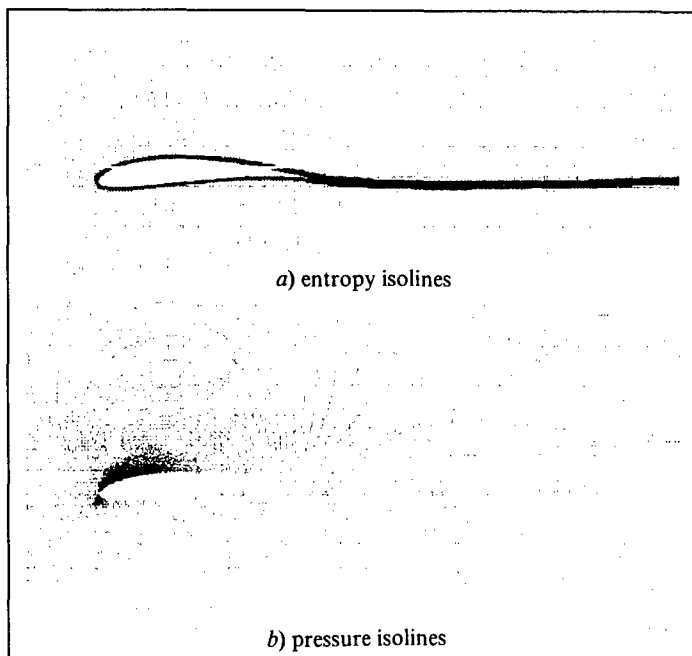


Fig. 11. Inviscid flow: the angle of attack 5° .

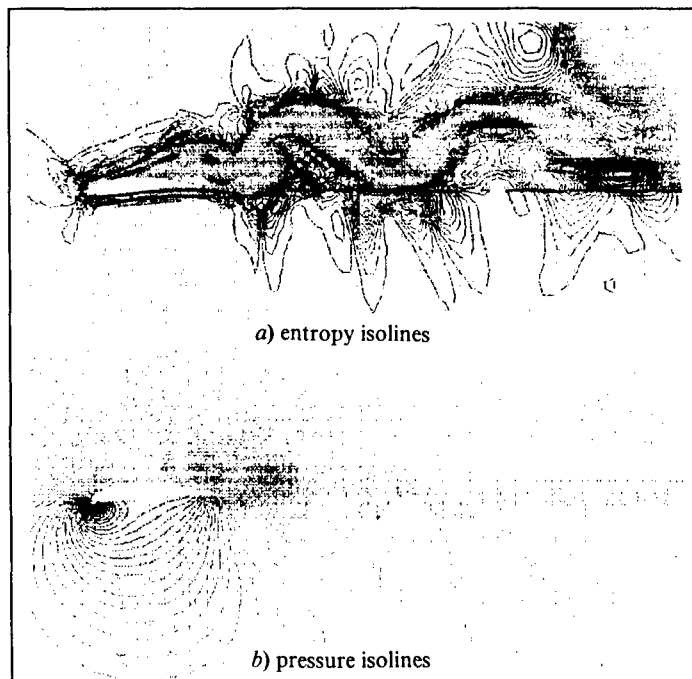


Fig. 12. Inviscid flow: the angle of attack 15° .

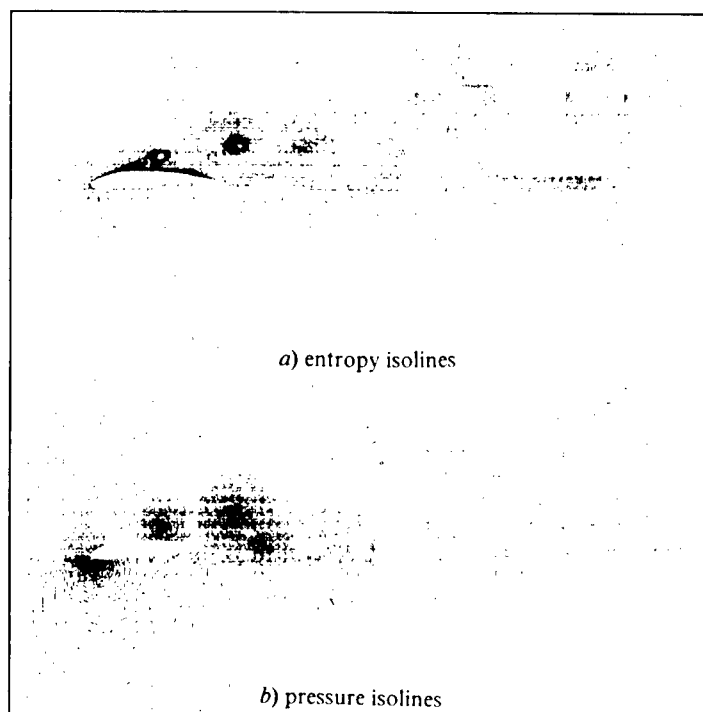


Fig. 13. Viscous flow: the angle of attack 15°.

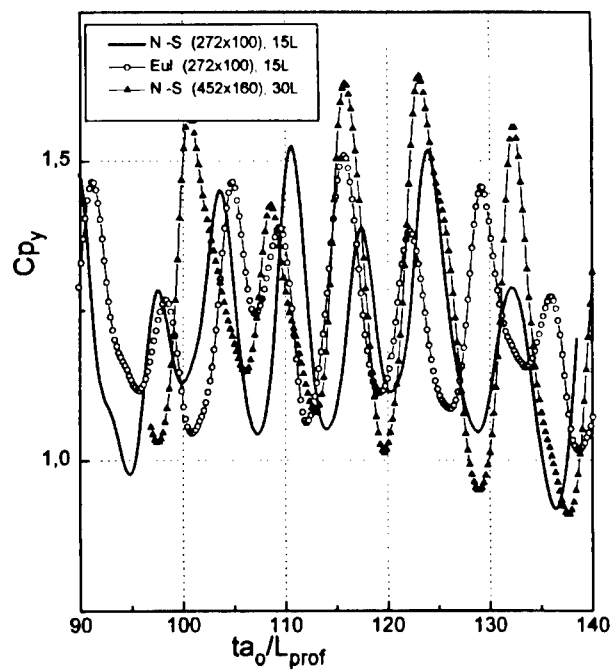


Fig. 14. Time distribution of the lifting force: the angle of attack 15°.

THE COMPLEX INVESTIGATION METHOD OF 3-D DISTURBANCES AT A CURVED SHEAR LAYER OF THE NONISOBARIC SUPERSONIC JET

V.I.Zapryagaev

Institute of Theoretical and Applied Mechanics SB RAS,
630090, Novosibirsk, Russia

The initial part of the mixing layer of a supersonic underexpanded jet exhausting from an axisymmetric nozzle was experimentally found to have a spatial structure. The three-dimensional flow character in the mixing layer of a supersonic jet at high Reynolds numbers is associated with the emergence and evolution of stationary streamwise vortex structures [1-6]. The curvature of streamlines at the initial part of the mixing layer of a supersonic nonisobaric jet involves the appearance of additional centrifugal forces which have a substantial effect on the evolution of small disturbances. The influence of streamlines curvature in the mixing layer both on the development of inviscid Kelvin-Helmholtz instability and on the formation and development of stationary disturbances of the Taylor-Goertler type is shown [7, 8]. The presence of streamwise vortex structures at the jet boundary affects the turbulent mixing processes, which determines to a large extent the importance of studying their physical nature and identification of methods of mixing control.

It is reasonable to represent the Taylor-Goertler disturbances in accordance with the form used in calculational works when the hydrodynamic flow stability is studied under the condition of curved streamlines [6, 7].

$$p = A(r) \exp[i(\alpha x - \omega t)] \cdot \cos(n \cdot \varphi); \quad \alpha = \alpha_r + i \cdot \alpha_i.$$

Here α_i is the spatial amplification rate in the streamwise direction, α_r is the streamwise wavenumber, n is the azimuthal wavenumber, x , r , φ are the streamwise and radial coordinates and the azimuthal angle in a cylindrical coordinate system, t is the time, A is the amplitude of disturbances. It is shown that the streamwise vortex structures are stationary (at least at the initial part of the supersonic jet), therefore, we can assume $\omega = 0$ in studying this type of disturbances.

Experimental researches of the streamwise vortex structures in the mixing layer of a supersonic jet at high Reynolds numbers are conducted using the methods of optical visualization of the flow (Schlieren technique, laser sheet method) [1,3,5,6], direct measurements in the flow by small-size pressure probes [1-6], and spectral analysis techniques for stationary azimuthal inhomogeneities [3,4], whose appearance is caused by stationary streamwise vortices in the mixing layer.

It seems important to study the influence of a local microroughness on the nozzle surface on the generation of streamwise vortices in the mixing layer, which is closely connected with the flow receptivity to the value and spectral composition of surface microroughnesses. The local character of the action of a single roughness is demonstrated in [3]. More detailed data on the structure of stationary disturbances in the mixing layer, which are generated by a local microroughness located on the inner surface of the nozzle, are presented below. The experiments

were performed in a jet facility using a system of automated data acquisition, which is described in [3]. The gas dynamic parameters of the three examined regimes for a convergent nozzle with diameter $D_a = 20$ mm and exit Mach number $M_a = 1.0$ are presented in the Table.

N	$P_s(kPa)$	x_l/R_a	M_l	$np=P_a/P_h$	$Re/10^6$
1	392.0	3.25	1.56	2.12	1.30
2	490.0	3.75	1.71	2.65	1.71
3	588.0	4.0	1.83	3.18	1.95

Here N is the regime number, P_s corresponds to the stagnation pressure in the plenum chamber of the jet facility, x_l/R_a is the length of the first cell of the jet normalized to the nozzle exit radius R_a ; M_l is the Mach number corresponding to isentropic expansion of the flow in an underexpanded jet from the nozzle exit pressure P_a to the ambient pressure P_h ($np=P_a/P_h$ is the jet pressure ratio); Re is the Reynolds number based on the nozzle exit diameter ($D_a=2R_a$) and flow parameters in the nozzle exit cross-section. The dependence of the measured relative thickness of the mixing layer at the jet boundary $\delta'=\delta/R_a$ on the relative distance $x'=x/R_a$ for three examined regimes within the range of azimuthal angles corresponding to an undisturbed flow can be represented by a single approximating formula ($x' < 8$) [3]:

$$\delta' = 0.157x' + 0.048.$$

The dependence of the measured pressure $Po(\varphi)$ on the azimuthal angle for three examined regimes (see the Table) for five various cross-sections of the jet is shown in Fig. 1. The presented plots $Po(\varphi)$ are obtained for a radius corresponding to the middle of the mixing layer, $r = r_{0.5}$, where $Po(r_{0.5}) \sim 0.5 \cdot Po(r_m)$, r_m is the radius corresponding to the internal boundary of the mixing layer of the jet. The position of a spherical particle 0.150 mm in diameter corresponds to $\varphi_0 = 122^\circ$. The microroughness diameter k is comparable with the measured displacement thickness δ^* of the boundary layer at the nozzle exit, i.e., $k/\delta^* \approx 1$.

The form of the total pressure versus the azimuthal angle plot changes as the distance from the nozzle exit increases, which manifests itself in the flattening of the $Po(\varphi)$ curves and decreasing the amplitude of the total pressure variation. The increased amplitude of variation of the total pressure Po corresponds to the range of azimuthal angles $\Delta\varphi = 90-190^\circ$, which is in agreement with disturbances in the mixing layer that resulted from the action of a localized microroughness located at $\varphi_0 = 122^\circ$. The center of the wave packet developing in the mixing layer from the microroughness is located approximately at $\varphi_w = 140^\circ$ and differs from the microroughness position by the value of $\varphi_w - \varphi_0$, which is significantly higher than the measurement accuracy of the azimuthal angle ($\sim 1^\circ$).

For $x \approx 2.0$ and 2.5, the form of the dependence $Po(\varphi)$ for various values of the jet pressure ratio differs insignificantly. The difference in the form of the curves $Po(\varphi)$ for different regimes in cross-section close to the end of the first cell can be explained by the different curvature of streamlines. The thickness of the mixing

layer for various regimes of jet exhaustion differs insignificantly [3]. This circumstance makes us consider more accurately the curvature of streamlines near the external boundary of the jet.

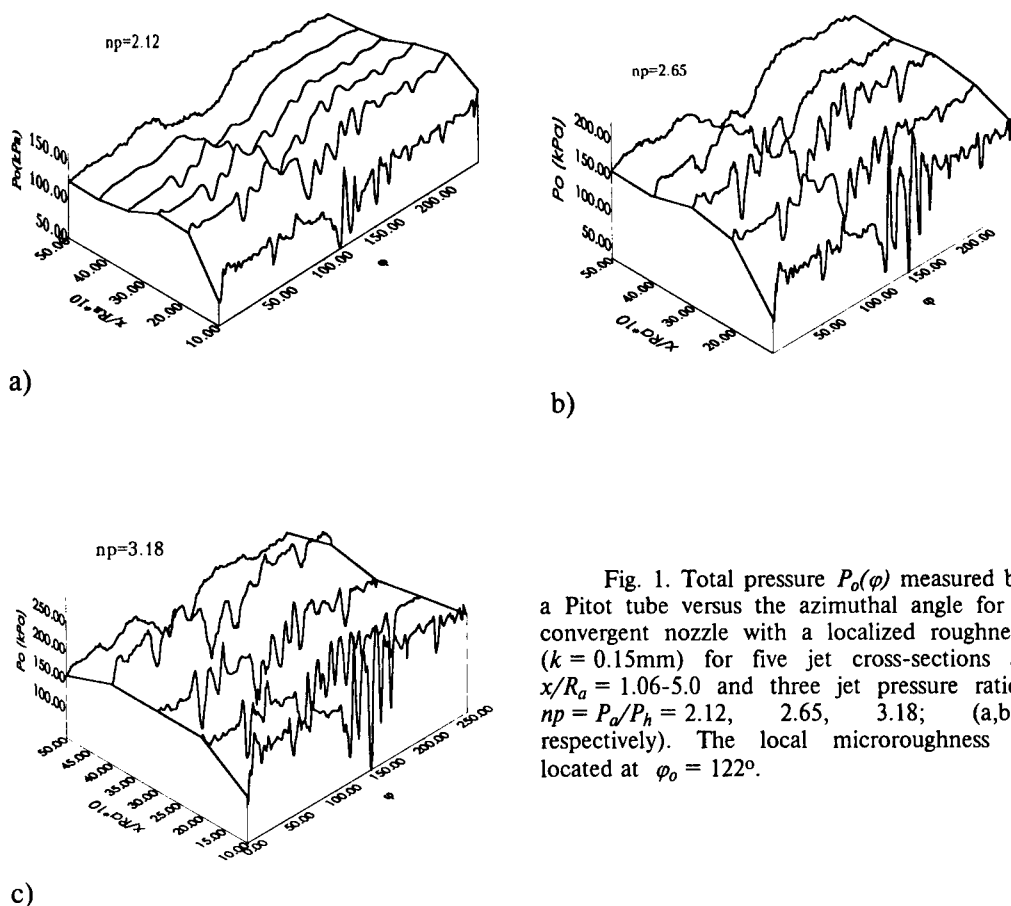


Fig. 1. Total pressure $P_o(\varphi)$ measured by a Pitot tube versus the azimuthal angle for a convergent nozzle with a localized roughness ($k = 0.15\text{mm}$) for five jet cross-sections at $x/R_a = 1.06-5.0$ and three jet pressure ratios $np = P_a/P_h = 2.12, 2.65, 3.18$; (a,b,c respectively). The local microroughness is located at $\varphi_0 = 122^\circ$.

The curvature of the jet boundary is not constant. The curvature changes its sign at the end of the first cell. According to available numerical data, the sign and the value of the curvature of streamlines are determining parameters for the development of Goertler-type disturbances [9]. An increase of curvature (a decrease of curvature radius) favors the amplification of this type of disturbances. The change of the curvature sign leads to the decay of disturbances (the case of a convex surface in a flow with a velocity gradient corresponding to a boundary layer flow) [9]. This is confirmed by the comparison of the form of the functions $P_o(\varphi)$ for the cross-section $x/R_a = 4.0$ for two jet pressure ratios $np = 2.12$ and 3.18 (Fig. 1,a and 1,c). For a smaller jet pressure ratio, the smaller length of the first cell of the jet is realized (see the Table).

A substantial increase of the amplitude of streamwise vortex structures has been registered as the jet pressure ratio increases, and hence, the initial curvature of streamlines, whose value is given in [2], also increases. Thus, the form of the

total pressure plotted versus the azimuthal angle and streamwise distance (see Fig. 1) are consistent with the fact that the observed inhomogeneity of the distribution of gas dynamic quantities in the shear layer of a supersonic jet is generated by streamwise vortices of the Taylor-Goertler type.

The influence of the radius, where the Pitot tube is located, on the shape of the curves $Po(\varphi)/P_s$ is shown in Fig. 2 which presents isobars for regime 2 (see the Table). Similar changes of the form of the plots $Po(\varphi)$ with radius are observed both for natural disturbances $0 < \varphi < 90^\circ$ and for the influence region of a single local roughness. When the pressure probe is located near the internal boundary of the mixing layer, which in our case corresponds to $r = 0.8 \cdot R_a$, almost complete vanishing of the total pressure variations for natural disturbances is observed, but a rather intense "valley" ($\varphi_w = 140^\circ$) is retained in the influence region of the single roughness element. As already stated, the position of this valley does not coincide with the position of the azimuthal inhomogeneity. To explain the latter, additional studies are necessary.

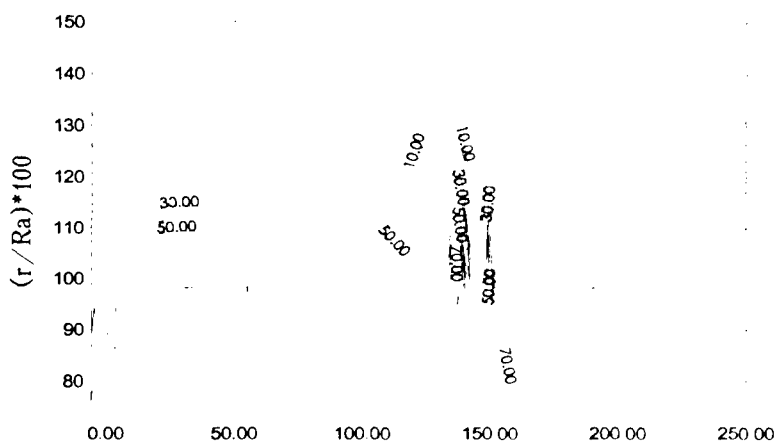


Fig. 2. Isobars of the measured relative total pressure P_o in the plane (r, φ) for a supersonic nonisobaric jet exhausting from a nozzle at $M_a = 1.0$, $np = 2.65$, $r/R_a = 0.74-1.50$, $x/R_a = 2.5$.

When the sign of the derivative with respect to radius dPo/dr changes, which is registered in this cross-section at $r/R_a = 1.0$, the character of the dependence $Po(\varphi)$ also changes. The maximum of $Po(\varphi)$ in the external part of the mixing layer where $dPo/dr < 0$ corresponds to the minimum in the compressed layer of the jet ($dPo/dr > 0$). In this case, small disturbances are hardly ever registered in the compressed layer. Higher-amplitude disturbances caused by the microroughness penetrate into the compressed layer of the jet (see Fig. 2).

The spectral analysis of azimuthal inhomogeneities observed is conducted under the assumption that disturbances from different portions of the surface with different roughness form different spectra in the mixing layer. An example of the spectrum of wavenumbers of inhomogeneities $P_{os}(n)$ for various jet cross-sections x/R_a and isolines of equal amplitude of the spectral components of disturbances are presented in Fig. 3. Fig. 3,a shows the data for the range of azimuthal angles $\Delta\varphi = 0-90^\circ$, for which the spectral analysis was performed, which corresponds to

disturbances in the mixing layer, originating from the natural roughness of the nozzle surface.

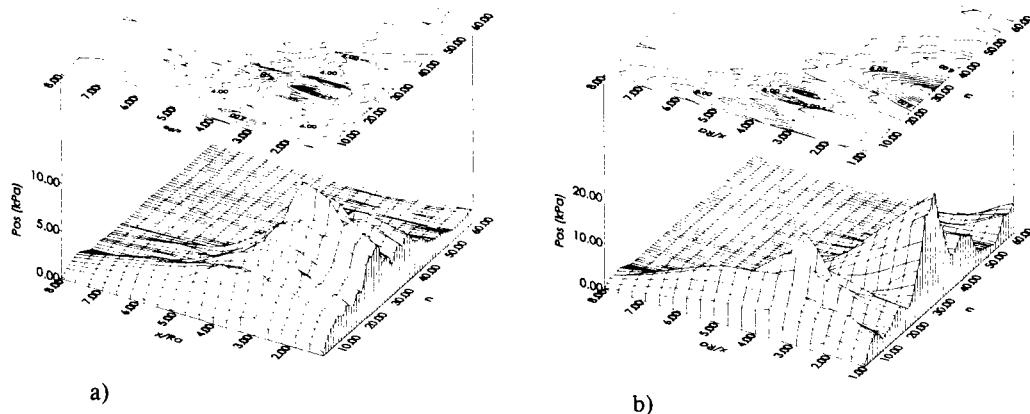


Fig. 3. Wavenumber spectra $P_{os}(n, x/R_n)$ obtained in the range of angles $\Delta\varphi = (0-90)^\circ$ (a) and $\Delta\varphi = (90-190)^\circ$ (b), and the corresponding isolines of equal amplitude of the spectral components versus the streamwise coordinate $x/R_n = 1.06 - 8.0$, $M_a = 1.0$; $np = 2.65$; $Re = 1.71 \cdot 10^6$.

The spectral composition of disturbances is limited by wavenumber values $n < 50$. Individual spectral components are clearly seen, which take the values $n=8, 20$, and 32 for natural disturbances in the range of azimuthal angles $\Delta\varphi=0 - 90^\circ$. For the range of azimuthal angles $\Delta\varphi=90-190^\circ$ corresponding to disturbances caused by a local inhomogeneity, the spectrum has a different form, the wavenumbers, corresponding to the maxima, are different from the influence region of natural disturbances and equal to $n=14; 28$ and 39 (Fig. 3,b).

The common feature in the character of variation of the wavenumber spectrum versus the streamwise distance is a dramatic decrease in the amplitude of some spectral components down to the noise level at distances $x/R_n > 4.0$, which corresponds to the end of the first cell of a supersonic jet. However, for distances $x/R_n < 4.0$, the behavior of individual modes at the initial part of the jet is different for the ranges of azimuthal angles with natural (Fig. 3,a) $\Delta\varphi = 0-90^\circ$ and artificial (Fig. 3,b) $\Delta\varphi = 90-190^\circ$ disturbances on the surface.

Natural disturbances have a maximum in the dependence $P_{os}(x')$ whose position shifts from the nozzle exit as the size of streamwise vortices increases (the wavenumber n decreases). The amplitudes of the spectral components for the range $\Delta\varphi = 90-190^\circ$, as well as for the range corresponding to the natural disturbances, have a maximum ($n=20$). An important factor is a drastic decrease of the amplitude of some spectral components ($n=28$ and 39) for $\Delta\varphi = 90-190^\circ$, which is explained by the fact that these spectral components are generated by a local microroughness.

Thus, it seems reasonable to use the approach employed to study the disturbance evolution in the boundary layer within the framework of the theory of hydrodynamic stability, which includes the consideration of the problems of stability, receptivity, level and type of initial disturbances [10]. The data of an

experimental study of the influence of a local microroughness positioned on the internal surface of a convergent nozzle near its exit support the previously made assumption about the important role of the level and character of initial disturbances of the nozzle surface roughness on the formation and development of streamwise vortices at the initial part of a supersonic jet. A strong influence of the boundary conditions at the nozzle exit supports the fact of existence of a transitional process at the initial part of a supersonic jet exhausting into the ambient space at Reynolds numbers $(2-5) \cdot 10^6$. The transitional process implies the transition from a laminar flow in the boundary layer of the nozzle to a turbulent flow in the mixing layer of a supersonic jet. The latter is in agreement with the experimental data on the transitional Reynolds number obtained in [11], and also with the numerical data of [12], which indicate a significant increase of flow stability in the mixing layer when passing to supersonic flow speeds. The transition in the initial part of a supersonic jet is apparently due to the initial development of stationary streamwise vortices of the Taylor-Goertler type with subsequent turbulization of the flow in the mixing layer or by means of development of the Kelvin-Helmholtz instability.

REFERENCES

1. Zapryagaev V.I., Solotchin A.V. Three-dimensional feature of the flow structure in a supersonic underexpanded jet // *J. Appl. Mech. Tech. Phys.* -1991.-No.4, P. 42-47.
2. Zapryagaev V.I., Solotchin A.V. An experimental study of the influence of nozzle roughness on streamwise vortex structures in a supersonic jet // *J. Appl. Mech. Tech. Phys.*-1997. Vol. 38, No. 1, P. 86-96.
3. Zapryagaev V.I., Solotchin A.V. Evolution of streamwise vortices at the initial part of a supersonic nonisobaric jet in the presence of microroughnesses of the internal surface of the nozzle // *Izvestiya AN, MZhG.*- 1997. - No. 3.- P.180-185.
4. Zapryagaev V.I., Mironov S.G., Solotchin A.V. Spectral composition of wavenumbers of streamwise vortices and specific features of the flow structure in a supersonic jet // *J. Appl. Mech. Tech. Phys.*-1993.-No.5, P.41-47.
5. Arnette S.A., Samimy M., Elliott G.S. On streamwise vortices in high Reynolds number supersonic axisymmetric jets// *Phys. Fluids A* -1993.-Vol.5, No.1.
6. Krothopalli A., Buzuna G., Lourenco L. Streamwise Vortices in an Underexpanded Axisymmetric Jet//*Phys. Fluids A*. Vol. 3 No. 8, August 1991. P.1848-1851.
7. Liou W.W. Linear instability of curved free shear layers//*Phys. Fluids*,Vol. 6, No. 2, February 1994. P.541-549.
8. Terekhova N.M. Streamwise vortices in axisymmetric jets // *J.Appl. Mech. Tech. Phys.*- 1996. Vol.37, No. 3. P.45-57.
9. Saric W.S. Gortler vortices. *Annual Rev. Fluid Mech* 1994. Vol.26. P.379-409.
10. Reshotko E. Boundary-layer stability and transition // *Annual Rev. Fluid Mech.* 1976 Vol.8, P.311-349.
11. Glotov G.F., Gozhenko G.F., Feiman M.I. A study of the additional mass of underexpanded gas jets // *Trudy TsAGI, Iss.1377.*- Moscow: TsAGI Publications, 1971 13 p.
12. Jackson T.L., Groesch G.E. Inviscid spatial stability of a compressible mixing layer//*J. Fluid Mech.* 1989. Vol.208. P.609-637.

ICMAR'98 PROGRAM COMMITTEE

Prof. V.M. FOMIN (Russia) – Co-Chairman
Prof. A.M. KHARITONOV (Russia) – Co-Chairman
Prof. V.A. LEBIGA (Russia) – Scientific Secretary

Prof. N.A. ANFIMOV (Russia)
Prof. S. BOGDONOFF (USA)
Prof. V.N. GUSEV (Russia)
Dr. Ph.E. CASSADY (USA)
Prof. J. COUSTEIX (France)
Prof. M.S. IVANOV (Russia)
Dr. R.A. KILGORE (USA)
Dr. G. KOPPENWALLNER (Germany)
Prof. V.V. KOZLOV (Russia)

Prof. E. KRAUSE (Germany)
Dr. G. LARUELLE (France)
Prof. A.A. MASLOV (Russia)
Prof. G.E.A. MEIER (Germany)
Dr. A.S. ROUDAKOV (Russia)
Prof. J. SCHETZ (USA)
Prof. A.F. SIDOROV (Russia)
Prof. A.V. ZABRODIN (Russia)

List of participants of ICMAR'98

1. Adamov N.P.,
ITAM, Novosibirsk, Russia
2. Agarkov A.A.,
Inst. Thermophysics, Novosibirsk, Russia
3. Alexandrov V.Yu.,
CIAM, Moscow, Russia
4. Alkhimov A.P.,
ITAM, Novosibirsk, Russia
5. Aulchenko S.M.,
ITAM, Novosibirsk, Russia
6. Baev V.K.,
ITAM, Novosibirsk, Russia
7. Bardakhanov S.P.,
ITAM, Novosibirsk, Russia
8. Belykh S.A., NIC CIAM,
Lytkarino, Russia
9. Bessonov M.B.,
ITAM, Novosibirsk, Russia
10. Bezgin L.V.,
CIAM, Moscow, Russia
11. Boiko V.M.,
ITAM, Novosibirsk, Russia
12. Borodulin V.I.,
ITAM, Novosibirsk, Russia
13. Bublik V.V.,
ITAM, Novosibirsk, Russia
14. Buzukov A.A.,
ITAM, Novosibirsk, Russia
15. Cassady Ph.,
Boeing, Seattle, USA.
16. Chirkashenko V.F.,
ITAM, Novosibirsk, Russia
17. Chugunova N.V.,
ITAM, Novosibirsk, Russia
18. Denisova N.V.,
ITAM, Novosibirsk, Russia
19. Derunov E.K.,
ITAM, Novosibirsk, Russia
20. Dikovskaya N.D.,
ITAM, Novosibirsk, Russia
21. Dolgushev S.V.,
ITAM, Novosibirsk, Russia
22. Dovgal A.V.,
ITAM, Novosibirsk, Russia
23. Ermolaev Yu.G.,
ITAM, Novosibirsk, Russia
24. Fedorov A.V.,
ITAM, Novosibirsk, Russia
25. Fedorov S.Yu.,
Inst. Thermophysics, Novosibirsk, Russia
26. Fedorova N.N.,
ITAM, Novosibirsk, Russia
27. Fomichev V.P.,
ITAM, Novosibirsk, Russia
28. Fomin V.M.,
ITAM, Novosibirsk, Russia
29. Gaitonde D.V.,
Air Force Research Laboratory,
Wright-Patterson, USA
30. Gaponenko V.R.,
ITAM, Novosibirsk, Russia
31. Gaponov S.A.,
ITAM, Novosibirsk, Russia
32. Garanin A.F.,
ITAM, Novosibirsk, Russia
33. Georgievsky P. Yu.,
IM MSU, Moscow, Russia
34. Giljov V.M.,
ITAM, Novosibirsk, Russia
35. Goldfeld M.A.,
ITAM, Novosibirsk, Russia
36. Goon'ko Yu.P.,
ITAM, Novosibirsk, Russia
37. Gousskov O.V.,
CIAM, Moscow, Russia
38. Grek G.R.,
ITAM, Novosibirsk, Russia
39. Gusev V.N.,
TsAGI, Zhukovsky, Russia
40. Harlamov G. V.,
NSABU, Novosibirsk, Russia
41. Ilyushin B.B.,
ITAM, Novosibirsk, Russia

42. Ivanov A.V.,
ITAM, Novosibirsk, Russia
43. Ivanchenko A.I.,
ITAM, Novosibirsk, Russia
44. Kachanov Y.S.,
ITAM, Novosibirsk, Russia
45. Katasonov M.M.,
ITAM, Novosibirsk, Russia
46. Khaidarov S.V.,
ITAM, Novosibirsk, Russia
47. Kharitonov A.M.,
ITAM, Novosibirsk, Russia
48. Khotyanovsky D.V.,
ITAM, Novosibirsk, Russia
49. Klemenkov G.P.,
ITAM, Novosibirsk, Russia
50. Klinkov S.V.,
ITAM, Novosibirsk, Russia
51. Klinkova G.I.,
ITAM, Novosibirsk, Russia
52. Konkin A.Ya.,
ITAM, Novosibirsk, Russia
53. Koptsev D.B.,
ITAM, Novosibirsk, Russia
54. Kornilov V.I.,
ITAM, Novosibirsk, Russia
55. Korotaeva T.A.,
ITAM, Novosibirsk, Russia
56. Kosarev V.F.,
ITAM, Novosibirsk, Russia
57. Kosinov A.D.,
ITAM, Novosibirsk, Russia
58. Kovrizhina V.N.,
ITAM, Novosibirsk, Russia
59. Kozlov V.V.,
ITAM, Novosibirsk, Russia
60. Kozlovsky V.A.,
TsNIMash, Korolev, Russia
61. Krause E.,
Aerodynamics Institute, RWTH,
Aachen, Germany
62. Kudryavtsev A.N.,
ITAM, Novosibirsk, Russia
63. Kuraev A.A.,
NSTU, Novosibirsk, Russia
64. Larichkin V.V.,
NSTU, Novosibirsk, Russia
65. Latypov A.F.,
ITAM, Novosibirsk, Russia
66. Lebiga V.A.,
ITAM, Novosibirsk, Russia
67. Lokotko A.V.,
ITAM, Novosibirsk, Russia
68. Lutsky A.E.,
Inst. Appl. Math., Moscow, Russia
69. Lysenko V.I.,
ITAM, Novosibirsk, Russia
70. Maslennikova I.I.,
ITAM, Novosibirsk, Russia
71. Maslov A.A.,
ITAM, Novosibirsk, Russia
72. Mazhul' I.I.,
ITAM, Novosibirsk, Russia
73. Medvedev A.E.,
ITAM, Novosibirsk, Russia
74. Meier G. E. A.,
DLR Institute of Fluid Mechanics,
Goettingen, Germany
75. Melamed B.M.,
ITAM, Novosibirsk, Russia
76. Merkulov V. I.,
ITAM, Novosibirsk, Russia
77. Migirenko G.S.,
NSTU, Novosibirsk, Russia
78. Mironov S.G.,
ITAM, Novosibirsk, Russia
79. Mosseichuk O.N.,
ITAM, Novosibirsk, Russia
80. Mutchnaja M. I.,
ITAM, Novosibirsk, Russia
81. Muylaert J.,
ESTEC, Noordwijk, The Netherlands
82. Nikiforov S.B.,
ITAM, Novosibirsk, Russia
83. Nikulichev Yu. V.,
ITAM, Novosibirsk, Russia
84. Novikov V. E.,
ITAM, Novosibirsk, Russia
85. Obukhovskiy A.D.,
NSTU, Novosibirsk, Russia
86. Ocheretny S.G.,
ITAM, Novosibirsk, Russia
87. Pak A.Yu.,
NSTU, Novosibirsk, Russia
88. Pavlov A.A.,
ITAM, Novosibirsk, Russia
89. Perepechko I.N.,
Inst. Thermophysics, Novosibirsk, Russia
90. Petrov A.P.,
ITAM, Novosibirsk, Russia
91. Popkov A.N.,
ITAM, Novosibirsk, Russia
92. Poplavskaya T.V.,
ITAM, Novosibirsk, Russia
93. Poplavsky S.V.,
ITAM, Novosibirsk, Russia
94. Potapkin A.V.,
ITAM, Novosibirsk, Russia
95. Prokhorov A.N.,
CIAM, Moscow, Russia
96. Proskuryakov V.A.,
Presidium of SB RAS ,
Novosibirsk, Russia
97. Rakhimov R.D.,
ITAM, Novosibirsk, Russia
98. Rebrov A.K.,
Inst. Thermophysics, Novosibirsk, Russia
99. Relin V.I.,
CIAM, Moscow, Russia

100. Rodionov S.P.,
ITAM Dept. at Tumen', Russia
101. Rudyak V.Ya.,
NSABU, Novosibirsk, Russia
102. Salenko S.D.,
NSTU, Novosibirsk, Russia
103. Sapozhnikov G.A.,
Presidium of SB RAS,
Novosibirsk, Russia
104. Sboev D. S.,
ITAM, Novosibirsk, Russia
105. Schetz J.,
Virginia Polytechnical Institute,
Blacksburg, USA.
106. Semionov N.V.,
ITAM, Novosibirsk, Russia
107. Shapeev V.P.,
ITAM, Novosibirsk, Russia
108. Shepelenko V.N.,
ITAM, Novosibirsk, Russia
109. Shevchenko A. M.,
ITAM, Novosibirsk, Russia
110. Shumsky V.V.,
ITAM, Novosibirsk, Russia
111. Shutov A.,
NIC CIAM, Lytkarino, Russia
112. Smorodsky B. V.,
ITAM, Novosibirsk, Russia
113. Sopka M. S.,
NSABU, Novosibirsk, Russia
114. Starov A.V.,
ITAM, Novosibirsk, Russia
115. Takagi S.,
Aircraft Aerodynamic Division, NAL,
Tokyo, Japan
116. Taran J. P.,
ONERA/LAERTE, Palaiseau, France
117. Tchernyshyev A.V.,
ITAM, Novosibirsk, Russia
118. Terekhov V.I.,
Inst. Thermophysics, Novosibirsk, Russia
119. Terekhova N.M.,
ITAM, Novosibirsk, Russia
120. Titov V.M.,
Inst. Hydrodyn., Novosibirsk, Russia
121. Topchiyan M.E.,
Inst. Hydrodyn., Novosibirsk, Russia
122. Tretyakov P.K.,
ITAM, Novosibirsk, Russia
123. Trofimov V.M.,
ITAM, Novosibirsk, Russia
124. Tyushin V.Yu.,
ITAM, Novosibirsk, Russia
125. Volchkov E.P.,
Inst. Thermophysics, Novosibirsk, Russia
126. Volkov V.F.,
ITAM, Novosibirsk, Russia
127. Vorob'ev N.F.,
ITAM, Novosibirsk, Russia
128. Vorozhtsov E.V.,
ITAM, Novosibirsk, Russia
129. Yakovenko S.N.,
ITAM, Novosibirsk, Russia
130. Yakovlev V. I.,
ITAM, Novosibirsk, Russia
131. Yakovlev V.N.,
ITAM, Novosibirsk, Russia
132. Yaroslavtsev M.I.,
ITAM, Novosibirsk, Russia
133. Yarygina N.I.,
Inst. Thermophysics, Novosibirsk, Russia
134. Yurin V.P.,
NIC CIAM, Lytkarino, Russia
135. Zaikovskii V.N.,
ITAM, Novosibirsk, Russia
136. Zamurayev V. P.,
ITAM, Novosibirsk, Russia
137. Zanin B.Yu.,
ITAM, Novosibirsk, Russia
138. Zapryagaev V. I.,
ITAM, Novosibirsk, Russia
139. Zharkova G.M.,
ITAM, Novosibirsk, Russia
140. Zheltovodov A.A.,
ITAM, Novosibirsk, Russia
141. Zhukov M.F.,
ITAM, Novosibirsk, Russia
142. Zinoviev V. N.,
ITAM, Novosibirsk, Russia
143. Zvegintsev V.I.,
ITAM, Novosibirsk, Russia

CONTENTS

1. N.P. Adamov, Yu.P. Goon'ko, A.M. Kharitonov, A.F. Latypov, I.I. Mazhul, M.I. Yaroslavl'tsev, Ph. Chalot, P. Perrier, Ph. Rostand. Study on drag-thrust forces of a scramjet model in blow-down and hot-shot wind tunnels	3
2. Yu.V. Afonin, A.P. Petrov. High-voltage pulse generator for velocity measurement in gas flows by spark tracer method	10
3. Yu.V. Afonin, A.P. Petrov. The conditions of using the multi-spark discharge for gas flow velocity measurements.	14
4. L.S. Alekseeva, V.M. Berkovich, M.M. Grigorev, G.S. Taranov, E.F. Shirokov-Bryukhov, K.A. Kolinko, A.N. Prekhorov, L.I. Semernyak. Experimental research of atomic power station building large-scale model aerodynamics in aerodynamic subsonic velocities wind tunnel with visualization of flow	18
5. V.Yu. Alexandrov, Yu.S. Mnatsakanyan, A.N. Prokhorov, V.L. Relin, A.A. Shutov, V.P. Yurin. OH ⁻ emission registration at hydrogen jet burning inside onway supersonic flow in the scramjet combustor model	25
6. V.Yu. Alexandrov, A.N. Prokhorov, A.S. Roudakov, S.A. Belykh, G.K. Vedeshkin, A.A. Shutov, V.P. Yurin, J. Hicks. Support and realization of tests of axisymmetric scramjet on test cell C16VK CIAM RTC	30
7. A.P. Alkhimov, S.V. Klinkov, V.F. Kosarev. A study of supersonic air jets exhausted from a rectangular nozzle	41
8. V.K. Baev, A.V. Nikulinskih, A.V. Potapkin, A.D. Frolov, V.N. Yakovlev. Aerodynamics and heat transfer in a disk rotor machine with tangential input and output of the working body	47
9. V.K. Baev, A.F. Garanin, P.K. Tretyakov. Creation of control forces on the vehicle surface by the external burning	52
10. V.K. Baev, D.Yu. Moskvichev, A.V. Potapkin. The influence of acoustic resonator on the air-breathing combustor operation under pulsation burning of hydrogen	55
11. V.K. Baev, P.K. Tretyakov, V.V. Shumsky. Unsteady processes in a combustion chamber with supersonic flow velocity	60
12. V.K. Baev, V.V. Shumsky. Specific features of the flow in gas dynamic shot-duration facilities	66
13. L.V. Bezgin, A.N. Ganzhelo, V.I. Kopchenov. Some results of detonation combustion regimes investigation	72
14. V.M. Boiko, V.M. Gil'gov, S.G. Ocheretny, S.V. Poplavsky. Software complex for velocity field measurement on the basis of multiframe shadow pictures of two-phase flow	78
15. A.A. Buzukov. High-speed cinematography study of an impulse high-pressure gas-liquid jet	84
16. N.V. Denisova. Maximum entropy based tomography of gas flows	88
17. N.D. Dikovskaya, G.I. Klinkova, V.Y. Levchenko. Numerical investigation of crossflow instability on 39°- swept wing	93
18. V.P. Fomichev, G.A. Pozdniakov, S.S. Pravdin. Modification of the method of spectral line inversion for panoramic temperature measurements in gas flow.	99
19. S.A. Gaponov, B.V. Smorodsky. Disturbance excitation in supersonic boundary layer by acoustics	103

20. A.F. Garanin, A.I. Glagolev. Effect of various methods of organization of gaseous and solid fuel burning for base drag reduction	109
21. A.F. Garanin, P.K. Tretyakov, V.F. Chirkashenko, Yu. N. Yudin. Control of shock wave parameters by means of mass and energy supply	114
22. B.N. Giljazetdinov, V.I. Zvegintsev. Inlet performances measurement in short-duration aerodynamic facility	119
23. V.M. Giljov, V.F. Kurmell, O.N. Mosseichuk, S.G. Ocheretny. The use of network technologies in aerophysical research at ITAM SB RAS	125
24. M.A. Goldfeld, A.V. Starov, V.A. Vinogradov. Preliminary investigations of scramjet module	130
25. Yu.P. Goon'ko, A.N. Kudryavtsev, R.D. Rakhimov. A numerical study on reducing the internal nonuniform shocked flows to equivalent one-dimensional streams	136
26. C. Greated, V.I. Kornilov, V.N. Kovrizhina, V.M. Khachatryan, A.A. Pavlov, G.M. Zharkova. Liquid crystal thermography and PIV method in investigations of unstationary processes in fluids	142
27. A.M. Kharitonov, V.I. Shyshov, Ju.I. Vyshenkov, V.I. Zvegintsev, V.N. Rychkov, M.E. Topchiyan, A.A. Mescherjakov, V.I. Pinakov. Simulation of hypersonic flight condition for scramjet-powered vehicles at wind tunnel with adiabatic compression	148
28. A.Ya. Konkin, V.A. Lebiga, V.N. Zinoviev. Determination of the dynamic characteristic of an aspirating probe using a shock tube	154
29. A.D. Kosinov, N.V. Semionov, A.I. Semisynov, M.B. Bessonov. Experimental study of mean and pulsational features in supersonic boundary layer on blunted flat plate	159
30. A.N. Kudryavtsev, D.V. Khotyanovsky. A numerical method for simulation of unsteady phenomena in high speed shear flows	165
31. A.N. Kudryavtsev, D.V. Khotyanovsky. Nonlinear evolution of shear layer disturbances in a supersonic plane jet	171
32. V.V. Larichkin. An aerodynamic study of column-type headframes	177
33. A.A. Maslov, S.G. Mironov. An experimental study of artificial disturbances in the shock layer on the flat plate	183
34. B.M. Melamed, V.N. Zaikovskii. An experimental study of vortex structures in gas dynamic duct with swivelling nozzle	189
35. O.N. Mosseichuk. The development of a database of aerodynamic experiments and computations performed at ITAM	193
36. M.I. Mutchaj. The results of numerical investigation of a gas flow in hypersonic nozzles at high Reynolds numbers	200
37. J. Muylaert, W. Berry. Overview of ESA aerothermodynamic research and project activities (1996 – 1999)	205
38. A.M. Pavlyuchenko, O.A. Bragin, A.A. Tyutin, A.N. Popkov. Laminar-turbulent transition, relaminarization, separated flows, interaction of transition and separation on rocket nose cones of two types in a trajectory flight at $Re_{L_{\infty}} \leq 10^8$, $M_{\infty} \leq 4.5$, $\alpha \leq 32^\circ$	213
39. V.V. Pickalov, N.V. Chugunova. Wide aperture tomography method in flow investigation	219
40. A.N. Popkov. On the theory of parametric equations of two-dimensional laminar boundary layer	225

41. A.G. Prudnikov, P.K. Tretyakov. The action of injection of inert and chemically active high-temperature gas mass on duct flow gas dynamics	231
42. V.Ya. Rudyak, A.A. Belkin, G.V. Harlamov. Numeric simulation of transport processes in suspensions and gas suspensions	235
43. S.D. Salenko, A.D. Obukhovsky. Parametric investigation of the multi-beam bridges aeroelasticity	241
44. S.D. Salenko, A.D. Obukhovsky. Pressure oscillations investigations on multi-beams bridges models	247
45. V.M. Trofimov. Convection and heat transfer in angular momentum nonequilibrium turbulent flows	252
46. V.M. Trofimov, V.N. Zaikovskii. Acoustic tones investigation in zone of turbulent heat transfer stratification at supersonic velocities	258
47. A.B. Vatazhin, O.V. Gouskov, V.I. Kopchenov. Numerical investigation of supersonic flow structure in the duct at the presence of magnetic field	262
48. V.N. Vetlutsky, T.A. Korotaeva, A.P. Shashkin. Force and heat loads on a pointed body in the wake of local energy source	268
49. V.I. Yakovlev. Flow gasdynamic structure space-time scales in aerophysical experiment with pulsating laser thermal source	273
50. A.V. Zabrodin, A.E. Lutsky, I.S. Men'shov, I.L. Petrushchenkov, V.A. Cherkashin. Numerical simulation of subsonic flows	277
51. V.I. Zapryagaev. The complex investigation method of 3-D disturbances at a curved shear layer of the nonisobaric supersonic jet	295
<i>List of participants</i>	301
<i>Contents</i>	304

International Conference on the Methods of Aerophysical
Research: Proc. Pt III. — Novosibirsk, 1998. — 306 p.

Ответственный за выпуск С.М. Аульченко
Технический редактор Т.В. Ветровская

Формат бумаги 70 × 100/16, Усл. п. л. 24.6, Уч.-изд. л. 26.0
Тираж 250 экз., Заказ № 205

Отпечатано в Издательстве СО РАН